UNIVERSITÉ DE GENÈVE

Archive ouverte UNIGE
https://archive-ouverte.unige.ch

Thèse 2022

Open Access

This version of the publication is provided by the author(s) and made available in accordance with the copyright holder(s).

Unraveling the Origins of Stellar Mass Black Hole Mergers

Bavera, Simone Sergio

How to cite

BAVERA, Simone Sergio. Unraveling the Origins of Stellar Mass Black Hole Mergers. Doctoral Thesis, 2022. doi: 10.13097/archive-ouverte/unige:162269

This publication URL: https://archive-ouverte.unige.ch/unige:162269
Publication DOI: 10.13097/archive-ouverte/unige:162269

© This document is protected by copyright. Please refer to copyright holder(s) for terms of use.

UNIVERSITÉ DE GENÈVE
Département d'Astronomie

FACULTÉ DES SCIENCES
Professeur Anastasios Fragkos

Unraveling the Origins of Stellar Mass Black Hole Mergers

THÈSE

Présenté à la Faculté des sciences de l'Université de Genève
pour obtenir le grade de Docteur ès sciences,
mention astronomie et astrophysique

par
Simone S. Bavera
de
Breggia (TI)

Thèse N° 5666

GENÈVE
Observatoire Astronomique de l'Université de Genève
June 2022

UNIVERSITÉ DE GENÈVE

FACULTÉ DES SCIENCES

DOCTORAT ÈS SCIENCES, MENTION ASTRONOMIE ET ASTROPHYSIQUE

Thèse de Monsieur Simone Sergio BAVERA

intitulée :

«Unraveling the Origins of Stellar Mass Black Hole Mergers»

La Faculté des sciences, sur le préavis de Monsieur A. FRAGKOS, professeur assistant et directeur de thèse (Département d'astronomie), Madame C. CHARBONNEL, professeure ordinaire (Département d'astronomie), Monsieur P. OESCH, professeur associé (Département d'astronomie), Monsieur C. BERRY, docteur (Institute for Gravitational Research, School of Physics & Astronomy, University of Glasgow, Glasgow, United Kingdom), autorise l'impression de la présente thèse, sans exprimer d'opinion sur les propositions qui y sont énoncées.

Genève, le 30 juin 2022

Thèse - 5666 -

Le Décanat

N.B. - La thèse doit porter la déclaration précédente et remplir les conditions énumérées dans les "Informations relatives aux thèses de doctorat à l'Université de Genève".

Abstract

The detections of gravitational waves from the collisions of stellar-mass black holes by the *LIGO Scientific & Virgo Collaboration* have opened a new window onto the Universe. Even though multiple formation mechanisms have been theorized in the literature, the question regarding their origin remains open. The first part of this thesis aims to study merging binary black holes formed from isolated binary evolution in galactic fields. In particular, we model the distribution of their observational properties such as black hole masses, spins, and their merger redshifts. To achieve this goal, we combine detailed stellar and binary evolution simulations of their progenitors with binary population synthesis techniques, which allow us to model the statistical distributions of the binary black hole population properties. In the second part, we consider model predictions for alternative formation channels, and illustrate how one could leverage these signatures to interpret and quantify the origin of the detected sample of binary black holes. In the last part, we discuss the implications on the observable population of electromagnetic transient events of our stellar binary models, which could potentially be used to constrain further the formation mechanisms of merging binary black holes.

Résumé

La première détection d'ondes gravitationnelles émis par la collision de deux trous noirs de masse stellaire par la collaboration de *LIGO-Virgo* a drastiquement modifié notre vision de l'Univers. Bien que plusieurs mécanismes de formation aient été théorisés dans la littérature, la question de leur origine reste ouverte. La première partie de cette thèse vise à étudier la formation de trous noirs binaires, formée par l'évolution des étoiles binaires isolées dans les champs galactiques. Nous modélisons en particulier la distribution de leurs propriétés d'observations telles que les masses des trous noirs, leurs spins et leurs redshifts de fusion. Pour atteindre cet objectif, nous générons des simulations détaillées de l'évolution stellaire et binaire de leurs progéniteurs et utilisons des techniques de synthèse de population binaire. Ceci nous permet par la suite de modéliser les distributions statistiques des propriétés de la population des trous noirs binaires. Dans la deuxième partie, nous considérons des prédictions des modèles des canaux de formation alternatifs et illustrons comment interpréter et quantifier l'origine de formation de trous noirs binaires détectés, grâce aux signatures spécifiques de chaque canal de formation. Dans la dernière partie, nous discutons des implications sur la population observable des événements transitoires électromagnétiques de nos modèles binaires stellaires, les quelles pourraient potentiellement être utilisées pour contraindre les mécanismes de formation des trous noirs binaires.

Members of the jury

- **Dr Christopher Berry**
  Institute for Gravitational Research, School of Physics & Astronomy
  University of Glasgow, Kelvin Building, University Avenue, Glasgow,
  G12 8QQ, Scotland

- **Prof. Corinne Charbonnel**
  Département d'Astronomie, Faculté des Sciences
  Université de Genève, Chemin Pegasi 51, CH-1290 Versoix, Switzerland

- **Prof. Tassos Fragos**
  Département d'Astronomie, Faculté des Sciences
  Université de Genève, Chemin Pegasi 51, CH-1290 Versoix, Switzerland

- **Prof. Pascal Oesch**
  Département d'Astronomie, Faculté des Sciences
  Université de Genève, Chemin Pegasi 51, CH-1290 Versoix, Switzerland

List of my publications

The contents presented in this thesis contain material appearing in some of the following list of co-authored publications. Only first- and second-authorship manuscripts appear as a whole in the thesis.

First author publications

1. **Bavera S. S.**, Fragos T., Qin Y., Zapartas E., Neijssel C. J., Mandel I., Batta A., Gaebel S. M., Kimball C., and Stevenson S. *The origin of spin in binary black holes: predicting the distributions of the main observables of Advanced LIGO.* A&A, 635:A97, March 2020 [open-access link]

2. **Bavera S. S.**, Fragos T., Zevin M., Berry C. P. L., Marchant P., Andrews J. J., Coughlin S., Dotter A., Kovlakas K., Misra D., Serra-Perez J. G., Qin Y., Rocha K. A., Román-Garza J., Tran N. H., and Zapartas E. *The impact of mass-transfer physics on the observable properties of field binary black hole populations.* A&A, 647:A153, March 2021 [open-access link]

3. **Bavera S. S.**, Zevin M., and Fragos T. *Approximations of the Spin of Close Black Hole-Wolf-Rayet Binaries.* RNAAS, 5(5):127, May 2021 [open-access link]

4. **Bavera S. S.**, Fragos T., Zapartas E., Ramirez-Ruiz E., Marchant P., Kelley L. Z., Zevin M., Andrews J. J., Coughlin S., Dotter A., Kovlakas K., Misra D., Serra-Perez J. G., Qin Y., Rocha K. A., Román-Garza J., Tran N. H., and Xing Z. *Probing the progenitors of spinning binary black-hole mergers with long gamma-ray bursts.* A&A, 657:L8, January 2022 [open-access link]

5. **Bavera S. S.**, Franciolini G., Cusin G., Riotto A., Zevin M., and Fragos T. *Stochastic gravitational-wave background as a tool to investigate multichannel astrophysical and primordial black-hole mergers.* A&A, 660:A26, April 2022 [open-access link]

6. **Bavera S. S.**, Fishbach M., Zevin M., Zapartas E., and Fragos T. *The $\chi_{\rm eff} - z$ correlation of field binary black hole mergers and how 3G gravitational-wave detectors can constrain it.* arXiv e-prints, page arXiv:2204.02619, accepted for publication in A&A, June 2022 [open-access link]

Second author publications

7. Zevin M., **Bavera S. S.**, Berry C. P. L., Kalogera V., Fragos T., Marchant P., Rodriguez C. L., Antonini F., Holz D. E., and Pankow C. *One Channel to Rule Them All? Constraining the Origins of Binary Black Holes Using Multiple Formation Pathways.* ApJ, 910(2):152, April 2021 [open-access link]

8. Román-Garza J., **Bavera S. S.**, Fragos T., Zapartas E., Misra D., Andrews J., Coughlin S., Dotter A., Kovlakas K., Serra J. G., Qin Y., Rocha K. A., and Tran N. H. *The Role of Core-collapse Physics in the Observability of Black Hole Neutron Star Mergers as Multimessenger Sources.* ApJ, 912(2):L23, May 2021 [open-access link]

9. Zevin M. and **Bavera S. S.** *Suspicious Siblings: The Distribution of Mass and Spin Across Component Black Holes in Isolated Binary Evolution.* ApJ, 933, 86, July 2022 [open-access link]

Other publications

10. Zapartas E., Renzo M., Fragos T., Dotter A., Andrews J. J., **Bavera S. S.**, Coughlin S., Misra D., Kovlakas K., Román-Garza J., Serra J. G., Qin Y., Rocha K. A., Tran N. H., and Xing Z. P. *Revisiting the explodability of single massive star progenitors of stripped-envelope supernovae.* A&A, 656:L19, December 2021 [open-access link]

11. Fragos T., Andrews J. J., **Bavera S. S.**, Berry C. P. L., Coughlin S., Dotter A., Giri P., Kalogera V., Katsaggelos A., Kovlakas K., Lalvani S., Misra D., Srivastava P. M., Qin Y., Rocha K. A., Roman-Garza J., Serra J. G., Stahle P., Sun M., Teng X., Trajcevski G., Hai Tran N., Xing Z., Zapartas E., and Zevin M. *POSYDON: A General-Purpose Population Synthesis Code with Detailed Binary-Evolution Simulations.* arXiv e-prints, pages arXiv:2202.05892, submitted to ApJS, February 2022 [open-access link]

12. Akira Rocha K., Andrews J. J., Berry C. P. L., Doctor Z., Marchant P., Kalogera V., Coughlin S., **Bavera S. S.**, Dotter A., Fragos T., Kovlakas K., Misra D., Xing Z., and Zapartas E. *Active Learning for Computationally Efficient Distribution of Binary Evolution Simulations.* arXiv e-prints, page arXiv:2203.16683, submitted to ApJ, March 2022 [open-access link]

13. Amaro-Seoane P., Andrews J., Arca Sedda M., Askar A., Balasov R., Bartos I., **Bavera S. S.**, Bellovary J., Berry C. P. L., Berti E., Bianchi S., Blecha L., Blondin S., Bogdanović T., Boissier S., Bonetti M., Bonoli S., Bortolas E., Breivik K., ... and Vigna-Gómez A. *Astrophysics with the Laser Interferometer Space Antenna.* arXiv e-prints, pagse arXiv:2203.06016, submitted to Living Rev. Relativ., March 2022 [open-access link]

Conference proceedings

14. Teng X., Corpstein A., Holm J., Knox W., Mathie B., Payne P., Wiel E. V., Giri P., Trajcevski G., Dotter A., Andrews J., Coughlin S., Qin Y., Serra- Perez J. G., Tran N., Roman-Garja J., Kovlakas K., Zapartas E., **Bavera S. S.**, Misra D., and Fragos T. *CACSE: Context Aware Clustering of Stellar Evolution.* SSTD '21: 17th International Symposium on Spatial and Temporal Databases, August 2021 [link]

15. Teng X., Beckler T., Gannon B., Huinker B., Huinker G., Kumar K., Marquez C., Spooner J., Trajcevski G., Dotter A., Andrews J., Coughlin S., Serra J. G., Qin Y., Tran N., Garja J. R., Kouvlakis K., Zapartas E., **Bavera S. S.**, Misra D., Fragkos A., and Giri P. *CSD-CMAD: Coupling Similarity and Diversity for Clustering Multivariate Astrophysics Data.* SIGSPATIAL '21: Proceedings of the 29th International Conference on Advances in Geographic Information Systems, November 2021 [link]

Contents

To Aurélie

Chapter 1

And then there were none

It is now established that most massive stars are members of binary or higher-order stellar systems (Sana et al. 2012; Moe & Di Stefano 2017). Some of these stars will interact during their evolution and eventually form compact objects, such as black holes (BHs), neutron stars (NSs), and white dwarfs. Over hundreds of millions of years, these systems slowly spiral inward toward each other, eventually colliding. These compact objects orbit each other at an ever-increasing rate during the last seconds of their life, emitting an extreme amount of energy in gravitational waves (GWs). Gravitational waves are ripples in *space-time* that travel at the speed of light and carry information about their source. The first detection of GWs, GW150914, from the merger of two BHs by the *Advanced LIGO* detectors (Abbott et al. 2016d), sparked the start of the new era of multi-messenger astronomy. Gravitational-wave astronomy gives us a new window on the Universe and has the potential to revolutionize our astrophysical understanding of multiple aspects of the Cosmos. For example, as the endpoint of massive-star evolution, merging binary black holes (BBHs) can encode unique information about their progenitor systems, such as the types of environments they were born in, their formation processes, and the complex stellar evolution that persisted throughout their lives. This chapter reviews the BBH detections made with GW detectors and introduces all the key ingredients needed to unravel the origin of merging BBHs.

1.1 Gravitational-wave astronomy

The existence of GWs in general relativity was first predicted by Albert Einstein one year after formulating the field equations in 1916 (Einstein 1916, 1918). Indirect evidence of their existence came in 1982 by Taylor & Weisberg (1982), who, in the previous years, measured the GW energy loss of the binary pulsar PSR B1913+16 as predicted by general relativity, in the system previously discovered by Hulse & Taylor (1975). This further motivated the construction of laser interferometry detectors which could directly observe GWs. By the early 2000s, a set of initial detectors was completed, including *TAMA 300* in Japan (Ando & TAMA Collaboration 2002), *GEO 600* in Germany (Willke et al. 2002), the *Laser Interferometer Gravitational-Wave Observatory (LIGO)* in the United States (Fritschel 2003), and *Virgo* in Italy (Marion & VIRGO Collaboration 2000). In 2015, *Advanced LIGO* (Aasi et al. 2015b) became the first of a significantly more sensitive network of advanced detectors to begin observations (Aso et al.

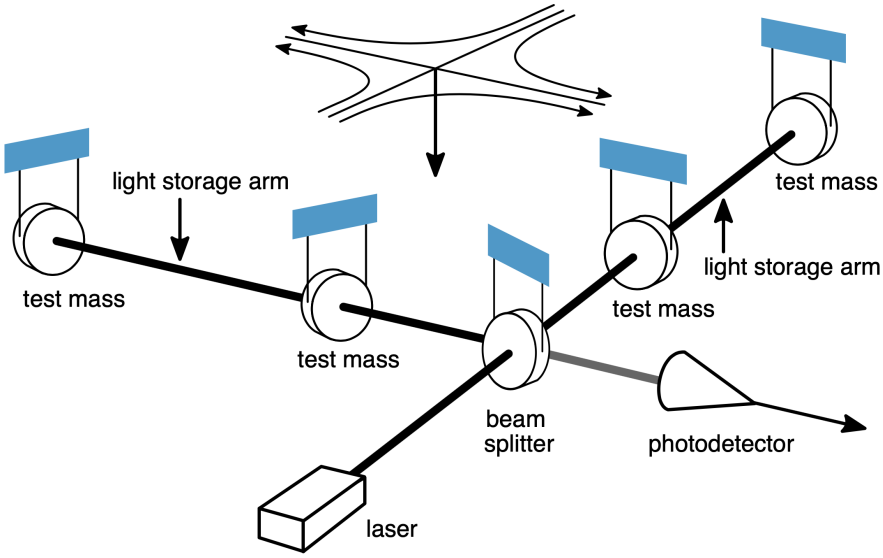

Figure 1.1: A schematic diagram of a laser interferometer with light storage arms. Credit: *LIGO Scientific Collaboration*.

2013; Affeldt et al. 2014; Aasi et al. 2015a; Acernese et al. 2015). On September 14, 2015, the *LIGO Hanford* and *Livingston* GW observatories detected GW150914, the first coincident GW signal coming from the merger of two stellar-mass BHs of roughly $30\,M_{\odot}$ in mass (Abbott et al. 2016d).

The global GW detector network currently consists of two *Advanced LIGO* detectors (Aasi et al. 2015b), the *Advanced Virgo* detector (Acernese et al. 2015), the GEO 600 detector (Dooley et al. 2016), the Japanese detector *KAGRA* (Aso et al. 2013; Akutsu et al. 2020), and soon, a third *Advanced LIGO* detector to be located in India (Unnikrishnan 2013). The first observing run (O1) of *Advanced LIGO* took place from mid-September 2015 until mid-January 2016. The second observing run (O2) for the *Advanced LIGO* detectors began at the end of November 2016 and lasted until the end of August 2017. The *Advanced Virgo* detector formally began observations during O2 at the beginning of August 2017, enabling the first three-detector observations of GWs (Abbott et al. 2019b). The third observing run (O3) of *LIGO-Virgo* detectors lasted from April 2019 until March 2020, with all three detectors operating with their best sensitivity to date. The upcoming O4 run will also see the joint operation of the *KAGRA* detector (Akutsu et al. 2019). In the following sections, we review how GW detectors work (§1.1.1), what are the BBH observable properties constrained from GW observations (§1.1.2) and review current GW detections of BBHs (§1.1.3).

1.1.1 Gravitational-wave detectors

The current second-generation GW detectors such as *Advanced LIGO* (Aasi et al. 2015b) and *Advanced Virgo* (Acernese et al. 2015) are large-scale enhanced Michelson interferometers. These detectors are sensitive to perturbations of space-time induced by passing GWs, causing the arms' lengths to vary over time. Terrestrial force and disturbances are equivalently measured by the detector and constitute noise that can mask the GW signals. When a GW passes through a detector, it causes differences in

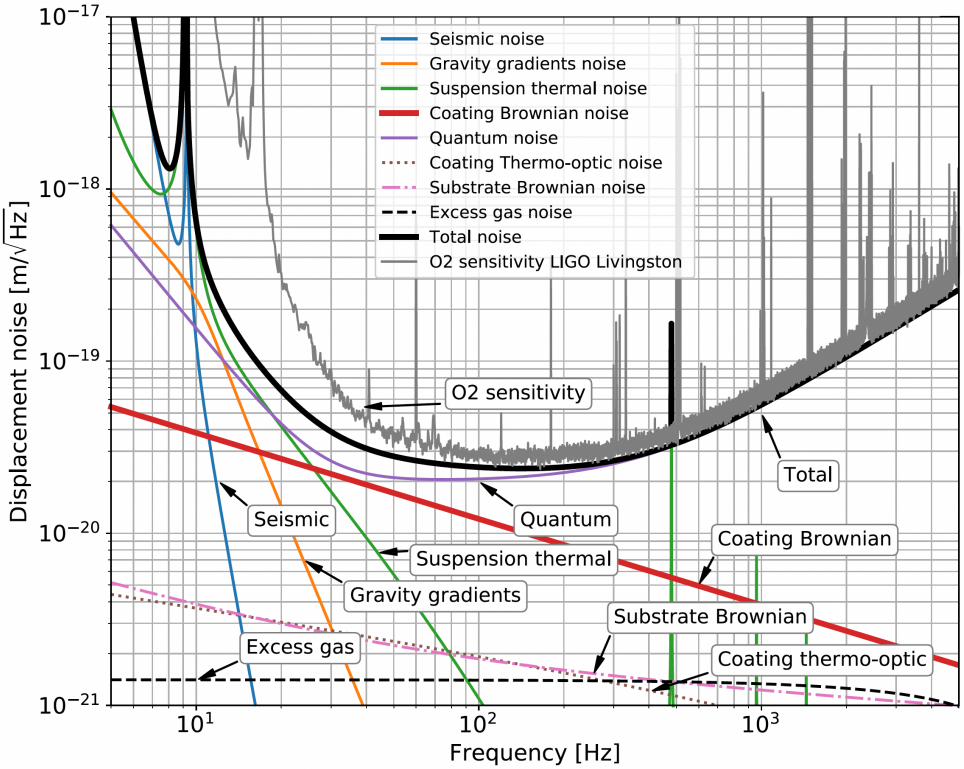

Figure 1.2: Design strain sensitivity of the *Advanced LIGO* detector, showing the main noise sources that contributes to limiting the sensitivity. For comparison, the measured sensitivity of the *Livingston LIGO* detector during the O2 run is displayed as an example of the typical performance of the GW detectors. Credit: Vajente et al. (2019)

the relative arm length, generating power variations in the laser output captured by photodiodes. The *Advanced LIGO* GW detectors are identical in design, with 4 km-long arms. *Advanced Virgo* has a similar design, with 3 km-long arms. Fabry-Perot cavities are used in the arms of the detectors to increase the interaction time with a GW, and power recycling is used to increase the effective laser power. A calibration procedure is applied to the interferometer photodiodes, making the detector operational between the GW frequencies of 10 Hz and 5 kHz. This frequency range correspond to the GW chirp frequency of merging stellar mass compact objects like BHs and NSs (e.g., Aasi et al. 2015b). The GW detector's performance is continuously monitored to characterize noise sources that could negatively impact the sensitivity of the GW searches or the source property estimation (Abbott et al. 2016a; Covas et al. 2018; Davis et al. 2021; Acernese et al. 2022). Figure 1.1 is a schematic diagram of the laser interferometer technique used in GW detectors.

The GW signals recorded by the *Advanced LIGO* and *Advanced Virgo* detector instruments are impacted by various types of noise sources, including quantum sensing, seismic, suspension thermal, mirror coating thermal, and gravity gradient (Aasi et al. 2015b). In addition, there are transient sources of noise such as, e.g., human activities, weather and equipment malfunctions (Abbott et al. 2016a), and occasional noise of unknown origin, commonly referred to as glitches (Cabero et al. 2019; Davis et al.

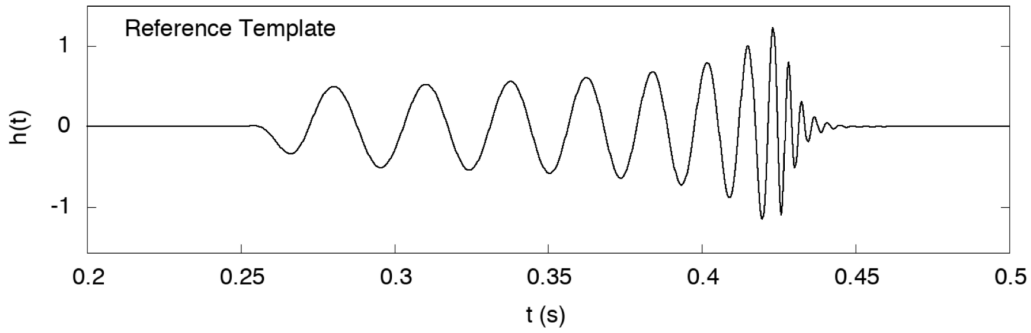

Figure 1.3: The gravitational waveform reference computed from the numerical relativity template for the GW150914 discovery paper (Abbott et al. 2016d) in the *LIGO* detector GW frequency band. Credit: Abbott et al. (2020b)

2021; Acernese et al. 2022). Finally, there is also elevated persistent noise confined to certain frequencies, referred to as spectral lines, which electrical and mechanical devices or resonances typically cause these (Covas et al. 2018). The impact of the different noise sourses to the GW detector strain sensitivity is shown in Figure 1.2. For comparison, the same figure also shows the measured sensitivity of one of the *Advanced LIGO* GW detectors during the second observing campaign. In the data analysis, the noise is modeled as a stochastic process with statistical properties given by the joint probability distribution of all the noise sources in a detector. The GW detection and parameter estimation techniques are briefly discussed in the following section, but e.g., see the guide in Abbott et al. (2020b) to the *LIGO-Virgo* detector noise and extraction of GW signals from the data for a more in depth review.

1.1.2 Gravitational waveforms and binary black-hole properties

Binary black holes lose orbital energy and angular momentum due to the emission of GWs. This causes their orbital separation to shrink until the two BHs collide and merge, forming a single BH of mass less than the sum of the two parent BHs. Three distinct stages characterize the BBH orbital evolution: the inspiral, the merger, and the ringdown phase of the remnant BH (for a review see Schmidt 2020). The GW signature encodes the properties characterizing the merging BBH. There are seven intrinsic parameters characterizing a BBH system composed of two Kerr BHs in a circular orbit, since for astrophysical BHs, one commonly assumes charge neutrality (see, e.g., Zajacek & Tursunov 2019). These parameters are the mass ratio $q = m_2/m_1$ where m_1 and m_2 are the BH masses (with the common convention being $m_2 \leq m_1$), and the two dimensionless spin vectors $\vec{\chi}_1$ and $\vec{\chi}_2$, which are defined as $\vec{\chi}_i = c\vec{J}_i/(Gm_i)^2$, where $\vec{J}_i$ is the angular-momentum vector of the BH with dummy index $i \in \{1, 2\}$. The total mass of the BBH system, $M = m_1 + m_2$, is not relevant intrinsically but determines the GW frequency in physical units, and is therefore relevant for the parameter estimation in GW detection.

The general relativistic two-body problem lacks analytic solutions. Therefore the dynamics and the corresponding GW signal must be approximated using a combination of analytic and numerical techniques. During the inspiral stage, where the orbital separation between two BHs is much larger than their size, the BHs can be treated as point particles. The GW signal can be calculated using the post-

Newtonian approximation. The post-Newtonian approximation is no longer valid at smaller separations, and the Einstein field equations must be solved numerically. Figure 1.3 shows the last moments of the gravitational waveform as predicted by numerical solutions of general relativity for GW150914; the first-ever detected merging BBH system.

Given the computational cost of solving the Einstein field equations numerically, GW data analysis relays on libraries of precomputed gravitational waveform models. Matched-filter search is the most common analysis used to extract GW signals of coalescing compact objects from the detector noise (e.g., Sathyaprakash & Dhurandhar 1991; Allen et al. 2012). This detection technique relays on comparing the measured GW detector signal with the gravitational waveform libraries. Complementary, the signal is scanned for unmodeled short-duration transient bursts (Klimenko et al. 2016). In both cases, once a candidate GW signal is identified and its significance is established, the next goal is to use the data to infer the physical parameters characterising the source that created the GWs. This is done by using Bayesian inference (e.g., Christensen & Meyer 1998, 2001, 2022; Röver et al. 2006; van der Sluys et al. 2008a,b; Veitch & Vecchio 2010; Veitch et al. 2015; Zackay et al. 2018; Biwer et al. 2019). The total number of physical parameters inferred from the GW signal of a merging BBH in a *circular orbit* is 15. In addition to the seven intrinsic BBH parameters and the total binary mass, M, we have the polarization angle ψ and the angle θ between the total orbital angular momentum $\vec{L}$ and the propagation direction of the GW, $\hat{\vec{n}}$, the source luminosity distance $D_{\rm L}$, the source right ascension α and declination δ, and a reference phase ϕ_0 and a reference time, typically the GW strain peak time, t_0. To the set of physical parameters, one must add another ten parameters per GW detector necessary to specify the calibration uncertainty model. Hence, for a typical three-detector analysis (*LIGO-Virgo*), 45 parameters for a quasi-circular system with generic spin orientations must be inferred. We refer to Abbott et al. (2020b) for a review of how such a high dimensional parameter space is efficiently explored. Additionally, we note that accounting for more complicated orbits, e.g., eccentric ones, or accoutring for tidal deformation of NSs, would consequently require additional parameters for the model.

Because GW signals are weak compared to the GW detector noise, there are, potentially large, uncertainties in the parameter estimation. Additionally, some of the source parameters are strongly correlated, leading to near-degeneracies when extracting them from a noisy dataset. For the heaviest BBHs, the total mass M is measured relatively accurately because the latest stage of the merger waveform, the ringdown, whose frequency is a function of the total mass, falls in the sensitive frequency band of current GW detectors. For lower-mass BBHs, the chirp mass $M_{\rm chirp}$ is the better-measured parameter since it determines to the lowest order the rate of frequency evolution during the earlier inspiral phase of the waveform. The chirp mass is defined as

$$M_{\rm chirp} = \frac{(m_1 m_2)^{3/5}}{M^{1/5}} \,. \tag{1.1}$$

Additionally, the mass ratio q is often poorly constrained. This parameter appears in the GW waveform inspiral phase at higher order corrections in the ratio of the orbital velocity to the speed of light, and is partially degenerate with the BH spins (Poisson & Will 1995; Hannam et al. 2013).

Similarly, placing precise constraints on the BH spins is challenging. Instead, a quantity that can be constrained better is the effective spin parameter, $\chi_{\rm eff}$: a mass-weighted linear combination of the BH

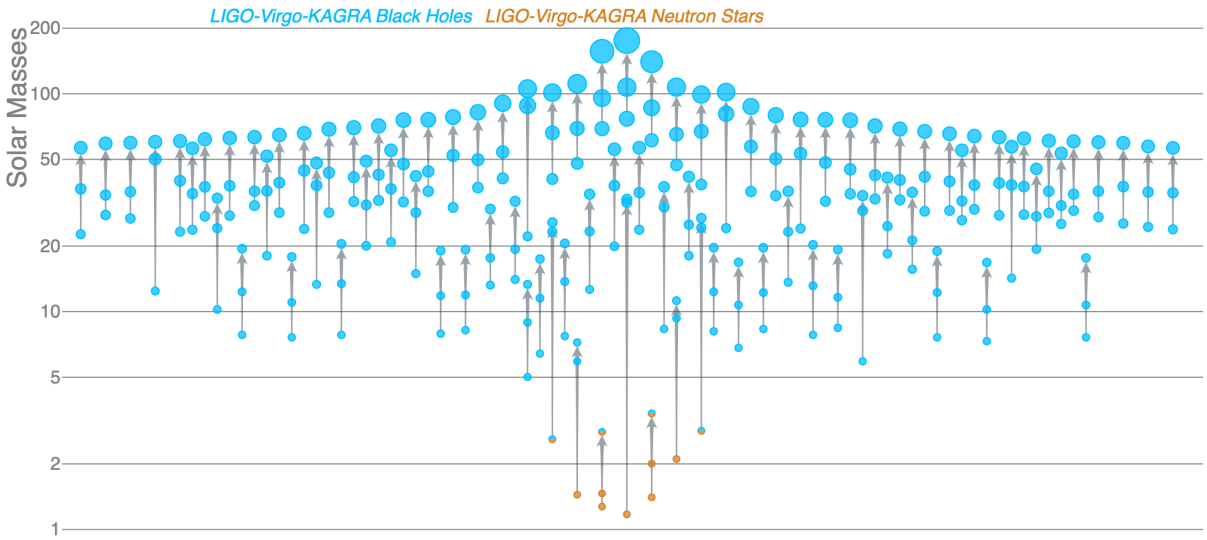

Figure 1.4: Diagram showing the masses of all BHs observed as GWs by the LVK Collaboration in GWTC-3 (blue) and NSs (orange). The resultant merger object mass is indicated with arrows. Credit: visualization by the LVK Collaboration, Aaron Geller at Northwestern University.

dimensionless spin components along the orbital angular-momentum direction $\vec{L}$ (e.g., Racine 2008; Ajith 2011)

$$\chi_{\rm eff} = \frac{m_1\vec{\chi}_1 + m_2\vec{\chi}_1}{M} \cdot \vec{L}. \tag{1.2}$$

This parameter is better constrained as it is proportional to the gravitational waveform amplitude.

Finally, as mentioned before, coupled with information from two or more GW detectors in a network, it is possible to infer the sky location, the orientation, and the luminosity distance to the source, or redshift assuming a cosmological model (e.g., Veitch et al. 2015; Abbott et al. 2016e; Ashton et al. 2019).

1.1.3 Current gravitational-wave detections

To date, 76 detections of GWs with a false alarm rate $< 1\,{\rm yr}^{-1}$ have been reported by the *LIGO-Virgo-KAGRA* (LVK) Collaboration (Abbott et al. 2016b, 2019b, 2021a,d,e). In the GW transient catalogs GWTC-1, GWTC-2, GWTC-2.1, and GWTC-3 released by the LVK Collaboration, we count 69 merging BBHs event, two merging binary NSs (BNSs; Abbott et al. 2017b, 2020a), two from the merger of BH-NS binaries (Abbott et al. 2021b), and three difficult-to-classify events GW190426_152155, GW190814, and GW190917_114630. The mass of the less massive component in these last three systems could be classified as a NS or a BH depending on where the threshold between NS and BH formation lies in the $2-3\,M_\odot$ mass range. Figure 1.4 shows an illustration of the mass distribution of the mentioned GW detections. Additional detections have also been reported by other groups' independent reanalysis of the data (Venumadhav et al. 2020; Nitz et al. 2021a,b; Olsen et al. 2022). For the remaining of this section, we will just focus on discussing the main BH observed properties through GWs, but see Mandel & Farmer (2022) for a general review of observed BH properties, which also includes a discussion about BHs detected in X-ray binaries.

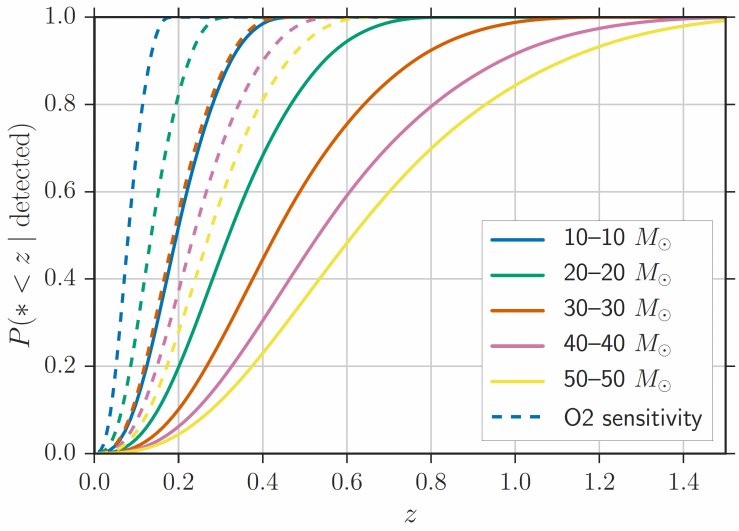

Figure 1.5: Cumulative probability distribution of the redshifts of detected BBHs of given masses, assuming that the underlying redshift distribution is uniform in comoving volume. The solid (dashed) lines show the expected distributions for *Advanced LIGO* at design (O2) sensitivity. If the merger rate evolves positively (negatively) with redshift, these curves would shift to the right (left). Credit: Fishbach et al. (2018)

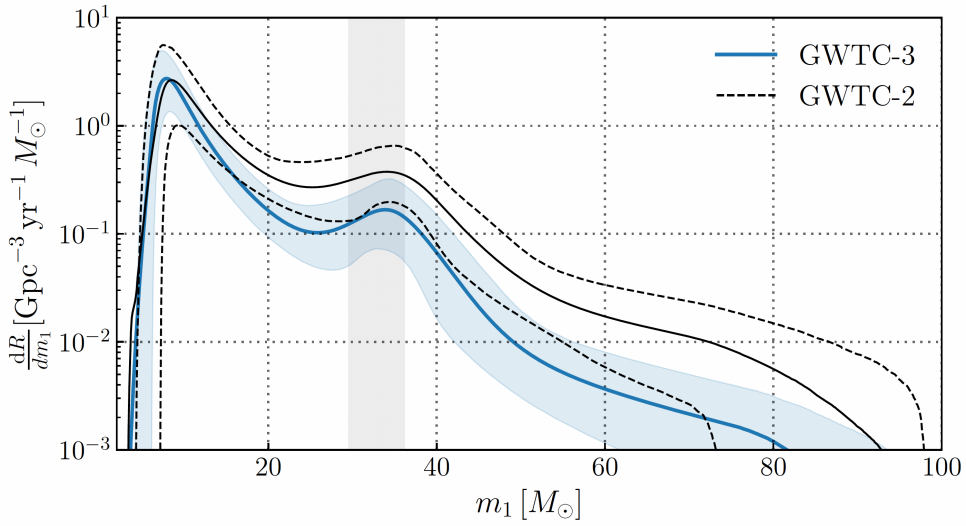

Figure 1.6: The astrophysical BBH primary mass distribution for the fiducial model analysis by the LVK Collaboration, showing the differential BBH merger rate as a function of primary mass. Credit: Abbott et al. (2021f)

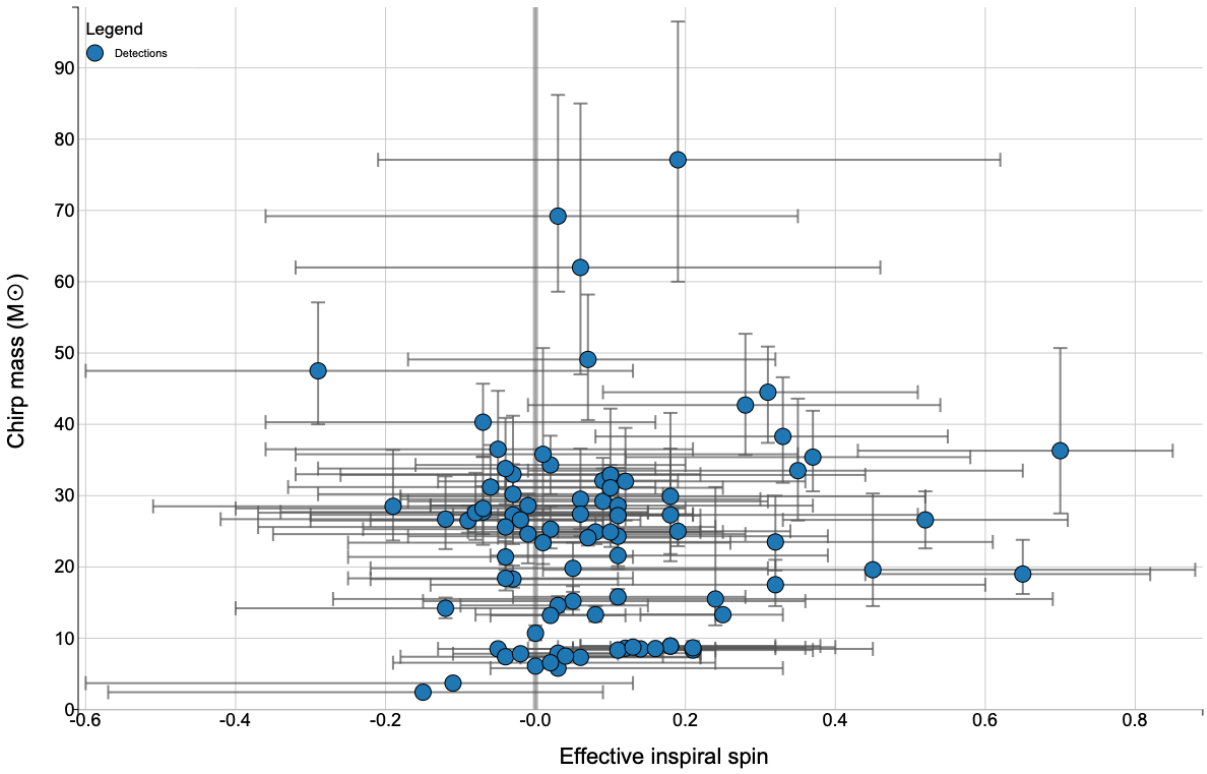

Figure 1.7: Diagram showing the chirp masses, $M_{\rm chirp}$, versus the effective spin parameters, $\chi_{\rm eff}$, of all BHs observed as GWs by the LVK Collaboration in GWTC-3 (blue). The error bars indicate the 90% credible interval. Credit: visualization by the LVK Collaboration (generated from `http://catalog.cardiffgravity.org`).

Assuming the lower-mass object in GW190814 is a BH rather than a NS (Abbott et al. 2020e), the observed BH masses range from $\sim 2.6\,M_\odot$ to $\sim 80\,M_\odot$ for GW190521 (Abbott et al. 2020d). In Figure 1.4, we see a significant selection bias toward detecting more massive BBHs. This occurs because the GW detector sensitivity depends on the observed BBH component masses. More massive BBHs have louder GW signals as the GW amplitude is mass dependent and the horizon distance at which a source is detectable, specifically scales as $M_{\rm chirp}^{5/6}$. Figure 1.5 shows the cumulative distribution of the redshifts of detected BBHs of given masses for *Advanced LIGO* at design and O2 sensitivity. More massive BBHs can be detected at larger redshifts. Correcting for GW detector selection effects, one can recover the underlying distribution of BH masses, which is consistent with a power-law for the most massive BH, i.e., $p(m_1) \propto m_1^{-3.4}$ (Abbott et al. 2021f). This power law is reminiscent of the stellar initial mass function (Salpeter 1955) with an additional peak at around $34\,M_\odot$ as shown in Figure 1.6. Additionally, the majority (99%) of observed merging BHs have masses below $45\,M_\odot$ (Abbott et al. 2021f).

Most observed BBH mergers have small spins, but some events show evidence of non-zero $\chi_{\rm eff}$. In Figure 1.7, we show the estimated $\chi_{\rm eff}$ parameters versus $M_{\rm chirp}$ for the detected BBHs. The population spin distribution of merging BBHs is a topic of ongoing discussion, and the official interpretation by the LVK Collaboration is debated (e.g., Abbott et al. 2021f,c; Roulet et al. 2021; Callister et al. 2021b;

Galaudage et al. 2021). See Section 1.4.3 for a discussion on this matter and its astrophysical implications. The official LVK Collaboration analysis hints at a sub-population of $\chi_{\rm eff} < 0$ BBHs (Abbott et al. 2021f,c). On the other hand, both Roulet et al. (2021) and Galaudage et al. (2021) contest such claims by finding that the majority of BBHs have negligible spins on both components (consistent with zero), while a small fraction has positive and preferentially aligned spins (with the orbital angular momentum) with no observed events displaying a definite negative $\chi_{\rm eff}$. These differences are the result of the adopted model used to interpret the BBH population $\chi_{\rm eff}$ distribution. Roulet et al. (2021) and Galaudage et al. (2021) claim that by assuming $\chi_{\rm eff}$ follows a simplistic Gaussian distribution (as done in the LVK Collaboration analysis), the original analysis miss-specify the real underlying BBH $\chi_{\rm eff}$ distribution. See also Miller et al. (2020) for a discuss on the overestimation of $\chi_{\rm eff}$ introduced by the assumption of uninformative spin priors given the observed population.

All BBH events were observed with distances of around 250 Mpc to 6 Gpc, corresponding to redshifts between 0.05 and 0.9. This is consistent with the detector sensitivity during the first three observing runs of *LIGO-Virgo* GW detectors (Abbott et al. 2021e). Moreover, a couple of events could potentially have residual eccentricity at the GW frequency of 10 Hz (Romero-Shaw et al. 2021, 2020, 2022). Still, these analyses are not conclusive as they do not account for possible degeneracy between eccentricity and precession (Bustillo et al. 2021). Finally, the LVK Collaboration constrains the merger rate to increase with redshift, where the merger rate at the local Universe ($z = 0$) is $10 - 30\,{\rm Gpc}^{-3}\,{\rm yr}^{-1}$ (Abbott et al. 2021f).

1.2 From stars to black holes

1.2.1 Stellar evolution of massive stars and core-collapse supernovae

The evolution post-main-sequence of stars more massive than $\gtrsim 8\,M_\odot$ differs from lower mass stars such as the Sun. After the hydrogen-burning phase, followed by helium burning and forming a carbon-oxygen core, the very high central temperature of massive stars can further trigger carbon and oxygen burning. Figure 1.8 shows the Hertzsprung-Russell diagram evolution of single stars in the mass range $0.5 - 300\,M_\odot$. The most massive stars will continue undergoing all nuclear burning phases up to forming an iron core. The iron core keeps growing by silicon shell burning to a mass of around the Chandrasekhar mass limit $\sim 1.44\,M_\odot$. This leads eventually to electron capture and dissociation of the core elements into alpha particles in a process known as photodisintegration. The first process removes the degeneracy-pressure support of the core, while the second removes the thermal support. Combined, these two mechanisms accelerate the collapse until the core reaches nuclear densities, and neutron degeneracy pressure halts the collapse. This sudden halt produces a bounce shock moving out of the core. The shock wave moves outwards until it deposits all its energy into the surrounding layers. A supernova explosion occurs if the deposited energy can overcome the ram pressure of the infalling stellar material. A fraction, $f_{\rm fb}$, of the material ejected by the supernova then falls back onto the stellar remnant. If the remnant is massive enough, neutron degeneracy pressure fails to halt the collapse, which leads to the formation of a BH. On the other end, the most massive stars can directly overcome the neutron degeneracy pressure

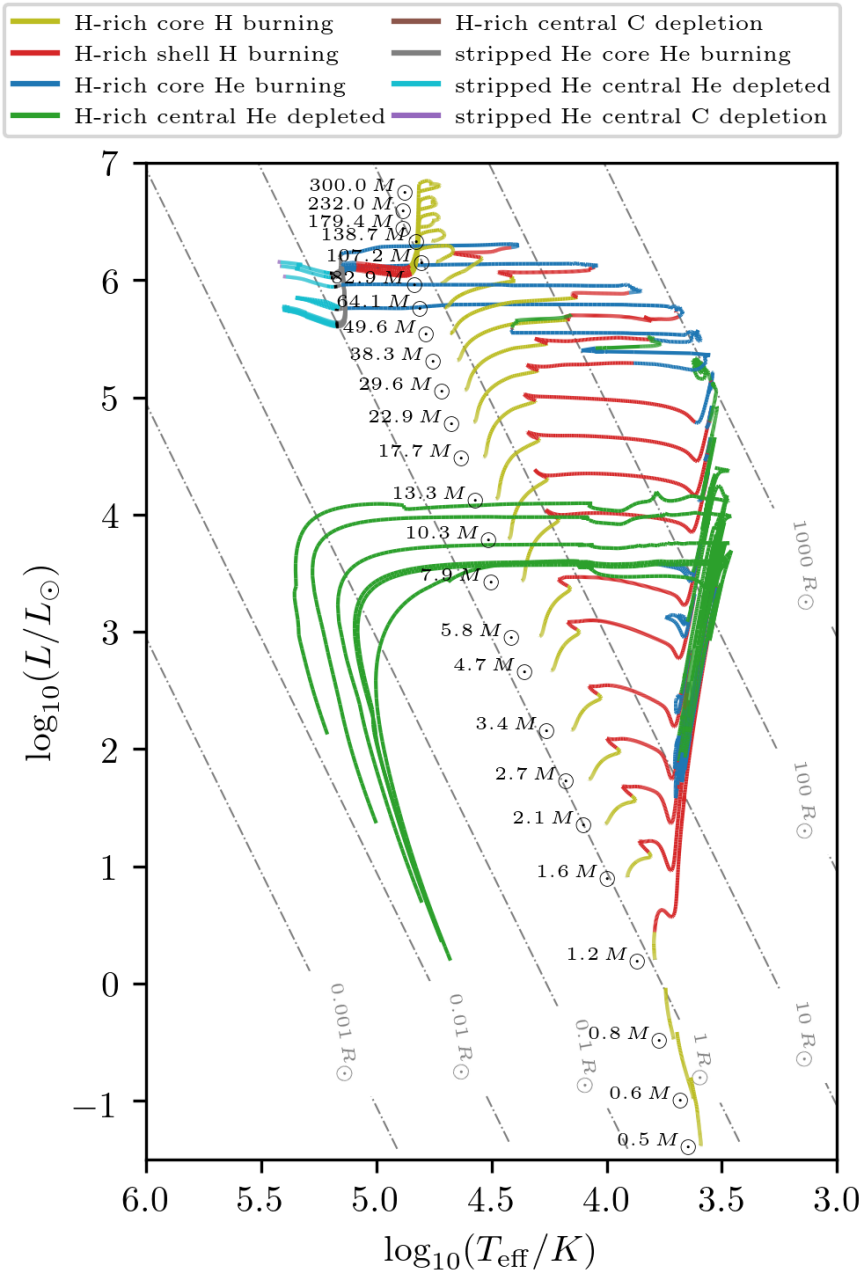

Figure 1.8: Hertzsprung-Russell diagram of `POSYDON` single-stellar models in the mass range $0.5-300\,M_\odot$ where different stellar burning phases are indicated according to the legend. The stars are evolved up to carbon depletion or until they reach the Hubble time. Credit: Fragos et al. (2022)

when the collapse starts, and implode to form a BH. This process is known as a core-collapse supernova (for a review see Janka et al. 2007).

The process of the core collapse was extensively studied during the past decades, and self-consistent simulations that model the core-collapse process are still the subject of active research. An extensive body of recent research showed that the star's final fate in core-collapse supernovae, i.e. implosion or explosion, depends sensitively on the structure of the stellar core immediately preceding the iron core-collapse, which in turn is set by the last few thousand years of evolution in the stellar core (e.g. Fryer 1999; Fryer et al. 2012; Woosley et al. 2002; O'Connor & Ott 2011; Ugliano et al. 2012; Pejcha & Thompson 2015; Sukhbold et al. 2016; Sukhbold & Adams 2020; Patton & Sukhbold 2020). We explicitly point out that the latest research shows that there is no unique boundary in the core mass of the pre-core-collapse star that transitions between the formation of NSs and BHs. This result is important and can potentially impact BBH formation models, however, is still commonly neglected in population synthesis modeling (see, e.g., Patton et al. 2022, and §1.5.1 for an introduction on this modeling technique). The most commonly used prescription to approximate the remnant baryonic mass left behind by the core-collapse supernova, given the pre-core-collapse stellar core mass, is the one of Fryer et al. (2012). Subsequently, the remnant baryonic mass is converted to gravitational mass, given some empirical prescriptions to account for neutrino mass loss during the collapse. See, e.g., the prescription in Appendix A.2 of Zevin et al. (2020), which is an updated version of the one by Lattimer & Yahil (1989) based on the neutrino observations of SN 1987A.

Finally, another important point about modeling the formation of BHs is the estimation of the fraction of angular momentum stored in the collapsing star that is passed to the BH. Highly rotating, massive stars are thought to support the formation of an accretion disk and potentially lead to the emission of a long-duration gamma-ray burst (LGRB; e.g., Woosley 1993; Paczyński 1998). Given the profile of a collapsing star and assuming the direct collapse of its shells, one can determine the portions of the collapsing star that will collapse directly toward the center, as well as those that will support the formation of an accretion disk (e.g., Batta & Ramirez-Ruiz 2019). Because this procedure is illustrated in multiple of my publications (and, hence, this thesis), we omit an explanation of the details of this mechanism here (e.g., Bavera et al. 2020, 2021a, 2022b; Fragos et al. 2022).

1.2.2 Pulsational pair-instability supernovae

During the post-carbon burning phase of massive stars, photons produced in the core can be energetic enough to produce electron-positron pairs, softening the equation of state and diminishing the pressure support of the core (see, e.g., Woosley et al. 2007; Langer 2012). In such stars, the core rapidly contracts. The temperature increases, leading to explosive oxygen burning (e.g., Woosley & Heger 2015), which creates a series of energetic pulses that eject material from the star's surface. This phenomenon is known as a pulsational pair-instability supernova (PPISN) and occurs for stars with helium core masses in the range $\sim 32 - 64\,M_\odot$ (Yoshida et al. 2016; Woosley 2017, 2019; Marchant et al. 2019; Renzo et al. 2020). For more massive stars with helium core masses in $\sim 64 - 133\,M_\odot$, the first pulse is so energetic that can unbind and destroy the whole star in a so-called pair-instability supernova (PISN; Fowler & Hoyle 1964; Rakavy & Shaviv 1967; Barkat et al. 1967; Heger & Woosley 2002), leaving no remnant. Figure 1.9 shows

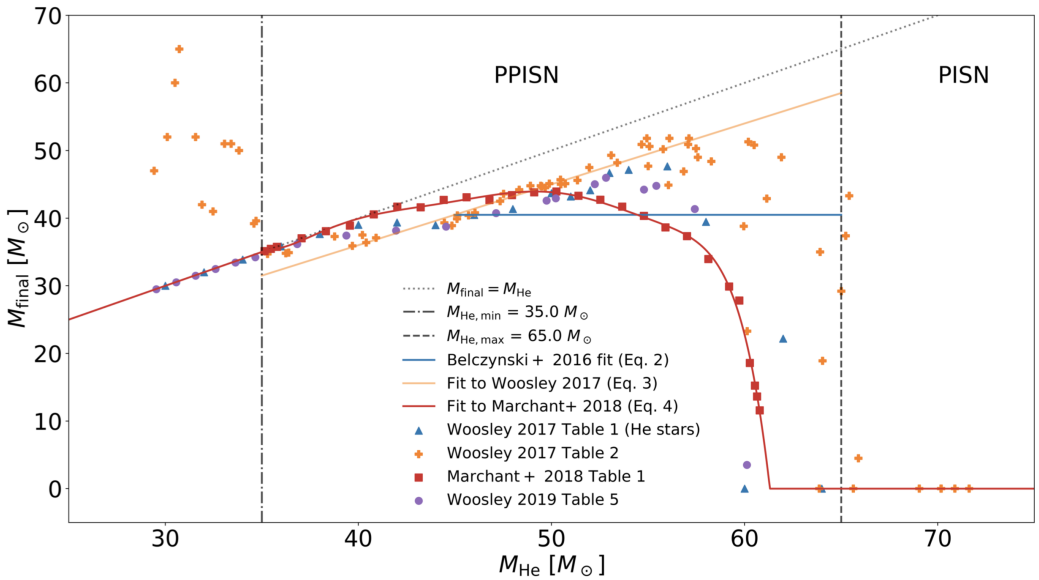

Figure 1.9: Final remnant mass $M_{\rm final}$ as a function of pre-supernova helium core mass $M_{\rm He}$ for stars in the PPISN and PISN mass regime. The results of different studies (Belczynski et al. 2016a; Woosley 2017, 2019; Stevenson et al. 2017; Marchant et al. 2019) are indicated with different color markers. Solid lines show analytical fits to these models as presented in Stevenson et al. (2019). All models demonstrate a turnover between pre-supernova helium core mass and final mass. Credit: Stevenson et al. (2019)

the relation of the final remnant mass of stars experiencing PPISN according to some of the mentioned aforementioned models.

We notice that the location of the PISN gap at BH mass $\sim 45\,M_\odot$ is robust against model uncertainties. For example, variations in the metallicity might shift it by $\lesssim 3M_\odot$, the treatment of internal mixing by $\lesssim 1\,M_\odot$, and stellar-wind mass loss $\lesssim 4\,M_\odot$ (Farmer et al. 2019). However, it was found that it is sensitive to the uncertain $^{12}{\rm C}(\alpha,\gamma)^{16}{\rm O}$ nuclear reaction rate. This nuclear reaction rate is of great astrophysical significance and governs the production of oxygen at the expense of carbon (Farmer et al. 2020).

1.2.3 Black-hole natal kicks

During the core collapse, the binary system experiences abrupt mass loss away from the center of mass, affecting its orbital parameters (Blaauw 1961; Boersma 1961). Furthermore, asymmetric ejection of matter (Janka & Mueller 1994; Burrows & Hayes 1996; Janka 2013) or asymmetric emission of neutrinos (Bisnovatyi-Kogan 1993; Socrates et al. 2005) can provide a momentum kick to the newly formed BH. Oftentimes, BH kicks are empirically assumed to be drawn from a Maxwellian distribution with dispersion $\sigma = 265\,{\rm km\,s^{-1}}$ (Hobbs et al. 2005) and resealed by some factor as, e.g., one minus $f_{\rm fb}$ (Fryer et al. 2012). Depending on the natal kick magnitudes, BH kicks can induce a statistically relevant fraction of BBH systems to have spins anti-align with the orbital angular momentum and have $\chi_{\rm eff} < 0$ (see, e.g., Rodriguez et al. 2016b; Gerosa et al. 2018; Steinle & Kesden 2021; Callister et al. 2021a; Stevenson 2022).

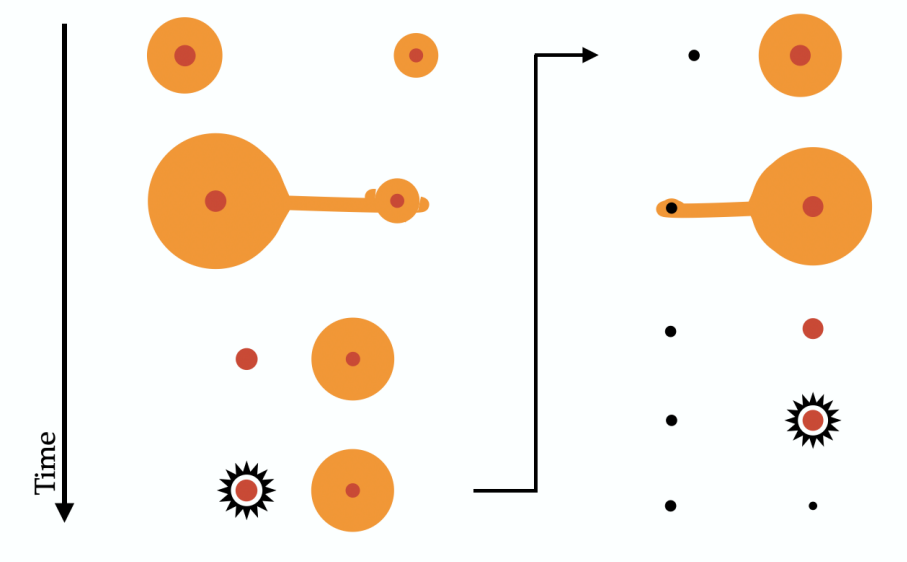

Figure 1.10: Diagram showing a binary black hole system forming through the canonical stable mass transfer formation channel.

1.3 Binary black-hole formation channels

General relativity puts upper constraints on the maximal orbital separation at the formation of the BBH system for the two BHs to coalesce within the age of the Universe ($t_{\rm H} = 13.8\,{\rm Gyr}$). The inspiral timescale can be approximated using the Peters (1964) formula. For example, assuming a circular orbit, the maximal orbital separation for the first-ever detected BBH system GW150914 composed of two BHs with mass $\sim 30\,M_\odot$ for the system to merge in isolation within the Hubble time $t_{\rm H}$ is $\leq 47\,R_\odot$. However, from isolated stellar evolution, we know that a star massive enough to generate such BHs will expand to become a supergiant of more than a thousand solar radii during its evolution. Naively, we might therefore expect that the stellar binary system would had merge long before the first BH formation. Therefore, a viable formation mechanism for merging BBHs would either (i) efficiently bring the stars closer together after they have expanded and formed the BH, (ii) prevent the stars from expanding during their evolution, or (iii) have the expanding star interact with the binary companion without merging or disrupting the system.

The present thesis mostly focuses on studying the BBH evolutionary pathways in the framework of detailed, isolated binary evolution models. This corresponds to formation mechanisms categories (ii) and (iii) listed above. However, many other formation channels have been discussed in the literature. The following sections review and summarize the main BBH formation channel discussed in the literature.

1.3.1 Isolated binary evolution in galactic fields

1.3.1.1 The canonical stable mass transfer and common envelope evolutionary pathways

In this formation channel (for a review see Mandel & Farmer 2022), two massive stars are born in a relatively wide binary. The first binary interaction happens after the initially more massive star

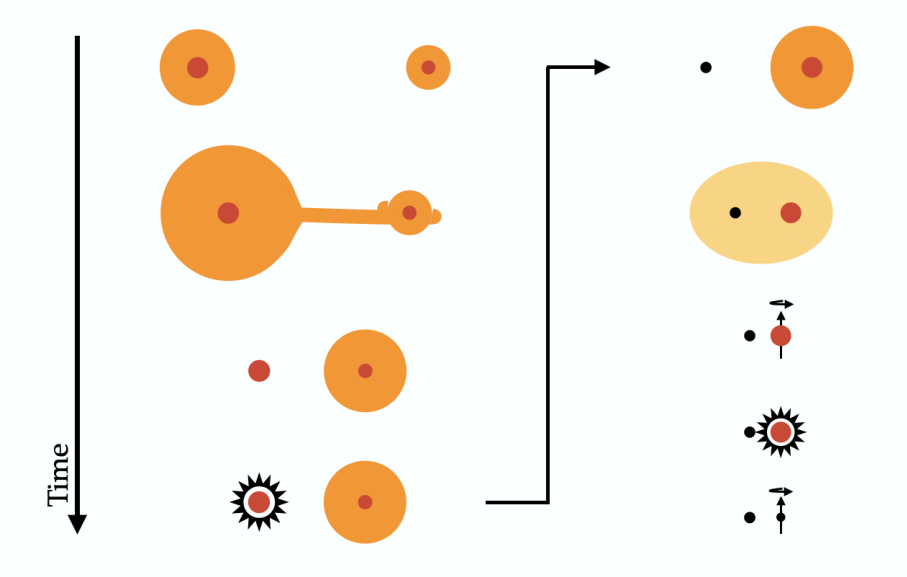

Figure 1.11: Diagram showing a binary black hole system forming through the canonical common envelope phase formation channel. We indicate the spin of the second-born BH acquired through tidal spin up during the BH-WR phase with an arrow.

(henceforth, *primary*) leaves the main sequence and expands to become a red supergiant star. The primary star inflates its hydrogen-rich envelope beyond its Roche lobe during this evolutionary phase, leading to the first mass-transfer episode. The mass transfer stops when the entire stellar envelope is lost, leaving behind a naked helium star known as Wolf-Rayet (WR) star. Depending on the mass-transfer accretion efficiency, which mostly depends on the surface rotation of the accreting star, the secondary star might accrete a small or large fraction of the transferred mass. Eventually, the primary star collapses to form the first-born BH.

The angular-momentum transport efficiency determines the spin of the first-born BH during the evolution of the progenitor star. Measurements of NS and white dwarf spins (Heger et al. 2005; Suijs et al. 2008), and asteroseismology studies (Fuller et al. 2014; Eggenberger et al. 2012; Cantiello et al. 2014), suggest that this mechanism must be efficient (Spruit 1999, 2002; Fuller & Ma 2019). Thus, upon expansion, the initial angular momentum of the star is mostly transported to the outer layers, which are subsequently lost due to the first mass transfer episode and wind mass loss. This leads to the formation of a slowly spinning first-born BH ($|\vec{\chi}_1| \simeq 0$), as initially suggested in the context of BH low-mass X-ray binary formation by Fragos & McClintock (2015), and subsequently quantitatively shown in Qin et al. (2018), Fuller & Ma (2019), and Belczynski et al. (2020).

The above process repeats for the secondary star (also referred as *companion*). The mass-transfer phase can be either stable or unstable, with the latter leading to the formation of a common envelope (CE) of gas engulfing the binary. From this point on, we will refer to the first evolutionary case as the stable mass-transfer (SMT) channel while the latter as the CE channel. If the stripping of the secondary's envelope is successful, we are left with either a tight BH–WR system in the case of the CE channel, or with a wider system in the case of the SMT channel. Eventually, the secondary star collapses to form

the second-born BH. Due to energy and angular-momentum loss from GW emission (Peters 1964), the BBH system merges to form a single BH.

In the case of the SMT channel, during the second mass-trasfer episode, the first-born BH may accrete material and spin up (Thorne 1974). This depends on the accretion rate onto BHs. If the accretion efficiency is Eddington limited, then the first-born BH will not accrete material and avoid any spin-up. In the case of super-Eddington accretion, the BH will spin up depending on the accreted mass (van Son et al. 2020; Bavera et al. 2021a; Qin et al. 2022; Zevin & Bavera 2022).

On the other hand, the spin of the second-born BH is determined by the net effect of the interplay between stellar-wind mass loss and the tidal interactions of the BH–WR binary system. Because of the efficiency of the angular-momentum transport, the WR star emerges from the second mass transfer event with a negligible spin. If the orbital separation is small enough and stellar winds do not widen the system significantly, the WR star can be spun up by tides. These conditions are met at low metallicities ($Z \lesssim 0.2 Z_{\odot}$) and for BH–WR systems mostly formed through the CE formation channel (Qin et al. 2018; Bavera et al. 2020). In contrast, in the case of the SMT channel, the orbit shrinks less efficiently, leading to wider BH–WR systems and less tidally spun-up second-born BHs than in the CE channel (Bavera et al. 2021a). The main evolutionary steps described here for the SMT and CE evolutionary channel are illustrated in Figures 1.10 and 1.11, respectively.

In recent years, a lot of focus was put on these two evolutionary pathways to explain the origin of coalescing BBHs detected by LVK GW detectors. Relevant studies about the SMT channel are, e.g., Pavlovskii et al. (2017); van den Heuvel et al. (2017); Neijssel et al. (2019); Inayoshi et al. (2017); van Son et al. (2021); Bavera et al. (2021a); Broekgaarden et al. (2022), while studies focusing on the CE channels are, e.g., Smarr & Blandford (1976); van den Heuvel (1976); Tutukov & Yungelson (1993); Kalogera et al. (2007); Dominik et al. (2012, 2013, 2015); Postnov & Yungelson (2014); Belczynski et al. (2016b, 2020); Breivik et al. (2016); Giacobbo & Mapelli (2018); Zaldarriaga et al. (2018); Spera et al. (2019); Bavera et al. (2020).

1.3.1.2 Chemically homogeneous evolution

Massive stars at the main sequence, in binary systems with short orbital periods ($p \lesssim 2\,\mathrm{days}$) and nearly equal masses ($q > 0.8$), tidally spin up to be highly rotating. The rapid rotation of the stars induces rotational mixing in the stellar interior, replenishing the core with elements for nuclear burning and never leading to significant expansion of the progenitor stars throughout core hydrogen burning (Maeder 1987; Langer 1992; Heger & Langer 2000). This evolutionary pathway is known as chemically homogeneous evolution (CHE). Detailed studies in binary systems have shown that this mechanism leads to the formation of merging BBHs only at low metallicities ($Z \lesssim 5 \cdot 10^{-3}$), where strong angular-momentum loss due to stellar winds can be avoided such that the stars remain fully mixed until core hydrogen exhaustion (Yoon & Langer 2005; Woosley & Heger 2006; Brott et al. 2011; Köhler et al. 2015; Szécsi et al. 2015). Studies focusing on the CHE channel in massive binaries targeting the formation of GW sources are de Mink & Mandel (2016); Mandel & de Mink (2016); Marchant et al. (2016) and, subsequently, follow-up studies (e.g., du Buisson et al. 2020; Riley et al. 2021). Figure 1.12 illustrates the evolution of a binary through this channel. Both stars born in a close binary system evolve chemically

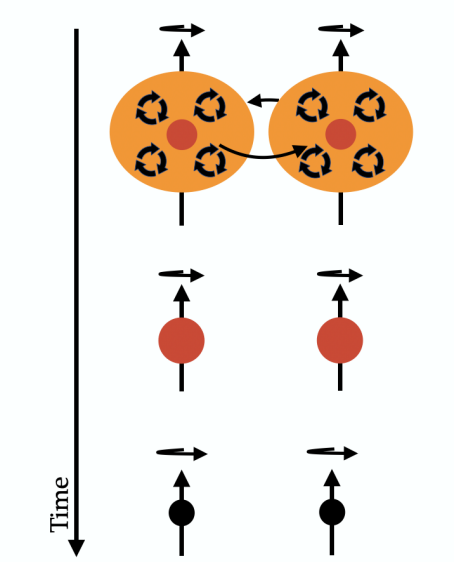

Figure 1.12: Diagram showing a binary black hole system forming through the chemically homogeneous evolutionary channel. We use arrows to indicate the star and BH spins.

homogeneously avoiding expansion, becoming directly rapidly rotating WR stars and eventually forming massive, nearly-equal mass and highly rotating BHs, which will eventually merge.

1.3.1.3 Other minor evolutionary pathways within isolated binary evolution

Another channel for forming BBHs is similar to the double-core CE channel first introduced by Brown (1995) and Dewi et al. (2006) for the formation of merging BNSs. In this scenario, both stars evolve beyond the Hertzsprung-gap, engaging in an unstable mass-transfer episode. Binaries that survive the CE phase will form close WR–WR systems, which can then undergo tidal spin-up (Hotokezaka & Piran 2017; Olejak & Belczynski 2021). Eventually, both stars will then collapse to form merging highly spinning BBHs. This evolutionary channel typically leads to near-equal-mass mergers and is often neglected because it is rare compare the other evolutionary pathways mentioned above (Neijssel et al. 2019).

1.3.2 Dynamical formation in dense stellar environments

In the isolated binary evolution channels, the companions are formed at the same time, and evolve in parallel, largely ignoring the effects of environment. Conversely, in dense stellar environments, merging BBHs may originate from stars of the same or different ages, in the same or different systems (single, binary or multiple), subject to internal (e.g., three-body) or external (from close encounters) forces. The evolution of one possible system in this channel is illustrated in Figure 1.13. This formation path is present in nuclear star clusters (e.g. Antonini & Rasio 2016; Petrovich & Antonini 2017; Antonini et al. 2019; Arca Sedda 2020; Fragione & Silk 2020), globular clusters (e.g., Portegies Zwart & McMillan 2000; O'Leary et al. 2006; Downing et al. 2010; Tanikawa 2013; Rodriguez et al. 2015, 2016a; Askar et al.

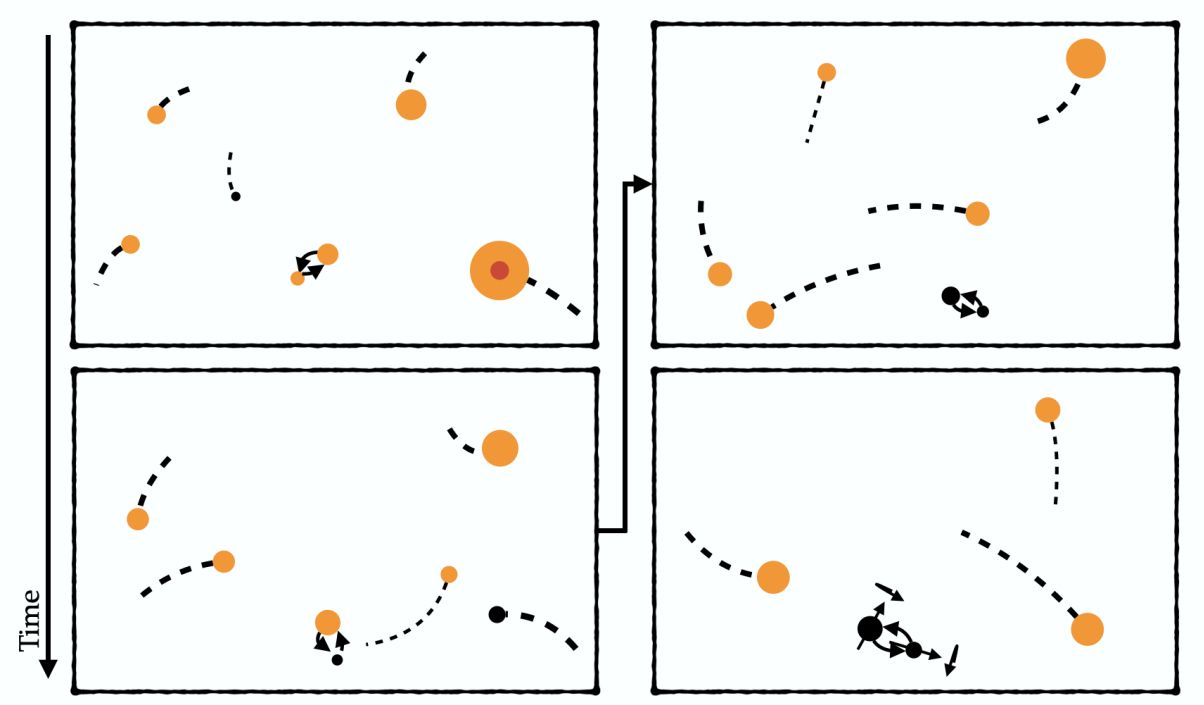

Figure 1.13: Diagram showing a binary black hole system forming through dynamical interactions in a dense stellar environment. The last drawing shows the BH spin vectors in case the BHs are born spinning. In contrast to isolated binary evolution channels, BH spins are not expected to be aligned with the orbital angular momentum.

2017; Fragione & Kocsis 2018; Choksi et al. 2018; Choksi & Gnedin 2019; Hong et al. 2018; Rodriguez & Loeb 2018), and young star clusters (e.g., Banerjee et al. 2010; Banerjee 2017, 2021; Ziosi et al. 2014; Mapelli 2016; Di Carlo et al. 2019, 2020b; Kumamoto et al. 2019, 2020; Rastello et al. 2019). The BHs formed from massive stars aggregate to the core of the cluster due to dynamical friction, creating a dense subsystem dominated by BH interactions (Lightman & Shapiro 1978; Sigurdsson & Hernquist 1993). Strong gravitational encounters between BH systems produce "hardened" binaries, typically extracting orbital energy from the more massive components of the interaction by ejecting the lighter components (McMillan et al. 1991; Hut et al. 1992; Sigurdsson & Phinney 1993; Miller & Hamilton 2002; Gültekin et al. 2006; Fregeau & Rasio 2007), leading to BBHs that can merge within the Hubble time (e.g., Samsing et al. 2014; Samsing & Ramirez-Ruiz 2017). Different dynamical environments have unique predictions for the properties of merging BBHs, since stellar densities, escape velocities, and stellar mass budgets differ in these scenarios. If the BHs are born spinning, then because of their formation nature, one would expect isotropically-distributed spins in contrast to isolated binary evolution, this evolutionary channel is expected to result in symmetric BBH $\chi_{\rm eff}$ distributions (see further discussion in §1.4.3).

1.3.3 Triple and multiples

Multiple systems of more than two stars, namely triples, quadruples, and so on, are abundant in galactic fields (Sana et al. 2014; Moe & Di Stefano 2017). For example, for solar-type stars, one in four binaries has a third companion (Raghavan et al. 2010; Tokovinin 2014). In contrast, for massive O and B-type stars, progenitors of BHs, the fraction of triples might be even higher than those of binaries (Moe & Di Stefano 2017). Based on stability arguments, we expect them to be hierarchical, consisting of multiple levels in which the stars of the lower levels can be treated as binaries. For example, a stable triple consists of an inner binary system, and a star orbiting the latter at a larger separation, while a quadruple star may be a stable triple with an orbiting outer star, or a binary of stable binaries. If a BBH is formed first as the inner binary in a hierarchical system, eccentricity can be imparted into the inner BBH from the outter star (referred as "tertiary") through the Lidov–Kozai mechanism (Kozai 1962; Lidov 1962). This process will expedite the inspiral time of the binary, allowing systems to merge as GW sources that, typically, would not merge within a Hubble time (Wen 2003; Toonen et al. 2016, 2020, 2021; Antonini et al. 2017; Silsbee & Tremaine 2017; Fragione & Kocsis 2019; Arca Sedda et al. 2021; Vigna-Gómez et al. 2021). The dynamical impact of the tertiary is strongest when the system is "less" hierarchical and close to dynamically unstable, which occurs when the separation of the tertiary from the inner binary is comparable to the separation of the latter. These interactions are complex to model as the hierarchy of an isolated stable triple can decrease and even break down because of its evolution (Perets & Kratter 2012). The majority of our intuition about unstable triples comes mostly in the context of stellar clusters.

1.3.4 Population III stars

Population III stars have also been proposed to form merging BBHs either in isolation or in stellar clusters at high redshifts. The absence of carbon, nitrogen, and oxygen in these metal-poor stars could

prevent the CNO cycle hydrogen fusion in the hydrogen shell around the helium-rich core, reducing radial expansion after the end of the main sequence (Marigo et al. 2001). In addition, this could allow the star to retain its tightly-bound hydrogen envelope when collapsing into a BH (Kinugawa et al. 2021). Since stellar winds are weaker in low-metallicity stars, population III stars experience reduced wind mass loss throughout their lifetime compared to present-day stars, producing BH masses in the range $40 - 140\,M_\odot$ (e.g., Bond et al. 1984; Schneider et al. 2000; Madau & Rees 2001; Bromm & Yoshida 2011; Hirano et al. 2014; Liu et al. 2021). There are two evolutionary pathways within the population III star channel: (i) in-situ formation in binaries, and (ii) ex-situ from dynamical capture of two BHs, either born into one dense star cluster or from two originally separate formation sites (e.g., during galaxy mergers). The first channel has been intensely studied before and after the first *LIGO* detection (Kinugawa et al. 2014, 2016; Hartwig et al. 2016; Inayoshi et al. 2016, 2017; Belczynski et al. 2017; Mapelli et al. 2019). There is disagreement among different studies, mostly dominated by uncertainties in the initial binary parameters and evolution models for population III binary stars (Stacy & Bromm 2013; Kinugawa et al. 2014; Belczynski et al. 2017). The second channel has been studied with semi-analytical models (e.g., Sesana et al. 2009, 2011; Dayal et al. 2019) in the context of cosmic structure formation (e.g., Tremmel et al. 2015; Roškar et al. 2015; Tamfal et al. 2018; Pfister et al. 2019; Ogiya et al. 2019; Liu & Bromm 2020a). The BH merger rate density of population III stars is expected to dominate over population I/II at large redshifts ($z \gtrsim 7$, e.g., Tanikawa et al. 2022).

1.3.5 Primordial black holes

Another well-studied formation channel for producing merging BBHs is merging primordial BHs (PBHs; Zel'dovich & Novikov 1967; Hawking 1974; Chapline 1975; Carr 1975), which may arise from the collapse of large overdensities in the radiation-dominated early Universe (Ivanov et al. 1994; Ivanov 1998; Garcia-Bellido et al. 1996; Blinnikov et al. 2016). Primordial BHs may have contributed to a sizeable ratio $f_{\rm PBH} \equiv \Omega_{\rm PBH}/\Omega_{\rm DM}$ of the dark matter energy density in a variety of mass ranges (for a recent review on constraints of $f_{\rm PBH}$, see Carr et al. 2020). The recent discovery of GWs has reewed the interest in PBHs, particularly as it has been noted that PBHs can produce observable mergers without conflicting with existing bounds on the PBH abundance (Bird et al. 2016; Clesse & García-Bellido 2017; Sasaki et al. 2016). This finding has motivated various works on the confrontation of the PBH scenario with the most recent data (see, e.g., the recent results of Eroshenko 2018; Wang et al. 2016, 2019; Clesse & García-Bellido 2018; Chen & Huang 2018; Raidal et al. 2019; Gow et al. 2020; Hütsi et al. 2019, 2021; Vaskonen & Veermäe 2020; De Luca et al. 2020b,a, 2021b,a; Hall et al. 2020; Wu 2020; Kritos et al. 2021; Deng 2021; Kimura et al. 2021). Current GW data imply an upper bound to $f_{\rm PBH} \lesssim \mathcal{O}(10^{-3})$ in the mass range of interest for current GW detectors (see, e.g., Wong et al. 2021). Finally, it was also shown (e.g., Ali-Haïmoud et al. 2017) that the dominant PBH merger rate comes from PBH binaries assembled via gravitational decoupling from the Hubble flow before matter-radiation equality (Nakamura et al. 1997; Ioka et al. 1998; Sasaki et al. 2018; Green & Kavanagh 2021).

1.3.6 Active galactic nuclei

Another favorable environment for facilitating BBH mergers is active galactic nuclei (AGN) disks. Multiple evolutionary pathways have been identified in the literature. In general, BBHs find themselves or get caught in resonance traps of AGN disks, where they are efficiently "hardened" via gas dynamical friction, potentially proceeding through many successive hierarchical mergers due to the high escape velocity in the vicinity of the supermassive BH (Goodman & Tan 2004; Levin 2007; Just et al. 2012; Antonini & Perets 2012; Antonini & Merritt 2012; McKernan et al. 2014, 2018, 2019; Bellovary et al. 2016; Bartos et al. 2017; Stone et al. 2017a; Leigh et al. 2018; Secunda et al. 2019; Yang et al. 2019a,b; Tagawa et al. 2020, 2021).

1.3.7 Ultra-compact dwarf galaxies

It has also been suggested that stellar-mass BBHs detected by *LIGO-Virgo* might also originate in the center of extremely low-mass ultra-compact dwarf galaxies that have merged in the distant past at $z > 1$. Ultra-compact dwarf galaxies, with masses in the $10^5 - 10^6\,\mathrm{M}_\odot$ range, have extremely high stellar densities. Therefore, they are considered birth places of BBHs formed from dynamical captures (Conselice et al. 2020; Palmese & Conselice 2021).

1.3.8 Stellar flybys

Finally, another exotic channel for binaries is stellar flybys. Close encounters with other stars can perturb ultra-wide BH binaries in galactic fields with orbital separations $> 1000\,\mathrm{AU}$. The frequent interactions with random stars can change the eccentricity of wide binaries and, in some cases, excite sufficiently high eccentricities, leading to the merger of the binary via GW emission at periastra causing them to merge within the Hubble time (Michaely & Perets 2019, 2020).

1.4 Distinguishing binary black-hole evolutionary channels

Understanding the origin of merging BBHs is currently one of the most pressing quests in astrophysics. The majority of the discussed formation channels have been shown to successfully lead to the formation of merging BBHs and, in most cases, predict a plausible range of merger-rate density consistent with current GW observational constraints (Mandel & Broekgaarden 2021). However, accurate rate estimates are often difficult to make, as they depend on unconstrained astrophysical processes. The most well-known uncertainties affecting the astrophysical models include initial stellar and binary properties (e.g., binary ratio, initial mass function, mass ratio, and initial orbital parameter distributions), stellar evolution physics (e.g., stellar winds of massive stars, core-collapse mechanism, supernova kicks, and PPISNe), binary evolution physics (e.g., mass-transfer stability and efficiency, and CE efficiency) as well as uncertainties in the star-formation and metallicity history of high-redshift galaxies (see, e.g., Antonini et al. 2017; Chatterjee et al. 2017; Chruslinska et al. 2019; Neijssel et al. 2019; Gröbner et al. 2020; Carr & Kühnel 2020; Riley et al. 2021; Belczynski et al. 2021). Combined, these unconstrained physical processes lead to order-of-magnitude uncertainties in the rates, hindering the interpretation of

BBH observations (for a review see Mandel & Broekgaarden 2021). Hence, most recent studies focus on key BBH observational features specific to a formation channel that might allow us to isolate its presence in the observed BBH sample. In the following sections, we discuss some of these features and how they can be used to interpret the origin of merging BBHs.

1.4.1 The pair-instability supernovae gap

Due to the PISN mass gap, isolated binary evolution cannot lead to the formation of BHs in the mass range $\sim 50\,M_\odot$ to $\sim 120\,M_\odot$ (Marchant et al. 2019; Stevenson et al. 2019; van Son et al. 2020, see also §1.2.2). To explain observed mergers of BHs in the PISN mass gap, also known as upper mass gap, dynamical formation is invoked. For example, stellar mergers in young star clusters (e.g., Portegies Zwart et al. 2004; Mapelli 2016; Di Carlo et al. 2020a; Rizzuto et al. 2021) or hierarchical BBH mergers (e.g., Miller & Hamilton 2002; Giersz et al. 2015; Fishbach & Holz 2017; Gerosa & Berti 2017; Rodriguez et al. 2019; Mapelli et al. 2021) could produce such massive BBHs. The discovery of BBH systems with one or two components lying within the upper mass gap is considered a smoking gun for dynamical origin (Fragione et al. 2020; Romero-Shaw et al. 2020; Kremer et al. 2020; Kimball et al. 2021; Liu & Lai 2021; Samsing & Hotokezaka 2021). This was indeed a matter of debate after detecting GW190521 with at least one BH within the upper mass gap (Abbott et al. 2020d,f). Alternatively, GW190521 was also interpreted in the context as having a primordial origin (Clesse & Garcia-Bellido 2020; De Luca et al. 2021a) or formed from population III stars avoiding PISN (Safarzadeh & Haiman 2020; Liu & Bromm 2020b; Farrell et al. 2021; Kinugawa et al. 2021; Tanikawa et al. 2021). However, we notice that (Fishbach & Holz 2020) reanalyzed the event using a population-informed prior consistent with the previously observed BBH sample finding that the lighter BH might lie below the upper mass gap with mass $< 48\,M_\odot$ at 90% credibility and the more massive BH to sit above the gap at 39% with mass $120\,M_\odot$ which further adds to the puzzle.

1.4.2 Eccentricity in the merging binary black hole

Another important property of BBH mergers that can potentially distinguish between isolated and dynamical formation is the eccentricity of the BBH merger in the LVK GW frequency band (e.g., Breivik et al. 2016; Samsing & Ramirez-Ruiz 2017; Rodriguez et al. 2018; Samsing & D'Orazio 2018; Zevin et al. 2019; Arca Sedda et al. 2021; Zevin et al. 2021b). Isolated binary evolution is expected to lead to near-circular BBH merger due to the rarity of BH natal kicks to impart extreme eccentricities which are not rapidly circularised by GW emissions (Peters 1964), while dynamical formation favors eccentric BBH mergers. In globular clusters, eccentric mergers from strong gravitational encounters have been shown to account for $\sim 10\%$ of the underlying population of BBH mergers, with approximately half of these having eccentricities larger than 0.1 at a GW frequency of 10 Hz. With current GW observatories, only eccentricities greater than 0.1 at GW frequency 10 Hz can be measured (Harry & LIGO Scientific Collaboration 2010; Lower et al. 2018). To date, a couple of events seem to have residual eccentricity at the GW frequency of 10 Hz (Romero-Shaw et al. 2021, 2020). Still, these analyses are not conclusive as they do not account for possible degeneracy between eccentricity and precession (Bustillo et al. 2021).

This is partly because of the difficulty in modeling eccentric signals (Loutrel 2020) and the computational burden of adding two extra dimensions to matched-filter template banks. Hence, current GW template banks used for matched-filter searches for GW signals typically assume quasi-circular binaries with aligned spins (Hooper et al. 2012; Allen et al. 2012; Dal Canton et al. 2014; Usman et al. 2016; Adams et al. 2016; Messick et al. 2017; Nitz et al. 2017; Chu et al. 2020; Davies et al. 2020; Aubin et al. 2021).

1.4.3 Black-hole spin orientations and magnitudes

Black-hole spin magnitudes and orientations might be another promising signature that might tell us about the environmental origin of merging BBHs (Farr et al. 2017). Systems formed through dynamical interactions among already formed BHs are expected to have isotropically distributed spin orientations (e.g., Sigurdsson & Hernquist 1993; Portegies Zwart & McMillan 2002; Rodriguez et al. 2015, 2016b; Stone et al. 2017b). In contrast, BBHs formed from isolated binary evolution are expected to have BH spins preferentially aligned with the binary orbital angular momentum (Tutukov & Yungelson 1993; Belczynski et al. 2016b, 2020; Bavera et al. 2020, 2021a). Observed BBHs spins have a small but non-zero magnitude with half of them being below $|\vec{\chi}| = 0.25$ (Wysocki et al. 2019; Roulet & Zaldarriaga 2019; Miller et al. 2020; García-Bellido et al. 2021; Biscoveanu et al. 2021; Abbott et al. 2021f). It was reported by several studies, including the official *LIGO-Virgo* collaboration analysis, that some of the observed BBHs have misaligned BH spin orientation with the orbital angular momentum (Talbot & Thrane 2017; Abbott et al. 2019a, 2021f). However, other studies have challenged such conclusions by applying a different population model to interpret the data (Roulet et al. 2021; Galaudage et al. 2021). Both Roulet et al. (2021) and Galaudage et al. (2021) analysis claim that there is no evidence for a negative $\chi_{\rm eff}$ sub-population in the data when analyzing the observed BBH sample with an astrophysical motivated prior, which allows for a sub-population of BHs with negligible spins. We point the reader to the recent review paper by Callister et al. (2022) who recently summarised what is under debate about BH spins. Given the huge potential of BHs spins in disentangling the origin of merging BBHs, my Ph.D. thesis focuses on deepening our current understanding of the origin of spin in BBHs formed through isolated binary evolution.

1.4.4 Correlations between binary black-hole properties

Recent studies have searched for correlation among BBH parameters such as mass, spin, and redshift in the observed BBHs. Such correlations can be the result of evolutionary processes within a single formation channel, or the presence of multiple populations arising from distinct formation channels. We discuss here the highlights of these studies.

Callister et al. (2021b) and Abbott et al. (2021f) found statistically significant evidence for an anti-correlation between the distribution of the effective spin parameter, $\chi_{\rm eff}$, and the binary mass ratio, q, where the mean of the $\chi_{\rm eff}$ distribution increases for extreme mass ratios. This result was also corroborated by the recent analysis of Biscoveanu et al. (2022). This anti-correlation is unexpected for most individual BBH formation models, with the possible exception of: BBH formation in AGN disks (e.g., McKernan et al. 2012, 2018, 2020; Stone et al. 2017a; Tagawa et al. 2021), super-Eddington accretion

during stable mass transfer for systems formed via isolated binary evolution (Bavera et al. 2021a; Broekgaarden et al. 2022; Zevin & Bavera 2022), or the superposition of multiple populations formed via independent channels with unique signatures.

Safarzadeh et al. (2020) looked for potential correlation between $\chi_{\rm eff}$ with various BH mass parameters of the binary, e.g., primary BH mass m_1, the chirp mass $M_{\rm chirp}$, and total mass M. The authors found a possible negative correlation between the mean $\chi_{\rm eff}$ and the parameters $m_1, M_{\rm chirp}$ and M, and a possible positive correlation between the effective spin and mass dispersion. However, neither finding reached high statistical significance at $\sim 80\%$ credibility depending on the mass and correlation parameters. One might interpret this finding as potential evidence for dynamically formed BBHs, which via successive mergers, might lead to more massive BHs and larger BH spins (e.g., Portegies Zwart & McMillan 2002; Miller & Lauburg 2009; Benacquista & Downing 2013; Rodriguez et al. 2015, 2019; Antonini & Rasio 2016; Fishbach et al. 2017; Kimball et al. 2020; Gerosa & Fishbach 2021). Similarly, Franciolini & Pani (2022) found evidence of an evolving $\chi_{\rm eff}$ distribution with increasing M by including the analysis the new events of the GWTC-3 catalog. These last authors interpret this correlation as evidence for either an astrophysical dynamical formation channel or primordial origin. However, one caveat of both analyses is that they do not account for potential correlations with the BBH merger redshift, which might bias the results.

Fishbach et al. (2021) and Abbott et al. (2021f) looked for potential correlations between the BBH mass and redshift distributions. Such correlations are expected for BBHs formed via isolated binary evolution channels as heavier BHs are predicted to form from low metallicity stellar progenitors, which are more abundant at higher redshifts (Belczynski et al. 2020; Mapelli et al. 2019; Neijssel et al. 2019). This might be the case, e.g., for systems formed via the CE formation channel at low metallicities (higher redshifts) which tend to widen less and have shorter delay times compared to higher metallicities (lower redshifts) (Bavera et al. 2020, 2021a; Broekgaarden et al. 2021b). However, see van Son et al. (2021), who pointed out that the majority of BBHs formed through isolate binary evolution with masses above $30\,M_\odot$ are formed from the SMT channel which produces wider BBHs compared to the CE channel and, hence, massive BBHs might become more scarce relative to less massive BBH systems due to their longer delay times. Additionally, Fishbach et al. (2021) find a redshift dependence of the maximum BH mass by fitting a model which assumes the BH mass distribution has a sharp upper cutoff dictated by PISNe with the observations.

Biscoveanu et al. (2022) recently found that the $\chi_{\rm eff}$ distribution broadens for increasing redshift. This might be explained by the existence of multiple sub-populations arising from distinct formation channels, each occupying a different region in the $\chi_{\rm eff} - z$ parameter space. For example, the $\chi_{\rm eff} \simeq 0$ component might be reconducted to BBHs dynamically assembled in dense stellar environments where BH birth spins are negligible (e.g., Portegies Zwart & McMillan 2002; Miller & Lauburg 2009; Benacquista & Downing 2013; Rodriguez et al. 2015, 2019; Antonini & Rasio 2016; Fishbach et al. 2017; Kimball et al. 2020; Gerosa & Fishbach 2021). In contrast, the preferentially-positive $\chi_{\rm eff}$ component corresponds to a sub-population of systems formed via isolated binary evolution in galactic fields experiencing tidal spin up (Gerosa et al. 2018; Qin et al. 2018; Zaldarriaga et al. 2018; Belczynski et al. 2020; Bavera et al. 2020, 2021a, 2022a). However, Biscoveanu et al. (2022) points out that such a mixture of two sub-populations

generally leads to a shift in the mean of the $\chi_{\rm eff}$ distribution with redshift. On the other hand, their analyses strongly favor the evolution of the width of the $\chi_{\rm eff}$ distribution with redshift.

1.4.5 Hierarchical Bayesian model selection

A quantitative and unbiased constraint to the formation mechanisms of coalescing BBHs comes from considering many prominent BBH formation channels and encompassing the wide range of model prescriptions for uncertain physical processes, which, as previously discussed, can affect BBH population properties in highly degenerate ways. Given the rapidly growing catalog of BBHs, we are now at the stage where such high-dimensional, multi-channel model selection, exploiting the different signatures of the aforementioned channels, can be informative. The statistical methodology employed to constrain the formation models and using the catalog of GW events, is known as hierarchical Bayesian model selection (see, e.g., Mandel et al. 2019; Vitale et al. 2020). The selection effects of the GW detectors are also accounted for this Bayesian framework. This approach allows for both measurement uncertainty in individual measurements and, crucially, selection biases on the population of measurements. The latter is an important bias that should be carefully considered to correctly extract the parameters of the intrinsic (underlying) BBH population, namely what a detector on Earth with infinite sensitivity would observe. This technique can be employed to constrain model uncertainties and obtain constraints on the branching fractions of formation channels (e.g., Bouffanais et al. 2021b; Franciolini et al. 2021; Wong et al. 2021; Zevin et al. 2021a; Mapelli et al. 2022). It is important to notice that only a model selection analysis that considers all model uncertainties and all BBH formation channels will lead to an unbiased and conclusive answer to which channel dominates the formation mechanism of merging BBHs. However, the current large number of proposed formation models and their model uncertainties, combined with the still limited observational sample, make this task currently computationally infeasible.

1.5 Modeling isolated binary evolution and populations

1.5.1 Binary population synthesis

Understanding BH mergers formed from the evolution of isolated binaries, requires modeling the formation and evolution of the progenitor systems. This is often achieved with a technique known as binary population synthesis. The evolution of stars and binaries can be modeled in either of two methods "detailed" and "rapid", which different in computational speed and accuracy.

The "detailed" method refers to detailed stellar structure and binary-evolution calculations. It simultaneously solves each star's stellar structure equations and the orbital evolution. Example of codes which use this technique are, e.g., `BEC` (Heger et al. 2000; Heger & Langer 2000), `BINSTAR` (Siess et al. 2013), the `Cambridge STARS` code (Eggleton 1971; Pols et al. 1995; Eldridge & Tout 2004; Stancliffe & Eldridge 2009), `MESA` (Paxton et al. 2011, 2013, 2015, 2018, 2019), and the `TWIN` code (Nelson & Eggleton 2001; Eggleton & Kiseleva-Eggleton 2002). A single system detailed binary simulation employing one of these codes typically requires $\sim$ 10–100 CPU hours (Paxton et al. 2019). Therefore studies that use detailed binary-evolution calculations often cover the initial binary parameter space in rectilinear grids

by varying, e.g., the masses of the two stars and the binary's orbital period (e.g., Nelson & Eggleton 2001; Podsiadlowski et al. 2002; de Mink et al. 2007; Marchant et al. 2017; Qin et al. 2018, 2019; du Buisson et al. 2020; Langer et al. 2020; Laplace et al. 2020; Misra et al. 2020; Laplace et al. 2021). Because of the computational cost, this approach is limited to a small part of the initial parameter space or focuses on a specific evolutionary phase.

The "rapid" method uses faster approximate methods typically aimed at the binary population synthesis approach. Over the last two decades, many general purpose binary population synthesis codes also known as *rapid* or *parametric* have been developed, e.g., `binary_c` (Izzard et al. 2004, 2006, 2009), `BPASS`[1] (Eldridge et al. 2017), the `Brussels' code` (Vanbeveren et al. 1998a,b), `BSE` (Hurley et al. 2002), `ComBinE` (Kruckow et al. 2018), `COMPAS` (Riley et al. 2022), `COSMIC` (Breivik et al. 2020), `MOBSE` (Giacobbo et al. 2018), the `Scenario Machine` (Lipunov et al. 1996, 2009), `SEVN` (Spera et al. 2015), `SeBa` (Portegies Zwart & Verbunt 1996; Toonen et al. 2012), `StarTrack` (Belczynski et al. 2002, 2008), and `TRES` (Toonen et al. 2016). Binary population synthesis modeling first generates initial binary populations, whose properties are randomly sampled from probability distributions that have been observationally constrained. Then, the population is evolved with parametrized stellar evolution tracks, which are fitted to detailed calculations to produce observable properties of the target population and rely on approximate prescriptions for modeling binary interactions (see next section for a discussion on the uncertainties introduced by this method). For a large enough sample of binaries, this technique can provide valuable insights into the expected rate and observable distribution of BBH properties, the different evolutionary pathways that lead to the formation of these systems, and the effect that different physical processes have on their evolution. These have been used in studies of a wide variety of binary populations, including the formation of merging BBHs. The key advantage of these codes is that they are computationally efficient, evolving a binary system in a fraction of a second. For most studies, one would need to model the evolution of many millions of binaries in a reasonable computational time.

1.5.2 `POSYDON`: A general-purpose population synthesis code with detailed binary-evolution simulations

The majorly of current rapid binary population synthesis codes approximate each star's evolution, employing either fitting formulae (e.g., `SSE`; Hurley et al. 2000) or look-up tables (e.g., `COMBINE`; Kruckow et al. 2018) for the properties of single stars based on grids of pre-calculated detailed, single-star models. The effects of binary interactions such as, e.g., mass-transfer episodes and tidal interactions are modeled using approximate prescriptions and parametrizations. Parametric binary population synthesis codes operate under the implicit assumption that the binary components have properties identical to single stars of the same mass in thermal equilibrium (e.g., abundance profiles, core sizes, mass-radius relations, and response to mass-loss). They also lack information about the star's internal structure at different

[1] In contrast to the other rapid population synthesis code, `BPASS` uses extensive grids of detailed binary evolution models computed with a custom version of the `Cambridge STARS` binary evolution code (Stancliffe & Eldridge 2009). In the grids of binary-star models employed in `BPASS`, both the primary and the secondary stars are followed in detail, but for computational-cost reasons only one at a time. During the primary's evolution, the properties of the secondary star are approximated by formulae based on single-star models (Hurley et al. 2000). Subsequently, once the modeling of the primary's evolution is completed, the secondary star's evolution is re-computed, accounting for mass-transfer and rejuvenation effects.

critical evolutionary phases, e.g., at the onset of a dynamically unstable mass transfer, at the end of stable and unstable mass-transfer phases, or the core collapse, which might introduce systematic uncertainties and inaccuracies. Instead, these caveats could be avoided by employing detailed stellar structure and binary-evolution simulations. Focusing on aspects that are relevant to the formation of BBH: detailed models (i) allow for a self-consistent estimation of the mass-transfer rate, especially during thermal-timescale mass-transfer phases, and therefore an accurate assessment of mass-transfer stability; (ii) allow for a more accurate description of the type and properties of the formed BH as well as any potential associated transient events, since the internal structure of pre-core-collapse stars is known, (iii) account for the transport of angular momentum between and within the binary components, including back-reaction on the structure and evolution of each star (e.g., rotational mixing which induces CHE), and (iv) allow for the self-consistent modeling of the end of a mass transfer phase (e.g., accounting for a potential partial stripping of the envelope). All the mentioned points are crucial in determining the evolutionary pathways leading to BBH formation and their observable properties.

During my Ph.D., I contributed as one of the key developers of the next general-purpose population synthesis code, which addresses the above points by employing detailed `MESA` stellar structure and binary-evolution simulations throughout the whole evolution of the binaries. The `POSYDON` (POpulation SYnthesis with Detailed binary-evolution simulatiONs) code was recently publicly released[2] (Fragos et al. 2022). In its first software version, `POSYDON` is limited to the evolution of stars of solar metallicity and binaries where the primary star is massive enough to form a BH or a NS. Future releases, which are already in development, will lift these limitations. The use of `POSYDON` enables the self-consistent treatment of physical processes in stellar and binary evolution, including realistic mass-transfer calculations and assessment of stability, internal angular-momentum transport and tides, stellar-core sizes, mass-transfer rates, and orbital periods. We foresee that `POSYDON` will have drastically impact and improve our understanding of binary evolution in general.

1.5.3 The hybrid binary population synthesis approach

At the beginning of my Ph.D. studies, a complete and fully functional population synthesis code that employs detailed stellar structure and binary-evolution simulation such as `POSYDON` did not exist. Furthermore, in its current version, `POSYDON` stellar and binary simulation tracks target only solar metallicity stellar populations, while the detected merging BHs are expected to have formed at lower-metallicity environments. Therefore, to overcome some limitations of the `POSYDON` (e.g., metallicity) and the current rapid population synthesis codes (e.g., accuracy), in my research projects I employed a hybrid technique between the two approaches. I combined detailed `MESA` stellar and binary simulations targeting key evolutionary phases of BBH progenitors with publicly available rapid population synthesis codes. This hybrid technique allowed me to gain accurate BBH property distributions such as, e.g., the distribution of BH spins rising from the BH-WR tidal spin up phase (see §2.1 and §2.2). Moreover, this allowed me to follow in detail the stellar profile core collapse of highly rotating massive stars which is not only important for determining the BH spins but it might also give rise to electromagnetic counterparts (see §4.1). In addition, this technique allowed me to obtain a complete BBH model of isolated binary evolution including

[2]See the `POSYDON` portal `https://posydon.org`

the evolutionary pathway through CHE, which cannot be modeled with most standard rapid population synthesis codes (see §3.2, §3.3, and §4.1).

Chapter 2

Dancing with the stars

Massive stars in close binary systems interact during their evolution. This chapter studies the population of massive binaries that evolve to become merging BBHs through the isolated binary evolutionary channel. We focus on studying the binary interactions responsible for determining the BBH spins in the CE and SMT evolutionary pathways (see §1.3.1.1). This is done by combining detailed `MESA` binary simulations with rapid binary population synthesis techniques (see §1.5.3). Our models allow us to make predictions of BBH observable distributions, which can then be leveraged to interpret the origins of coalescing BBHs detected by the *LIGO-Virgo* GW detectors.

2.1 The origin of spin in merging binary black holes

2.1.1 A brief introduction

Isolated BHs, located in systems where binary interactions prior to the collapse of the helium core do not cause significant spin-up, are thought to be born with negligible spins due to efficient angular-momentum transport in stellar interiors (Spruit 1999, 2002; Fuller & Ma 2019, but see also the discussion in §1.3.1.1). Nevertheless, during the BH-WR evolutionary phase of BBH progenitors, tidal interaction can induce spin-up via tidal torques exercised by the first-born BH on its stellar companion (Qin et al. 2018; Zaldarriaga et al. 2018; Piran & Piran 2020; Fuller & Lu 2022). Hence, quantifying the fraction of tidally spun-up BBHs formed from isolated binary evolution is timely and critical in interpreting the origin of currently detected coalescing BHs (see §1.4.3). In this project, we used a hybrid approach to combine detailed binary BH-WR `MESA` simulations based on Qin et al. (2018) with the `COMPAS` (Riley et al. 2022) rapid binary population synthesis model of Neijssel et al. (2019) targeting the CE formation channel. See §1.5.3 for further details about the hybrid binary population synthesis technique.

The discussed CE formation channel is thought to lead to the formation of close BH-WR systems, which potentially spin up. In practice, the efficiency of tides is highly dependent on the orbital separation (Zahn 1977; Hut 1981), which can be altered by metallicity-dependent stellar-wind mass-loss rates (Vink et al. 2001). At lower metallicities, binaries widen on average less because of weaker stellar-wind mass-loss rates, and tides will more efficiently spin up the second-born BH progenitor than at larger metallicities

(Qin et al. 2018). In this project, we aim to interpret the future (now current) GW detectable BBH population by obtaining the effective spin ($\chi_{\rm eff}$) distribution of BBHs formed through the CE formation channel. While working on this project, the *LIGO-Virgo* collaboration released the first catalog of GW transient events, GWTC-1, with a sample of ten BBHs (Abbott et al. 2019b). Thanks to this sample, we could leverage BBH observations to verify our theoretical model predictions.

2.1.2 Manuscript

The conducted study Bavera et al. (2020) was published in *Astronomy & Astrophysics* in March 2020. The arXiv open-access version of the manuscript is presented in the following pages.

Astronomy & Astrophysics manuscript no. aanda
January 27, 2020
©ESO 2020

arXiv:1906.12257v3 [astro-ph.HE] 24 Jan 2020

The origin of spin in binary black holes:

Predicting the distributions of the main observables of Advanced LIGO

Simone S. Bavera[1,⋆], Tassos Fragos[1], Ying Qin[1], Emmanouil Zapartas[1], Coenraad J. Neijssel[2], Ilya Mandel[3,2,4], Aldo Batta[5,6,7], Sebastian M. Gaebel[2], Chase Kimball[8], Simon Stevenson[9,4]

[1] Geneva Observatory, University of Geneva, Chemin des Maillettes 51, 1290 Versoix, Switzerland
[2] Birmingham Institute for Gravitational Wave Astronomy and School of Physics and Astronomy, University of Birmingham, Birmingham, B15 2TT, United Kingdom
[3] Monash Centre for Astrophysics, School of Physics and Astronomy, Monash University, Clayton, Victoria 3800, Australia
[4] ARC Centre of Excellence for Gravitational Wave Discovery – OzGrav
[5] Instituto Nacional de Astrofísica, Óptica y Electrónica, Tonantzintla, Puebla 72840, México
[6] Consejo Nacional de Ciencia y Tecnología, Av. Insurgentes Sur 1582, Col. Crédito Constructor, CDMX, C.P. 03940, Mexico
[7] Niels Bohr Institute, University of Copenhagen, Blegdamsvej 17, 2100 Copenhagen, Denmark
[8] Center for Interdisciplinary Exploration and Research in Astrophysics (CIERA), Northwestern University, 2145 Sheridan Road, Evanston, IL 60208, USA
[9] Centre for Astrophysics and Supercomputing, Swinburne University of Technology, Hawthorn, VIC 3122, Australia

Accepted on January 21, 2020

ABSTRACT

Context. After years of scientific progress, the origin of stellar binary black holes is still a great mystery. Several formation channels for merging black holes have been proposed in the literature. As more merger detections are expected with future gravitational-wave observations, population synthesis studies can help to distinguish between them.

Aims. We study the formation of coalescing binary black holes via the evolution of isolated field binaries that go through the common envelope phase in order to obtain the combined distributions of observables such as black-hole spins, masses and cosmological redshifts of mergers.

Methods. To achieve this aim, we used a hybrid technique that combines the parametric binary population synthesis code COMPAS with detailed binary evolution simulations performed with the MESA code. We then convolved our binary evolution calculations with the redshift- and metallicity-dependent star-formation rate and the selection effects of gravitational-wave detectors to obtain predictions of observable properties.

Results. By assuming efficient angular momentum transport, we are able to present a model that is capable of simultaneously predicting the following three main gravitational-wave observables: the effective inspiral spin parameter $\chi_{\rm eff}$, the chirp mass $\mathrm{M_{chirp}}$ and the cosmological redshift of merger $z_{\rm merger}$. We find an excellent agreement between our model and the ten events from the first two advanced detector observing runs. We make predictions for the third observing run O3 and for Advanced LIGO design sensitivity. We expect approximately 80% of events with $\chi_{\rm eff} < 0.1$, while the remaining 20% of events with $\chi_{\rm eff} \geq 0.1$ are split into $\sim 10\%$ with $\mathrm{M_{chirp}} < 15\,\mathrm{M_\odot}$ and $\sim 10\%$ with $\mathrm{M_{chirp}} \geq 15\,\mathrm{M_\odot}$. Moreover, we find that $\mathrm{M_{chirp}}$ and $\chi_{\rm eff}$ distributions are very weakly dependent on the detector sensitivity.

Conclusions. The favorable comparison of the existing LIGO/Virgo observations with our model predictions gives support to the idea that the majority, if not all of the observed mergers, originate from the evolution of isolated binaries. The first-born black hole has negligible spin because it lost its envelope after it expanded to become a giant star, while the spin of the second-born black hole is determined by the tidal spin up of its naked helium star progenitor by the first-born black hole companion after the binary finished the common-envelope phase.

Key words. black-hole spin – isolated field binaries – common envelope channel – gravitational waves – aLIGO

1. Introduction

During the first and second observing runs O1/O2 of the advanced gravitational-wave (GW) detector network, Advanced LIGO (aLIGO) (Aasi et al. 2015) and Advanced Virgo (Acernese et al. 2015) detected 10 GWs from binary black holes (BBHs). With the third observing run O3 that just started, this number is expected to increase. In the near future, sometime around 2020, the detectors will be upgraded to reach design sensitivity and we expect the detection of hundreds of such mergers (Abbott et al. 2019).

To date, the origin of these BBHs is still an open scientific question. Various explanations of different formation channels for merging BBHs have entered into the scientific literature (see, e.g., Abbott et al. 2016b; Miller 2016; Mandel & Farmer 2018, for reviews). The most popular ones are as follows: isolated binary evolution where (i) the stars go through a common envelope (CE) phase due to an unstable mass transfer after the formation of the first-born black hole (BH) (e.g., Smarr & Blandford 1976; van den Heuvel 1976; Tutukov & Yungelson 1993; Kalogera et al. 2007; Postnov & Yungelson 2014; Belczynski

⋆ E-mail:simone.bavera@unige.ch

et al. 2016a), (ii) massive stars with a nonextreme mass ratio after the formation of the first-born BH goes through stable mass transfer avoiding the CE phase (e.g., van den Heuvel et al. 2017; Pavlovskii et al. 2017; Inayoshi et al. 2017), (iii) massive stars in close orbits experiencing strong internal mixing go through chemically homogeneous evolution and produce massive BBHs (e.g., de Mink et al. 2009; Mandel & de Mink 2016; Marchant et al. 2016); dynamical formation (iv) in globular clusters and (v) galactic nuclear clusters where the BBHs are formed from stars not born in the same binary (e.g., Sigurdsson & Hernquist 1993; Portegies Zwart & McMillan 2000; Miller & Lauburg 2009; Rodriguez et al. 2015; Antonini et al. 2016); or (vi) Lidov-Kozai resonance bringing the inner binary to merge in hierarchical triple systems (e.g., Silsbee & Tremaine 2017). All of these scenarios possess some significant uncertainties in the prediction of merger rates due to the poorly constrained underlying physics or unconstrained distributions of initial conditions. The merger rate predictions for the isolated binary evolution via the CE phase are consistent (Abbott et al. 2017a) with the observed rate of BBH mergers of around $\sim 24 - 112\ \mathrm{Gpc^{-3}yr^{-1}}$ (Abbott et al. 2018b). The same holds for the stable mass transfer channel (Neijssel et al. 2019), while formation via chemically homogeneous evolution could yield tens of mergers per $\mathrm{Gpc^{-3}yr^{-1}}$ (Mandel & de Mink 2016; Marchant et al. 2016). Finally, predicted rates via the dynamical formation channel are closer to the lower end of the observed range (Fragione et al. 2018; Park et al. 2017); for example Rodriguez & Loeb (2018) find $4 - 18\ \mathrm{Gpc^{-3}yr^{-1}}$ from globular cluster in the local Universe.

Any astrophysical BH can be fully described by only two quantities: its mass M and its dimensionless spin parameter, $\mathbf{a} = c\mathbf{J}/(GM^2)$, where $\mathbf{J}$ is the angular momentum of the BH. Using matched-filtering analysis, GW observations provide estimates for each of the above-mentioned quantities for both parent BHs. Although individual BH spin magnitudes and orientations are poorly constrained with present GW measurements, the effective inspiral spin parameter

$$\chi_{\rm eff} = \frac{M_1\mathbf{a}_1 + M_2\mathbf{a}_2}{M_1 + M_2}\hat{\mathbf{L}}\,, \tag{1}$$

the mass-weighted spin of the system projected onto the orbital angular momentum $\mathbf{L}$, is reasonably well constrained (Abbott et al. 2019). This is explained by the fact that the leading spin-orbit-coupling term in the post-Newtonian waveforms is dominated by this parameter (Santamaría et al. 2010). From the ten observed $\chi_{\rm eff}$, 8 are consistent with 0 within the 90% credible interval while the remaining two are determined with a positive value of $\chi_{\rm eff}$. Another important quantity characterizing the waveforms is the chirp mass

$$M_{\rm chirp} = \frac{(M_1M_2)^{3/5}}{(M_1 + M_2)^{1/5}}\,, \tag{2}$$

which, to first-order approximation, determines the frequency evolution of the GW signal emitted during the BBH's inspiral phase (Cutler & Flanagan 1994). The ten observed $M_{\rm chirp}$ span the range of $7.9 - 35.7\ \mathrm{M_\odot}$ with a pile-up around $26\ \mathrm{M_\odot}$. In addition, the luminosity distance can be measured using the GW amplitude and, assuming a cosmological model, the cosmological redshift of the merger can be inferred. The distributions of these parameters for a population of merging BBHs can be used to distinguish between different formation channels. As pointed out in the literature, the effective inspiral spin parameter is sensitive to the evolutionary path of BBHs (see e.g., Rodriguez et al. 2016). For isolated field binary channels, the spins of the two BHs are expected to be preferentially aligned with the orbital angular momentum, whereas, assuming effective exchange interaction, the spin directions of BBHs formed in dynamical environments are expected to be randomly, isotropically distributed (Abbott et al. 2016b; Farr et al. 2017).

In this study, we focus on BBHs formed through classical isolated binary evolution that go through the CE phase. The main evolutionary phases of this pathway are now summarized. At the beginning, the stars are born in a relatively wide binary where the initially more massive star, called the "primary", reaches the end of its main sequence first. At this stage the primary star expands its hydrogen-rich envelope past the Roche-lobe and begins transferring mass to the secondary until it loses its entire envelope, leaving a naked helium-burning star. Following wind-driven mass loss the primary collapses to form a BH. When the secondary reaches the end of its main sequence, the process repeats itself in reverse. This time, the mass transfer onto the black hole is unstable and this leads to the formation of a CE of gas around the binary (Paczynski 1976). The physical details of this phase are still not fully understood (Ivanova et al. 2013). The drag force on the BH from the envelope leads to a rapid inspiral and the dissipated orbital energy leads to the expulsion of the envelope and a decay of the orbital separation by more than two orders of magnitude. At this stage we are left with the immediate progenitor of the BBH system, namely a BH - He-star binary. Finally, the secondary eventually collapses into a BH and potential asymmetries in the core collapse may impart a kick on the newly formed BH and alter the orbit further. Eventually, due to energy and angular momentum loss from GW emission, the BBH system can coalesce into a single, more massive BH.

Previous theoretical works focused on the first few observed GW events suggest that these BBHs are consistent with having been formed through the CE formation channel (Stevenson et al. 2017; Giacobbo et al. 2018; Kruckow et al. 2018). These authors show how, at the respective appropriate metallicity regime, the observed BH masses are produced by their binary evolution models. Furthermore, their inferred merger rates are consistent with the one obtained from GW observations. In another study in favor of the CE formation channel, Belczynski et al. (2016b) carried out a detailed analysis of merger rates and found that BBHs formed though this channel should dominate the event rates in Advanced LIGO and Virgo.

In the CE formation channel, the physical process determining the spin of the first-born BH is the efficiency of angular momentum (AM) transport through the evolution of the progenitor star during the red supergiant phase. From observations of astroseismology (Fuller et al. 2014; Cantiello et al. 2014), as well as neutron star and white dwarf spins (Heger et al. 2005; Suijs et al. 2008), it is known that this mechanism must be efficient (Spruit 1999, 2002; Fuller et al. 2019). Thus, upon expansion, the initial angular momentum is mostly transported to the outer layers of the star which are subsequently lost due to Roche-lobe overflow mass transfer and wind mass loss. This leads to very slowly spinning BHs ($a_1 \simeq 0$) as was shown by Qin et al. (2018) (see also Fuller & Ma 2019). Assuming efficient AM transport, the angular momentum of the second-born BH is mainly determined by the net effect of the stellar winds and the tidal interaction of the BH-He-star binary system. This is because any initial or acquired rotation during the evolution of the secondary is erased through mass transfer and wind mass loss by the time it becomes a He-star. Several studies attempted to model the last evolutionary phase of this channel and derived constraints on the spin using analytical arguments and semi-analytical calculations (Kushnir et al. 2016; Hotokezaka & Piran 2017; Zaldar-

riaga et al. 2018). These studies found out that around half of the secondary BHs have zero spin and the other half are maximally spinning. When using detailed models to simulate the binary evolution and the stellar structure of the two components, Qin et al. (2018) did not reproduce this prediction of a bi-modal distribution of spins. Both Hotokezaka & Piran (2017) and Zaldarriaga et al. (2018) results are based on the approach outlined in Kushnir et al. (2016). Compared to the detailed binary simulations of Qin et al. (2018), these authors did not model self-consistently the orbit evolution of the binary due to the combined effects of tides and stellar winds, which in most cases leads to the widening of the orbit. Even when tides are initially efficient at synchronizing the spin of the helium star to the orbit, such wind-driven orbital widening can lead to tidal decoupling. Ignoring this effects underestimates the impact of stellar winds on the final spin of the second-born BH. Moreover they used approximate timescales for the process of tidal synchronization that do not take into account changes in the structure of the star during its lifetime and assumed that tides allow the He-star to remain tidally locked indefinitely. These approximations lead to results that disagree with what is found in our detailed binary simulations. Belczynski et al. (2017) used parametric binary population synthesis models, which share all the same approximations as the studies discussed above, to compare three different prescriptions for the efficiency of AM transport. They found that efficient AM transport is favored, as it results to distributions of $\chi_{\rm eff}$ and BH masses qualitatively consistent with observations, while inefficient AM transport would lead to rapidly spinning BHs which are currently not observed by aLIGO.

In this paper, we present a model capable of predicting simultaneously the spin, mass and redshift distributions of coalescing BBHs formed from isolated field binaries that go through the CE phase. This aim is achieved by combining the parametric binary population syntheses code COMPAS with the detailed MESA stellar structure and binary evolution simulations. The study is structured as follows. In Sec. 2 we explain the methods used to generate a Monte-Carlo population of isolated field BBHs and how we take into account the redshift and metallicity dependence of the star formation rate and the observational selection effects. In Sec. 3 we present our main results and make detailed predictions for observing runs of the future GW detector network, distinguishing three regions of the BBH parameter space. Our model is able to successfully reproduce the observed $\chi_{\rm eff}$ distribution providing strong support for the CE channel being the dominant formation channel. We then discuss our results in Sec. 4 where we compare our work to the current literature and demonstrate the importance of detailed binary evolution calculations. Finally, the conclusions of our work are given in Sec. 5.

2. Method

We use the parametric binary population synthesis code COMPAS (e.g., Stevenson et al. 2017, 2019; Barrett et al. 2017, 2018; Vigna-Gómez et al. 2018; Neijssel et al. 2019) to evolve isolated stellar binaries until the formation of BH - He-star systems, namely the immediate progenitors of BBHs. In Sec. 2.1 we briefly describe the COMPAS-model assumptions used in the simulation. Since we are not interested in a parameter study, we specifically picked a model capable of reproducing a BBHs merger rate which is in agreement with the observed one from Abbott et al. (2019). For the last step of the evolution, which we consider to be the one that determines the spin distribution of the secondary BH, we use the stellar structure and evolution code MESA (Paxton et al. 2011, 2013, 2015, 2018, 2019) to simulate the evolution of the binary systems. Assuming that the first-born black hole can be treated as a point-like particle, this approach allows us to track the angular momentum profile evolution of the He-star until the formation of the secondary BH (see Sec. 2.2). In Sec. 2.3, we explain in detail how we treat the collapse of the He-stars into BHs. Finally, taking into account the redshift dependence of metallicity, star-formation rate (SFR) and aLIGO sensitivity, we can distribute the population across cosmic time and compute the expected detection rate (see Sec. 2.5).

2.1. COMPAS model assumptions

We use the results from the simulations of Neijssel et al. (2019) and here we only highlight the main physical assumptions. We assume that the underlying stellar population spans the mass range $0.01\,{\rm M}_\odot < m_1 < 200\,{\rm M}_\odot$ following the initial mass function of Kroupa (2001). The mass distribution of the less massive secondary star is given by $m_2 = m_1 q_0$ where q_0 is the initial mass ratio ($0 < q_0 < 1$) drawn from a flat distribution (Sana et al. 2012). We are interested in binaries with a primary star that ends up forming a BH, thus we restrict the initial mass distribution of primary masses between $5\,{\rm M}_\odot < m_1 < 150\,{\rm M}_\odot$. This means we only model a fraction $f_{\rm corr}$ of the underlying stellar population mass. We calculate this by assuming a binary fraction of 70% (Sana et al. 2012), see Appendix A. We assume that, at formation, binaries are distributed uniformly in log-orbital separation restricted to $0.1 < A/{\rm AU} < 1000$ (Abt 1983) and have zero eccentricity. We assume that all these distributions are independent from each other as well as independent of metallicity. For the metallicity distribution of binaries we divide uniformly in 30 bins the log-metallicity range $Z \in [0.0001, 0.0349]$. We then evolve three million binaries per metallicity bin ΔZ_j with a total of star forming mass on the order of $M_{{\rm sim},\Delta Z_j} = 6.5 \cdot 10^7\,{\rm M}_\odot$.

COMPAS evolves stars according to the stellar models of Pols et al. (1998) and uses analytical fits of these models to rapidly evolve binaries (Hurley et al. 2000, 2002). We adopt wind mass loss rates as prescribed by Hurley et al. (2000) for stars with effective temperatures smaller than 12,500 K, and for hotter stars the winds of Vink et al. (2001) as implemented by Belczynski et al. (2008). If stars during their evolution cross the Humphrey-Davidson limit (Humphreys & Davidson 1994) and enter a region of the Hertzsprung-Russel diagram in which no stars are observed, we apply an additional wind mass loss rate of $1.5 \cdot 10^{-4}\,{\rm M}_\odot\,{\rm yr}^{-1}$ (Belczynski et al. 2010).

When the primary star reaches the end of its main sequence, the star expands and loses its entire envelope through Roche-lobe overflow. In binaries where the first mass transfer episode is stable, the companion can accrete some mass with an efficiency that we assume depends on the ratio of the thermal timescales of the two stars (Hurley et al. 2002; Schneider et al. 2015; Neijssel et al. 2019), while the mass not accreted by the other star leaves the system carrying away the specific angular momentum of the accretor. Eventually, the envelope of the primary is stripped, leaving a naked helium burning star which, following wind-driven mass loss, collapses into a BH. The star collapses into a point-like BH following the "delayed" model of Fryer et al. (2012).

When the secondary reaches the end of its main sequence the process repeats in reverse and the mass transfer between the BH and the He-star can be either dynamically stable or unstable. Since we focus only on the subchannel that goes through the CE phase, we consider exclusively systems with dynamically unsta-

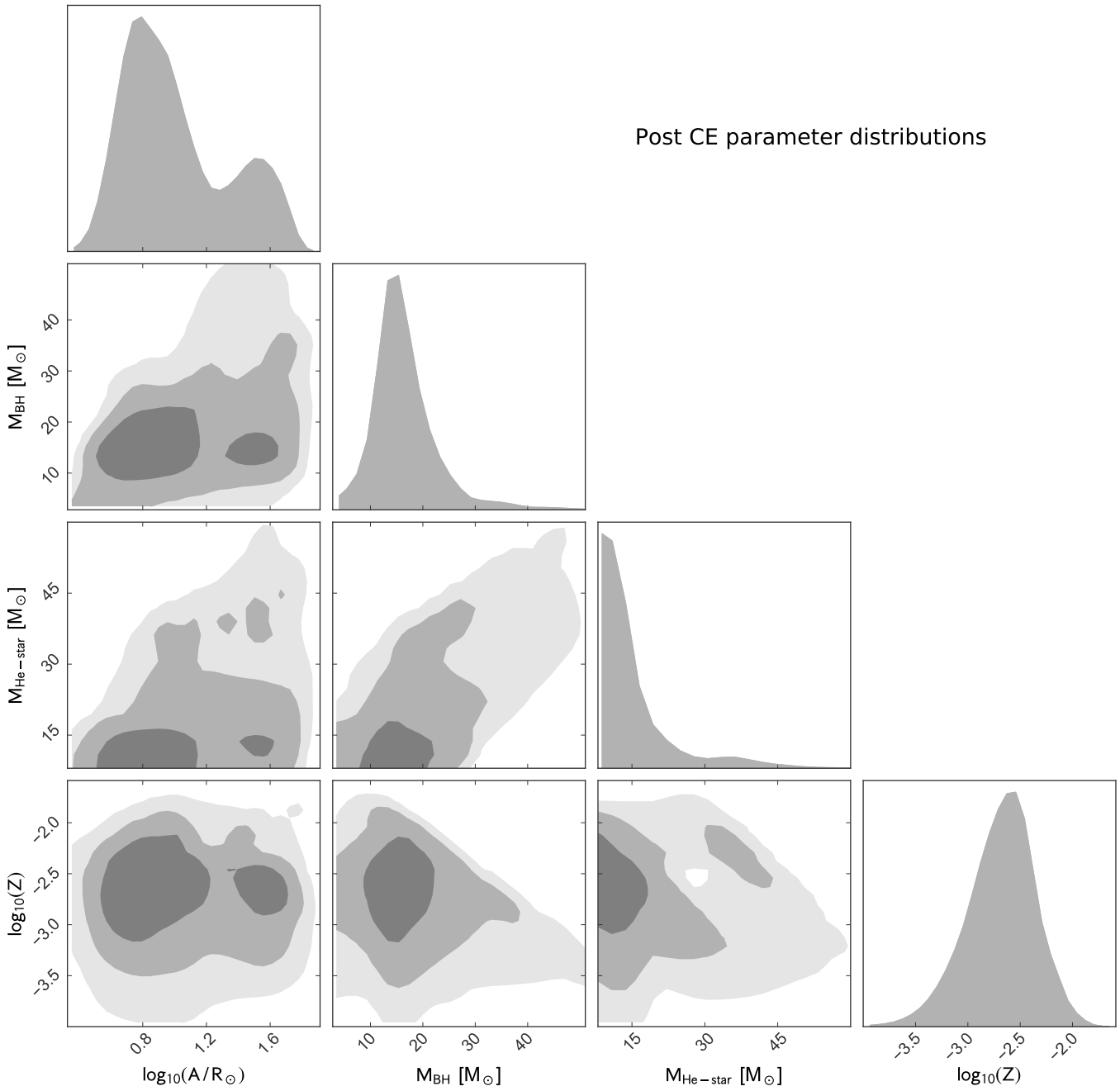

Fig. 1: Parameter distributions of the binary population after the CE phase. These BH – He-star binaries include systems that are going to form BH-NS binaries and BBHs with GW inspiral timescales bigger than the Hubble time. We show the distributions of orbital separation A, first-born BH mass M_{BH}, He-star mass $M_{He-star}$ and metallicity Z weighted by the integrated redshift- and metallicity-dependent SFR over the cosmic time (see Eq. B.10). The lighter shades represent larger contour levels, 68, 95 and 99%, respectively, constructed with pygtc (Bocquet & Carter 2016).

ble mass transfer which produces a non co-rotating CE of gas engulfing the binary. This represents only a subset of all merging binary black holes in the models of Neijssel et al. (2019). While uncertainties in the stability of mass transfer could reduce the importance of the non-CE channel, a self-consistent variation of the assumptions regarding mass transfer stability would also change the population of systems that evolve through a CE phase. This analysis is beyond the scope of this work, but could impact, in particular, our overall rate predictions for BBH mergers, which should be compared directly to Neijssel et al. (2019).

COMPAS uses the classical energy $\alpha_{CE} - \lambda$ formalism (Webbink 1984; de Kool 1990; Dewi & Tauris 2000; Xu & Li 2010) to parameterize the uncertainties in the physics of the CE phase. During this phase the two stars spiral in due to friction with the envelope. The loss of orbital energy can heat up and expand the envelope. The efficiency of this energy transfer is parameterized by the α_{CE} parameter which can vary (Livio & Soker 1988). We assume that all of the dissipated orbital energy goes into expelling the envelope, $\alpha_{CE} = 1$. The λ parameter, which characterizes the binding energy of the CE, depends on the structure of the donor's envelope (de Kool 1990). We chose our λ according

to the fits of Xu & Li (2010) as implemented by Dominik et al. (2012).

Within the CE subchannel, we distinguish two different scenarios for donor stars which are on the Hertzsprung-gap (HG). In the optimistic scenario we apply the usual $\alpha - \lambda$ prescription to evolve these systems. In the pessimistic scenario we assume that Hertzsprung-gap stars have not yet developed a sufficiently sharp density gradient at the core-envelope boundary to allow the inspiral during the CE to stop. Thus any CE event from donors in this evolutionary phase results in a merger which reduces the BBH merger rate (Belczynski et al. 2007). In this paper we present the results for the latter scenario. Both scenarios yield a similar distribution of spins, but the pessimistic one predicts fewer low-mass BHs compared to the optimistic. This is because a greater fraction of the total post-main-sequence expansion occurs during the HG for high-metallicity stars (Linden et al. 2010). Therefore, forbidding the channel with HG CE donors has a particularly strong effect at high metallicity, which yields lower-mass BHs due to metallicity-enhanced stellar winds.

In Fig. 1 we show the distributions of orbital separation, first-born BH mass, He-star mass and metallicity of our BH-He-star binaries after the CE phase. These distributions are weighted by the redshift- and metallicity-dependent star-formation rate (SFR) integrated over the cosmic time, see Eq. (B.10) in Appendix B. We note that these distributions include all binaries, including those systems that are going to become BH-NS binaries and BBHs with GW inspiral timescales longer than the Hubble time. After the CE phase the orbital separations are no longer uniformly log-distributed and most of the first-born BHs have masses smaller than 30 $M_\odot$. Moreover, we see that formation metallicities of progenitors of merging compact-object binaries follow a skewed log-normal distribution. This is because the mean metallicity of the Universe decreases as a function of the look-back time and the star-formation rate peaks at a redshift ~ 2 , that is a look-back time of ~ 10.5 Gyr, where most of the binaries are formed. These distributions are used as an initial condition for our detailed modeling.

2.2. MESA model assumptions

We perform detailed stellar structure and binary evolution calculations that take into account wind mass loss, internal differential rotation of the He-star and tidal interaction between the BH and the He-star. These simulations[1] are based on the work of Qin et al. (2018) and are adapted for MESA r-10398.

Stellar winds play an important role in binary evolution. Here, we take a slightly different approach compared to Qin et al. (2018), and we follow the wind prescriptions outlined in Belczynski et al. (2010), which is the same as the ones used in COMPAS. Namely, for helium stars we adopt a wind mass-loss rate of

$$\frac{dM}{dt} = 10^{-13} \left(\frac{L}{L_\odot}\right)^{1.5} \left(\frac{Z}{Z_\odot}\right)^{0.86} \mathrm{M_\odot\,yr^{-1}}\,, \tag{3}$$

where L and Z are the star's luminosity and metallicity, respectively. This prescription is a combination of Hamann & Koesterke (1998) and Vink & de Koter (2005) and takes into account He-star winds clumping and a strong dependence on the metallicity. Furthermore, we adopt $Z_\odot = 0.017$ as solar metallicity (Grevesse & Sauval 1998).

[1] The detailed list of parameters used for the simulations can be found at http://mesastar.org/results.

Tidal forces are responsible for synchronising the spin of the He-star with the orbit. We assume that the CE ejection leaves a circular binary, and the system remains circular during He-star evolution. It has been suggested that dynamical tides are dominant for stars with a radiative envelope and a convective core (Zahn 1977; Hut 1981). The strength of the interaction depends on the ratio of the stellar radius R to the orbital separation A. The timescale for synchronization is defined as

$$\frac{1}{T_{\rm sync}} = 3E_2\,(1+q)^{5/6}\,\frac{q^2}{r_{\rm g}^2}\left(\frac{GM}{R^3}\right)^{1/2}\left(\frac{R}{A}\right)^{17/2}\,, \tag{4}$$

where the He-star has mass M, radius R and moment of inertia I, r_g given by $r_{\rm g}^2 = I/(MR^2)$ is the dimensionless gyration radius of the He-star, q is the mass ratio of the BH mass to the He-star mass, and E_2 is the second order tidal coefficient. We take the new fitting formula of E_2 as suggested by Qin et al. (2018) for He-stars

$$E_2 = 10^{-0.93}\left(\frac{R_{\rm conv}}{R}\right)^{6.7}\,, \tag{5}$$

where $R_{\rm conv}$ is the radius of the convective core (see Appendix A in Qin et al. 2018, for an in-depth discussion of E_2). We highlight here that a variation of the implementation of tides is used (Qin et al. 2019). Instead of the standard tides prescription in MESA (Paxton et al. 2015) that synchronize the whole star, the tides here only operate on the radiative regions. However it has been verified that this slight variation has a very small impact on our results.

Rotational mixing and angular momentum transport are treated as diffusion processes (Heger et al. 2000, 2005), which mainly involve the effects of Eddington-Sweet circulation, the Goldreich-Schubert-Fricke instability, and secular as well as dynamical shear mixing. In addition, diffusion element mixing is included with an efficiency parameter of $f_c = 1/30$ (Chaboyer & Zahn 1992; Heger et al. 2000) for all processes above. Furthermore, an efficient angular momentum transport mechanism (i.e., Tayler-Spruit dynamo: Spruit (1999, 2002)) is included. For comparison, we also ran a small grid without the Tayler-Spruit dynamo and found that there is a negligible impact on our results. More details on this can be found in the discussion. Furthermore, efficient AM transport allows us to assume that all He-stars emerging from the CE phase are initially not rotating. This is because any initial or acquired rotation during the evolution of the secondary is erased by mass transfer and wind mass loss by the time it becomes a He-star.

Running these simulations for all binary systems computed by COMPAS is computationally too expensive. Therefore we run a grid that allows us to infer through interpolation the six parameters we are interested in, namely: the He-star mass before the supernova, the carbon-oxygen (CO) core mass pre-supernova, the resultant second-born BH mass, the orbital period pre-supernova, the lifetime of the BH-He-star binary system (from the expulsion of the CE to the collapse of the He-star) and the spin of the second-born BH, as a function of the initial parameters of the BH - He-star binary: initial mass of the first-born BH, $m_{\rm BH}$, initial mass of the He-star, $m_{\rm He-star}$, initial orbital period, p, and He-star metallicity, Z. In order to optimally construct our grid, we first randomly generate 3 000 points to cover the parameter space spanned by the binaries after the CE phase, namely, $m_{\rm BH} \in [2.5\,\mathrm{M_\odot}, 60\,\mathrm{M_\odot}]$, $m_{\rm He-star} \in [2.5\,\mathrm{M_\odot}, 89\,\mathrm{M_\odot}]$, $p \in [0.05\,\mathrm{days}, 8.5\,\mathrm{days}]$ and $Z \in [0.0001, 0.0349]$, to which we add 1,500 points drawn from a kernel density estimator (KDE)

trained with the post CE phase parameters of the synthetic population. In Appendix C we explain how we try to minimize linear interpolation errors by running more simulations where the interpolator is under-performing. The accuracy of the linear interpolator at each step is verified conducting 50 "leave 5% of the sample out" tests. We run a total of 18,000 simulations and show how the median relative errors stabilize at 0.01% and 0.04% for the He-star mass pre-supernova and resultant BH mass respectively, 0.20% for the CO core mass of the He-star, 0.01% for the orbital period, 0.04% for the lifetime of the BH-He-star binary and 0.41% for the log-spin of the second-born BH. In the Appendix we also show the spread of the relative errors. If in the 50 leave 5% of the sample out tests we also count non-fittable points, such as remote points at the boundary of the parameter space, we find the following percentages of test systems that have relative errors above 10% in the estimated quantities: 5% and 8% of the He-star mass pre-supernova and resultant BH mass, 8% of the CO core mass of the He-star, 6% of the orbital period, 6% of the lifetime of the BH-He-star binary and 17% of the log-spin of the second-born BH .

2.3. Core-collapse physics

Black holes are formed during the core collapse of massive stars and, in some cases, their formation may be accompanied by supernova explosions. The collapse occurs when the stellar core begins to contract under its own weight without being able to trigger any more nuclear burning in its iron core. This leads eventually to electron capture and dissociation of the core elements into alpha particles. The first process removes the degeneracy pressure support of the core while the second removes the thermal support. These two mechanisms combined accelerate the collapse until the core reaches nuclear densities and neutron degeneracy pressure halts the collapse. This sudden halt produces a bounce shock moving out of the core. The shock-wave moves outwards until it deposits all its energy into the surrounding layers. A supernova explosion occurs if the deposited energy can overcome the ram pressure of the infalling stellar material. A fraction, f_{fb}, of the material ejected by the supernova then falls back onto the stellar remnant. If the remnant is massive enough, neutron degeneracy pressure fails to halt the collapse and a black hole is formed. Moreover, the most massive stars can directly overcome the neutron degeneracy pressure when the collapse starts and implode to form a black hole. For a thorough review of our current understanding of the core-collapse process see for example Janka et al. (2007).

We use Fryer et al. (2012) delayed supernova prescription to model how much baryonic remnant mass is left behind after the collapse of the secondary star. This differs from their rapid prescription which produces a mass gap between BHs and neutron stars by assuming a strong convection which allows instabilities to grow quickly after the core bounce, producing more energetic SN explosion. The two prescriptions are not expected to lead to significant differences in the detected BBH merger rate (Belczynski et al. 2016b) as the population is dominated, due to aLIGO's selection effects, by more massive BHs.

Using the delayed prescription, we calculated the fraction of the star that collapses to form the BH, and we assume that any remaining outer layers that do not collapse are instantaneously ejected. In order to estimate the spin of the resulting BH we follow the framework described in Batta & Ramirez-Ruiz (2019). We assume that there is no pressure stopping or slowing down the collapse. We can think of the star mass distribution $M(r)$ as a collection of shells with mass $m_{\rm shell}$ and angular frequency $\Omega_{\rm shell}$, that falls one by one onto the center of the star. We assume that at the center, the shells up to 2.5 $M_\odot$ collapse directly to form a black hole conserving their angular momentum and mass. Once a shell reaches the BH's event horizon, it is accreted by it. The amount of angular momentum of the infalling material determines the properties of the accretion flow. Low angular momentum material collapses directly onto the BH transferring its entire mass and angular momentum to the BH, while material with enough angular momentum can create a disk around it. The maximum amount of angular momentum the disk material can give to the BH is determined by the specific angular momentum at the innermost circular orbit (ISCO) around the BH (Bardeen et al. 1972),

$$j_{\rm isco} = \frac{GM_{\rm BH}}{c}\frac{2}{3^{3/2}}\left(1+2\left(\frac{3c^2 r_{\rm isco}}{GM_{\rm BH}}-2\right)^{1/2}\right), \tag{6}$$

where $r_{\rm isco}$ is the radius at ISCO for prograde equatorial orbits,

$$r_{\rm isco} = \frac{GM_{\rm BH}}{c^2}\left(3+z_2-((3-z_1)(3+z_1+2z_2))^{1/2}\right), \tag{7}$$

with $z_1 = 1+(1-a^2)^{1/3}((1+a)^{1/3}+(1-a)^{1/3})$ and $z_2 = (3a^2+z_1^2)^{1/2}$ where a is the spin of the BH. Assuming that the disk formed from the collapse of a shell is accreted before the next shell collapses, as the viscous timescale of the disk is shorter than the dynamical timescale of the collapsing shells, we can evolve the BH's mass and spin as it accretes material through the accretion disk. Each mass shell then contributes to the angular momentum of the BH by

$$J_{\rm shell} = \int_0^{\theta_{\rm disk}} m_{\rm shell}\Omega_{\rm shell}(r) r^2 \sin^3\theta\, d\theta + \int_{\theta_{\rm disk}}^{\pi/2} m_{\rm shell} j_{\rm isco}\sin\theta\, d\theta, \tag{8}$$

where the disk formation angle is given by

$$\theta_{\rm disk} = \arcsin\left(\left(\frac{j_{\rm isco}}{\Omega_{\rm shell}(r) r^2}\right)^{1/2}\right) \tag{9}$$

and if the argument of arcsin exceeds 1, there is no disk formation. The first term in Eq. (8) represents material with low angular momentum that collapses directly onto the BH, while the second term corresponds to the material that forms the accretion disk with mass $m_{\rm disk} = m_{\rm shell}\cos\theta_{\rm disk}$. The mass-energy accreted from the disk onto the BH is $\Delta M_{\rm disk} = m_{\rm disk}(1-2GM_{\rm BH}/(3c^2 r_{\rm isco}))^{1/2}$ and the accreted angular momentum is $\Delta J_{\rm disk} = m_{\rm disk} j_{\rm isco}$ (Bardeen 1970; Thorne 1974). When treating the accretion of the portions of the shell that collapse directly onto the BH, we take into account 10% of baryonic mass loss through neutrinos (Fryer et al. 2012).

In our population synthesis study we neglect the effects of pair-instability supernovae (PISNe) and pulsational pair-instability supernovae (PPISNe). Both events are caused by the production of electron-positron pairs in the cores of very massive stars. In a PISN, pair production leads to a drop in the radiation pressure support in the core, causing the core to contract and the core temperature to increase. This results in explosive oxygen burning which reverses the collapse, unbinding the star. A PPISN is similar but the release of energy is insufficient to completely disrupt the star. This create a series of energetic pulses which eject material from the star before it collapses into a BH. PISNe cause massive stars with He-core masses between

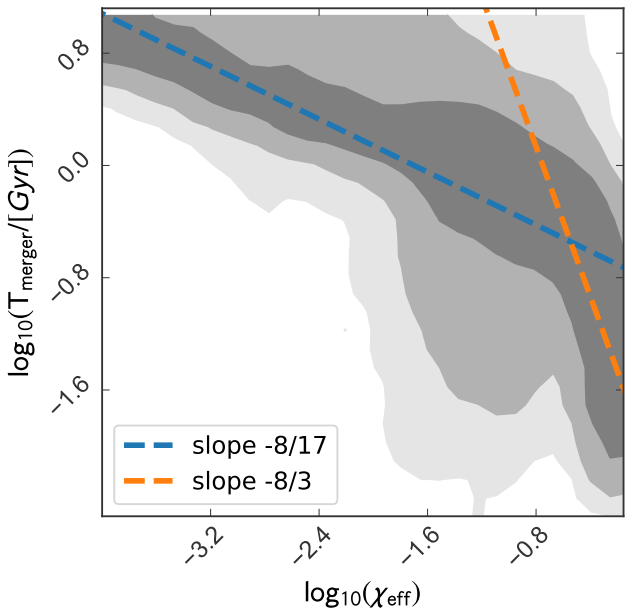

Fig. 2: Combined distribution of the BBH merger timescale T_{merger} versus the effective inspiral spin parameter χ_{eff} for our synthetic BBH population at metallicity $\log_{10}(Z) = -2.5$, in gray. The lighter shades represent larger contour levels, 68, 95 and 99%, respectively. Tidally locked systems follow the relation $\log_{10}(T_{merger}) \sim -\frac{8}{3}\log_{10}(\chi_{eff})$, orange dashed line, while the others systems follow $\log_{10}(T_{merger}) \sim -\frac{8}{17}\log_{10}(\chi_{eff})$ dictated by the tidal synchronization timescale, blue dashed line. Both lines are drawn at an arbitrary ordinate.

approximately 60 and 150 $M_\odot$ to be completely disrupted. Therefore, PISNe put a second theoretical mass gap into the distribution of BH masses (Fowler & Hoyle 1964; Rakavy & Shaviv 1967; Barkat et al. 1967). On the other hand, PPISNe affect presupernovae stars with He-core masses between around 35 and 60 $M_\odot$ enhancing the loss of mass before the supernova event and resulting in less massive BHs (Yoshida et al. 2016; Woosley 2017; Marchant et al. 2019). Neglecting these two phenomena leads us to overestimate the mass of the most massive BHs with $M_{BH} \gtrsim 35\,M_\odot$. For a recent population synthesis study of the effect of PISNe and PPISNe on the population of coalescing BBHs using the same code as in this work see Stevenson et al. (2019).

During a supernova, the asymmetric ejection of matter (Janka & Mueller 1994; Burrows & Hayes 1996; Janka 2013) or asymmetric emission of neutrinos (Bisnovatyi-Kogan 1993; Socrates et al. 2005) can provide a momentum kick to the newly formed compact object. Here we assume that the birth kicks of BHs follow a Maxwellian distribution with $\sigma = 265$ km/s (Hobbs et al. 2005), which is then rescaled by one minus the fall-back mass fraction f_{fb} (Fryer et al. 2012). In the Fryer et al. (2012) that we adopt, this quantity depends on the carbon-oxygen core mass m_{core} of the star before the collapse. For core masses grater than 11 $M_\odot$, $f_{fb} = 1$, which means that in our model all heavy black holes receive no natal kicks. These kicks can tilt the orbit of the BBH, which may generate a negative χ_{eff}, add eccentricity to the orbit or disrupt the binary. We take into account all these orbital changes, as well as orbital changes due to symmetric mass loss, following the analytical calculations of Kalogera (1996) and Abbott et al. (2017b).

2.4. Inspiral due to gravitational waves

After the birth of the second-born BH, GW emission removes energy and angular momentum from the orbit, shrinking it, and eventually leading to the merger of the two compact objects. The merger timescale for eccentric BBHs is computed as

$$T_{merger} = \frac{15}{304}\frac{c^5}{G^3}\frac{1}{m_1 m_2 (m_1+m_2)} A^4 f(e)\,, \tag{10}$$

where m_1 and m_2 are the masses of the BHs, A is the orbital separation (Peters 1964) and $f(e)$ is a numerical factor that account for the orbital eccentricity:

$$f(e) = \frac{\left(1-e^2\right)^4 \int_0^e \frac{e'^{29/19}(1+\frac{121}{304}e'^2)^{1181/2299}}{(1-e'^2)^{3/2}} de'}{e^{48/19}(1+\frac{121}{304}e^2)^{3480/2299}}\,. \tag{11}$$

There is an important point to make here. As was already explained by other authors (e.g., Kushnir et al. 2016; Zaldarriaga et al. 2018; Qin et al. 2018), the merger timescale is anti-correlated with the spin of the second-born BH, a_2, or the observed quantity χ_{eff}. This is because in order to form a fast rotating BH, tides should be strong and therefore the orbital separation between the parent He-star and the BH companion should be small. Since the merger timescale scales as the fourth power of the orbital separation, for tidally locked systems we can recover the following proportionality $T_{merger} \sim A^4 \sim \omega^{-8/3} \sim a_2^{-8/3} \sim \chi_{eff}^{-8/3}$. In the second relation we used Kepler's third law with ω being the orbital frequency matching the He-star's angular frequency Ω and in the last one $a_1 = 0$ as assumed in our model. Meanwhile, for the wider binaries partially synchronized by dynamical tides on a synchronization timescale $T_{sync}^{-1} = |\dot{\Omega}|/\Omega$, we recover small spins $a_2 \sim \Omega \sim \exp(1/T_{sync}) \sim 1/T_{sync} \sim A^{-17/2}$ (cf. Eq. (4)) and therefore $T_{merger} \sim A^4 \sim a_2^{-8/17} \sim \chi_{eff}^{-8/17}$. In Fig. 2 we show the combined distribution of the merger timescale and the effective spin parameter for a specific metallicity bin (centered at $\log_{10}(Z) = -2.5$) of our synthetic BBH population, namely not integrating over redshift and not accounting for any selection effect, in gray. Indeed, systems with high χ_{eff} follow the scaling relation for tidally locked systems (orange dashed line), while those with low χ_{eff} follow the scaling dictated by the tidal synchronization timescale (blue dashed line).

2.5. Detection rate

To compute the expected rate of detectable GW events, we need to convolve the star-formation rate (SFR) and metallicity distribution at different redshift epochs with the selection effects of the detectors. To do this we follow a similar approach to the one used in Belczynski et al. (2016b). Here we briefly summarize our approach, which is described in detail in Appendix B.

In our cosmological calculation we adopt the flat ΛCDM model with $H_0 = 67.7\,\frac{\mathrm{km/s}}{\mathrm{Mpc}}$ and $\Omega_m = 0.307$ (Planck Collaboration et al. 2016). Every simulated BBH k with BH masses $m_{1,k}$ and $m_{2,k}$, born at redshift $z_{f,i}$ and merging at redshift $z_{m,i,k}$ set by the delay time of this binary contributes to the detection rate by the following weight

$$w_{i,j,k} = \frac{\mathrm{fSFR}(z_{f,i})}{M_{\mathrm{sim},\Delta Z_j}} f_{\mathrm{corr}}\, 4\pi c\, D_c^2(z_{m,i,k})\, p_{\mathrm{det}}(z_{m,i,k}, m_{1,k}, m_{2,k})\, \Delta t_i \tag{12}$$

where subscripts f and m refer to formation and merger, respectively, and fSFR is the fractional star-formation rate, that is

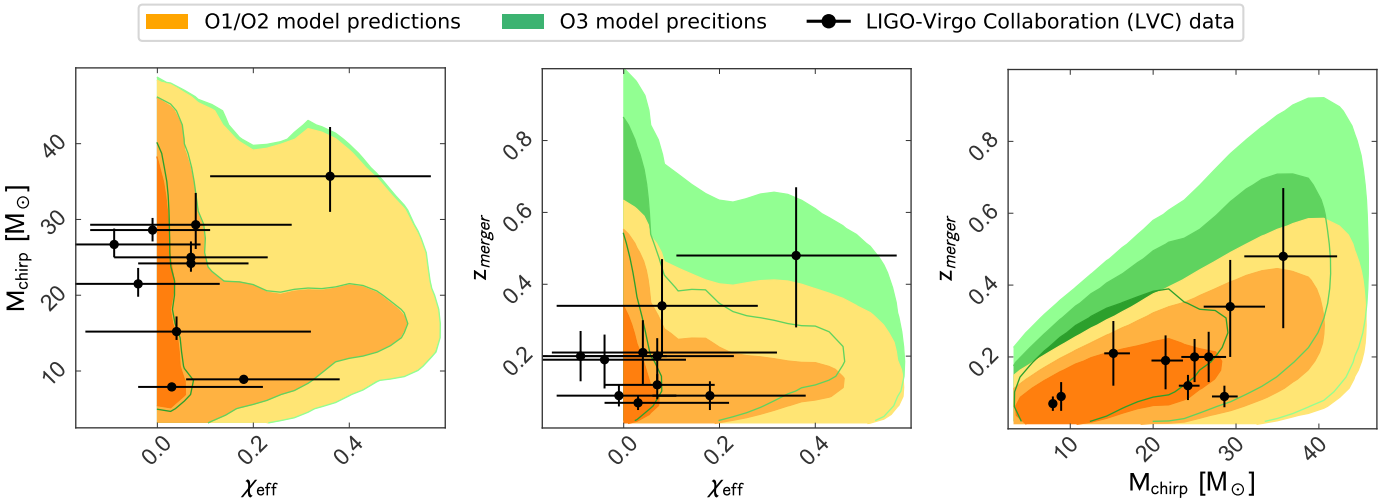

Fig. 3: Model predictions for binary black hole observables: chirp mass M_{chirp}, effective inspiral spin parameter χ_{eff} and cosmological redshift of merger z_{merger} distributions. We represent O1/O2 observing runs in orange and O3 in green, while lighter colors represent larger contour levels of 68, 95 and 99%, respectively. We overlaid in black the O1/O2 LIGO-Virgo Collaboration (LVC) data with their 90% credible intervals.

the total mass of stars formed per comoving volume per year per metallicity interval ΔZ_j. We adopt the SFR and metallicity distribution of Madau & Fragos (2017). The SFR formula we adopt is computed from UV and infrared surveys and is an updated version of Madau & Dickinson (2014) that better reproduces recent results at high redshifts $4 \leq z \leq 10$ (Bowler et al. 2015; Finkelstein et al. 2015; Ishigaki et al. 2015; McLeod et al. 2015; Oesch et al. 2015; McLeod et al. 2016). The metallicities are log-normally distributed with standard deviation 0.5 dex around the mean metallicity function of Madau & Fragos (2017). The mean metallicity function is obtained fitting observations assuming that the galaxy mass – metallicity relation holds at any redshift (Kajisawa et al. 2009; Baldry et al. 2012; Lee et al. 2012; Ilbert et al. 2013; Grazian et al. 2015). Furthermore, $M_{\mathrm{sim},\Delta Z_j}/f_{\mathrm{corr}}$ is the matter simulated in the metallicity bin ΔZ_j rescaled by the normalization factor f_{corr} (see Appendix A), $D_c(z) = c/H_0 \int_0^z (\Omega_m(1+z')^3 + \Omega_\Lambda)^{-1/2} dz'$ is the comoving distance to the source and p_{det} accounts for the selection effects of the detector. The total rate of detectable BBH mergers for a given detector network is calculated from the Monte Carlo simulations as a sum

$$R_{\mathrm{det}} = \sum_{\Delta t_i} \sum_{\Delta Z_j} \sum_{k} w_{i,j,k} \,, \tag{13}$$

where we add the contribution of every binary placed at the center of each formation time bin Δt_i in its corresponding metallicity bin ΔZ_j. The population synthesis predictions are performed in finite time bins of $\Delta t = 100$ Myr and the log-metallicity range $Z \in [0.0001, 0.0349]$ is divided in 30 bins.

The sensitivity of a GW detector to a source depends on the distance to the source, its orientation and position relative to the detector and on its physical characteristics. The detectability of a signal depends on its signal-to-noise ratio (S/R). In our model we assume that signals are detected if their single-detector S/R exceeds a threshold value of 8 (Aasi et al. 2016). For the two observing runs O1/O2 of aLIGO, we assumed a detector sensitivity equal to the target "early high sensitivity" (Abbott et al. 2018a). This simplification is motivated by the fact that the sensitivity of O2 was close to that of O1 (Abbott et al. 2018a). We assume a target "late low sensitivity" for the third observing run O3 and for design sensitivity the corresponding one (Abbott et al. 2018a). We follow the methodology and implementation of Barrett et al. (2018) [see their section 3.2] to compute the detection probability p_{det} for a given set of parameters (m_1, m_2, z). The optimal S/R (for a face-on, i.e. zero inclination, directly overhead source) is computed for a single detector using the sensitivity above with GW waveforms from `lalsuite` (LIGO Scientific Collaboration 2018). This S/R is then convolved with the antenna pattern function distribution (Finn & Chernoff 1993) in order to efficiently sample over the four angles involved, two for the sky location and two for the source orientation, which allows us to estimate the probability of detection. In our simplification we ignored the impact of BH spin on detectability, although high χ_{eff} may slightly enhance p_{det}.

3. Results

We use our model to predict the distributions of the three main observables inferred from GW detections: the chirp mass, the effective inspiral spin parameter and the cosmological merger redshift (Abbott et al. 2016). Every binary in our population synthesis model contributes to the total distributions of every observable quantity with the weight given in Eq. (12).

Our detailed binary evolution models give predictions about the spin of the second-born BH and its misalignment with the orbit. However, in order to estimate the observable χ_{eff}, we need to also have information about the spin of the first-born BH. As we already discussed earlier, here we assume that the spin of the first-born BH is very low, $a_1 \simeq 0$. This is due to two reasons. First, while the progenitor of the BH evolves through the red supergiant phase, most of the angular momentum is transported to the outer layers of the star upon expansion (because of the assumed efficient AM transport). This depletes the angular momentum of the core and eventually, due to mass transfer or stellar winds which remove the outer layers of the star, leads to a slowly rotating naked He-star. Second, the initial orbital separation of the two stars is quite large compared to the later stage of the evolution. Thus, even if tides can efficiently synchronize the rotation of the star to the orbit, the angular frequency of the envelope is too low to efficiently spin up the core. To quantita-

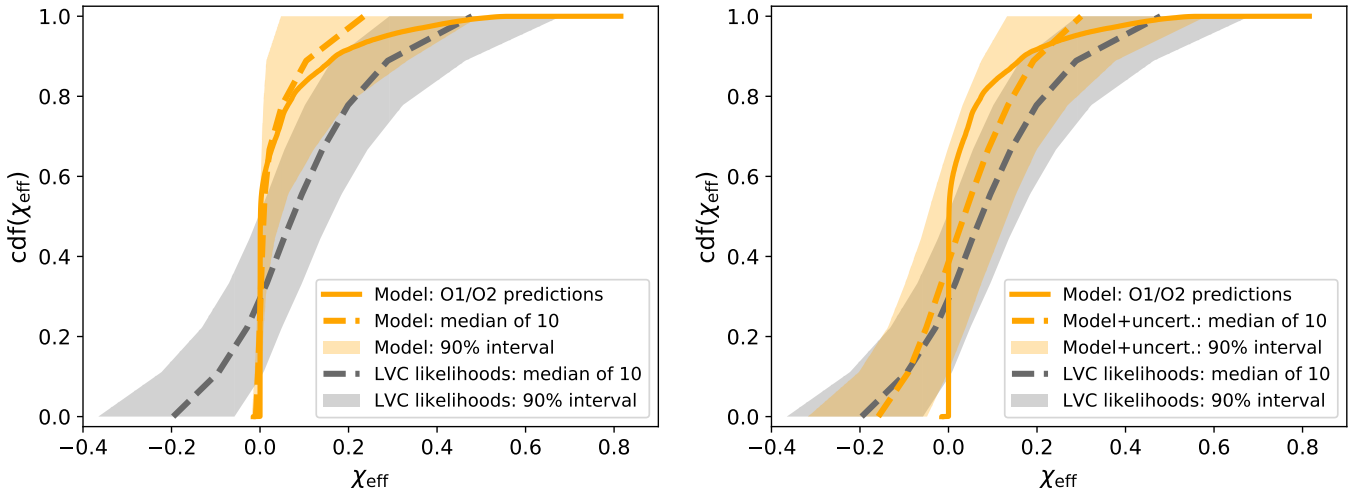

Fig. 4: Cumulative distribution functions (cdfs) of the effective inspiral spin parameter $\chi_{\rm eff}$ as predicted for O1/O2 by our model (solid orange line). (*Left*) From our model we generate 5,000 sets of 10 measurements and plot the median cdf (dashed orange line) together with the 90% credible interval (shaded orange region). (*Right*) We generate again 5,000 sets of 10 measurements from our model to which we now add mock measurement uncertainties generated from the zero-centered LVC data likelihoods. We plot the median cdf (dashed orange line) and the 90% credible interval (shaded orange region). For both graphs, in gray, we plot the median cdf (dashed line) and the 90% credible interval (shaded region) of 5,000 samples from the 10 actual observations generated from their respective LVC data likelihoods.

tively check these assumptions, Qin et al. (2018) used detailed stellar-evolution simulations to show that main sequence stars with initial angular rotations up to $\Omega_{\rm initial} \lesssim 0.5\,\Omega_{\rm critical}$ evolve to yield BHs with negligible spins at all metallicities, even when assuming that the angular momentum of the core is conserved in the collapse. A small subset of the most rapidly spinning stars undergo efficient internal mixing and evolve chemically homogeneously. These stars never expand to become giant stars and hence do not evolve through the standard CE formation channel.

3.1. aLIGO O1, O2, & O3 observing runs

The first and second observing runs of aLIGO (and, for parts of it, Advanced Virgo) lasted for 4 and 9 months, respectively, resulting in a total of 166 days of data suitable for coincident analysis (Abbott et al. 2016a). Ten GW signals from BBH mergers were detected (Abbott et al. 2019). These ten detections translate to a rate of 22 BBH mergers per year. In our model comparison to the data we only include these ten detections from the LIGO-Virgo Collaboration's catalog, although evidence for additional signals in O1/O2 data has been presented by Zackay et al. (2019a,b); Venumadhav et al. (2019). Our goal here is to model the combined distributions of observable quantities of the CE formation channel, with a special focus on the spins of the BHs which we investigate in detail. We intentionally picked a population synthesis model that approximately matches the observed rate for this study. Using Eq. (13), our model predicts for O1/O2 a detection rate of 27 $\rm yr^{-1}$, while for the ongoing observing run O3, we predict a detection rate of around 100 $\rm yr^{-1}$. However, the predicted event rate depends sensitively on a number of uncertain evolutionary model parameters (e.g., Dominik et al. 2015; Giacobbo et al. 2018; Barrett et al. 2018) and metallicity-specific star formation history (e.g., Chruslinska et al. 2019; Neijssel et al. 2019).

In Fig. 3 we show the predicted two-dimensional distributions of chirp mass, effective inspiral spin parameter and cosmological merger redshift for O1/O2 in orange and O3 in green. Lighter colors delineate larger contour levels of 68, 95 and 99%, respectively. For a comparison with the observations, we overlay the ten GW detections with their 90% credible intervals in black. These detections agree visually very well with our model prediction. In the first histogram, $\rm M_{chirp}$ vs. $\chi_{\rm eff}$, we see that the selection effects of the detectors at different sensitivities do not significantly affect the chirp mass and the effective inspiral spin parameter distributions. Meanwhile in the other two histograms, $z_{\rm merger}$ vs. $\chi_{\rm eff}$ and $z_{\rm merger}$ vs. $\rm M_{chirp}$, we see that at higher detector sensitivity we are able to detect events at higher cosmological redshift, namely at further distances, and that more massive sources can be observed out to a higher redshift, as one might trivially expect.

To provide a qualitative comparison between our theoretical predictions of $\chi_{\rm eff}$ and LIGO-Virgo Collaboration (LVC) measurements, we conducted a visual cumulative distribution function (cdf) graphical check and a Bayesian model comparison between our model and the LVC prior (uniform spin magnitudes $a_{1,2} \in [0, 1]$ and isotropic spin directions). For the graphical check, shown in Fig. 4, we generate 5,000 sets of 10 mock events from a KDE of our O1/O2 model predictions (solid orange line in Fig. 4) and compute the corresponding cdf. In the left panel of Fig. 4 we plot the median cdf (dashed orange line) and 90% credible interval (shaded orange region) of these sets of mock observations without any measurement uncertainty. Our model mostly predicts positive $\chi_{\rm eff}$ and only a few slightly negative $\chi_{\rm eff}$ but cannot reproduce $\chi_{\rm eff} \ll 0$. In the right panel of Fig. 4 we plot the same quantities, but this time we add uncertainties to the 5,000 sets generated from our model. These uncertainties are generated from the zero-centered LVC likelihoods. We show the cdfs from 5,000 sets of 10 samples, one each from the LVC data likelihoods of the 10 observed events, in gray in both panels of Fig. 4. These likelihoods are obtained by weighting the posteriors of the ten O1/O2 GW observations by the inverse of the average projected

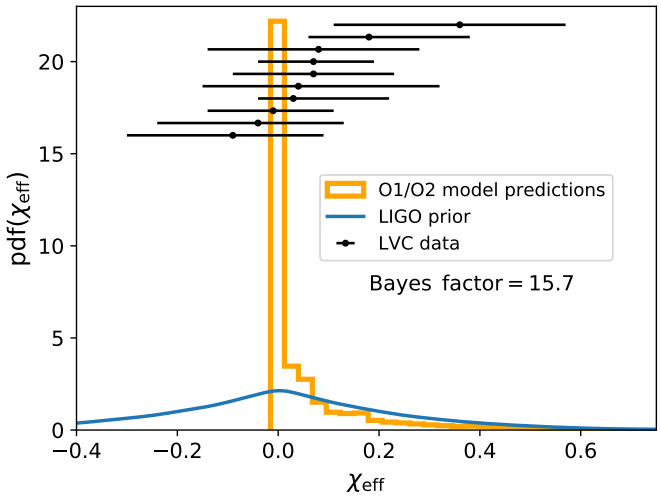

Fig. 5: Probability density function of $\chi_{\rm eff}$ predicted by our O1/O2 model (orange) and the average LIGO prior (blue). At an arbitrary vertical position, we plot in black the LVC data with their respective 90% credible intervals. The Bayes factor between our model and the LIGO prior is 15.7.

LVC prior, which is found by combining the samples of all ten priors. We see that, when accounting for observational uncertainties, we can also reproduce negative values of $\chi_{\rm eff}$ as in the observed cdf tail. We conclude that, visually, our model agrees well with the data. Of course, there is no single statistical check to unambiguously test the goodness of a model. In addition to the graphical check described above, we could ask, for example, whether the existing observations are statistically consistent with a model that predicts a negligible number of events with negative $\chi_{\rm eff}$. They are indeed consistent. All individual observations allow for zero or positive values of $\chi_{\rm eff}$ well within their 90% credible intervals. However, if future GW observations have significant negative $\chi_{\rm eff}$ inconsistent with zero, this will be an indication that those systems have been formed through alternative channels, such as dynamical formation. In Fig. 5 we show the probability density function of $\chi_{\rm eff}$ as predicted by our O1/O2 model, in orange, and the average projection of the LVC prior onto $\chi_{\rm eff}$. For reference we added the ten LVC GW observations with their 90% credible intervals at an arbitrary vertical position. We carried out a Bayesian model comparison between our model and the LVC prior given the observational data. This test results in a Bayes factor of 15.7 which favors our model.

3.2. aLIGO design sensitivity

We use the target design sensitivity curve of Abbott et al. (2018a) and predict a BBH merger rate of around 400 $\rm yr^{-1}$ for advanced detectors operating at design sensitivity. In Fig. 6, we show the expected properties of the BBH population detectable at aLIGO design sensitivity: the effective inspiral spin parameter, chirp mass and cosmological merger redshift, as well as the BBH merger timescale, metallicity and binary mass ratio.

As pointed out previously, the two-dimensional distribution of the effective inspiral spin parameter vs. the chirp mass does not change with different detector sensitivities. We arbitrarily divide the parameter space and identify three regions: Region-A with $\chi_{\rm eff} < 0.1$, Region-B with $\chi_{\rm eff} \geq 0.1$ and $\rm M_{chirp} < 15\,M_\odot$ and Region-C with $\chi_{\rm eff} \geq 0.1$ and $\rm M_{chirp} \geq 15\,M_\odot$. Our model predicts that 80, 10 and 10% of detectable BBH mergers fall into these three regions, respectively.

To understand these different regions of the parameter space, we recall that there is an anti-correlation between the merging timescale of the BBHs $T_{\rm merger}$ and the spin of the second-born BH a_2 or equivalently the observed quantity $\chi_{\rm eff}$ (see Sec. 2.4). Region-A contains systems with low spins which translate into long merger timescales. For reference, at formation of the second-born BH most of the orbital periods are between 1 and 5 days. These systems might have formed at redshifts up to 10 and they probe a wide range of metallicities and chirp masses. BBHs in Region-B have short merger timescales since they have a high $\chi_{\rm eff}$: at the formation of the second-born BH they are in close orbits with periods smaller than 1 day. These BBHs are formed in the local Universe, at redshifts close to zero, where the average metallicity is high and the chirp mass is low because high metallicity massive stars tend to lose a lot of mass due to stellar winds and thus the resulting BH masses are lower. Finally, systems in Region-C have high spins and high chirp masses. These are binaries that formed with low metallicity and merge quickly, that is at $\rm z_{merger} \simeq z_{formation}$. This part of the parameter space really probes the low-end tail of the metallicity distribution out to the observational redshift horizon of aLIGO. These are intrinsically rare systems but are amplified by aLIGO's higher sensitivity to high BH masses.

In Fig. 7 we further investigate GW selection effects that favor high BH masses. We show, in blue, the model prediction for aLIGO at design sensitivity against the overall BBH underlying population that one would observe with an infinitely-sensitive detector, in gray. The entire population of merging BBHs has a peak in the merger redshift at around $\rm z_{merger} \simeq 2$. While aLIGO is not sensitive to mergers at such high redshifts, future third generation GW detectors, such as the Einstein Telescope (Punturo et al. 2010; Kalogera et al. 2019), are able to observe them. The selection effects in favor of higher BH masses are clearly visible in the distribution of $\rm M_{chirp}$. Our observable predictions show a bimodal distribution of chirp masses with peaks at 11 $\rm M_\odot$ and 33 $\rm M_\odot$, while the underlying population has only one peak at around 10 $\rm M_\odot$. Selection effects allow us to observe massive BHs formed at high redshifts where the mean metallicity is lower than today. GW detectors preferentially observe BBHs that do not merge quickly, namely have wider orbits and slower spin (see the peak at $\chi_{\rm eff} \simeq 0$ in the $\chi_{\rm eff}$ histogram). We note that in our treatment of the selection effects we did not take into account the potentially greater sensitivity to GWs from BBHs with high $\chi_{\rm eff}$; this may influence the tail of the effective inspiral spin parameter distribution, accentuating the second peak at $\chi_{\rm eff} = 0.4$.

4. Discussion

4.1. Angular momentum efficiency

Our results are obtained assuming efficient angular momentum transport (Spruit 1999, 2002; Fuller et al. 2019) which plays an important role in determining the spin of the first-born BH. Meanwhile, the spin of the second-born BH is mainly determined by the combined effects of stellar wind and tidal interaction during the binary evolution. Although the Tayler-Spruit dynamo model helps to reproduce the flat rotation profile of our Sun (Fuller et al. 2014; Cantiello et al. 2014) as well as neutron star and white dwarf spins (Heger et al. 2005; Suijs et al. 2008), it cannot reproduce the asteroseismic constrains for sub-

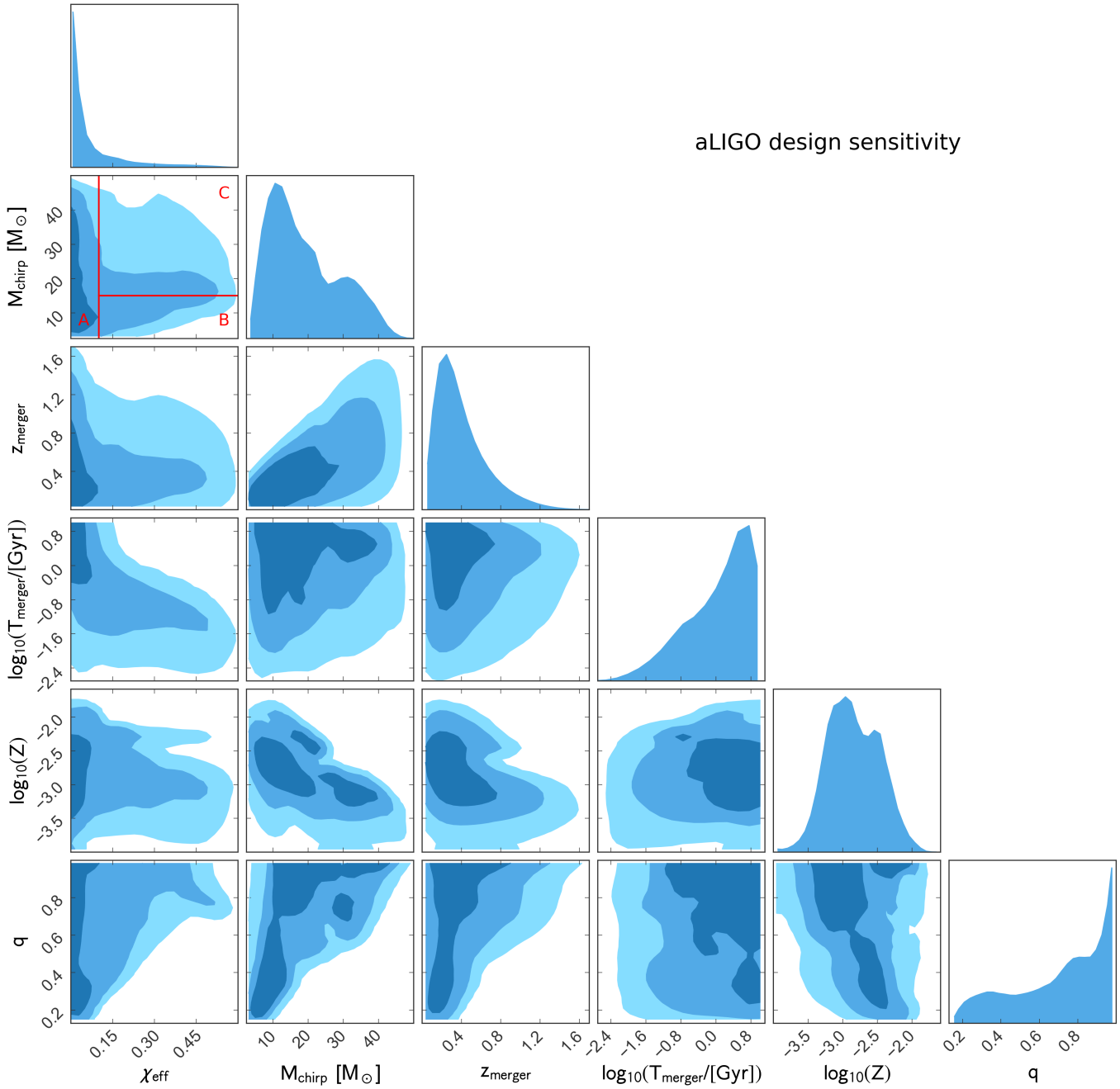

Fig. 6: Model predictions for the chirp mass $M_{\rm chirp}$, effective inspiral spin parameter $\chi_{\rm eff}$, cosmological redshift of merger $z_{\rm merger}$, BBH merger timescale $T_{\rm merger}$, metallicity Z and the binary mass ratio q distributions of binary black holes observables at design sensitivity. Lighter colors represent larger contour levels of 68, 95 and 99%. We arbitrarily divide the two dimensional histogram $M_{\rm chirp}$ vs $\chi_{\rm eff}$ with red lines into three regions at $\chi_{\rm eff} = 0.1$ and $M_{\rm chirp} = 15\,M_\odot$. Region-A contains 80% of the events, 10% are in Region-B and 10% are in Region-C. For illustrative purposes, all histograms are plotted with a smoothing scale of 0.8 bins with the exception of $z_{\rm formation}$ vs. $\chi_{\rm eff}$, $z_{\rm formation}$ vs. $z_{\rm merger}$, q vs. $\chi_{\rm eff}$ that have no smoothing

.

giants and red giants (Gehan et al. 2018), which would require an even higher efficiency in angular momentum transport. Alternatively, a model with inefficient angular momentum transport predicts highly spinning BHs, $\chi_{\rm eff} \simeq 1$ (Belczynski et al. 2017; Arca Sedda & Benacquista 2019), which do not match current GW observations. To test that angular momentum transport efficiency affects only the spin of the first born BH, and perhaps the initial rotation of the helium star after the common envelope, but not how tides can spin up an initially non-spinning helium star, we ran a grid of 5,000 MESA simulations of BH-He-star binaries with inefficient angular momentum transport, namely without the Tayler-Spruit dynamo. We found that there is a negligible impact on the spin of the second-born BH.

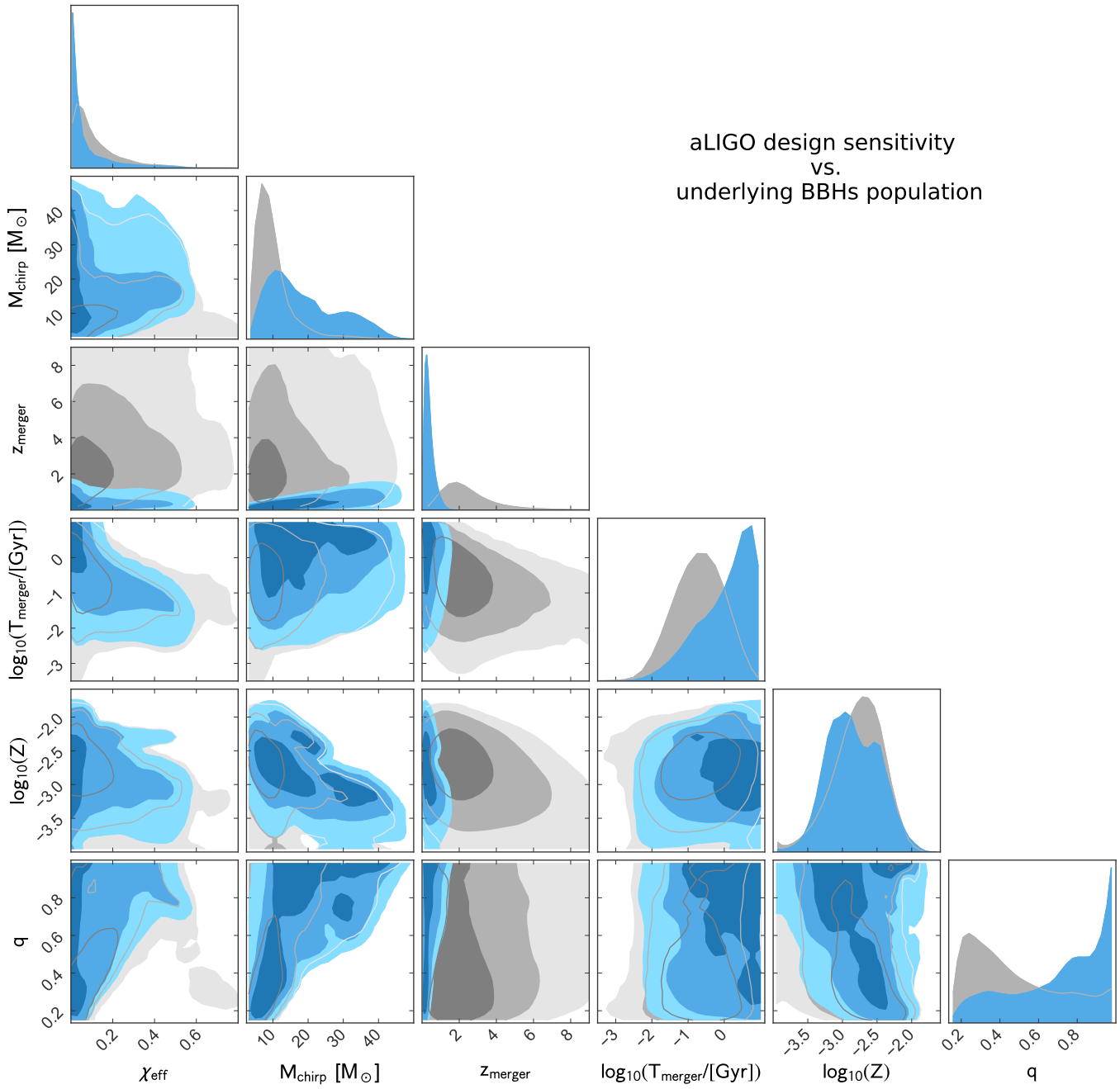

Fig. 7: Model predictions for the chirp mass $M_{\rm chirp}$, effective inspiral spin parameter $\chi_{\rm eff}$, cosmological redshift of merger $z_{\rm merger}$, BBH merger timescale $T_{\rm merger}$, metallicity Z and the binary mass ratio q distributions of binary black holes observables at design sensitivity, in blue, versus the underlying population of merging BBHs one would observe with a GW detector with infinite sensitivity, in gray. Lighter shades represent larger contour levels of 68, 95 and 99%, respectively.

4.2. Comparison with other studies

When comparing our results with other studies of the CE channel, we find some discrepancies. For example Zaldarriaga et al. (2018) found a bimodal distribution of spins of the second-born BH, with around half of the BHs having spin zero and the other half maximally spinning. When accounting for stellar winds and tidal interaction between the BH and He-star in a detailed binary evolution calculation we find that this bimodal distribution is an oversimplification. In Fig. 8 we show the normalized distribution of the spin of the second-born BH a_2 from detailed BH-He-star binaries simulations with masses $M_{\rm BH} = 30\,M_\odot$, $M_{\rm He-star} = 35\,M_\odot$ and metallicities $Z_\odot, 10^{-1}Z_\odot, 10^{-2}Z_\odot$ assuming a uniform distribution in log-orbital separation. Indeed, we find an approximately bimodal distribution of spins (similar to Fig. 4 from Zaldarriaga et al. (2018)) at low metallicity where stellar winds are weak and do not affect the orbital evolution. However, at higher metallicity the wind-driven mass loss causes the binaries to widen and the tidal interaction which spins up the He-star gradually becomes less effective. In the same figure we also show our predicted a_2 distribution from our model of BBH mergers observable at the aLIGO design sensitivity (blue shaded region) versus the underlying population of merging BBHs (gray shaded region). The

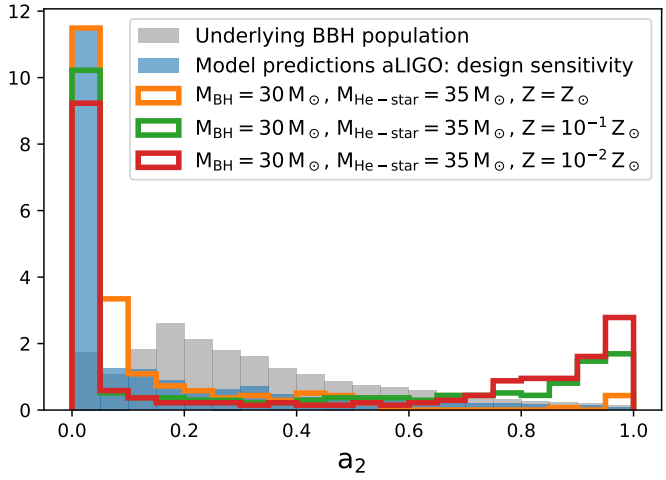

Fig. 8: Normalized distribution of the spin of the second-born BH as predicted by our model for GWs observable at aLIGO design sensitivity, in light blue, versus the underlying population of merging BBHs, in gray. For comparison, we show the same distribution obtained with MESA simulations of BH-He-star binary systems with $M_{BH} = 30\,M_\odot$, $M_{He-star} = 35\,M_\odot$ and metallicities $Z_\odot$ (orange), $10^{-1}\,Z_\odot$ (green) and $10^{-2}\,Z_\odot$ (red) under the assumption that the initial separation is log-uniform in $5 < A/R_\odot < 63$.

former one has a peak at around $a_2 = 0$ while the latter has a peak at around $a_2 = 0.2$. Although it has a peak at $a_2 = 0$, it is much flatter and both do not show the second peak at high spins. A key reason is that we did not assume a log-normal distribution of orbital separation after the CE phase, as was assumed by Zaldarriaga et al. (2018), but used the predictions of our population synthesis model (cf. Fig 1). Moreover, we also take into account the redshift- and metallicity-dependent star formation rate and apply aLIGO selection effects. The anti-correlation between T_{merger} and a_2 means that binary systems with high spins merge quickly. Thus, their merger redshift distribution follows the SFR evolution with a peak around $z \simeq 2$, beyond aLIGO sensitivity. This further reduces the number of rapidly spinning BHs detectable by aLIGO. We believe that the non-inclusion of detailed binary evolution calculations that carefully track the angular momentum evolution due to tidal interaction and stellar winds is also the reason for overestimated χ_{eff} distributions derived in other studies (Gerosa et al. 2018; Postnov & Kuranov 2019).

4.3. Comparison with other formation scenarios

We now compare our findings with theoretical results from other formation scenarios. All isolated binary evolution channels produce BH spins which are expected to be mostly aligned. It was shown by Marchant et al. (2016) that the chemically homogeneous evolution channel mostly produce highly spinning BHs ($a_{1,2} > 0.4$), which are currently not observed. An indicator that would rule in favor of this scenario are the detections of high effective spin parameters, say $\chi_{eff} > 0.8$, which are not predicted by the CE channel. Zackay et al. (2019b) recently reported the finding of a new BBH merger by reanalyzing the publicly available raw data from O1, using an independently developed pipeline. Assuming a flat χ_{eff} prior they found an event with high chirp mass, $M_{chirp} = 31^{+2}_{-3}\,M_\odot$, and high effective spin parameter, $\chi_{eff} = 0.81^{+0.15}_{-0.21}$, which is marginally consistent with our model. If similar events with better-measured parameters are found in the future, such BBHs would probably have been formed through the chemically homogeneous evolution channel, since the high χ_{eff} is outside our model prediction range for the CE channel. For dynamically-formed BBHs in dense star cluster, Rodriguez et al. (2018) found a symmetric distribution of χ_{eff} with a peak at $\chi_{eff} = 0$, regardless of the BH birth spins. Therefore, anti-aligned systems ($\chi_{eff} < 0$) would be a key indicator of the dynamical formation channel, as these are not predicted for either the CE channel or the chemically homogeneous evolution channel.

4.4. Uncertainties

Our model may be limited by some uncertainties which can alter the merger rate and, to a lesser degree, the predicted BBH property distributions. Uncertainties in (i) how the CE phase is accounted for, namely different choices of the α_{CE} parameter which characterizes the efficiency of transferring orbital energy into unbinding the CE might lead to different rate predictions (see e.g., Giacobbo & Mapelli 2018). For example, Fragos et al. (2019) report a very efficient (high) α_{CE} for a specific binary neutron stars (BNSs) system analyzed with 1D hydrodynamic simulations. However, in their estimate of α_{CE} they do not include the envelope's thermal energy in the calculation of the envelope's binding energy, and, most importantly, their results may not carry over to BBH formation, which tends to happen at lower metallicities, with more similar donor and accretor masses at common envelope onset. Indeed, Mapelli & Giacobbo (2018) showed that uncertainties in α_{CE} correspond to a variation of a factor of around 1.5 in the BBH merger rate estimates while a factor of 10 for BNS merger rates. Another example are uncertainties in the (ii) physics of the supernova explosions, such as the kicks strength, which can influence rates and affect the parameter distribution of BBH mergers (Dominik et al. 2013). To test how the delayed SN mechanism affects our results, we relaxed the model to account for direct collapse of the second born BH (still assuming a possible 10% of mass defect). We found similar distributions to the one of the delayed collapse with only a slight increase around $M_{chirp} \simeq 11\,M_\odot$ and $\chi_{eff} \simeq 0.2$ for detectable binaries and an increase of the merger rate by $\sim 10\%$ due to the survival of BBHs disrupted by natal kicks in the Fryer et al. (2012) model and the detectability of the slightly more massive BBHs are greater distances. Furthermore, in our binary population, (iii) the He-stars after the CE phase are not necessarily zero-age helium main sequence stars, as assumed in the second step of our detailed binary evolution calculations. This is because some of the progenitors of the helium stars overflowed their Roche lobes and entered the common envelope phase after helium burning was initiated in their core. The remaining lifetime of these stars is shorter than the duration of their zero-age helium main sequence. They lose less mass through stellar winds in their remaining lifetimes, which cause the orbits to not widen as much and result in more massive BHs with higher spins. However, we expect that the fraction of stars that enter the CE while burning helium in their core is higher at low metallicities, as low-metallicity stars tend to expand later in their lives. At the same time, stellar winds in these stars are weaker due to the low metallicity, so the overall effect on the population of BBHs is expected to be limited. Moreover, our detection rate calculation is affected by (iv) uncertainties in the redshift dependent SFR, (v) redshift-dependent metallicity distribution and (vi) the initial mass function (de Mink & Belczynski 2015; Chruslinska et al. 2019; Nei-

jssel et al. 2019) which may not be universal (e.g., Kroupa 2001; Schneider et al. 2018), but see Farr & Mandel (2018). For example there is an uncertainty in the UV and IR data used to infer the SFR and mean metallicity at high redshift $z > 4$ (Madau & Dickinson 2014). A SFR favoring lower formation metallicities than the one assumed here would skew our result in favor of systems in Region-C in the $\chi_{\rm eff} - M_{\rm chirp}$ histogram of Fig. 6, namely BBHs with high $M_{\rm chirp}$ and high $\chi_{\rm eff}$, at the expense of systems in Region-A, namely BBHs with low $\chi_{\rm eff}$.

5. Conclusions

One of the biggest open questions in GW astrophysics today is how merging binary black holes are formed. Isolated binaries that go through the CE phase are one of the main proposed formation channels for BBHs. In this work we investigate the combined distributions of masses, spins and merger redshifts of a population of BBHs formed through this channel that would be detectable by advanced GW detectors. We combine binary population synthesis studies with detailed stellar structure and binary evolution simulations. Rapid population synthesis allows us to obtain a population of BBH progenitors: BH-He-star binaries. Meanwhile, the detailed simulations that take into account the effects of differential stellar rotation, tidal interactions, wind mass loss and the evolution of the structure of the He-star, allow us to accurately predict the distribution of the properties of BBH systems at their formation. We then take into account the redshift and metallicity dependence of the star-formation rate together with the selection effects of the detectors to build a model capable of reproducing all observable properties of the current sample of 10 BBH mergers. We also predict what future GW experiments are likely to observe. Our main findings can be summarized in the following points:

- Our model is the first one to use detailed stellar structure and binary evolution simulations to successfully reproduce the observed $\chi_{\rm eff}$ population: most with $\chi_{\rm eff} \simeq 0$ and a few with positive $\chi_{\rm eff}$. Hence, it provides strong support for the CE channel as the dominant formation channel for the observed BBH mergers.
- We find that the ten O1/O2 GW detections are consistent with having formed through the CE channel. We predict a detection rate of 27 $\rm yr^{-1}$ for a particular set of population-synthesis model assumptions and a specific choice of a metallicity-specific star formation history, which is consistent with the 10 GW detections found in 167 days of total coincident observing time during the first two advanced detector observing runs.
- We predict the combined distributions of $\rm M_{chirp}$, $\chi_{\rm eff}$ and $z_{\rm merger}$ for the current O3 observing run and for future data at design sensitivity.
- We distinguish three different regions of observable BBH mergers. At design sensitivity, we expect around 80% of events with $\chi_{\rm eff} < 0.1$ and a wide range of chirp masses: these systems formed in relatively wide orbits (mostly with periods of 1-5 days at the formation of the second-born BH) and might have formed at redshifts up to 10, probing a wide range of metallicities. Around 10% of events with $\chi_{\rm eff} \geq 0.1$ and $\rm M_{chirp} < 15\,M_\odot$ are BBHs born in close orbits (with orbital periods of less than 1 day at the formation of the second-born BH) in the local Universe at redshift close to 0 where the metallicity is high. These systems merge promptly. Finally, the remaining 10% of events with $\chi_{\rm eff} \geq 0.1$ and $\rm M_{chirp} \geq 15\,M_\odot$ are BBHs formed at low metallicity at a range of redshifts; these systems again merge promptly. Efficient spin-up of the secondary, which yields high $\chi_{\rm eff}$, requires the BBH to be born in a close orbit, which then allows for a prompt merger through GW emission.
- We find that the total population of merging BBHs, namely the one that would be observed by a GW detector with infinite sensitivity, has a peak in the merger redshift at around 2, far beyond aLIGO sensitivity. This peak is set by a combination of the star formation rate, which peaks at a redshift of 2; the metallicity of star formation, which is lower in the early Universe and favors more efficient BBH formation; and the delay time distribution until merger.
- We show that in order to understand the distribution of BBH spins, population synthesis studies of isolated field binary formation channels should include detailed binary evolution calculations that carefully track the angular momentum evolution due to the tidal interaction and stellar winds which are the origin of the spin of the second-born BH. Moreover, we find that the assumption of efficient angular momentum transport has a negligible impact on the spin of the second-born BH.

Acknowledgements. We would like to thank Pablo Marchant, Michael Zevin, Vicky Kalogera and Christopher Berry for helpful suggestions regarding Section 2.4 and Appendix B. This work was supported by the Swiss National Science Foundation Professorship grant (project number PP00P2 176868). This project has received funding from the European Union's Horizon 2020 research and innovation program under the Marie Sklodowska-Curie RISE action, grant agreement No 691164 (ASTROSTAT). This work was performed in part at the Aspen Center for Physics, which is supported by National Science Foundation grant PHY-1607611. The computations were performed in part at the University of Geneva on the Baobab and Lesta computer clusters and at the University of Birmingham. AB is funded by the program Cátedras CONACYT para Jóvenes Investigadores and by the Danish National Research Foundation (project number DNRF132). SS is supported by the Australian Research Council Centre of Excellence for Gravitational Wave Discovery (OzGrav), through project number CE170100004. All figures were made with the free Python modules Matplotlib (Hunter 2007) and pygtc (Bocquet & Carter 2016). This research made use of Astropy,[2] a community-developed core Python package for Astronomy (Astropy Collaboration et al. 2013; Price-Whelan et al. 2018).

References

Aasi, J., Abbott, B. P., Abbott, R., et al. 2015, Classical and Quantum Gravity, 32, 074001
Aasi, J., Abbott, B. P., Abbott, R., et al. 2016, Phys. Rev. D, 93, 042006
Abbott, B. P., Abbott, R., Abbott, T. D., et al. 2016, Phys. Rev. Lett., 116, 241102
Abbott, B. P., Abbott, R., Abbott, T. D., et al. 2018a, Living Reviews in Relativity, 21, 3
Abbott, B. P., Abbott, R., Abbott, T. D., et al. 2016a, Physical Review X, 6, 041015
Abbott, B. P., Abbott, R., Abbott, T. D., et al. 2016b, ApJ, 818, L22
Abbott, B. P., Abbott, R., Abbott, T. D., et al. 2018b, arXiv e-prints, arXiv:1811.12940
Abbott, B. P., Abbott, R., Abbott, T. D., et al. 2019, Physical Review X, 9, 031040
Abbott, B. P., Abbott, R., Abbott, T. D., et al. 2017a, Phys. Rev. Lett., 118, 221101
Abbott, B. P., Abbott, R., Abbott, T. D., et al. 2017b, ApJ, 850, L40
Abt, H. A. 1983, Annual Review of Astronomy and Astrophysics, 21, 343
Acernese, F., Agathos, M., Agatsuma, K., et al. 2015, Classical and Quantum Gravity, 32, 024001
Antonini, F., Chatterjee, S., Rodriguez, C. L., et al. 2016, ApJ, 816, 65
Arca Sedda, M. & Benacquista, M. 2019, MNRAS, 482, 2991
Astropy Collaboration, Robitaille, T. P., Tollerud, E. J., et al. 2013, A&A, 558, A33
Baldry, I. K., Driver, S. P., Loveday, J., et al. 2012, MNRAS, 421, 621
Bardeen, J. M. 1970, Nature, 226, 64
Bardeen, J. M., Press, W. H., & Teukolsky, S. A. 1972, ApJ, 178, 347
Barkat, Z., Rakavy, G., & Sack, N. 1967, Phys. Rev. Lett., 18, 379

[2] http://www.astropy.org

Barrett, J. W., Gaebel, S. M., Neijssel, C. J., et al. 2018, MNRAS, 477, 4685
Barrett, J. W., Mandel, I., Neijssel, C. J., Stevenson, S., & Vigna-Gómez, A. 2017, in IAU Symposium, Vol. 325, Astroinformatics, ed. M. Brescia, S. G. Djorgovski, E. D. Feigelson, G. Longo, & S. Cavuoti, 46–50
Batta, A. & Ramirez-Ruiz, E. 2019, arXiv e-prints, arXiv:1904.04835
Belczynski, K., Bulik, T., Fryer, C. L., et al. 2010, ApJ, 714, 1217
Belczynski, K., Holz, D. E., Bulik, T., & O'Shaughnessy, R. 2016a, Nature, 534, 512
Belczynski, K., Kalogera, V., Rasio, F. A., et al. 2008, ApJS, 174, 223
Belczynski, K., Klencki, J., Meynet, G., et al. 2017, arXiv e-prints, arXiv:1706.07053
Belczynski, K., Repetto, S., Holz, D. E., et al. 2016b, ApJ, 819, 108
Belczynski, K., Taam, R. E., Kalogera, V., Rasio, F. A., & Bulik, T. 2007, ApJ, 662, 504
Bisnovatyi-Kogan, G. S. 1993, Astronomical and Astrophysical Transactions, 3, 287
Bocquet, S. & Carter, F. W. 2016, The Journal of Open Source Software, 1
Bowler, R. A. A., Dunlop, J. S., McLure, R. J., et al. 2015, MNRAS, 452, 1817
Broekgaarden, F. S., Justham, S., de Mink, S. E., et al. 2019, arXiv e-prints [arXiv:1905.00910]
Burrows, A. & Hayes, J. 1996, Phys. Rev. Lett., 76, 352
Cantiello, M., Mankovich, C., Bildsten, L., Christensen-Dalsgaard, J., & Paxton, B. 2014, ApJ, 788, 93
Chaboyer, B. & Zahn, J. P. 1992, A&A, 253, 173
Chruslinska, M., Nelemans, G., & Belczynski, K. 2019, MNRAS, 482, 5012
Cutler, C. & Flanagan, É. E. 1994, Phys. Rev. D, 49, 2658
de Kool, M. 1990, ApJ, 358, 189
de Mink, S. E. & Belczynski, K. 2015, ApJ, 814, 58
de Mink, S. E., Cantiello, M., Langer, N., et al. 2009, A&A, 497, 243
Dewi, J. D. M. & Tauris, T. M. 2000, A&A, 360, 1043
Dominik, M., Belczynski, K., Fryer, C., et al. 2013, ApJ, 779, 72
Dominik, M., Belczynski, K., Fryer, C., et al. 2012, ApJ, 759, 52
Dominik, M., Berti, E., O'Shaughnessy, R., et al. 2015, ApJ, 806, 263
Farr, W. M. & Mandel, I. 2018, Science, 361, aat6506
Farr, W. M., Stevenson, S., Miller, M. C., et al. 2017, Nature, 548, 426
Figer, D. F. 2005, Nature, 434, 192
Finkelstein, S. L., Ryan, Russell E., J., Papovich, C., et al. 2015, ApJ, 810, 71
Finn, L. S. & Chernoff, D. F. 1993, Phys. Rev. D, 47, 2198
Fowler, W. A. & Hoyle, F. 1964, ApJS, 9, 201
Fragione, G., Ginsburg, I., & Kocsis, B. 2018, ApJ, 856, 92
Fragos, T., Andrews, J. J., Ramirez-Ruiz, E., et al. 2019, ApJ, 883, L45
Fryer, C. L., Belczynski, K., Wiktorowicz, G., et al. 2012, ApJ, 749, 91
Fuller, J., Lecoanet, D., Cantiello, M., & Brown, B. 2014, ApJ, 796, 17
Fuller, J. & Ma, L. 2019, ApJ, 881, L1
Fuller, J., Piro, A. L., & Jermyn, A. S. 2019, MNRAS, 485, 3661
Gehan, C., Mosser, B., Michel, E., Samadi, R., & Kallinger, T. 2018, A&A, 616, A24
Gerosa, D., Berti, E., O'Shaughnessy, R., et al. 2018, Phys. Rev. D, 98, 084036
Giacobbo, N. & Mapelli, M. 2018, MNRAS, 480, 2011
Giacobbo, N., Mapelli, M., & Spera, M. 2018, MNRAS, 474, 2959
Grazian, A., Fontana, A., Santini, P., et al. 2015, A&A, 575, A96
Grevesse, N. & Sauval, A. J. 1998, Space Sci. Rev., 85, 161
Hamann, W. R. & Koesterke, L. 1998, A&A, 335, 1003
Heger, A., Langer, N., & Woosley, S. E. 2000, ApJ, 528, 368
Heger, A., Woosley, S. E., & Spruit, H. C. 2005, ApJ, 626, 350
Hobbs, G., Lorimer, D. R., Lyne, A. G., & Kramer, M. 2005, MNRAS, 360, 974
Hotokezaka, K. & Piran, T. 2017, ApJ, 842, 111
Humphreys, R. M. & Davidson, K. 1994, PASP, 106, 1025
Hunter, J. D. 2007, Computing In Science & Engineering, 9, 90
Hurley, J. R., Pols, O. R., & Tout, C. A. 2000, MNRAS, 315, 543
Hurley, J. R., Tout, C. A., & Pols, O. R. 2002, MNRAS, 329, 897
Hut, P. 1981, A&A, 99, 126
Ilbert, O., McCracken, H. J., Le Fèvre, O., et al. 2013, A&A, 556, A55
Inayoshi, K., Hirai, R., Kinugawa, T., & Hotokezaka, K. 2017, MNRAS, 468, 5020
Ishigaki, M., Kawamata, R., Ouchi, M., et al. 2015, ApJ, 799, 12
Ivanova, N., Justham, S., Chen, X., et al. 2013, Astronomy and Astrophysics Review, 21, 59
Janka, H.-T. 2013, MNRAS, 434, 1355
Janka, H. T., Langanke, K., Marek, A., Martínez-Pinedo, G., & Müller, B. 2007, Phys. Rep., 442, 38
Janka, H. T. & Mueller, E. 1994, A&A, 290, 496
Kajisawa, M., Ichikawa, T., Tanaka, I., et al. 2009, ApJ, 702, 1393
Kalogera, V. 1996, ApJ, 471, 352
Kalogera, V., Belczynski, K., Kim, C., O'Shaughnessy, R., & Willems, B. 2007, Phys. Rep., 442, 75
Kalogera, V., Berry, C. P., Colpi, M., et al. 2019, arXiv e-prints [arXiv:1903.09220]
Kroupa, P. 2001, Monthly Notices of the Royal Astronomical Society, 322, 231
Kruckow, M. U., Tauris, T. M., Langer, N., Kramer, M., & Izzard, R. G. 2018, MNRAS, 481, 1908
Kushnir, D., Zaldarriaga, M., Kollmeier, J. A., & Waldman, R. 2016, MNRAS, 462, 844
Lee, K.-S., Ferguson, H. C., Wiklind, T., et al. 2012, ApJ, 752, 66
LIGO Scientific Collaboration. 2018, LIGO Algorithm Library - LALSuite, free software (GPL)
Linden, T., Kalogera, V., Sepinsky, J. F., et al. 2010, ApJ, 725, 1984
Livio, M. & Soker, N. 1988, ApJ, 329, 764
Madau, P. & Dickinson, M. 2014, Annual Review of Astronomy and Astrophysics, 52, 415
Madau, P. & Fragos, T. 2017, ApJ, 840, 39
Mandel, I. & de Mink, S. E. 2016, MNRAS, 458, 2634
Mandel, I. & Farmer, A. 2018, arXiv e-prints, arXiv:1806.05820
Mapelli, M. & Giacobbo, N. 2018, MNRAS, 479, 4391
Marchant, P., Langer, N., Podsiadlowski, P., Tauris, T. M., & Moriya, T. J. 2016, A&A, 588, A50
Marchant, P., Renzo, M., Farmer, R., et al. 2019, ApJ, 882, 36
McLeod, D. J., McLure, R. J., & Dunlop, J. S. 2016, MNRAS, 459, 3812
McLeod, D. J., McLure, R. J., Dunlop, J. S., et al. 2015, MNRAS, 450, 3032
Miller, M. C. 2016, General Relativity and Gravitation, 48, 95
Miller, M. C. & Lauburg, V. M. 2009, ApJ, 692, 917
Neijssel, C. J., Vigna-Gómez, A., Stevenson, S., et al. 2019, MNRAS, 490, 3740
Oesch, P. A., Bouwens, R. J., Illingworth, G. D., et al. 2015, ApJ, 808, 104
Paczynski, B. 1976, in IAU Symposium, Vol. 73, Structure and Evolution of Close Binary Systems, ed. P. Eggleton, S. Mitton, & J. Whelan, 75
Park, D., Kim, C., Lee, H. M., Bae, Y.-B., & Belczynski, K. 2017, MNRAS, 469, 4665
Pavlovskii, K., Ivanova, N., Belczynski, K., & Van, K. X. 2017, MNRAS, 465, 2092
Paxton, B., Bildsten, L., Dotter, A., et al. 2011, ApJS, 192, 3
Paxton, B., Cantiello, M., Arras, P., et al. 2013, ApJS, 208, 4
Paxton, B., Marchant, P., Schwab, J., et al. 2015, ApJS, 220, 15
Paxton, B., Schwab, J., Bauer, E. B., et al. 2018, ApJS, 234, 34
Paxton, B., Smolec, R., Schwab, J., et al. 2019, ApJS, 243, 10
Peters, P. C. 1964, Phys. Rev., 136, B1224
Planck Collaboration, Ade, P. A. R., Aghanim, N., et al. 2016, A&A, 594, A13
Pols, O. R., Schröder, K.-P., Hurley, J. R., Tout, C. A., & Eggleton, P. P. 1998, MNRAS, 298, 525
Portegies Zwart, S. F. & McMillan, S. L. W. 2000, ApJ, 528, L17
Postnov, K. A. & Kuranov, A. G. 2019, MNRAS, 483, 3288
Postnov, K. A. & Yungelson, L. R. 2014, Living Reviews in Relativity, 17, 3
Price-Whelan, A. M., Sipőcz, B. M., Günther, H. M., et al. 2018, AJ, 156, 123
Punturo, M., Abernathy, M., Acernese, F., et al. 2010, Classical and Quantum Gravity, 27, 194002
Qin, Y., Fragos, T., Meynet, G., et al. 2018, A&A, 616, A28
Qin, Y., Marchant, P., Fragos, T., Meynet, G., & Kalogera, V. 2019, ApJ, 870, L18
Rakavy, G. & Shaviv, G. 1967, ApJ, 148, 803
Rodriguez, C. L., Amaro-Seoane, P., Chatterjee, S., & Rasio, F. A. 2018, Phys. Rev. Lett., 120, 151101
Rodriguez, C. L. & Loeb, A. 2018, ApJ, 866, L5
Rodriguez, C. L., Morscher, M., Pattabiraman, B., et al. 2015, Phys. Rev. Lett., 115, 051101
Rodriguez, C. L., Zevin, M., Pankow, C., Kalogera, V., & Rasio, F. A. 2016, ApJ, 832, L2
Sana, H., de Mink, S. E., de Koter, A., et al. 2012, Science, 337, 444
Santamaría, L., Ohme, F., Ajith, P., et al. 2010, Phys. Rev. D, 82, 064016
Schneider, F. R. N., Izzard, R. G., Langer, N., & de Mink, S. E. 2015, ApJ, 805, 20
Schneider, F. R. N., Sana, H., Evans, C. J., et al. 2018, Science, 359, 69
Sigurdsson, S. & Hernquist, L. 1993, Nature, 364, 423
Silsbee, K. & Tremaine, S. 2017, ApJ, 836, 39
Smarr, L. L. & Blandford, R. 1976, ApJ, 207, 574
Socrates, A., Blaes, O., Hungerford, A., & Fryer, C. L. 2005, ApJ, 632, 531
Spruit, H. C. 1999, A&A, 349, 189
Spruit, H. C. 2002, A&A, 381, 923
Stevenson, S., Sampson, M., Powell, J., et al. 2019, ApJ, 882, 121
Stevenson, S., Vigna-Gómez, A., Mandel, I., et al. 2017, Nature Communications, 8, 14906
Suijs, M. P. L., Langer, N., Poelarends, A. J., et al. 2008, A&A, 481, L87
Thorne, K. S. 1974, ApJ, 191, 507
Tutukov, A. V. & Yungelson, L. R. 1993, MNRAS, 260, 675
van den Heuvel, E. P. J. 1976, in IAU Symposium, Vol. 73, Structure and Evolution of Close Binary Systems, ed. P. Eggleton, S. Mitton, & J. Whelan, 35
van den Heuvel, E. P. J., Portegies Zwart, S. F., & de Mink, S. E. 2017, MNRAS, 471, 4256
Venumadhav, T., Zackay, B., Roulet, J., Dai, L., & Zaldarriaga, M. 2019, arXiv e-prints, arXiv:1904.07214
Vigna-Gómez, A., Neijssel, C. J., Stevenson, S., et al. 2018, MNRAS, 481, 4009
Vink, J. S. & de Koter, A. 2005, A&A, 442, 587
Vink, J. S., de Koter, A., & Lamers, H. J. G. L. M. 2001, A&A, 369, 574
Webbink, R. F. 1984, ApJ, 277, 355
Woosley, S. E. 2017, ApJ, 836, 244
Xu, X.-J. & Li, X.-D. 2010, ApJ, 716, 114
Yoshida, T., Umeda, H., Maeda, K., & Ishii, T. 2016, MNRAS, 457, 351
Zackay, B., Dai, L., Venumadhav, T., Roulet, J., & Zaldarriaga, M. 2019a, arXiv e-prints, arXiv:1910.09528
Zackay, B., Venumadhav, T., Dai, L., Roulet, J., & Zaldarriaga, M. 2019b, Phys. Rev. D, 100, 023007
Zahn, J. P. 1977, A&A, 500, 121
Zaldarriaga, M., Kushnir, D., & Kollmeier, J. A. 2018, MNRAS, 473, 4174

Appendix A: Mass renormalization of the population synthesis simulation

We used COMPAS to run a Monte-Carlo simulation and generate a sample of half a million BH - He-star binaries. When we perform binary population synthesis simulations, we only model binary systems, neglecting the population of single stars. Furthermore, to save on computational costs, we restrict the mass of the primary star to a suitable range $m_A < m_{\rm primary} < m_B$ so that we only consider initial binaries that can be progenitors of the systems we want to study (this is a basic version of the importance sampling approach described by Broekgaarden et al. (2019)). This means that we model only a fraction of the underlying stellar population. Here we show how to renormalize the population synthesis simulation to the total stellar mass of the underlying stellar population.

Let us consider a stellar population of total mass M_* with an initial mass function (IMF) of single star masses:

$$f(m) = \begin{cases} f_0 \left(\frac{m}{m_{\rm min}}\right)^{-\alpha_1} & m_{\rm min} \le m \le m_1 \\ f_0 \left(\frac{m_1}{m_{\rm min}}\right)^{-\alpha_1} \left(\frac{m}{m_1}\right)^{-\alpha_2} & m_1 \le m \le m_2 \\ f_0 \left(\frac{m_1}{m_{\rm min}}\right)^{-\alpha_1} \left(\frac{m_2}{m_1}\right)^{-\alpha_2} \left(\frac{m}{m_2}\right)^{-\alpha_3} & m_2 \le m \le m_{\rm max} \end{cases} \tag{A.1}$$

where the constant f_0 is defined such that $\int_{m_{\rm min}}^{m_{\rm max}} f(m)\, dm = 1$. Let $f_{\rm bin}$ be the fraction of stars in binaries and assume that the distribution of mass ratios in binaries is flat between 0 and 1, that is $g(q) = 1$. Then, the mean mass of a stellar system in the population is

$$\begin{aligned} \bar{m}_\star &= (1 - f_{\rm bin}) \int_{m_{\rm min}}^{m_{\rm max}} m f(m)\, dm + f_{\rm bin} \int_{m_{\rm min}}^{m_{\rm max}} \int_0^1 \left[f(m) g(q)\, (m + qm)\right]\, dq dm = \\ &= f_0 \left(1 + \frac{f_{\rm bin}}{2}\right) \left[\frac{1}{2 - \alpha_1} \left(\frac{m_1^{2-\alpha_1} - m_{\rm min}^{2-\alpha_1}}{m_{\rm min}^{-\alpha_1}} \right) + \frac{1}{2 - \alpha_2} \left(\frac{m_1}{m_{\rm min}}\right)^{-\alpha_1} \left(\frac{m_2^{2-\alpha_2} - m_1^{2-\alpha_2}}{m_1^{-\alpha_2}} \right) + \frac{1}{2 - \alpha_3} \left(\frac{m_1}{m_{\rm min}}\right)^{-\alpha_1} \left(\frac{m_2}{m_1}\right)^{-\alpha_2} \left(\frac{m_{\rm max}^{2-\alpha_3} - m_2^{2-\alpha_3}}{m_2^{-\alpha_3}} \right) \right]. \end{aligned} \tag{A.2}$$

In the case when $m_A, m_B > m_2$, we only model the following fraction of all systems:

$$f_{\rm model} = f_{\rm bin} \int_{m_A}^{m_B} f(m)\, dm = f_{\rm bin} f_0 \frac{1}{1 - \alpha_3} \left(\frac{m_1}{m_{\rm min}}\right)^{-\alpha_1} \left(\frac{m_2}{m_1}\right)^{-\alpha_2} \left(\frac{m_B^{1-\alpha_3} - m_A^{1-\alpha_3}}{m_2^{-\alpha_3}} \right). \tag{A.3}$$

The mean mass of a binary system in our simulated population is;

$$\bar{m}_{*,\rm model} = \frac{1}{\int_{m_A}^{m_B} f(m) dm} \int_{m_A}^{m_B} \int_0^1 f(m) g(q) (m + qm)\, dq dm = \frac{3}{2} \frac{1 - \alpha_3}{2 - \alpha_3} \left(\frac{m_B^{2-\alpha_3} - m_A^{2-\alpha_3}}{m_B^{1-\alpha_3} - m_A^{1-\alpha_3}} \right). \tag{A.4}$$

Thus, the total modeled mass $M_{*,\rm model}$ represents only a fraction of the total stellar population mass M_*:

$$f_{\rm corr} = \frac{M_{*,\rm model}}{M_*} = f_{\rm model} \frac{\bar{m}_{*,\rm model}}{\bar{m}_*} \tag{A.5}$$

and we must renormalize by the inverse of $f_{\rm corr}$ in order to return to the population we intended to simulate.

Adopting the Kroupa (2001) IMF, namely $\alpha_1 = 0.3$, $\alpha_2 = 1.3$, $\alpha_3 = 2.3$, $m_1 = 0.08\,{\rm M}_\odot$, $m_2 = 0.5\,M_\odot$, using the observed $f_{\rm bin} = 0.7$ (Sana et al. 2012), arbitrarily choosing $m_{\rm min} = 0.01\,{\rm M}_\odot$ and $m_{\rm max} = 200\,{\rm M}_\odot$ as the minimum and the maximum stellar mass, and carrying out the simulation for primary masses in the range between $m_A = 5\,{\rm M}_\odot$ and $m_B = 150\,{\rm M}_\odot$ (Figer 2005), we obtain $f_{\rm corr}^{-1} = 4.78$.

Appendix B: Detection rate

To compute the detected BH merger rate by GW detectors, we follow a similar procedure to the one of Belczynski et al. (2016b) which is a refined version of Dominik et al. (2015). In our cosmological calculation, we adopt the flat ΛCDM model with $H_0 = 67.7\,\frac{\rm km/s}{\rm Mpc}$ and $\Omega_m = 0.307$ (Planck Collaboration et al. 2016). We follow the model of Madau & Fragos (2017) for the star formation rate (SFR) model as a function of redshift, which is an updated version of Madau & Dickinson (2014),

$${\rm SFR}(z) = \frac{0.01 \cdot (1 + z)^{2.6}}{1 + ((1 + z)/3.2)^{6.2}}\ {\rm M}_\odot\, {\rm yr}^{-1}\, {\rm Mpc}^{-3}\,. \tag{B.1}$$

We assume that the metallicities of the binaries follow a truncated log-normal distributed,

$$\mathcal{N}(\log_{10}(Z)\,|\,\mu(z), \sigma) \equiv \frac{dP}{d\log_{10}(Z)}(z) = \frac{1}{\sigma\sqrt{2\pi}} \exp\left(-\frac{(\log_{10}(Z) - \mu(z))^2}{2\sigma^2} \right) \tag{B.2}$$

with standard deviation $\sigma = 0.5$ and mean $\mu = \log_{10}\left(\bar{Z}(z)\right) - \frac{\ln(10)}{2}\sigma^2$ where the mean metallicity is (Madau & Fragos 2017)

$$\bar{Z}(z) = Z_\odot \cdot 10^{0.153-0.074\cdot z^{1.34}} . \tag{B.3}$$

The log-normal distribution is truncated at the highest metallicity bin edge, $Z_{\max} = 0.034923$, and the distribution is accordingly renormalized to ensure that $\int_{-\infty}^{\log_{10} Z_{\max}} \mathcal{N}(\log_{10}(Z)\,|\,\mu(z),\sigma)\, d\log_{10} Z = 1$. Portions of the distribution extending beyond the lower limit edge $Z_{\min} = 0.000091$ are included in the edge bin when integrating over metallicity.

We compute the detection rate by integrating the cosmological merger rate $R(z_m) = \frac{dN}{dm_1 dm_2 dV_c dt_m}$ per unit masses, per unit comoving volume, per unit time as measured in the source frame at the redshift of the merger as in Eq. (5) of Dominik et al. (2015), that is

$$R_{\rm det} = \iiint R(z_m)\frac{dt_m}{dt_{\rm det}} p_{\rm det}(z_m, m_1, m_2)\, dm_1 dm_2 dV_c \,, \tag{B.4}$$

where the factor $\frac{dt_m}{dt_{det}} = \frac{1}{1+z_m}$ account for the difference in clock rates at merger and at the detector and $p_{\rm det}$ is the detection probability accounting for the detector's selection effects. The integration over the comoving volume can be calculated with a change of variable over the redshift of merger, namely $dV_c = \frac{dV_c}{dz_m} dz_m$, where

$$\frac{dV_c}{dz_m} = \frac{4\pi c}{H_0}\frac{D_c^2(z_m)}{E(z)} \,, \tag{B.5}$$

and $D_c(z)$ is the comoving distance which is related to the luminosity distance as $D_L(z) = D_c(z)(1+z)$ and is computed as follows

$$D_c(z) = \frac{c}{H_0}\int_0^z \frac{dz'}{E(z')} \tag{B.6}$$

where $E(z) = \sqrt{\Omega_m(1+z)^3 + \Omega_\Lambda}$. The merger rate $R(z_m)$ can be rewritten as the convolution of the star-formation rate, SFR= $\frac{d^2 M_f}{dV_c dt_f}$, that is the total mass of stars formed per comoving volume per year, and the number density of binaries per unit star forming mass M_f per unit masses m_1, m_2 per unit log-metallicity interval Z per unit time delay $\tau = t_m - t_f$:

$$R(z_m) \equiv R(z(t_m)) = \int_0^{t_m}\int \frac{d^2 M_f}{dV_c dt_f}(z_f)\,\frac{d^5 N}{dM_f dm_1 dm_2 d\tau d\log_{10} Z}(\tau)\,\mathcal{N}\left(\log_{10}(Z)\,\middle|\,\mu = \log_{10}\left(\bar{Z}(z_f)\right) - \frac{\ln(10)}{2}\sigma^2, \sigma = 0.5\right) d\log_{10} Z\, dt_f \,, \tag{B.7}$$

where we used the compact notation $z_f \equiv z(t_f)$. The time delay τ is mostly set by $T_{\rm merger}$, since the GW-driven merger takes much longer than stellar evolution for BH progenitors. Performing the change of variable $dz_m = \frac{dz_m}{dt_m} dt_m = H_0(1+z_m)E(z_m)dt_m$, the integral of Eq. (B.4) translates into the following Monte-Carlo sum over the formation time intervals arbitrarily chosen as $\Delta t_i = 100\,$Myr and 30 uniformly-distributed log-metallicity intervals for $Z \in [Z_{\min}, Z_{\max}]$

$$R_{\rm det} = \sum_{\Delta t_i}\sum_{\Delta Z_j}\sum_k \frac{\rm fSFR(z_{f,i})}{M_{{\rm sim},\Delta Z_j}}\, f_{\rm corr}\, 4\pi c\, D_c^2(z_{m,i,k})\, p_{\rm det}(z_{m,i,k}, m_{1,k}, m_{2,k})\, \Delta t_i \,, \tag{B.8}$$

where $M_{{\rm sim},\Delta Z_j}$ is the total mass simulated per log-metallicity interval ΔZ_j and fSFR is the total mass of stars formed per comoving volume per year per log-metallicity interval ΔZ_j,

$$\begin{aligned}{\rm fSFR}(z_{f,i}) &= \int_{\Delta Z_j} {\rm SFR}\left(z_{f,i}\right)\,\mathcal{N}\left(\log_{10}(Z)\,\middle|\,\mu = \log_{10}\left(\bar{Z}(z_f)\right) - \frac{\ln(10)}{2}\sigma^2, \sigma = 0.5\right) d\log_{10} Z = \\ &= {\rm SFR}(z_{f,i})\left[CDF\left(\log_{10}(Z_j) + \frac{\Delta Z_j}{2}\right) - CDF\left(\log_{10}(Z_j) - \frac{\Delta Z_j}{2}\right)\right]\ {\rm M_\odot\,yr^{-1}\,Mpc^{-3}} \,,\end{aligned} \tag{B.9}$$

where Z_j is the center of the log-metallicity bin ΔZ_j corresponding to the metallicity Z_k of the binary k. Meanwhile, the integrated SFR (iSFR) over the cosmic time used to obtain the weighted distributions of parameters after the CE phase is computed with the change of variable $dt = \frac{dt}{dz} dz = (H_0(1+z)E(z))^{-1}\, dz$,

$${\rm iSFR}(Z) = \int_0^\infty {\rm SFR}\,(z)\,\mathcal{N}\left(\log_{10}(Z)\,\middle|\,\mu = \log_{10}\left(\bar{Z}(z_f)\right) - \frac{\ln(10)}{2}\sigma^2, \sigma = 0.5\right)\frac{dt}{dz} dz\ \ {\rm M_\odot\,Mpc^{-3}} \,, \tag{B.10}$$

which gives the total mass of stars formed per comoving volume at a given metallicity Z.

Appendix C: Linear interpolation of the MESA simulations

Running MESA simulations on the entire simulated binary population is too computationally expensive. Instead, we use linear interpolation over a simulated grid to estimate the physical observables of the binaries that we are interested in. To generate the first simulations we sample stochastically in the logarithmic parameter space of initial masses, orbital periods and metallicities. We generate 3,000 initial points with $m_{\rm BH} \in [2.5\,{\rm M}_\odot, 60\,{\rm M}_\odot]$, $m_{\rm He-star} \in [2.5\,{\rm M}_\odot, 89\,{\rm M}_\odot]$, $p \in [0.05\,{\rm days}, 8.5\,{\rm days}]$ and $Z \in [0.0001, 0.0349]$. We add to these 1,500 points drawn from a kernel density estimator (KDE) of the parameter distribution of the synthetic binary population.

We cover these points by running MESA binary simulations as described in section 2.2. We want to interpolate six quantities: the He-star mass and its CO core mass before the supernova, the resulting BH mass, the orbital period before the supernova, the lifetime of the BH-He-star binary and the spin of the second-born black hole. All physical quantities are log-transformed and rescaled to the interval $[-1, 1]$ before going through the interpolation algorithm. The interpolation itself relies on building a Delaunay triangulation of the input data points followed by barycentric linear interpolation over the vortices of the (hyper)triangle containing the location of interest. The relative error on each quantity X_i is computed as $\Delta_i = (X_{\rm true,i} - X_{\rm interp.,i})/X_{\rm true,i}$ (in the original units, except for spins, where the relative error is computed on the spin logarithm to avoid excessive sensitivity to true values close to zero). We then combine the relative errors of the quantities to obtain the combined relative error

$$\Delta = \min\left(\sqrt{\sum_{i=1}^{6}\Delta_i^2},\ \sqrt{6}\right), \tag{C.1}$$

where we arbitrarily limit the maximal combined relative error to $\sqrt{6}$, that is a point with all relative errors equal to $|\Delta_i| = 1$.

We check the accuracy of the linear interpolator by conducting 50 leave 5% of the sample out tests. We use the combined relative errors as weights to sample an additional 500 points where the interpolator is performing the worst. We iterate this procedure 21 times for a total of 10,500 simulations, stopping because almost all the new points generated through this procedure in the 22nd iteration would be on the boundaries. The triangulation scheme can still fail near the parameter space boundaries; in this case, we find that 2.5% of synthetic population systems cannot be interpolated, and we run 3000 simulations to bring the parameter space coverage to 100%.

Fig. C.1 shows the relative errors in the interpolated quantities over the series of 50 leave 5% of the sample out tests. The left panel shows the median percentage relative errors excluding non-fittable points. These stabilize at 0.01%, 0.20% and 0.04% for the He-star mass before supernova, its CO core mass, and resultant BH mass; 0.01% for the orbital period; 0.04% for the lifetime of the BH-He-star binary and 0.4% for the log-spin of the second-born BH. The log spin is the parameter which shows the biggest relative errors because it can have very large negative values for spins close to zero. The right panel of Fig. C.1 shows the fraction of relative errors larger than 10% as a function of the number of simulations for the different interpolated quantities where we also count non-fittable points, such as points at the boundary of the parameter space or isolated regions of the parameter space. At the last iteration the mean of the 50 leave 5% of the sample out tests shows the following fraction of relative errors greater than 10%: 5% for the He-star mass before the supernova, 8% for its CO core mass and the resulting BH mass, 6% for the orbital period, 6% for the lifetime of the BH-He-star binary and 17% for the log-spin of the second-born BH. The apparent increase in the fraction of relative errors larger than 10% with the number of simulations happens because with the last iterations we are sampling mostly the boundaries of the parameter space and the test picks up more points that cannot be interpolated (we note that the median relative errors does not show this trend and stabilizes). The last simulations used to bring the coverage of the parameter space to 100% are run in disconnected and remote regions of the parameter space, and the "leave out" tests pick up the newly added samples, artificially increasing the apparent fraction of large relative errors.

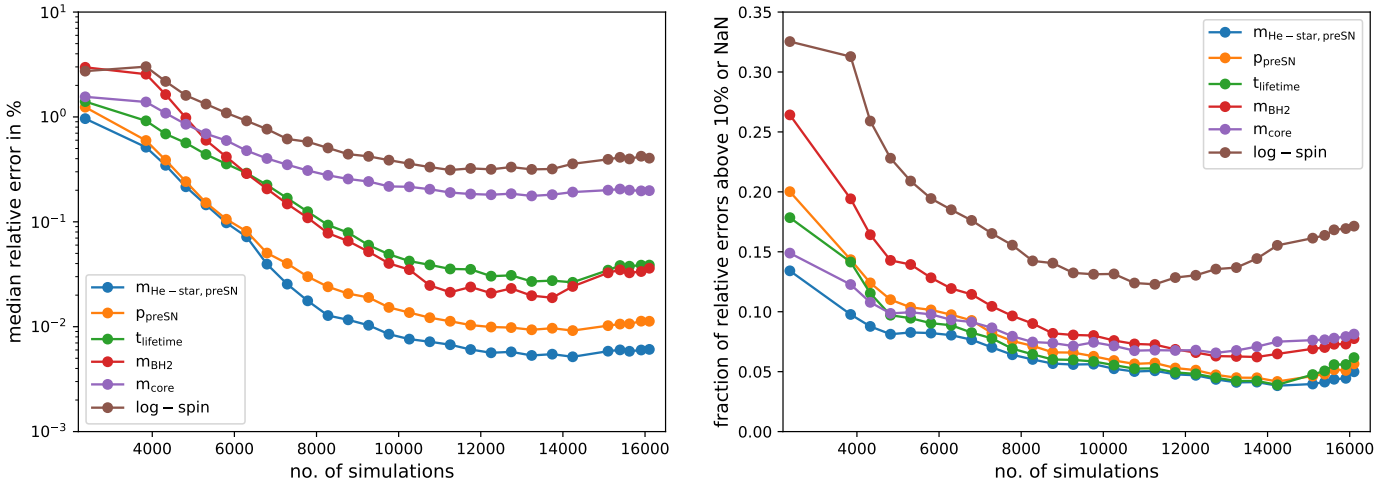

Fig. C.1: Median relative error of the interpolation expressed as a percentage (*Left*) and the fraction of relative errors above 10% (*Right*) from all iterations of the 50 leave 5% of the sample out tests for six interpolated quantities. The points on each plot, moving from left to right, represent the different iterations; we exclude all simulations that stopped due to initial Roche-lobe overflow (indicating a difference between COMPAS and MESA models). The right plot includes NaNs (obtained from non-fittable points, e.g., points at the boundary of the parameter space) when counting relative errors larger than 10%, while the left plot excludes them.

2.1.3 Impact on the current field of research

The presented model had an important impact on GW astrophysics as it quantified the fraction of tidally spun-up BBHs formed through the CE formation channel to be $\sim 20\%$ with $\chi_{\rm eff} \geq 0.1$. In contrast, the remaining $\sim 80\%$ has negligible spins with $0 \lesssim \chi_{\rm eff} < 0.1$. At the time of publication, the model was consistent with current GW observations of BBHs from GWTC-1. Later observations of BBHs, e.g., those included in the GWTC-2 and GWTC-3, have hinted at a BBH sub-population having negative $\chi_{\rm eff}$, which is inconsistent with the CE channel if BH natal kicks are assumed to be small (Abbott et al. 2021c,e). However, other independent studies have challenged such interpretations, claiming that current GW observations still show support for a dominant BBH population with negligible spins ($\chi_{\rm eff} \simeq 0$) and a smaller sub-population with spins positive-aligned with the orbital angular momentum ($\chi_{\rm eff} > 0$, e.g., Roulet et al. 2021; Galaudage et al. 2021). We refer to the discussion about the interpretation and implications of observed BBH spins in Sections 1.1.3 and 1.4.3. In the remaining part of this section, we discuss the major impact that this publication had on the current field of GW astrophysics research.

In parallel to our work, under similar model assumptions but using `StarTrack` (Belczynski et al. 2002, 2008), Belczynski et al. (2020) independently reached at a similar conclusion with ours. In contrast to our approach, Belczynski et al. (2020) employed approximations to model the tidal spin-up phase of BH-WR binaries. These approximations include assuming that the WR stellar profile is tidally locked to the orbital period and solid-body rotation of the WR stellar structure as implemented in (Belczynski et al. 2008). This approximate modeling cannot capture in detail the rich features of this evolutionary phase regarding the impact of stellar-wind mass loss and the WR stellar structure evolution onto the tidal spin-up efficiency. See Bavera et al. (2020)'s discussion about previous studies, which used even more simplistic parametric approximations and over-predicted the fraction of highly spinning BBHs from the CE formation channel (Kushnir et al. 2016; Hotokezaka & Piran 2017; Zaldarriaga et al. 2018; Gerosa et al. 2018). Additionally, Belczynski et al. (2020) also explored the possibility that post-CE WR stars are highly rotating, as well as the impact of inefficient angular-momentum transport on such a hypothetical scenario. They obtained a model predicting an overabundance of highly rotating BBHs which are currently non observed by GW detectors. Using a similar parametric approach of tidal spin-up but without using binary population synthesis, Piran & Piran (2020) also found that BBHs formed from isolated binary evolution and experiencing tidal spin-up during the BH-WR evolutionary phase could explain the observed sub-population of spinning BBHs.

Using detailed `MESA` binary simulations in a recent study, Fuller & Lu (2022) corroborated our results about tidal spin-up efficiency in close BH-WR binary systems. Similar to our findings, the authors report that spin-up of the WR stellar companion takes place for orbital periods $\lesssim 1\,$day. Further findings of Fuller & Lu (2022) are discussed in §4.1.3.

Finally, we explicitly point out that the results presented in Bavera et al. (2020) are currently the reference for studies of BBH spin distribution of systems formed through the canonical CE formation channel. In this research project, Bavera et al. (2020) quantified the $\chi_{\rm eff}$ distribution of BBH formed through the CE channel employing detailed `MESA` binary simulations targeting the tidal spin-up phase of BBH progenitors. Before this work, the understanding of this evolutionary channel was leading to a pre-

diction of a highly rotating BBH population, mainly due to an over-simplistic parametric approximation of the BH-WR tidal spin-up phase.

2.2 The impact of mass-transfer physics on the observable properties of field binary black hole populations

2.2.1 A brief introduction

The previous section was restricted to the tidal spin-up of close BBH progenitors formed through the CE channel. Alternatively, as discussed in §1.3.1.1, the second mass-transfer episode could be stable (Pavlovskii et al. 2017; van den Heuvel et al. 2017; Neijssel et al. 2019; van Son et al. 2021). Following the footsteps of the project presented in the previous section, we investigated the potential spin-up of BH-WR systems formed through the SMT channel. Additionally, we investigated multiple mass-transfer uncertainties that might affect the $\chi_{\rm eff}$ distribution of BBHs formed from both the CE and SMT channels in this project. These uncertainties include the efficiency of CE, which is parameterized by $\alpha_{\rm CE}$ in the $\alpha_{\rm CE} - \lambda$ parametrization (for a review about CE evolution, see Ivanova et al. 2013), super-Eddington accretion spin-up on the first-born BH during the second SMT episode, and uncertainties in the parametrization of mass-transfer stability ($q_{\rm crit}$) which governs the relative fraction of systems evolving either through the CE or SMT channels (see §1.3.1.1). Similarly to Bavera et al. (2020), the project presented in this section adopts the hybrid approach to binary population synthesis, combining the `COSMIC` rapid binary population synthesis code (Breivik et al. 2020) with the same detailed BH-WR simulations.

We also explicitly mention that the BH-WR `MESA` simulations presented in Bavera et al. (2020), and based on the previous work of Qin et al. (2018), were reconfigured to follow the same stellar and binary assumptions made by du Buisson et al. (2020). In this last study, du Buisson et al. (2020) used `MESA` to study the BBH formation through the CHE channel (see §1.3.1.2). The BH-WR `MESA` models were updated in preparation for the follow-up studies presented in Chapters 3 and 4, which require complementing our BBH model targeting the CE and SMT formation channels with the CHE BBH model of du Buisson et al. (2020). As previously discussed in Section 1.5.2, publicly available rapid population synthesis codes, when this project was carried out, could not model the evolution through the CHE channel.

Additionally, the newer version of the BH-WR simulation ensures that the BH-WR simulations only start once the WR stellar profiles reach local thermal equilibrium after `MESA` relaxes the metallicity to the desired value. Local thermal equilibrium is reached after the inflated (nonphysical) WR stellar profiles contract to ignite helium in their stellar cores, namely when the stars find themselves at zero-age helium main sequence. This last improvement to Qin et al. (2018) BH-WR `MESA` simulations is important to accurately model close BH-WR systems, as we found that a non-relaxed profile might overestimate the radius of the WR star up to a factor of two, depending on the WR stellar mass. The updated BH-WR `MESA` simulation configuration was made publicly available after the publication of the project (Bavera 2021).

2.2.2 Manuscript

The conducted study Bavera et al. (2021a) was published in *Astronomy & Astrophysics* in March 2021. The arXiv open-access version of the manuscript is presented in the following pages.

Astronomy & Astrophysics manuscript no. aanda
February 16, 2021
©ESO 2021

arXiv:2010.16333v2 [astro-ph.HE] 15 Feb 2021

The impact of mass-transfer physics on the observable properties of field binary black hole populations

Simone S. Bavera[1,⋆], Tassos Fragos[1], Michael Zevin[2,3,⋆⋆], Christopher P. L. Berry[2,4], Pablo Marchant[5], Jeff J. Andrews[2], Scott Coughlin[2], Aaron Dotter[2], Konstantinos Kovlakas[6,7], Devina Misra[1], Juan G. Serra-Perez[2], Ying Qin[2], Kyle A. Rocha[2], Jaime Román-Garza[1], Nam H. Tran[8] and Emmanouil Zapartas[1]

[1] Geneva Observatory, University of Geneva, Chemin des Maillettes 51, 1290 Versoix, Switzerland
[2] Center for Interdisciplinary Exploration and Research in Astrophysics (CIERA) and Department of Physics and Astronomy, Northwestern University, 1800 Sherman Avenue, Evanston, IL 60201, USA
[3] Enrico Fermi Institute and Kavli Institute for Cosmological Physics, The University of Chicago, 5640 South Ellis Avenue, Chicago, Illinois 60637, USA
[4] SUPA, School of Physics and Astronomy, University of Glasgow, Glasgow G12 8QQ, UK
[5] Institute of Astrophysics, KU Leuven, Celestijnenlaan 200D, 3001, Leuven, Belgium
[6] Physics Department, University of Crete, GR 71003, Heraklion, Greece
[7] Institute of Astrophysics, Foundation for Research and Technology-Hellas, GR 71110 Heraklion, Greece
[8] DARK, Niels Bohr Institute, University of Copenhagen, Jagtvej 128, 2200 Copenhagen, Denmark

Accepted January 25, 2021

ABSTRACT

We study the impact of mass-transfer physics on the observable properties of binary black hole populations that formed through isolated binary evolution. We used the `POSYDON` framework to combine detailed `MESA` binary simulations with the `COSMIC` population synthesis tool to obtain an accurate estimate of merging binary black hole observables with a specific focus on the spins of the black holes. We investigate the impact of mass-accretion efficiency onto compact objects and common-envelope efficiency on the observed distributions of the effective inspiral spin parameter $\chi_{\rm eff}$, chirp mass $\mathrm{M_{chirp}}$, and binary mass ratio q. We find that low common envelope efficiency translates to tighter orbits following the common envelope and therefore more tidally spun up second-born black holes. However, these systems have short merger timescales and are only marginally detectable by current gravitational-wave detectors as they form and merge at high redshifts ($z \sim 2$), outside current detector horizons. Assuming Eddington-limited accretion efficiency and that the first-born black hole is formed with a negligible spin, we find that all non-zero $\chi_{\rm eff}$ systems in the detectable population can come only from the common envelope channel as the stable mass-transfer channel cannot shrink the orbits enough for efficient tidal spin-up to take place. We find that the local rate density ($z \simeq 0.01$) for the common envelope channel is in the range of $\sim$ 17–113 $\mathrm{Gpc^{-3}\,yr^{-1}}$, considering a range of $\alpha_{\rm CE} \in [0.2, 5.0]$, while for the stable mass transfer channel the rate density is $\sim 25\ \mathrm{Gpc^{-3}\,yr^{-1}}$. The latter drops by two orders of magnitude if the mass accretion onto the black hole is not Eddington limited because conservative mass transfer does not shrink the orbit as efficiently as non-conservative mass transfer does. Finally, using GWTC-2 events, we constrained the lower bound of branching fraction from other formation channels in the detected population to be ~ 0.2. Assuming all remaining events to be formed through either stable mass transfer or common envelope channels, we find moderate to strong evidence in favour of models with inefficient common envelopes.

Key words. black hole physics – gravitational waves – stars: black holes – stars: binaries: close – stars: evolution – stars: massive – accretion

1. Introduction

Stars in binary systems are common in the Universe (Sana et al. 2012), but the details of their evolution are uncertain. For massive binaries, it is difficult to observationally constrain the details of physical processes, such as mass-transfer (MT), as the lifetimes of these interacting binary phases are short and hence it is unlikely to observe many of them directly. However, with gravitational-wave (GW) observations, one can search for the imprints of these processes on the properties of their stellar remnant populations, such as the binary black hole (BBH) population.

The LIGO Scientific and Virgo Collaboration (LVC) has recently released the new GW catalogue GWTC-2 (Abbott et al. 2020a), which includes 37 new potential BBH detections[1] from the first half of the third observing run (O3a). In total, GWTC-2 contains 47 BBHs detections (Abbott et al. 2019; Abbott et al. 2020a), and the intrinsic rate density of BBH mergers is currently estimated to be $23.9^{+14.9}_{-8.6}\ \mathrm{Gpc^{-3}\,yr^{-1}}$ (Abbott et al. 2020b). Each GW detection can constrain some combination of the astrophysical BH parameters: spin and mass. Convenient well-measured quantities are the chirp mass

$$\mathrm{M_{chirp}} = \frac{(m_1 m_2)^{3/5}}{(m_1 + m_2)^{1/5}}\,, \tag{1}$$

⋆ E-mail: simone.bavera@unige.ch
⋆⋆ NASA Hubble Fellow

[1] Here we consider GW190814 as a possible BBH.

where m_1 and m_2 ($m_1 \geq m_2$) are the BHs masses, the binary mass ratio $q = m_2/m_1 \leq 1$, and the effective inspiral spin parameter

$$\chi_{\rm eff} = \frac{m_1 \boldsymbol{a}_1 + m_2 \boldsymbol{a}_2}{m_1 + m_2} \cdot \hat{\boldsymbol{L}}, \quad (2)$$

where $\hat{\boldsymbol{L}}$ is the orbital angular momentum (AM) unit vector and $\boldsymbol{a}_1$ and $\boldsymbol{a}_2$ are the BH dimensionless spin vectors. The dimensionless spin vectors are defined as

$$\boldsymbol{a_i} = \frac{c\boldsymbol{J}_i}{Gm_i^2}, \quad i \in \{1, 2\}, \quad (3)$$

where c is the speed of light, G is the gravitational constant and $\boldsymbol{J}_i$ is the spin AM vector of the BH. There is a degeneracy between $\chi_{\rm eff}$ and q which limits the accuracy to which each quantity can be measured independently (Poisson & Will 1995; Hannam et al. 2013). Nevertheless, the combination of the three observables provide a robust constraint on the properties of a BBH.

Multiple formation channels have been proposed to explain the origin of merging BBHs. They can be divided into two broad categories: (i) isolated binary evolution and (ii) dynamical assembly.

The former occurs during isolated stellar evolution in the field under some specific binary evolution interactions. Interacting binaries that after the formation of the first BH go through (A) stable mass transfer (SMT; e.g. van den Heuvel et al. 2017; Inayoshi et al. 2017; Neijssel et al. 2019) or (B) unstable mass transfer leading to a common envelope (CE) phase (e.g. Smarr & Blandford 1976; van den Heuvel 1976; Tutukov & Yungelson 1993; Kalogera et al. 2007; Postnov & Yungelson 2014; Belczynski et al. 2016) have been shown to form merging BBHs. Another possibility is the formation of BBHs from massive stars with low metallicities and orbital period less than ∼4 days, which due to their tidal interaction, can maintain an almost critical rotation and are going to evolve (C) chemically homogeneously (e.g. de Mink et al. 2009; Mandel & de Mink 2016; Marchant et al. 2016; du Buisson et al. 2020).

The second category of formation channels category occurs in dense stellar environments where stars and binaries can dynamically interact with each other and assemble new binary systems with more massive BHs and tighter orbits, that may eventually merge within the Hubble time. This formation path is present in (D) globular, open, and nuclear stellar clusters (e.g. Kulkarni et al. 1993; Sigurdsson & Hernquist 1993; Portegies Zwart & McMillan 2000; Miller & Lauburg 2009; Banerjee et al. 2010; Rodriguez et al. 2015; Antonini & Rasio 2016; Arca-Sedda & Gualandris 2018; Fragione & Kocsis 2018; Rodriguez et al. 2019) and (E) active galactic nuclei disks (e.g. Bartos et al. 2017; Stone et al. 2017; McKernan et al. 2018; Tagawa et al. 2020). Finally (F) triple or higher-order stellar systems can also lead to the formation of BBHs (e.g. Silsbee & Tremaine 2017; Rodriguez & Antonini 2018; Gupta et al. 2020; Toonen et al. 2020). Within their uncertainties, almost all of these formation channels have been shown to have rate estimates consistent or marginally consistent with the empirical LVC rates.

In this study we consider the formation of BBHs in isolated binary evolution (A and B) though the SMT and CE phase. In these formation channels, two massive stars are born in a relatively wide binary (orbital separations of order $\sim 1000\,{\rm R}_\odot$), where binary interactions happen after the more massive star leaves the main sequence (MS). At this stage, the star expands to become a red supergiant, and inflates its hydrogen-rich envelope beyond its Roche lobe, leading to the first MT episode. The MT stops when the entire stellar envelope is lost, leaving behind a naked helium (He)-star which eventually collapses to form a BH. When the companion reaches the end of its MS, the process repeats itself for the companion star. This MT phase can be either stable or unstable, with the latter leading to the formation of a CE of gas engulfing the binary. If the stripping of the secondary's envelope is successful, we are left with either a tight BH–He-star system in the case of CE, or with a somewhat wider system in the case of SMT. Eventually the secondary star also collapses to form the second-born BH, and due to energy and AM loss from GW emission (Peters 1964), the BBH system coalesces to form a single, more massive BH.

In the SMT and CE formation channels, the spin of the first-born BH is determined by the AM transport efficiency during the evolution of the progenitor star. Measurements of neutron star and white dwarf spins (Heger et al. 2005; Suijs et al. 2008) and asteroseismology studies (Fuller et al. 2014; Cantiello et al. 2014) suggest that this mechanism must be efficient (Spruit 1999, 2002; Fuller & Ma 2019). Thus, upon expansion, the initial AM of the star is mostly transported to the outer layers which are subsequently lost due to MT and wind mass loss. This leads to the formation of slowly spinning BHs ($a_1 \simeq 0$), as initially suggested in the context of BH low-mass X-ray binary formation by Fragos & McClintock (2015) and subsequently quantitatively shown in Qin et al. (2018), Fuller & Ma (2019) and Belczynski et al. (2020). In the case of the SMT channel, during the second MT episode, the first born BH may accrete material and spin up (Thorne 1974), depending on the accretion efficiency rate. On the other hand, the spin of the second-born BH is determined by the net effect of the stellar wind and the tidal interaction of the BH–He-star binary system. Because of the efficiency of the AM transport, the He-star emerges from the second MT event with a negligible spin. If the orbital separation is small enough and stellar winds do not widen the system significantly, the He-star can be spun up by tides. These conditions are met at low metallicities for BBHs formed through the CE formation channel (Bavera et al. 2020). In contrast, in the case of SMT, the orbits shrink less efficiently leading to less tidally spun up second-born BHs compared to the CE channel.

All formation channels can be investigated through population synthesis studies which adopt stellar and binary models to rapidly evolve millions of binary stars. This approach gives us insights on the overall population observables given a set of physical assumptions. To explore a wide landscape of parameter values and generate many realisations of the studied population, we need to efficiently evolve millions of binaries. This can be achieved through parametric population synthesis codes which employ fits of single stellar evolution with analytical models to simulate the binary interactions at the expense of coarser approximations when modelling these interactions. Despite this limitation, rapid population synthesis still allows for investigation into how the observable distributions of a population change within the astrophysical model uncertainties. Bavera et al. (2020) recently showed how, given a specific theoretical framework, one can adopt detailed stellar and binary simulations in a population synthesis study to obtain new observable estimates such as the BH spin distributions. In this paper we study how these model predictions are affected by the uncertainties of MT physics such as MT stability and efficiency, CE efficiency and initial orbital distributions.

In Sec. 2 we present the framework we use to generate the population of BBHs and how we convolve the synthetic BBH population with the redshift- and metallicity-dependent star formation rate, as well as incorporate GW detector selection effects. We also summarise the key differences between this work and

Bavera et al. (2020). The BBH observable distributions for different MT and CE efficiencies are presented in Sec. 3, where we also show how the $\chi_{\rm eff}$, $\rm M_{chirp}$ and q distributions change for these different physical assumptions and determinate thorough model selection which CE efficiency is supported by GWTC-2 BBHs events. The impact of MT stability and initial orbital distributions on the uncertainties of our models is discussed in Sec. 4. We conclude by summarising our findings in Sec. 5.

2. Methods

We generate our populations of BBHs by modelling isolated binary evolution with the POSYDON code.[2] POSYDON, among many other functionalities, can run and combine detailed stellar and binary evolution simulations performed with the MESA code (Paxton et al. 2011, 2013, 2015, 2018, 2019) to existing parametric binary population synthesis codes. This integration lets us target particular evolutionary phases with more detailed modelling. Similar hybrid approaches have been used in previous population synthesis studies (e.g. Nelson 2012; Chen et al. 2014; Fragos et al. 2015; Shao & Li 2015; Shao et al. 2019). In this work, we use COSMIC (Breivik et al. 2020) to model the evolution of binaries starting from zero age MS (ZAMS) until the formation of the BH–He-star system. We then use MESA to model in detail the subsequent evolution until the formation of the BBH which is the evolutionary phase that determines the spin of the second-born BH (Qin et al. 2018; Bavera et al. 2020).

2.1. Binary black hole population

We create synthetic BBH populations similar to Bavera et al. (2020), but with some key differences.

We assume similar initial binary properties with the exception of the initial orbital periods which here are drawn from an extended Sana et al. (2012) log-power law with coefficient $\pi = -0.55$ in the range $p \in [10^{0.15}, 10^{5.5}]$ days and extrapolated down to $p = 0.4$ days assuming a log-flat distribution (as the power law is not defined for $p < 10^{0.15}$ day). This extension includes the portion of the parameter space leading to chemical homogeneous evolution (du Buisson et al. 2020). All initial binary property assumptions are explained in Appendix A and discussed in Sec 4.1.

To determine the MT stability, we adopt critical mass ratios $q_{\rm crit}$ as in Neijssel et al. (2019) with one exception. For stars in the giant branch (GB) and asymptotic giant branch (AGB) we use the same $q_{\rm crit}$ fits as in Neijssel et al. (2019) but do not adopt Soberman et al. (1997) radial response to adiabatic mass loss for evolved stars beyond the Hertzsprung gap (HG) because they are not currently available in COSMIC. For our reference models, the stable mass-accretion efficiency onto degenerate objects is Eddington-limited. This leads to a highly non-conservative mass-transfer phase where the first-born BH accretes a negligible amount of matter and cannot spin up due to accretion. Unstable MT is parameterised with the standard $\alpha_{\rm CE}$–λ formalism (see e.g. Ivanova et al. 2013, for a review). In contrast to Bavera et al. (2020), we adopt λ fits as in Claeys et al. (2014) while we explore different $\alpha_{\rm CE}$ efficiencies: $\alpha_{\rm CE} \in [0.2, 0.35, 0.5, 0.75, 1.0, 2.0, 5.0]$. Since, approximately, $\alpha_{\rm CE}$ scales linearly with the orbital separation post CE, see Eq. (B.2), low CE efficiencies lead to tighter orbital separations post CE. Therefore, we expect that more BH–He-star systems will undergo tidal spin up at lower $\alpha_{\rm CE}$. We describe the details of our COSMIC model, MT stability and CE in Appendix B. In Sec. 4.2 and 4.3 we discuss how our BBH population distributions and rates are affected by these assumptions.

The late-end phase of the binary evolution of BBHs formed through CE and SMT channels are BH–He-star systems. We update our MESA models (Qin et al. 2018; Bavera et al. 2020) to match the stellar model assumptions of du Buisson et al. (2020). In contrast to Bavera et al. (2020), we relax the He-star models to zero age helium MS (ZAHeMS) before initiating the binary evolution. This ensures that the He-star model is in thermal and hydrostatic equilibrium when the binary interactions begin. In order to verify that the He-star will not overfill the L2 Roche volume throughout the binary evolution, we include the prescription of Misra et al. (2020). The ingredients of our MESA model are explained in Appendix C.

Once the He-star reaches carbon depletion, the MESA simulations are stopped. We then collapsed the profile of the He-star according to the procedure used in Bavera et al. (2020) which accounts for disk formation. Here we adopted a different treatment of neutrino mass loss where we assume that the innermost 3 $\rm M_\odot$ forms a proto-neutron star which collapses to form a BH of 2.5 $\rm M_\odot$ while 0.5 $\rm M_\odot$ are converted into neutrinos and escape the system carrying away AM (cf. Zevin et al. 2020c). The complete procedure used to collapse the He-star profiles is explained in detail in Appendix D.

We use our detailed binary stellar models to cover the four-dimensional parameter space of initial metallicity Z, BH mass $M_{\rm BH}$, He-star mass $M_{\rm He-star}$ and orbital period p. We run grids for 30 different metallicities ranging from $\log_{10}(Z) = -4.0$ to $\log_{10}(1.5Z_\odot) \simeq -1.593$ in steps of $\log_{10}(Z) \simeq 0.083$ where we adopt the solar reference $Z_\odot = 0.017$ (Grevesse et al. 1996). For each metallicity we run 11 BH masses in the log-range $[2.5, 54.4]\,\rm M_\odot$, 17 He-star masses in the log-range $[8, 80]\,\rm M_\odot$ and 20 initial binary periods in the log-range $[0.09, 8]$ days. In total, we calculated roughly 110,000 new binary evolution sequences. These grids were used to determine the final outcomes and final parameters of the late-end evolution stage of the binary systems through linear interpolation for each metallicity, independently. The features of these grids and the interpolation accuracy are discussed in Appendix E.

In Fig. 1 we show an example of a two-dimensional slice from our four-dimensional grid. The parameter space is sliced at $Z = 0.001$ and $M_{\rm BH} = 29.4\,\rm M_\odot$. We show the final second-born BH mass and spin, as well as the BBH merger timescale as a function of initial orbital period and He-star mass at ZAHeMS. We see that the binary interactions determining the spin of the second-born BH create a gradual transition between tidally locked systems and non-spinning systems. The complex interactions of stellar winds, tides, internal differential rotation and (in some cases) mass transfer are important in determining the spin of the second-born BH, and therefore require a detailed treatment which traditional rapid population codes cannot offer.

Once a BBH system is formed, GW inspiral leads to the system's eventual merger. We calculate the merger timescale $T_{\rm merger}$ as in Peters (1964) accounting for eccentricity. In our models, this timescale is anti-correlated with the observable $\chi_{\rm eff}$. This is caused by tides, as they are the only mechanism able to spin up the progenitor of the second-born BH. Their efficiency is highly dependent on the orbital separation, see Eq. (C.1). For tidally locked systems one recovers $T_{\rm merger} \propto a_2^{-8/3} \propto \chi_{\rm eff}^{-8/3}$ while for the other systems $T_{\rm merger} \propto a_2^{-8/17} \propto \chi_{\rm eff}^{-8/17}$ (Bavera et al. 2020). We therefore expect systems with $\chi_{\rm eff} > 0$ to have, on average,

[2] See Fragos et al. (2021), to be submitted by the POSYDON collaboration, www.posydon.org.

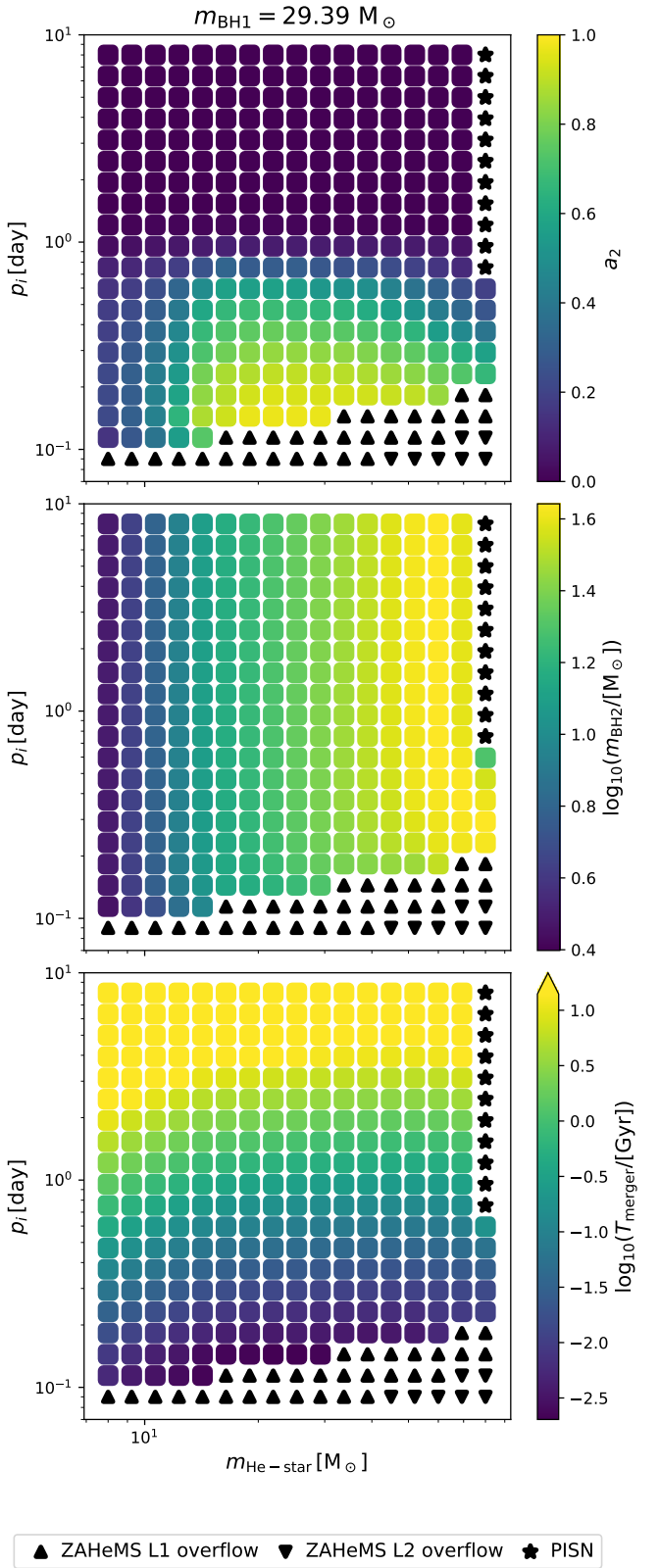

Fig. 1. Example of a two-dimensional slice of the four-dimensional grid showing their initial BH–He-star orbital period p_i (in days) and initial He-star mass $m_{\rm He-star}$ (in $\rm M_\odot$) for $\log_{10}(Z) \simeq -3$ and $m_{\rm BH1} = 29.39\,\rm M_\odot$. The final mass $m_{\rm BH2}$ and spin a_2 of the second-born BH, as well as merger timescale $T_{\rm merger}$, are coloured according to the legend of each panel. All successful `MESA` simulation stopped at carbon depletion (square markers) while other termination flags are shown in the bottom legend. The merger timescale colour bar is capped at 14 Gyr.

shorter merger timescales compared to systems with $\chi_{\rm eff} = 0$. This anti-correlation is the key to understanding the translation from the underlying BBH population (what one would observe with an infinitely sensitive detector) to the observed population. Current GW detectors are probing small redshifts ($z \lesssim 1$) and cannot explore the peak of the Universe's SFR at $z \simeq 2$ where most of the highly spinning BBHs form and merge (as they are preferentially formed in low metallicity environments, e.g. Stevenson et al. 2017).

2.2. Rate estimates

To compute the expected rate of detectable GW events, we need to convolve the redshift- and metallicity-dependent star-formation rate (SFR) with the selection effects of the detector array. To do this, we follow the approach shown in Appendix B of Bavera et al. (2020). We assume a flat ΛCDM cosmology with $H_0 = 67.7\ {\rm km\,s^{-1}\,Mpc^{-1}}$ and $\Omega_m = 0.307$ (Planck Collaboration et al. 2016), a cosmic SFR history as in Madau & Fragos (2017) and metallicities following a truncated log-normal distribution with standard deviation 0.5 dex around the empirical mean metallicity function derived by Madau & Fragos (2017). The log-normal distribution is truncated at the highest metallicity bin edge and the distribution is accordingly renormalised to ensure that $\int_{-\infty}^{Z_{\rm max}} N(\log_{10}(Z)\,|\,\mu(z),\sigma)\,{\rm d}\log_{10} Z = 1$, where $Z_{\rm max}$ is our highest metallicity edge bin. Portions of the distribution extending beyond the lower limit edge are included in the edge bin when integrating over metallicity. The population synthesis predictions are performed in finite time bins of $\Delta t_i = 100$ Myr and log-metallicity bins ΔZ_j. The detection rate of BBH mergers for a given detector network is calculated from the Monte Carlo simulations, cf. Eq. (13) in Bavera et al. (2020),

$$R_{\rm det} = \sum_{\Delta t_i} \sum_{\Delta Z_j} \sum_{k} f_{\rm corr} \frac{{\rm fSFR}(z_{{\rm f},i})}{M_{{\rm sim},\,\Delta Z_j}} 4\pi c\, D_{\rm c}^2(z_{{\rm m},i,k})\, p_{{\rm det},i,k}\, \Delta t_i \ \ {\rm yr}^{-1}, \tag{4}$$

where the argument of the summation is the cosmological weight contribution of the k-th binary born at redshift $z_{{\rm f},i}$ with BH mass $m_{1,k}$ and $m_{2,k}$, spin $\boldsymbol{a}_{1,k}$ and $\boldsymbol{a}_{2,k}$ and merging at redshift $z_{{\rm m},i,k}$. Furthermore, $M_{{\rm sim},\Delta Z_j}$ is the simulated mass per log-metallicity bin ΔZ_j and $f_{\rm corr}$ the normalisation constant which converts the simulated mass to the total stellar population (see Appendix A in Bavera et al. 2020). Here, $D_{\rm c}(z)$ is the comoving distance to the source, ${\rm fSFR}(z)$ is the SFR per log-metallicity range ΔZ_j and $p_{\rm det,i,k} \equiv p_{\rm det}(z_{{\rm m},i,k}, m_{1,k}, m_{2,k}, \boldsymbol{a}_{1,k}, \boldsymbol{a}_{2,k})$ accounts for the selection effects of the detector array.

In contrast to Bavera et al. (2020), we calculate the sensitivity of a GW detector to a source accounting for its network configuration as well as include the selection effects on the BH spins. We assume a 3-detector network configuration composed of LIGO–Hanford, LIGO–Livingston, and Virgo with simulated O3 sensitivity (mid high/late low from Abbott et al. 2018). Detector response functions are calculated using the `PyCBC` package (Nitz et al. 2020). For each compact binary merger, we calculate the signal-to-noise ratio (S/R) as

$$\rho^2 = 4\Re \int_0^\infty \frac{\tilde{h}^\star(f)\tilde{h}(f)}{S_n(f)} {\rm d}f \tag{5}$$

for each detector in the network, where $S_n(f)$ is the one-sided power spectral density of the noise, and $\tilde{h}(f)$ is the GW strain, determined using the `IMRPhenomPv2` waveform approximant

(Hannam et al. 2014; Khan et al. 2016). The network S/R is the quadrature sum of the S/Rs in all the three detectors. Assuming a network detection threshold of $\rho_{\rm det} = 12$, we Monte Carlo sample the sky location, inclination, and phase N times for each system and calculate $\rho_{\rm net}$. The detection probably $p_{{\rm det},i,k}$ is thus determined as

$$p_{{\rm det},i,k} = \frac{1}{N}\sum_{l=1}^{N} \mathcal{H}(\rho_{{\rm net},\,l,i,k} - \rho_{\rm det}), \tag{6}$$

where each l represents a random draw of extrinsic parameters and $\mathcal{H}$ is the Heaviside step function; we perform $N = 1000$ realisations of extrinsic parameters for each system.

The total BBH merger rate density $R_{\rm BBH}(z)$ is the number of BBHs per comoving volume per year as a function of redshift. This quantity can be calculated knowing the contribution of each binary k placed at the centre of each formation time bin Δt_i in its corresponding metallicity bin ΔZ_j assuming $p_{\rm det,i,k} = 1$,

$$R_{\rm BBHs}(z_i) = \sum_{\Delta Z_j}\sum_{k} f_{\rm corr}\frac{{\rm fSFR}(z_{{\rm f},i})}{M_{{\rm sim},\,\Delta Z_j}}\frac{4\pi c\, D_{\rm c}^2(z_{{\rm m},i,k})}{\Delta V_{\rm c}(z_i)}\,\Delta t_i \;\; {\rm Gpc^{-3}yr^{-1}}, \tag{7}$$

where $\Delta V_{\rm c}(z)$ is the comoving volume shell corresponding to the cosmic time bin Δt_i,

$$\Delta V_{\rm c}(z_i) \equiv \int_{\Delta z_i}\frac{1}{1+z}\frac{{\rm d}V_{\rm c}}{{\rm d}z}{\rm d}z = \frac{4\pi c}{H_0}\int_{\Delta z_i}\frac{D_{\rm c}^2(z)}{E(z)(1+z)}{\rm d}z\,, \tag{8}$$

where $E(z) = \sqrt{\Omega_m(1+z)^3 + \Omega_\Lambda}$. Here Δz_i is the redshift interval corresponding to the cosmic time bin Δt_i centered at $z_i \equiv z_{f,i}$.

3. Results

We use our models to predict the distributions of some of the main GW observables: the effective inspiral spin parameter $\chi_{\rm eff}$, the chirp mass $\mathrm{M_{chirp}}$ and the binary mass ratio q. We investigate how these distributions change for different CE and accretion efficiencies. The distributions for SMT and CE channels are obtained by distributing the synthetic BBH population across the cosmic history of the Universe as described in Sec. 2.2.

Our models use detailed binary evolution simulations to determine the spin of the second-born BH, assuming that the first-born BH is formed with a negligible spin $a_1 \simeq 0$ because of the assumed efficient AM transport (Qin et al. 2018; Fuller & Ma 2019). If the second MT is stable the first-born BH can accrete material and spin up (Thorne 1974). Nevertheless, because in our reference models we assume Eddington-limited accretion efficiency onto compact objects, the accreted mass is small; this leads to small $a_1 \simeq 0$ also for the SMT channel. The Eddington limited accretion onto the BH is a crucial assumption for the existence of this channel. In Sec. 3.1.2 we show that if highly super-Eddington accretion onto the BH is allowed, the SMT channel contributes to a negligible part to the BBH rate density compared to the CE channel.

3.1. Underlying BBH population

3.1.1. Common envelope channel

In our CE channel, only the spin of the second-born BH is non-zero and, hence, contributes to the $\chi_{\rm eff}$ parameter. The BH progenitor can be tidally spun up during binary evolution after the CE event. The efficiency of tides depends strongly on the orbital separation as the synchronisation timescale $T_{\rm syn} \propto A^{17/2}$, see Eq. (C.1). On the other hand, stellar winds can cause the binary to lose mass, widening the orbit and reducing or neutralising the effects of tides. He-stars have wind mass loss rates that strongly depend on metallicity. Hence, a second-born, tidally spun-up BH can only occur at low metallicity as shown in our detailed binary simulation (see Fig. D.1). A key point is that our detailed simulations do not show a dichotomy between tidally locked and non-spinning second-born BHs, but smoothly cover the whole range of $a_2 \in [0, 1]$, (e.g. top panel of Fig. 1). This was pointed out by Qin et al. (2018) and Bavera et al. (2020) and is in contrast with results from semi-analytical models (Hotokezaka & Piran 2017; Zaldarriaga et al. 2018; Gerosa et al. 2018).

In the top panels of Fig. 2 we show the joint distribution of $\chi_{\rm eff}$ and $\mathrm{M_{chirp}}$ for the underlying BBH population of the CE channel for the reference model with $\alpha_{\rm CE} = 1$ alongside the SMT channel and their combination. For the CE channel, we can see that the underlying BBH population has a non-negligible amount of positive $\chi_{\rm eff}$ mergers due to the tidal spin-up of the second born BH's progenitor. This is in agreement with our previous models (Bavera et al. 2020) obtained using the `COMPAS` code (Stevenson et al. 2017; Vigna-Gómez et al. 2018) which is based on the same stellar model fits but implements binary interactions differently (a comparison between the two codes is beyond the scope of this work). Because of the anti-correlation between the merger timescale $T_{\rm merger}$ and $\chi_{\rm eff}$ (Sec. 2.1), these highly spinning systems merge soon after their formation. Current GW detectors probe only small redshifts ($z \lesssim 1$), well below the peak of the cosmic SFR ($z \sim 2$) where most of these systems are created and merge, as low metallicity environments are required for efficient tidal spin up.

CE efficiency has an important role in the determination of the post-CE orbital distribution. This is because $\alpha_{\rm CE}$ correlates approximately linearly with the post-CE orbital separation $A_{\rm postCE}$, see Eq. (B.2). Models assuming inefficient CE ejection ($\alpha_{\rm CE} < 1.0$) result in tighter post-CE orbits and more systems merging during CE compared to larger $\alpha_{\rm CE}$ values (see Fig. 3). This occurs because the binaries need to deposit more orbital energy into the envelopes to successfully eject them. The opposite is true when assuming an efficient CE ejection ($\alpha_{\rm CE} > 1.0$). We expect, on average, larger $\chi_{\rm eff}$ values for models with lower CE efficiency parameters, as more systems will undergo tidal spin up and small $\chi_{\rm eff}$ for models assuming ultra-efficient CE ejection, as tides are weaker at larger orbital separations. Indeed, this trend is what we find. In Table 1, we report the median $\chi_{\rm eff}$, $\mathrm{M_{chirp}}$ and q with their 90% confidence interval (CI) for our different CE efficiencies models. For the underlying (intrinsic) BBH population, we observe a monotonic decrease of all these quantities for increasing $\alpha_{\rm CE}$ (from 0.2 to 5.0). This trend is also found if we look at the relative fractions of massive and highly spinning BBHs, namely with $\chi_{\rm eff} > 0.1$ and $\mathrm{M_{chirp}} > 15\,\mathrm{M_\odot}$, in Table 2. In both tables we see that on average models with small $\alpha_{\rm CE}$ have larger $\mathrm{M_{chirp}}$ and q. This is because for the same orbital separation, massive binaries have a larger orbital energy reservoir compared to lighter systems and, hence, can deposit more energy into the envelope without shrinking to the point where they merge in the CE phase.

In Table 1 we also report the local rate density for the cosmic time bin centreed at $z = 0.01$. The reference model with $\alpha_{\rm CE} = 1.0$ has a local rate density of 42.6 $\mathrm{Gpc^{-3}\,yr^{-1}}$. If we increase $\alpha_{\rm CE}$, the post-CE orbital separations are larger, hence, the rate density decreases because fewer systems merge within the Hubble time. On the other hand, if we decrease $\alpha_{\rm CE}$, more sys-

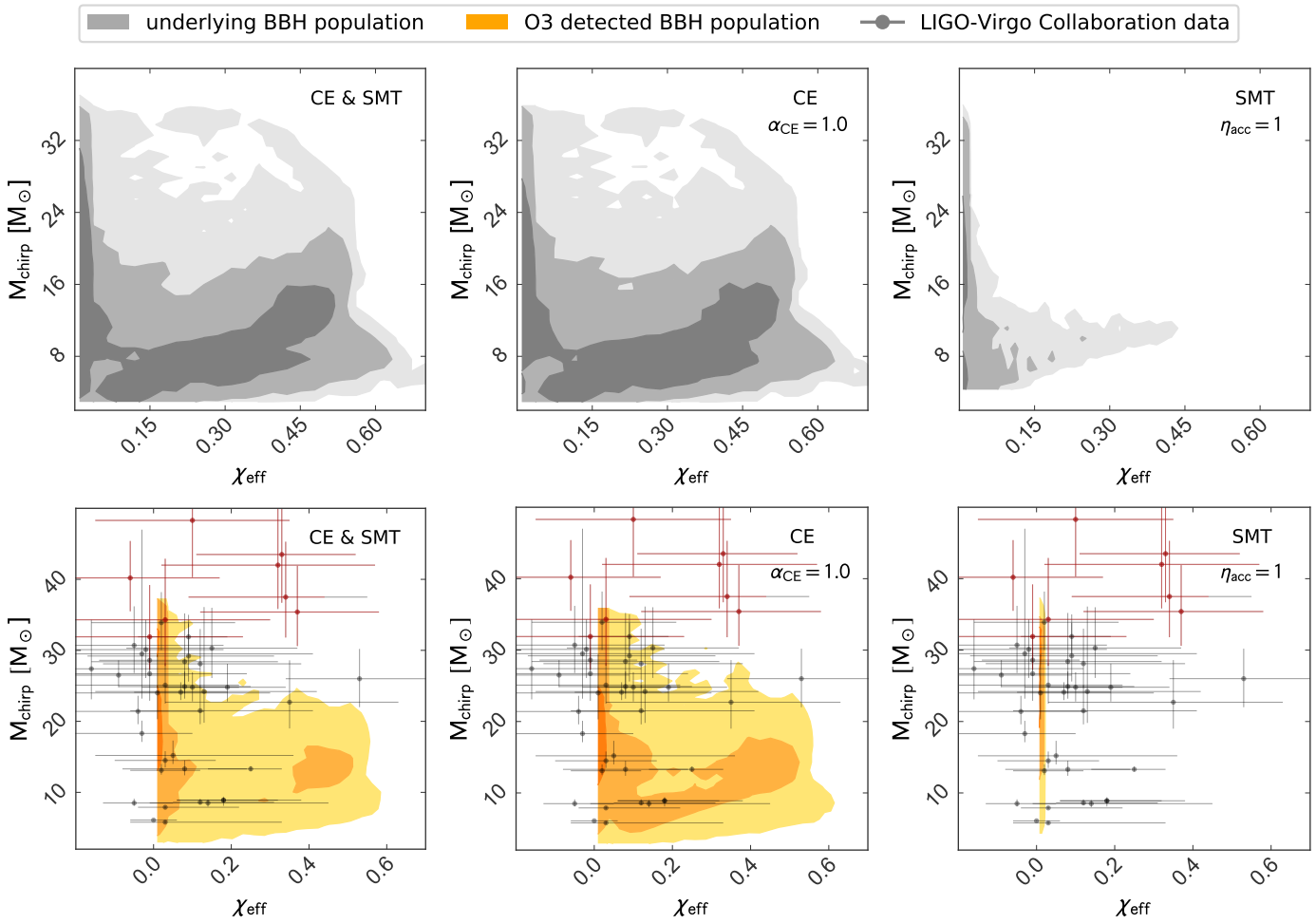

Fig. 2. Model predictions for the underlying (intrinsic) BBH population (grey) and the O3 detected BBH population (orange) for our reference model with $\alpha_{CE} = 1.0$ and $\eta_{acc} = 1$. We show the joint distributions of chirp mass M_{chirp} and effective inspiral spin parameter χ_{eff} for the combined CE and SMT channels (Left), CE formed BBHs (Centre) and SMT formed BBHs (Right). Lighter colours represent larger contour levels of 68%, 95% and 99%, respectively, constructed with `pygtc` module (Bocquet & Carter 2016). All histograms are plotted with 30 bins in the same range without any bin smoothing. We overlaid in grey the O1, O2 and O3a LVC GWTC-2 data with their 90% credible intervals. The 9 events of GWTC-2 in tension with our models are indicated in red (see Sec. 3.3), GW190521 is outside the plotted window.

tems merge during the CE event and the rate density decreases as well. This trend is not followed by the model with $\alpha_{CE} = 0.2$ where the rate density suddenly jumps up to 113.0 Gpc^{-3} yr^{-1}. To understand the sudden increase in the rate density of this model, we need to carefully look at the post-CE binary orbital separations. In Fig. 3 we show a histogram of all BH–He-star orbital separations surviving CE for $\alpha_{CE} \in [0.2, 0.5, 1.0]$ (solid lines). The synthetic BBH population is weighted according to Eq. (B.10) of Bavera et al. (2020) which integrates the redshift- and metallicity-dependent SFR across the cosmic history of the Universe. In grey, we show the 90% CI of systems forming merging BBHs with $T_{merger} < 14$ Gyr for the model with $\alpha_{CE} = 0.2$ (the other models have similar CIs). Systems with orbital separations smaller than the left boundary of the CI either form BH-NS binaries, merge during the BH–He-star evolution or widen the orbits (because of wind driven mass loss rate) past the point where they will merge within the Hubble time. Systems on the right of the CI form double compact objects with merging timescales larger than the Hubble time. In this figure we see that as the CE efficiency decreases, the orbital separations decrease. The total orbital separation distributions present a large peak of orbital separation preceded by a smaller flatter distribution of orbital separation. For $\alpha_{CE} = 0.2$ we see that this large peak of orbital separation enters the merging BBH population (grey area of Fig. 3). This is the source of the sudden increase of the rate density.

The peak of BH–He-star orbital separations post CE is a metallicity product. All binaries going through CE are evolving during the He-burning phase. In our models, systems that are in the HG at onset of CE are considered to merge during the CE (because we assume the pessimistic CE scenario; see Belczynski et al. 2007). The maximum stellar radius of a star in the HG is metallicity dependent. Even though, on average stars with high metallicity have larger radii during this phase compared to lower metallicity stars, they have similar super-giant phase radii, see for example, Fig. 7 of Linden et al. (2010). This implies that binaries with high metallicities sample a smaller range of orbital separations at onset of CE, with the donor star having passed the HG phase, compared to binaries with lower metallicities. Therefore, low metallicity BH–He-star binaries sample a wide (approximately flat) A_{preCE} distribution which result to a wide (also approximately flat) range of A_{postCE}, while high metallicity systems sample a narrow A_{preCE} distribution which result in a narrow A_{postCE} range. Fig. 3 shows the combination of these

channel	$\alpha_{\rm CE}$	$\eta_{\rm acc}$	Rate density at $z = 0.01$ [Gpc^{-3} yr^{-1}]	Detection rate O3 sensitivity [yr^{-1}]	$M_{\rm chirp}$ [$M_\odot$] intrinsic pop.	$M_{\rm chirp}$ [$M_\odot$] detected pop.	$\chi_{\rm eff}$ intrinsic pop.	$\chi_{\rm eff}$ detected pop.	q intrinsic pop.	q detected pop.
CE	0.20	1	113.0	412	$15.8^{+8.7}_{-8.9}$	$18.5^{+8.6}_{-5.5}$	$0.38^{+0.13}_{-0.38}$	$0.00^{+0.42}_{-0.00}$	$0.92^{+0.07}_{-0.18}$	$0.95^{+0.04}_{-0.14}$
CE	0.35	1	17.2	56	$14.7^{+11.0}_{-7.8}$	$18.1^{+14.2}_{-8.7}$	$0.37^{+0.17}_{-0.29}$	$0.32^{+0.18}_{-0.32}$	$0.84^{+0.12}_{-0.19}$	$0.84^{+0.13}_{-0.15}$
CE	0.50	1	20.4	61	$13.7^{+11.5}_{-7.6}$	$18.1^{+13.7}_{-8.8}$	$0.27^{+0.26}_{-0.26}$	$0.09^{+0.39}_{-0.09}$	$0.81^{+0.13}_{-0.20}$	$0.82^{+0.14}_{-0.15}$
CE	0.75	1	29.6	92	$12.5^{+11.8}_{-7.4}$	$18.9^{+13.4}_{-9.2}$	$0.18^{+0.33}_{-0.18}$	$0.00^{+0.40}_{-0.00}$	$0.80^{+0.14}_{-0.22}$	$0.82^{+0.14}_{-0.14}$
CE	**1.00**	**1**	**42.6**	**108**	$11.0^{+12.1}_{-6.6}$	$17.9^{+15.5}_{-8.1}$	$0.19^{+0.32}_{-0.18}$	$0.00^{+0.30}_{-0.00}$	$0.79^{+0.14}_{-0.24}$	$0.82^{+0.14}_{-0.14}$
CE	2.00	1	35.0	47	$7.6^{+10.4}_{-4.1}$	$16.0^{+14.8}_{-9.1}$	$0.21^{+0.30}_{-0.21}$	$0.00^{+0.24}_{-0.00}$	$0.76^{+0.16}_{-0.27}$	$0.79^{+0.17}_{-0.21}$
CE	5.00	1	22.7	15	$5.9^{+9.5}_{-2.8}$	$12.7^{+8.6}_{-8.0}$	$0.16^{+0.35}_{-0.16}$	$0.00^{+0.13}_{-0.00}$	$0.69^{+0.22}_{-0.26}$	$0.80^{+0.16}_{-0.29}$
SMT	-	**1**	**24.6**	**86**	$15.3^{+14.2}_{-10.4}$	$24.5^{+8.4}_{-11.2}$	$0.00^{+0.07}_{-0.00}$	$0.00^{+0.00}_{-0.00}$	$0.72^{+0.20}_{-0.29}$	$0.74^{+0.12}_{-0.07}$
CE	1.00	10^3	43.1	108	$10.9^{+12.0}_{-6.6}$	$17.8^{+15.4}_{-8.1}$	$0.18^{+0.29}_{-0.18}$	$0.00^{+0.29}_{-0.00}$	$0.79^{+0.17}_{-0.30}$	$0.82^{+0.14}_{-0.14}$
SMT	-	10^3	23.5	85	$15.5^{+14.2}_{-10.6}$	$24.8^{+8.2}_{-11.3}$	$0.01^{+0.03}_{-0.00}$	$0.01^{+0.00}_{-0.00}$	$0.72^{+0.19}_{-0.30}$	$0.75^{+0.12}_{-0.07}$
CE	1.00	10^5	40.8	97	$10.3^{+12.0}_{-6.0}$	$17.6^{+15.3}_{-8.1}$	$0.18^{+0.29}_{-0.18}$	$0.00^{+0.26}_{-0.00}$	$0.79^{+0.17}_{-0.31}$	$0.82^{+0.14}_{-0.15}$
SMT	-	10^5	3.7	13	$7.3^{+22.1}_{-2.0}$	$29.4^{+6.6}_{-16.4}$	$0.53^{+0.21}_{-0.27}$	$0.32^{+0.13}_{-0.04}$	$0.35^{+0.54}_{-0.16}$	$0.89^{+0.09}_{-0.13}$
CE	1.00	10^9	38.6	93	$10.3^{+11.9}_{-6.0}$	$17.4^{+15.6}_{-7.9}$	$0.18^{+0.29}_{-0.18}$	$0.00^{+0.26}_{-0.00}$	$0.79^{+0.17}_{-0.31}$	$0.83^{+0.14}_{-0.15}$
SMT	-	10^9	0.2	0.3	$8.5^{+3.2}_{-1.6}$	$13.9^{+6.8}_{-6.0}$	$0.78^{+0.08}_{-1.15}$	$0.78^{+0.08}_{-0.16}$	$0.14^{+0.07}_{-0.03}$	$0.24^{+0.15}_{-0.11}$

Table 1. This table summarises the results of our different models. The columns report the model's channel, either CE or SMT, CE efficiency $\alpha_{\rm CE}$, the mass-transfer accretion efficiency limit onto compact objects $\eta_{\rm acc}$ in units of Eddington-limit, the local rate density at $z = 0.01$ (in Gpc^{-3} yr^{-1}), the detection rate (in yr^{-1}) and the median chirp mass $M_{\rm chirp}$, effective inspiral spin parameter $\chi_{\rm eff}$ and binary mass ratio q with their 90% CI for the intrinsic (underlying) and observed BBH populations. Bold text is used to indicate our reference model.

CE + SMT		$\chi_{\rm eff} > 0.1$ & $M_{\rm chirp} > 15\,M_\odot$		$\chi_{\rm eff} > 0.1$ & $M_{\rm chirp} < 15\,M_\odot$		$M_{\rm chirp} > 15\,M_\odot$		$q > 0.8$	
		intrinsic	detected	intrinsic	detected	intrinsic	detected	intrinsic	detected
$\alpha_{\rm CE}$	$\eta_{\rm acc}$	pop.	pop.	pop.	pop.	pop.	pop.	pop.	pop.
0.20	1	0.33	0.05	0.27	0.01	0.56	0.88	0.77	0.83
0.35	1	0.38	0.22	0.44	0.08	0.48	0.83	0.61	0.40
0.50	1	0.22	0.12	0.46	0.08	0.42	0.82	0.52	0.37
0.75	1	0.11	0.04	0.46	0.05	0.34	0.83	0.47	0.41
1.00	1	0.09	0.02	0.49	0.03	0.27	0.80	0.45	0.42
2.00	1	0.06	0.01	0.59	0.03	0.15	0.78	0.39	0.29
5.00	1	0.01	0.00	0.53	0.01	0.13	0.82	0.28	0.24
1.00	10^3	0.08	0.02	0.50	0.03	0.27	0.81	0.45	0.43
1.00	10^5	0.07	0.13	0.55	0.06	0.22	0.74	0.47	0.68
1.00	10^9	0.07	0.02	0.55	0.06	0.22	0.71	0.48	0.65

Table 2. This table summarises the relative fractions of BBHs formed through CE and SMT channels combined for some arbitrary parameter space divisions (according to the column labels) for both the intrinsic (underlying) and observed BBH populations. The columns report the CE efficiency $\alpha_{\rm CE}$, mass-transfer accretion efficiency limit onto compact objects $\eta_{\rm acc}$ in units of Eddington-limit and the relative fraction of events in the parameter space slices: $\chi_{\rm eff} > 0.1$ & $M_{\rm chirp} > 15\,M_\odot$, $\chi_{\rm eff} > 0.1$ & $M_{\rm chirp} < 15\,M_\odot$, $M_{\rm chirp} > 15\,M_\odot$, and $q > 0.8$.

distributions for all metallicities. Since the average metallicity in the Universe is a monotonically increasing function, the yield of binaries at low metallicities is smaller than the yield at larger metallicities, hence the larger $A_{\rm postCE}$ peak.

3.1.2. Stable mass transfer channel

In our SMT channel, the spin of both BHs can be non-zero and hence affect the $\chi_{\rm eff}$ parameter. Since in our reference model we assume Eddington-limited MT, the amount of accreted material is negligible compared to the BH mass and leads to small spins ($a_1 \simeq 0.002$ is the largest value in our population). In Table 1 we show that models with super-Eddington accretion efficiency limits result in larger first-born BH spins, as the BH is allowed to accrete at highly super-Eddington rates, and, hence, result in larger median $\chi_{\rm eff}$. After the second MT phase, tides can further spin up the second-born BH progenitor if the orbits are tight enough (this requires $p < 1$ day). Since the orbits cannot shrink as efficiently as in the CE channel, most of the systems formed through this evolutionary path will not undergo tidal spin up. Since the CE efficiency does not affect this evolutionary path, here we report only values from the model with $\alpha_{\rm CE} = 1.0$.

In Fig. 2 we show the underlying joint distribution of $\chi_{\rm eff}$ and $M_{\rm chirp}$ for the SMT channel alongside the CE channel and their combination. We see that the underlying SMT BBH population presents a non-zero $\chi_{\rm eff}$ contour at the 95% level. These are the systems accreting during the second MT event with tidal spin up during the subsequent phase. Even though the non-zero $\chi_{\rm eff}$ distribution is a small part of the overall population (cf. median $\chi_{\rm eff}$ in Table 1) this subpopulation has an astrophysical consequence. During the second MT, the accreting BHs are thought to form an accretion disk with strong X-ray emission. This partly explains

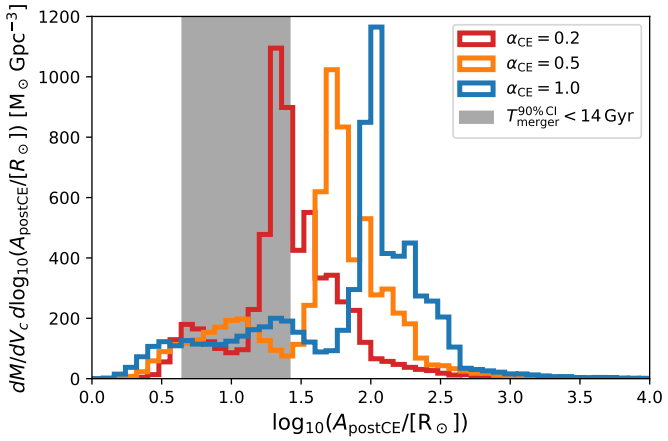

Fig. 3. Orbital separation of BH–He-star binaries post CE for $\alpha_{CE} \in [0.2, 0.5, 1.0]$ represented with solid lines according to the legend. The histogram has units of $M_\odot$ Gpc^{-3} and accounts for the total stellar mass formed per comoving volume integrated over the Universe cosmic history per log-orbital period bin. The grey shaded area represent the 90% CI of the systems forming merging BBHs with $T_{merger} < 14$ Gyr for the $\alpha_{CE} = 0.2$ model (the other models have similar CIs). As the CE efficiency is lowered, the orbital separations become smaller and the distributions move to the left: for $\alpha_{CE} = 0.2$ the orbital separation peak enters the grey area boosting the merger rate.

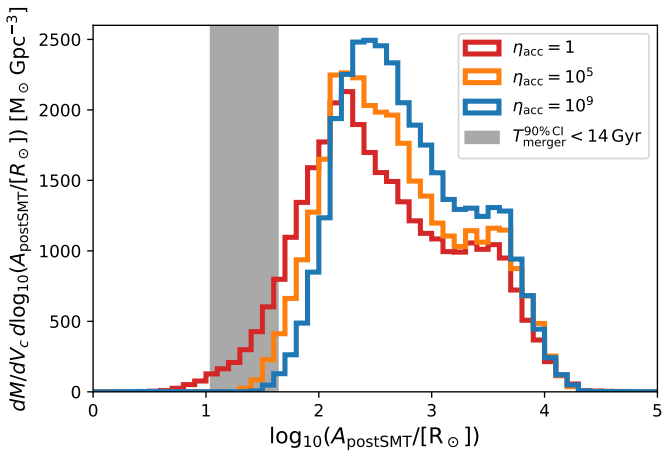

Fig. 4. Orbital separation of BH–He-star binaries post SMT for accretion efficiency limit $\eta_{acc} \in [1, 10^5, 10^9]$ (in units of Eddington-limit) represented with solid lines according to the legend. The histogram has units of $M_\odot$ Gpc^{-3} and accounts for the total stellar mass formed per comoving volume integrated over the Universe cosmic history per log-orbital period bin. The grey shaded area represent the 90% CI of the systems forming merging BBHs with $T_{merger} < 14$ Gyr for the model with $\eta_{acc} = 1$ (the other models have similar CIs). As the accretion efficiency is increased, the orbital separations become larger and the distributions move to the right: for highly super-Eddington accretion efficiency $\eta_{acc} = 10^9$ the tail almost exits the grey area, hence, decreasing the merger rate.

the high-end of the luminosity function of stellar X-ray sources in galaxies (e.g. ultraluminous X-ray sources; Begelman 2002; Swartz et al. 2004; Kovlakas et al. 2020).

In Table 1 we report the rate density contribution of SMT channel to be 24.6 Gpc^{-3} yr^{-1}. This value is comparable to the contribution of the CE channel for $\alpha_{CE} \in [0.35, 5.0]$. This result is consistent with other studies (e.g. Neijssel et al. 2019) and is strongly dependent on the assumed accretion efficiency limit onto the BH. If we allow for super-Eddington accretion the BBH rate density will decrease. The drop in the rate density when allowing for super-Eddington accretion occurs because conservative MT does not shrink the orbit as efficiently as non-conservative MT (in the case of Eddington-limited accretion) and thus the BBHs formed post-MT are more commonly too wide to merge within the Hubble time. This can be seen in Fig. 4 where we show a histogram of all BH–He-star orbital separation post SMT for different accretion efficiency limits $\eta_{acc} \in [1, 10^5, 10^9]$ (in units of Eddington-limit), solid lines, and the 90% CI of systems forming merging BBHs with $T_{merger} < 14$ Gyr, in grey. For not Eddington-limited accretion (here arbitrarily limited to up to 10^9 times the Eddington-limit) the rate density contribution of this channels drops by two orders of magnitudes down to 0.2 Gpc^{-3} yr^{-1} while just decreasing the CE channel rate by $\sim 10\%$. This is a negligible contribution to the BBH merger rate compared to the yield of the CE channel.

When allowing for super-Eddington accretion, the first-born BH accretes a non-negligible amount of matter leading to a different mass radio distribution compared to Eddington-limited SMT models. In Table 1 we can see that the median mass ratio decreases from 0.72 to 0.35 and 0.14 for increasing η_{acc}. Small mass ratios are also found by the BPASS team (Eldridge et al. 2017) who, in their models, allow for super-Eddington accretion onto BHs. As mentioned above, the first-born BH is spun-up when mass is accreted onto it. Indeed, for increasing η_{acc}, our SMT models predict larger median χ_{eff}.

3.2. Detected BBH population

O3a lasted 6 months and saw the detection of 37 GW signals from BBH mergers resulting in a total of 177.3 days of data suitable for coincident analysis. These detections translate to a detection rate of 76 yr^{-1}. In our model comparison with the data we include also the BBH detections of the first two observing runs O1 and O2 (Abbott et al. 2019) for a total of 47 events. Although evidence for additional signals in O1 and O2 data has been presented by other groups (e.g. Zackay et al. 2019a,b; Venumadhav et al. 2020; Nitz et al. 2020), we do not include them in order to simplify our analysis and only consider a single treatment of selection effects. At the same time, adding a few additional, low significance events in the observed population is not expected to add significant discriminating power. For all events, we assume simulated O3 sensitivity (mid high and late low from Abbott et al. 2018) as the observable distributions of χ_{eff} and M_{chirp} are weakly dependent on the detector sensitivity for the channels considered (Bavera et al. 2020).

The detected joint distributions of χ_{eff} and M_{chirp} of our reference model with $\alpha_{CE} = 1.0$ are presented in the bottom panels of Fig. 2. The figure shows CE and SMT channels alongside their combination. For a visual comparison with the observations, we add the LVC GW detections with their 90% credible intervals in grey. We can clearly see that the SMT channel only contributes with zero χ_{eff} and large M_{chirp} systems to the detected population. Hence, in our model, the only source of non-zero χ_{eff} in the detected BBH population comes from the CE channel.

In Fig. 5 we show the predicted two-dimensional distributions of χ_{eff}, M_{chirp} and q for the combined CE and SMT detected population at different CE efficiencies. We can clearly see how the models with inefficient CE ($\alpha_{CE} < 1$) lead to overall larger χ_{eff} values compared to ultra efficient CE in the detected population ($\alpha_{CE} > 1$). Next to each panel we also include the normalised one-dimensional histogram of each quantity where we also show the underlying BBH population for comparison. The

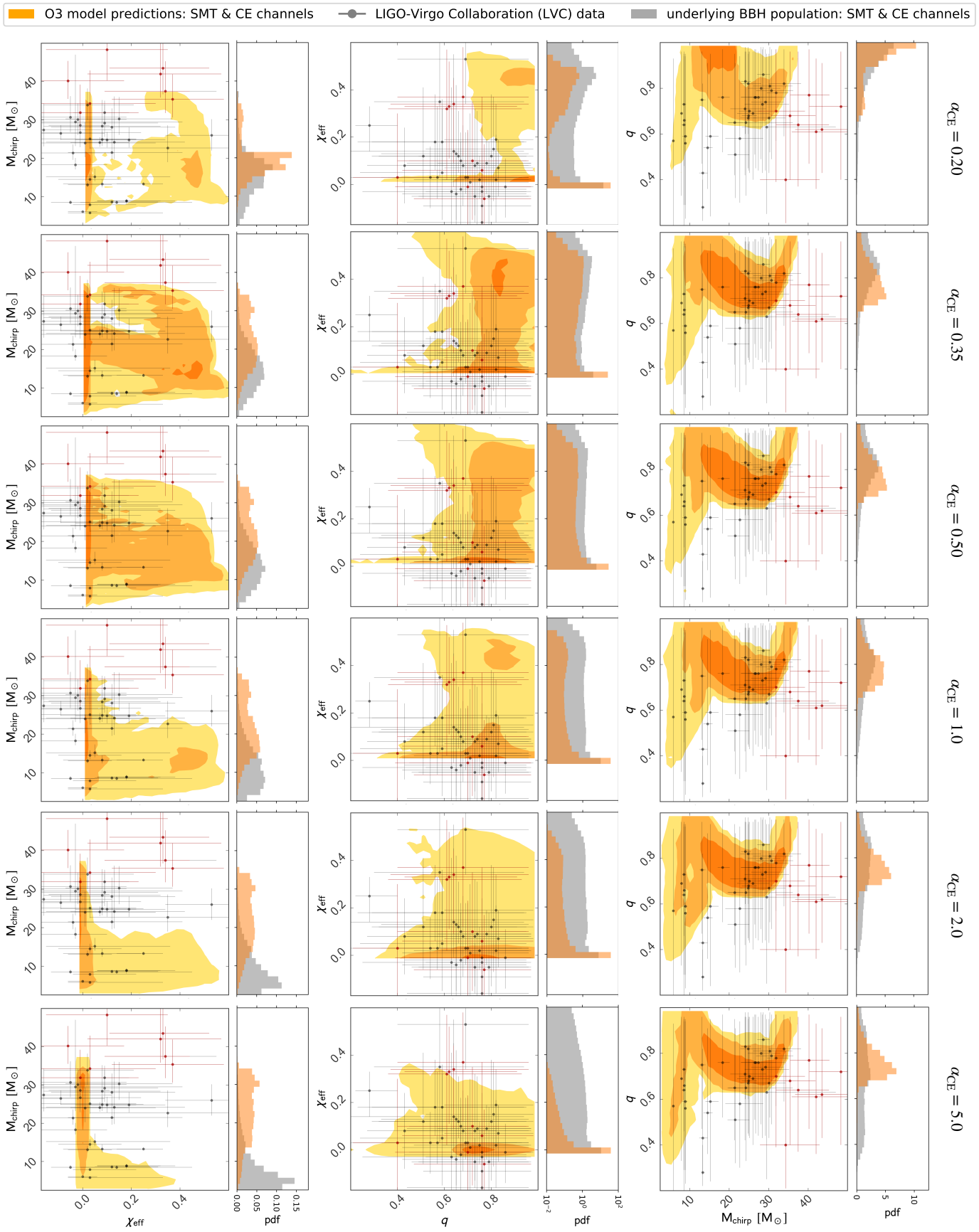

Fig. 5. Model predictions for the O3 detected BBH population of CE and SMT channels combined for $\alpha_{CE} \in [0.2, 0.35, 0.5, 1.0, 2.0, 5.0]$ and $\eta_{acc} = 1$, in orange. We show the joint distributions of chirp mass M_{chirp}, effective inspiral spin parameter χ_{eff} and binary mass ratio q. Lighter colours represent larger contour levels of 68%, 95% and 99%, respectively, constructed with `pygtc` (Bocquet & Carter 2016). All histograms are plotted with 30 bins without any bin smoothing. We overlaid in grey the LVC GWTC-2 data with their 90% credible intervals. The 9 events of GWTC-2 in tension with our models are indicated in red (see Sec. 3.3). We also show the one-dimensional projection of each quantity overplotted on the underlying (intrinsic) BBH population, in grey. For visualisation purposes, the χ_{eff} probability density function (pdf) is plotted in log-scale. For a visualisation of each model separately see Appendix G.

one-dimensional M_{chirp} histograms show how the selection effect favouring higher BH masses changes the distribution, while in the one-dimensional χ_{eff} histograms we can see how the detectable population mostly probes low χ_{eff}. This happens because the GW detectors probes small redshifts ($z \lesssim 1$) while highly spinning systems tend to form at high redshifts ($z \sim 2$) and low metallicity environments, and merge quickly at a redshift close to the one of their formation (see the discussion about the anti-correlation between χ_{eff} and T_{merger} in Sec. 2.1). These high redshifts are outside current GW detection horizons.

In Table 1 we report the detection rate of each model for O3 sensitivity. For the SMT channel our model predicts a detection rate of 86 yr^{-1} while the detection rate for the CE model with $\alpha_{CE} = 1.0$ is 108 yr^{-1}. As we increase or decrease CE efficiency we lower the detection rate to 56 yr^{-1} for $\alpha_{CE} = 0.35$ and 15 yr^{-1} for $\alpha_{CE} = 5.0$. The model with $\alpha_{CE} = 0.2$ overpredicts the detections with 412 yr^{-1} (see Sec. 3.1.1 for an explanation). On the other hand, the SMT model with highly super-Eddington accretion efficiency limit predicts a detection rate of 0.2 yr^{-1} which is negligible compared to the CE channel contribution. Within the probed mass-transfer physics uncertainties, the combination of the two channels is roughly consistent with the observed rate. While our models are consistent with observations, the event rate does depend on many other uncertain evolutionary parameters (e.g. Dominik et al. 2015; Giacobbo et al. 2018; Barrett et al. 2018) and metallicity-specific star formation history (e.g. Chruslinska et al. 2019; Neijssel et al. 2019) which we have not explored. Therefore, while our results can illustrate the expected trend when varying CE efficiency, we cannot make definitive statements on the true value of α_{CE} without also considering the other evolutionary parameters.

3.3. Evidence for additional formation channels

In GWTC-2 there are BBH events that appear marginally consistent or inconsistent explained by our models of isolated binary evolution through CE or SMT. Using individual events to discriminate between models should be done with caution, as the information that individual events carry can be strongly affected by the choice of priors used in the analysis (e.g. Mandel & Fragos 2020; Zevin et al. 2020b; Fishbach & Holz 2020). Instead, one should attempt to derive conclusions based on the combined detected population. In this section we discuss such events which may originate from other active formation scenarios (see the discussion in Sec. 1), while in the following section we perform a model comparison based on the combined sample of events.

In the catalogue we have two high-significance events with asymmetric masses: GW190412 and GW190814. GW190412 has a binary mass ratio of $q = 0.28^{+0.13}_{-0.06}$ (Abbott et al. 2020b) while GW190814 has $q = 0.112^{+0.008}_{-0.009}$ (Abbott et al. 2020c). We find that these small mass ratios are consistent at the 90% level of BBHs formed though SMT with highly super-Eddington accretion. In these models the first-born BH accretes material during the second MT phase leading to unequal mass ratios. However, these models predict large χ_{eff} values as the first-born BH is spun up during accretion (Thorne 1974). The 90% CI of χ_{eff} in this model is not consistent with the $\chi_{eff} = 0.25^{+0.08}_{-0.11}$ and $\chi_{eff} = -0.002^{+0.060}_{-0.061}$ of GW190412 and GW190814, respectively. If one assumes a different, astrophysically-motivated prior, such as a prior that assumes non-spinning primary BHs (different formation channels have different priors), rather than the one used in the LVC analysis, GW190412's inferred mass ratio increases to $0.34 \leq q \leq 0.47$ at the 90% level (Zevin et al. 2020b). The latter is marginally consistent with our models. The case of GW190814, with its lower-mass component being a $2.6\,M_\odot$ compact object, remains a challenge to explain with isolated BBH formation (Zevin et al. 2020c).

GW190521 is a GW signal with a BBH source with high component masses, $85^{+21}_{-14}\,M_\odot$ and $66^{+17}_{-18}\,M_\odot$ (Abbott et al. 2020a). Accounting for pulsational pair instability (PPI; Yoshida et al. 2016; Woosley 2017; Marchant et al. 2019) and a pair instability supernova (PISN; Fowler & Hoyle 1964; Rakavy & Shaviv 1967; Barkat et al. 1967) uncertainties, the primary mass falls in the mass gap predicted by PISN at around $[40–65, 120]\,M_\odot$ (Heger et al. 2003; Spera & Mapelli 2017; Giacobbo et al. 2018; Takahashi 2018; Woosley 2019; Marchant et al. 2019; Farmer et al. 2019; Marchant & Moriya 2020). Our work adopt fits to PPI and PISN models of Marchant et al. (2019) which for metallicity $0.1\,Z_\odot$ find that the maximum BH mass is $\sim 44\,M_\odot$. Hence, this system is a poor fit to our CE and SMT models. This conclusion is consistent with other studies; for example, van Son et al. (2020) investigated isolated binary evolution with super-Eddington accretion without finding any merging BBH systems with a total mass exceeding $100\,M_\odot$. Alternatively, Fishbach & Holz (2020) showed that if the event is analysed with a prior on the less massive BH of $m_{BH2} < 48\,M_\odot$ at 90% credibility, then, the primary BH has a 39% probability of being above the PISN gap. In our models we did not explore stellar and binary evolution above the PISN gap and hence, cannot rule out the formation through CE or SMT.

Amongst the O2 detections there is one event marginally consistent with our models: GW170729 (Abbott et al. 2019). This event has high chirp mass of $M_{chirp} = 35.4^{+6.5}_{-4.8}\,M_\odot$ and a high effective inspiral spin of $\chi_{eff} = 0.37^{+0.21}_{-0.25}$ (Abbott et al. 2019). Fig. 5 shows that only models with low α_{CE} are consistent with this event at the 99% level. When we calculate the likelihood of this system originating from our CE and SMT models using Eq. (F.2), we find it to be extremely small compared to the other events.

Similarly, we can identify a groups of events in GWTC-2 with primary BH masses which support masses larger than our PPI maximum BH mass $\sim 44\,M_\odot$ (Marchant et al. 2019). These are GW190413_134308, GW190519_153544, GW190521, GW190602_175927, GW190620_030421, GW190701_203306, GW190706_222641 and GW190929_012149. These events, given our CE and SMT models, have extremely small likelihoods with respect to others, and hence cannot be readily explained by our models.

All the events discussed in this section, perhaps with the exception of GW190412 and GW190814, are likely not the outcome of isolated binary evolution though CE or SMT, given our models. Without considering explicitly models for alternative channels, which is outside the scope of our study, we cannot make a conclusive statement on their origins. However, if we assume that all these systems originated from a different formation channel we can put a lower bound on the contamination fraction in the detected BBH population from other channels to be $9/47 \simeq 0.2$.

3.4. Models comparison

The real statistical power of model comparison lies in the combined information from all detected events. In Appendix F we explain how to compute the likelihood of observing N independent GW events, described by the physical parameters $\boldsymbol{\theta} = (\chi_{eff}, M_{chirp}, q)$, given an astrophysical model described by

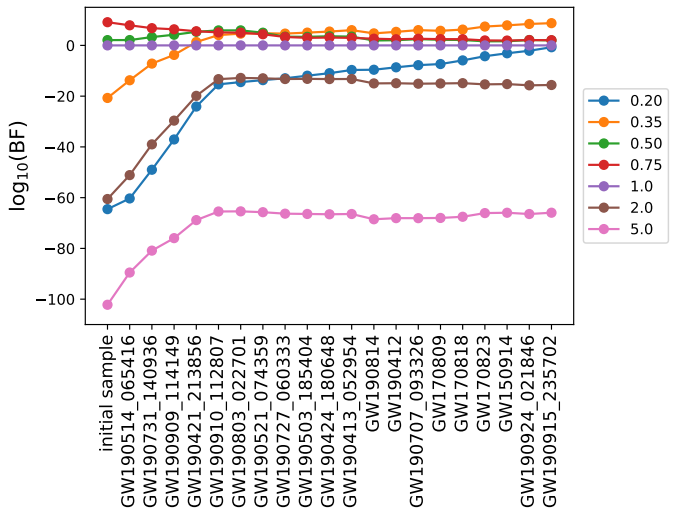

Fig. 6. BFs of CE and SMT models with respect to the reference model with $\alpha_{\rm CE} = 1.0$ and Eddington-limited accretion efficiency as a function of sample size. The initial sample contains 38 GW events of GWTC-2 and exclude GW170729, GW190413_134308, GW190519_153544, GW190521, GW190602_175927, GW190620_030421, GW190701_203306, GW190706_222641, GW190929_012149. At each iteration the event with lowest likelihood with respect to the reference model is removed and indicated on the horizontal axis until 20 events are removed. By definition the BF of the model with $\alpha_{\rm CE} = 1.0$ is equal to 1. The data show moderate to strong support for the models with low CE efficiency, $\alpha_{\rm CE} < 1.0$. This result is robust because the BFs show a constant behaviour as a function of sample size.

Channel	orbital dist.	RLOF ZAMS	Rate density [Gpc^{-3} yr^{-1}]	Detection rate [yr^{-1}]
CE	fiducial	incl.	42.6	108
SMT	fiducial	incl.	24.6	86
CE	fiducial	excl.	55.8	142
SMT	fiducial	excl.	31.4	111
CE	log-unif.	incl.	73.3	184
SMT	log-unif.	incl.	23.1	78
CE	log-unif.	excl.	78.5	198
SMT	log-unif.	excl.	24.8	83

Table 3. Rate densities at $z = 0.01$ and O3 detection rate for SMT and CE models with $\alpha_{\rm CE} = 1.0$ and $\eta_{\rm acc} = 1$ for different initial binary properties. The second column indicates which orbital distribution is used, either log-uniform or fiducial (the extended Sana et al. (2012) distribution, see Eq. (A.1)). The third column indicates if we include or exclude binary systems with Roche-lobe overflow at ZAMS.

the set of parameters $\boldsymbol{\lambda}$. How well the data are described by one model compared to another is described by the Bayes factor (BF), see Eq. (F.4). To compute the BFs, we use as our reference the model of CE and SMT with $\alpha_{\rm CE} = 1.0$ and Eddington-limited accretion onto the BH. For our model comparisons we remove the GW events discussed in the previous section (GW170729, GW190413_134308, GW190519_153544, GW190521, GW190602_175927, GW190620_030421, GW190701_203306, GW190706_222641, GW190929_012149) and consider them to not have been formed through the CE and SMT channels in this work. Of course, in the remaining population of events we cannot exclude contamination from other formation channels. A proper analysis would require a model comparison that includes all promising formation channels for BBHs and their branching fractions as model hyperparameters (Zevin et al. 2020a), this is beyond the scope of this paper as here we are only considering two formation channels.

To estimate which model describes best the events, and how sensitive this result is to the selection of events, we iterate the computation of the BF and remove at each iteration the event with lowest likelihood (with respect to the reference model) until the BF converges to a given value. In Fig. 6 we show the BFs of our reference model to the others as a function of sample size; this converge to a constant value after 5–6 events are removed. The BFs indicate moderate to strong evidence in favour of models with inefficient CE, namely $\alpha_{\rm CE} < 1.0$, while excluding the model with lowest $\alpha_{\rm CE} = 0.2$. If another model is chosen as the reference, then the order of events removed changes, but the end results is the same.

Another question we could ask ourselves is which parameter out of the three ($\chi_{\rm eff}$, $\mathrm{M_{chirp}}$, q) has the most discriminatory power in the BF analysis and, hence, carries most of the information about CE efficiency. To answer this question we repeat the analysis considering each parameter separately in $\boldsymbol{\theta}$. We find that the parameter carrying the least information is the mass ratio q which strongly disfavour only the model with $\alpha_{\rm CE} = 0.2$. Most of the information is contained in $\mathrm{M_{chirp}}$; considering there is the greatest variation in BFs, for instance, for the model with $\alpha_{\rm CE} = 5.0$ the BF is initially disfavoured at $\sim 10^{-12}$ and BF at $\sim 10^{-4}$ for the one with $\alpha_{\rm CE} = 2.0$. The only other model disfavoured by the $\mathrm{M_{chirp}}$ dimension is $\alpha_{\rm CE} = 0.2$ at BF $\sim 10^{-20}$. The $\mathrm{M_{chirp}}$ parameter has the largest discriminating power because is the one affected the most by the variation of $\alpha_{\rm CE}$ in the underlying distributions (cf. Table 1 and Table 2). Larger $\alpha_{\rm CE}$ leads to a smaller fraction of systems with $\mathrm{M_{chirp}} > 15\mathrm{M}_\odot$ which is what most of the LVC data support. In contrast, the $\chi_{\rm eff}$ dimension favours models with efficient CE ejection the most: models with $\alpha_{\rm CE} = 2.0$ at BF $\sim 10^{7}$–10^{4} and $\alpha_{\rm CE} = 5.0$ at BF $\sim 10^{2.6}$–10^{0} while it strongly disfavours $\alpha_{\rm CE} \in [0.2, 0.35]$. This result is a direct consequence of the majority of LVC data supporting small $\chi_{\rm eff}$ which in our models are achieved for ultra efficient $\alpha_{\rm CE}$. Finally, when we calculate the BFs with $\boldsymbol{\theta} = (\chi_{\rm eff}, \mathrm{M_{chirp}})$ we find similar results to the original analysis with $\boldsymbol{\theta} = (\chi_{\rm eff}, \mathrm{M_{chirp}}, q)$. Moreover, we find that, in contrast to the three-dimensional BF analysis, the two-dimensional one shows rather constant BFs starting from the initial sample. The variation in the first 6 iterations of the three-dimensional analysis is caused by the q dimension. We should stress, however, that the model with $\alpha_{\rm CE} = 0.2$ significantly overpredicts the rate of events. Hence, overall an $\alpha_{\rm CE}$ in the range $0.2 < \alpha_{\rm CE} < 1.0$ is favoured.

The result of our model section analysis needs to be interpret with caution. Here we only explored one parameter of the models which is degenerate with others, for example MT stability and efficiency, BHs birth spin, etc. Moreover we found a non-negligible fraction (≥ 0.2) of BBHs originating from other formation channels and, hence, cannot rule out an even greater contamination in the studied population. Finally, other formation channels have been shown to predict BBH observable distributions degenerate with the CE and SMT channels (see references in Sec. 1). Hence, a proper analysis would require a model comparison of all promising formation scenarios (cf. Zevin et al. 2020a).

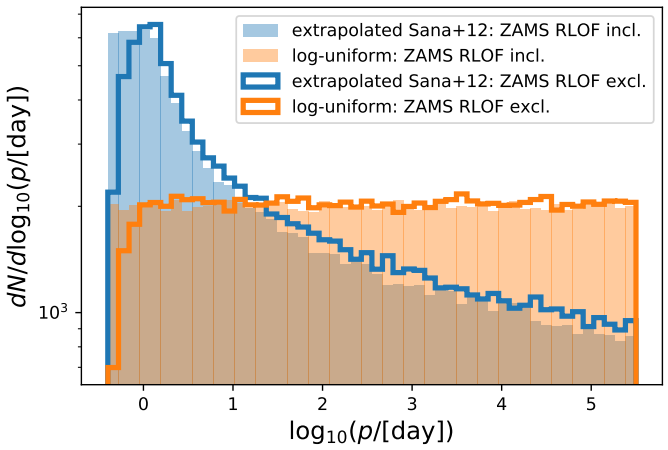

Fig. 7. Initial orbital separation of 10^5 binaries sampled from the extended Sana et al. (2012) distribution, cf. Eq. (A.1), in blue, and from a log-uniform distribution, in orange. Both distributions sample the range $p \in [0.4, 10^{5.5}]$ days and are independent of metallicity. With a solid line, we show the same distributions after removing systems with Roche-lobe overflow at ZAMS for $Z = 0.1\,Z_\odot$.

channel	$q_{\rm crit}$	Rate density [Gpc^{-3} yr^{-1}]	Detection rate [yr^{-1}]	q intrinsic pop.	q detected pop.
CE	F	42.6	108	$0.79^{+0.17}_{-0.30}$	$0.82^{+0.14}_{-0.14}$
SMT	F	24.6	86	$0.72^{+0.20}_{-0.29}$	$0.74^{+0.12}_{-0.07}$
CE	C	50.9	124	$0.78^{+0.18}_{-0.27}$	$0.81^{+0.15}_{-0.14}$
SMT	C	118.8	354	$0.66^{+0.22}_{-0.09}$	$0.69^{+0.14}_{-0.09}$
CE	B	24.5	28	$0.79^{+0.18}_{-0.30}$	$0.84^{+0.13}_{-0.28}$
SMT	B	31.3	212	$0.94^{+0.05}_{-0.10}$	$0.94^{+0.05}_{-0.09}$

Table 4. Rate densities at $z = 0.01$ and O3 detection rate for SMT and CE models with $\alpha_{\rm CE} = 1.0$ and $\eta_{\rm acc} = 1$ for different $q_{\rm crit}$ prescriptions. The fiducial model (F) assumes the values presented in Sec. B.2 while the other two options (C) and (B) uses values of Claeys et al. (2014) and Belczynski et al. (2008), respectively. For comparison, we also report the median BH mass ratio q with its 90% interval.

4. Model uncertainties

4.1. Initial binary properties

Lack of knowledge of the initial binary properties are a source of uncertainty in population synthesis studies. We assume that the primary mass follows the Kroupa (2001) initial-mass function (IMF). This is a power law which comes with uncertainties that can affect the rate estimate and to a lesser degree the observed distribution of BBHs (e.g. de Mink & Belczynski 2015). Moreover, the IMF may not be universal (e.g. Schneider et al. 2018; Farr & Mandel 2018). An additional source of uncertainty can be the initial binary mass fraction distribution and birth eccentricities, which we did not investigate here. We expect the impact of these uncertainties to be smaller compared to that of the IMF (de Mink & Belczynski 2015).

Another important assumption is the distribution of the birth orbital separation of the binaries. In our model, we assumed it follows an extended Sana et al. (2012) power law in log-orbital period $p \in [0.4, 10^{5.5}]$ days, cf. Eq. (A.1). Here, we investigate the sensitivity of our results to this assumption. In Fig. 7 we show the histogram of 10^5 initial orbital separations drawn from the assumed distribution, in blue, compared to a log-uniform distribution, in orange. We find that the rate density of the reference CE model with $\alpha_{\rm CE} = 1.0$ raises from 42.6 Gpc^{-3} yr^{-1} to 73.3 Gpc^{-3} yr^{-1} when assuming log-uniform orbital separation at birth. On the other hand, the rate density of SMT channel remains almost the same. This happens because the log-uniform distribution increases the yield of merging BBHs at large initial orbital periods ($p \gtrsim 10^2$ days), which are the binaries going through the CE evolutionary path, while it does not affect the yield of SMT BBHs as both initial orbital period distributions create roughly the same number of systems at $p \sim 10$ days.

Moreover, the sampled orbital period range can affect our results. In our model we lowered the smallest orbital period, compared to that measured by Sana et al. (2012), to include the portion of the parameter space leading to the chemical homogeneous formation of BBH (Mandel & de Mink 2016; Marchant et al. 2016; du Buisson et al. 2020). By default, we included systems overfilling their Roche lobe at ZAMS. Marchant et al. (2016) found that binaries that are already in contact at ZAMS can potentially survive and lead to the formation of BBHs through chemically homogeneous evolution. However, we only have observations of massive binaries when they are well-past their ZAMS, as in prior evolutionary phases they are still embedded in the formation clouds, undergoing accretion. Accretion onto a pre-MS binary significantly complicates its evolution (e.g. Sørensen et al. 2018), and thus including those binaries in our population models may be problematic. We now investigate how our results change if we exclude these systems. To exclude systems that are initially Roche lobe filling, we adopt the stellar radii fits of Tout et al. (1996). These fits are specific for ZAMS and offer more accuracy than the one of Hurley et al. (2000) which are meant to cover the entire stellar evolution and thus sacrifice some accuracy at ZAMS. By removing these binaries, we decrease the number of systems in small orbital periods as shown by the solid lines for both distributions in Fig. 7. The new way of drawing initial orbital periods is metallicity dependent because, in general, stars have larger radii at larger metallicities (Tout et al. 1996). In Table 3 we summarise the rates of all these models. As expected, we find for both distributions that excluding RLOF ZAMS increases the rates for both channels. We conclude that this uncertainty can affect our results by a factor of $\lesssim 2$.

4.2. Mass-transfer stability

The critical mass ratio $q_{\rm crit}$ determines weather the MT is dynamically stable or unstable (cf. Sec. B.2). We chose our $q_{\rm crit}$ values to match the assumptions of our previous work (Bavera et al. 2020), which is based on the population synthesis model of Neijssel et al. (2019) obtained using the `COMPAS` code (Stevenson et al. 2017; Vigna-Gómez et al. 2018). In contrast to Neijssel et al. (2019), we implement the same $q_{\rm crit}$ fits to the GB and asymptotic AGB (Hjellming & Webbink 1987) but do not adopt Soberman et al. (1997) radial response to adiabatic mass loss for evolved stars beyond the HG (this option is not present in the current version of `COSMIC`). Despite this and other differences in the model assumptions (such as different CE λ fits) which might affect the results, we reached similar conclusions for the detected population of the CE channel with $\alpha_{\rm CE} \sim 1.0$. Even though both models converge on similar detected population distributions, the two models have different mass-ratio distributions for the underlying BBH population. We suspect that this discrepancy is caused by the different $q_{\rm crit}$ assumption for

GB and AGB stars as all our merging BBH systems are evolving through central He burning at onset of CE. In order to verify the source of the difference, a thorough code comparison is needed, which is outside the scope of this project.

To test the sensitivity of our results to this assumption, we run two additional models with different $q_{\rm crit}$ choices: model (C) with $q_{\rm crit}$ values corresponding to Claeys et al. (2014) and model (B) with $q_{\rm crit}$ values similar to Belczynski et al. (2008). We find model (C) to have similar rate density to our fiducial CE channel but almost five times larger rate density of the SMT channel. On the other hand, the model (B) CE rate density is half of our fiducial model and slightly larger rate densities for the SMT channel. These results are summarised in Table 4 where we also report for comparison the median mass ratio of the intrinsic and detected BBH populations. Both $q_{\rm crit}$ choices do not have a significant impact on the detected observable distributions even though they have different impact on the underlying populations. To determine $q_{\rm crit}$, `COSMIC` uses the evolutionary type of the donor (as defined in Hurley et al. 2000) rather than the actual structure of its envelope. Recently, Klencki et al. (2021) showed that this tends to overpredict the number of systems that evolve through and survive a CE phase. This shows the limitation of parametric population synthesis codes. In fact, $q_{\rm crit}$ can be numerically determined by detailed binary evolution simulations, given the profile of the donor star. In the future, next-generation population synthesis tools based on detailed binary and stellar evolution simulations will remove this degree of freedom.

Finally, in our models we only explore the effects of MT accretion efficiency onto BHs, and did not investigate the effects of MT accretion efficiency between two non-degenerate objects. A recent study (Bouffanais et al. 2020) showed that, assuming Eddington-limited accretion onto BHs, stars need to accrete more than 30% of the mass lost by the donor stars during the first MT episode in order to explain O1 and O2 BBHs. MT efficiency between two non-degenerate stars depends strongly on the assumed specific AM of the material that reaches the surface of the mass-gaining star. In turns, this depends on the accretion disk physics and the coupling of the accretion disk to the star's surface. The assumption that the accreted material carries the Keplerian specific AM of the accretor's surface leads to a very efficient spin up of the mass-gaining star. The accretor then quickly reaches critical rotation and halts further accretion, leading to a highly inefficient mass transfer (a few to a few tens percent; e.g. de Mink et al. 2013; Langer et al. 2020). On the other hand, if one assumes that the AM is dissipated efficiently before it reached the accretor's surface, and that that the material that is added onto the star has similar specific AM to that of its own surface layers, then MT can be significantly more efficient.

4.3. Effect of angular momentum transport & accretion efficiency on black hole spin

Our models assume efficient AM transport (Spruit 1999, 2002) which leads to the formation of non-spinning first-born BHs (Fragos & McClintock 2015; Qin et al. 2018). Although the Tayler–Spruit dynamo model helps to reproduce the flat rotation profile of our Sun (Fuller et al. 2014; Cantiello et al. 2014), as well as, neutron star and white dwarf spins (Heger et al. 2005; Suijs et al. 2008), it cannot reproduce the asteroseismic constrains for subgiants and red giants (Gehan et al. 2018). This would require an even higher efficiency in AM transport. Alternatively, a model with inefficient AM transport predicts highly spinning BHs (e.g. Arca Sedda & Benacquista 2019; Belczynski et al. 2020), which do not match current GW observations. If the second MT episode is stable, then the first-born BH can be spun up by accretion (Thorne 1974). If the MT accretion onto BHs is Eddignton-limited, the BH accretes a negligible amount of matter leading to $a_1 \simeq 0$. On the other hand, a super Eddington-limited MT accretion will result in larger spins. The extreme case of this would be highly super-Eddington accretion efficiency where the spin of the first-born BH can even approach to $a_1 \simeq 1$, but in this case the contribution to the merging BBH population of the SMT channel almost vanishes (Table 1).

The spin of the second-born BH is determined by the combined effects of stellar winds and tidal interactions during the BH–He-star binary evolution which we model in detail. During this evolutionary phase, the AM transport does not play an important role as the He-star is compact and will not expand during its final evolution (Bavera et al. 2020). The strength of the tidal interaction is primarily determined by the orbital separation during the BH–He-star evolutionary phase, see Eq. (C.1). In our SMT models, the orbital separation is determined by the accretion efficiency. Models where super-Eddington accretion is allowed will result in larger orbits than our reference model, decreasing further the small effect of tides on this evolutionary path.

4.4. Common-envelope prescription

In our CE models, the post-CE orbital separation, $A_{\rm postCE}$, is linearly dependent on the CE parameterisation uncertainties as, approximately, $\delta A_{\rm postCE}/A_{\rm preCE} \propto \delta\alpha_{\rm CE}\,\lambda$. Even though we did not explore different λ fits in our models, our parameter study of $\alpha_{\rm CE} \in [0.2, 5.0]$ covers an uncertainty on $\delta A_{\rm postCE}/A_{\rm preCE} \propto 5.0/0.2 \simeq 25$. Recently, Klencki et al. (2021) showed that λ fits similar to the one we used could underestimate the envelope binding energies of massive radiative-envelope giants, leading to an overestimation of the systems surviving CE. An additional free parameter in the calculation of λ which complicates a detailed treatment of CE is the assumed boundary down to which the envelope will be ejected. Unfortunately detailed stellar models cannot robustly predict this (e.g. Tauris & Dewi 2001) and hydrodynamic simulations of the CE phase are necessary. For example, Fragos et al. (2019) showed that for progenitors of binary neutron stars, a non-negligible fraction of hydrogen rich material will remain bound to the core after the successful ejection of the CE, that would in turn imply a relatively efficient ejection of the CE.

4.5. Other uncertainties

Our model may be limited by other uncertainties we did not explore which can alter the merger rate and, to a lesser degree, the predicted BBH property distributions. Uncertainties in the (i) physics of the supernova explosions, such as the kicks strength, can influence rates and affect the parameter distribution of BBH mergers (e.g. Dominik et al. 2013). When connecting the population synthesis code to our detailed `MESA` simulations we (ii) assumed the BH–He-star systems post second MT to be at ZAHeMS. This is not always the case as the binaries are evolving through central He burning at onset of the MT. This leads us to overestimate the lifetime of these He-stars. This overestimation is negligible as the binary only spends a few hundred thousand years in this state compared to its overall life of a few million years and much longer BBH inspiral. This overestimation might lead to less massive second-born BHs and smaller spins as winds act for a larger time window. However, we expect that the frac-

tion of stars entering the MT on advanced He-burning phase is higher at low metallicities, as low-metallicity stars tend to expand later in their lives (Linden et al. 2010). At the same time, stellar winds in these stars are weaker due to the low metallicity, so the overall effect on the population of BBHs is expected to be limited. The uncertainty of the (iii) metallicity dependence of stellar winds for massive stars is another important ingredient of population synthesis studies which affects M_{chirp} distributions and the rates (cf. Barrett et al. 2018). The detection rate and density calculation is also affected by uncertainties in the (iv) redshift and metallicity dependent SFR (Chruslinska et al. 2019; Neijssel et al. 2019; Tang et al. 2020). A SFR favouring higher formation metallicities than the one assumed here would skew our results in favour of smaller χ_{eff} and lower rates as low metallicity systems are responsible for high χ_{eff} and the short merger timescales.

5. Conclusions

Mass-transfer physics is one of the most uncertain physical processes determining the observable properties of field binary black holes. The critical mass ratio q_{crit} determines the fraction of the parameter space going trough SMT and CE phases. Mass-accretion efficiency onto compact objects determines how efficiently binaries going through SMT will shrink, while CE efficiency α_{CE} determines post-CE orbital separations. In this work we investigated how the detected joint distributions of M_{chirp}, χ_{eff} and q of BBH formed through the CEe and SMT formation channels change given the uncertainties on these input physics. We investigated this by combining rapid binary population synthesis studies with detailed stellar and binary simulations. Rapid population synthesis studies allow us to obtain different BH–He-star populations for different input physics, while detailed simulations which take into account differential stellar rotation, tidal interaction, stellar winds and the evolution of the He-star stellar structure allow us to accurately determine the distributions of BBH observables. We then convolved the synthetic BBH population with the redshift- and metallicity-dependent star-formation rate, as well as selection effects from a 3-detector network to build a model capable of describing LIGO–Virgo detections. Our main findings are:

- We calculated the O3 detected joint distributions of χ_{eff}, M_{chirp} and q for CE and SMT channels. Assuming efficient AM transfer inside stars and Eddington-limited accretion efficiency, both channels lead to similar rate densities in the local Universe. We find that the CE channel is the only evolutionary path leading to non-zero χ_{eff} in the detected population as SMT channel cannot shrink the orbits enough for efficient tidal spin-up to take place.
- Inefficient CE (small α_{CE} values) leads to smaller orbital separation post CE. On average, these models lead to more systems being tidally spun up. However, the majority of these systems are not detected by current GW detectors because most of these systems are formed in low metallicity environments (otherwise stellar winds widen the binaries) and merge quickly at a redshift close to their formation ($z \sim 2$ where the SFR peaks), far outside current GW detector horizons ($z \lesssim 1$).
- Highly super-Eddington accretion efficiency onto compact objects reduces the rate densities of CE by $\sim 10\%$, while it reduces the contribution of SMT channel by two orders of magnitude, making the contribution of this channel almost negligible compared to the CE channel.
- The GW events GW170729, GW190413_134308, GW190519_153544, GW190521, GW190602_175927, GW190620_030421, GW190701_203306, GW190706_222641 and GW190929_012149 of GWTC-2 are not well explained by our models of isolated binary evolution through either CE or SMT. If we assume that these systems originate from other formation channels then we can put a lower bound on the detected branching fraction from other formation channels: $9/47 \simeq 0.2$.
- We conducted a model comparison given the events of GWTC-2 consistent with our CE and SMT models to determine which CE efficiency is best supported by the data. The GW events show moderate to strong evidence in favour of the models with inefficient CE, $0.2 < \alpha_{CE} < 1.0$. We find this result to be robust considering different selections of events in our calculations. This analysis did not include rate estimates which the $\alpha_{CE} = 0.2$ model significantly overpredicts.

We conclude that future works aiming to properly infer model parameters through model comparison will need to consider correlation between parameters as well as contamination from other formation channels in order to properly determine model parameters.

Acknowledgements. We would like to thank Simon Stevenson and Katerina Chatziioannou for useful discussions. This work was supported by the Swiss National Science Foundation Professorship grant (project number PP00P2 176868). This project has received funding from the European Union's Horizon 2020 research and innovation program under the Marie Sklodowska-Curie RISE action, grant agreement No 691164 (ASTROSTAT). MZ is supported by NASA through the NASA Hubble Fellowship grant HST-HF2-51474.001-A awarded by the Space Telescope Science Institute, which is operated by the Association of Universities for Research in Astronomy, Incorporated, under NASA contract NAS5-26555. CPLB is supported by the CIERA Board of Visitors Research Professorship. PM is supported by the FWO junior postdoctoral fellowship No. 12ZY520N. JJA and SC are supported by CIERA and AD, JGSP, and KAR are supported by the Gordon and Betty Moore Foundation through grant GBMF8477. KK received funding from the *European Research Council* under the European Union's *Seventh Framework Programme* (FP/2007-2013) / *ERC* Grant Agreement n. 617001. YQ acknowledges funding from the Swiss National Science Foundation under grant P2GEP2_188242. The computations were performed in part at the University of Geneva on the Baobab and Lesta computer clusters and at Northwestern University on the Trident computer cluster (the latter funded by the GBMF8477 grant). All figures were made with the free Python modules Matplotlib (Hunter 2007) and pygtc (Bocquet & Carter 2016). This research made use of Astropy,[3] a community-developed core Python package for Astronomy (Astropy Collaboration et al. 2013, 2018).

References

Abbott, B. P., Abbott, R., Abbott, T. D., et al. 2018, Living Reviews in Relativity, 21, 3
Abbott, B. P., Abbott, R., Abbott, T. D., et al. 2019, Physical Review X, 9, 031040
Abbott, R., Abbott, T. D., Abraham, S., et al. 2020a, arXiv e-prints, arXiv:2010.14527
Abbott, R., Abbott, T. D., Abraham, S., et al. 2020b, arXiv e-prints, arXiv:2010.14533
Abbott, R., Abbott, T. D., Abraham, S., et al. 2020a, Phys. Rev. Lett., 125, 101102
Abbott, R., Abbott, T. D., Abraham, S., et al. 2020b, arXiv e-prints, arXiv:2004.08342
Abbott, R., Abbott, T. D., Abraham, S., et al. 2020c, ApJ, 896, L44
Antonini, F. & Rasio, F. A. 2016, ApJ, 831, 187
Arca Sedda, M. & Benacquista, M. 2019, MNRAS, 482, 2991
Arca-Sedda, M. & Gualandris, A. 2018, MNRAS, 477, 4423
Astropy Collaboration, Price-Whelan, A. M., Sipőcz, B. M., et al. 2018, AJ, 156, 123
Astropy Collaboration, Robitaille, T. P., Tollerud, E. J., et al. 2013, A&A, 558, A33

[3] www.astropy.org

Banerjee, S., Baumgardt, H., & Kroupa, P. 2010, MNRAS, 402, 371
Bardeen, J. M. 1970, Nature, 226, 64
Bardeen, J. M., Press, W. H., & Teukolsky, S. A. 1972, ApJ, 178, 347
Barkat, Z., Rakavy, G., & Sack, N. 1967, Phys. Rev. Lett., 18, 379
Barrett, J. W., Gaebel, S. M., Neijssel, C. J., et al. 2018, MNRAS, 477, 4685
Bartos, I., Kocsis, B., Haiman, Z., & Márka, S. 2017, ApJ, 835, 165
Batta, A. & Ramirez-Ruiz, E. 2019, arXiv e-prints, arXiv:1904.04835
Bavera, S. S., Fragos, T., Qin, Y., et al. 2020, A&A, 635, A97
Begelman, M. C. 2002, ApJ, 568, L97
Belczynski, K., Holz, D. E., Bulik, T., & O'Shaughnessy, R. 2016, Nature, 534, 512
Belczynski, K., Kalogera, V., Rasio, F. A., et al. 2008, ApJS, 174, 223
Belczynski, K., Klencki, J., Fields, C. E., et al. 2020, A&A, 636, A104
Belczynski, K., Taam, R. E., Kalogera, V., Rasio, F. A., & Bulik, T. 2007, ApJ, 662, 504
Bisnovatyi-Kogan, G. S. 1993, Astronomical and Astrophysical Transactions, 3, 287
Bocquet, S. & Carter, F. W. 2016, The Journal of Open Source Software, 1
Böhm-Vitense, E. 1958, ZAp, 46, 108
Bouffanais, Y., Mapelli, M., Santoliquido, F., et al. 2020, arXiv e-prints, arXiv:2010.11220
Breivik, K., Coughlin, S., Zevin, M., et al. 2020, ApJ, 898, 71
Brott, I., de Mink, S. E., Cantiello, M., et al. 2011, A&A, 530, A115
Burrows, A. 2013, Reviews of Modern Physics, 85, 245
Callister, T. A., Farr, W. M., & Renzo, M. 2020, arXiv e-prints, arXiv:2011.09570
Camacho, J., Torres, S., García-Berro, E., et al. 2014, A&A, 566, A86
Cantiello, M., Langer, N., Brott, I., et al. 2009, A&A, 499, 279
Cantiello, M., Mankovich, C., Bildsten, L., Christensen-Dalsgaard, J., & Paxton, B. 2014, ApJ, 788, 93
Chaboyer, B. & Zahn, J. P. 1992, A&A, 253, 173
Chen, H.-L., Woods, T. E., Yungelson, L. R., Gilfanov, M., & Han, Z. 2014, MNRAS, 445, 1912
Chruslinska, M., Nelemans, G., & Belczynski, K. 2019, MNRAS, 482, 5012
Claeys, J. S. W., Pols, O. R., Izzard, R. G., Vink, J., & Verbunt, F. W. M. 2014, A&A, 563, A83
de Mink, S. E. & Belczynski, K. 2015, ApJ, 814, 58
de Mink, S. E., Cantiello, M., Langer, N., et al. 2009, A&A, 497, 243
de Mink, S. E., Langer, N., Izzard, R. G., Sana, H., & de Koter, A. 2013, ApJ, 764, 166
Dominik, M., Belczynski, K., Fryer, C., et al. 2013, ApJ, 779, 72
Dominik, M., Berti, E., O'Shaughnessy, R., et al. 2015, ApJ, 806, 263
du Buisson, L., Marchant, P., Podsiadlowski, P., et al. 2020, MNRAS[arXiv:2002.11630]
Eggleton, P. P. 1983, ApJ, 268, 368
Eldridge, J. J., Stanway, E. R., Xiao, L., et al. 2017, PASA, 34, e058
Farmer, R., Renzo, M., de Mink, S. E., Marchant, P., & Justham, S. 2019, ApJ, 887, 53
Farr, W. M. & Mandel, I. 2018, Science, 361, aat6506
Fishbach, M. & Holz, D. E. 2020, ApJ, 904, L26
Fowler, W. A. & Hoyle, F. 1964, ApJS, 9, 201
Fragione, G. & Kocsis, B. 2018, Phys. Rev. Lett., 121, 161103
Fragos, T., Andrews, J. J., Ramirez-Ruiz, E., et al. 2019, ApJ, 883, L45
Fragos, T., Linden, T., Kalogera, V., & Sklias, P. 2015, ApJ, 802, L5
Fragos, T. & McClintock, J. E. 2015, ApJ, 800, 17
Fryer, C. L., Belczynski, K., Wiktorowicz, G., et al. 2012, ApJ, 749, 91
Fuller, J., Lecoanet, D., Cantiello, M., & Brown, B. 2014, ApJ, 796, 17
Fuller, J. & Ma, L. 2019, ApJ, 881, L1
Ge, H., Webbink, R. F., Chen, X., & Han, Z. 2015, ApJ, 812, 40
Gehan, C., Mosser, B., Michel, E., Samadi, R., & Kallinger, T. 2018, A&A, 616, A24
Gerosa, D., Berti, E., O'Shaughnessy, R., et al. 2018, Phys. Rev. D, 98, 084036
Giacobbo, N. & Mapelli, M. 2019, MNRAS, 482, 2234
Giacobbo, N., Mapelli, M., & Spera, M. 2018, MNRAS, 474, 2959
Grevesse, N., Noels, A., & Sauval, A. J. 1996, in Astronomical Society of the Pacific Conference Series, Vol. 99, Cosmic Abundances, ed. S. S. Holt & G. Sonneborn, 117
Gupta, P., Suzuki, H., Okawa, H., & Maeda, K.-i. 2020, Phys. Rev. D, 101, 104053
Hamann, W. R., Koesterke, L., & Wessolowski, U. 1995, A&A, 299, 151
Hannam, M., Brown, D. A., Fairhurst, S., Fryer, C. L., & Harry, I. W. 2013, ApJ, 766, L14
Hannam, M., Schmidt, P., Bohé, A., et al. 2014, Phys. Rev. Lett., 113, 151101
Heger, A., Fryer, C. L., Woosley, S. E., Langer, N., & Hartmann, D. H. 2003, ApJ, 591, 288
Heger, A. & Langer, N. 2000, ApJ, 544, 1016
Heger, A., Langer, N., & Woosley, S. E. 2000, ApJ, 528, 368
Heger, A., Woosley, S., Baraffe, I., & Abel, T. 2002, in Lighthouses of the Universe: The Most Luminous Celestial Objects and Their Use for Cosmology, ed. M. Gilfanov, R. Sunyeav, & E. Churazov, 369
Heger, A., Woosley, S. E., & Spruit, H. C. 2005, ApJ, 626, 350
Hjellming, M. S. & Webbink, R. F. 1987, ApJ, 318, 794
Hobbs, G., Lorimer, D. R., Lyne, A. G., & Kramer, M. 2005, MNRAS, 360, 974
Hotokezaka, K. & Piran, T. 2017, ApJ, 842, 111
Hunter, J. D. 2007, Computing in Science & Engineering, 9, 90
Hurley, J. R., Pols, O. R., & Tout, C. A. 2000, MNRAS, 315, 543
Hurley, J. R., Tout, C. A., & Pols, O. R. 2002, MNRAS, 329, 897
Hut, P. 1981, A&A, 99, 126
Iglesias, C. A. & Rogers, F. J. 1996, ApJ, 464, 943
Inayoshi, K., Hirai, R., Kinugawa, T., & Hotokezaka, K. 2017, MNRAS, 468, 5020
Ivanova, N., Justham, S., Chen, X., et al. 2013, A&A Rev., 21, 59
Janka, H. T. & Mueller, E. 1994, A&A, 290, 496
Kalogera, V. 1996, ApJ, 471, 352
Kalogera, V., Belczynski, K., Kim, C., O'Shaughnessy, R., & Willems, B. 2007, Phys. Rep., 442, 75
Khan, S., Husa, S., Hannam, M., et al. 2016, Phys. Rev. D, 93, 044007
Klencki, J., Nelemans, G., Istrate, A. G., & Chruslinska, M. 2021, A&A, 645, A54
Kolb, U. & Ritter, H. 1990, A&A, 236, 385
Kovlakas, K., Zezas, A., Andrews, J. J., et al. 2020, MNRAS, 498, 4790
Kroupa, P. 2001, MNRAS, 322, 231
Kulkarni, S. R., Hut, P., & McMillan, S. 1993, Nature, 364, 421
Kumar, S. S. 1963, ApJ, 137, 1121
Langer, N. 1991, A&A, 252, 669
Langer, N. 1997, in Astronomical Society of the Pacific Conference Series, Vol. 120, Luminous Blue Variables: Massive Stars in Transition, ed. A. Nota & H. Lamers, 83
Langer, N., Fricke, K. J., & Sugimoto, D. 1983, A&A, 126, 207
Langer, N., Schürmann, C., Stoll, K., et al. 2020, A&A, 638, A39
Linden, T., Kalogera, V., Sepinsky, J. F., et al. 2010, ApJ, 725, 1984
Madau, P. & Fragos, T. 2017, ApJ, 840, 39
Mandel, I. & de Mink, S. E. 2016, MNRAS, 458, 2634
Mandel, I., Farr, W. M., & Gair, J. R. 2019, MNRAS, 486, 1086
Mandel, I. & Fragos, T. 2020, ApJ, 895, L28
Marchant, P., Langer, N., Podsiadlowski, P., Tauris, T. M., & Moriya, T. J. 2016, A&A, 588, A50
Marchant, P. & Moriya, T. J. 2020, A&A, 640, L18
Marchant, P., Renzo, M., Farmer, R., et al. 2019, ApJ, 882, 36
McKernan, B., Ford, K. E. S., Bellovary, J., et al. 2018, ApJ, 866, 66
Miller, M. C. & Lauburg, V. M. 2009, ApJ, 692, 917
Misra, D., Fragos, T., Tauris, T. M., Zapartas, E., & Aguilera-Dena, D. R. 2020, A&A, 642, A174
Moe, M. & Di Stefano, R. 2017, ApJS, 230, 15
Neijssel, C. J., Vigna-Gómez, A., Stevenson, S., et al. 2019, MNRAS, 490, 3740
Nelson, L. 2012, in Journal of Physics Conference Series, Vol. 341, Journal of Physics Conference Series, 012008
Nitz, A., Harry, I., Brown, D., et al. 2020, gwastro/pycbc: PyCBC Release 1.16.4
Nitz, A. H., Dent, T., Davies, G. S., et al. 2020, ApJ, 891, 123
Paczynski, B. 1976, in IAU Symposium, Vol. 73, Structure and Evolution of Close Binary Systems, ed. P. Eggleton, S. Mitton, & J. Whelan, 75
Paxton, B., Bildsten, L., Dotter, A., et al. 2011, ApJS, 192, 3
Paxton, B., Cantiello, M., Arras, P., et al. 2013, ApJS, 208, 4
Paxton, B., Marchant, P., Schwab, J., et al. 2015, ApJS, 220, 15
Paxton, B., Schwab, J., Bauer, E. B., et al. 2018, ApJS, 234, 34
Paxton, B., Smolec, R., Schwab, J., et al. 2019, ApJS, 243, 10
Peters, P. C. 1964, Physical Review, 136, 1224
Planck Collaboration, Ade, P. A. R., Aghanim, N., et al. 2016, A&A, 594, A13
Poisson, E. & Will, C. M. 1995, Phys. Rev. D, 52, 848
Pols, O. R., Schröder, K.-P., Hurley, J. R., Tout, C. A., & Eggleton, P. P. 1998, MNRAS, 298, 525
Portegies Zwart, S. F. & McMillan, S. L. W. 2000, ApJ, 528, L17
Postnov, K. A. & Yungelson, L. R. 2014, Living Reviews in Relativity, 17, 3
Qin, Y., Fragos, T., Meynet, G., et al. 2018, A&A, 616, A28
Qin, Y., Marchant, P., Fragos, T., Meynet, G., & Kalogera, V. 2019, ApJ, 870, L18
Rakavy, G. & Shaviv, G. 1967, ApJ, 148, 803
Rodriguez, C. L. & Antonini, F. 2018, ApJ, 863, 7
Rodriguez, C. L., Morscher, M., Pattabiraman, B., et al. 2015, Phys. Rev. Lett., 115, 051101
Rodriguez, C. L., Zevin, M., Amaro-Seoane, P., et al. 2019, Phys. Rev. D, 100, 043027
Sana, H., de Mink, S. E., de Koter, A., et al. 2012, Science, 337, 444
Schneider, F. R. N., Sana, H., Evans, C. J., et al. 2018, Science, 359, 69
Shao, Y. & Li, X.-D. 2015, ApJ, 802, 131
Shao, Y., Li, X.-D., & Dai, Z.-G. 2019, ApJ, 886, 118
Sigurdsson, S. & Hernquist, L. 1993, Nature, 364, 423
Silsbee, K. & Tremaine, S. 2017, ApJ, 836, 39
Smarr, L. L. & Blandford, R. 1976, ApJ, 207, 574

Soberman, G. E., Phinney, E. S., & van den Heuvel, E. P. J. 1997, A&A, 327, 620
Socrates, A., Blaes, O., Hungerford, A., & Fryer, C. L. 2005, ApJ, 632, 531
Sørensen, M., Fragos, T., Meynet, G., & Haemmerlé, L. 2018, arXiv e-prints, arXiv:1808.06488
Spera, M. & Mapelli, M. 2017, MNRAS, 470, 4739
Spruit, H. C. 1999, A&A, 349, 189
Spruit, H. C. 2002, A&A, 381, 923
Stevenson, S., Sampson, M., Powell, J., et al. 2019, ApJ, 882, 121
Stevenson, S., Vigna-Gómez, A., Mandel, I., et al. 2017, Nature Communications, 8, 14906
Stone, N. C., Metzger, B. D., & Haiman, Z. 2017, MNRAS, 464, 946
Suijs, M. P. L., Langer, N., Poelarends, A. J., et al. 2008, A&A, 481, L87
Swartz, D. A., Ghosh, K. K., Tennant, A. F., & Wu, K. 2004, ApJS, 154, 519
Tagawa, H., Haiman, Z., Bartos, I., & Kocsis, B. 2020, ApJ, 899, 26
Takahashi, K. 2018, ApJ, 863, 153
Tang, P. N., Eldridge, J. J., Stanway, E. R., & Bray, J. C. 2020, MNRAS, 493, L6
Tauris, T. M. & Dewi, J. D. M. 2001, A&A, 369, 170
Thorne, K. S. 1974, ApJ, 191, 507
Toonen, S. & Nelemans, G. 2013, A&A, 557, A87
Toonen, S., Portegies Zwart, S., Hamers, A. S., & Band opadhyay, D. 2020, A&A, 640, A16
Tout, C. A., Pols, O. R., Eggleton, P. P., & Han, Z. 1996, MNRAS, 281, 257
Tutukov, A. V. & Yungelson, L. R. 1993, MNRAS, 260, 675
van den Heuvel, E. P. J. 1976, in IAU Symposium, Vol. 73, Structure and Evolution of Close Binary Systems, ed. P. Eggleton, S. Mitton, & J. Whelan, 35
van den Heuvel, E. P. J., Portegies Zwart, S. F., & de Mink, S. E. 2017, MNRAS, 471, 4256
van Son, L. A. C., De Mink, S. E., Broekgaarden, F. S., et al. 2020, ApJ, 897, 100
Venumadhav, T., Zackay, B., Roulet, J., Dai, L., & Zaldarriaga, M. 2020, Phys. Rev. D, 101, 083030
Vigna-Gómez, A., Neijssel, C. J., Stevenson, S., et al. 2018, MNRAS, 481, 4009
Vink, J. S., de Koter, A., & Lamers, H. J. G. L. M. 1999, A&A, 350, 181
Vink, J. S., de Koter, A., & Lamers, H. J. G. L. M. 2001, A&A, 369, 574
Woosley, S. E. 2017, ApJ, 836, 244
Woosley, S. E. 2019, ApJ, 878, 49
Woosley, S. E., Blinnikov, S., & Heger, A. 2007, Nature, 450, 390
Woosley, S. E. & Heger, A. 2015, Astrophysics and Space Science Library, Vol. 412, The Deaths of Very Massive Stars, ed. J. S. Vink, 199
Wyrzykowski, Ł. & Mandel, I. 2020, A&A, 636, A20
Yoshida, T., Umeda, H., Maeda, K., & Ishii, T. 2016, MNRAS, 457, 351
Zackay, B., Dai, L., Venumadhav, T., Roulet, J., & Zaldarriaga, M. 2019a, arXiv e-prints, arXiv:1910.09528
Zackay, B., Venumadhav, T., Dai, L., Roulet, J., & Zaldarriaga, M. 2019b, Phys. Rev. D, 100, 023007
Zahn, J. P. 1977, A&A, 500, 121
Zaldarriaga, M., Kushnir, D., & Kollmeier, J. A. 2018, MNRAS, 473, 4174
Zevin, M., Bavera, S. S., Berry, C. P. L., et al. 2020a, arXiv e-prints, arXiv:2011.10057
Zevin, M., Berry, C. P. L., Coughlin, S., Chatziioannou, K., & Vitale, S. 2020b, ApJ, 899, L17
Zevin, M., Spera, M., Berry, C. P. L., & Kalogera, V. 2020c, ApJ, 899, L1
Zorotovic, M., Schreiber, M. R., Gänsicke, B. T., & Nebot Gómez-Morán, A. 2010, A&A, 520, A86

Appendix A: Initial binary distributions

The parameters describing the initial conditions of a binary system are primary and secondary masses, m_1 and m_2, orbital period p, eccentricity e and metallicity Z of the stars at ZAMS. We assumed that the primary masses follow the initial mass function (IMF) of Kroupa (2001) which spans the mass range $0.01\,\mathrm{M}_\odot \leq m_1 \leq 150\,\mathrm{M}_\odot$. The upper limit is an extrapolation of the Kroupa (2001) IMF which is measured only up to $50\,\mathrm{M}_\odot$. In our model, the lower limit represents the smallest theoretical mass for a star to support nuclear fusion (cf. Kumar 1963) while the arbitrary maximum stellar mass exclude BH formation above the upper mass-gap (e.g. Heger et al. 2002). The mass distribution of the less massive secondary star is given by $m_2 = m_1 q$ where the initial mass ratio q is drawn from a flat distribution (Sana et al. 2012) in the range $q \in [0, 1]$. Furthermore, we adopt a binary fraction of $f_{\rm bin} = 0.7$ (Sana et al. 2012) and assume that at birth the distribution of log-orbital periods follow Sana et al. (2012) power law with coefficient $\pi = -0.55$ in the range $p \in [10^{0.15}, 10^{5.5}]$ days and extrapolate down to the range $p \in [0.4, 10^{0.15}]$ days assuming a log-flat distribution (as the power low is not defined for $p < 10^{0.15}$ days), that is

$$f(p) = \begin{cases} C \times 0.15^{-0.55} & 0.4 \leq p/\mathrm{days} < 10^{0.15} \\ C \log_{10}(p/\mathrm{days})^{-0.55} & 10^{0.15} \leq p/\mathrm{days} \leq 10^{5.5} \end{cases}, \quad \text{(A.1)}$$

where the normalisation constant C is determined by the condition $\int_{p_{\rm min}}^{p_{\rm max}} f(p)\,\mathrm{d}p = 1$. The lower limit of 0.4 days will ensure that we probe all the available parameter space, see for example, the detailed simulations of du Buisson et al. (2020) where they find binaries with initial orbital periods as small as 0.4 days forming BBHs. Finally, we assume that all binaries are born with circular orbits, namely with zero e. We assume that all these distributions are both independent of each other, as well as, independent of metallicity which in reality might not be the case (Moe & Di Stefano 2017). This oversimplification means that we also include systems overfilling the L1 and L2 Roche-lobe surfaces at ZAMS. In Sec. 4.1 we discuss how our BBH rate estimates are affected by omitting these systems or by assuming a log-uniform distribution. The omission of this portion of the parameter space does not lead to a qualitative difference in the predicted observable distributions.

In order to optimise the absolute number of binaries becoming BBHs per number of simulated binaries, we restrict the primary mass to the range $5\,\mathrm{M}_\odot \leq m_1 \leq 150\,\mathrm{M}_\odot$. For the metallicity, we divide uniformly the log-metallicity range $Z \in [0.0001, 0.0309]$ in 30 bins. The largest metallicity bin was chosen to have a centre at $1.5\,Z_\odot$ where we adopt the solar reference $Z_\odot = 0.017$ (Grevesse et al. 1996). This metallicity range is where the stellar model fits of Hurley et al. (2000) we use are defined. We evolve 5 million binaries per metallicity bin ΔZ for a total simulated mass per ΔZ of $M_{\mathrm{sim},\,\Delta Z} \simeq 1.05 \times 10^8\,\mathrm{M}_\odot$. Since we restricted the primary mass, we only model a fraction of the underlying stellar population. Hence, we need to re-normalise the simulated stellar mass $M_{\mathrm{sim},\,\Delta Z}$ to obtain the total stellar population; the normalisation constant for our choice of initial binary properties is $f_{\rm corr}^{-1} = 4.72$, see Appendix A in Bavera et al. (2020) for a derivation of this quantity.

Appendix B: COSMIC population synthesis model

Appendix B.1: Single stellar models

To generate our BBH population models, we used `COSMIC` version `v3.3.0`. Stellar evolution in `COSMIC` (Breivik et al. 2020) is based on the analytical fits of Hurley et al. (2000, 2002) to the single stellar models of Pols et al. (1998). For O and B stars we adopt mass loss through stellar winds according to the prescription of Vink et al. (2001), which covers separately the temperature ranges $12,500\,\mathrm{K} < T_{\rm eff} < 22,500\,\mathrm{K}$ and $27,500\,\mathrm{K} < T_{\rm eff} < 50,000\mathrm{K}$. Around $T \simeq 25,000\,\mathrm{K}$ there is a bi-stability jump that leads to a mass-loss increase of a factor of about five. This jump is due to the recombination of the Fe IV to the Fe III ion in the lower part of the wind (Vink et al. 1999). For Wolf–Rayet stars mass-loss rate we adopt stellar winds as in Brott et al. (2011) who assume Hamann et al. (1995) reduced by a factor of 10 to correct for clumping and use a metallicity scaling of $(Z/Z_\odot)^{0.85}$ (Vink et al. 2001). For all these wind prescriptions we adopt the solar reference $Z_\odot = 0.017$ (Grevesse et al. 1996).

During the post-carbon burning phase of massive stars, photons produced in the core are energetic enough to produce electron–positron pairs which softens the equation of state, diminishing the pressure support of the core (Woosley et al. 2007). This causes the core to rapidly contract and the temperature to increase, allowing for explosive oxygen burning (e.g. Woosley & Heger 2015). For He-core masses in the range $\sim [30, 64]\,\mathrm{M}_\odot$ the released energy is insufficient to completely disrupt the star. This create a series of energetic pulses which eject material from the star before it collapses into a BH. This is the PPI (Yoshida et al. 2016; Woosley 2017; Marchant et al. 2019). If the He-core mass is in the range $\sim [64, 133]\,\mathrm{M}_\odot$ the released energy is enough to reverse the collapse, unbinding and destroying the star. This event is a PISN (Fowler & Hoyle 1964; Rakavy & Shaviv 1967; Barkat et al. 1967). Similar to Stevenson et al. (2019), we adopt the fit to the grid of simulations from Marchant et al. (2019, see Table 1), which demonstrate a turnover in the relation between pre-supernova He-core mass and final mass. We use the 9th-order polynomial fit of Breivik et al. (2020), cf. their Eq. (4), to map the pre SN stellar mass in the range $31.99 \leq M_{\rm preSN}/\mathrm{M}_\odot \leq 61.10$ to the baryonic mass collapsing to form the BH.

Appendix B.2: Mass-transfer stability and common envelope

The stability of Roche-lobe overflow mass transfer is determined by the rate at which the Roche-lobe radius is changing as a result of mass-transfer $\mathrm{d}\log(R_{\rm L})/\mathrm{d}\log(m)$ to the response of the radius of a star as its mass is changing $\mathrm{d}\log(R_*)/\mathrm{d}\log(m)$. We use the approximation of Eggleton (1983) for the Roche-lobe radius while we approximate the radial response of the star depending on its stellar type. We adopt the values assumed in Neijssel et al. (2019); Bavera et al. (2020). The stability of the mass transfer can then be determined by solving this equation with respect to the critical mass ratio, defined as $q_{\rm crit} = m_{\rm donor}/m_{\rm accretor}$. For MS stars we use $\mathrm{d}\log(R_*)/\mathrm{d}\log(m) = 2.0$ which correspond to $q_{\rm crit} \simeq 1.72$ while for HG stars $\mathrm{d}\log(R_*)/\mathrm{d}\log(m) = 6.5$ which correspond to $q_{\rm crit} \simeq 3.83$ (Ge et al. 2015). For stars on the GB and AGB we use fits from Hjellming & Webbink (1987). For stripped stars we adopt $q_{\rm crit}$ as in Claeys et al. (2014). Different choices of $q_{\rm crit}$, especially for GB and AGB stars have an impact on the parameter space that leads to the formation of BBHs, hence on the merger rate, see Sec. 4.3 for a discussion of this uncertainty.

If the mass transfer is stable the companion star accretes a fraction of mass lost by the donor star. Any mass that is not accreted leaves the system instantaneously, taking away the specific AM of the accretor (Hurley et al. 2002). For our fiducial models we assume that the accretion of degenerate objects is Eddington-limited, this results in a highly non-conservative

mass-transfer phase where degenerate objects accrete negligible amount of mass, hence the first-born BH will not spin up because of accretion during the second mass-transfer phase (Thorne 1974). For the Eddington-limited accretion efficiency onto a compact object, COSMIC uses the definition of Hurley et al. (2002),

$$\dot{M}_{\rm edd} = 2.08 \times 10^{-3}(1+X)^{-1}(R_{\rm acc}/{\rm R}_\odot)\ {\rm M}_\odot\,{\rm yr}^{-1} \equiv 1 = \eta_{\rm acc}\,, \tag{B.1}$$

where X is the hydrogen mass fraction of the donor and $R_{\rm acc}$ is the accretion radius of the compact object which for a BH is chosen to be the Schwarzschild radius. In this work we define $\eta_{\rm acc}$ to be the MT accretion efficiency limit in units of the Eddington-limit. To investigate how our results depend on this limit, we explore different MT efficiency limits: $\eta_{\rm acc} \in [1, 10^3, 10^5, 10^9]$.

If the mass transfer is unstable, the donor star will expand to form a CE of gas around the binary which can be expelled by the injection of orbital energy from the binary (Paczynski 1976). This is a complex phase and we parameterise it with the $\alpha_{\rm CE}$–λ formalism (see, e.g. Ivanova et al. 2013, for a review). In this parameterisation $\alpha_{\rm CE}$ determines the efficiency factor for injecting orbital energy into the envelope, while λ characterises the binding energy of the envelope to its stellar core which depends on the structure of the donor's envelope. Assuming that the pre-CE orbital energy is much smaller than the post-CE orbital energy, the initial and final orbital period of the CE event, $A_{\rm preCE}$ and $A_{\rm postCE}$, are related by the following expression (Ivanova et al. 2013)

$$A_{\rm postCE} \simeq \frac{1}{2}\alpha_{\rm CE}\,\lambda\frac{m_1\,m_{2,\rm postCE}}{m_{2,\rm preCE}\,m_{2,\rm env}}\,\hat{r}_L\,A_{\rm preCE}, \tag{B.2}$$

where $\hat{r}_L$ is the dimensionless Roche-lobe radius, m_1 is the mass of the accretor, $m_{2,\rm preCE}$ and $m_{2,\rm postCE}$ are the donor star masses before and after the CE event and $m_{2,\rm env}$ the envelope mass. Previous studies of post-CE binaries have shown that the efficiency could be as low as $\alpha_{\rm CE} = 0.2$ (Zorotovic et al. 2010; Toonen & Nelemans 2013; Camacho et al. 2014) while other using detailed modelling of the CE phase for binary neutron star progenitors (Fragos et al. 2019), suggests CE efficiencies as high as $\alpha_{\rm CE} = 5.0$ (see also Giacobbo & Mapelli 2019). Approximately, uncertainties on $\alpha_{\rm CE}$ or on λ linearly scale to uncertainties on the orbital separation post CE as $\delta A_{\rm postCE}/A_{\rm preCE} \propto \delta\alpha_{\rm CE}\times\lambda + \alpha_{\rm CE}\times\delta\lambda$. For λ we adopt the fits as in Claeys et al. (2014).

Within the CE channel we distinguish and adopt a pessimistic scenario, in which unstable mass transfer from a donor star without a well-developed core-envelope structure, namely when a star finds itself in the HG, is always assumed to lead to a merger (Belczynski et al. 2007). An optimistic scenario which include these systems would result in an overestimation of the observed local BBHs merger rate density (Neijssel et al. 2019; Belczynski et al. 2020).

Appendix C: MESA detailed BH–He-star models

In our previous works (Qin et al. 2018; Bavera et al. 2020) we explored the evolution of tight BH–He-star systems computing grids of detailed binary evolution models using MESA (Paxton et al. 2011, 2013, 2015, 2018, 2019). This is the late-end phase of the binary evolution of BBHs formed through the CE and SMT channels. Here we iterate on this work by adapting those models to the newer MESA version r11701, computing an even larger grid and modifying our stellar models to match the physical stellar assumptions made in the work of du Buisson et al. (2020), which expand on the work of Marchant et al. (2016) on chemical homogeneous evolution.

Appendix C.1: Single stellar physics

All mixing processes are treated as diffusive processes. Convection is modelled using the Ledoux criterion, adopting a mixing-length parameter of $\alpha_{\rm MLT} = 1.5$ (Böhm-Vitense 1958). Semi-convection is modelled according to Langer et al. (1983) with an efficiency parameter $\alpha_{\rm SEM} = 1.0$ (Langer 1991). We also take into account exponential core-overshooting and thermohaline mixing with $\alpha_{\rm TH} = 1.0$ (cf. Cantiello et al. 2009). Opacities are computed using CO-enhanced opacity tables from the OPAL project (Iglesias & Rogers 1996), computed using solar-scaled abundances based on Grevesse et al. (1996). As we are not interested in following the nucleosynthesis in detail, we use the simple networks provided with MESA basic.net which MESA automatically extend to co_burn.net to resolve carbon burning. Our models are stopped at C depletion. Finally, PPI and PISN are treated as in the single stellar models of COSMIC. We assume that the mass loss through PPI of any stellar model is lost from the surface of the star and only consider the AM of the remaining layers in the collapse of the star.

Rotational mixing and AM transport are also treated as diffusion processes (Heger et al. 2000, 2005), which involve the effects of Eddington–Sweet circulation, secular and dynamical shear mixing and the Goldreich–Schubert–Fricke instability with an efficiency parameter of $f_c = 1/30$ (Chaboyer & Zahn 1992; Heger et al. 2000). We include the effect of magnetic fields on the transport of AM assuming an efficient AM transport mechanism: the Tayler–Spruit dynamo (Spruit 1999, 2002). An efficient AM transport allows us to assume that all He-stars emerging from the CE or SMT phases are initially not rotating. This is because any initial or acquired rotation during the evolution of the secondary is erased by mass transfer and wind mass loss by the time it becomes a He-star. Assuming instead that the He-star is initially synchronized with the orbit, right after the formation of the BH–He-star binary, has been shown to have negligible effects in the final properties of the resulting BBH system (Qin et al. 2018).

We implement the same WR stars wind prescription as in COSMIC where we also include the enhancement of winds through rotation as in Heger & Langer (2000). When the rotation rate exceeds a given threshold, $\Omega/\Omega_{\rm crit} > 0.98$, we implicitly compute the mass-loss rate required for the rotation rate to remain just below this value (Paxton et al. 2015). For a star with mass M and radius R, $\Omega_{\rm crit} \equiv [(1-\Gamma)GM/R]^{1/2}$ where $\Gamma = \kappa L/(4\pi cGM)$ is the Eddington factor and κ is the true flux-mean opacity coefficient (Langer 1997).

Appendix C.2: Binary stellar physics

We use MESA single star module to first create a He-star with the desired mass and with abundances $Y = 0.98$ and $Z = 0.02$. We then load the model in the MESA binary module, relax the metallicity to the desired value and allow the star to relax until it reaches ZAHeMS. We define ZAHeMS to be the moment when the central luminosity becomes larger than $\sim 99\%$ of the surface luminosity. To facilitate the relaxation of the star to ZAHeMS we adopt MLT++ treatment of convection (Paxton et al. 2013) which reduces the superadiabaticity in some radiation-dominated convective regions. Once the star reaches ZAHeMS we turn off MLT++. At ZAHeMS we check if the He-star overfill

its Roche lobe, if this is the case we stop the evolution and assume the system to be non-physical. Whenever one component in the system attempts to overflow its Roche lobe during the binary evolution, we implicitly compute the mass-transfer rate using the Kolb scheme (Kolb & Ritter 1990). If the mass transfer exceed 10 $M_\odot\,yr^{-1}$ we stop the run and assume that the binary will merge. Furthermore, we use the prescription of Misra et al. (2020) to check that the He-star does not overflow the L2 Roche volume of the binary. If this is the case, either at ZAHeMS or during the evolution of the binary, we stop the run and assume that it will lead to a merger.

Tidal forces are responsible for synchronising the spin of the He-star with the orbit (Zahn 1977; Hut 1981). Tidal effects are implemented as in Qin et al. (2019) for the case of stars with radiative envelope. This is a variation of the standard tidal prescription of `MESA` (Paxton et al. 2015) which synchronize the whole star. Here tides only operate on the radiative regions. This slight variation has a negligible impact on our results because the Tayler–Spruit dynamo guarantees strong coupling between the star's layers. We assume that the orbits after the second MT phase are circular and the system remains circular during binary evolution. The strength of the interaction depends on the ratio of the stellar radius R to the orbital separation A, the He-star mass M, the binary mass ratio q and the moment of inertia I. The timescale for synchronization is given by (Hurley et al. 2002)

$$\frac{1}{T_{\rm syn}} = 3E_2(1+q)^{5/6}\frac{q^2}{r_{\rm g}^2}\left(\frac{GM}{R^3}\right)^{1/2}\left(\frac{R}{A}\right)^{17/2}, \tag{C.1}$$

where $r_{\rm g} = [I/(MR^2)]^{1/2}$ is the dimensionless gyration radius of the He-star and E_2 is the second order tidal coefficient. As in our previous work, we use the fitting formula of E_2 for He-star from Qin et al. (2018).

Appendix D: Core collapse

BHs are formed during the core collapse of massive stars and, in some cases, their formation is associated with a supernova explosion. As in Bavera et al. (2020), we use Fryer et al. (2012) delayed supernova prescription to model how much baryonic remnant mass is left behind after the core collapse. This model avoids an enforced mass gap between neutron stars and BHs which are not consistent with current microlensing observations (Wyrzykowski & Mandel 2020) or with GW190814 (Abbott et al. 2020c). During the collapse of the star, asymmetric ejection of matter (Janka & Mueller 1994; Burrows 2013) or asymmetric emission of neutrinos (Bisnovatyi-Kogan 1993; Socrates et al. 2005) can provide a momentum kick to the newly formed BHs. We assume that the birth kicks of BHs follow a Maxwellian distribution with $\sigma = 265\ {\rm km\,s^{-1}}$ (Hobbs et al. 2005) rescaled by $1 - f_{\rm fb}$ where $f_{\rm fb}$ is the fallback mass fraction (Fryer et al. 2012). For massive stars with carbon–oxygen core masses grater than 11 $M_\odot$, Fryer et al. (2012) prescription assumes a direct collapse, that is $f_{\rm fb} = 1$. This implies that in our model all heavy BHs receive no natal kicks. The kicks impacted on the lighter BHs can tilt the orbit, which may generate a negative $\chi_{\rm eff}$, add eccentricity to the orbit or disrupt the binary. In practise systems with negative $\chi_{\rm eff}$ are not statistically relevant in our models as the kicks are not strong enough to flip the orbits by more than 90°. Recently, Callister et al. (2020) showed that a $\sigma \simeq 1,000$ km/s is required in order to explain negative $\chi_{\rm eff}$ in GWTC-2 data with CE BBHs. We take into account all these orbital changes, as well as, orbital changes due to neutrinos symmetric mass loss, following the analytical calculations of Kalogera (1996).

We estimate the spin of the resulting second-born BH following the framework presented in Bavera et al. (2020). Here, we adopt a different treatment of neutrino mass loss motivated by Zevin et al. (2020c) which prescribes that a collapsing proto-neutron star can lose up to $0.5\,M_\odot$ through neutrino emission. In order to calculate the final mass and spin of the BH resulting from the collapse, we need to consistently follow its accretion history soon after it is formed. We assume that the innermost $3\,M_\odot$ form a proto-neutron star, which collapse to form a BH of $2.5\,M_\odot$, while $0.5\,M_\odot$ are converted into neutrinos and leave the systems carrying away a fraction $(0.5/3)$ of the proto-neutron star AM. We consider a collapsing star to be a collection of shells with mass $m_{\rm shell}$ and angular frequency $\Omega_{\rm shell}$ that falls one by one onto the central BH. Once a shell reaches the BH's event horizon, it is accreted by it. The amount of specific AM of the in-falling material, $j(r,\theta) = \Omega_{\rm shell}(r) r^2 \sin(\theta)$ where θ is the polar angle, determines the properties of the accretion flow. Low AM material collapses directly onto the BH transferring its entire mass and AM to the hole, while material with enough AM can create a disk around it. The mass $M_{\rm BH}$ and spin a of the accreting BH determine the threshold for disk formation and is given by the specific AM at the innermost stable circular orbit (ISCO; Bardeen et al. 1972)

$$j_{\rm ISCO} = \frac{GM_{\rm BH}}{c}\frac{2}{3^{3/2}}\left[1 + 2\left(\frac{3c^2 r_{\rm ISCO}}{GM_{\rm BH}} - 2\right)^{1/2}\right], \tag{D.1}$$

where $r_{\rm ISCO}$ is the radius of the ISCO for prograde equatorial orbits,

$$r_{\rm ISCO} = \frac{GM_{\rm BH}}{c^2}\left\{3 + z_2 - [(3-z_1)(3+z_1+2z_2)]^{1/2}\right\}, \tag{D.2}$$

with $z_1 = 1+(1-a^2)^{1/3}[(1-a)^{1/3}+(1+a)^{1/3}]$ and $z_2 = (3a^2+z_1^2)^{1/2}$. From the disk formation condition $j(r,\theta) > j_{\rm ISCO}$ we can define the polar angle at which disk formation occurs as

$$\theta_{\rm disk} = \arcsin\left(\frac{j_{\rm ISCO}}{\Omega_{\rm shell}(r) r^2}\right)^{1/2}. \tag{D.3}$$

The portion of the shell with $\theta < \theta_{\rm disk}$ will collapse directly onto the BH on a dynamical timescale, $t_{\rm dyn} \simeq [r^3/(GM(r))]^{1/2}$, transferring $j(r,\theta)$ to the hole, while the portion of the shell with $\theta \geq \theta_{\rm disk}$ will form a disk and transfer only $j_{\rm ISCO}$ to the BH. The disk will be accreted on a viscous timescale $t_\nu \simeq \alpha_\nu^{-1}(R_{\rm circ}/H)^2 t_{\rm circ}$ assumed to be much smaller than $t_{\rm dyn}$ (Batta & Ramirez-Ruiz 2019). Here H is the disk's scale height, α_ν is the viscosity parameter and $t_{\rm circ}$ is the Keplerian orbital period at the accretion radius also known as circularisation radius $R_{\rm circ} = j_{\rm shell}^2/(GM_{\rm BH})$. The collapsing shell contributes therefore to the AM of the BH by

$$J_{\rm shell} \equiv J_{\rm direct} + J_{\rm disk} = \int_0^{\theta_{\rm disk}} m_{\rm shell}\Omega_{\rm shell}(r)\, r^2 \sin^3(\theta)\, {\rm d}\theta + \\ + \int_{\theta_{\rm disk}}^{\pi/2} m_{\rm shell} j_{\rm ISCO} \sin(\theta)\, {\rm d}\theta. \tag{D.4}$$

The accretion disk has mass $m_{\rm disk} = m_{\rm shell}\cos(\theta_{\rm disk})$ and the mass-energy accreted onto the BH from the disk is $\Delta M_{\rm disk} = m_{\rm disk}[1 - 2GM_{\rm BH}/(3c^2 r_{\rm ISCO})]^{1/2}$ (Bardeen 1970; Thorne 1974).

Appendix E: Grids of detailed BH–He-star models

We use our detailed binary stellar models to cover the 4D parameter space defined by initial metallicity Z, black hole mass

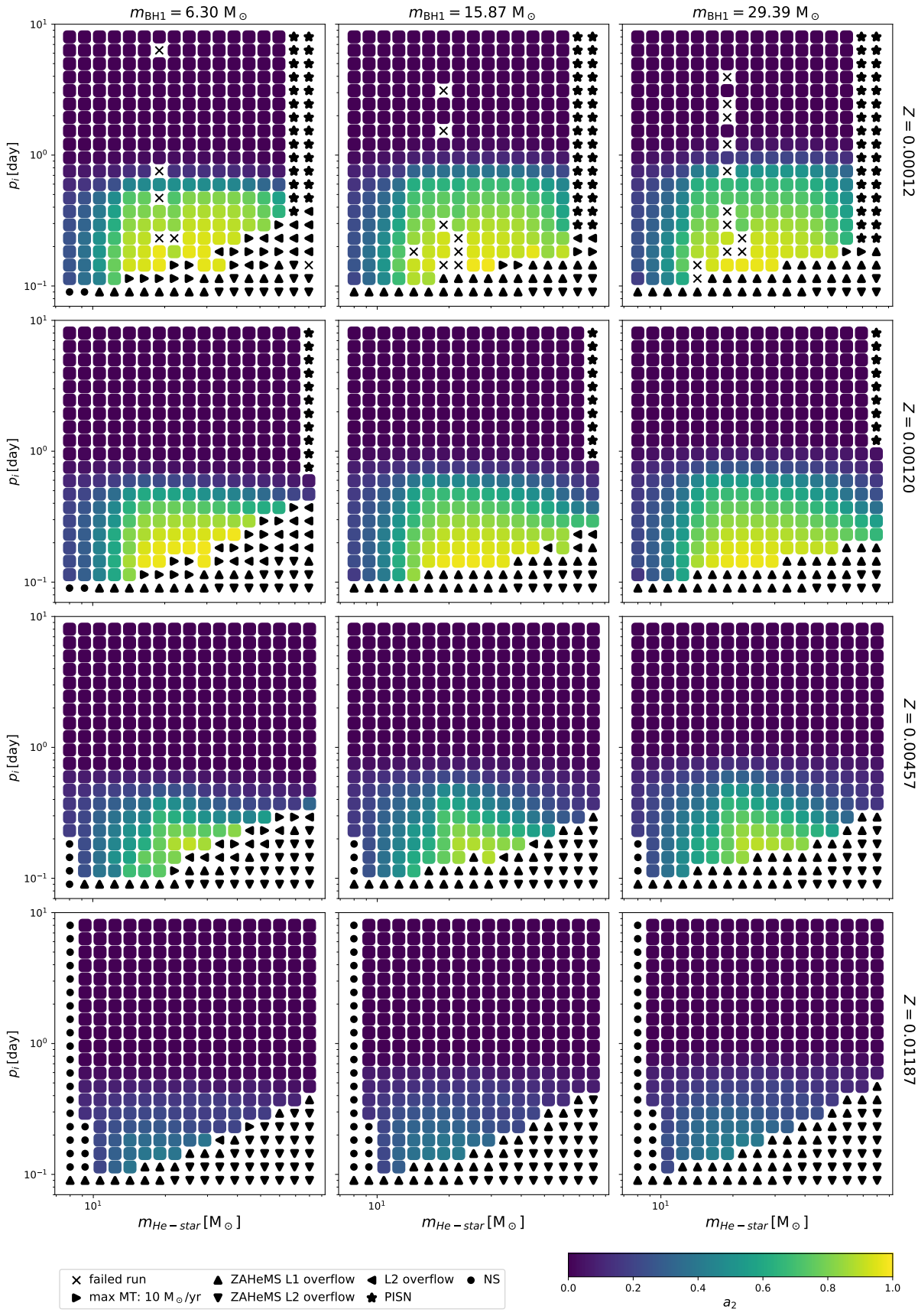

Fig. D.1. These are examples of two-dimensional slices of the four-dimensional grid for 4 different metallicities, $Z \in [0.00012, 0.00120, 0.00457, 0.01187]$, and 3 different BH masses $m_{BH} \in [6.3, 15.87, 29.38]$ $M_\odot$. The final second-born BH spin value a_2 is coloured for each successful track according to the legend. Each successful run stopped because of carbon depletion (square markers) while other termination flags are shown in the bottom legend.

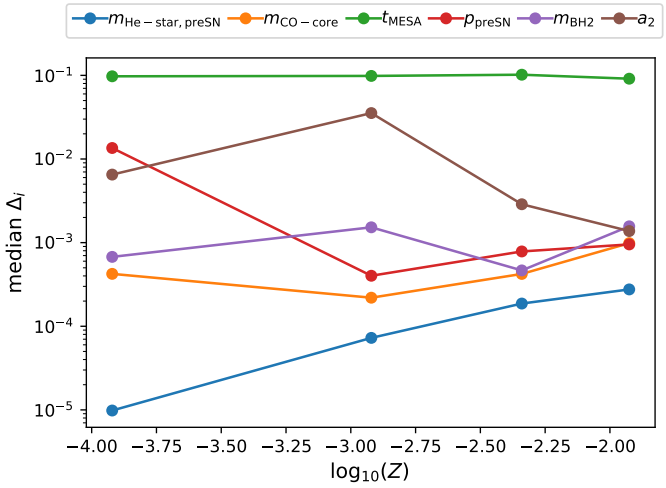

Fig. E.1. Median relative error as a function of metallicity of the log-transformed and re-scaled six quantities B_i: the He-star mass (blue) and its carbon-oxygen core mass (orange) before the supernova, the orbital period before the supernova (red), the second-born BH mass (violet), the spin of the second-born black hole (brown), and the lifetime of the BH–He-star binary (green).

$m_{\rm BH1}$, He-star mass $m_{\rm He-star}$ and orbital period p. We run grids for 30 different metallicities ranging from $\log_{10}(Z) = -4.0$ to $\log_{10}(Z) = \log_{10}(1.5Z_\odot) \simeq -1.593$ in steps of $\log_{10}(Z) \simeq 0.083$. For each metallicity, we run 11 BH masses in the log-range $[2.5, 54.4]\,{\rm M}_\odot$ in steps of $\log_{10}(m_{\rm BH1}/{\rm M}_\odot) \simeq 0.134$. The lower limit is the smallest theoretical BH mass (in our model) while the maximum BH mass is chosen to have the second to last BH mass at 40 $\rm M_\odot$ near the PISN cut. For each metallicity and BH mass we run 17 He-star masses in the log-range $[8, 80]\,{\rm M}_\odot$ in steps of $\log_{10}(m_{\rm He-star}/{\rm M}_\odot) \simeq 0.063$ and 20 binary periods in the log-range $[0.09, 8]$ days in steps of $\log_{10}(p/{\rm days}) \simeq 0.103$. We verified that smaller He-star masses do not lead to BH formation for any metallicity we consider. The maximum He-star mass and smallest orbital period where chosen to include any BH–He-star system produced by our `COSMIC` models. The maximal orbital period range ensure that we cover the parameter space well past the point where the BBH systems are merging within the Hubble time.

In total, we calculated roughly 110,000 new binary evolution sequences, as compared to about 16,000 used in Bavera et al. (2020). The fraction of failed `MESA` runs vary from 3% to 0.1% depending on metallicity. To minimise the loss of information created by the failed runs we rerun those models with an He-star mass increased by 5% which reduced the failed runs by a factor of 3. In Fig. D.1 we show the spin of the second-born BH for different two-dimensional slices of the four-dimensional parameter space for four different metallicities, $Z \in [0.00012, 0.00120, 0.00457, 0.01187]$, and three different BH masses, $m_{\rm BH} \in [6.3, 15.87, 29.38]$ $\rm M_\odot$. We can see how the tides are more efficient at lower metallicities. This is because the stellar winds of He-stars are metallicity dependent $\propto (Z/Z_\odot)^{0.85}$ (Vink et al. 2001) and widen more efficiently the binaries at larger metallicities and hence reduce the impact of tides.

These grids were used to determine the final outcomes and final parameters of the late-end evolution stage of the binary systems through linear interpolation. Each metallicity is interpolated separately. We want to interpolate six quantities B_i: the He-star mass and its carbon-oxygen core mass before the supernova, the resulting BH mass, the orbital period before the supernova, the lifetime of the BH–He-star binary and the spin of the second-born BH. Before interpolating each quantity, we log-transformed it and re-scale it to the interval $[-1, 1]$ to reduce the interpolation error. The interpolation itself relies on building a Delaunay triangulation of the input data points followed by barycentric linear interpolation over the vertices of the (hyper)triangle containing the location of interest. To test the accuracy of the interpolation: we computed around 1000 new `MESA` tracks for each of the four metallicities shown in Fig. D.1 and calculate the relative error of each transformed and rescaled quantity $X_i \equiv \log_{10}(B_i)^{[-1,1]}$ as $\Delta_i = |X_{\rm true,i} - X_{\rm interp,i}|/X_{\rm true,i}$. In Fig. E.1 we show the median relative errors of these quantities as a function of metallicity. In the median calculation we exclude all the systems not becoming BBHs. Half of the quantities have median relative errors independent of metallicity with the exception of the second-born BH spin, He-star mass and orbital period before supernova. The decrease of median error for a_2 and $p_{\rm preSN}$ is explained by the fact that at high metallicities the orbits widen more, neutralising tides and resulting in systems with zero spin. On the other hand, the median error of $m_{\rm He-star}$ increases because at higher metallicities this quantity does not depend linearly on the initial He star mass which is caused by stellar winds that cause the He-star to lose a non-negligible amount of mass. The largest relative median error is the lifetime of the BH–He-star system. This is not a problem by itself as the delay time between the binary formation and merger is dominated by the GW inspiral which is many order of magnitudes larger than this timescale. The increase of interpolation accuracy compared to Bavera et al. (2020) is due to the larger data set used here, the fact that we use a regular grid and interpolate each metallicity independently.

Appendix F: Model comparison

We use Bayesian hierarchical modelling to determine the likelihood of observing N independent GW events $\{x_i\}_{i=1}^N$ given an astrophysical model described by a set of parameters $\boldsymbol{\lambda}$ (e.g. Mandel et al. 2019). We assume that each GW event is an independent observation and is characterised by a set of physical parameters $\boldsymbol{\theta}$,

$$p(\{x_i\}_{i=1}^N \,|\, \boldsymbol{\lambda}) = \prod_{i=1}^N \frac{p(x_i \,|\, \boldsymbol{\lambda})}{\xi(\boldsymbol{\lambda})} = \prod_{i=1}^N \frac{1}{\xi(\boldsymbol{\lambda})} \int p(x_i \,|\, \boldsymbol{\theta})\, p(\boldsymbol{\theta} \,|\, \boldsymbol{\lambda})\, {\rm d}\boldsymbol{\theta} = \\ = \prod_{i=1}^N \frac{p(x_i)}{\xi(\boldsymbol{\lambda})} \int \frac{p(\boldsymbol{\theta} \,|\, x_i)}{p(\boldsymbol{\theta})} p(\boldsymbol{\theta} \,|\, \boldsymbol{\lambda})\, {\rm d}\boldsymbol{\theta}\,, \tag{F.1}$$

where we have marginalised over the physical parameters of the individual events and used Bayes' theorem to obtain the final line. Here $p(\boldsymbol{\theta})$ is the prior on the physical parameters that are used to generate the posterior samples. The normalisation factor $\xi(\boldsymbol{\lambda}) = \int p_{\rm det}(\boldsymbol{\theta}) p(\boldsymbol{\theta}|\boldsymbol{\lambda}) {\rm d}\boldsymbol{\theta}$ accounts for the overall probability of making an observation given a particular choice $\boldsymbol{\lambda}$. Since in GWTC-2 we have samples drawn from the posterior $p(\boldsymbol{\theta} \,|\, x_i)$, we can approximate posterior-weighted integrals as a sum over samples as

$$p(\{x_i\}_{i=1}^N \,|\, \boldsymbol{\lambda}) \simeq \prod_{i=1}^N \frac{p(x_i)}{\xi(\boldsymbol{\lambda})} \frac{1}{S} \sum_{k=1}^S \frac{p(\boldsymbol{\theta}_k \,|\, \boldsymbol{\lambda})}{p(\boldsymbol{\theta}_k)}\,, \tag{F.2}$$

where S the number of posterior samples. Again, $\boldsymbol{\theta}_k$ are the astrophysical parameters drawn from the GW posterior distribu-

tion and $p(\boldsymbol{\theta}_k \,|\, \boldsymbol{\lambda})$ are their likelihood given by our astrophysical model (underlying distribution). Similarly, the normalisation constant $\xi(\boldsymbol{\lambda})$ can be approximated as a sum over the weighed underlying BBH distribution $p(\boldsymbol{\theta}|\boldsymbol{\lambda})$ as

$$\xi(\boldsymbol{\lambda}) \simeq \frac{1}{T \sum_{j=1}^{T} w_j} \sum_{j=1}^{T} p_{\rm det}(\boldsymbol{\theta}_j)\, w_j \,, \tag{F.3}$$

where $\boldsymbol{\theta}_j$ is the set of parameters describing the BBH j with a cosmological weight w_j given by the argument of the summation in Eq. (4) and T the total number of samples. Finally, to approximate the probability density functions of each event $p(\boldsymbol{\theta})$ and each model $p(\boldsymbol{\theta}|\boldsymbol{\lambda})$ we use a three-dimensional kernel density estimator (KDE) where we graphically verify the accuracy by comparing random draws from the KDE with the real marginalised one-dimensional and two-dimensional sample distributions.

We can now compare two models, M_1 and M_2, described by $\boldsymbol{\lambda}_1$ and $\boldsymbol{\lambda}_2$, respectively. The amount by which the data supports a specific model is described by the BF, defined as:

$$\mathrm{BF}_{12} \equiv \frac{p(\{x_i\}_{i=1}^{N} \,|\, \boldsymbol{\lambda}_1)}{p(\{x_i\}_{i=1}^{N} \,|\, \boldsymbol{\lambda}_2)} \,. \tag{F.4}$$

In the ratio of the two likelihoods the multiplicative constant $p(x_i)$ is canceled out, leaving us with all the information required to compute the BF. This factor indicates whether any model is favoured or disfavoured by the data compared to another. Values larger than 1 favour the model M_1 while values smaller than 1 favours the model M_2. In our analysis, we adopt the convention of having M_2 as our reference model.

Appendix G: Model results

Here we present some extra figures which were not included in the paper because of their size. Fig. G.1 and G.2 show the combined distributions of the main GW observables $\chi_{\rm eff}$, $\mathrm{M}_{\rm chirp}$ and q of the CE channel for the detected and underlying BBH population, respectively, for different $\alpha_{\rm CE}$ values. Similarly, Fig. G.3 and Fig. G.4 show the combined distributions of these observables of the SMT channel for the detected and underlying BBH population, respectively, for different $\eta_{\rm acc}$ values.

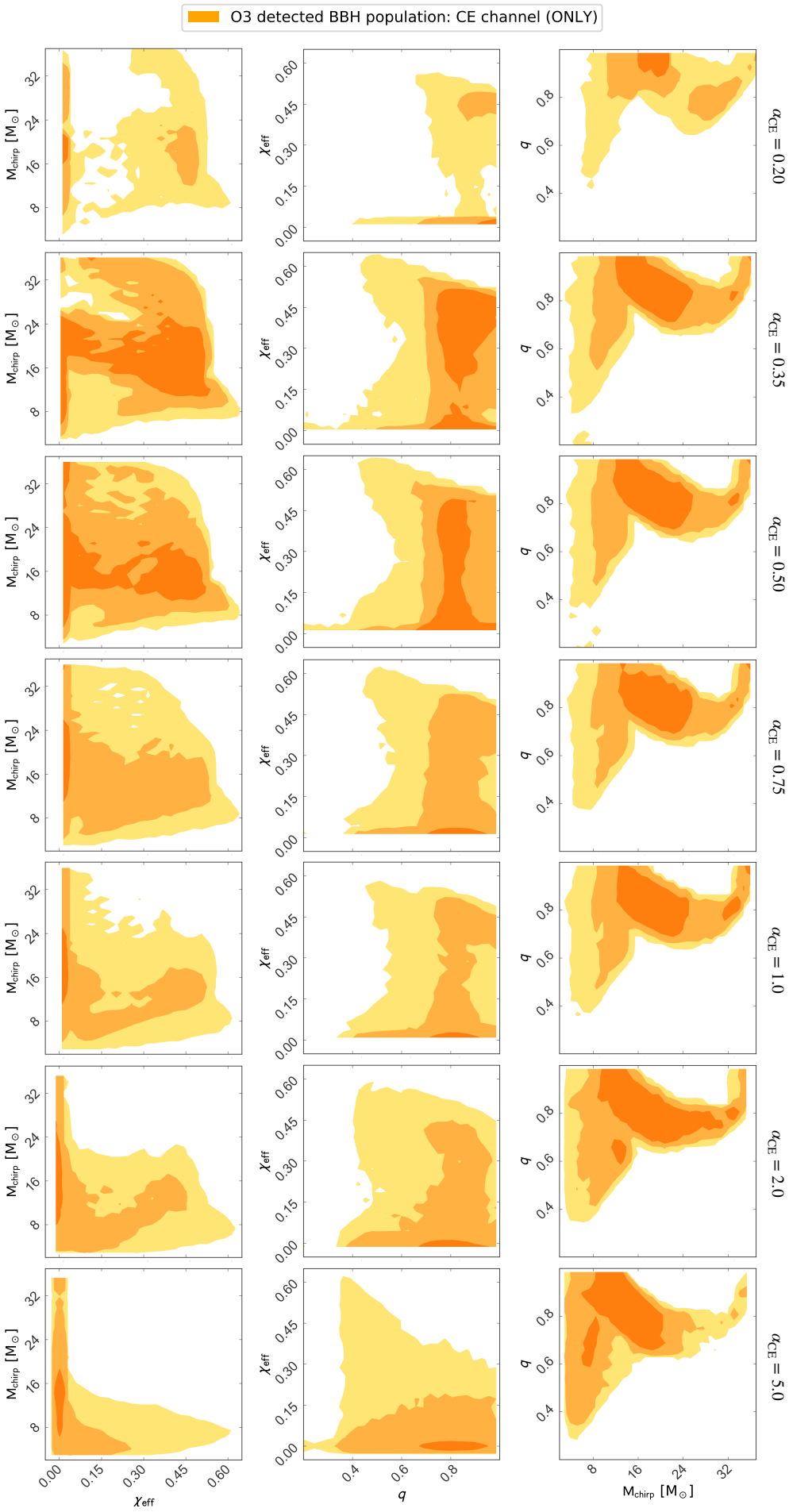

Fig. G.1. Model predictions for the O3 detected BBH population of the CE channel for different α_{CE} values according to the legend, in orange. We show the joint distributions of chirp mass M_{chirp}, effective inspiral spin parameter χ_{eff} and binary mass ratio q. Lighter colours represent larger contour levels of 68%, 95% and 99%, respectively, constructed with `pygtc` (Bocquet & Carter 2016). All histograms are plotted with 30 bins without any bin smoothing.

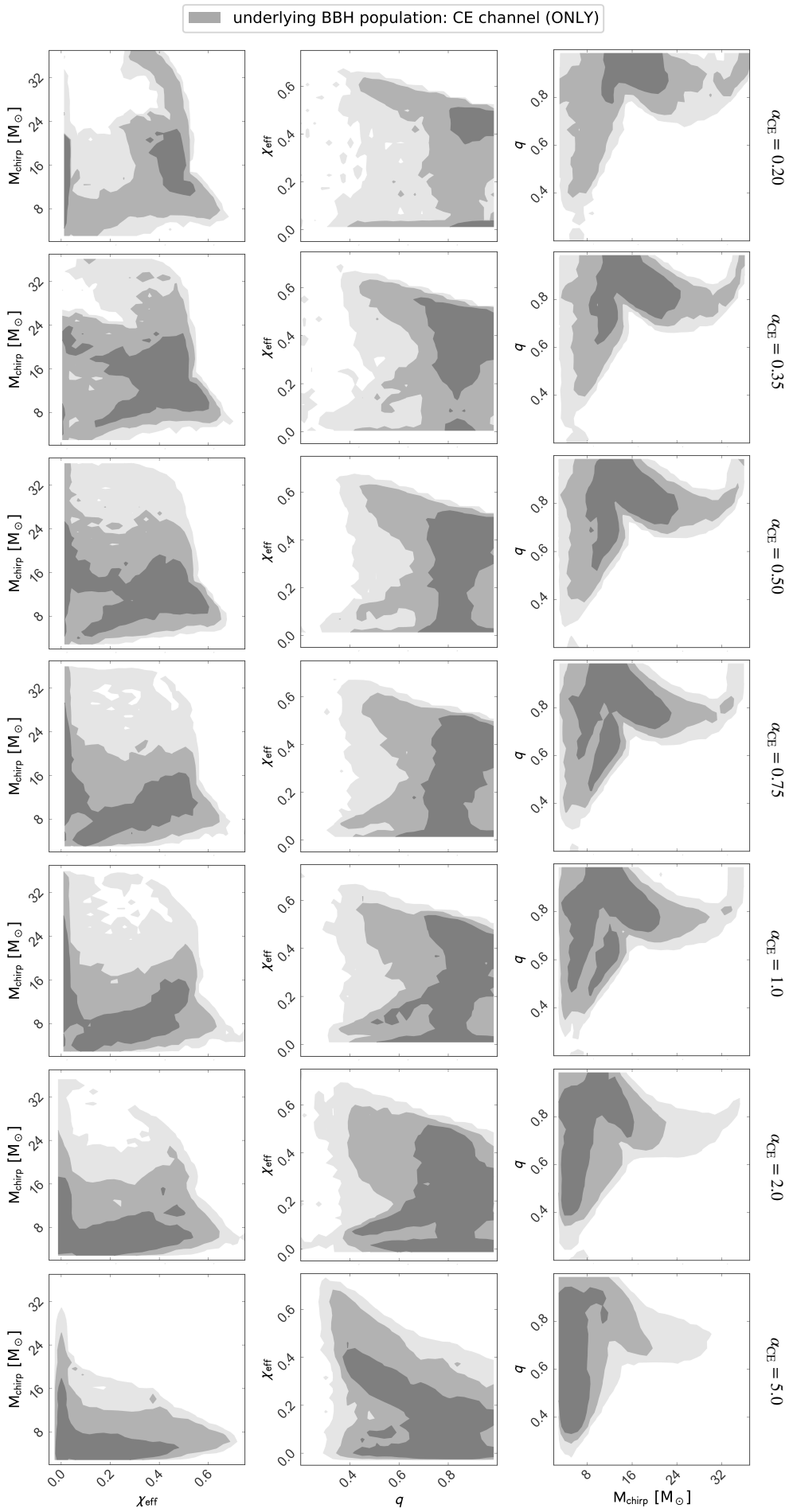

Fig. G.2. Model predictions for the underlying (intrinsic) BBH population of the CE channel for different α_{CE} values according to the legend, in grey. We show the joint distributions of chirp mass M_{chirp}, effective inspiral spin parameter χ_{eff} and binary mass ratio q. Lighter colours represent larger contour levels of 68%, 95% and 99%, respectively, constructed with `pygtc` (Bocquet & Carter 2016). All histograms are plotted with 30 bins without any bin smoothing.

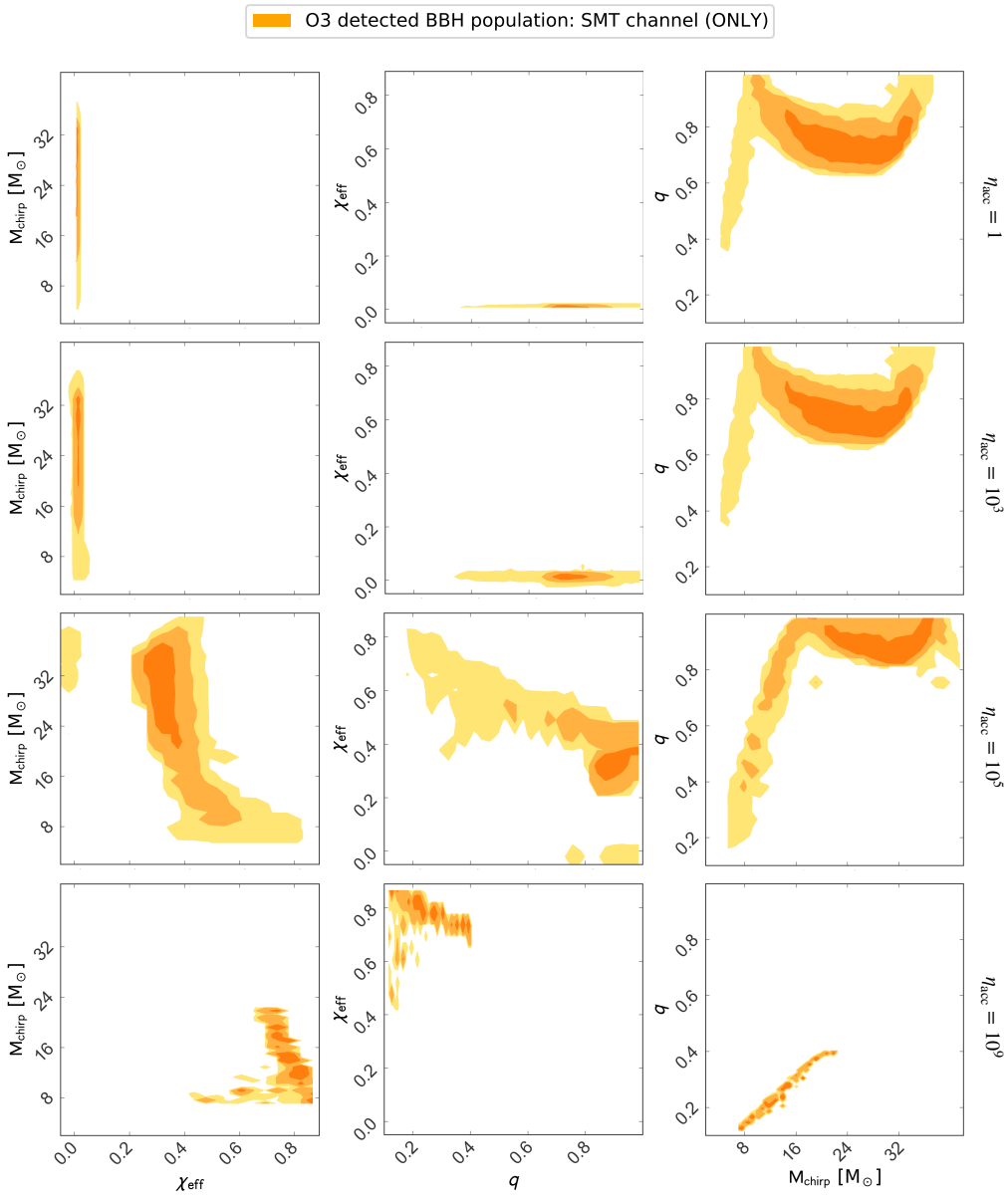

Fig. G.3. Model predictions for the O3 detected BBH population of the SMT channel for different η_{acc} values according to the legend, in orange. We show the joint distributions of chirp mass M_{chirp}, effective inspiral spin parameter χ_{eff} and binary mass ratio q. Lighter colours represent larger contour levels of 68%, 95% and 99%, respectively, constructed with `pygtc` (Bocquet & Carter 2016). All histograms are plotted with 30 bins without any bin smoothing.

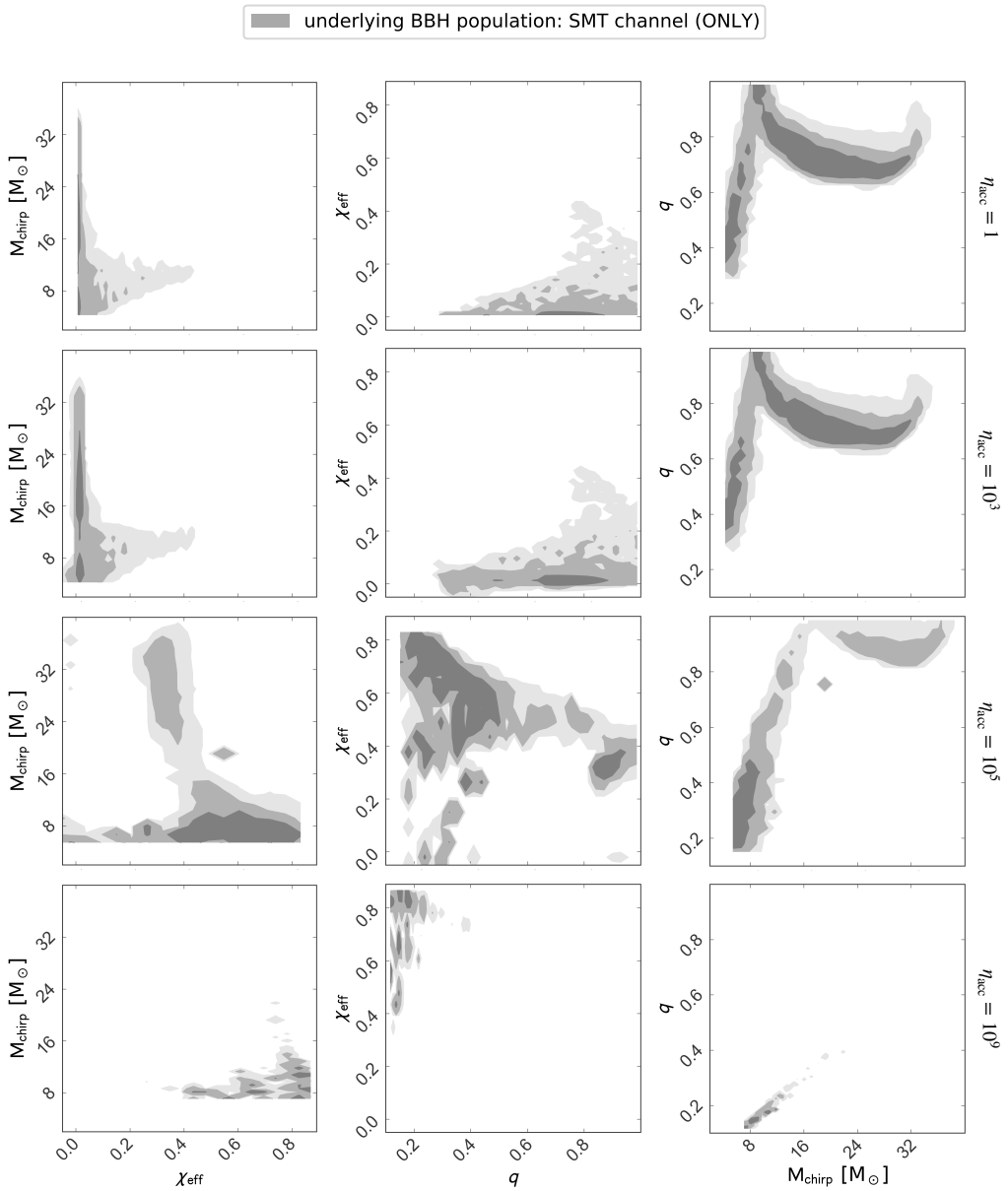

Fig. G.4. Model predictions for the underlying (intrinsic) BBH population of the SMT channel for different η_{acc} values according to the legend, in grey. We show the joint distributions of chirp mass M_{chirp}, effective inspiral spin parameter χ_{eff} and binary mass ratio q. Lighter colours represent larger contour levels of 68%, 95% and 99%, respectively, constructed with `pygtc` (Bocquet & Carter 2016). All histograms are plotted with 30 bins without any bin smoothing.

2.2.3 Impact on the current field of research

The current project complemented our understanding of BBH spin distributions from the evolution of binaries evolving through the canonical CE and SMT channels. In contrast to Bavera et al. (2020), the present study used a different rapid population synthesis code (`COSMIC`) to evolve the binaries from zero-age main sequence to the second mass-transfer episode. Nevertheless, model predictions of the tidal spin-up of BBHs through the CE channels presented in Bavera et al. (2020) were confirmed by Bavera et al. (2021a). We also showed how potential uncertainties on the efficiency of the CE phase affect the $\chi_{\rm eff}$ distribution. Independently of this model uncertainty, Bavera et al. (2021a) showed that BBHs formed through the CE channel are expected to have a highly spinning sup-population. Another interesting result of this project is that it is in line with the new finding of other research groups using different rapid population synthesis codes (e.g., Neijssel et al. 2019; van Son et al. 2021; Olejak et al. 2021; Broekgaarden et al. 2022), which predict the existence if not the dominance of the SMT channel over the CE channel to the formation of merging BBHs in the local Universe, in contrast to previous studies of isolated binary evolution (e.g., Dominik et al. 2012, 2013, 2015; Belczynski et al. 2016b).

Overall, the research project presented in Bavera et al. (2021a) advanced our understanding of the origin of spin in BBHs formed from the CE and SMT evolutionary channels. We find that, on average, these two channels have comparable merger rates at low redshifts. BBHs formed through the CE channel are less massive than those formed through the SMT channel. The SMT channel, on average, leads to wider BH-WR orbital separations compared to the CE channel and, hence, the bulk of BBH formed through the SMT channel avoids efficient tidal spin-up, leading to a BBH population with mostly $\chi_{\rm eff} \simeq 0$ in contrast to BBHs formed from the CE channel which manifests a statistically relevant sub-population of highly spinning BBHs. Consequently, BBHs formed through the SMT channel have, on average, longer delay times than BBHs formed through the CE channel. This result agrees with van Son et al. (2021) recent results. Overall, our BBH models predict correlations between the BBH masses, spins, and delay times, having importance in the interpretation of GW observations. We discuss in these implications in the following chapters of this thesis.

2.3 Approximations to the spin of close black-hole–Wolf-Rayet binaries

2.3.1 A brief introduction

In Section 2.2, we presented a research project that used more than 110,000 detailed BH-WR `MESA` simulations. This simulation grid was used to determine the outcomes and parameters of the late-end evolution stage of highly rotating BBH progenitors. As explained in Bavera et al. (2021a), the simulations cover the 4D parameter space of initial metallicity Z, BH mass, WR star mass, and orbital period. The simulation grid was run for 30 different metallicities ranging from $Z \in [10^{-4}, 1.5 Z_{\odot}]$. For each metallicity, we run 11 BH masses in the range $[2.5, 54.4]\,{\rm M}_{\odot}$, 17 WR star masses in the range $[8, 80]\,{\rm M}_{\odot}$, and 20 initial binary periods in the range $[0.09, 8]$ days. The grid was evenly spaced in log-space across all dimensions.

The simulations took into account differential stellar rotation, tidal interaction, WR stellar winds, the evolution of WR stellar structure, and up to date core-collapse prescriptions accounting for angular momentum supported disk formation during the collapse of the WR stellar structure, which guarantees the general relativistic limit of the second-born BH spin $|\vec{\chi}_2| < 1$.

Building such a simulation library was computationally expensive as, on average, each evolutionary track required several CPU hours. Additionally, the raw simulation output of $\sim 2.5\,\mathrm{TB}$ limits data sharing. Hence, we thought that the scientific community would benefit from having a computationally inexpensive analytical fit of the tidal spin-up second-born BH spin $|\vec{\chi}_2|$ as determined by the detailed `MESA` simulations. After multiple attempts, we found a simple relation between the orbital period at helium or carbon depletion of the WR star, the WR stellar mass and the final spin of the second-born BH. We note that the analytical approximation of $|\vec{\chi}_2|$ is model dependent on the core-collapse assumptions made in Bavera et al. (2021a). These assumptions include the delayed core-collapse mechanism of Fryer et al. (2012), the fit to the PPISN models of Marchant et al. (2019), neutrino mass and angular-momentum loss up to $0.5\,M_\odot$ as implemented in Zevin et al. (2020), and the minimum BH mass of $2.5\,M_\odot$.

2.3.2 Manuscript

The study Bavera et al. (2021b) was published in *Research Notes of the American Astronomical Society* in May 2021. The arXiv open-access version of the manuscript is presented in the following pages.

Draft version May 20, 2021
Typeset using LaTeX default style in AASTeX631

arXiv:2105.09077v1 [astro-ph.HE] 19 May 2021

Approximations to the spin of close Black-hole–Wolf-Rayet binaries

Simone S. Bavera,[1,*] Michael Zevin,[2,3,†] and Tassos Fragos[1]

[1]*Departement d'Astronomie, Université de Genève, Chemin Pegasi 51, CH-1290 Versoix, Switzerland*
[2]*Kavli Institute for Cosmological Physics, The University of Chicago, 5640 South Ellis Avenue, Chicago, Illinois 60637, USA*
[3]*Enrico Fermi Institute, The University of Chicago, 933 East 56th Street, Chicago, Illinois 60637, USA*

ABSTRACT

Population synthesis studies of binary black-hole mergers often lack robust black-hole spin estimates as they cannot accurately follow tidal spin-up during the late black-hole–Wolf-Rayet evolutionary phase. We provide an analytical approximation of the dimensionless second-born black-hole spin given the binary orbital period and Wolf-Rayet stellar mass at helium depletion or carbon depletion. These approximations are obtained from fitting a sample of around 10^5 detailed MESA simulations that follow the evolution and spin up of close black-hole–Wolf-Rayet systems with metallicities in the range $[10^{-4}, 1.5Z_{\odot}]$. Following the potential spin up of the Wolf-Rayet progenitor, the second-born black-hole spin is calculated using up-to-date core collapse prescriptions that account for any potential disk formation in the collapsing Wolf-Rayet star. The fits for second-born black hole spin provided in this work can be readily applied to any astrophysical modeling that relies on rapid population synthesis, and will be useful for the interpretation of gravitational-wave sources using such models.

Keywords: black-hole, gravitational-waves

Isolated binary evolution is one of the leading astrophysical mechanisms proposed for generating merging binary black holes (BBHs). In the standard BBH formation scenarios through isolated binary evolution, BBH progenitors either proceed through a stable mass transfer and a common envelope phase (e.g., Bethe & Brown 1998; Belczyński et al. 2002; Kalogera et al. 2007; Dominik et al. 2012; Bavera et al. 2020) or a double stable mass-transfer episode (e.g., van den Heuvel et al. 2017; Neijssel et al. 2019; Bavera et al. 2021). In both cases, after the second mass-transfer event the binary emerges as a black-hole–Wolf-Rayet (BH-WR) system. The first-born BH spin is determined by the angular momentum (AM) transport of the progenitor star during the red supergiant evolutionary phase. Asteroseismic observations hint at efficient AM transport (Spruit 1999, 2002; Fuller et al. 2019), and hence, upon expansion, any initial AM is mostly transported to the outer layers of the star which are subsequently lost due to mass transfer and wind mass loss. The dimensionless spin parameter of the first-born BH is therefore $a_{\rm BH1} \simeq 0$ (Fragos & Mcclintock 2015; Qin et al. 2018; Fuller & Ma 2019). During the BH-WR evolutionary phase, if the binary orbit is tight enough, the WR star experiences tidal spin up from the compact-object companion, which can lead to rapid rotation and, after core collapse, to the formation of a rapidly rotating BH (Qin et al. 2018; Bavera et al. 2020, 2021). However, during the BH-WR evolution, mass loss through metallicity-dependent stellar winds can widen the binary and might lead to tidal decoupling. A careful treatment of binary interactions, as well as the WR stellar structure evolution and core collapse, are thus essential to properly determine the second-born BH spin $a_{\rm BH2}$. In this research note, we present an analytical model to approximate $a_{\rm BH2}$ given the BH-WR orbital period and WR mass at helium (He) or carbon (C) depletion. Though the BH-WR orbital period and WR mass are implicitly dependent on BH companion mass and the zero age He main sequence (ZAHeMS) metallicity, we find that accurate fits for $a_{\rm BH2}$ can be obtained using this two-parameter model. This approximation is well suited for isolated binary evolution population synthesis studies aiming to study merging BBHs as well as modeling of other formation channels that rely on rapid population synthesis.

To approximate $a_{\rm BH2}$, we use the results of around 10^5 detailed BH-WR `MESA` simulations presented in Bavera et al. (2021). These simulations take into account differential stellar rotation, tidal interaction, WR stellar winds, the evolution of WR stellar structure, and up to date core-collapse prescriptions accounting for AM supported disk formation during collapse which guaran-

* simone.bavera@unige.ch
† NASA Hubble Fellow

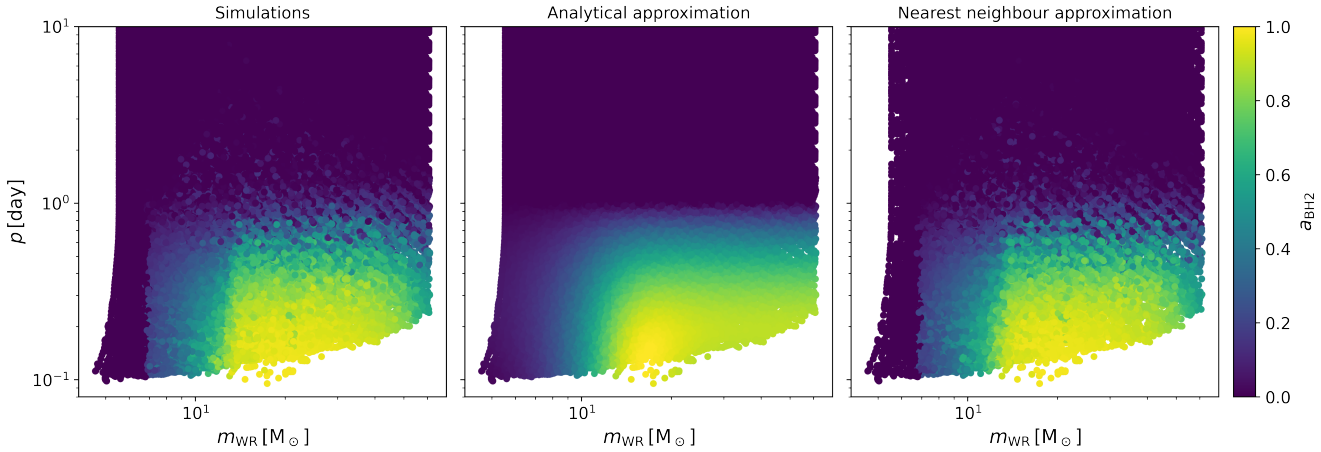

Figure 1. Second-born black hole spin of close BH-Wolf-Rayet systems as a function of binary orbital period and Wolf-Rayet mass at carbon depletion. *Left:* The result of the $\sim 10^5$ post-processed `MESA` simulation for all BH companion masses ($m_{\rm BH1} \in [2.5, 55]\,{\rm M}_\odot$) and metallicities ($Z \in [10^{-4}, 1.5Z_\odot]$). *Center:* Analytical approximation for the second-born BH spin presented in this work (Eq. 1-2). *Right:* Nearest neighbour approximation for the second-born BH spin determined via performing 20 realizations where 5% of the original dataset is used to test the nearest neighbor algorithm.

tees the general relativistic limit $a_{\rm BH2} \leq 1$. The $a_{\rm BH2}$ approximation presented in this work is therefore model dependent on the assumptions made, which include Fryer et al. (2012) delayed core-collapse mechanism, fit to the (pulsational) pair-instability supernovae models of Marchant et al. (2019), up to 0.5 $\rm M_\odot$ neutrino mass and AM loss as implemented in Zevin et al. (2020), and the arbitrary minimum BH mass of 2.5 $\rm M_\odot$. The initial conditions of the simulations at ZAHeMS cover the range of BH-WR orbital periods $p^i \in [0.09, 8]$ day, WR masses $m^i_{\rm WR} \in [8, 80]\,{\rm M}_\odot$, BH masses $m^i_{\rm BH1} \in [2.5, 55]\,{\rm M}_\odot$, and metallicities $Z^i \in [10^{-4}, 1.5Z_\odot]$, all of which are uniformly sampled in log. All assumptions about these simulations are explain in detail in Appendixes C and D of Bavera et al. (2021). The simulation dataset used in this work is made available, including the second-born BH mass $m_{\rm BH2}$.

We empirically determine that $a_{\rm BH2}$ can be approximated by the following analytical function, given the BH-WR orbital period, p, and Wolf-Rayet mass, $m_{\rm WR}$, at He or C depletion:

$$a_{\rm BH2} = \begin{cases} \alpha \log_{10}(p/[\rm day])^2 + \beta \log_{10}(p/[\rm day]) & p \leq 1\,\rm day \\ 0 & \rm otherwise \end{cases} \tag{1}$$

where $\alpha = f(m_{\rm WR}, c^\alpha_1, c^\alpha_2, c^\alpha_3)$ and $\beta = f(m_{\rm WR}, c^\beta_1, c^\beta_2, c^\beta_3)$ for

$$f(m_{\rm WR}, c_1, c_2, c_3) = \frac{-c_1}{c_2 + \exp(-c_3\, m_{\rm WR}/[\rm M_\odot])}\,. \tag{2}$$

The coefficients $c^{\alpha,\beta}_{1,2,3}$ are determined through non-linear least-square minimization to be $(c^\alpha_1, c^\alpha_2, c^\alpha_3) = (0.059305, 0.035552, 0.270245)$ and $(c^\beta_1, c^\beta_2, c^\beta_3) = (0.026960, 0.011001, 0.420739)$ for input p and $m_{\rm WR}$ at He depletion, or $(c^\alpha_1, c^\alpha_2, c^\alpha_3) = (0.051237, 0.029928, 0.282998)$ and $(c^\beta_1, c^\beta_2, c^\beta_3) = (0.027090, 0.010905, 0.422213)$ for input p and $m_{\rm WR}$ at C depletion. Though our simulations and analytical approximation always return $0 \leq a_{\rm BH2} \leq 1$, one may wish to impose the extra condition $a'_{\rm BH2} = \max(a_{\rm BH2}, 1)$ to ensure that BHs are spinning at the physical limit according to general relativity if the fit is extrapolated to regimes outside the parameter space of our models.

We compare the absolute errors $|a^{true}_{\rm BH2} - a^{approx.}_{\rm BH2}|$ from our analytical approximation to the absolute errors determined by k-fold validation of a nearest neighbor interpolant trained on the normalized input parameters $(\log_{10}(p), \log_{10}(m_{\rm WR}))$. We find the absolute errors to be comparable: over the whole population for all orbital periods (orbital periods less than 1 day), the absolute error of the analytical approximation is $0.00^{+0.13}_{-0.00}$ ($0.04^{+0.14}_{-0.04}$) whereas the absolute error of the nearest neighbor algorithm is $0.00^{+0.09}_{-0.00}$ ($0.02^{+0.12}_{-0.02}$), where we quote the median and symmetric 90% credible interval. A visual comparison between the simulation results, analytical approximation, and nearest neighbour algorithm is shown in Figure 1. The accuracy of the two-parameter approximation to the full 4D parameter space $(p, m_{\rm WR}, m_{\rm BH1}, Z)$ is achieved due to the fact that the orbital period p at He or C depletion is itself a function of $m_{\rm WR}$, $m_{\rm BH1}$, and Z. Approximately, because for ZAHeMS $p^i < 1$ day the BH-WR

evolutionary timescale of a few 100 kyr is larger than the tidal synchronisation timescale (Qin et al. 2018), to prove this point, one can assume that at He or C depletion any binary undergoing tidal spin-up is tidally synchronized. One therefore finds $a_{\rm BH2} = cJ_{\rm WR}/Gm_{\rm WR}^2 \propto \Omega/m_{\rm WR}^2$ for tidally spun up BHs, where $\Omega \propto 1/p$ is the orbital frequency. On the other hand, for wide BH-WR binaries, here $p \geq 1$ day, it holds $cJ_{\rm WR} << Gm_{\rm WR}^2$ and hence $a_{\rm BH2} = 0$.

We anticipate that the flexible analytical approximation presented in this work will be useful for various population modeling endeavors. Spins are one of the key observational signatures of BBHs detected via gravitational waves, and an accurate physical representation of BH spins from theoretical models is essential for the interpretation of gravitational-wave events.

1. DATA RELEASE STATEMENT

We provide the dataset of BH-WR binaries at He and C depletion used in the work as well as a notebook with our analytical models on GitHub https://github.com/ssbvr/approximating_BH_spins. The `MESA` inlists used to run the BH-WR simulations are available at http://cococubed.asu.edu/mesa_market/ or on Zenodo (Bavera 2021).

We would like to thank Christopher Berry and Emmanouil Zapartas for comments on the manuscript. This work was supported by the Swiss National Science Foundation Professorship grant (project number PP00P2_176868). Support for M.Z. was provided by NASA through the NASA Hubble Fellowship grant HST-HF2-51474.001-A awarded by the Space Telescope Science Institute, which is operated by the Association of Universities for Research in Astronomy, Inc., for NASA, under contract NAS5-26555. This study made use of the following open-sources Python modules `Matplotlib` (Hunter 2007), `Numpy` (Harris et al. 2020), `Scikit-learn` (Pedregosa et al. 2011), and `Scipy` (Virtanen et al. 2020).

REFERENCES

Bavera, S. S. 2021, MESA Black-hole-Wolf-Rayet binary inlists used in "The impact of mass-transfer physics on the observable properties of field binary black hole populations", Zenodo, doi: 10.5281/zenodo.4767090

Bavera, S. S., Fragos, T., Qin, Y., et al. 2020, Astronomy & Astrophysics, 635, A97, doi: 10.1051/0004-6361/201936204

Bavera, S. S., Fragos, T., Zevin, M., et al. 2021, Astronomy and Astrophysics, 647, A153, doi: 10.1051/0004-6361/202039804

Belczyński, K., Kalogera, V., & Bulik, T. 2002, The Astrophysical Journal, 527, 407, doi: 10.1086/340304

Bethe, H. A., & Brown, G. E. 1998, The Astrophysical Journal, 506, 780, doi: 10.1086/306265

Dominik, M., Belczynski, K., Fryer, C., et al. 2012, The Astrophysical Journal, 759, 52, doi: 10.1088/0004-637X/759/1/52

Fragos, T., & Mcclintock, J. E. 2015, Astrophysical Journal, 800, 17, doi: 10.1088/0004-637X/800/1/17

Fryer, C. L., Belczynski, K., Wiktorowicz, G., et al. 2012, The Astrophysical Journal, 749, 14, doi: 10.1088/0004-637X/749/1/91

Fuller, J., & Ma, L. 2019, The Astrophysical Journal Letters, 881, L1, doi: 10.3847/2041-8213/ab339b

Fuller, J., Piro, A. L., & Jermyn, A. S. 2019, Monthly Notices of the Royal Astronomical Society, 485, 3661, doi: 10.1093/mnras/stz514

Harris, C. R., Millman, K. J., van der Walt, S. J., et al. 2020, arXiv e-prints. https://arxiv.org/abs/2006.10256

Hunter, J. D. 2007, Computing in Science and Engineering, 9, 99, doi: 10.1109/MCSE.2007.55

Kalogera, V., Belczynski, K., Kim, C., O'Shaughnessy, R., & Willems, B. 2007, Physics Reports, 442, 75, doi: 10.1016/j.physrep.2007.02.008

Marchant, P., Renzo, M., Farmer, R., et al. 2019, The Astrophysical Journal, 882, 36, doi: 10.3847/1538-4357/ab3426

Neijssel, C. J., Vigna-Gómez, A., Stevenson, S., et al. 2019, Monthly Notices of the Royal Astronomical Society, 490, 3740, doi: 10.1093/mnras/stz2840

Pedregosa, F., Varoquaux, G., Gramfort, A., et al. 2011, Journal of Machine Learning Research, 12, 2825. https://arxiv.org/abs/1201.0490

Qin, Y., Fragos, T., Meynet, G., et al. 2018, Astronomy & Astrophysics, 616, A28, doi: 10.1051/0004-6361/201832839

Spruit, H. C. 1999, Astronomy and Astrophysics, 349, 189. https://arxiv.org/abs/9907138

—. 2002, Astronomy & Astrophysics, 381, 923, doi: 10.1051/0004-6361

van den Heuvel, E. P., Portegies Zwart, S. F., & de Mink, S. E. 2017, Monthly Notices of the Royal Astronomical Society, 471, 4256, doi: 10.1093/mnras/stx1430

Virtanen, P., Gommers, R., Oliphant, T. E., et al. 2020, Nature Methods, 17, 261, doi: 10.1038/s41592-019-0686-2

Zevin, M., Spera, M., Berry, C. P. L., & Kalogera, V. 2020, The Astrophysical Journal, 899, L1, doi: 10.3847/2041-8213/aba74e

2.3.3 Impact on the current field of research

The analytical approximation of the spin of the second-born BH in tidally spun-up BH-WR binaries obtained from the detailed `MESA` simulations has already impacted the current field of GW astrophysics. In this section, we summarise a few relevant uses of the fit presented in Bavera et al. (2021b), mainly constraining uncertain astrophysical processes, which expand on the work done during my Ph.D.

Recently, Stevenson (2022) used the analytical fit to generate a $\chi_{\rm eff}$ phenomenological model of field-formed BBHs to contradict recent results by Callister et al. (2021a). In the latter study, the authors assumed a phenomenological model of BH spins for the tidally spin-up scenario resulting from the CE channel to analyze the *LIGO-Virgo* GWTC-2 catalog of GW detections and constrain BH natal kick magnitudes, assuming all observed BBHs originate from said channel (see §1.2.3). Given their phenomenological model, Callister et al. (2021a) find that to explain the presence of BH spins misaligned with the orbital angular momentum, BBHs formed through isolated binary evolution would require extreme natal kicks, with a Maxwellian dispersion greater than $\sigma = 260\,{\rm km\,s^{-1}}$ at 99% credibility. This is greater than what is currently assumed in BBH population synthesis models (see §1.4.3). However, Stevenson (2022), who employed the Bavera et al. (2021b) fit to obtain a simulation-based phenomenological model of BBHs formed through tidal spin-up BH-WR systems, highlights that the Callister et al. (2021a) results might be biased by their assumption that *all* secondary BHs can be tidally spun up. This is not motivated by recent physically motivated models which show the formation of wider BH-WR systems from the SMT channel avoiding spin up (Bavera et al. 2021a; Zevin & Bavera 2022; Broekgaarden et al. 2022). By accounting for a population of wider merging binaries where tidal synchronization is ineffective, Stevenson (2022) finds that the spin-orbit misalignment observed in the GWTC-2 BBH population can be explained by more typical BH kicks with $\sigma \simeq 100\,{\rm km\,s^{-1}}$, consistent with kicks inferred from Galactic X-ray binaries (Brandt et al. 1995; Mirabel et al. 2001; Repetto et al. 2012, 2017). At the same time, other BHs might not receive any kick at all (Mirabel & Rodrigues 2003) as often assumed.

Finally, an example of how this analytical fit can be employed in current generation rapid population synthesis endeavors is presented in the following section. The application of the BH spin fit was used to study the formation of unequal-mass, highly-rotating BBHs (Zevin & Bavera 2022). Similarly, Broekgaarden et al. (2022) also employed the Bavera et al. (2021b) BH spin fit to study the same problem of mass ratio reversal with highly-rotating primary BHs in the context of isolated binary evolution.

2.4 Investigating the $\chi_{\rm eff} - q$ anti-correlation of field binary black hole mergers

By analyzing the observed sample of merging BBHs, some authors have suggested that merging BBHs might have effective spin parameters ($\chi_{\rm eff}$) anti-correlated to their mass ratio (q), i.e., the mean of the $\chi_{\rm eff}$ distribution increasing for smaller mass ratios (Abbott et al. 2021f; Callister et al. 2021b; Biscoveanu et al. 2022, and see §1.4.4 for more details). Looking at individual events, GW190412 was a BBH merger with unequal mass ratio where the most massive BH was constrained to be highly rotating with $|\vec{\chi}_1| \geq 0.22$ at 95% credibility (Abbott et al. 2020c). Models of isolated binary evolution presented in §2.2 showed that

BBHs formed through the SMT channel and experiencing super-Eddington accretion during the second mass-transfer episode, or systems experiencing mass ratio reversal and undergoing tidal spin up through the CE channel, might lead to such signatures (Bavera et al. 2021a).

Motivated by this sparked interest in these evolutionary channels, we further study whether BBH systems formed in galactic fields from isolated binary evolution can achieve final configurations with unequal mass ratios and large effective spins. To achieve this, we leverage the analytical fit of Bavera et al. (2021b) to the second-born BH spin of tidally spun-up BH-WR systems (see §2.3). The analytical approximation to the detailed simulations is convenient, as it can be directly employed in rapid population synthesis studies. This technique allows us then to efficiently investigate multiple astrophysical uncertainties impacting the formation of highly spinning BBHs with unequal BH masses.

Section 2.2 discussed the impact of mass-transfer physics uncertainties on BBHs spins. In addition to the investigated uncertainties of CE efficiency, mass transfer stability and accretion efficiency onto BHs, one could and should consider the uncertainty of mass-transfer accretion efficiency onto stars and angular-momentum transport in massive stars. The first uncertainty could have a major impact on the stellar mass distribution of the secondary star after the first mass transfer phase, depending on the mass accreted and, consequently, alter BBH formation and their observable properties. The second uncertainty directly impacts the BH spin distributions. In Appendix A, we discuss the Zevin & Bavera (2022) publication where, using a rapid population synthesis approach, we investigated the ability of isolated binary evolution to form highly spinning, asymmetric mass BBH systems through either super-Eddington accretion onto the first-born BH (SMT channel) or mass ratio reversal and tidal spin-up of the second-born BH progenitor (CE channel). This work showed that the production of systems with significant mass asymmetries and spin residing in the primary BH is unlikely to originate from isolated binary evolution abundantly enough to explain observed BBHs. We point to Appendix A for an in-depth discussion of the study and its implication for GW astrophysics.

Chapter 3

If not me, who? If not now, when?

Multiple formation mechanisms other than isolated binary evolution in the galactic field have been theorized to explain the origin of merging BBHs. After more than half a decade since the first detection of GWs from the merger of two BHs, the question about their origin remains open. This chapter aims to show how one may quantify how much and when the different theorized formation channels contribute to the formation of merging BBHs in the Universe. This challenging task is further complicated by unconstrained astrophysical processes, which make accurate theoretical estimates of BBH merger rates impossible. In addition, there are multiple degeneracies between BBH observational property distributions across the different formation channels. The effort that could maximize our current chances to disentangle the formation mechanisms, is to rely on key BBH observational features specific to them, which, in turn, might allow us to isolate their presence in the observed BBH sample (see §1.4). Complementary, it exists a quantitative analysis that leverages these features with BBH observations. To constrain the formation mechanisms of coalescing BBHs and their model uncertainties one could use hierarchical Bayesian model selection (see §1.4.5). In this chapter, we illustrate such an approach.

3.1 Unraveling the origins of merging binary black holes

We analyze the GWTC-2, the second catalog of GW detections containing 46 BBH events, using a suite of five state-of-the-art BBH population models covering a range of isolated and dynamical formation channels. We illustrate how one can use hierarchical model selection to infer branching fractions between channels as well as constrain uncertain physical processes that impact the observational properties of BBH mergers. We consider the three evolutionary pathways for the isolated binary evolution channel in galactic fields: CE, SMT, and CHE. We adopt the models of Bavera et al. (2021a) for the CE and SMT channels, which we combined with the CHE models of du Buisson et al. (2020). We complement Bavera et al. (2021a) simulations with du Buisson et al. (2020) one because the former could not cover the parameter space with short orbital periods at zero-age main sequence, leading to CHE. With this purpose in mind, the CE and SMT models were designed to match the same stellar and binary physical assumptions made in the du Buisson et al. (2020) CHE model (see §2.2). For the dynamical formation channels in dense stellar environments, we consider the models for BBH mergers in globular clusters of

Rodriguez et al. (2019) and the model of Antonini et al. (2019) for nuclear star clusters. Each formation channel model has unique predictions for BBH mass and spin distributions, and merger rate density evolution with redshift. The models were made publicly available upon publication of the manuscript (Zevin 2021).

To illustrate how this Bayesian analysis can put constraints on model uncertainties, across all models, we vary the natal spin magnitude of BHs born in isolation or in binary systems where binary interactions before the collapse of the helium core do not cause significant spin-up. Variations in the BH natal spin magnitudes act as a proxy for the efficiency of angular-momentum transport in massive stars. If angular momentum is efficiently transported from the core to the envelope, the birth spins of BHs are predicted to be low (e.g., Qin et al. 2018; Fuller & Ma 2019, but also see the discussion in §1.3.1.1), while for inefficient angular-momentum transport the opposite is true. In addition, we also consider different assumptions for the efficiency of the CE phase ejection as presented in Bavera et al. (2021a). This last model uncertainty significantly impacts the BH mass and spin distributions only for BBHs formed from the CE channel.

The results of this project (Zevin et al. 2021a) are presented in detail in Appendix B. Here, we limit ourselves to summarizing some key results. Given the assumed BBHs modes, our analysis showed a significant difference between the branching fractions of the underlying and detectable BBH populations. This is due to the GW detector selection effects skewing detections in favour of massive BBHs that can be detected at further distances (see Figure 1.5). The diversity of detections suggests that multiple formation channels are at play. A mixture of channels is strongly preferred over any single channel dominating the detected population: any individual channel does not contribute to more than $\sim 70\%$ of the observational sample of BBHs. Additionally, we find preference for some BH natal spin assumptions and common-envelope efficiencies in our models. The analysis favors models where the natal spins of isolated BHs are $|\vec{\chi}| \leq 0.1$, indirectly implying that the angular-momentum transport of massive stars must be efficient and strongly disfavoring highly inefficient CE phases. We notice that this latter result is the opposite of what Bavera et al. (2021a) found. This contradicting result shows how neglecting the contribution of the aforementioned formation scenarios leads to biases in the analysis. Therefore, a conclusive and unbiased answer to which channel truly dominates the formation mechanism of merging BBHs in the Universe, would require the consideration of all possible formation channels and model uncertainties, which today is still a computationally unfeasible task.

3.2 Stochastic gravitational-wave background as a tool to investigate multi-channel astrophysical and primordial black-hole mergers

3.2.1 A brief introduction

In this research project, we show how the stochastic GW background (SGWB) can provide an additional input for the origin of merging BBHs. The SGWB is generated by the incoherent superposition of signals emitted by many resolved and unresolved astrophysical sources at any redshift in the Universe.

In the GW frequency ranges of current GW observatories, the SGWB is thought to be dominated by coalescing compact binaries (Abbott et al. 2016c, 2018), where BBHs mergers are thought to dominate the SGWB over NS-NS or BH-NS systems (e.g., de Freitas Pacheco 2020; Périgois et al. 2021a,b).

The previous section introduced hierarchical model selection analyses to constrain the origin of merging BBHs. However, such a technique has discriminating power only up to the GW detector horizons, currently at redshifts $z \lesssim 1$ for LVK detectors. This project illustrates a methodology that uses the SGWB to complement multi-channel hierarchical model selection analysis by putting an additional independent constraint on the validity of model selection results. As a working example, we adopt the results of the hierarchical model selection analysis of Franciolini et al. (2021) and add further model constraints using the SGWB. The latter study consider BBHs formed through isolated binary evolution as modeled by Bavera et al. (2021a), dynamical formation in the globular cluster as modeled by Rodriguez et al. (2019), and included the potential contribution of the primordial BH formation channel (see §1.3.5). Primordial BHs are thought to be formed from the collapse of large overdensities in the radiation-dominated era of the early Universe (Ivanov et al. 1994; Garcia-Bellido et al. 1996; Ivanov 1998; Blinnikov et al. 2016). Therefore, they are expected to dominate the BBH merger rate density at much larger redshifts ($z \gtrsim 10$). Consequently, the SGWB is an additional tool to constrain the relative contribution of the BBH formation channels.

3.2.2 Manuscript

The conducted study Bavera et al. (2022c) was published in *Astronomy & Astrophysics* in April 2022. The arXiv open-access version of the manuscript is presented in the following pages.

Astronomy & Astrophysics manuscript no. aanda
December 22, 2021
©ESO 2021

arXiv:2109.05836v2 [astro-ph.CO] 21 Dec 2021

Stochastic gravitational-wave background as a tool to investigate multi-channel astrophysical and primordial black-hole mergers

Simone S. Bavera[1], Gabriele Franciolini[2], Giulia Cusin[2], Antonio Riotto[2], Michael Zevin[3,4], and Tassos Fragos[1]

[1] Departement d'Astronomie, Université de Genève, Chemin Pegasi 51, CH-1290 Versoix, Switzerland
e-mail: simone.bavera@unige.ch
[2] Département de Physique Théorique and Centre for Astroparticle Physics, Université de Genève, 24 quai E. Ansermet, CH-1211 Geneva, Switzerland
[3] Kavli Institute for Cosmological Physics, The University of Chicago, 5640 South Ellis Avenue, Chicago, Illinois 60637, USA
[4] Enrico Fermi Institute, The University of Chicago, 933 East 56th Street, Chicago, Illinois 60637, USA

Accepted December 21, 2021

ABSTRACT

The formation of merging binary black holes can occur through multiple astrophysical channels such as, e.g., isolated binary evolution and dynamical formation or, alternatively, have a primordial origin. Increasingly large gravitational-wave catalogs of binary black-hole mergers have allowed for the first model selection studies between different theoretical predictions to constrain some of their model uncertainties and branching ratios. In this work, we show how one could add an additional and independent constraint to model selection by using the stochastic gravitational-wave background. In contrast to model selection analyses that have discriminating power only up to the gravitational-wave detector horizons (currently at redshifts $z \lesssim 1$ for LIGO–Virgo), the stochastic gravitational-wave background accounts for the redshift integration of all gravitational-wave signals in the Universe. As a working example, we consider the branching ratio results from a model selection study that includes potential contribution from astrophysical and primordial channels. We renormalize the relative contribution of each channel to the detected event rate to compute the total stochastic gravitational-wave background energy density. The predicted amplitude lies below the current observational upper limits of GWTC-3 by LIGO–Virgo, indicating that the results of the model selection analysis are not ruled out by current background limits. Furthermore, given the set of population models and inferred branching ratios, we find that, even though the predicted background will not be detectable by current generation gravitational-wave detectors, it will be accessible by third-generation detectors such as the Einstein Telescope and space-based detectors such as LISA.

Key words. Gravitational waves – Stars: black holes – Black hole physics – Cosmology: dark matter

1. Introduction

Coalescing binary black holes (BBHs) are the primary sources of gravitational-waves (GWs) currently detectable by the LIGO (Aasi et al. 2015), Virgo (Acernese et al. 2015) and KAGRA (Aso et al. 2013) detectors. To date, counting only events with false alarm rate of $< 1\,\mathrm{yr}^{-1}$, the signals of 69 confident BBH mergers have been reported along with 2 binary neutron stars (BNSs), 2 black hole–neutron star (BHNS) systems (Abbott et al. 2019, 2021a,b,d,e).

In addition to events that are individually detectable, the entire population of unresolved and resolved events generates a stochastic gravitational-wave background (SGWB) signal. Other than compact binary coalescences, there are multiple astrophysical and cosmological sources contributing to the SGWB. Possible sources include core-collapse supernovae, magnetars, cosmic strings and GWs produced during inflation (e.g. Regimbau 2011; de Freitas Pacheco 2020). However in the frequency ranges of current GW observatories, the SGWB is thought to be dominated by coalescing compact binaries (Abbott et al. 2016, 2018) where BBHs mergers are thought to dominate the SGWB over BNS or BHNS systems (de Freitas Pacheco 2020; Périgois et al. 2021a,b).

The SGWB is characterized by a spectral energy spectrum, $\Omega_{\mathrm{GW}}(\nu)$, which can be measured by cross-correlating the data streams from multiple detectors (Christensen 1992; Allen & Romano 1999). Using the data of the first three observing runs (O1, O2 and O3), the LIGO Scientific and Virgo Collaboration (LVC) did not find evidence of the SGWB. Hence, the LVC was able to put an upper limit to the SGWB energy density spectrum of $\Omega_{\mathrm{GW}}(\nu = 25\,\mathrm{Hz}) \leq 1.04 \times 10^{-9}$ for a power-law SGWB with a spectral index of 2/3, consistent with expectations for coalescing compact binary (Abbott et al. 2021f).

Multiple astrophysical evolutionary pathways may contribute to the formation of coalescing BBHs, which are often divided into categories. The isolated binary evolution family of pathways includes binaries evolving through a stable mass transfer (MT) and a common envelope (CE) phase (e.g. Bethe & Brown 1998; Kalogera et al. 2007; Postnov & Yungelson 2014; Belczynski et al. 2016; Bavera et al. 2020), double stable MT (SMT) (e.g., van den Heuvel et al. 2017; Neijssel et al. 2019; Bavera et al. 2021b), and chemically homogeneous evolution (CHE) (e.g. de Mink et al. 2009; Mandel & de Mink 2016; Marchant et al. 2016; du Buisson et al. 2020). Dynamical formation of BBHs in dense stellar environments may occur in globular clusters (GCs) (e.g. Sigurdsson & Hernquist 1993; Miller & Hamilton 2002; Downing et al. 2010; Rodriguez et al. 2015), nuclear star clusters (NSCs) (e.g. Miller & Lauburg 2009; Petrovich & Antonini 2017; Antonini et al. 2019; Arca Sedda 2020) or young open star clusters (e.g. Ziosi et al. 2014; Mapelli 2016; Banerjee 2017; Kumamoto et al. 2020). Population III stars have

also been proposed to lead to merging BBH either in isolation or in stellar cluster (e.g. Madau & Rees 2001; Kinugawa et al. 2014; Inayoshi et al. 2017; Liu et al. 2021). Furthermore, alternative proposed channels exists such as the formation of merging BBHs in active galactic nuclei disks (e.g. Antonini & Perets 2012; McKernan et al. 2014; Bartos et al. 2017; Tagawa et al. 2020) and in triple or multiples systems (e.g. Antonini et al. 2016, 2017; Fragione & Loeb 2019; Vigna-Gómez et al. 2021).

Another well-studied formation channel for producing merging BBHs is through primordial origins (PBHs) (Zel'dovich & Novikov 1967; Hawking 1974; Chapline 1975; Carr 1975). PBHs may arise from the collapse of large overdensities in the radiation-dominated early universe (Ivanov et al. 1994; Garcia-Bellido et al. 1996; Ivanov 1998; Blinnikov et al. 2016) and could contribute to a sizeable ratio $f_{\rm PBH} \equiv \Omega_{\rm PBH}/\Omega_{\rm DM}$ of the dark matter energy density in a variety of mass ranges (see Carr et al. 2020, for a recent review about constraints on $f_{\rm PBH}$). The recent discovery of GWs has ignited a new wave of interest on PBHs as it was soon realised that PBHs could produce observable mergers without conflicting with existing bounds on the PBH abundance (Bird et al. 2016; Clesse & García-Bellido 2017; Sasaki et al. 2016). This motivated various works on the confrontation of the PBH scenario with the most recent data (see, for example, the recent results of Wang et al. 2016, 2019; Hall et al. 2020; Kritos et al. 2021; Hütsi et al. 2021; De Luca et al. 2021b; Deng 2021; Kimura et al. 2021). Current GW data imply an upper bound $f_{\rm PBH} \lesssim O(10^{-3})$ in the mass range of interest for current GW detectors (see e.g., Wong et al. 2021). The constraining power of GW observations of either resolved mergers or the SGWB will improve significantly with future GW detectors (De Luca et al. 2021c; Pujolas et al. 2021).

All these channels have been shown to successfully lead to the formation of merging BBHs and, in most cases, predict a plausible range of merger-rate density approximately consistent with current GW observational constraints. However, accurate rate estimates are often difficult to be made, as they are highly dependent on uncertain and sometimes unconstrained astrophysical processes. The most well-known uncertainties affecting the astrophysical models include initial stellar and binary properties (e.g., binary ratio, initial mass function, mass ratio and initial orbital parameter distributions), stellar evolution physics (e.g., stellar winds of massive stars, core-collapse mechanism, supernova kicks and pulsational pair instability), binary evolution physics (e.g., MT stability and efficiency, and CE efficiency) as well as uncertainties in the star formation rate and metallicity distribution of their environment at high redshifts (see e.g., Antonini et al. 2017; Chatterjee et al. 2017; Chruslinska et al. 2019; Neijssel et al. 2019; Gröbner et al. 2020; Riley et al. 2021; Belczynski et al. 2021). The primordial channel also suffers from large uncertainties on the overall PBH abundance and initial mass distribution, which are mostly unconstrained in the mass range of interest for LVC mergers (Carr et al. 2020). Combined, these unconstrained physical processes lead to order-of magnitudes uncertainties in the rates while often have minor effects on the BBH observable distributions (see e.g., Mandel & Broekgaarden 2021, for a review). Such large uncertainties translate to the SGWB energy spectrum and also bias relative $\Omega_{\rm GW}$ estimates between channels.

Given the large uncertainty on the modelled BBH rates, comparison between theoretical predictions and GW observations are often done by normalising the theoretical rate to the observed one. Recent attempts of model selection involving multiple formation channels and GWTC-2 events (Wong et al. 2021; Zevin et al. 2021a; Franciolini et al. 2021) indicate that, given the state-of-the-art formation models considered, multiple formation channels are needed to explain the detected population of BBHs. To date, Zevin et al. (2021a) work is the most inclusive analysis which accounts for CE, SMT, CHE, GC and NSC channels. Even though Zevin et al. (2021a) find that a mixture of channels is preferred over a single dominant channel, at face value, the analysis shows that isolated BBH formation might dominate the underlying BBH merging population. It is important to note that only the uncertainties of CE efficiency (cf. Bavera et al. 2021b) and isolated BH spin as a proxy for angular momentum transport were explored in that analysis. The consideration of all model uncertainties and the other prominent BBH formation channel are key in obtaining an unbiased and conclusive answer, though the large number of proposed formation models and model uncertainties, combined with the still limited observational sample, make this task currently computationally infeasible. Following an analysis similar to Zevin et al. (2021a), Franciolini et al. (2021) expanded the set of considered models by also including the PBH channel. The Bayesian evidence for PBHs against an astrophysical-only multi-channel model was found decisive, due to the fact that the astrophysical models considered there did not produce significant numbers of high-mass events, such as those observed by the LVC. However, the evidence weakens in the presence of a dominant SMT isolated formation channel, which is more efficient at producing high-mass BBHs.

In this work we compute the contribution to the SGWB energy spectrum of astrophysical and primordial BBHs using the results of the model comparison by Franciolini et al. (2021) as a working example. The relative contribution of each channel is directly dictated by the comparison of the models with the GWTC-2 data, and their total contribution normalised against the BBH detection rate of 44 events, including GW190521.[1] This assumption is complementary to previous studies which use phenomenological astrophysical models (e.g. Callister et al. 2020a; Zhao & Lu 2021) and arbitrarily fix the relative contribution of primordial to astrophysical BBHs (e.g. Chen et al. 2019; Mukherjee & Silk 2021; Mukherjee et al. 2021). Moreover, our analysis gives a further model constraint to model selection studies as the SGWB includes the rate contribution across all redshift compared to current GW detectors horizons of $z \lesssim 1$ (Abbott et al. 2020a). The results presented in this work are meant to illustrate a methodology which can be applied to and extended with future catalogs of BBH events, putting more stringent constraints on model selection studies. The best fit parameters of astrophysical and PBH models, with the corresponding branching ratios, can change drastically with adjustments in the population models or the formation channels considered. However, accounting for the measurement or upper limits on the SGWB provides a new additional constraint on the validity of model selection results, which to our best knowledge is considered here for the first time.

The paper is structured as follows. In Section 2 we present the main assumption of each considered astrophysical and primordial BBH channel and explain how we estimate the SGWB

[1] Following Abbott et al. (2021c), Franciolini et al. (2021) discarded from the GWTC-2 catalog the events with large false-alarm rates (GW190426, GW190719, GW190909) and two events involving neutron stars (GW170817, GW190425). Also, as the secondary mass ($m_2 \approx 2.6\,{\rm M}_\odot$) of GW190814 (Abbott et al. 2020b) would correspond to either the lowest-mass astrophysical BH or to the highest-mass NS observed to date, challenging current understanding of compact objects, it was assumed that the secondary component of GW190814 is a neutron star and this event was neglected. Notice, however, that its inclusion would not affect our conclusions (Franciolini et al. 2021).

energy density spectrum. Section 3 presents the SGWB energy density spectrum of our models compared to current and planned ground- and space-based GW observatories such as the Einstein Telescope (ET) (Punturo et al. 2010) and the Laser Interferometer Space Antenna (LISA) (Amaro-Seoane et al. 2017). Finally, in Section 4 we discuss how our results depend on model uncertainties and we quantify the effect of neglecting other prominent channels. In Section 5 we summarise our findings.

2. Methods

We compute the SGWB energy density spectrum of merging BBHs from astrophysical and primordial origins. For the astrophysical channels we include isolated binary evolution evolving through CE and SMT channels, and dynamical formation in GC. We adopt BBH models of isolated binary evolution by Bavera et al. (2021b), a GC model by Rodriguez et al. (2019) as released by Zevin et al. (2021a) and a PBH model by Franciolini et al. (2021). The key assumptions of all these models are summarised in Appendix A. More precisely, as favoured by the model comparison with GWTC-2 data in Franciolini et al. (2021) (but also see Zevin et al. 2021a), we use models with isolated BHs birth spins of zero and for the CE channel the model with common envelope efficiency $\alpha_{\rm CE} = 5$. Here, an $\alpha_{\rm CE}$ value grater than 1 does not mean that other sources of energy partake in the CE ejection, but more likely points to an inaccurate assumption of core-envelope boundaries in the $\alpha_{\rm CE} - \lambda$ parametrization of CE (see, e.g. Ivanova et al. 2013, for a review). The fact that envelope stripping stops earlier than what currently assumed in population synthesis models has been suggested in multiple recent studies (Fragos et al. 2019; Quast et al. 2019; Klencki et al. 2021; Marchant et al. 2021). Finally, the combined and relative detection rate and, hence indirectly, the local merger rate density of these channels are calibrated against the model selection comparison of Franciolini et al. (2021) with GWTC-2 events.

For a graphical visualisation of the intrinsic distributions of the main BBH observables of all considered channels, in Figure 1, we show the underlying distributions of chirp mass $\mathcal{M}$ and effective spin parameter χ. The intrinsic (underlying) BBH distribution is what a GW detector with infinite sensitivity would observe on Earth. Here, the chirp mass is defined as $\mathcal{M} = (m_1 m_2)^{3/5}/(m_1+m_2)^{1/5}$ where m_1 and m_2 are the BH masses and the effective spin parameter $\chi = (m_1 \mathbf{a}_1 + m_2 \mathbf{a}_2)/M \cdot \hat{\mathbf{L}}$ where $\mathbf{a_1}$ and $\mathbf{a_2}$ are the BHs dimensionless spins and $\hat{\mathbf{L}}$ is the orbital angular momentum unit vector. The probability density functions (PDFs) of astrophysical channels are constructed using kernel density estimators (KDE) on the BBH discrete model results, while for the PBH channel the PDFs are semi-analytically determined using Eq. (6).

In Figure 1, the maximum $\mathcal{M}$ of the isolated binary evolution channels CE and SMT is dictated by pulsational pair instability supernovae (e.g., Fowler & Hoyle 1964; Woosley 2017; Marchant et al. 2019) while this is not the case for the GC channel since merger products can be retained in the cluster and merge again. PBHs form from the collapse of large overdensities in the early universe and their mass is related to the mass contained in the cosmological horizon at the time of collapse. For this reason, PBHs can form in a much wider range of masses compared to astrophysical BHs and can cover the mass gap (e.g. De Luca et al. 2021a). Even though we assume astrophysical BHs are born with zero spin in isolation, tidal interactions in the later phase of close BH-Walf-Rayet systems can tidally spin up second born BHs in the CE and SMT channels (e.g., Qin et al. 2018; Bavera et al. 2020). The spin of the resultant BH is mostly aligned with the orbital angular momentum since BH natal kicks are not typically strong enough to flip the orbits by more than 90° (e.g., Rodriguez et al. 2016; Callister et al. 2020b). Hence, the minimum effective spin parameter of CE and SMT channels is $\chi \simeq 0$. In contrast, GC channel might lead to negative χ given the random dynamical assembly of the BBH systems. Since the majority of these systems are the results of first-generation mergers whose components do not proceed through tidal spinup, the effective spin distribution peaks at $\chi \simeq 0$. However, merger products retained in the cluster are imparted spin due to the angular momentum of the inspiraling binary, and thus hierarchical mergers lead to a symmetric distribution of χ about zero. While PBHs form with negligible spin in the standard scenario, efficient accretion can spin up PBHs along independent directions and lead to large magnitudes for χ symmetrically distributed around zero, see more details in Appendix A.2.

The SGWB energy density spectrum, $\Omega_{\rm GW}$, for each model as well as the GW detectors' power-law-integrated sensitivity curves are calculated as explained in the following Sections.

2.1. SGWB energy density spectrum

Under the cosmological assumption of the ΛCDM model, the fractional energy density content of the Universe today is dominated by matter $\Omega_m \simeq 0.307$ and dark energy $\Omega_\Lambda \simeq 1 - \Omega_m$. These energy density ratios are defined in terms of closure density $\rho_c = 3H_0^2/(8\pi G)$ with a current Universe relative rate of expansion $H_0 = 67 {\rm km/s/Mpc}$ (Planck Collaboration et al. 2016).

In comparison, the energy density ratio of the SGWB, $\Omega_{\rm GW}$, is small and often expressed as a spectrum, namely as a function of frequency. This is done in order to compare it with GW detectors' power-law-integrated sensitivity curves which are frequency dependent. Here, we consider frequencies of current ad future ground-based detectors such as LIGO, Virgo, KAGRA and ET, which are sensitive to the $[1, 10^3]$ Hz band, as well as space-based detectors like LISA, which are sensitive to $[10^{-4}, 0.1]$ Hz. In such bands, the spectral GW energy density is dominated by merging BBHs (de Freitas Pacheco 2020; Périgois et al. 2021a).

The SGWB spectral energy density ratio is defined as (e.g. Zhu et al. 2011)

$$\Omega_{\rm GW}(\nu_{\rm obs}) = \frac{\nu_{\rm obs}}{c^3 \rho_c} F_\nu(\nu_{\rm obs}) \,, \tag{1}$$

where $\nu_{\rm obs}$ is the observed GW frequency related to the source frame by $\nu = \nu_{\rm obs}(1+z)$, F_ν is the GW spectral energy density and c the speed of light. Here, we can express

$$F_\nu(\nu_{\rm obs}) = \int_0^{z_{\rm max}} f_\nu(\nu_{\rm obs}, z) \frac{{\rm d}R}{{\rm d}z}(z) \, {\rm d}z \,, \tag{2}$$

where dR/dz is the differential GW event rate given by each BBH formation channel (see Sections 2.2 and 2.3 for astrophysical and primordial models, respectively) and f_ν the energy flux per unit frequency emitted by a source at a luminosity distance $d_{\rm L}(z)$ which is related to the comoving distance, $d_c(z) = c/H_0 \int_0^z E(z')^{-1} {\rm d}z$ where $E(z) = \sqrt{\Omega_m (1+z)^3 + \Omega_\Lambda}$, by the relation $d_{\rm L}(z) = (1+z)\, d_c(z)$. Here, the integration limit $z_{\rm max} = \frac{\nu_{\rm cut}}{\nu_{\rm obs}} - 1$ is given by the maximal emitting GW frequency $\nu_{\rm cut}$. We can express

$$f_\nu(\nu_{\rm obs}, z) = \frac{1}{4\pi d_{\rm L}^2(z)} \frac{{\rm d}E}{{\rm d}\nu_{\rm obs}} = \frac{1}{4\pi d_{\rm c}^2(z)} \frac{1}{1+z} \left.\frac{{\rm d}E}{{\rm d}\nu}\right|_{\nu=\nu_{\rm obs}(1+z)} \,, \tag{3}$$

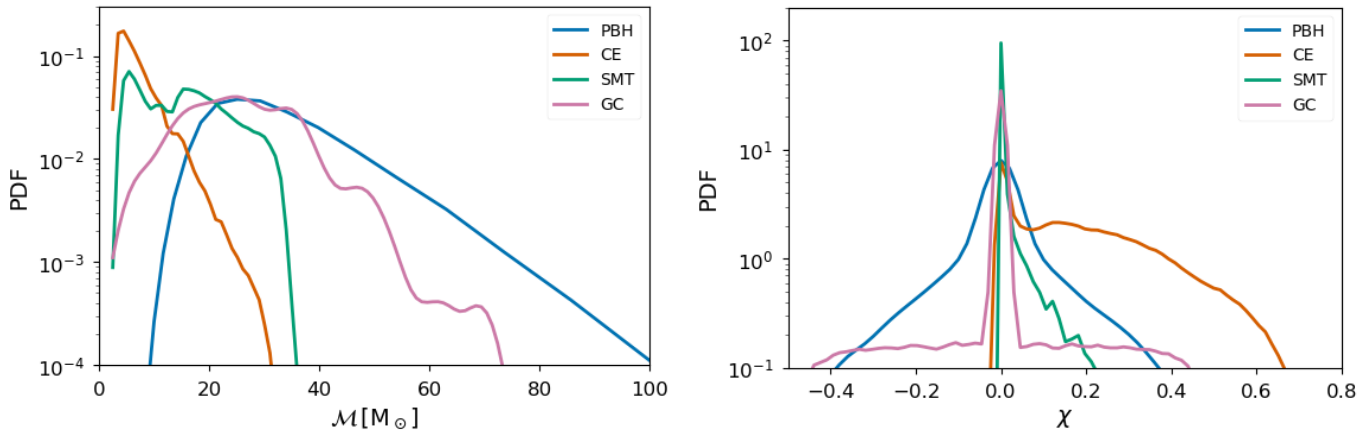

Fig. 1. Gravitational-wave observables for the intrinsic distribution of merging BBHs in the Universe for different formation channels according to the legends. (*Left*) We show the normalised chirp mass, $\mathcal{M}$, distributions where we can see that the PBH and GC channels leads to more massive BHs, whereas the maximum BH mass of CE and SMT channels is dictated by pulsational pair instability supernovae. (*Right*) We show the normalised effective spin parameter, χ, distributions where we see that only the CE channel generates a large ratio of positive χ due to tidal spin up, while both the GC and PBH channels lead to a symmetric distribution of χ (allowing for negative values) because of isotropically oriented spins in hierarchical mergers (GC) or uncorrelated spin growth (PBHs).

where we used the coordinate transformation $\mathrm{d}\nu/\mathrm{d}\nu_{\rm obs} = (1+z)$ to change from the observer frame to source frame of reference. Here, $\mathrm{d}E/\mathrm{d}\nu$ is the GW energy spectrum emitted by the BBH system evaluated in the source frame. Assuming the BBH systems are in quasi-circular orbits when they reach the $[10^{-4}, 10^{3}]$ Hz band, we approximate $\mathrm{d}E/\mathrm{d}\nu$ using Eq. (B.1) and the waveform approximations for non-precessing spinning BBHs by Ajith et al. (2011), as explained in Appendix B. Ignoring the precession of spins in the waveforms approximation will not affect our results as the majority of spins in the considered channels are small. In Figure 2 we show the GW energy spectrum $\mathrm{d}E/\mathrm{d}\nu$ for BBH systems with varying component masses and χ.

2.2. Astrophysical binary black hole merger rates

For each astrophysical channel, we define $w^{\rm intrinsic}_{i,j,k}$ to be the contribution of a binary k to the intrinsic GW event rate (cf. e.g., Bavera et al. 2020, 2021a,b).[2] This binary is described by component masses $m_{1,k}$ and $m_{2,k}$, and spin vectors $\mathbf{a}_{1,k}$ and $\mathbf{a}_{2,k}$. Each binary is placed at the cosmic time bin Δt_i with its redshift of formation $z_{\mathrm{f},i}$ at the center of the bin, and merges at redshift $z_{\mathrm{m},i,k}$ for its corresponding metallicity bin ΔZ_j. Here, the "intrinsic" superscript indicates that we assume an infinite detector sensitivity and thus detection probabilities of $p_{\mathrm{det},i,k} = 1$, following the notation of Eq. (D.4) in Bavera et al. (2021a). Therefore, the BBH event rate observed on Earth for a detector with infinite sensitivity is $N = \int \frac{\mathrm{d}R}{\mathrm{d}z} dz = \sum_{\Delta t_i, \Delta Z_j, k} w^{\rm intrinsic}_{i,j,k}$. We can thus calculate the SGWB energy density spectrum of Eq. (1), given any arbitrary intrinsic event rate normalisation N', as

$$\Omega_{\rm GW}(\nu_{\rm obs}) = \frac{\nu_{\rm obs}}{c^3 \rho_c} N' \sum_{\Delta t_i, \Delta Z_j, k} f_\nu(\nu_{\rm obs}, z_{\mathrm{m},i,k})\, \tilde{w}^{\rm intrinsic}_{i,j,k}\,, \tag{4}$$

where $\tilde{w}^{\rm intrinsic}_{i,j,k} = w^{\rm intrinsic}_{i,j,k} / \sum_{\Delta t'_i, \Delta Z'_j, k'} w^{\rm intrinsic}_{i',j',k'}$ is the normalized cosmological weight. The normalisation constants N' are given by the model selection result of Franciolini et al. (2021). For each considered astrophysical channel we have a median intrinsic event rate value for the Universe observed on Earth of $N'_{\rm CE} = 16729.4\,\mathrm{yr}^{-1}$, $N'_{\rm SMT} = 905.1\,\mathrm{yr}^{-1}$ and $N'_{\rm GC} = 779.6\,\mathrm{yr}^{-1}$, respectively.

Similar to the BBH event rates, we can calculate the BBH rate density by dividing the normalised cosmological weight contribution of the binary k by the integrated differential comoving volume over Δz_i corresponding to the comic time bin Δt_i, i.e.

$$\mathcal{R}(z) = N' \sum_{\Delta Z_j, k} \tilde{w}^{\rm intrinsic}_{i,j,k} / \Delta V_{\rm c}(z_i) \;\; [\mathrm{Gpc}^{-3}\mathrm{yr}^{-1}]\,, \tag{5}$$

where $\Delta V_{\rm c}(z_i) = \frac{4\pi c}{H_0} \int_{\Delta z_i} d_{\rm c}^2(z)/(E(z)(1+z))\,\mathrm{d}z$ as in Eq. (D.2) of Bavera et al. (2021a).

2.3. Primordial binary black hole merger rate

For the computation of the rate density of binaries in the primordial model, we closely follow the parametrisation of the merger rate as in Franciolini et al. (2021) and Refs. therein. We refer the reader to App. A.2 for more details on the predictions of the PBH scenario.

Depending on the initial abundance $f_{\rm PBH}$ and mass function $\psi(m)$, one can estimate the probability of forming binaries in the early Universe due to PBHs decoupling from the Hubble flow. The initial distribution of orbital parameters is defined by the spatial distribution of the surrounding population of PBHs, as well as density perturbations adding an initial torque to the binary system (see e.g. Ali-Haïmoud et al. (2017)). Then, one can compute the differential PBH merger rate density as a function of masses using (De Luca et al. 2020a)

$$\begin{aligned}\frac{\mathrm{d}^2\mathcal{R}_{\rm PBH}}{\mathrm{d}m_1^{\rm i}\mathrm{d}m_2^{\rm i}} &= \frac{1.6\times10^6}{\mathrm{Gpc}^3\,\mathrm{yr}} f_{\rm PBH}^{\frac{53}{37}} \eta^{-\frac{34}{37}}(z_{\rm i}) \left(\frac{t}{t_0}\right)^{-\frac{34}{37}} \left(\frac{M^{\rm i}}{M_\odot}\right)^{-\frac{32}{37}} \\ &\times S\left(M^{\rm i}, f_{\rm PBH}, \psi\right) \psi(m_1^{\rm i}, z_{\rm i}) \psi(m_2^{\rm i}, z_{\rm i}) \left(\frac{M(z_{\text{cut-off}})}{M(z_{\rm i})}\right)^{9/37} \\ &\times \left(\frac{\eta(z_{\text{cut-off}})}{\eta(z_{\rm i})}\right)^{3/37} \exp\left(\frac{12}{37}\int_{t_{\rm i}}^{t_{\text{cut-off}}} \left(\frac{\dot{M}(t)}{M(t)} + 2\frac{\dot{\mu}(t)}{\mu(t)}\right)\mathrm{d}t\right),\end{aligned} \tag{6}$$

[2] For the GC model (Rodriguez et al. 2019) we take the weights as released by Zevin et al. (2021a) where we divide out the coefficient $(1+z_i)^{-1}\,\frac{\mathrm{d}V_{\rm c}}{\mathrm{d}z}\big|_{z_i}$ and multiplied each weight by $\Delta V_{\rm c}(z_i)$ to obtain $w^{\rm intrinsic}_{i,j,k}$.

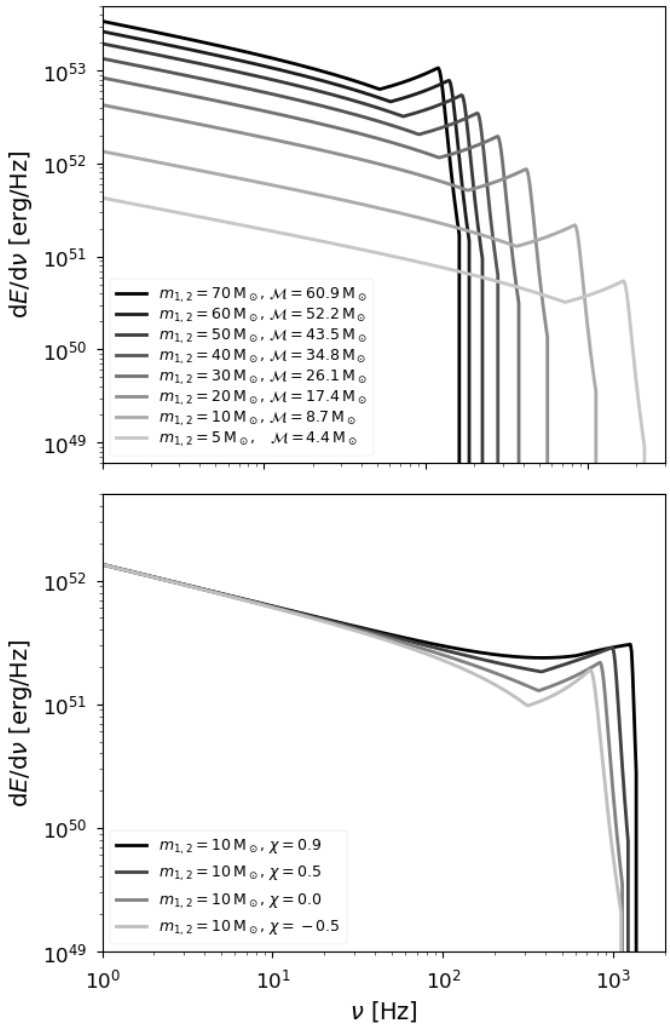

Fig. 2. Gravitational-wave energy spectrum, $\mathrm{d}E/\mathrm{d}\nu$, as a function of frequency. (*Top*) We show the energy spectrum for different non-spinning equal mass BBHs according to the legend. The more massive the BBH systems is, the more energetic the GW signals and the smaller the merger frequencies. More precisely, the GW energy spectrum scales as $\mathrm{d}E/\mathrm{d}\nu \propto \nu^{-1/3}\mathcal{M}^{5/3}$ for $\nu < \nu_{\rm merger}$ and $\mathrm{d}E/\mathrm{d}\nu \propto \nu^{2/3}\mathcal{M}^{5/3}$ for $\nu < \nu_{\rm ringdown}$ (cf. Eq. B.1), while $\nu_{\rm merger} \propto M^{-1}$ where $M = m_1 + m_2$ is the total mass (cf. Eq. B.4). (*Bottom*) We show the energy spectrum for a BBH system composed of two BHs of mass $10\,\mathrm{M}_\odot$ and different effective spins according to the legend. Larger χ values lead to more energetic GW signals as $\mathrm{d}E/\mathrm{d}\nu \propto \nu^{-1/3}\,(1 + O(\chi))$ for $\nu < \nu_{\rm merger}$ and $\mathrm{d}E/\mathrm{d}\nu \propto \nu^{2/3}\,(1 + O(\chi))$ for $\nu < \nu_{\rm ringdown}$ (cf. Eq. B.1).

where $M = m_1 + m_2$, $\mu = m_1 m_2/M$, $\eta = \mu/M$, t is the cosmic time and t_0 is the current age of the Universe. Integrating Eq. (6) in both masses provides the PBH merger rate density as a function of redshift which we adopt in the following. This formula also accounts for the corrective factors introducing the evolution of PBH masses from the initial redshift $z_{\rm i}$ (i generally indicates high-z quantities before PBH accretion took place) to the cut-off redshift $z_{\rm cut\text{-}off}$ and the shrinking of the binary semi-major axis due to accretion (De Luca et al. 2020a). This effect drives the binary evolution up to $z_{\rm cut\text{-}off}$, after which the binary evolves through the energy loss induced by GW emission (Peters & Mathews 1963). The suppression factor $S(M_{\rm tot}, f_{\rm PBH}, \psi) \equiv S_1 \times S_2$ accounts for both the effect of surrounding DM matter inhomogeneities (not in the form of PBHs) and the disruption of binaries due to interactions with neighbouring PBHs (Raidal et al. 2019; Vaskonen & Veermäe 2020; Young & Hamers 2020; Jedamzik 2021, 2020; De Luca et al. 2020; Tkachev et al. 2020; Hütsi et al. 2021). In particular, the second piece S_2 specifically includes the effect of disruption of PBH binaries in early substructures formed throughout the history of the universe.[3] The two pieces read (Hütsi et al. 2021)

$$S_1(M, f_{\rm PBH}, \psi) \approx 1.42 \left(\frac{\langle m^2\rangle/\langle m\rangle^2}{\bar{N}(y) + C} + \frac{\sigma_{\rm M}^2}{f_{\rm PBH}^2} \right)^{-21/74} \exp\left(-\bar{N}\right),$$
$$S_2(x) \approx \min\left[1, 9.6 \cdot 10^{-3} x^{-0.65} \exp\left(0.03 \ln^2 x\right)\right], \quad (7)$$

with $x \equiv f_{\rm PBH}(t(z)/t_0)^{0.44}$ and the number of neighbouring PBHs being $\bar{N} \equiv M/\langle m\rangle \times f_{\rm PBH}/(f_{\rm PBH} + \sigma_{\rm M})$. The constant C appearing in Eq. (7) is defined in Eq. (A.5) of Hütsi et al. (2021). Notice that, for $f_{\rm PBH} \lesssim 0.003$, one always finds $S_2 \simeq 1$, i.e. the suppression of the merger rate due to disruption inside PBH clusters is negligible. This is supported by the results obtained through a cosmological N-body simulation finding that PBHs are essentially isolated for a small enough values of the abundance (Inman & Ali-Haïmoud 2019). Therefore, for the small values of $f_{\rm PBH}$ adopted in our analysis following Franciolini et al. (2021), the clustering of PBHs does not play a significant role (Inman & Ali-Haïmoud 2019; Vaskonen & Veermäe 2020; De Luca et al. 2020).

In order to compute the SGWB energy density $\Omega_{\rm GW}(\nu_{\rm obs})$ emitted by the PBH population, we calculate the differential merger rate as a function of redshift as

$$\frac{\mathrm{d}R}{\mathrm{d}z} = \int \frac{1}{1+z} \frac{\mathrm{d}V_c(z)}{\mathrm{d}z} \frac{\mathrm{d}^2\mathcal{R}_{\rm PBH}}{\mathrm{d}m_1 \mathrm{d}m_2} \mathrm{d}m_1 \mathrm{d}m_2 \quad (8)$$

and feed this information in Eqs. (1) and (2). Finally, the energy spectrum $\mathrm{d}E/\mathrm{d}\nu$ is computed by integrating over the distribution of PBH binary masses as implied by Eq. (6). Also in this case, consistently with the previous section, the PBH model hyper-parameters (i.e. $[M_c, \sigma]$ determining the PBH mass distribution, the abundance $f_{\rm PBH}$ and $z_{\rm cut\text{-}off}$ characterising PBH accretion, see more details in App. A.2), are assumed to be given by the population inference result of Franciolini et al. (2021). In particular, we adopt $M_c = 34.54 M_\odot$, $\sigma = 0.41$, $f_{\rm PBH} = 10^{-3.64}$ and $z_{\rm cut\text{-}off} = 23.90$, such that the PBH channel is compatible with explaining around $(1 - 21)\%$ of the detectable events in the O1/O2/O3a run of LVC, and given the associated astrophysical models considered, the mass gap event GW190521.

2.4. Power-law-integrated sensitivity curves

The power-law-integrated (PI) sensitivity curve of a given detector (see Thrane & Romano 2013) can be computed once the noise spectral density and the averaged overlap functions are known following the procedure detailed in Appendix C. For the extended LVC network, we assume instrumental noise in different detectors to be uncorrelated. For triangular detectors we take into account the fact that the three nested inteferometers have correlated noise. All PI sensitivity curves are computed using the public code `schNell` (Alonso et al. 2020). We choose a (optimistic) SNR threshold of $\rho = 2$ to claim a detection, as commonly done in the literature on the subject (see e.g., Périgois et al. 2021a). Notice that the PI sensitivity curves scale linearly with ρ, see Eq. (C.8).

[3] Recent numerical results on PBH clustering confirm the suppression factors we adopt taking into account that the ratio of PBH binaries not entering in clusters is sizeable (Jedamzik 2021).

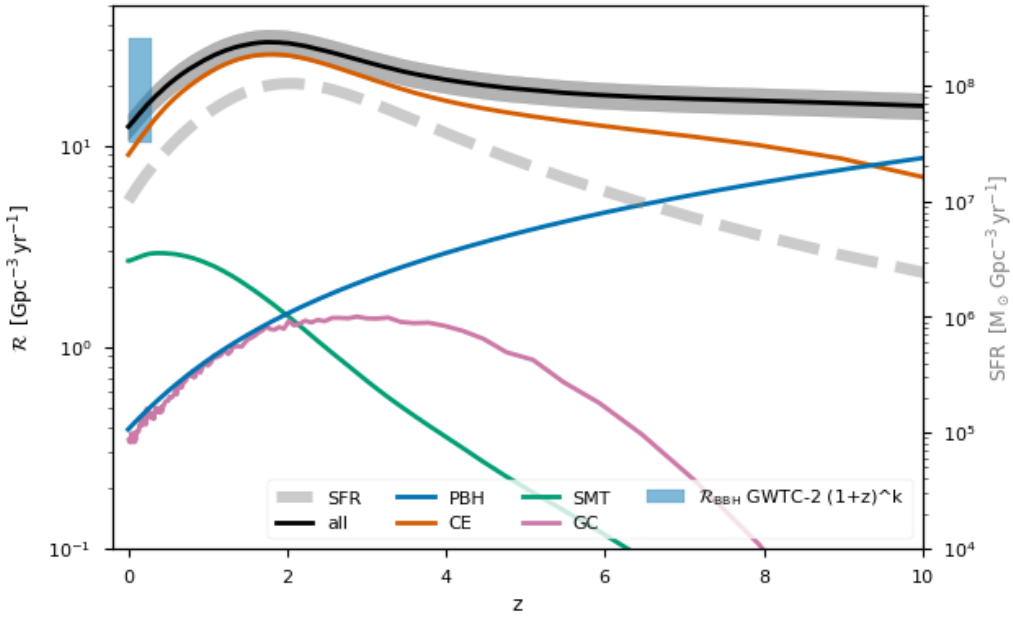

Fig. 3. Binary black hole rate density evolution normalised to the model selection results of Franciolini et al. (2021) compared to the local merger rate density inferred from GWTC-2 events assuming a power-law evolution of the merger rate with redshift. We show, in black, the contribution of all channels with relative Poisson error, in gray, computed on the detection rate of the 44 confident BBH events in the O1/O2/O3a observing runs. The model prediction can be directly compared to the local rate constrained by GWTC-2 displayed in blue. With different colors we show the contribution of each channel: common envelope (CE), stable mass transfer (SMT), globular cluster (GC) and primordial black holes (PBH). For comparison, we show the assumed SFR for isolated BBHs which the CE and SMT channels follow, in dashed gray.

The current official model for the power spectral density of the LISA noise (for both auto and cross-correlations) is based on the Payload Description Document, and is referenced in the LISA Strain Curves document LISA-LCST- SGS-TN-001.[4]

For ET one might argue that any estimate of correlated noise is quite arbitrary at the moment. We assume that the noise in ET is 20% correlated between detectors with an arm in common. This means that magnetic noise lies about a factor 2 in amplitude below other instrument noise. This is a robust assumption at lowest frequencies (< 20Hz). At higher frequencies, if one considers subtraction of magnetic noise, the correlation is expected to be substantially less than 20%. It is difficult to predict how much one can remove magnetic noise from data with subtraction, but it could even be by another factor 10 in amplitude. A level of correlation of 20% is therefore quite conservative. As the site for ET has not yet been chosen, we arbitrarily choose a location in Sardinia, close to one of the surveyed sites (see Alonso et al. (2020) for the specific coordinates and orientation angle of the triangular network). We use the sensitivity curve of the instrument in the so-called D-configuration (Hild et al. 2011). The resulting PI sensitivity curve is in quantitative agreement with the one of Maggiore et al. (2020).

3. Results

We compute the SGWB of astrophysical and primordial BBHs models given the relative event rate contribution determined by the model selection comparison against GWTC-2 events of Franciolini et al. (2021). For each channel, in Figure 3, we show the BBH merger rate density as a function of redshift as well as their combination. Given our event rate normalisation against the observed 44 events of GWCT-2, the modelled combined local rate density is consistent with the LVC redshift-dependent estimation at $19.3^{15.1}_{-9}$ Gpc^{-3}yr^{-1} (Abbott et al. 2021c)[5]. For comparison, in Figure 3, we also plot the assumed SFR density of the Universe. The rate density redshift evolution of the CE and SMT channels follow the SFR density. The GC BBH rate density does not mimic the star formation history of the host galaxies, instead peaking at $z \in [2, 3]$ (see e.g., Rodriguez & Loeb 2018). In contrast to the astrophysical channels, primordial BBHs have a monotonically increasing merger rate density with redshift as (Ali-Haïmoud et al. 2017; Raidal et al. 2019; De Luca et al. 2020a)

$$\mathcal{R}_{\rm PBH}(z) \approx \left(\frac{t(z)}{t(z=0)}\right)^{-34/37}, \tag{9}$$

extending up to redshifts $z = O(10^3)$. Notice that the evolution of the merger rate with time shown in Eq. (9) is entirely determined by the binary formation mechanism (i.e. how pairs of PBHs decouple from the Hubble flow) before the matter-radiation equality era. Eq. (9) is, therefore, a robust prediction of the PBH model assuming the standard formation scenario where PBHs are generated with an initial spatial Poisson distribution. In our case, given the local normalisation we assume, the PBH contribution grows to overcome the rate density of the astrophysical channels at high redshift ($z > 9.5$). In contrast, the BBH merger rate density at low redshifts is dominated by the CE and SMT channels up to $z = 2$ where the PBH and GC dominate over SMT. The

[4] We stress that some care has to be taken when comparing different PI sensitivity curves in the literature, as different references assume different arm length for LISA, different observation times and different SNR threshold ρ, see e.g. Petiteau (2015) for an overview. We consider the official configuration with 2.5 Gm arms and 4 yr of activity. Our results for the PI agree with Fig. 11 of Babak et al. (2021).

[5] Notice that the new GWTC-3 rate estimate $17.3 - 45\,\mathrm{Gpc^{-3}yr^{-1}}$ at $z = 0.2$ is consistent with the GWTC-2 estimate (Abbott et al. 2021f).

SMT channel shows a stronger rate suppression over redshift compared to the CE channel as their delay times, i.e. the time between binary formation and BBH merger, are much longer. This occurs because the second MT episode is not as efficient as the CE phase to shrink the BH-Wolf-Rayet binary systems progenitors of the BBHs (Bavera et al. 2021b).

The SGWB energy density spectrum of astrophysical and primordial BBH channels is shown in Figure 4. We find that, even though the BBH merger rate density is dominated by the CE channel up to redshifts $z \simeq 9.5$, $\Omega_{\rm GW}$ is dominated by the PBH channel in the frequency range $\nu \in [10^{-4}, 400]$ Hz. The dominance of the PBH channel over astrophysical channels is explained by two factors. First, contrary to the astrophysical channels, the merger rate density of primordial BBHs is a monotonic increasing function (see Figure 3) peaking at high redshifts of $z \gtrsim 9.5$. Second, given the model inference results of Franciolini et al. (2021), primordial BBHs are more massive than those produced by the astrophysical channels (see Figure 1) whose coalescence will lead to more energetic GW signals (see Figure 2). The combinations of these two factors leads to the dominance of the PBH channel in the SGWB since $\Omega_{\rm GW}$ accounts for the integration over all redshifts. Furthermore, we find that the astrophysical channels dominate $\Omega_{\rm GW}$ at $\nu \in [400, 1100]$ Hz. The suppression of $\Omega_{\rm GW}$ at higher frequencies is explained by the fact that the astrophysical channels can produce less massive BBHs compared to our fiducial PBH model (see Figure 1). Given that the inspiral and merger frequency scales as $\nu_{\rm merger} \propto M^{-1}$ (cf. Eq. B.4, but also see Figure 2) the astrophysical channels contribute to $\Omega_{\rm GW}$ above the PBH channel frequency turning point.

Our model predicts[6] $\Omega_{\rm GW}(\nu = 25\,{\rm Hz}) = 1.11^{+0.16}_{-0.05} \times 10^{-10}$, roughly ten times smaller than the current observational upper limits by the LVC of $\Omega_{\rm GW}(\nu = 25\,{\rm Hz}) \leq 1.04 \times 10^{-9}$ (Abbott et al. 2021f). Notice that this is not a trivial result generated by our normalisation assumption but rather a new constraint to model selection since these SGWB estimates include the integration over all redshifts whereas the constraints from GW events only probe the models up to the detectors horizons ($z \lesssim 1$). Further, we can predict whether our BBH SGWB estimate will be detected by future GW observing runs. To this end, in Figure 4, we show the PI sensitivity curves for the ground base detectors LIGO-Virgo (HLV), LIGO-Virgo-KAGRA (HLVK) with auto-correlations and ET accounting for 2 yr of integrated data collection at their design sensitivities as well as the space-based detector LISA for the nominal 4 yr mission. Given our model assumptions, we find that the SGWB of merging BBH lies below the current generation of GW detectors. However, we find that LISA and the third-generation (3G) GW detectors such as ET will be able to detect the BBH SGWB.

4. Discussion

Compared to the analysis of Zevin et al. (2021a), in Franciolini et al. (2021) the CHE channel was excluded, while the inclusion of the NSC channel was not found to lead to a larger Bayesian evidence, still reaching similar conclusions regarding the relative contributions of CE, SMT and GC channels. This is due to the CHE and NSC models contributing $< 8\%$ and $< 13\%$, respectively, to the underlying merging BBH distribution in Zevin et al. (2021a) at 95% credibility. More precisely, the CHE channel mostly leads to highly spinning and massive BHs which are favoured due to GW detector selection effects and a smaller contribution to the underlying BBH distribution is required to explain the events in GWTC-2. A similar argument can be made for the NSC channel where in contrast to CHE channel BH spins are smaller. Given the small predicted contribution of these two channels to the intrinsic merger rate distribution we expect a subdominant contribution to $\Omega_{\rm GW}$, much smaller than the GC contribution in Figure 4, and hence, will not affect our results.

Our analysis neglected the contribution from the population of non-merging binaries, which previous studies on isolated binary evolution (Périgois et al. 2021a) have found to be negligible compared to the merging population in the frequency bands we consider. Furthermore, we also did not include eccentric corrections to the GW energy spectrum and assumed that the BBHs will reach the LISA or ground based detector sensitive frequencies with quasi-circular orbits. Périgois et al. (2021a,b) showed that this is the case for isolated binary evolution, while a number of semi-analytic and numerical studies (Breivik et al. 2016; Samsing & Ramirez-Ruiz 2017; Rodriguez et al. 2018; Samsing & D'Orazio 2018; Zevin et al. 2019, 2021b) have shown that for dynamically formed systems a sizable fraction of the BBH population can retain appreciable eccentricity when they enter the LIGO or LISA bands. However, since the GC channel shows a subdominant contribution to the total $\Omega_{\rm GW}$ at one part in 20 at $\nu = 3$ mHz, any boost to the GW background from this channel will not change our conclusion significantly.

In this work we presented our SGWB analysis as an additional constraint to multi-channel Bayesian model selection where $\Omega_{\rm GW}$ is computed a posteriori to be much smaller than the observational constraint. Alternatively, if we had a more stringent constraint to $\Omega_{\rm GW}$, one could include the SGWB constraint in the inference of such model selection frameworks, providing the analysis with a direct discriminatory power to models over-predicting $\Omega_{\rm GW}$. Because in our analysis the SGWB is found to be much smaller than the LVC observational constraint, the result of our model selection would remain the same. On a similar end, given a phenomenological model, Callister et al. (2020a) recently used the SGWB and informations about individually resolvable events from O1 and O2 to place joint constraints on the BBH merger rate density peak and slope for low redshifts. Notice that the two analysis are complementary as the one presented here simultaneously constrains the potential contribution of each channel to the total BBH merger rate density while Callister et al. (2020a) puts a direct constraints on the overall joint merger rate density.

A future detection of the SGWB would also possibly help in distinguishing between astrophysical and primordial channels through the SGWB anisotropies (Wang & Kohri 2021). Another example for distinguishing between channels is that in the case the GC channel dominates the SGWB, one would expect to be able to identify a cusp in $\Omega_{\rm GW}$ in LISA frequency band (D'Orazio & Samsing 2018). Other possible ways to discriminate among different channels is the measurement of the merger bias at 3G detectors through the study of the cross-correlation with the large scale structure (Cusin et al. 2017, 2018; Scelfo et al. 2018; Mukherjee & Silk 2020a,b; Calore et al. 2020; Yang et al. 2021), the study of the time evolution of the high redshift merger rates (De Luca et al. 2021b; Ng et al. 2021), and the reconstruction of the spectral shape pre-merger via small band searches.

5. Conclusions

With the aim of further constraining multi-channel BBH Bayesian model selection, as a working example in this work,

[6] We report the value of $\Omega_{\rm GW}$ at $\nu = 25$ Hz where the current LVC sensitivity has its maximum, see Figure 4.

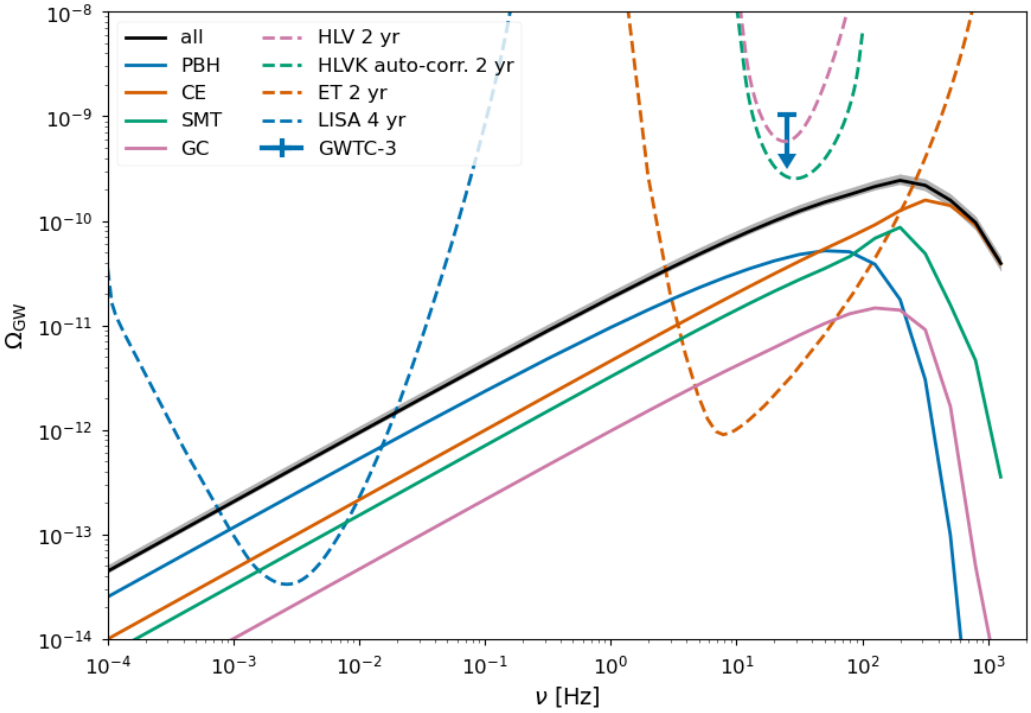

Fig. 4. Stochastic gravitational-wave background energy density spectrum of merging astrophysical and primordial BBHs (solid lines). The fiducial model assumes combined BBH event rate normalized against the 44 confident BBH detections of GWTC-2 and branching ratios of each channel inferred by the model selection analysis of Franciolini et al. (2021). We show with individual lines the partial contribution of each channel: common envelope (orange), stable mass transfer (green), globular cluster (pink) and primordial black holes (blue). The total SGWB is indicated in black where the gray band indicates the Poisson error. The upper constraint to the SGWB from GWTC-3 is indicated with a blue bar marker and an arrow. For comparison, we indicate with dashed lines the PI sensitivity curves of different detectors for corresponding continuous observation time. The detector configurations include LIGO-Virgo at design sensitivity (HLV), the same configuration including KAGRA with auto-correlations (HLVK auto-corr.), Einstein Telescope (ET) and the Laser Interferometer Space Array (LISA).

we computed the SGWB of an astrophysical and primordial BBH population resulting from a model selection comparison with GWTC-2. Because our study did not include all potentially prominent channels leading to merging BBHs or span all model uncertainties (cf. Section 1), the results of the analysis need to be carefully interpreted. Rather than being a definitive answer to which channel dominates the SGWB, our analysis is intended to provide a complementary tool to model selection that can be used to further constrain the contribution of particular formation channels. In principle, it provides an additional constraint to model selection as the SGWB probes the theoretical prediction over all redshifts. This is in contrast to model selection analyses that focus on the resolved population, which have discriminating power only up to the GW detector horizons, currently at $z \lesssim 1$ for LIGO–Virgo. Our methodology can therefore be extended to all future model selection studies aiming to unravel the origin of merging BBHs independently from which channel dominates the BBH merger rate density.

To mitigate the large model uncertainties on the merger rate density estimation of each channel which directly correlate to Ω_{GW}, we have normalized the event rate to the 44 confident detections of GWTC-2 and the relative contribution of each channel to the branching ratio results in the model selection analysis of Franciolini et al. (2021). We predict a SGWB of $\Omega_{GW}(\nu = 25\,\mathrm{Hz}) = 1.11^{+0.16}_{-0.05} \times 10^{-10}$ which lies below the current observational upper limits published by the LVC. Moreover, we find that such background will be accessible only to 3G GW observatories such as ET and the space-based detector LISA.

Finally, with 3G Earth-based detectors, a catalogue of individual events and background mapping provide complementary information on the underlying source population. Combining the two approaches can be useful to gain information on a high redshift population of sources which cannot be detected and studied individually, even with large-horizon instruments.

Acknowledgements. The authors would like to thank Valerio De Luca for useful discussions on early stages of the project. This work was supported by the Swiss National Science Foundation Professorship grant (project number PP00P2 176868). G.F. and A.R. are supported by the Swiss National Science Foundation (SNSF), project *The Non-Gaussian Universe and Cosmological Symmetries*, project number: 200020-178787. The work of G.C. is supported by SNSF Ambizione grant - *Gravitational waves propagation in the clustered universe*. M.Z. is supported by NASA through the NASA Hubble Fellowship grant HST-HF2-51474.001-A awarded by the Space Telescope Science Institute, which is operated by the Association of Universities for Research in Astronomy, Inc., for NASA, under contract NAS5-26555.

References

Aasi, J., Abbott, B. P., Abbott, R., et al. 2015, Classical and Quantum Gravity, 32, 074001
Abbott, B. P., Abbott, R., Abbott, T. D., et al. 2016, Phys. Rev. Lett., 116, 131102
Abbott, B. P., Abbott, R., Abbott, T. D., et al. 2019, Physical Review X, 9, 031040
Abbott, B. P., Abbott, R., Abbott, T. D., et al. 2018, Phys. Rev. Lett., 120, 091101
Abbott, R., Abbott, T. D., Abraham, S., et al. 2021a, ApJ, 915, L5
Abbott, R., Abbott, T. D., Abraham, S., et al. 2021b, Physical Review X, 11, 021053
Abbott, R., Abbott, T. D., Abraham, S., et al. 2021c, ApJ, 913, L7
Abbott, R., Abbott, T. D., Abraham, S., et al. 2020a, Phys. Rev. Lett., 125, 101102

Abbott, R., Abbott, T. D., Abraham, S., et al. 2020b, ApJ, 896, L44
Abbott, R., Abbott, T. D., Acernese, F., et al. 2021d, arXiv e-prints, arXiv:2108.01045
Abbott, R., Abbott, T. D., Acernese, F., et al. 2021e, arXiv e-prints, arXiv:2111.03606
Abbott, R., Abbott, T. D., Acernese, F., et al. 2021f, arXiv e-prints, arXiv:2111.03634
Acernese, F., Agathos, M., Agatsuma, K., et al. 2015, Classical and Quantum Gravity, 32, 024001
Ajith, P., Hannam, M., Husa, S., et al. 2011, Phys. Rev. Lett., 106, 241101
Ali-Haïmoud, Y. 2018, Phys. Rev. Lett., 121, 081304
Ali-Haïmoud, Y., Kovetz, E. D., & Kamionkowski, M. 2017, Phys. Rev., D96, 123523
Allen, B. & Romano, J. D. 1999, Phys. Rev. D, 59, 102001
Alonso, D., Contaldi, C. R., Cusin, G., Ferreira, P. G., & Renzini, A. I. 2020, Phys. Rev. D, 101, 124048
Amaro-Seoane, P., Audley, H., Babak, S., et al. 2017, arXiv e-prints, arXiv:1702.00786
Antonini, F., Chatterjee, S., Rodriguez, C. L., et al. 2016, ApJ, 816, 65
Antonini, F., Gieles, M., & Gualandris, A. 2019, MNRAS, 486, 5008
Antonini, F. & Perets, H. B. 2012, ApJ, 757, 27
Antonini, F., Toonen, S., & Hamers, A. S. 2017, ApJ, 841, 77
Arca Sedda, M. 2020, ApJ, 891, 47
Aso, Y., Michimura, Y., Somiya, K., et al. 2013, Phys. Rev. D, 88, 043007
Babak, S., Hewitson, M., & Petiteau, A. 2021, arXiv e-prints, arXiv:2108.01167
Ballesteros, G., Serpico, P. D., & Taoso, M. 2018, JCAP, 10, 043
Banerjee, S. 2017, MNRAS, 467, 524
Bardeen, J. M., Bond, J., Kaiser, N., & Szalay, A. 1986, Astrophys. J., 304, 15
Bartos, I., Kocsis, B., Haiman, Z., & Márka, S. 2017, ApJ, 835, 165
Bavera, S. S., Fragos, T., Qin, Y., et al. 2020, A&A, 635, A97
Bavera, S. S., Fragos, T., Zapartas, E., et al. 2021a, arXiv e-prints, arXiv:2106.15841
Bavera, S. S., Fragos, T., Zevin, M., et al. 2021b, A&A, 647, A153
Bavera, S. S., Zevin, M., & Fragos, T. 2021c, Research Notes of the American Astronomical Society, 5, 127
Belczynski, K., Holz, D. E., Bulik, T., & O'Shaughnessy, R. 2016, Nature, 534, 512
Belczynski, K., Romagnolo, A., Olejak, A., et al. 2021, arXiv e-prints, arXiv:2108.10885
Bellomo, N., Bernal, J. L., Raccanelli, A., & Verde, L. 2018, J. Cosmology Astropart. Phys., 2018, 004
Berger, L., Koester, D., Napiwotzki, R., Reid, I. N., & Zuckerman, B. 2005, A&A, 444, 565
Bethe, H. A. & Brown, G. E. 1998, ApJ, 506, 780
Bird, S., Cholis, I., Muñoz, J. B., et al. 2016, Phys. Rev. Lett., 116, 201301
Blinnikov, S., Dolgov, A., Porayko, N. K., & Postnov, K. 2016, JCAP, 1611, 036
Breivik, K., Coughlin, S., Zevin, M., et al. 2020, ApJ, 898, 71
Breivik, K., Rodriguez, C. L., Larson, S. L., Kalogera, V., & Rasio, F. A. 2016, ApJ, 830, L18
Callister, T., Fishbach, M., Holz, D. E., & Farr, W. M. 2020a, ApJ, 896, L32
Callister, T. A., Farr, W. M., & Renzo, M. 2020b, arXiv e-prints, arXiv:2011.09570
Calore, F., Cuoco, A., Regimbau, T., Sachdev, S., & Serpico, P. D. 2020, Physical Review Research, 2, 023314
Carr, B., Kohri, K., Sendouda, Y., & Yokoyama, J. 2020, arXiv e-prints, arXiv:2002.12778
Carr, B., Raidal, M., Tenkanen, T., Vaskonen, V., & Veermäe, H. 2017, Phys. Rev., D96, 023514
Carr, B. J. 1975, Astrophys. J., 201, 1
Chapline, G. F. 1975, Nature, 253, 251
Chatterjee, S., Rodriguez, C. L., & Rasio, F. A. 2017, ApJ, 834, 68
Chen, Z.-C., Huang, F., & Huang, Q.-G. 2019, ApJ, 871, 97
Christensen, N. 1992, Phys. Rev. D, 46, 5250
Chruslinska, M., Nelemans, G., & Belczynski, K. 2019, MNRAS, 482, 5012
Clesse, S. & García-Bellido, J. 2017, Phys. Dark Univ., 15, 142
Cusin, G., Dvorkin, I., Pitrou, C., & Uzan, J.-P. 2018, Phys. Rev. Lett., 120, 231101
Cusin, G., Pitrou, C., & Uzan, J.-P. 2017, Phys. Rev. D, 96, 103019
de Freitas Pacheco, J. A. 2020, arXiv e-prints, arXiv:2001.09663
De Luca, V., Desjacques, V., Franciolini, G., Malhotra, A., & Riotto, A. 2019, JCAP, 1905, 018
De Luca, V., Desjacques, V., Franciolini, G., Pani, P., & Riotto, A. 2021a, Phys. Rev. Lett., 126, 051101
De Luca, V., Desjacques, V., Franciolini, G., & Riotto, A. 2020, J. Cosmology Astropart. Phys., 2020, 028
De Luca, V., Franciolini, G., Pani, P., & Riotto, A. 2020a, JCAP, 06, 044
De Luca, V., Franciolini, G., Pani, P., & Riotto, A. 2020b, JCAP, 04, 052
De Luca, V., Franciolini, G., Pani, P., & Riotto, A. 2021b, J. Cosmology Astropart. Phys., 2021, 003
De Luca, V., Franciolini, G., Pani, P., & Riotto, A. 2021c, arXiv e-prints, arXiv:2106.13769
de Mink, S. E., Cantiello, M., Langer, N., et al. 2009, A&A, 497, 243
Deheuvels, S., Ballot, J., Beck, P. G., et al. 2015, A&A, 580, A96
Deng, H. 2021, JCAP, 04, 058
Desjacques, V. & Riotto, A. 2018, Phys. Rev. D, 98, 123533
Dolgov, A. & Silk, J. 1993, Phys. Rev. D, 47, 4244
D'Orazio, D. J. & Samsing, J. 2018, MNRAS, 481, 4775
Downing, J. M. B., Benacquista, M. J., Giersz, M., & Spurzem, R. 2010, MNRAS, 407, 1946
du Buisson, L., Marchant, P., Podsiadlowski, P., et al. 2020, MNRAS, 499, 5941
Fowler, W. A. & Hoyle, F. 1964, ApJS, 9, 201
Fragione, G. & Loeb, A. 2019, MNRAS, 486, 4443
Fragos, T., Andrews, J. J., Ramirez-Ruiz, E., et al. 2019, ApJ, 883, L45
Fragos, T. & McClintock, J. E. 2015, ApJ, 800, 17
Franciolini, G., Baibhav, V., De Luca, V., et al. 2021, arXiv e-prints, arXiv:2105.03349
Fuller, J. & Ma, L. 2019, ApJ, 881, L1
Garcia-Bellido, J., Linde, A. D., & Wands, D. 1996, Phys. Rev. D, 54, 6040
Gehan, C., Mosser, B., Michel, E., Samadi, R., & Kallinger, T. 2018, A&A, 616, A24
Gow, A. D., Byrnes, C. T., & Hall, A. 2020, arXiv e-prints, arXiv:2009.03204
Green, A. M. 2016, Phys. Rev. D, 94, 063530
Green, A. M. & Kavanagh, B. J. 2021, Journal of Physics G Nuclear Physics, 48, 043001
Gröbner, M., Ishibashi, W., Tiwari, S., Haney, M., & Jetzer, P. 2020, A&A, 638, A119
Hall, A., Gow, A. D., & Byrnes, C. T. 2020, Phys. Rev. D, 102, 123524
Hasinger, G. 2020, J. Cosmology Astropart. Phys., 2020, 022
Hawking, S. W. 1974, Nature, 248, 30
Hénon, M. 1971a, Ap&SS, 13, 284
Hénon, M. H. 1971b, Ap&SS, 14, 151
Hild, S., Abernathy, M., Acernese, F., et al. 2011, Classical and Quantum Gravity, 28, 094013
Hütsi, G., Raidal, M., Vaskonen, V., & Veermäe, H. 2021, JCAP, 2103, 068
Hütsi, G., Raidal, M., & Veermäe, H. 2019, Phys. Rev. D, 100, 083016
Inayoshi, K., Hirai, R., Kinugawa, T., & Hotokezaka, K. 2017, MNRAS, 468, 5020
Inman, D. & Ali-Haïmoud, Y. 2019, Phys. Rev. D, 100, 083528
Ioka, K., Chiba, T., Tanaka, T., & Nakamura, T. 1998, Phys. Rev. D, 58, 063003
Ivanov, P. 1998, Phys. Rev. D, 57, 7145
Ivanov, P., Naselsky, P., & Novikov, I. 1994, Phys. Rev. D, 50, 7173
Ivanova, N., Justham, S., Chen, X., et al. 2013, A&A Rev., 21, 59
Jedamzik, K. 2020, JCAP, 09, 022
Jedamzik, K. 2021, https://agenda.infn.it/event/23799/contributions/125718/attachments/78986/102370/rome110221.pdf,
Jedamzik, K. 2021, Phys. Rev. Lett., 126, 051302
Joshi, K. J., Rasio, F. A., & Portegies Zwart, S. 2000, ApJ, 540, 969
Kalogera, V., Belczynski, K., Kim, C., O'Shaughnessy, R., & Willems, B. 2007, Phys. Rep., 442, 75
Kimura, R., Suyama, T., Yamaguchi, M., & Zhang, Y.-L. 2021, JCAP, 04, 031
Kinugawa, T., Inayoshi, K., Hotokezaka, K., Nakauchi, D., & Nakamura, T. 2014, MNRAS, 442, 2963
Klencki, J., Nelemans, G., Istrate, A. G., & Chruslinska, M. 2021, A&A, 645, A54
Kritos, K., De Luca, V., Franciolini, G., Kehagias, A., & Riotto, A. 2021, J. Cosmology Astropart. Phys., 2021, 039
Kühnel, F. & Freese, K. 2017, Phys. Rev. D, 95, 083508
Kumamoto, J., Fujii, M. S., & Tanikawa, A. 2020, MNRAS, 495, 4268
Kurtz, D. W., Saio, H., Takata, M., et al. 2014, MNRAS, 444, 102
Liu, B., Meynet, G., & Bromm, V. 2021, MNRAS, 501, 643
Madau, P. & Rees, M. J. 2001, ApJ, 551, L27
Maggiore, M., Van Den Broeck, C., Bartolo, N., et al. 2020, J. Cosmology Astropart. Phys., 2020, 050
Mandel, I. & Broekgaarden, F. S. 2021, arXiv e-prints, arXiv:2107.14239
Mandel, I. & de Mink, S. E. 2016, MNRAS, 458, 2634
Mapelli, M. 2016, MNRAS, 459, 3432
Marchant, P., Langer, N., Podsiadlowski, P., Tauris, T. M., & Moriya, T. J. 2016, A&A, 588, A50
Marchant, P., Pappas, K. M. W., Gallegos-Garcia, M., et al. 2021, A&A, 650, A107
Marchant, P., Renzo, M., Farmer, R., et al. 2019, ApJ, 882, 36
McKernan, B., Ford, K. E. S., Kocsis, B., Lyra, W., & Winter, L. M. 2014, MNRAS, 441, 900
Miller, M. C. & Hamilton, D. P. 2002, MNRAS, 330, 232
Miller, M. C. & Lauburg, V. M. 2009, ApJ, 692, 917
Mirbabayi, M., Gruzinov, A., & Noreña, J. 2020, JCAP, 2003, 017
Moradinezhad Dizgah, A., Franciolini, G., & Riotto, A. 2019, JCAP, 11, 001

Mukherjee, S., Meinema, M. S. P., & Silk, J. 2021, arXiv e-prints, arXiv:2107.02181
Mukherjee, S. & Silk, J. 2020a, arXiv e-prints, arXiv:2008.01082
Mukherjee, S. & Silk, J. 2020b, MNRAS, 491, 4690
Mukherjee, S. & Silk, J. 2021, MNRAS, 506, 3977
Nakamura, T., Sasaki, M., Tanaka, T., & Thorne, K. S. 1997, Astrophys. J. Lett., 487, L139
Neijssel, C. J., Vigna-Gómez, A., Stevenson, S., et al. 2019, MNRAS, 490, 3740
Ng, K. K. Y., Chen, S., Goncharov, B., et al. 2021, arXiv e-prints, arXiv:2108.07276
Oh, S. P. & Haiman, Z. 2003, Mon. Not. Roy. Astron. Soc., 346, 456
Pattabiraman, B., Umbreit, S., Liao, W.-k., et al. 2013, ApJS, 204, 15
Paxton, B., Bildsten, L., Dotter, A., et al. 2011, ApJS, 192, 3
Paxton, B., Cantiello, M., Arras, P., et al. 2013, ApJS, 208, 4
Paxton, B., Marchant, P., Schwab, J., et al. 2015, ApJS, 220, 15
Paxton, B., Schwab, J., Bauer, E. B., et al. 2018, ApJS, 234, 34
Paxton, B., Smolec, R., Schwab, J., et al. 2019, ApJS, 243, 10
Périgois, C., Belczynski, C., Bulik, T., & Regimbau, T. 2021a, Phys. Rev. D, 103, 043002
Périgois, C., Santoliquido, F., Bouffanais, Y., et al. 2021b, arXiv e-prints, arXiv:2112.01119
Peters, P. C. & Mathews, J. 1963, Phys. Rev., 131, 435
Petiteau, A. 2015, Note for eLISA cosmology working group on sensitivity curve and detection estimation for a stochastic background (version 0.3), https://apc.u-paris.fr/Downloads/lisa/eLISA/Sensitivity/Cfgv1/StochBkgd/Notes_eLISASensitivityAndCosmology_v0.3.pdf, [Online; accessed 2-September-2021]
Petrovich, C. & Antonini, F. 2017, ApJ, 846, 146
Planck Collaboration, Ade, P. A. R., Aghanim, N., et al. 2016, A&A, 594, A13
Postnov, K. A. & Yungelson, L. R. 2014, Living Reviews in Relativity, 17, 3
Pujolas, O., Vaskonen, V., & Veermäe, H. 2021, arXiv e-prints, arXiv:2107.03379
Punturo, M., Abernathy, M., Acernese, F., et al. 2010, Classical and Quantum Gravity, 27, 194002
Qin, Y., Fragos, T., Meynet, G., et al. 2018, A&A, 616, A28
Quast, M., Langer, N., & Tauris, T. M. 2019, A&A, 628, A19
Raidal, M., Spethmann, C., Vaskonen, V., & Veermäe, H. 2019, JCAP, 02, 018
Regimbau, T. 2011, Research in Astronomy and Astrophysics, 11, 369
Ricotti, M. 2007, Astrophys. J., 662, 53
Ricotti, M., Ostriker, J. P., & Mack, K. J. 2008, Astrophys. J., 680, 829
Riley, J., Mandel, I., Marchant, P., et al. 2021, MNRAS, 505, 663
Rodriguez, C. L., Amaro-Seoane, P., Chatterjee, S., & Rasio, F. A. 2018, Phys. Rev. Lett., 120, 151101
Rodriguez, C. L. & Loeb, A. 2018, ApJ, 866, L5
Rodriguez, C. L., Morscher, M., Pattabiraman, B., et al. 2015, Phys. Rev. Lett., 115, 051101
Rodriguez, C. L., Zevin, M., Amaro-Seoane, P., et al. 2019, Phys. Rev. D, 100, 043027
Rodriguez, C. L., Zevin, M., Pankow, C., Kalogera, V., & Rasio, F. A. 2016, ApJ, 832, L2
Samsing, J. & D'Orazio, D. J. 2018, MNRAS, 481, 5445
Samsing, J. & Ramirez-Ruiz, E. 2017, ApJ, 840, L14
Sasaki, M., Suyama, T., Tanaka, T., & Yokoyama, S. 2016, Phys. Rev. Lett., 117, 061101, [erratum: Phys. Rev. Lett.121,no.5,059901(2018)]
Scelfo, G., Bellomo, N., Raccanelli, A., Matarrese, S., & Verde, L. 2018, J. Cosmology Astropart. Phys., 2018, 039
Sigurdsson, S. & Hernquist, L. 1993, Nature, 364, 423
Tagawa, H., Haiman, Z., Bartos, I., & Kocsis, B. 2020, ApJ, 899, 26
Thorne, K. S. 1974, ApJ, 191, 507
Thrane, E. & Romano, J. D. 2013, Phys. Rev. D, 88, 124032
Tkachev, M., Pilipenko, S., & Yepes, G. 2020, Mon. Not. Roy. Astron. Soc., 499, 4854
van den Heuvel, E. P. J., Portegies Zwart, S. F., & de Mink, S. E. 2017, MNRAS, 471, 4256
Vaskonen, V. & Veermäe, H. 2020, Phys. Rev. D, 101, 043015
Vigna-Gómez, A., Toonen, S., Ramirez-Ruiz, E., et al. 2021, ApJ, 907, L19
Wang, S. & Kohri, K. 2021, arXiv e-prints, arXiv:2107.01935
Wang, S., Terada, T., & Kohri, K. 2019, Phys. Rev. D, 99, 103531
Wang, S., Wang, Y.-F., Huang, Q.-G., & Li, T. G. F. 2016, arXiv e-prints, arXiv:1610.08725
Wong, K. W. K., Breivik, K., Kremer, K., & Callister, T. 2021, Phys. Rev. D, 103, 083021
Wong, K. W. K., Franciolini, G., De Luca, V., et al. 2021, Phys. Rev., D103, 023026
Woosley, S. E. 2017, ApJ, 836, 244
Yang, K. Z., Mandic, V., Scarlata, C., & Banagiri, S. 2021, MNRAS, 500, 1666
Young, S. & Hamers, A. S. 2020, JCAP, 10, 036
Zel'dovich, Y. B. & Novikov, I. D. 1967, Soviet Astron. AJ (Engl. Transl.),, 10, 602
Zevin, M., Bavera, S. S., Berry, C. P. L., et al. 2021a, ApJ, 910, 152
Zevin, M., Romero-Shaw, I. M., Kremer, K., Thrane, E., & Lasky, P. D. 2021b, arXiv e-prints, arXiv:2106.09042
Zevin, M., Samsing, J., Rodriguez, C., Haster, C.-J., & Ramirez-Ruiz, E. 2019, ApJ, 871, 91
Zhao, Y. & Lu, Y. 2021, MNRAS, 500, 1421
Zhu, X.-J., Howell, E., Regimbau, T., Blair, D., & Zhu, Z.-H. 2011, ApJ, 739, 86
Ziosi, B. M., Mapelli, M., Branchesi, M., & Tormen, G. 2014, MNRAS, 441, 3703

Appendix A: Binary black hole models

Appendix A.1: Astrophysical BBH models

Appendix A.1.1: Isolated binary evolution models

We consider the SMT and CE channels for the formation of merging BBH through isolated binary evolution. In both cases a typical binary evolves first through a stable MT episode which is caused by the primary star evolving faster and expanding first to overfill the Roche-lobe when the star leaves the main sequence to become a red supergiant. Stripped from its envelope, the primary eventually collapse to form a BH. Similarly, when the companion star leaves its main sequence, the secondary will expand to overfill the Roche-lobe leading to the second mass transfer episode which can be either be stable (SMT channel) or unstable (CE channel). The latter case leads to a CE phase where the envelope of the secondary engulf the BH companion. If the binary survives the MT episode, namely it avoids merging, a BH-Wolf-Rayet systems is formed. Compared to the SMT channel, the CE channel leads to smaller orbital separations post MT (Bavera et al. 2021b). For BH-Wolf-Rayet orbital periods smaller than 1 day tidal interactions from the BH onto the companion can lead to the spin-up of the Wolf-Rayet star which subsequently leads to the formation of a highly spinning second-born BH (Qin et al. 2018; Bavera et al. 2020, 2021b,c).

In this work we adopt the CE and SMT models of Bavera et al. (2021b) which used `POSYDON`[7] (Fragos et al. 2021, in prep.) to combine the rapid parametric population synthesis code `COSMIC` (Breivik et al. 2020) with detailed `MESA` (Paxton et al. 2011, 2013, 2015, 2018, 2019) binary evolution simulations. `COSMIC` was used to rapidly evolve binaries from zero-age main sequence to post second MT while `MESA` to target the BH-Wolf-Rayet evolutionary phase leading to the tidal spin-up of the secondary. The spin of the first-born BH is assumed to be zero, a direct consequence of the assumed efficient angular transport (Fragos & McClintock 2015; Qin et al. 2018; Fuller & Ma 2019) which finds support in asteroseismic measurements (Kurtz et al. 2014; Deheuvels et al. 2015; Gehan et al. 2018), observations of white dwarfs spins (Berger et al. 2005) and recent gravitational-wave observations (Zevin et al. 2021a). Moreover we assume Eddington-limited accretion efficiency onto compact objects, which leads to negligible mass accretion onto the first-born BH and prevent any mass-accretion spin-up in the SMT channel (Thorne 1974). For a detailed description of all the model parameters we point the reader to Bavera et al. (2021b).

Appendix A.1.2: Dynamical formation models in GC

In addition to isolated evolution channels, we also consider the astrophysical formation channel of BBH mergers that are synthesized in dense stellar environments. In particular, we use the set of globular cluster models from Rodriguez et al. (2019), which are simulated using the Henon-style cluster Monte Carlo code `CMC` (Hénon 1971a,b; Joshi et al. 2000; Pattabiraman et al. 2013). These cluster models span a range of initial masses, half-mass radii and metallicities and show present-day consistency with observational properties of globular clusters in the Milky Way and nearby galaxies. We use the models from Rodriguez et al. (2019) in which black holes are born with near-zero spin, as spin has only a minor effect on the GW energy spectrum and this model is preferred by the data (Zevin et al. 2021a; Franciolini et al. 2021). Cluster formation, and therefore the redshift distribution of mergers, follow the prescriptions in Rodriguez & Loeb (2018), and the cluster population is weighted based on the metallicity distribution of Milky Way globular clusters.

[7] https://posydon.org

Appendix A.2: Primordial BBH model

The formation of PBHs occurs from the collapse of large overdensities in the primordial Universe (see Green & Kavanagh 2021, for a recent review). The formation of a PBH of mass m takes place deep in the radiation-dominated era at a typical redshift $z_{\rm i} \simeq 2 \cdot 10^{11} (m/M_\odot)^{-1/2}$. The distribution of masses is determined by the characteristic size and statistical properties of the density perturbations, corresponding to curvature perturbations generated during the inflationary epoch. As typically done in the literature, we assume a model-independent parametrization of the mass function at formation redshift $z_{\rm i}$ of the form

$$\psi(m, z_{\rm i}) = \frac{1}{\sqrt{2\pi}\sigma m} \exp\left(-\frac{\log^2(m/M_c)}{2\sigma^2}\right), \tag{A.1}$$

in terms of its width σ and reference mass scale M_c (not to be confused with the chirp mass denoted here with $\mathcal{M}$). This mass function describes a PBH population resulting from a symmetric peak in the curvature spectrum and recovers a wide variety of models (Dolgov & Silk 1993; Green 2016; Carr et al. 2017).[8]

As extreme perturbations tend to have nearly-spherical shape (Bardeen et al. 1986) and the collapse takes place in a radiation-dominated Universe, the initial adimensional Kerr parameter $\mathbf{a}$ is expected to be below the percent level (De Luca et al. 2019; Mirbabayi et al. 2020). However, a non-zero spin can be acquired by PBHs forming binaries through an efficient phase of accretion (De Luca et al. 2020a,b) prior the reionization epoch. Therefore, a defining characteristics of the PBH model is the expected correlation between large values of binary total masses and large values of spins of their PBH constituents. Also, the spin directions of PBHs in binaries are independent and they randomly distribute on the sphere. PBH accretion is still affected by large uncertainties, in particular coming from the impact of feedback effects (Ricotti 2007; Ali-Haïmoud et al. 2017), structure formation (Hasinger 2020; Hütsi et al. 2019) and early X-ray pre-heating (Oh & Haiman 2003). Therefore, an additional hyper-parameter, the cut-off redshift $z_{\rm cut\text{-}off} \in [10, 30]$, was introduced by De Luca et al. (2020b) accounting for this accretion model uncertainties. For each value of $z_{\rm cut\text{-}off}$ there exists a one-to-one correspondence between the initial and final masses which can be computed according to the accretion model described in details in Refs. (Ricotti 2007; Ricotti et al. 2008; De Luca et al. 2020a,b). We highlight, for clarity, that a lower cut-off is associated to stronger accretion and vice-versa. Values above $z_{\rm cut\text{-}off} \simeq 30$ correspond to negligible accretion in the mass range of interest for the LVC observations.

In the absence of primordial non-Gaussianities, the PBH locations in space at the formation epoch follow a Poisson distribution (Ali-Haïmoud 2018; Desjacques & Riotto 2018; Ballesteros et al. 2018; Moradinezhad Dizgah et al. 2019). This feature, describing the spatial distribution of PBHs at formation in the stadard scenario, is used to compute the properties of the population of PBH binaries formed at high redshift and contributing to the merger rate described in Sec. 2.3. Notice, finally, that that the dominant PBH merger rate comes from PBH binaries assembled

[8] In the literature, other PBH mass functions were also considered (e.g. Kühnel & Freese 2017; Bellomo et al. 2018; Hall et al. 2020; Gow et al. 2020). In this work, we follow Franciolini et al. (2021) and adopt Eq. (A.1).

via gravitational decoupling from the Hubble flow before matter-radiation equality (Nakamura et al. 1997; Ioka et al. 1998) and, as shown for example in Ali-Haïmoud et al. (2017), the merger rate of binaries formed through dynamical capture in the present day halos is subdominant and, therefore, neglected in our computations.

Appendix B: Gravitational-wave energy spectrum

We approximate the gravitational-wave energy spectrum, $\frac{dE}{d\nu}$, of a coalescing BBH using the phenomenological templates models of Ajith et al. (2011) which are obtained using frequency domain matching of post-Newtonian inspiral waveforms with coalescence waveforms from numerical simulations. These models approximate the inspiral, merger and ringdown waveforms in the frequency Fourier space domain, ν, for BBHs with component masses, m_1 and m_2, and non-precessing spins, $\mathbf{a_1}$ and $\mathbf{a_2}$. Assuming circular orbits, we have (Zhu et al. 2011)

$$\frac{dE}{d\nu} = \frac{(G\pi)^{2/3}\mathcal{M}^{5/3}}{3}\begin{cases}\nu^{-1/3}f_1^2 & \nu < \nu_{\rm merger}\\ \omega_1\nu^{2/3}f_2^2 & \nu_{\rm merger} \le \nu < \nu_{\rm ringdown}\\ \omega_2 f_3^2 & \nu_{\rm ringdown} \le \nu < \nu_{\rm cut}\end{cases} \tag{B.1}$$

where in the above expression

$$\begin{aligned} f_1 &\equiv f_1(\nu, M, \eta, \chi) = 1 + \alpha_2\nu'^2 + \alpha_3\nu'^3\,,\\ f_2 &\equiv f_2(\nu, M, \eta, \chi) = 1 + \varepsilon_1\nu' + \varepsilon_2\nu'^2\,,\\ f_3 &\equiv f(\nu, \nu_{\rm ringdown}, M, \chi) = \frac{\nu}{1 + \left(\frac{2(\nu-\nu_{\rm ringdown})}{\sigma}\right)^2}\,, \end{aligned} \tag{B.2}$$

with $\nu' = (\pi MG\nu/c^3)^{1/3}$ and

$$\begin{aligned} \alpha_2 &= -\frac{323}{224} + \frac{451}{168}\eta\,,\\ \alpha_3 &= \left(\frac{27}{8} - \frac{11}{6}\eta\right)\chi\,,\\ \varepsilon_1 &= 1.4547\chi - 1.8897\,,\\ \varepsilon_2 &= -1.8153\chi + 1.6557\,. \end{aligned} \tag{B.3}$$

Here, the merge, ringdown and cut frequencies, as well as σ, are approximated by

$$\begin{aligned} \nu_{\rm merger} &= \frac{c^3}{\pi MG}\left(1 - 4.455(1-\chi)^{0.217} + 3.521(1-\chi)^{0.26} + \mu_{\rm merger}\right),\\ \nu_{\rm ringdown} &= \frac{c^3}{\pi MG}\left(\left(1 - 0.63(1-\chi)^{0.3}\right)/2 + \mu_{\rm ringdown}\right),\\ \nu_{\rm cut} &= \frac{c^3}{\pi MG}\left(0.3236 + 0.04894\chi + 0.01346\chi^2 + \mu_{\rm cut}\right),\\ \sigma &= \frac{c^3}{\pi MG}\left(\left(1 - 0.63(1-\chi)^{0.3}\right)(1-\chi)^{0.45}/4 + \mu_\sigma\right), \end{aligned} \tag{B.4}$$

where $\mu_k^{(ij)}$ with $k \in [\text{merger}, \text{ringdown}, \text{cut}, \sigma]$ are computed as

$$\mu_k \equiv \mu_k(\eta,\chi) = \sum_{i=1}^{3}\sum_{j=0}^{\min(3-i,2)} y_k^{(ij)}\eta^i\chi^j\,, \tag{B.5}$$

with y_k coefficents given in Table 1 of Ajith et al. (2011). Finally, ω_1 and ω_2 are normalisation constants that guarantee continuity at $\nu_{\rm merger}$ and $\nu_{\rm ringdown}$, respectively,

$$\begin{aligned} \omega_1 &= \nu_{\rm merger}^{-1} f_1^2(\nu_{\rm merger}, M, \eta, \chi)/f_2^2(\nu_{\rm merger}, M, \eta, \chi)\,,\\ \omega_2 &= \omega_1 \nu_{\rm ringdown}^{-4/3} f_2^2(\nu_{\rm ringdown}, M, \eta, \chi)\,. \end{aligned} \tag{B.6}$$

Appendix C: Power-law-integrated sensitivity curve

Let us assume to have a network of N detectors. The antenna pattern for a detector pair AB is given by

$$\mathcal{A}_{AB}(\mathbf{n}, \nu) = \gamma_{AB}(\mathbf{n})\, e^{-i2\pi\nu\mathbf{n}\cdot\mathbf{b}_{AB}}. \tag{C.1}$$

These functions are already defined in `schNell` (Alonso et al. 2020) for different detector classes. We define the average antenna patter function, often referred to in the literature as average overlap function (i.e. the exponential factor in Eq. (C.1) is often included in the definition of γ_{AB}) as

$$\bar{\gamma}_{AB}(\nu) = \int \frac{\mathcal{A}_{AB}(\nu, \mathbf{n})}{4\pi} d^2\mathbf{n}\,. \tag{C.2}$$

We start from the effective noise power spectral density. In full generality this is given by

$$S_{\rm eff} = \left[\sum_{ABCD}(N_\nu^{-1})^{AB}\bar{\gamma}_{BC}(\nu)(N_\nu^{-1})^{CD}\bar{\gamma}_{DA}(\nu)\right]^{-1/2}, \tag{C.3}$$

for the case of uncorrelated detectors

$$(N_\nu^{-1})^{AB} = \frac{\delta_{AB}}{N_\nu^A}\,, \tag{C.4}$$

where N_ν^A is the noise power spectral density (PSD). In this case Eq. (C.3) simplifies to

$$S_{\rm eff} = \left[\sum_{A=1}^{N}\sum_{B>A}^{N}\frac{\bar{\gamma}_{AB}}{N_\nu^A N_\nu^B}\right]^{-1/2}. \tag{C.5}$$

However, for triangular detectors such as LISA and ET one needs to know both the noise variance (auto-correlation) N_ν^{11}, and the cross-detector covariance N_ν^{12}. We convert Eq. (C.3) to energy density units using

$$S_{\rm eff}(\nu) = \frac{3H_0^2}{2\pi^2}\frac{\Omega_{\rm eff}(\nu)}{\nu^3}\,. \tag{C.6}$$

For a set of power low indices β, we compute the value of the amplitude Ω_β such that the integrated signal to noise ratio ρ has some fixed value, here we assume $\rho = 2$. This is given by

$$\Omega_\beta = \frac{\rho}{\sqrt{2T}}\left[\int_{\nu_{\rm min}}^{\nu_{\rm max}}\frac{(\nu/\nu_{\rm ref})^{2\beta}}{\Omega_{\rm eff}^2(\nu)}\right]^{-1/2} d\nu\,. \tag{C.7}$$

Note that the choice of $\nu_{\rm ref}$ is arbitrary and will not affect the sensitivity curve. For each pair of values (β, Ω_β), we compute $\Omega_{\rm GW} = \Omega_\beta(\nu/\nu_{\rm ref})^\beta$. The envelope is the power low integrated sensitivity curve. Formally it is given by

$$\Omega_{\rm PI}(\nu) = \max_\beta\left[\Omega_\beta\left(\frac{\nu}{\nu_{\rm ref}}\right)^\beta\right]. \tag{C.8}$$

Any line (on a log-log plot) that is tangent to the power-law integrated sensitivity curve corresponds to a gravitational-wave background power-law spectrum with an integrated signal-to-noise ratio $\rho = 2$. This implies that if the curve for a predicted background lies everywhere below the sensitivity curve, then $\rho < 2$ for such a background.

3.2.3 Impact on the current field of research

The fiducial model of astrophysical and primordial BHs presented in Bavera et al. (2022c) predicts a SGWB spectral energy density ratio of $\Omega_{\rm GW}(\nu = 25\,{\rm Hz}) \leq 1.3 \times 10^{-10}$, which lies below the optimistic upper limits of the LVK detectors at design sensitivity. Hence, given our model, the SGWB of merging BBHs will only be accessible by the third-generation of ground-based GW detectors such as the *Einstein Telescope* (Punturo et al. 2010) and the *Cosmic Explorer* (Reitze et al. 2019) and, in the future, also by the space-based detector *LISA* (Amaro-Seoane et al. 2017).

Recently, Périgois et al. (2021b) studied the SGWB of coalescing double compact objects formed from both isolated binary evolution and dynamical formation channels. For merging BBHs, Périgois et al. (2021b)'s model predictions corroborate Bavera et al. (2022c) results that the SGWB will only be accessible by the next generation of GW detectors. Périgois et al. (2021b) also modeled the SGWB contribution of coalescing BH-NS and NS-NS systems in the $[10^{-5}, 10^{3}]\,{\rm Hz}$ frequency regime. When considering the contribution of all coalescing double compact objects and model uncertainties, the authors find that the combined SGWB might be detectable after 8 yr of data collection by the *LIGO-Virgo* GW detectors.

As previously discussed, the SGWB is a powerful tool that can be used to constrain BBH formation at high redshifts. Formation channels other than primordial BHs are predicted to have abundant merger rates at large redshifts ($z \gtrsim 10$), such as population III stars (see §1.3.4). Both Callister et al. (2020) and Atal et al. (2022) discussed how current upper limits on the estimates of the SGWB by the LVK Collaboration put constraints on a phenomenological model for the merger rate up to redshifts higher than the current detector horizon of LVK detectors at $z \lesssim 1$. This different approach does not rely on model selection analysis, and puts direct constraints on the total intrinsic redshift evolution on the BBH merger rate density redshift evolution. The two different methodologies are complementary, while the Bavera et al. (2022c) approach has the advantage of simultaneously constraining the potential contribution of each channel to the total BBH merger rate density.

Finally, we note that the power-law-integrated sensitivity curves for the *Einstein Telescope* and *LISA* detectors presented in Bavera et al. (2022c), computed with the `schNell` code (Alonso et al. 2020), and used to compare the model predictions with GW detectors sensitivities, have been adopted in other publications as a reference (e.g., Balaji et al. 2022). We explicitly point out that, because both detectors are yet to be built, care must be taken when comparing different power-law-integrated sensitivity curves in the literature, as different references assume different detector configurations. Our derived future power-law-integrated sensitivity curves agree with Babak et al. (2021) for *LISA* and Maggiore et al. (2020) for the *Einstein Telescope*.

3.3 The $\chi_{\rm eff} - z$ correlation of field binary black hole mergers and how 3G gravitational-wave detectors can constrain it

3.3.1 A brief introduction

The growing GW source catalog by the LVK Collaboration allows for ever-increasingly precise characterization of the population properties of merging BBHs as well as their correlations (see §1.4.4). Such correlations might be imprinted via evolutionary processes within a single formation pathway or can be caused by the presence of multiple populations arising from distinct formation channels. In this research project, we presented the theoretical existence of a correlation between BH effective spins and BBH merger redshifts for coalescing BHs formed through isolated binary evolution in galactic fields. Similarly to the work presented in Section 3.1, we consider the formation of merging BBHs through the CE, SMT, and CHE evolutionary channels using the updated model of Bavera et al. (2022b, see §4.1). In contrast to the models used in Zevin et al. (2021a), the new variation adopts an improved assumption of the metallicity-dependent star formation history based on the Illustris TNG simulation (Nelson et al. 2015), and excludes initial initial binary configurations which overfill the Roche-lobe at zero-age main sequence from the BBH merger rate normalisation. Both assumptions aim to further improve our estimates of the relative BBH merger rates of the different channels. For a more detailed discussion of the new assumptions, we point to the discussions in Appendix D of Bavera et al. (2022b) and Section 4.1 of Bavera et al. (2021a), respectively.

3.3.2 Manuscript

The conducted study Bavera et al. (2022a) was accepted for publication in *Astronomy & Astrophysics* in June 2022. The arXiv open-access version of the manuscript is presented in the following pages.

Astronomy & Astrophysics manuscript no. aanda
June 28, 2022
©ESO 2022

arXiv:2204.02619v2 [astro-ph.HE] 27 Jun 2022

The $\chi_{\rm eff} - z$ correlation of field binary black hole mergers and how 3G gravitational-wave detectors can constrain it

Simone S. Bavera[1,2], Maya Fishbach[3], Michael Zevin[4,5], Emmanouil Zapartas[1,6], and Tassos Fragos[1,2]

[1] Département d'Astronomie, Université de Genève, Chemin Pegasi 51, CH-1290 Versoix, Switzerland
e-mail: Simone.Bavera@unige.ch
[2] Gravitational Wave Science Center (GWSC), Université de Genève, CH1211 Geneva, Switzerland
[3] Center for Interdisciplinary Exploration and Research in Astrophysics (CIERA) and Department of Physics and Astronomy, Northwestern University, 1800 Sherman Ave, Evanston, IL 60201, USA
[4] Kavli Institute for Cosmological Physics, The University of Chicago, 5640 South Ellis Avenue, Chicago, Illinois 60637, USA
[5] Enrico Fermi Institute, The University of Chicago, 933 East 56th Street, Chicago, Illinois 60637, USA
[6] IAASARS, National Observatory of Athens, Vas. Pavlou and I. Metaxa, Penteli, 15236, Greece

Accepted on June 20, 2022 – ET-0058A-22

ABSTRACT

Understanding the origin of merging binary black holes is currently one of the most pressing quests in astrophysics. We show that if isolated binary evolution dominates the formation mechanism of merging binary black holes, one should expect a correlation between the effective spin parameter, $\chi_{\rm eff}$, and the redshift of the merger, z, of binary black holes. This correlation comes from tidal spin-up systems preferentially forming and merging at higher redshifts due to the combination of weaker orbital expansion from low metallicity stars given their reduced wind mass loss rate, delayed expansion and have smaller maximal radii during the supergiant phase compared to stars at higher metallicity. As a result, these tightly bound systems merge with short inspiral times. Given our fiducial model of isolated binary evolution, we show that the origin of a $\chi_{\rm eff} - z$ correlation in the detectable LIGO–Virgo binary black hole population is different from the intrinsic population, which will become accessible only in the future by third-generation gravitational-wave detectors such as Einstein Telescope and Cosmic Explorer. Given the limited horizon of current gravitational-wave detectors, $z \lesssim 1$, highly rotating black hole mergers in the LIGO–Virgo observed $\chi_{\rm eff} - z$ correlation are dominated by those formed through chemically homogeneous evolution. This is in contrast to the subpopulation of highly rotating black holes in the intrinsic population, which is dominated by tidal spin up following a common evolve event. The different subchannel mixture in the intrinsic and detected population is a direct consequence of detector selection effects, which allows for the typically more massive black holes formed through chemically homogeneous evolution to be observable at larger redshifts and dominate the LIGO–Virgo sample of spinning binary black holes from isolated evolution at $z > 0.4$. Finally, we compare our model predictions with population predictions based on the current catalog of binary black hole mergers and find that current data favor a positive correlation of $\chi_{\rm eff} - z$ as predicted by our model of isolated binary evolution.

Key words. Gravitational waves – Black hole physics – Stars: binaries: close

1. Introduction

The detection of gravitational waves (GWs) from coalescing binary black holes (BBHs) by the LIGO–Virgo–KAGRA (LVK) collaboration has opened a new window for the study of stellar and binary astrophysics (Aasi et al. 2015; Acernese et al. 2015; Akutsu et al. 2021). To date, the LVK collaboration has reported 69 BBH events with a false alarm rate (FAR) smaller than 1 $\rm yr^{-1}$ (Abbott et al. 2019, 2021a,e,c). However, after more than half a decade since the first detection of GWs, the origin of merging BBHs remains an open question. This is not due to a lack of theoretical predictions but rather because of the degeneracy between different formation channel model predictions and unconstrained astrophysical processes of these models (see, e.g., Mandel & Broekgaarden 2022; Zevin et al. 2021).

Improved sensitivity of the LVK detectors and planned third-generation (3G) GW detectors such as the Einstein Telescope (Punturo et al. 2010) and the Cosmic Explorer (Reitze et al. 2019) will increase BBH detection rates by orders of magnitude. A larger sample size allows for detailed investigations of correlations between BBH observable properties (e.g., Maggiore et al. 2020; Tiwari 2021), which might enable different astrophysical formation channels to be distinguished. For example, multiple studies have looked for potential correlations between masses and redshifts (Fishbach et al. 2021; Abbott et al. 2021d), $M_{\rm chirp} - \chi_{\rm eff}$ (Safarzadeh et al. 2020; Abbott et al. 2021d; Franciolini & Pani 2022), $\chi_{\rm eff} - q$ (Callister et al. 2021b; Abbott et al. 2021d), and $\chi_{\rm eff} - z$ (Biscoveanu et al. 2022). The redshift at which the BBH systems merge, z, is a proxy for the distance to the source, $M_{\rm chirp} = (m_1 m_2)^{3/5}/(m_1 + m_2)^{1/5}$ is the chirp mass where m_1 and m_2 are the BH component masses, $q = m_2/m_1$ is the mass ratio defined with $m_2 < m_1$, and $\chi_{\rm eff} = (m_1 \mathbf{a_1} + m_2 \mathbf{a_2})/(m_1 + m_2) \cdot \hat{\mathbf{L}}$ is the effective spin parameter where $\mathbf{a_1}$ and $\mathbf{a_2}$ are the component BH dimensionless spin vectors and $\hat{\mathbf{L}}$ the orbital angular momentum unit vector.

Here, we demonstrate that field-formed BBHs naturally predict a $\chi_{\rm eff} - z$ correlation. Under the assumptions of efficient angular momentum transport inside stars, supported by asteroseismology observational constraints (Kurtz et al. 2014; Deheuvels et al. 2014; Gehan et al. 2018) and current GW observations (Belczynski et al. 2020; Zevin et al. 2021), and Eddington lim-

ited mass accretion efficiency onto BHs, the origin of BH spin in field BBHs arises from tidal interactions during the late BH–Wolf-Rayet (BH-WR) (Qin et al. 2018; Bavera et al. 2020; Fuller & Lu 2022) or WR-WR (Hotokezaka & Piran 2017; Olejak & Belczynski 2021) evolutionary phases or, alternatively, through chemically homogeneous evolution induced by rotational mixing caused from tidal spin-up during the early evolutionary stage of close binaries (Mandel & de Mink 2016; Marchant et al. 2016). From first principles, such correlation should exist since the strength of tidal interaction steeply depends on the orbital separation (Zahn 1977; Hut 1981), and the distribution of orbital separation pre core collapse evolves with redshift. The redshift evolution of the orbital separation distribution originates from the metallicity-dependent stellar winds (Nugis & Lamers 2000; Vink et al. 2001) whose intensity increases as a function of metallicity. Stronger wind-mass loss (during the BH-WR binary evolution phase) widens the binary more efficiently, inhibiting or even canceling the effects of tides. Because the mean metallicity of the Universe decreases as a function of redshift (Madau & Dickinson 2014; Madau & Fragos 2017), we empirically expect an increasing fraction of BBH mergers with highly spinning BH components from tidal spin up as a function of redshift. Additionally, low metallicity stars are more compact at zero-age-main-sequence (ZAMS), expand later in their evolution and have smaller maximal radii during the supergiant phase compare to stars at higher metallicity.

In this paper, we discuss the evolving $\chi_{\rm eff}$ distribution as a function of redshift for field BBHs from the common envelope (CE), stable mass transfer (SMT), and the chemically homogeneous evolution (CHE) channels. The paper is structured as follows. First, we introduce our fiducial model and describe how we quantify the $\chi_{\rm eff} - z$ correlation in Section 2. In Section 3, we present the redshift evolution of the $\chi_{\rm eff}$ distribution for the intrinsic and detectable BBH population as predicted by our model of isolated binary evolution. We then compare our model predictions against the LIGO–Virgo catalog of BBHs. In Section 4, we discuss how potential uncertainties in our model might affect the $\chi_{\rm eff}$ distribution of field BBHs and how a possible change in the mixing fraction of the different channels predicted from isolated binary evolution might impact our results. All findings are summarised in Section 5.

2. Methods

2.1. The binary black-hole population synthesis model

This study uses the isolated binary evolution model presented in Bavera et al. (2022a), calculated using the `POSYDON` framework (Fragos et al. 2022), which accounts for BBH formation through the CE, SMT, and CHE channels. It was shown that this model (i) leads to BBH observable properties consistent with the events of the second LIGO–Virgo GW transient catalog (GWTC-2) (Zevin et al. 2021), (ii) have BBH merger rate estimates compatible with observational constraints of GWTC-2 and, now GWTC-3, (Bavera et al. 2021a; du Buisson et al. 2020), (iii) the subpopulation of highly spinning BBHs might explain the observed population of luminous LGRBs across the cosmic history of the Universe (Bavera et al. 2022a), and (iv) does not violate current upper limit estimates of the stochastic GW background (Bavera et al. 2022b).

In contrast to most rapid population synthesis studies, our simulations accurately model the late tidal spin-up phase of the second-born BH and CHE due to rotational-induced mixing of tidally spun-up ZAMS binaries. The former is done by following the evolution of the binaries from ZAMS up to the formation of the BH-WR systems after the second mass transfer phase with the rapid population synthesis code `COSMIC` (Breivik et al. 2020) and then uses detailed `MESA` (Paxton et al. 2011, 2013, 2015, 2018, 2019) BH-WR simulations (Bavera et al. 2021a) to accurately model the final tidal spin-up phase of the BH-WR system up to central carbon exhaustion of the WR star, as done in Bavera et al. (2022a). The detailed BH-WR simulations self-consistently model the angular momentum evolution of the WR star, which is determined by the interplay of tides, WR stellar wind mass loss, and the evolution of the WR stellar structure.

Massive stars in short orbital periods ($p < 2$ days) at ZAMS with nearly equal masses tidally spin up to be highly rotating, which induces rotational mixing and eventually leads to CHE. Because `COSMIC` cannot model the parameter space leading to CHE as the code cannot accurately follow the back-reaction on the stellar structure and evolution from rotational-induced mixing, CHE is done by matching ZAMS binary conditions to detailed `MESA` simulations targeting CHE according to du Buisson et al. (2020), as implemented in Bavera et al. (2022a).

Given the availability of the stellar profile at carbon exhaustion from the `MESA` simulations, in both cases, the core collapse considers disk formation during the collapse of highly spinning stars. Additionally, we account for mass loss through neutrinos, pulsational pair-instability and pair-instability supernovae (PPISNe & PISNe) (Marchant et al. 2019), and orbital changes resulting from anisotropic mass loss and isotropic neutrinos mass loss (Kalogera 1996), as explained in Appendix D of Bavera et al. (2021a). Because we implement the Fryer et al. (2012) delayed collapse mechanism which assigns zero velocity kicks to collapsing stars with carbon-oxygen cores with masses above 11 $M_\odot$, in practice, we find a statistically small number of systems with $\chi_{\rm eff} < 0$. Alternatively, non-negligible kicks would lead to a more considerable fraction of negative $\chi_{\rm eff}$ (see, e.g., Rodriguez et al. 2016; Gerosa et al. 2018; Callister et al. 2021a; Stevenson 2022). For a detailed explanation of the main features and the physical assumptions made in this model, we refer the reader to the extensive discussions in Bavera et al. (2022a).

2.2. Detection rates

Merger rates are computed by convolving the redshift and metallicity dependent star formation rate as predicted by the Illustris-TNG simulation (Nelson et al. 2015) with the synthetic catalog of merging BBHs obtained by evolving initial ZAMS conditions at different discrete metallicities with `POSYDON`. Following the notation of Bavera et al. (2020, 2021a, 2022a), the BBH detection rate of a GW detector network can be expressed as a Monte Carlo sum over the synthetic population of merging BBHs, i.e., $R_{\rm det} = \sum_{i,j,k} w_{i,j,k}(p_{\rm det})\,{\rm yr}^{-1}$ where $w_{i,j,k}$ is the weighted contribution of a binary k forming at redshift $z_{{\rm f},i}$ and merging at redshift $z_{{\rm m},k} \equiv z_k$. Here the dummy index j indicates the discrete sum over the 30 simulated log-binned metallicity intervals ΔZ_j. The synthetic BBH population is distributed across the cosmic history of the Universe in the center of time bins of size $\Delta t_i = 100\,{\rm Myr}$ with center the formation redshift $z_{{\rm f},i}$. We chose the time bin size to be small enough to ensure the convergence of our results (see Appedinx D of Bavera et al. 2022a for the details of the calculation).

To compute the BBH detection rate of LIGO–Virgo, we account for the detectors' selection effects, $p_{\rm det}$, given the source redshift, BH masses, and spins. Here, we assume a GW detector network configuration composed by LIGO Hanford, LIGO Livingston, and Virgo at O3 `mid-high/late-low` sensitivity

(Abbott et al. 2018) with a network signal-to-noise ratio (S/N) threshold of 12 as implemented in Bavera et al. (2021a).

We also consider the sensitivity of the future 3G ground-based GW detector Einstein Telescope. To approximate the BBH detection rate of the Einstein Telescope, we account for detector selection effects given the source redshift and BH masses assuming a theorized noise-sensitive curve `ET-D` (Hild et al. 2011) as implemented by Barrett et al. (2018) in `COMPAS` (Team COMPAS et al. 2022). Here, we assume a conservative S/N threshold of 12 for the Einstein Telescope, similar to what Hild et al. (2011) assumed. In practice, we find that this assumption sets the horizon of a BBH with $m_1 = m_2 = 15\,M_\odot$ at $z = 10$, namely $p^{\rm ET}_{\rm det}(z = 10, m_1 = m_2 = 15\,M_\odot) \simeq 0$.

Finally, we will distinguish the intrinsic detection rate, i.e., what a GW detector with infinite sensitivity would observe on Earth, using the notation $\tilde{w}_{i,j,k} = w_{i,j,k}(p_{\rm det} = 1)$ as first introduced in Bavera et al. (2022a).

2.3. Relative channel contribution

Once detection rates are defined, we can compute the relative contribution to the intrinsic detection rate from each one of the isolated binary evolution channels (CE, SMT, and CHE) at a given redshift as

$$f_{\rm channel}(z) = \sum_{i,j,k} \left. \frac{\tilde{w}_{i,j,k}(k \,|\, k \in \text{channel})}{\tilde{w}_{i,j,k}} \right|_{z_k \in \Delta z} \tag{1}$$

where $z \in [0, 10]$ is discredited in bins, Δz, taken to have a constant cosmic time width of $\Delta t = 200\,$Myr. Similarly, for the detectable population, we define $f^{\rm det}_{\rm channel}(z)$ where we use $w_{i,j,k}$ instead of $\tilde{w}_{i,j,k}$ in $z \in [0, 1]$ for LIGO–Virgo and $z \in [0, 10]$ for the Einstein Telescope.

2.4. Quantifying the $\chi_{\rm eff} - z$ correlation

To quantify the redshift evolution of the $\chi_{\rm eff}$ distribution, we define $f_{\chi_{\rm eff}>\chi_0}(z)$ to be the fraction of merging BBHs with $\chi_{\rm eff}$ above the arbitrary value χ_0 at a given redshift for the modeled intrinsic BBH population. This quantity is calculated as

$$f_{\chi_{\rm eff}>\chi_0}(z) = \sum_{i,j,k} \left. \frac{\tilde{w}_{i,j,k}(\chi_{{\rm eff},k} | \chi_{\rm eff} > \chi_0)}{\tilde{w}_{i,j,k}} \right|_{z_k \in \Delta z} \tag{2}$$

and, similarly, for the detectable populations, we define $f^{\rm det}_{\chi_{\rm eff}>\chi_0}(z)$ with the same redshift spacing and bounds as in Eq. (1).

3. Results

We now investigate the $\chi_{\rm eff} - z$ correlation of field-formed BBHs and assert its detectability given current and planned GW observatories. We first look at the intrinsic and detectable $\chi_{\rm eff}$ distributions as a function of redshift in our fiducial model, which includes potential contribution from the CE, SMT, and CHE channels described in Section 3.1. We then quantify the intrinsic and detectable $\chi_{\rm eff} - z$ correlation by computing the quantities $f_{\chi_{\rm eff}>\chi_0}(z)$ and $f^{\rm det}_{\chi_{\rm eff}>\chi_0}(z)$ and the relative channel contributions $f_{\rm channel}(z)$ and $f^{\rm det}_{\rm channel}(z)$, in Section 3.2. Finally, we look for evidence of the modeled $f_{\chi_{\rm eff}>\chi_0}(z)$ and $f^{\rm det}_{\chi_{\rm eff}>\chi_0}(z)$ in LIGO–Virgo GWTC-3 data in Section 3.3.

3.1. The $\chi_{\rm eff}$ distribution of field BBHs

First, we show the $\chi_{\rm eff}$ distribution as a function of discrete redshift bins for the intrinsic and detectable BBH populations in Figure 1. At low redshifts, the intrinsic distribution manifests a peak at $\chi_{\rm eff} = 0$ plus an almost flat distribution up to $\chi_{\rm eff} \simeq 0.5$ which then progressively decays. Similarly, the detectable LIGO–Virgo $\chi_{\rm eff}$ distribution also exhibit a similar narrow peak at $\chi_{\rm eff} = 0$. However, in contrast to the intrinsic distribution, we observe a second broader peak at around $\chi_{\rm eff} \simeq 0.35$ with an elongated tail reaching large $\chi_{\rm eff}$ depending on redshift. Both distributions evolve with redshift; with the $\chi_{\rm eff}$ distribution in the intrinsic population showing a slow evolution with redshift, while in the LIGO–Virgo observable population the distribution evolves significantly over the redshift range between 0 and 1. The median $\bar{\chi}_{\rm eff}$ value of the intrinsic distribution grows from $\bar{\chi}^{z\in[0,1]}_{\rm eff} \simeq 0.12$ to $\bar{\chi}^{z\in[5,6]}_{\rm eff} \simeq 0.33$ while for the LIGO–Virgo detectable population the model predicts that $\bar{\chi}^{z\in[0,0.2]}_{\rm eff} \simeq 0.13$ grows to $\bar{\chi}^{z\in[0.8,1]}_{\rm eff} \simeq 0.41$.

The origin of the redshift evolution of the $\chi_{\rm eff}$ distribution is different between the intrinsic and the detectable LIGO–Virgo BBH populations as they probe different redshift horizons, $z \in [0, \infty]$ and $z \in [0, 1]$, respectively. The former encapsulates all merging BBHs at any redshifts and probes the increasing fraction of systems experiencing tidal spin up prior to BBH formation at increasing redshifts (see Section 1). In contrast, the detectable LIGO–Virgo population is biased by the BBH mass-dependent selection effects. More massive BHs can be detected at further distances than lighter BHs. We note that at the highest redshifts detectable by LIGO–Virgo ($z \simeq 1$), only systems with large positive $\chi_{\rm eff}$ are detected due to the increased duration of the inspiral and therefore the S/N. However, the impact of $\chi_{\rm eff}$ on detectability is minor compared to mass selection effects (Ng et al. 2018).

In the following section, we show how the different evolutionary channels CE, SMT, and CHE, which have distinct spin distributions, have different detector horizons due to their inherent mass spectrum. For a discussion about the intrinsic and LIGO–Virgo observable joint distributions of $\chi_{\rm eff}$ vs. $M_{\rm chirp}$, we refer the reader to Figure 1 of Bavera et al. (2022a). Finally, because the Einstein Telescope has a much more distant horizon than current generation GW detectors, the planned GW observatory will be able to detect the majority of the underlying BBH population up to large redshifts, see e.g., $z \in [4, 5]$ in Figure 1. We therefore find that the Einstein Telescope will observe an evolving $\chi_{\rm eff}$ distribution similar to the intrinsic one.

3.2. The $\chi_{\rm eff} - z$ correlation of field BBHs

The $\chi_{\rm eff} - z$ correlation of field BBHs in the intrinsic population, $f_{\chi_{\rm eff}>\chi_0}(z)$, is shown in the leftmost column of Figure 2 for $\chi_0 = 0.2$ and $\chi_0 = 0.5$. In both cases, $f_{\chi_{\rm eff}>\chi_0}(z)$ is monotonically increasing and reaches an asymptotic plateau at high redshifts, $z > 5$ and $z > 8$ for $\chi_0 = 0.2$ and $\chi_0 = 0.5$, respectively. To understand the origin of the $f_{\chi_{\rm eff}>\chi_0}(z)$ shape, we need to look at this quantity channel-wise and consider the relative contribution of each channel $f_{\rm channel}(z)$ to the total BBH intrinsic population. In Figure 2, we can see that at low redshifts the intrinsic BBH merging population is composed of a mix of channels, $f_{\rm CE}(z = 0) = 30\%$, $f_{\rm SMT}(z = 0) = 55\%$, and $f_{\rm CHE}(z = 0) = 15\%$. In contrast, at higher redshifts, the total population of merging BBHs is dominated by the CE channel, with $f_{\rm CE}(z \geq 2) \geq 80\%$.

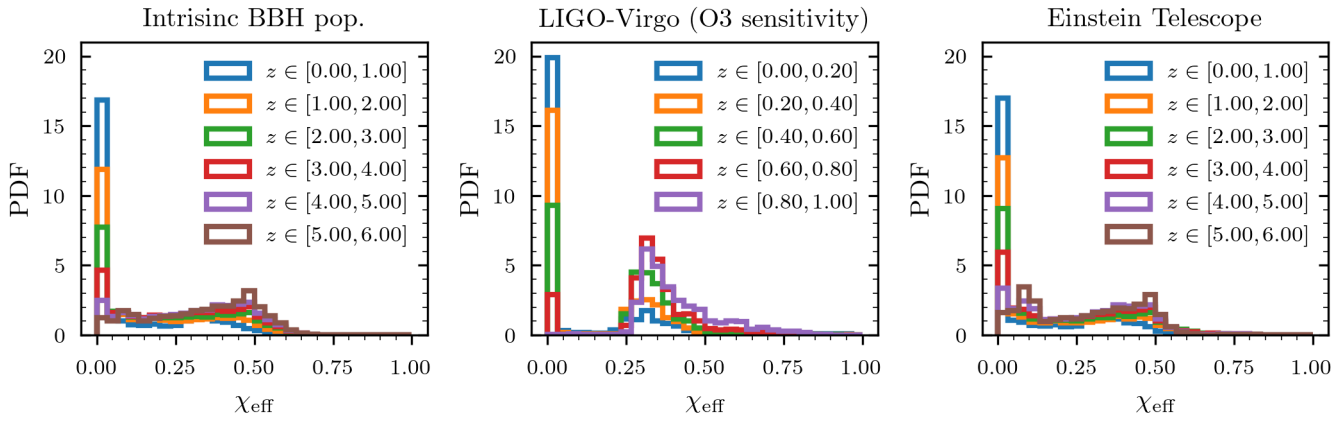

Fig. 1. Effective spin parameter, $\chi_{\rm eff}$, distribution of field BBHs as a function of redshift, z. (*Left*) We show the modeled intrinsic (underlying) population of field merging BBHs. (*Center*) We show the modeled detectable LIGO–Virgo BBH population assuming simulated O3 detector sensitivity selection effects. (*Right*) We show the modeled Einstein Telescope detectable BBH population assuming a forecast detector sensitivity as in Hild et al. (2011). In all cases, the fraction of non-spinning BBHs decreases as a function of redshift, shifting the $\chi_{\rm eff}$ distribution to larger $\chi_{\rm eff}$ values.

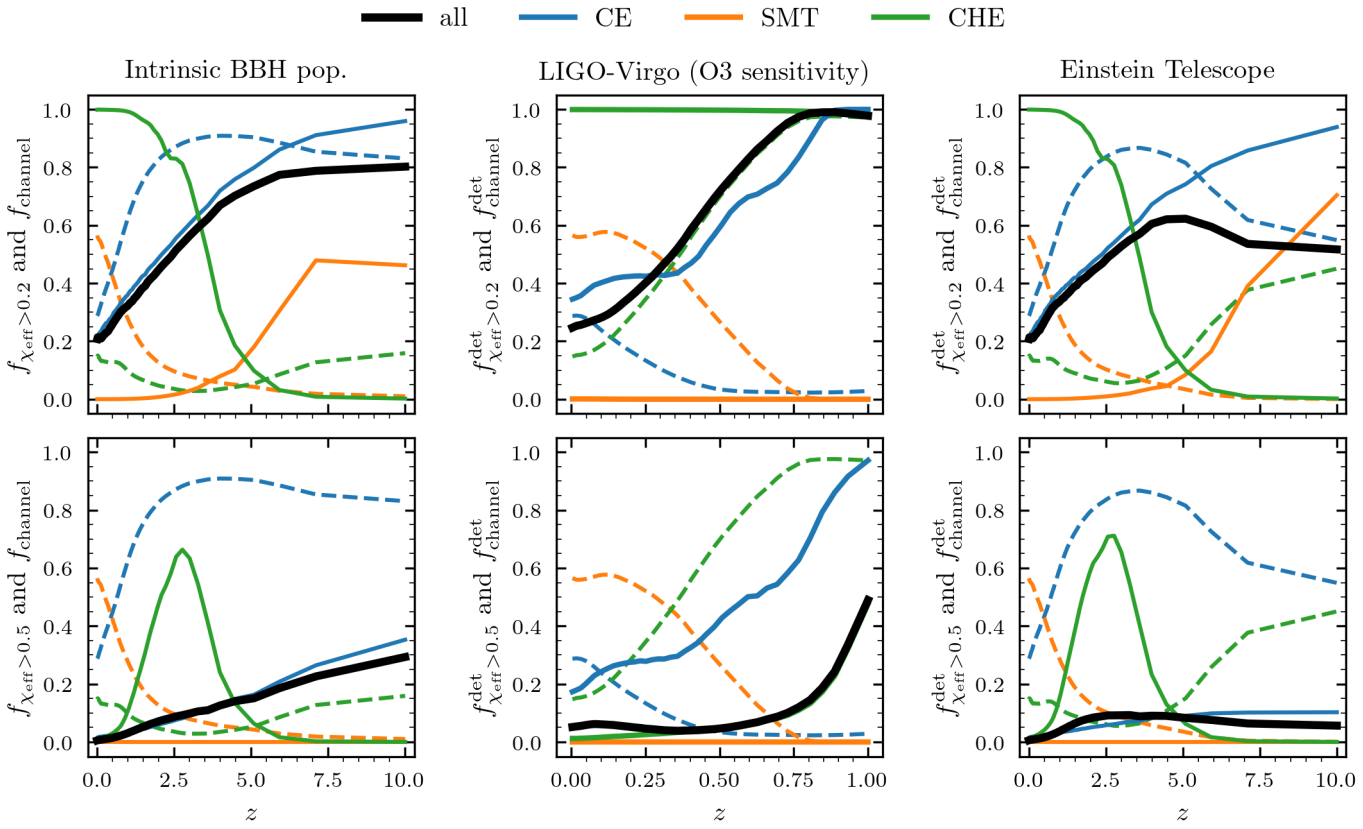

Fig. 2. Fractions of BBHs with $f_{\chi_{\rm eff}>0.2}$ and $f_{\chi_{\rm eff}>0.5}$ as a function of redshift (solid lines), and the relative contribution of each field BBH channel, $f_{\rm channel}$, according to the legend (dashed lines). Black solid lines show the fraction of systems that satisfy a given $\chi_{\rm eff}$ criteria for the combined CE, SMT, and CHE channels with redshift-dependent branching fractions accounted for. (*Left*) We show the modeled intrinsic (underlying) population of field merging BBHs. (*Center*) We show the modeled LIGO–Virgo detectable BBH population assuming simulated O3 detector sensitivity selection effects. (*Right*) We show the modeled Einstein Telescope detectable BBH population assuming forecast detector sensitivity as in Hild et al. (2011). In most cases, the fraction of highly spinning BBHs increases as a function of redshift.

Channel-wise, we can see that $f^{\rm CE}_{\chi_{\rm eff}>\chi_0}(z)$ increases monotonically due to a larger fraction of systems experiencing tidal spin-up as a function of redshift. On average, at higher redshifts, binary systems are born at lower metallicities and experience reduced stellar wind mass loss. Hence, an increased fraction of binaries can maintain short orbital separations and tidal locking during the BH-WR phase. A similar argument can be made for the SMT channel. However, because SMT leads on average to wider BH-WR orbital separations than the CE channel (Bavera et al. 2021a); we find $f^{\rm SMT}_{\chi_{\rm eff}(z)>\chi_0}(z) < f^{\rm CE}_{\chi_{\rm eff}>\chi_0}(z)$ for any redshift. Moreover, we find that at low redshifts $f^{\rm SMT}_{\chi_{\rm eff}>0.2}(z \simeq 0) = 0$,

which steadily increases to $f^{\rm SMT}_{\chi_{\rm eff}>0.2}(z \simeq 10) \simeq 0.5$. On the contrary, $f^{\rm CHE}_{\chi_{\rm eff}>0.2}(z)$ manifests a monotonically decreasing behavior. At low redshifts, $f^{\rm CHE}_{\chi_{\rm eff}>0.2}(z \simeq 0) = 1$, i.e. all BBHs from the CHE channel are fast spinning, while at higher redshifts most systems possess negligible $\chi_{\rm eff}$, with $f^{\rm CHE}_{\chi_{\rm eff}>0.2}(z = 10) = 0$. We also notice that highly rotating CHE systems with $\chi_{\rm eff} > 0.5$ are not present in the local universe $f^{\rm CHE}_{\chi_{\rm eff}>0.5}(z = 0) = 0$ but their presence peaks at $f^{\rm CHE}_{\chi_{\rm eff}>0.5}(z = 2.5) = 0.6$ before decreasing again to $f^{\rm CHE}_{\chi_{\rm eff}>0.5}(z = 10) = 0$. The decreasing fraction of highly rotating CHE systems as a function of redshift is a direct consequence of angular momentum loss due PPISNe. The CHE channel only operates at low metallicities ($Z < 5 \cdot 10^{-3}$) but only binaries with metallicities $Z \leq 10^{-4}$ experience mass loss due to PPISNe (in the considered ZAMS primary masses range $\leq 150\,M_\odot$). During these pulses, the mass ejection from the stellar surface depletes the angular momentum content of these stars and leads to slowly rotating BHs, see Appendix A for more details. Because at large redshifts ($z > 3$) the metallicity-dependent star formation rate leads to an increasing relative fraction of extremely low metallicity binaries, we expect to observe a decreasing $f^{\rm CHE}_{\chi_{\rm eff}>\chi_0}$ as a function of increasing redshift. The three channels combined lead to the monotonically increasing behavior of $f_{\chi_{\rm eff}>\chi_0}(z)$ we see in Figure 2, which is mainly dominated by the CE channel. In Appendix B, we show how our fiducial model predictions would change if one of these three channels would be neglected, see Section 4 for a discussion of these alternative scenarios.

The $\chi_{\rm eff} - z$ correlation of field BBHs in the detectable populations, $f^{\rm det}_{\chi_{\rm eff}>\chi_0}(z)$, is shown in the center and right columns of Figure 2 for LIGO–Virgo detectors at O3 sensitivity and the Einstein Telescope, respectively, for $\chi_0 = 0.2$ and $\chi_0 = 0.5$. For LIGO–Virgo detectability, $f^{\rm det}_{\chi_{\rm eff}>\chi_0}(z)$ is a monotonically increasing function growing from $f^{\rm det}_{\chi_{\rm eff}>0.2}(z = 0) = 0.25$ to $f^{\rm det}_{\chi_{\rm eff}>0.2}(z = 1) = 1$, and $f^{\rm det}_{\chi_{\rm eff}>0.5}(z = 0) = 0.05$ to $f^{\rm det}_{\chi_{\rm eff}>0.5}(z = 1) = 0.5$. On the other hand, the Einstein Telescope $f^{\rm det}_{\chi_{\rm eff}>\chi_0}(z)$ mimics the intrinsic distribution up to $z \simeq 5$ above which it shows a suppression. The similarity between the Einstein Telescope detectable distribution and the underlying distribution is due to the Einstein Telescope GW horizon being much more distant than that of LIGO–Virgo. The suppression for the detectable Einstein Telescope $f^{\rm det}_{\chi_{\rm eff}>\chi_0}(z > 5)$ is caused by the fact that the detector cannot resolve all distant low mass highly rotating BBHs formed through the CE channel. To understand the difference between the LIGO–Virgo $f^{\rm det}_{\chi_{\rm eff}>\chi_0}$ redshift evolution compared to the Einstein Telescope and the intrinsic BBH population, we need to once again consider the relative contribution of each channel. Similar to the intrinsic distribution, for LIGO–Virgo at low redshift, we have a mixed contribution of the different channels, $f^{\rm det}_{\rm CE}(z = 0) = 30\%$, $f^{\rm det}_{\rm SMT}(z = 0) = 55\%$, and $f^{\rm det}_{\rm CHE}(z = 0) = 15\%$. Up to redshift $z = 0.4$ the SMT channel dominates over CE and CHE, above which the CHE channel dominates the LIGO–Virgo detectable population to the point where $f^{\rm det}_{\rm CHE}(z \geq 0.75) \simeq 1$. This is notably different than the behavior of the intrinsic BBH population and is a direct consequence of selection effects favouring high BH masses. The different channels have different BH mass distributions, which result in different observational horizons for each channel. Notably, the CHE channel leads to more massive BBHs compared to CE and SMT, and hence this channel can be probed by LIGO–Virgo at larger redshifts compared to BBHs formed from the CE and SMT channels. The described signature leads to a bimodal distribution of $\chi_{\rm eff}$ in the LIGO-Virgo detectable BBH population in Figure 1.

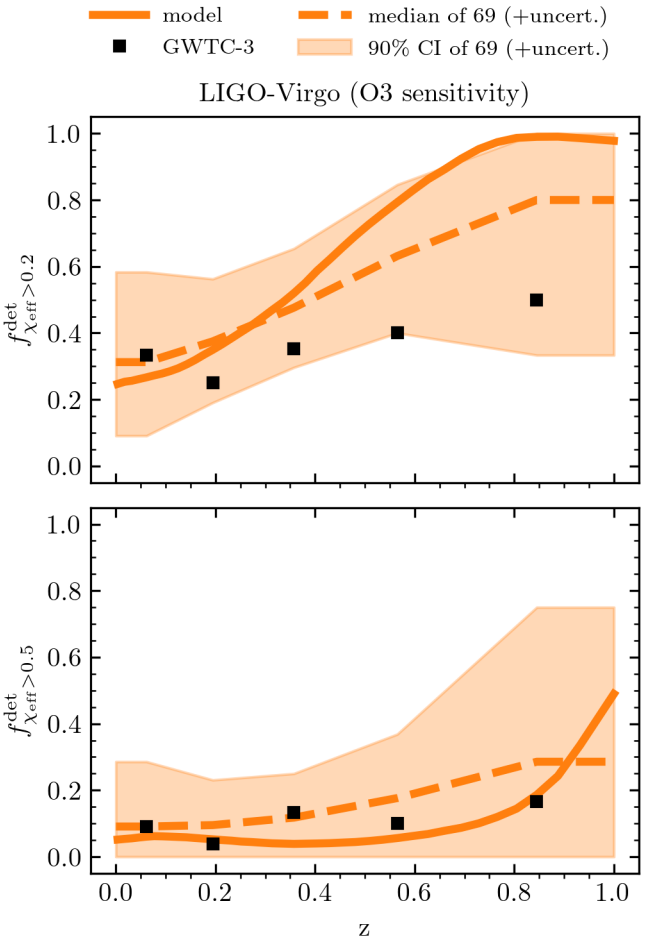

Fig. 3. Modeled and observed fractions of BBHs satisfying $f^{\rm det}_{\chi_{\rm eff}>\chi_0}$ as a function of the redshift. Samples are placed into redshift bins with a bin size of $\Delta t = 1.6$ Gyr. The observed fractions $f^{\rm det}_{\chi_{\rm eff}>0.2}$ and $f^{\rm det}_{\chi_{\rm eff}>0.5}$ are obtained from the median of 10,000 GWTC-3 mock catalog events obtained by sampling the 69 events with FAR $< 1\,{\rm yr}^{-1}$ likelihoods. The modeled prediction for O3 sensitivity is shown with a solid orange line. To compare the model with the data, we generated 10,000 mock catalogs of 69 events, to which we added mock measurements uncertainties. We indicate the median and 90% CI modeled fractions with orange dashed line and shaded area, respectively. Mock uncertainties are obtained from the zero-centered GWTC-3 event likelihoods.

The second peak is mostly composed of BBHs formed through the CHE channel (see Bavera et al. 2022a, for further discussions). This bimodal feature is not present in the $\chi_{\rm eff}$ distribution of the intrinsic BBH population for $z \in [0, 1]$ (see the right panel of Figure 1). Because intrinsically $f^{\rm CHE}_{\chi_{\rm eff}>0.2}(z \leq 1) \simeq 1$, $f^{\rm SMT}_{\chi_{\rm eff}>0.2}(z \leq 1) \simeq 0$, and $f^{\rm CE}_{\chi_{\rm eff}>0.2}(z)$ is monotonically increasing at low redshifts, we also find a monotonically increasing $f^{\rm det}_{\chi_{\rm eff}>0.2}(z)$ function for LIGO–Virgo sensitivity. A similar argument can be made for $f^{\rm det}_{\chi_{\rm eff}>0.5}(z)$, where for low redshifts, it holds that $f^{\rm SMT}_{\chi_{\rm eff}>0.5}(z \leq 1) \simeq 0$ while both $f^{\rm CHE}_{\chi_{\rm eff}>0.5}(z \leq 1)$ and $f^{\rm CE}_{\chi_{\rm eff}>0.5}(z \leq 1)$ are monotonically increasing, which results in $f^{\rm det}_{\chi_{\rm eff}>0.5}(z)$ monotonically increasing. Finally, notice that the CHE dominance is not present in the Einstein Telescope detectable population as the 3G detector, given our theorised sensitivity curve, will be able to observe the entire intrinsic BBH population up to redshift $z \simeq 4 - 5$.

3.3. Evidence for the $\chi_{\rm eff} - z$ correlation in GWTC-3 data

Our model provides a falsifiable prediction that both the underlying and detected high-$\chi_{\rm eff}$ fractions $f_{\chi_{\rm eff}>\chi_0}(z)$ and $f^{\rm det}_{\chi_{\rm eff}>\chi_0}(z)$ for the O3 LIGO–Virgo detector network should increase as a function of redshift if isolated evolution channels dominate the BBH merger rate at low redshifts. We notice that at low redshifts, $z < 1$, the evolution of this fraction for the intrinsic BBH population is mild, but can be amplified by the selection effects of current ground-based detectors. We use BBH events from GWTC-3 to infer both $f_{\chi_{\rm eff}>\chi_0}(z)$ and $f^{\rm det}_{\chi_{\rm eff}>\chi_0}(z)$ and compare them against our model predictions. As in Abbott et al. (2021d), we only consider GWTC-3 events with a false alarm rate (FAR) smaller than $1\,{\rm yr}^{-1}$. In GWTC-3, there are 76 events satisfying this condition from which we exclude the binary neutron stars (NSs) GW170817 and GW190425_081805, the NS-BH systems GW190426_152155, GW200105_162426, GW200115_042309, and the events GW190814, GW190917_114630 in which the less massive compact objects have masses that could be either a massive NS or a BH. Our BBH sample therefore includes a total of 69 BBH events.

We first approximate the observed $f^{\rm det}_{\chi_{\rm eff}>\chi_0}(z)$ for O3, or $f^{\rm GWTC-3}_{\chi_{\rm eff}>\chi_0}(z)$, in a model agnostic way directly from the observed events. We measure $f^{\rm GWTC-3}_{\chi_{\rm eff}>\chi_0}(z)$ on a sample of 10,000 mock GWTC-3 catalogs composed of 69 BBH events. A mock catalog of events, $\{x_i\}_{i=1}^{N=69}$, is generated by drawing a 2D sample, $x_i^k = (\chi_{\rm eff}^k, z^k)_i$, from each event's x_i 2D posterior distribution[1] $p(\chi_{\rm eff}, z|x_i)$ weighted by the inverse of the prior 2D probability density $p(\chi_{\rm eff}, z)$ in order to sample from the likelihood. The events' posterior and prior distributions are publicly released by the LIGO–Virgo collaboration. We approximate the discretely-sampled prior distribution probability density function (PDF) with a 2D kernel density estimator (KDE) trained on the GWTC-3 event samples where the bandwidth of the KDE is set by Scott's rule (Scott 2015) as implemented in the Gaussian KDE function of the `SciPy` Python module (Virtanen et al. 2020). The accuracy of our KDE method to represent the inferred 2D distributions is verified by comparing the histogram of the original samples and samples generated from the KDEs.

To perform a fair comparison of our model with the observations, we need to account for (i) the statistical variance of drawing a sample of 69 events from our model and (ii) to account for the measurement uncertainty for BBH parameters. This is done by generating 10,000 mock samples of 69 events from our model, to which we add mock uncertainty to each event. We approximate measurement uncertainties following a procedure first shown in Bavera et al. (2020) for the $\chi_{\rm eff}$ parameter. Here, we extend this procedure to the 2D case. Mock uncertainties are obtained by shifting another set of 10,000 mock GWTC-3 catalogs by each event's median value $\bar{x}_i = (\bar{\chi}_{\rm eff}, \bar{z})_i$. When the mock uncertainty is added to the model mock samples, we find that this methodology overestimates the measurement uncertainty of events with low redshift of merger. This occurs because this methodology does not assign smaller measurement uncertainties to events with smaller redshifts of merger. Such correlation is expected because of the larger measurement uncertainty for more distant events, which is due to their typically smaller S/N compared to events merging at lower redshifts. In practice, we find that this procedure only leads to 0.6% of the sample having nonphysical values $|\chi_{\rm eff}| > 1$ and 4.2% of systems having nonphysical $z < 0$, which we map back to $|\chi_{\rm eff}| = 1$ or $z = 0$. We claim that this bias is small and does not affect our results as we still find that events with larger $\bar{z}$ have broader $\chi_{\rm eff}$ distributions.

In Figure 3, we show the comparison of the median $f^{\rm GWTC-3}_{\chi_{\rm eff}>\chi_0}(z)$ computed on the sample of mock GWTC-3 catalogs with the model prediction. The GWTC-3 quantity is independently measured for each mock catalog in the interval $z \in [0, 1]$ by counting the events meeting the $\chi_{\rm eff} > \chi_0$ condition in the discrete redshift bin Δz with constant cosmic time bin of size of $\Delta t = 1.6\,{\rm Gyr}$ and then quote the median value at each redshift bin. We then compare our model predictions with the inclusion of mock uncertainties by overlaying the median and 90% CI $f^{\rm det}_{\chi_{\rm eff}>\chi_0}(z)$. We conclude that our model cannot be ruled out given the current GWTC-3 sample. Even though our model 90% CI overlaps with the median inferred GWTC-3 value, a closer comparison with the model median indicates that our model slightly overpredicts the fraction of highly spinning BBHs. This could be due, e.g., to an overprediction of the fraction of highly spinning BBHs formed from the CHE channel which dominates over BBHs formed from the CE channel in the LIGO–Virgo detectable population (see Appendix B) or the existence of an additional channel contributing to the detectable BBH population with small BH spins (see e.g., dynamical formation in globular clusters, Zevin et al. 2021). Other model uncertainties are discussed in Section 4.

We next infer the underlying fraction $f_{\chi_{\rm eff}>\chi_0}(z)$ by fitting a model for the astrophysical BBH population to the GWTC-3 data. We jointly fit the mass (m_1, m_2), spin $\chi_{\rm eff}$, and redshift z distribution, allowing the $\chi_{\rm eff}$ distribution to evolve redshift but for simplicity neglecting possible correlations between other parameters:

$$p_{\rm pop}(m_1, m_2, \chi_{\rm eff}, z) = p(m_1, m_2) p(\chi_{\rm eff} \mid z) p(z). \tag{3}$$

For the mass distribution, $p(m_1, m_2)$, we use the Broken Power Law model from Abbott et al. (2021b) and for the redshift distribution, $p(z)$, we assume the merger rate evolves as a power law in $(1 + z)$ (Fishbach et al. 2018). We model the redshift-dependent spin distribution $p(\chi_{\rm eff} \mid z)$ as a mixture model between a "zero-spin" component, approximated as a narrow Gaussian centered at $\chi_{\rm eff} = 0$ with standard deviation 0.03, and a "positive spin" component, for which we use a Gaussian distribution $\mathcal{N}^{\rm T}$ with mean $0.2 < \mu_p < 0.5$ and standard deviation $0.05 < \sigma_p < 0.5$ truncated to the range [0, 1] to reflect our model predictions. We take the mixture fraction A between the zero and positive spin components to be a logistic function of z (so that it is always within $0 < A < 1$), described by two free parameters, $A(z = 0)$ and $A(z = 1)$. We therefore have

$$p(\chi_{\rm eff} \mid z) = (1 - A(z))\, \mathcal{N}_{\mu=0,\sigma=0.03}(\chi_{\rm eff}) + A(z) \mathcal{N}^{\rm T}(\chi_{\rm eff} \mid \mu_p, \sigma_p), \tag{4}$$

where

$$A(z) = (1 + B \exp(kz))^{-1}, \tag{5}$$

with $B = A^{-1}(z = 0) - 1$ and $k = \log\left(A^{-1}(z = 1) - 1\right) - \log(B)$. We fit for all population parameters by sampling from a hierarchical Bayesian likelihood with PyMC3 (Salvatier et al. 2016) (see e.g., Thrane & Talbot 2019; Mandel et al. 2019; Vitale et al. 2020), using the GWTC-3 detector sensitivity estimates covering the first three observing runs and the parameter estimation

[1] In contrast to the GWTC-3 official analysis, for events in O3b we use posterior samples from the IMRPhenomXPHM analysis as the Mixed and SEOBNRv4PHM analyses do not come with associated prior samples in the 8th November 2021 data release (LIGO Scientific Collaboration, Virgo Collaboration and KAGRA Collaboration 2021c).

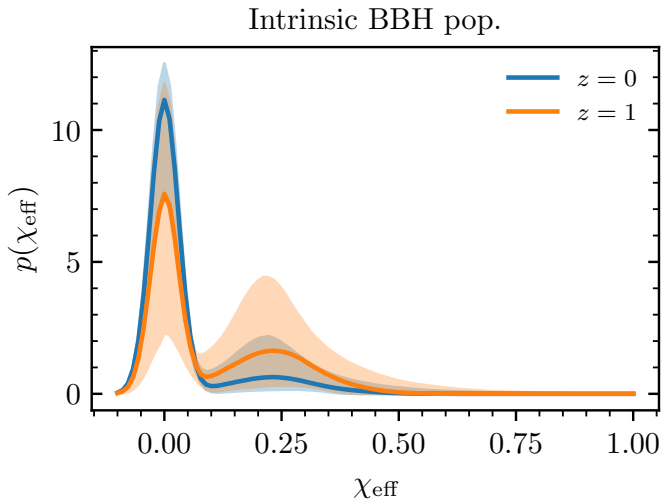

Fig. 4. Underlying $\chi_{\rm eff}$ distribution from fitting the population model of Eq. (4) to the GWTC-3 BBH events. We plot the $\chi_{\rm eff}$ population distribution at two redshift slices, $z = 0$ (blue) and $z = 1$ (orange). Solid lines denote the median and shaded bands denote the 90% CI.

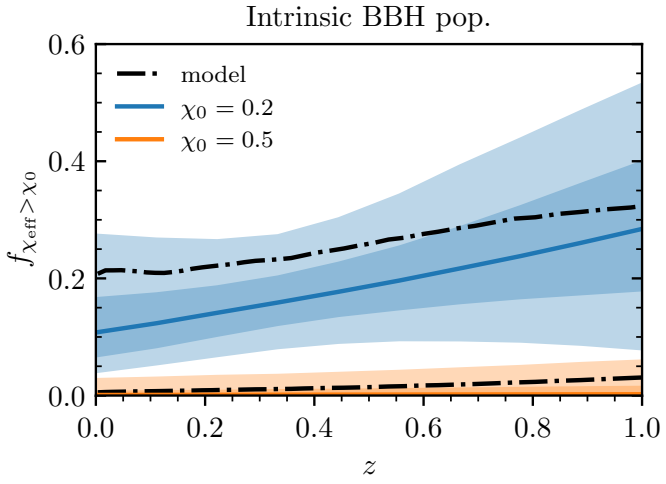

Fig. 5. High-$\chi_{\rm eff}$ fractions in the underlying distribution inferred from the population fit described in Section 3.3, in blue and orange according to the legend. Lighter contour colors indicate larger CIs of 50% and 90%, respectively. The fraction of BBH systems with large positive spins in the underlying population may increase with increasing redshift (credibility 82%), consistent with our model predictions (black). We do not yet have enough BBH events at $z \sim 1$ to accurately measure the $\chi_{\rm eff}$ distribution at high z and therefore cannot confidently conclude that the distribution is evolving.

samples for the GWTC-3 BBH events (LIGO Scientific Collaboration, Virgo Collaboration and KAGRA Collaboration 2019, 2020, 2021a,b,c). We use flat priors on all parameters within their ranges specified above.

The inferred intrinsic $\chi_{\rm eff}$ population distribution at two redshifts, $z = 0$ and $z = 1$, is shown in Figure 4. At $z = 0$ the positive-spin component is constrained to be small, whereas at $z = 1$, the data permit a larger fraction of systems with high $\chi_{\rm eff}$, although the overall constraints are more uncertain and more closely resemble the prior. We can directly compare the underlying high-$\chi_{\rm eff}$ fractions $f_{\chi_{\rm eff}>0.2}$ and $f_{\chi_{\rm eff}>0.5}$ inferred under this fit to the low-redshift $z < 1$ predictions in the leftmost panel of

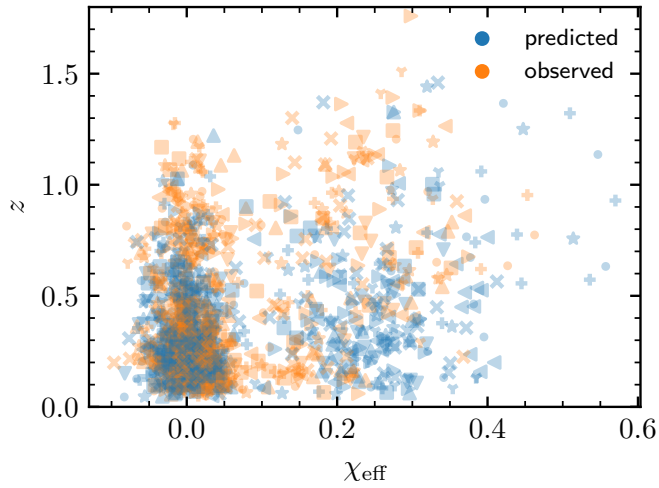

Fig. 6. Redshift and effective spin parameters of the 69 confident BBH observations drawn from the GWTC-3 posteriors (orange; "observed") compared to 69 draws from the inferred distribution fit (blue; "predicted") described in Section 3.3. Each marker shape corresponds to a different set of 69 draws. We plot ten total sets. The inferred model sometimes over-predicts the largest observed $\chi_{\rm eff}$, while the bulk of both observed and predicted draws cover an equivalent portion of the $z - \chi_{\rm eff}$ plane in a comparable abundance, confirming that the inferred model is a good fit for the data.

Figure 2. In Figure 5, we show the inferred intrinsic $f_{\chi_{\rm eff}>0.2}(z)$ and $f_{\chi_{\rm eff}>0.5}(z)$ versus our astrophysical model predictions. The intrinsic fractions are broadly consistent with the model predictions, although the data prefer slightly smaller fractions of large positive $\chi_{\rm eff}$ at all z, similar to the conclusions of Figure 3 regarding the observed fractions. To reiterate, this could be due, e.g., to an overprediction of the contribution of the CHE channel (see Appendix B) or the non-negligible contribution of an additional channel with small BH spins. Other model uncertainties are discussed in Section 4.

We verify the goodness-of-fit of the inferred model by performing posterior predictive checks. Figure 6 shows the comparison between the $(z, \chi_{\rm eff})$ parameters of ten mock GWTC-3 catalogs versus ten sets of 69 events drawn from the inferred model. This test is analogous to the posterior predictive check in Figure 2 of Fishbach et al. (2021). Each of the ten sets (plotted with a different marker size) corresponds to one draw from the inferred population hyperposterior. We reweight the single-event posterior from each GWTC-3 event to the population distribution specified by the hyperposterior draw, and draw one $(z, \chi_{\rm eff})$ sample per event. We then draw a set of 69 predicted events from the same population distribution, conditioned on detection. We can see that the inferred model sometimes over-predicts the largest observed $\chi_{\rm eff}$, while the bulk of both the observed and predicted draws cover an equivalent portion of the $z - \chi_{\rm eff}$ plane in a comparable abundance, confirming that the inferred model is a good fit to the data.

Despite the suggestive hint that $f_{\chi_{\rm eff}>0.2}(z)$ increases with z, we are not yet able to confidently identify that the $\chi_{\rm eff}$ distribution varies with redshift under our parameterization. More precisely, we constrain $f_{\chi_{\rm eff}>0.2}(z = 0.3) > 0.06$ at 99% credibility and find that $f_{\chi_{\rm eff}>0.2}(z)$ increases with increasing redshift at 82% credibility. Our conclusions are consistent with the results of Biscoveanu et al. (2022), who find that the width of the $\chi_{\rm eff}$ distribution likely broadens with increasing redshift, but do not find compelling evidence that the mean $\chi_{\rm eff}$ evolves with red-

shift.[2] Our model for field BBH formation predicts that the mean of the $\chi_{\rm eff}$ distribution must increase with redshift.

We further caution that our phenomenological population fit makes the simplifying assumption that the mass distribution is independent of spin and redshift, despite the fact that we predict a correlation between total mass, $\chi_{\rm eff}$, and redshift. However, given current statistical uncertainties on the inferred intrinsic $f_{\chi_{\rm eff}>\chi_0}(z)$, we do not expect our systematic errors on this inferred quantity from mismodeling the population distribution to be significant. However, with future data it will be important to allow for $\chi_{\rm eff}$ to vary with both mass and redshift in BBH population fits, because as Figures. 1 and 2 show, some of the observed $\chi_{\rm eff}$ evolution in the LIGO-Virgo catalog will be due to an underlying correlation between $\chi_{\rm eff}$ and mass. These conclusions are corroborated by Biscoveanu et al. (2022), who find that the preference for $\chi_{\rm eff}$ to correlate with redshift is stronger than a possible correlation with primary mass, although the two scenarios can be confused for each other.

4. Discussion

In this work, we considered a fiducial model for isolated binary evolution. However, model uncertainties can potentially alter BBH observable distributions and rates (see e.g. Broekgaarden et al. 2021 for an extended overview of such uncertainties). Here, we are interested in astrophysical uncertainties which may alter the $\chi_{\rm eff} - z$ joint distribution.

Our fiducial model assumes efficient angular momentum transport inside stars which leads to the formation of non-spinning first-born BHs for the CE and SMT channels. Alternatively, a less efficient angular momentum transport would lead to non-negligible birth spins (see e.g. some model variations in Belczynski et al. 2020) which would consequently raise our estimated fraction of highly spinning BBHs $f_{\chi_{\rm eff}>\chi_0}(z)$ as the CE and SMT channels dominate the intrinsic BBH population. Nevertheless, current observations are consistent with low birth spins of $\lesssim 0.1$ for isolated BHs (Abbott et al. 2021b,d; Miller et al. 2020; Zevin et al. 2021).

In Bavera et al. (2021a), the impact of mass-transfer physics uncertainties on the $\chi_{\rm eff}$ distribution of BBHs formed from the CE and SMT channels was investigated, accounting for uncertainties in (i) the unknown efficiency of CE ejection in the $\alpha_{\rm CE}-\lambda$ parametrization (see, e.g., Ivanova et al. 2013, for a review), (ii) the SMT accretion efficiency onto BHs, and (iii) the criteria for mass-transfer stability. The first uncertainty directly impacts the relative fraction of highly rotating BBHs in the CE channel as the $\alpha_{\rm CE}$ parameter approximately linearly scales with the orbital separation post CE. For a wide range of $\alpha_{\rm CE} \in [0.2, 5]$, Bavera et al. (2021a) showed that the BBH fraction of systems with $\chi_{\rm eff} > 0.1$ formed from the CE channel can vary from 0.54 to 0.82 where the merger rate density might also vary by up to one order of magnitude. Nevertheless, Bavera et al. (2021a) showed how both $\alpha_{\rm CE}$ extremes include a non-zero fraction of tidally spun-up BBHs in the CE channel. The second uncertainty affects the initially negligible spin of the first-born BH of a BBH systems formed through the SMT channel. In the case of highly super-Eddington accretion efficiency onto BHs, Bavera et al. (2021a) showed how a non-negligible fraction of first-born BHs could be spun up due to accretion. However, in such cases, depending on the super-Eddington accretion efficiency, Bavera et al. (2021a) found a suppression of the SMT merger rate density up to two orders of magnitude. This occurs because conservative mass transfer is less efficient than unconservative mass transfer in leading to tight BH-WR systems, leading to less BBH systems that can merge in a Hubble time. Finally, the third uncertainty directly impacts the relative fraction of systems that undergo either stable or unstable mass transfer and, hence, CE or SMT evolution. We now examine how these uncertainties might affect the presented $\chi_{\rm eff} - z$ correlation.

In the present study, we assumed inefficient CE ejection, namely the model with $\alpha_{\rm CE} = 0.5$ of (Bavera et al. 2021a). A smaller value than what was assumed here would lead to a more significant fraction of tidal spun-up BBHs. Because the CE channel dominates the intrinsic BBH population, such a scenario would increase the predicted quantity $f_{\chi_{\rm eff}>\chi_0}(z)$. In contrast, a more efficient assumption for CE ejection would lead to a smaller fraction of systems that are tidally spun up. For the detectable fraction $f^{\rm det}_{\chi_{\rm eff}>\chi_0}(z)$, we expect a small impact of this assumption as the detectable population of BBHs is dominated by the SMT and CHE channels. Since Bavera et al. (2021a) showed that at $\alpha_{\rm CE} = 5$ there is still a fraction of highly rotating BBHs formed from the CE channel with a median $\bar{\chi}^{\rm CE}_{\rm eff} = 0.16$, we can claim that our model will always display a monotonically increasing $f_{\chi_{\rm eff}>\chi_0}(z)$ regardless of the $\alpha_{\rm CE}$ value in the CE parameterization.

Our fiducial model assumed Eddington limited mass-transfer accretion efficiency onto BHs. A super-Eddington accretion efficiency onto BHs would boost the fraction of highly spinning BBHs formed from the SMT channel, and, hence, positively contribute to larger values of $f_{\chi_{\rm eff}>\chi_0}(z)$ and $f^{\rm det}_{\chi_{\rm eff}>\chi_0}(z)$. However, given that the BBH merger rate from the SMT channel (both detected and intrinsic) drops by up to two orders of magnitude compared to our fiducial model when increasing the allowed accretion rate onto BHs (see Table 1 of Bavera et al. 2021a), we would expect a smaller intrinsic contribution to the SMT channel than the one modeled here.

Both uncertainties (i) and (iii) might lead to a smaller relative contribution of the CE channel to the total BBH population than what is assumed here, where the CE channel dominates the $f_{\chi_{\rm eff}>\chi_0}(z)$ behavior. Moreover, recent studies employing detailed binary simulations point towards an overestimation of systems evolving through and surviving CEs due to envelope stripping during the CE ceasing earlier than what is assumed in rapid population synthesis codes (Fragos et al. 2019; Quast et al. 2019; Klencki et al. 2021; Marchant et al. 2021; Gallegos-Garcia et al. 2021). Therefore, it is natural to ask ourselves what would happen to the modeled $f_{\chi_{\rm eff}>\chi_0}(z)$ fraction if the CE channel is negligible compared to SMT and CHE. In such a scenario, given our model, one would expect that most binaries evolving through CE would either evolve through SMT or successfully emerge from the CE at wider orbital separations. In the first case this would lead to a SMT contribution that is similar or greater than what is modeled here. The second case would lead to a reduced fraction of tidally spun-up CE systems, similarly to the outcome of choosing an efficient $\alpha_{\rm CE}$ values. If the remaining SMT and CHE channels retain a similar fraction of highly spinning BBHs to what is modeled here, one would find $f_{\chi_{\rm eff}>0.2}(z < 4) \simeq 0.2$ which would eventually decay at larger redshifts while the LIGO–Virgo detectable population would still exhibit a monotonically increasing behaviour since the contribution of CE systems to the LIGO–Virgo detectable population is

[2] Our parameterization for the $\chi_{\rm eff}$ distribution is most similar to the model Biscoveanu et al. (2022) consider in their Section 4.3 with the "Prior 3" variation. Biscoveanu et al. (2022) analysis consider alternative models for the parameterization of the redshift evolving $\chi_{\rm eff}$ distribution other than the one assumed here, still reaching similar conclusions.

small ($f^{\rm det}_{\rm CE}(z > 0.25) < 10\%$). In Appendix B, we show how Fig. 2 would change given the omission of the CE channel from our fiducial model. At low redshifts, $z < 1$, we find that the intrinsic fraction $f_{\chi_{\rm eff}>0.2}$ of this alternative model is still consistent with the 90% CI of GWTC-3 constraints shown in Figure 5.

Similar to this last point, we alternatively entertain the idea of what would happen to the $\chi_{\rm eff} - z$ correlation if either the SMT or CHE channels contributions are negligible. This might happen, for example, if we overestimate the contribution of the initial conditions parameter space at low orbital periods that leads to SMT or CHE evolution. In Appendix B, we show that the presented correlation would still be observed. In both cases we still recover monotonically increasing fractions $f_{\chi_{\rm eff}>\chi_0}(z)$ and $f^{\rm det}_{\chi_{\rm eff}>\chi_0}(z)$. However, we note that the model with the omission of the SMT channel manifests a larger, relatively constant $f_{\chi_{\rm eff}>0.2}(z < 1) \simeq 0.45$ which is inconsistent with the 90% CI of GWTC-3 constraints in Figure 5 of $f_{\chi_{\rm eff}>0.2}(z < 0.4) < 0.3$. Finally, we find that the model that excludes the CHE channel has both an intrinsic $f_{\chi_{\rm eff}>\chi_0}$ and LIGO–Virgo detectable $f^{\rm det}_{\chi_{\rm eff}>\chi_0}$ closer to the median GWTC-3 inferred constrains of Figures 3 and 5.

5. Conclusions

In this paper, we investigated the $\chi_{\rm eff} - z$ correlation of field-formed merging BBHs. An increasing fraction of highly spinning BBHs as a function of redshift is expected. At higher redshifts, stars are formed at lower metallicities, experience weaker stellar wind mass loss, and consequently can maintain their short orbital separations and undergo tidal spin up. We quantified this correlation by the fraction of systems with $\chi_{\rm eff} > \chi_0$ as a function of redshift, $f_{\chi_{\rm eff}>\chi_0}(z)$. For our fiducial model of field BBHs, which includes the potential contribution of CE, SMT, and CHE channels, this quantity for $\chi_0 \in [0.2, 0.5]$ shows a monotonically increasing behavior as a function of redshift in the underlying BBH population. We also presented predictions for the detectable $f^{\rm det}_{\chi_{\rm eff}>\chi_0}(z)$ for the LIGO–Virgo detector network at O3 sensitivity and the Einstein Telescope. Because of the smaller horizons of current GW detectors ($z \simeq 1$), the origin of the monotonically increasing LIGO–Virgo $f^{\rm det}_{\chi_{\rm eff}>\chi_0}(z)$ quantity is different than the intrinsic BBH population or that which the Einstein Telescope will observe in the future. Such differences originate from different BH mass distributions of the various channels. On average, highly rotating BBHs formed from the CHE channel are more massive than tidally spun up BBH systems formed from the CE channel. Hence, LIGO–Virgo detector selection effects favour high BH masses and lead to different observational horizons for different channels. We find that, in contrast to the intrinsic distribution where the $\chi_{\rm eff} - z$ correlation is dominated by tidal spun-up BBHs from the CE channel, the CHE channel dominates the LIGO–Virgo detected $\chi_{\rm eff} - z$ correlation above $z > 0.4$.

Finally, assuming isolated binary evolution dominates the detected population of merging BBHs, we performed a model comparison between our fiducial model and LIGO–Virgo GWTC-3 data. We find that current observations favor the prediction of our model that there is a positive correlation between $\chi_{\rm eff}$ and z. Such a conclusion is consistent with the results of Biscoveanu et al. (2022) who found that the width of the $\chi_{\rm eff}$ distribution likely broadens with increasing redshift, event though they did not find compelling evidence in favor of a redshift evolving mean $\chi_{\rm eff}$. Additionally, our model prediction at low redshifts of a large zero-spin BBH population with an additional subpopulation of systems with spin vectors preferentially aligned to the orbital angular momentum is in agreement with Roulet et al. (2021) and Galaudage et al. (2021) reanalysis of GWTC-2 events. Moreover, our results are consistent with the findings that investigated field BBH observable properties and rates (Bavera et al. 2020, 2021a), multi-channel model selection with GWTC-2 data (Zevin et al. 2021), potential constraints from LGRBs (Bavera et al. 2022a), and the current upper limits of the stochastic GW background (Bavera et al. 2022b).

Considering future 3G GW detector facilities, we demonstrated that if isolated binary evolution plays a dominant role in the formation of merging BBHs in the Universe, 3G GW detectors will observe more of the merging BBHs in the Universe and a $\chi_{\rm eff} - z$ correlation that is more indicative of the behavior of the underlying population.

Acknowledgements. We thank Sylvia Biscoveanu and Christopher Berry for useful comments on this manuscript. This work was supported by the Swiss National Science Foundation Professorship grant (project number PP00P2_176868). MF and MZ are supported by NASA through NASA Hubble Fellowship grants HST-HF2-51455.001-A and HST-HF2-51474.001-A awarded by the Space Telescope Science Institute, which is operated by the Association of Universities for Research in Astronomy, Incorporated, under NASA contract NAS5-26555. EZ acknowledges funding support from the European Research Council (ERC) under the European Union's Horizon 2020 research and innovation programme (Grant agreement No. 772086). This material is based upon work supported by NSF's LIGO Laboratory which is a major facility fully funded by the National Science Foundation. All figures were made with the open-source Python module `Matplotlib` (Hunter 2007). This research made use of the python modules `Astropy` (Price-Whelan et al. 2018), `iPhyton` (Pérez & Granger 2007), `Numpy` (Harris et al. 2020) and `SciPy` (Virtanen et al. 2020).

References

Aasi, J., Abbott, B. P., Abbott, R., et al. 2015, Classical and Quantum Gravity, 32, 074001
Abbott, B. P., Abbott, R., Abbott, T. D., et al. 2018, Living Reviews in Relativity, 21, 3
Abbott, B. P., Abbott, R., Abbott, T. D., et al. 2019, Physical Review X, 9, 031040
Abbott, R., Abbott, T. D., Abraham, S., et al. 2021a, Physical Review X, 11, 021053
Abbott, R., Abbott, T. D., Abraham, S., et al. 2021b, ApJ, 913, L7
Abbott, R., Abbott, T. D., Acernese, F., et al. 2021c, arXiv e-prints, arXiv:2111.03606
Abbott, R., Abbott, T. D., Acernese, F., et al. 2021d, arXiv e-prints, arXiv:2111.03634
Abbott, R., Abbott, T. D., Acernese, F., et al. 2021e, arXiv e-prints, arXiv:2108.01045
Acernese, F., Agathos, M., Agatsuma, K., et al. 2015, Classical and Quantum Gravity, 32, 024001
Akutsu, T., Ando, M., Arai, K., et al. 2021, Progress of Theoretical and Experimental Physics, 2021, 05A101
Barrett, J. W., Gaebel, S. M., Neijssel, C. J., et al. 2018, MNRAS, 477, 4685
Bavera, S. S., Fragos, T., Qin, Y., et al. 2020, A&A, 635, A97
Bavera, S. S., Fragos, T., Zapartas, E., et al. 2022a, A&A, 657, L8
Bavera, S. S., Fragos, T., Zevin, M., et al. 2021a, A&A, 647, A153
Bavera, S. S., Franciolini, G., Cusin, G., et al. 2022b, A&A, 660, A26
Bavera, S. S., Zevin, M., & Fragos, T. 2021b, Research Notes of the American Astronomical Society, 5, 127
Belczynski, K., Klencki, J., Fields, C. E., et al. 2020, A&A, 636, A104
Biscoveanu, S., Callister, T. A., Haster, C.-J., et al. 2022, ApJ, 932, L19
Breivik, K., Coughlin, S., Zevin, M., et al. 2020, ApJ, 898, 71
Broekgaarden, F. S., Berger, E., Stevenson, S., et al. 2021, arXiv e-prints, arXiv:2112.05763
Callister, T. A., Farr, W. M., & Renzo, M. 2021a, ApJ, 920, 157
Callister, T. A., Haster, C.-J., Ng, K. K. Y., Vitale, S., & Farr, W. M. 2021b, ApJ, 922, L5
Deheuvels, S., Doğan, G., Goupil, M. J., et al. 2014, A&A, 564, A27
du Buisson, L., Marchant, P., Podsiadlowski, P., et al. 2020, MNRAS, 499, 5941
Fishbach, M., Doctor, Z., Callister, T., et al. 2021, ApJ, 912, 98
Fishbach, M., Holz, D. E., & Farr, W. M. 2018, ApJ, 863, L41
Fragos, T., Andrews, J. J., Bavera, S. S., et al. 2022, arXiv e-prints, arXiv:2202.05892
Fragos, T., Andrews, J. J., Ramirez-Ruiz, E., et al. 2019, ApJ, 883, L45

Franciolini, G. & Pani, P. 2022, arXiv e-prints, arXiv:2201.13098
Fryer, C. L., Belczynski, K., Wiktorowicz, G., et al. 2012, ApJ, 749, 91
Fuller, J. & Lu, W. 2022, MNRAS, 511, 3951
Galaudage, S., Talbot, C., Nagar, T., et al. 2021, ApJ, 921, L15
Gallegos-Garcia, M., Berry, C. P. L., Marchant, P., & Kalogera, V. 2021, ApJ, 922, 110
Gehan, C., Mosser, B., Michel, E., Samadi, R., & Kallinger, T. 2018, A&A, 616, A24
Gerosa, D., Berti, E., O'Shaughnessy, R., et al. 2018, Phys. Rev. D, 98, 084036
Harris, C. R., Millman, K. J., van der Walt, S. J., et al. 2020, Nature, 585, 357
Hild, S., Abernathy, M., Acernese, F., et al. 2011, Classical and Quantum Gravity, 28, 094013
Hotokezaka, K. & Piran, T. 2017, ApJ, 842, 111
Hunter, J. D. 2007, Computing in Science & Engineering, 9, 90
Hut, P. 1981, A&A, 99, 126
Ivanova, N., Justham, S., Chen, X., et al. 2013, A&A Rev., 21, 59
Kalogera, V. 1996, ApJ, 471, 352
Klencki, J., Nelemans, G., Istrate, A. G., & Chruslinska, M. 2021, A&A, 645, A54
Kurtz, D. W., Saio, H., Takata, M., et al. 2014, MNRAS, 444, 102
LIGO Scientific Collaboration, Virgo Collaboration and KAGRA Collaboration. 2019, Parameter estimation sample release for GWTC-1, https://dcc.ligo.org/LIGO-P1800370/public
LIGO Scientific Collaboration, Virgo Collaboration and KAGRA Collaboration. 2020, GWTC-2 Data Release: Parameter Estimation Samples and Skymaps, https://dcc.ligo.org/LIGO-P2000223/public/
LIGO Scientific Collaboration, Virgo Collaboration and KAGRA Collaboration. 2021a, GWTC-2.1: Deep Extended Catalog of Compact Binary Coalescences Observed by LIGO and Virgo During the First Half of the Third Observing Run - Parameter Estimation Data Release, https://doi.org/10.5281/zenodo.5117703
LIGO Scientific Collaboration, Virgo Collaboration and KAGRA Collaboration. 2021b, GWTC-3: Compact Binary Coalescences Observed by LIGO and Virgo During the Second Part of the Third Observing Run — O1+O2+O3 Search Sensitivity Estimates, https://doi.org/10.5281/zenodo.5636816
LIGO Scientific Collaboration, Virgo Collaboration and KAGRA Collaboration. 2021c, GWTC-3: Compact Binary Coalescences Observed by LIGO and Virgo During the Second Part of the Third Observing Run — Parameter estimation data release, https://doi.org/10.5281/zenodo.5546663
Madau, P. & Dickinson, M. 2014, ARA&A, 52, 415
Madau, P. & Fragos, T. 2017, ApJ, 840, 39
Maggiore, M., Van Den Broeck, C., Bartolo, N., et al. 2020, J. Cosmology Astropart. Phys., 2020, 050
Mandel, I. & Broekgaarden, F. S. 2022, Living Reviews in Relativity, 25, 1
Mandel, I. & de Mink, S. E. 2016, MNRAS, 458, 2634
Mandel, I., Farr, W. M., & Gair, J. R. 2019, MNRAS, 486, 1086
Marchant, P., Langer, N., Podsiadlowski, P., Tauris, T. M., & Moriya, T. J. 2016, A&A, 588, A50
Marchant, P., Pappas, K. M. W., Gallegos-Garcia, M., et al. 2021, A&A, 650, A107
Marchant, P., Renzo, M., Farmer, R., et al. 2019, ApJ, 882, 36
Miller, S., Callister, T. A., & Farr, W. M. 2020, ApJ, 895, 128
Nelson, D., Pillepich, A., Genel, S., et al. 2015, Astronomy and Computing, 13, 12
Ng, K. K. Y., Vitale, S., Zimmerman, A., et al. 2018, Phys. Rev. D, 98, 083007
Nugis, T. & Lamers, H. J. G. L. M. 2000, A&A, 360, 227
Olejak, A. & Belczynski, K. 2021, ApJ, 921, L2
Paxton, B., Bildsten, L., Dotter, A., et al. 2011, ApJS, 192, 3
Paxton, B., Cantiello, M., Arras, P., et al. 2013, ApJS, 208, 4
Paxton, B., Marchant, P., Schwab, J., et al. 2015, ApJS, 220, 15
Paxton, B., Schwab, J., Bauer, E. B., et al. 2018, ApJS, 234, 34
Paxton, B., Smolec, R., Schwab, J., et al. 2019, ApJS, 243, 10
Pérez, F. & Granger, B. E. 2007, Computing in Science and Engineering, 9, 21
Price-Whelan, A. M., Sipőcz, B., Günther, H., et al. 2018, The Astronomical Journal, 156, 123
Punturo, M., Abernathy, M., Acernese, F., et al. 2010, Classical and Quantum Gravity, 27, 194002
Qin, Y., Fragos, T., Meynet, G., et al. 2018, A&A, 616, A28
Quast, M., Langer, N., & Tauris, T. M. 2019, A&A, 628, A19
Reitze, D., Adhikari, R. X., Ballmer, S., et al. 2019, in Bulletin of the American Astronomical Society, Vol. 51, 35
Rodriguez, C. L., Zevin, M., Pankow, C., Kalogera, V., & Rasio, F. A. 2016, ApJ, 832, L2
Roulet, J., Chia, H. S., Olsen, S., et al. 2021, Phys. Rev. D, 104, 083010
Safarzadeh, M., Farr, W. M., & Ramirez-Ruiz, E. 2020, ApJ, 894, 129
Salvatier, J., Wiecki, T. V., & Fonnesbeck, C. 2016, PeerJ Computer Science, 2, e55
Scott, D. W. 2015, Multivariate Density Estimation: Theory, Practice, and Visualization
Stevenson, S. 2022, ApJ, 926, L32
Team COMPAS, :, Riley, J., et al. 2022, ApJS, 258, 34
Thrane, E. & Talbot, C. 2019, PASA, 36, e010
Tiwari, V. 2021, arXiv e-prints, arXiv:2111.13991
Vink, J. S., de Koter, A., & Lamers, H. J. G. L. M. 2001, A&A, 369, 574
Virtanen, P., Gommers, R., Oliphant, T. E., et al. 2020, Nature Methods, 17, 261
Vitale, S., Gerosa, D., Farr, W. M., & Taylor, S. R. 2020, arXiv e-prints, arXiv:2007.05579
Zahn, J. P. 1977, A&A, 500, 121
Zevin, M. & Bavera, S. S. 2022, arXiv e-prints, arXiv:2203.02515
Zevin, M., Bavera, S. S., Berry, C. P. L., et al. 2021, ApJ, 910, 152

Appendix A: Angular momentum loss due to pulsational pair-instability supernovae

Mass loss due to PPISNe can play a role in depleting the angular-momentum reservoir of a collapsing star. Because the pulsations carry away the outer layers of the stars that carry most of the angular-momentum content of the star, this phenomena could have a major impact in reducing the spins of massive BHs.

The impact of PPISNe on the spin of the second-born BH of tidally spun up BH-WR systems was briefly discussed in Zevin & Bavera (2022). For tidally spun-up systems with orbital periods $p < 1$ day and WR stellar masses of $M_{\rm WR} > 40\,M_\odot$ at carbon depletion, the first panel of Figure 1 in Bavera et al. (2021b) shows a small suppression of the second-born BH spin obtained from the WR stellar profile collapse of `MESA` BH-WR simulations from Bavera et al. (2021a). Because WR stellar wind rates scale as a function of metallicity (Vink et al. 2001), only binaries born at low metallicities (prevalently formed at high redshifts) will evolve to have WR stars in such a mass regime. Hence, for the CE channel, we expect this phenomena to have a small impact as on average the channel operates at smaller WR stellar mass. For the SMT channel, we find that in practice this phenomena is relevant only at large redshifts as this channel leads on average to more massive BH-WR star systems compared to the CE channel, resulting in a $f^{\rm SMT}_{\chi_{\rm eff}>0.2}(z \geq 7) \simeq 0.45$ plateau in Figure 2.

In contrast, we find that the impact of PPISNe onto the spin of BHs formed from the CHE channel is not negligible as this channel only operates at low metallicities ($Z < 5 \cdot 10^{-3}$) and for massive stars. For metallicities $Z \leq 10^{-4}$ the entire sample of merging BBHs evolving through the CHE channel is formed by stars with ZAMS primary masses $40\,M_\odot \lesssim M_1 \lesssim 70\,M_\odot$ which undergo PPISN. This occurs because at these low metallicities stellar wind mass loss is weaker compared to larger metallicities, and the stars reach the mass regime of PPISN, see Figure A1 of du Buisson et al. (2020). We note that in our fiducial model we do not simulate BBH formation above ZAMS primary masses of $150\,M_\odot$, hence Figure A1 of du Buisson et al. (2020) should be read accordingly. On the other hand, the $10^{-4} < Z \leq 5 \cdot 10^{-3}$ parameter space leading to the formation of merging BBHs allows for direct collapse and, hence, conservation of angular momentum during the stellar profile collapse (with the exception of extremely highly rotating stars inducing disk formation). In Figure A.1, we show the ZAMS binary conditions leading to merging BBH formation through the CHE channel, showing their final primary BH spins as a function of ZAMS initial orbital period and primary mass which can be directly compared to Figure A1 of du Buisson et al. (2020). We can see that for $Z \leq 10^{-4}$ and ZAMS primary masses $\lesssim 70\,M_\odot$ the entire population of BBHs is composed of BBH systems with negligible spins as they have lost their high stellar angular momentum due to PPISN mass ejection. The gap in the parameter space at $1.8 \lesssim \log_{10}(M_1/M_\odot) \lesssim 2.1$ for $Z \leq 10^{-4}$ binaries in Figure A.1 is due to pair-instability supernovae leaving no remnant. For binaries with $Z > 10^{-4}$, this portion of the parameter space is present at larger ZAMS primary masses and orbital periods (see Figure A1 of du Buisson et al. 2020). The impact of PPISN onto the BH spin of BBHs formed from the CHE channel at extremely low metallicities explains the monotonically decreasing behaviour of $f^{\rm CHE}_{\chi_{\rm eff}>\chi_0}(z)$ as a function of increasing redshift as the Universe forms more stars at these low metallicities.

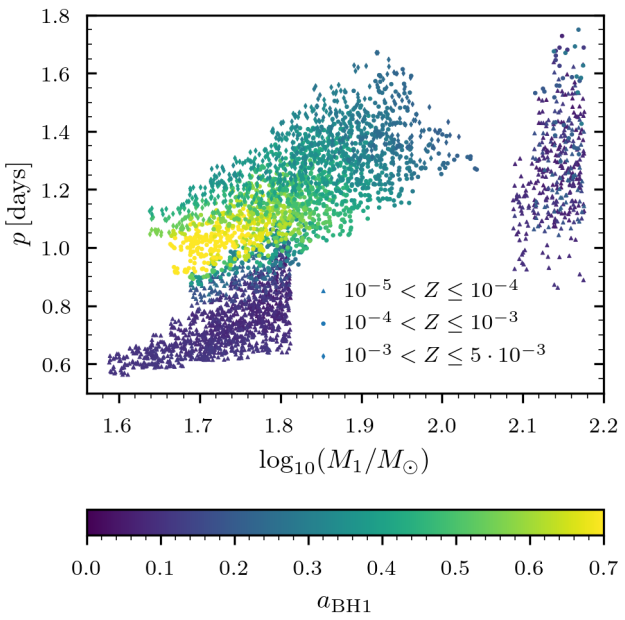

Fig. A.1. Distribution of ZAMS binary orbital period, p, primary mass, M_1, and the final primary BH spin of systems evolving thorough the CHE channel to become merging BBHs in our fiducial model. In this sample we only include BBH systems with inspiral times less than the age of the Universe. Different markers differentiate metallicity regimes according to the legend. For visualisation purposes, we capped the color bar at $a_{\rm BH1} = 0.7$ even though there are BHs approaching the general relativistic limit $a_{\rm BH1} = 1$. Though binaries with $p < 1$ day do tidally spin up and evolve through CHE, they later undergo mass loss due to PPISN which depletes the WR star of its angular momentum reservoir.

Appendix B: The $\chi_{\rm eff} - z$ correlation with channel exclusion

In this appendix section we show the impact to our results presented in Figure 2 in the hypothetical scenario that one of the three channels considered has a negligible contribution to the formation of merging BBHs.

First, let us consider neglecting the CE channel. Factors that might lead to this hypothetical scenario are discussed in Section 4. Figure B.1 shows how the results presented in Figure 2 would change under this assumption. In this alternative model, the intrinsic fraction $f_{\chi_{\rm eff}>0.2}(z)$ is mainly supported by highly spinning BBHs formed from the CHE channel at $z < 5$, while at larger redshift the SMT channel contributes with a larger fraction of tidally spun-up BHs. However, we notice that in contrast to our fiducial model the intrinsic fraction $f_{\chi_{\rm eff}>0.2}(z)$ is monotonically decreasing. On the other hand the LIGO–Virgo detectable BBH population shows a similar behaviour as the fiducial model. This occurs as the CE channel contribution to the LIGO–Virgo detectable population is small compared to the SMT and CHE channels, since the CE channel leads to less massive BBHs (cf. Figure 2).

Second, let us consider neglecting the SMT channel. Figure B.2 shows how the results presented in Figure 2 would change under this assumption. Because at low redshifts ($z < 5$) the SMT channel mostly contributes to the intrinsic distribution with non-spinning BBHs, this alternative scenario leads to a larger $f_{\chi_{\rm eff}>0.2}(z)$ fraction compared to the fiducial model. This hypothetical scenario would result in a LIGO–Virgo detectable

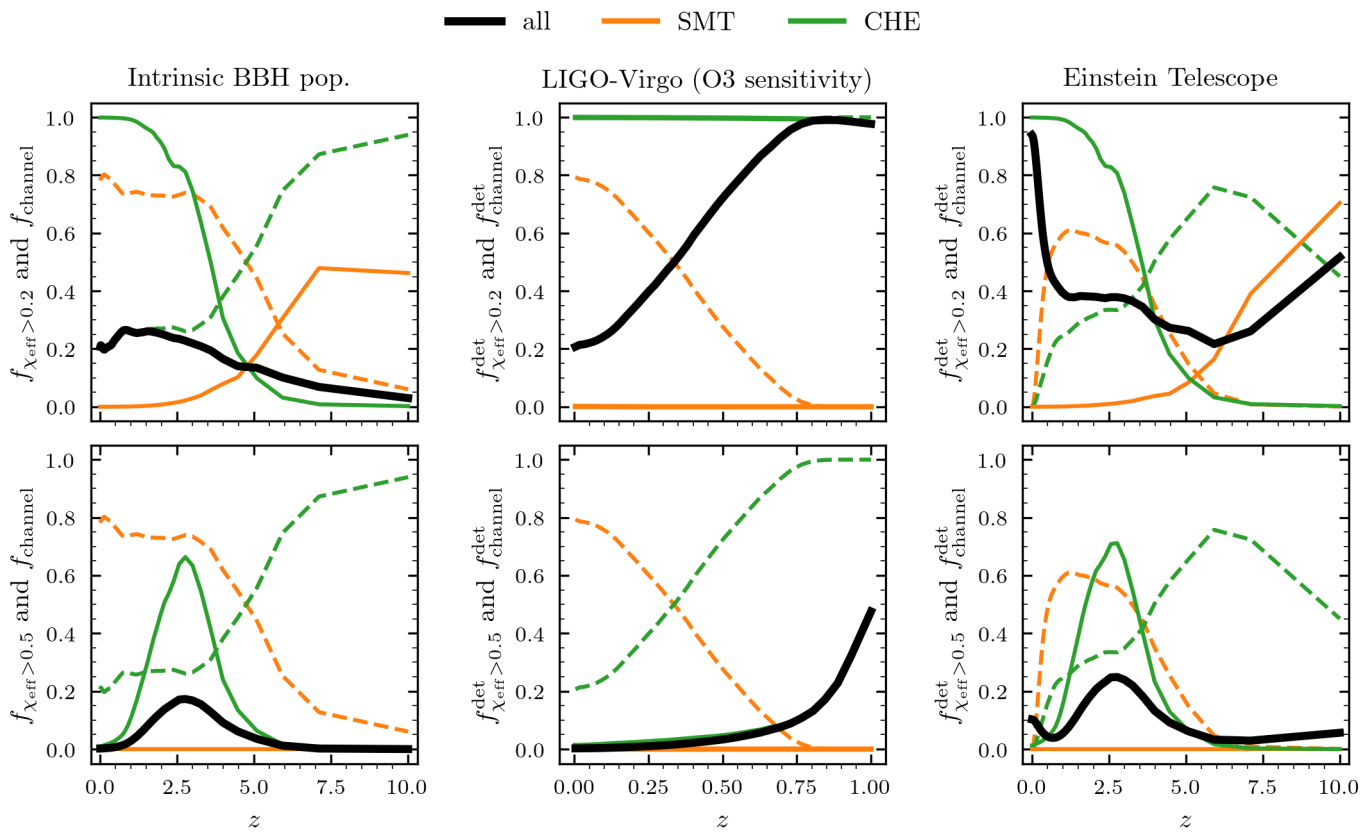

Fig. B.1. Same as Figure 2 but the model of isolated binary evolution excludes the CE channel.

BBH population $f^{\rm det}_{\chi_{\rm eff}>0.2}(z) \gtrsim 0.6$, in tension with GWTC-3 observations.

Last, let us consider neglecting the CHE channel. As discussed in Section 4 this might occur, for example, in the hypothetical case where the abundance of binary stars at ZAMS with short orbital periods ($p < 2$ days) is overestimated. This alternative model is presented in Figure B.3. We can see that the $f_{\chi_{\rm eff}>\chi_0}(z)$ distribution is similar to what is presented in Figure 2. This is explained by the fact that for any redshift the CHE channel has a small contribution to the intrinsic population of merging BBHs at $f_{\rm CHE}(z) < 0.2$. On The other hand the LIGO–Virgo detectable $f^{\rm det}_{\chi_{\rm eff}>\chi_0}(z)$ manifests an almost flat behaviour up to $z = 0.6$ above which it sharply increases to reach unity at $z \simeq 1$. This sharp monotonic increase of $f^{\rm det}_{\chi_{\rm eff}>\chi_0}(z > 0.6)$ is due to the contribution of tidally spun up BBHs formed from the CE channel completely dominates over BBHs formed from the SMT channel at $z > 0.75$, as $f^{\rm det}_{\rm CE}(z > 0.75) \gg f^{\rm det}_{\rm SMT}(z > 0.75)$.

A comparison between the intrinsic $f_{\chi_{\rm eff}>0.2}(z)$ when excluding one of the three field channels and the inferred distribution given the phenomenological model presented in Eq. (4) is shown in Figure B.4. We can see that a model without the CHE channel is closer to the median inferred intrinsic fraction of $f_{\chi_{\rm eff}>0.2}$ than the fiducial model. Additionally, the model excluding the SMT channel is incompatible with the 90% CI of the inferred fraction as it overpredicts the fraction of highly rotating BBHs.

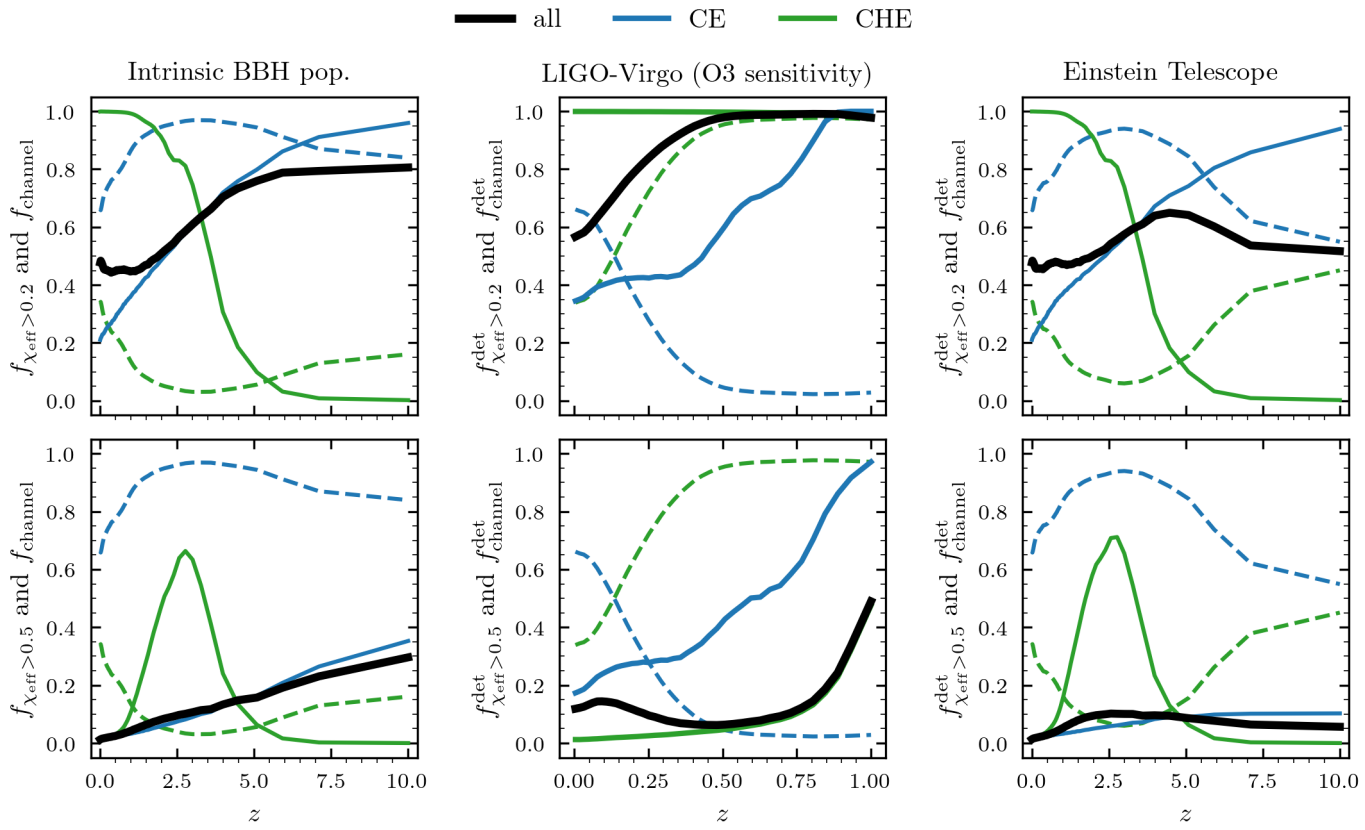

Fig. B.2. Same as Figure 2 but the model of isolated binary evolution excludes the SMT channel.

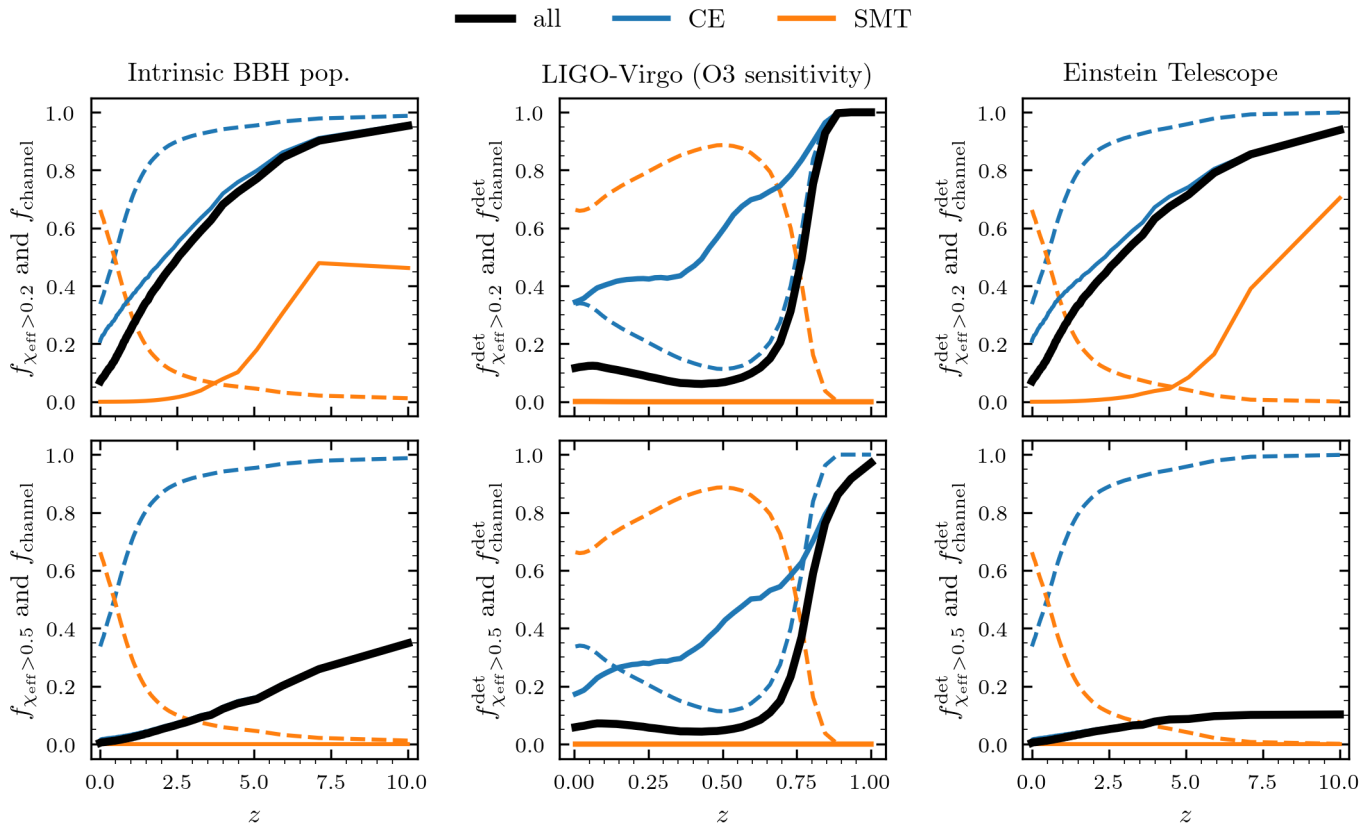

Fig. B.3. Same as Figure 2 but the model of isolated binary evolution excludes the CHE channel.

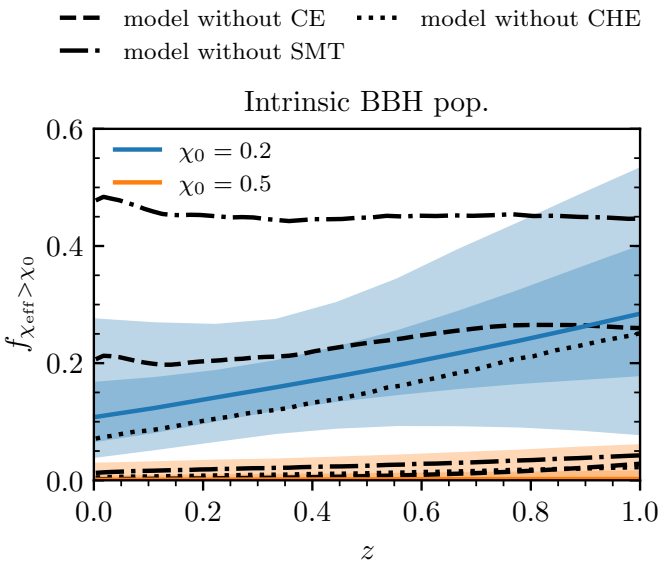

Fig. B.4. Same as Figure 5 but we show the models excluding one of the three channels according to the legend.

3.3.3 Impact on the current field of research

The presented redshift evolution of the $\chi_{\rm eff}$ distribution for BBH mergers is a distinct feature of isolated binary evolution that can be used to identify the presence of this formation channel in the detected population of merging BBHs. Assuming isolated binary evolution is the dominant BBH formation channel in the Universe, we showed how the future third-generation GW detectors such as the *Einstein Telescope*, which have wider observational horizons than current GW detectors, might directly observe this evolution.

Simultaneously to the publication of the Bavera et al. (2022a) manuscript, Biscoveanu et al. (2022) reported that the current observed BBH sample (GWTC-3) show that the $\chi_{\rm eff}$ distribution broadens with increasing redshift. This conclusion is consistent with our analysis of GWTC-3 events Bavera et al. (2022a). However, in contrast to Bavera et al. (2022a) BBH models for the isolated binary evolution previously presented, Biscoveanu et al. (2022) analysis does not find compelling evidence that the *mean* of the $\chi_{\rm eff}$ distribution evolves with redshift, but only an increasing *dispersion*. A $\chi_{\rm eff}$ distribution evolving with redshift is constrained at $\sim 80\%$ credibility in both cases. Compared to Bavera et al. (2022a), Biscoveanu et al. (2022) carefully considers potential biases introduced in the analysis. For example, the authors ruled out that this signature is caused by the marginalization over a potential correlation between BH primary mass and effective spin. The authors also conclude that the measured trend is robust against considering alternative astrophysically-motivated phenomenological models. These trends are discussed, among others in Section 1.4.4.

Chapter 4

Now you see me

Merging BBHs formed from isolated binary evolution are expected to be generated in a gas-free environment. Hence, the merger event is not expected to be associated with an electromagnetic (EM) counterpart. Given the right conditions, BBHs formed in gaseous environments like AGN disks might lead to prompt EM emission during the merger of the two BHs (e.g., McKernan et al. 2019). Nonetheless, the core collapse of massive rapidly spinning stars and the formation of BHs in isolation has been linked to long-duration gamma-ray bursts (LGRBs) under the collapsar model (Woosley 1993; Paczyński 1998). Being bright transient events, LGRBs are detectable to high redshifts (e.g., $z \simeq 9$ Cucchiara et al. 2011). This chapter investigates and quantifies the contribution to LGRBs of the sub-population of highly rotating merging BBHs formed from isolated binary evolution. Additionally, we discuss the implications of our tidal spin-up models of isolated binary evolution to the observability of EM counterparts in BH-NS mergers. In contrast to merging BBHs, merging BH-NS systems are expected to lead to EM counterparts if the tidal disruption radius of the NS is outside the innermost stable circular orbit (ISCO) of the BH, which, in turn, depends on the BH spin.

4.1 Probing the progenitors of spinning binary black-hole mergers with long gamma-ray bursts

4.1.1 A brief introduction

The collapse of a massive, rapidly rotating star is thought to lead to the formation of a gaseous disk around a centrally formed BH which accretion can successively power an electromagnetic jet. This process, known as the collapsar scenario, is thought to be responsible for the emission of observed LGRBs. These are transient events in which the detected signal lasts more than two seconds (Kouveliotou et al. 1993), as opposed to short-duration gamma-ray bursts, which last less than two seconds and are thought to be emitted during the merger event of two compact objects (Abbott et al. 2017c). We point out that this classical picture was recently challenged by Rastinejad et al. (2022) claim of observing a LGRB event with a kilonova-like light curve similar to the one observed after the EM observation of GW170817 following the merger of two NSs (Abbott et al. 2017a).

Efficient angular-momentum transport in stellar interiors, currently supported by asteroseismic and gravitational-wave constraints, leads to predominantly slowly-spinning stellar cores (see §1.3.1.1 and §3.1). However, tidal interactions in close binaries can explain the observed sub-population of spinning and merging BBHs (see Chapeters 2 and 3). In the CE, SMT, and CHE evolutionary channels, high BH spins result from tidal spin-up in the BBH progenitor system, which leads to a high angular-momentum content in the pre-collapse core. At core collapse, portions of the star supported by their extreme angular momentum do not fall directly toward the center, forming an accretion disk. As the newly-formed central BH accretes from the disk, a fraction of the accreted material's rest mass is converted into energy, powering a jet that pierces a hole through the collapsing star's poles, giving rise to the LGRB. In this research project, we quantify the contribution of the isolated binary evolutionary channel to the observed sample of LGRBs and look for potential candidates in the observed GW sample for BBHs systems that were associated with a LGRB at the moment of BBH formation.

4.1.2 Manuscript

The conducted study Bavera et al. (2022b) was published as a *Letter* in *Astronomy & Astrophysics* in January 2022. The arXiv open-access version of the manuscript is presented in the following pages.

Astronomy & Astrophysics manuscript no. aanda
December 6, 2021
©ESO 2021

LETTER TO THE EDITOR

Probing the progenitors of spinning binary black-hole mergers with long gamma-ray bursts

Simone S. Bavera,[1,⋆] Tassos Fragos,[1] Emmanouil Zapartas,[1] Enrico Ramirez-Ruiz,[2,3] Pablo Marchant,[4] Luke Z. Kelley,[5] Michael Zevin,[6] Jeff J. Andrews,[5] Scott Coughlin,[5] Aaron Dotter,[5] Konstantinos Kovlakas,[1] Devina Misra,[1] Juan G. Serra-Perez,[5] Ying Qin,[5,7] Kyle A. Rocha,[5] Jaime Román-Garza,[1] Nam H. Tran[3] and Zepei Xing[1]

[1] Département d'Astronomie, Université de Genève, Chemin Pegasi 51, CH-1290 Versoix, Switzerland
[2] Department of Astronomy and Astrophysics, University of California, Santa Cruz, CA 95064, USA
[3] DARK, Niels Bohr Institute, University of Copenhagen, Jagtvej 128, 2200 Copenhagen, Denmark
[4] Institute of Astrophysics, KU Leuven, Celestijnenlaan 200D, 3001, Leuven, Belgium
[5] Center for Interdisciplinary Exploration and Research in Astrophysics (CIERA) and Department of Physics and Astronomy, Northwestern University, 1800 Sherman Avenue, Evanston, IL 60201, USA
[6] Enrico Fermi Institute and Kavli Institute for Cosmological Physics, The University of Chicago, 5640 South Ellis Avenue, Chicago, Illinois 60637, USA
[7] Department of Physics, Anhui Normal University, Wuhu, Anhui 241000, China

Accepted December 03, 2021

arXiv:2106.15841v3 [astro-ph.HE] 3 Dec 2021

ABSTRACT

Long-duration gamma-ray bursts are thought to be associated with the core-collapse of massive, rapidly spinning stars and the formation of black holes. However, efficient angular momentum transport in stellar interiors, currently supported by asteroseismic and gravitational-wave constraints, leads to predominantly slowly-spinning stellar cores. Here, we report on binary stellar evolution and population synthesis calculations, showing that tidal interactions in close binaries not only can explain the observed sub-population of spinning, merging binary black holes but also lead to long gamma-ray bursts at the time of black-hole formation. Given our model calibration against the distribution of isotropic-equivalent energies of luminous long gamma-ray bursts, we find that ≈10% of the GWTC-2 reported binary black holes had a luminous long gamma-ray burst associated with their formation, with GW190517 and GW190719 having a probability of ≈85% and ≈60%, respectively, being among them. Moreover, given an assumption about their average beaming fraction, our model predicts the rate density of long gamma-ray bursts, as a function of redshift, originating from this channel. For a constant beaming fraction $f_B \sim 0.05$ our model predicts a rate density comparable to the observed one, throughout the redshift range, while, at redshift $z \in [0, 2.5]$, a tentative comparison with the metallicity distribution of observed LGRB host galaxies implies that between 20% to 85% of the observed long gamma-ray bursts may originate from progenitors of merging binary black holes. The proposed link between a potentially significant fraction of observed, luminous long gamma-ray bursts and the progenitors of spinning binary black-hole mergers allows us to probe the latter well outside the horizon of current-generation gravitational wave observatories, and out to cosmological distances.

Key words. Gravitational waves – Black hole physics – Stars: binaries: close – Gamma rays: bursts – Accretion, accretion disks

1. Introduction

The substantial increase in the sample size of merging binary black holes (BBHs) detected by the Advanced LIGO (Aasi et al. 2015) and Advanced Virgo (Acernese et al. 2015) detectors has allowed for significant improvement in our understanding of BBH assembly, primarily driven by meaningful population inferences. The second gravitational-wave transient catalog, GWTC-2, contains 46 confident BBH detections (Abbott et al. 2020b). Each system can be characterised by the chirp mass M_{chirp} and the effective spin parameter χ_{eff}. Here, $M_{chirp} = (m_1 m_2)^{3/5}/(m_1 + m_2)^{1/5}$ where m_1 and m_2 are the BH masses and $\chi_{eff} = (m_1 \mathbf{a}_1 + m_2 \mathbf{a}_2)/(m_1 + m_2) \cdot \hat{\mathbf{L}}$ where $\mathbf{a}_1$ and $\mathbf{a}_2$ the BH dimensionless spin vectors and $\hat{\mathbf{L}}$ the orbital angular momentum (AM) unit vector. The majority of the detected BBHs have a χ_{eff} consistent with zero, 9 events have positive χ_{eff} at 95% credibility, while no individual BBH events are observed with confidently negative χ_{eff}. These observations indicate the existence of a sub-population of spinning BBHs.

Although several formation pathways of coalescing BBHs have been proposed in the literature, recent works suggest that the evolution of isolated binaries dominates the underlying, local merging BBH population (Zevin et al. 2021; Franciolini et al. 2021; Bavera et al. 2021b) over dynamical formation in dense stellar environments (e.g., Rodriguez et al. 2019; Antonini et al. 2019) or primordial merging BBHs (e.g., Sasaki et al. 2016; De Luca et al. 2020). However, There is not yet enough observational evidence to make a definite conclusion regarding the origin of BBHs.

The isolated binary formation pathways include (i) a stable mass transfer (MT) and a common envelope (CE) phase (e.g., Smarr & Blandford 1976; van den Heuvel 1976; Tutukov & Yungelson 1993; Kalogera et al. 2007; Postnov & Yungelson 2014;

⋆ E-mail: simone.bavera@unige.ch

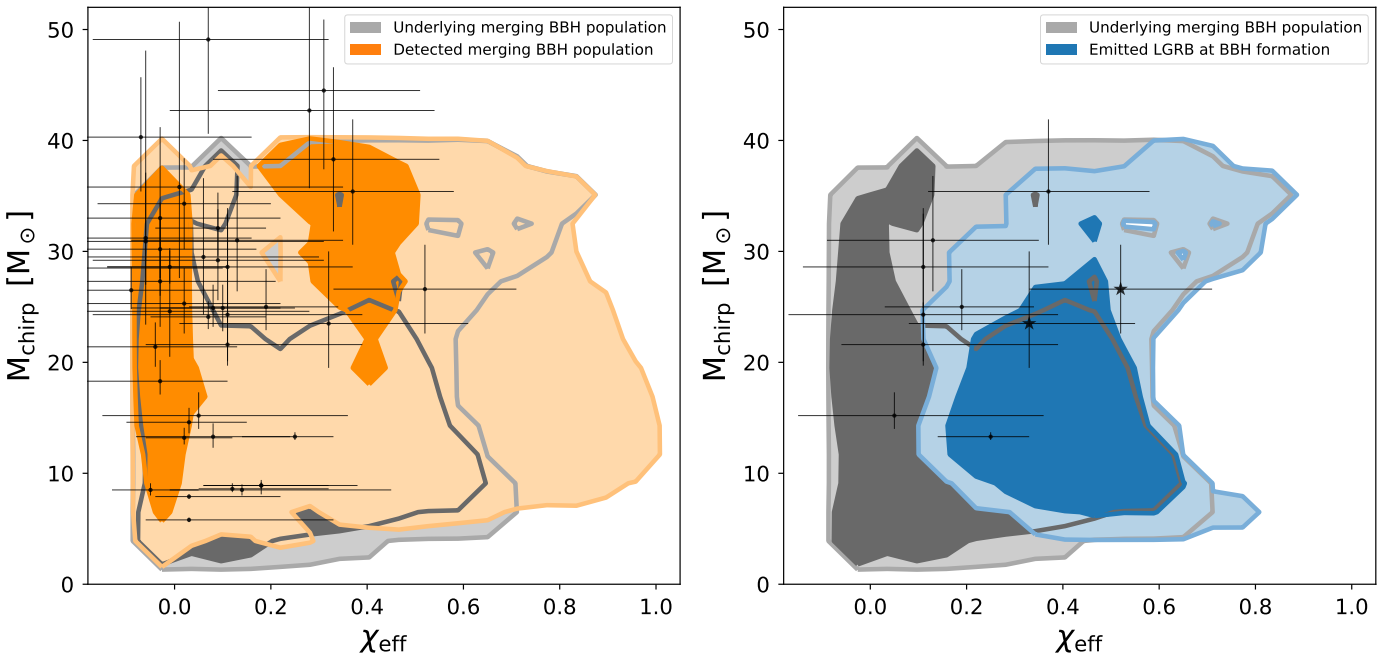

Fig. 1: Joint distribution of the chirp mass M_{chirp} and the effective inspiral spin parameter χ_{eff} for the combined CE, SMT, and CHE channels. For all figures, the model predictions for the underlying (intrinsic) BBH population are shown in gray where lighter colors represent larger contour levels of 90% and 99.9%, respectively. *Left:* The detected BBH population with O3 sensitivity is shown in orange. Overlaid in black are the O1, O2, and O3a LVC GWTC-2 (Abbott et al. 2020a) data with their 90% credible intervals; GW190521 is outside the plotted window. *Right:* The BBH sub-population which emitted LGRBs at BBH formation is shown in blue. The 10 events in GWTC-2 with chances > 10% to have emitted a luminous LGRB at BBH formation are indicated in black. The 2 events, GW190517 and GW190719, with > 50% probabilities are indicated with star markers. No bin smoothing was applied to construct the contour levels.

Belczynski et al. 2016; Bavera et al. 2020), (ii) double stable MT (SMT) (e.g., van den Heuvel et al. 2017; Inayoshi et al. 2017; Neijssel et al. 2019; Bavera et al. 2021a) or (iii) chemically homogeneous evolution (CHE) (e.g., de Mink et al. 2009; Mandel & de Mink 2016; Marchant et al. 2016; du Buisson et al. 2020). In these channels, high BH spins are the result of tidal spin-up in the BBH progenitor system, which leads to a high AM content in the pre-collapse cores. The high spins of the cores are retained until collapse, even in the case of efficient AM transport (Spruit 1999, 2002; Fuller et al. 2019). In contrast, efficient AM coupling in isolated single-star evolution or in wide binaries is expected to lead to BHs with negligible spin (Qin et al. 2018; Fuller & Ma 2019) which AM transport efficiency is supported by asteroseismic data (Kurtz et al. 2014; Deheuvels et al. 2015; Gehan et al. 2018), observations of white dwarfs spins (Berger et al. 2005) and recent gravitational-wave observations (Zevin et al. 2021).

The collapse of a spinning stellar core has been linked to long-duration gamma-ray bursts (LGRBs) under the "collapsar" model (Woosley 1993; Paczyński 1998). In this scenario, portions of the star supported by their extreme AM do not fall directly towards the center when they collapse, forming instead an accretion disk. As the newly-formed central BH accretes from the disk, a fraction of the accreted material's rest mass is converted into energy powering a jet that pierces a hole through the collapsing star's poles, giving rise to the LGRB. Being bright transient events, LGRBs are detectable up to very high redshifts (e.g., $z \approx 9$, Cucchiara et al. 2011) and have $T_{90} > 2$ s, where T_{90} is the time over which a burst emits 90% of its total measured counts (Kouveliotou et al. 1993). Furthermore, several LGRBs have been associated with Type Ic-broad-line supernovae (Woosley & Bloom 2006). These supernovae show broad spectral lines due to their high kinetic energy and lack H- and He-lines, which indicate that the progenitors are stripped stars (Modjaz et al. 2016). There are only a few unbiased and redshift-complete catalogs of LGRBs, as they require a rapid follow-up response from the ground to obtain redshift measurements. The largest of these catalogs is the SHOALS survey which counts 110 LGRBs and is considered complete for all LGRBs with fluence $S_{15-150\,\mathrm{keV}} > 10^{-6}$ erg cm^{-2} which corresponds to isotropic-equivalent energies of $E^{\mathrm{iso}}_{\mathrm{LGRB}} > 10^{51}$ erg in the 45−450 keV band (Perley et al. 2016).

Detailed stellar models of tidally spun-up stars have shown that binary configurations, such as those involved in the formation of fast-spinning merging BBHs from isolated binary scenarios, can lead to LGRBs (van den Heuvel & Yoon 2007; Detmers et al. 2008; Marchant et al. 2016; Qin et al. 2018; Chrimes et al. 2020). Notably, one of the first quantitative studies by Detmers et al. (2008) concluded that only a small fraction of LGRBs can come from tidal spin-up, in contrast to findings of more recent studies, including this work.

In this work, we make the working assumption that the isolated binary evolution pathway dominates the formation of merging BBHs in the Universe. We adopt a formation model that combines the CE, SMT, and CHE BBH channels and is consistent with observed BBH merger rates and their observable distributions (du Buisson et al. 2020; Bavera et al. 2021a; Zevin et al. 2021), and explore the hypothesis of a direct link between

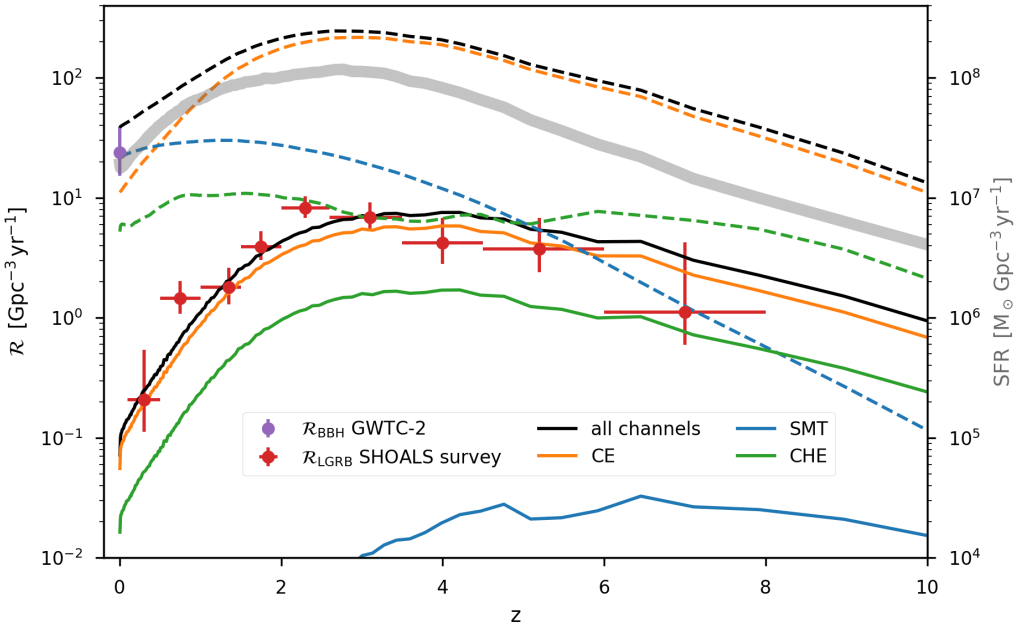

Fig. 2: Modeled merging BBH and luminous LGRB rate densities as a function of redshift from isolated binary evolution in dashed and solid black lines, respectively. The CE, SMT, and CHE channel contributions are indicated in orange, blue, and green colors, respectively. The violet marker denotes observable constraints of local BBH rate densities at $z = 0$ from LVC GWTC-2 (Abbott et al. 2020a) and the red markers the luminous LGRB rate densities from the SHOALS survey (Perley et al. 2016). The SHOALS survey LGRB rate densities are not beaming-corrected and hence probe the observed and not the intrinsic LGRB population. Our fiducial model assumes LGRB efficiency $\eta = 0.01$, constant beaming factor $f_{\rm B} = 0.05$, and IllustrisTNG redshift- and metallicity-dependent star formation rate (Nelson et al. 2019).

a potentially significant fraction of the observed long gamma-ray bursts and the progenitors of highly spinning, merging BBHs.

2. Methods

The modeling of the BBH population combines detailed binary stellar MESA (Paxton et al. 2011) models that follow in detail the tidal spin-up of the collapsing cores, with rapid population synthesis techniques (Breivik et al. 2020) under the same software framework called POSYDON.[1] The key assumptions of these models are summarised in Appendicies A to C. To compute the corresponding rate densities, we assume a redshift- and metallicity-dependent star formation rate (SFR) density according to the IllustrisTNG cosmological simulation (Nelson et al. 2019) as explained in Appendix D.

3. Results

The combined gravitational-wave (GW) observable predictions of $\chi_{\rm eff}$ and $\rm M_{chirp}$ for the modeled underlying population of merging BBHs is shown in gray in Figure 1. The CE evolutionary pathway leads to BH–Wolf-Rayet systems in close orbits where a subsequent tidal spin-up phase may occur (Bavera et al. 2020, 2021a,c). The SMT channel leads, on average, to wider orbital separations and, hence, the majority of these systems will avoid efficient tidal spin-up (Bavera et al. 2021a). CHE occurs in initially close binaries with stars that have nearly equal masses and orbital periods between 0.4 and 4 days (du Buisson et al. 2020). Both stars experience strong tidal spin-up since early in their evolution, which leads to efficient rotational mixing throughout their interior, avoiding a super-giant phase and associated stellar expansion. Therefore, the CE and CHE scenarios are mostly responsible for BBHs with non-zero $\chi_{\rm eff}$ (Bavera et al. 2020, 2021a), where the CHE BBHs primarily probe high $\rm M_{chirp}$ (du Buisson et al. 2020).

Contemporary GW detectors can probe only the low redshift subset ($z \lesssim 1$, Abbott et al. 2020b) of the underlying BBH population. Observations are biased towards high $\rm M_{chirp}$ as the signals of massive BBHs are louder and, hence, can be detected at further distances. Current GW observatories are therefore unable to individually resolve a large fraction of merging BBHs in the Universe. In the left panel of Figure 1, we indicate in orange the observed distribution of $\chi_{\rm eff}$ and $\rm M_{chirp}$ predicted by our model, assuming a three detector configuration with a network signal-to-noise ratio threshold of 12 and "mid-high/late-low" sensitivity (Abbott et al. 2018), consistent with the third observing run of LIGO and Virgo detectors. For a direct comparison with the observations, we overlay the 46 BBH events with their 90% credible interval (CI) in black. The GW detector selection effects distort the observable distributions to high $\rm M_{chirp}$ and $\chi_{\rm eff}$ values compared to the underlying BBH distribution, which is shown in gray.

A fraction of the underlying merging BBH population with highly spinning BHs is expected to give rise to LGRB events at the moment of BBH formation. For each BBH formation, we calculate from the structure profile of the BH progenitor star whether a sufficiently massive accretion disk is formed during the core collapse, which will give rise to a luminous LGRB (see Appendix C for details). In the CE channel, only the second-born BH is associated with a LGRB as tidal interactions are only relevant in the BH–Wolf-Rayet evolution phase of the BBH progenitor. In contrast, a highly spinning CHE BBH system can

[1] posydon.org

be associated with two LGRB events, as tides cause both stars to be rapidly spinning. The sub-population of BBHs associated with LGRBs is indicated in blue in the right panel of Figure 1. These systems have $\chi_{\rm eff} \gtrsim 0.2$ (90% CI) while favoring $M_{\rm chirp} \in [5, 30]\,M_\odot$. In contrast to the observed GW population, there is no observational bias for high-$M_{\rm chirp}$ BHs in the LGRB population. We find that the expected number of GWTC-2 events that had emitted a LGRB at BBH formation is ≈ 4. Among all the GWTC-2 events, GW190517 and GW190719 have the highest probabilities, ≈85% and ≈60% respectively, of having had a LGRB precursor, while 8 more events have a probability $p_{\rm LGRB} > 10\%$. Those 10 events are highlighted in the right panel of Figure 1. The details of the calculation of these probabilities are presented in Appendix E.

The combined local ($z = 0$) BBH merger rate density of our CE, SMT, and CHE fiducial models is $38.3\,{\rm Gpc^{-3}\,yr^{-1}}$, with each channel contributing 57%, 29%, and 14%, respectively. The predicted local rate density is within the observational constraints from GWTC-2 with $[15.3, 38.8]\,{\rm Gpc^{-3}\,yr^{-1}}$ at 90% credibility (Abbott et al. 2020a). In Figure 2, we show the redshift evolution of each channel's BBH merger rate density as well as their combination (dashed lines). The CE BBH merger rate density peaks at a redshift $z \in [2, 3]$, close to the peak of the SFR density, shown in gray. The CE BBH merger rate closely follows the SFR because of the short delay times between the formation and merger of tight BBH systems produced by the CE channel. In contrast, SMT and CHE BBHs have longer delay timescales as there is no mechanism to shrink the orbits as efficiently as the CE phase does. Therefore, the SMT rate density does not follow the SFR density and peaks at lower redshifts. Finally, we note that the CHE rate density is not as suppressed at high redshift as in the other two channels. This is because the CHE channel operates with higher efficiency at extremely low metallicity environments, which are more abundant at high redshifts.

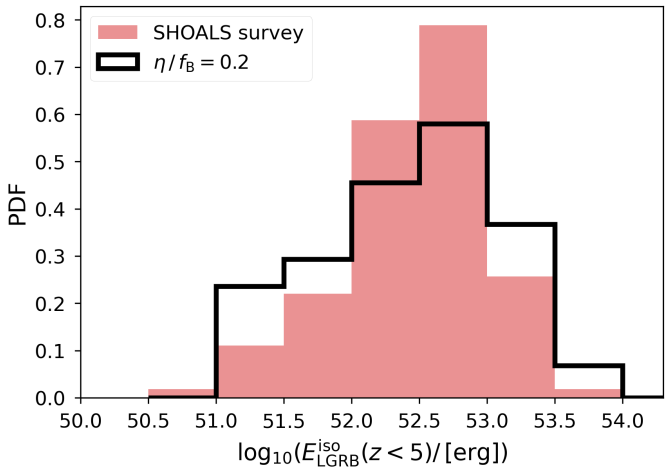

Fig. 3: Normalized histogram of the observed luminous LGRB isotropic-equivalent energies with redshift $z < 5$ from the SHOALS survey, in light red, compared to the modeled LGRB isotropic-equivalent energies. Our fiducial model was calibrated such that the modeled LGRB energies peak near the observed energy distribution. This is achieved for $\eta/f_{\rm B} = 0.2 \propto E^{\rm iso}_{\rm LGRB}$.

Luminous LGRB rate densities from our fiducial model are shown in Figure 2 as a function of redshift, for each channel and their combination (solid lines). The fiducial model assumes a LGRB energy efficiency $\eta = 0.01$ and beaming fraction

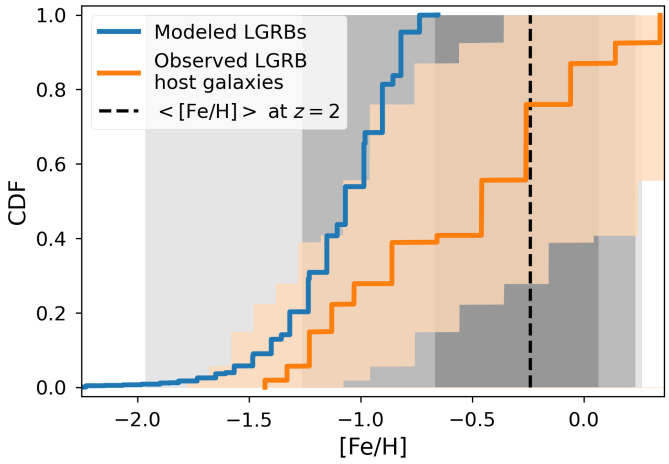

Fig. 4: Cumulative distribution function (CDF) of the modeled LGRB progenitors' metallicities for redshifts $z < 2.5$, in blue. The CDF of the observed SHOALS LGRBs host galaxy metallicities for $z < 2.5$ (Graham et al. 2019) are indicated in orange. The light orange shaded area shows the uncertainty in the observed CDF due to systematic offsets in the measurement of $\log_{10}$(O/H) depending on the calibrations used, and the stellar mass of the galaxy which can be as high as $\Delta[\log_{10}({\rm O/H})] \approx 0.7$ dex (Kewley & Ellison 2008). As a reference, we indicate with a vertical dashed black line the median metallicity from the IllustrisTNG simulation at redshift $z = 2$ and lighter gray shaded areas delineate larger CI of 68, 95 and 99% for the assumed star formation metallicity distribution.

$f_{\rm B} = 0.05$, whose ratio is calibrated to match the peak of observed luminous LGRB energy distributions as described in Appendix C and shown in Figure 3. The majority of LGRBs originate through the CE evolutionary pathway while only 21-25%, for any $z < 10$, come from CHE. The SMT channel leads to the smallest LGRB rate densities ($< 0.03\,{\rm Gpc^{-3}\,yr^{-1}}$) for any redshift, as tidally spun-up second-born BHs are rare in this evolutionary pathway. To confront our model predictions, we compare our theoretical luminous LGRB rate estimates with the SHOALS survey estimates using red markers in Figure 2. The combination of CE and CHE LGRB rates for our fiducial model are consistent with the observations of luminous LGRBs throughout the redshift range. A discussion about the sensitivity of our rate estimates about the choice of beaming fraction and SFR are presented in Appendices C and D.

LGRBs probe the formation of highly spinning merging BBHs formed at low metallicity because, at such metallicities, stellar winds are weaker, which allows the BBHs' progenitors to remain rapidly spinning and in close orbits until the formation of the BHs. These systems are therefore mostly formed at high redshifts where low metallicity environments are more abundant. Measurements of the metallicity of LGRB host galaxies have shown that LGRB rates are indeed enhanced at low metallicities (Fruchter et al. 2006). In our model, the threshold for LGRB formation is $Z_{\rm max} \approx 0.2\,Z_\odot$ where we adopt $Z_\odot = 0.017$ (Grevesse et al. 1996). In Figure 4, we compare the progenitors' metallicities of modeled LGRBs to the sub-sample of the SHOALS LGRBs with identified host galaxies which have measured metallicities for $z < 2.5$ (Graham et al. 2019). At face value, we find that 40% of the observed LGRB host galaxies have metallicities lower than $Z_{\rm max}$. However, when taking into account possible systematic uncertainties in the measurement of

$\log_{10}$(O/H) abundances (Kewley & Ellison 2008) our model can be consistent with at most ∼85% of observed LGRBs, see Appendix F for more details. Selection effects in LGRB host galaxies for which metallicity measurements are possible, biases the sample towards low red-shift and high-mass galaxies, and hence potentially towards higher metallicities (Graham et al. 2019). This comparison implies that in order to associate the entirety of luminous LGRBs to the formation of BBHs, a potentially significant fraction of LGRB progenitors at low redshifts ($z < 2.5$) must originate in low metallicity pockets of the host galaxies. Finally, we should stress that theoretical model uncertainties due to the uncertain metallicity dependence of stellar wind mass loss during the late Wolf-Rayet phase of the stars evolution as well as the uncertainties in the metallicity dependent SFR make this comparison less conclusive. A detailed parameter study would improve such a comparison but is outside the scope of this letter.

4. Discussion & Conclusions

In this study, we only consider a contribution to the LGRB rate from merging BBH progenitors. Other pathways to fast-spinning, BH progenitor stars, in single or binary stars, have been proposed to lead to LGRBs (e.g., Yoon et al. 2006; Cantiello et al. 2007), none of which though at a rate that matches the observed one, when considering efficient angular momentum transport in stellar interiors (Fryer et al. 2007). Observed high mass X-ray binaries, containing highly spinning BHs, such as Cygnus X-1 (e.g., Gou et al. 2011; Zhao et al. 2021), may have also been progenitors of LGRBs. The formation of these systems is puzzling (e.g. Wong et al. 2012; Neijssel et al. 2021), and it is uncertain whether the BH spin in these systems originates from highly-spinning pre-collapse cores (see e.g., Moreno Méndez et al. 2008; Batta et al. 2017; Schrøder et al. 2018). It is interesting to note that a simple estimate of the LGRB rate density from Cyg X-1 like systems, assuming that there is one such binary per Milky Way like galaxy with $\mathrm{SFR_{MW}} \simeq 1\,\mathrm{M_\odot\,yr^{-1}}$, and a typical lifetime of $\tau_{\mathrm{HMXB}} \simeq 10^5$ yr, far exceeds the observationally determined one at $\mathcal{R}_{\mathrm{LGRB}}(z \simeq 0) < 0.6\,\mathrm{Gpc^{-3}\,yr^{-1}}$ at

$$\mathcal{R}^{\mathrm{HMXB}}_{\mathrm{LGRB}}(z \simeq 0) = 10 \times \left(\frac{\tau_{\mathrm{HMXB}}}{10^5\,\mathrm{yr}}\right) \times \left(\frac{f_{\mathrm{B}}}{0.05}\right) \mathrm{Gpc^{-3}\,yr^{-1}}\,. \quad (1)$$

In this estimate, we assumed a $\mathrm{SFR}(z \simeq 0) = 2 \times 10^7\,\mathrm{M_\odot\,Gpc^{-3}\,yr^{-1}}$ for the local Universe (cf. Figure 1). Another possible viable alternative for the origin of LGRBs includes the formation of a fast rotating neutron star with an ultrahigh magnetic field (Duncan & Thompson 1992). While our analysis cannot exclude other potential progenitors of LGRBs, consideration of the salient uncertainties of our model demonstrates that progenitors of fast-spinning BBH mergers, formed via isolated binary evolution, are likely a major contribution to the observed luminous LGRB rate.

Fast-spinning BBHs have typically short merger timescales. Because of this, current gravitational wave detectors cannot probe them efficiently, as their formation and merger rate is maximal approximately where the SFR density peaks at $z \in [2, 3]$. Luminous LGRBs, on the other hand, are observable up to redshift of ≈ 9, and can therefore be used as a cosmological probe, empirically constraining the sub-population of progenitors of fast-spinning BBH merger events far beyond the horizons of current-generation gravitational wave observatories. We have used two types of multi-messenger, albeit asynchronous, types of observations, gravitational waves, and gamma-rays, to chart BBH formation across cosmic time. Using combinations of observations like this opens a new avenue to constrain the currently uncertain physics of binary evolution and compact object formation.

Acknowledgements We would like to thank Christopher Berry for his comments on the manuscript. This work was supported by the Swiss National Science Foundation Professorship grant (project number PP00P2_176868). E.R.-R. acknowledges support from the Heising-Simons Foundation, the Danish National Research Foundation (DNRF132) and NSF (AST-1911206 and AST-1852393). P.M. is supported by the FWO junior postdoctoral fellowship No. 12ZY520N. L.Z.K. is supported by CIERA. M.Z. is supported by NASA through the NASA Hubble Fellowship grant HST-HF2-51474.001-A awarded by the Space Telescope Science Institute, which is operated by the Association of Universities for Research in Astronomy, Inc., for NASA, under contract NAS5-26555. J.J.A. and S.C. are supported by CIERA and A.D., J.G.S.P., and K.A.R. are supported by the Gordon and Betty Moore Foundation through grant GBMF8477. Y.Q. acknowledges funding from the Swiss National Science Foundation under grant P2GEP2_188242. The computations were performed in part at the University of Geneva on the Baobab and Yggdrasil computer clusters and at Northwestern University on the Trident computer cluster (the latter funded by the GBMF8477 grant). All figures were made with the open-source Python modules `Corner` (Foreman-Mackey 2016) and `Matplotlib` (Hunter 2007). This research made use of the python modules (Virtanen et al. 2020), `Astropy` (Price-Whelan et al. 2018), and `PyCBC` (Nitz et al. 2019).

References

Aasi, J., Abbott, B. P., Abbott, R., et al. 2015, Classical and Quantum Gravity, 32, 074001
Abbott, B. P., Abbott, R., Abbott, T. D., et al. 2018, Living Reviews in Relativity, 21, 3
Abbott, R., Abbott, T. D., Abraham, S., et al. 2020a, arXiv e-prints, arXiv:2010.14533
Abbott, R., Abbott, T. D., Abraham, S., et al. 2020b, arXiv e-prints, arXiv:2010.14527
Acernese, F., Agathos, M., Agatsuma, K., et al. 2015, Classical and Quantum Gravity, 32, 024001
Antonini, F., Gieles, M., & Gualandris, A. 2019, MNRAS, 486, 5008
Bardeen, J. M. 1970, Nature, 226, 64
Batta, A. & Ramirez-Ruiz, E. 2019, arXiv e-prints, arXiv:1904.04835
Batta, A., Ramirez-Ruiz, E., & Fryer, C. 2017, ApJ, 846, L15
Bavera, S. S., Fragos, T., Qin, Y., et al. 2020, A&A, 635, A97
Bavera, S. S., Fragos, T., Zevin, M., et al. 2021a, A&A, 647, A153
Bavera, S. S., Franciolini, G., Cusin, G., et al. 2021b, arXiv e-prints, arXiv:2109.05836
Bavera, S. S., Zevin, M., & Fragos, T. 2021c, Research Notes of the American Astronomical Society, 5, 127
Belczynski, K., Holz, D. E., Bulik, T., & O'Shaughnessy, R. 2016, Nature, 534, 512
Belczynski, K., Klencki, J., Fields, C. E., et al. 2020, A&A, 636, A104
Berger, L., Koester, D., Napiwotzki, R., Reid, I. N., & Zuckerman, B. 2005, A&A, 444, 565
Breivik, K., Coughlin, S., Zevin, M., et al. 2020, ApJ, 898, 71
Cantiello, M., Yoon, S. C., Langer, N., & Livio, M. 2007, A&A, 465, L29
Chrimes, A. A., Stanway, E. R., & Eldridge, J. J. 2020, MNRAS, 491, 3479
Claeys, J. S. W., Pols, O. R., Izzard, R. G., Vink, J., & Verbunt, F. W. M. 2014, A&A, 563, A83
Cucchiara, A., Levan, A. J., Fox, D. B., et al. 2011, ApJ, 736, 7
De Luca, V., Franciolini, G., Pani, P., & Riotto, A. 2020, J. Cosmology Astropart. Phys., 2020, 044
de Mink, S. E., Cantiello, M., Langer, N., et al. 2009, A&A, 497, 243
Deheuvels, S., Ballot, J., Beck, P. G., et al. 2015, A&A, 580, A96
Detmers, R. G., Langer, N., Podsiadlowski, P., & Izzard, R. G. 2008, A&A, 484, 831
du Buisson, L., Marchant, P., Podsiadlowski, P., et al. 2020, MNRAS, 499, 5941
Duncan, R. C. & Thompson, C. 1992, ApJL, 392, L9
Eggleton, P. P. 1983, ApJ, 268, 368

Foreman-Mackey, D. 2016, The Journal of Open Source Software, 1, 24
Fragos, T., Andrews, J. J., Ramirez-Ruiz, E., et al. 2019, ApJ, 883, L45
Fragos, T. & McClintock, J. E. 2015, ApJ, 800, 17
Frail, D. A., Kulkarni, S. R., Sari, R., et al. 2001, ApJL, 562, L55
Franciolini, G., Baibhav, V., De Luca, V., et al. 2021, arXiv e-prints, arXiv:2105.03349
Fruchter, A. S., Levan, A. J., Strolger, L., et al. 2006, Nature, 441, 463
Fryer, C. L., Belczynski, K., Wiktorowicz, G., et al. 2012, ApJ, 749, 91
Fryer, C. L., Mazzali, P. A., Prochaska, J., et al. 2007, PASP, 119, 1211
Fuller, J. & Ma, L. 2019, ApJL, 881, L1
Fuller, J., Piro, A. L., & Jermyn, A. S. 2019, MNRAS, 485, 3661
Gehan, C., Mosser, B., Michel, E., Samadi, R., & Kallinger, T. 2018, A&A, 616, A24
Goldstein, A., Connaughton, V., Briggs, M. S., & Burns, E. 2016, ApJ, 818, 18
Gou, L., McClintock, J. E., Reid, M. J., et al. 2011, ApJ, 742, 85
Graham, J. F., Schady, P., & Fruchter, A. S. 2019, arXiv e-prints, arXiv:1904.02673
Grevesse, N., Noels, A., & Sauval, A. J. 1996, in Astronomical Society of the Pacific Conference Series, Vol. 99, Cosmic Abundances, ed. S. S. Holt & G. Sonneborn, 117
Grevesse, N. & Sauval, A. J. 1998, SSR, 85, 161
Heger, A., Woosley, S., Baraffe, I., & Abel, T. 2002, in Lighthouses of the Universe: The Most Luminous Celestial Objects and Their Use for Cosmology, ed. M. Gilfanov, R. Sunyeav, & E. Churazov, 369
Hobbs, G., Lorimer, D. R., Lyne, A. G., & Kramer, M. 2005, MNRAS, 360, 974
Hunter, J. D. 2007, Computing in Science & Engineering, 9, 90
Inayoshi, K., Hirai, R., Kinugawa, T., & Hotokezaka, K. 2017, MNRAS, 468, 5020
Ivanova, N., Justham, S., Chen, X., et al. 2013, A&A Rev., 21, 59
Kalogera, V. 1996, ApJ, 471, 352
Kalogera, V., Belczynski, K., Kim, C., O'Shaughnessy, R., & Willems, B. 2007, Phys. Rep., 442, 75
Kewley, L. J. & Ellison, S. L. 2008, ApJ, 681, 1183
Klencki, J., Nelemans, G., Istrate, A. G., & Chruslinska, M. 2021, A&A, 645, A54
Kobulnicky, H. A. & Kewley, L. J. 2004, ApJ, 617, 240
Kouveliotou, C., Meegan, C. A., Fishman, G. J., et al. 1993, ApJL, 413, L101
Kroupa, P. 2001, MNRAS, 322, 231
Kurtz, D. W., Saio, H., Takata, M., et al. 2014, MNRAS, 444, 102
Madau, P. & Fragos, T. 2017, ApJ, 840, 39
Mandel, I. & de Mink, S. E. 2016, MNRAS, 458, 2634
Marchant, P., Langer, N., Podsiadlowski, P., Tauris, T. M., & Moriya, T. J. 2016, A&A, 588, A50
Marchant, P., Pappas, K. M. W., Gallegos-Garcia, M., et al. 2021, A&A, 650, A107
Marchant, P., Renzo, M., Farmer, R., et al. 2019, ApJ, 882, 36
Modjaz, M., Liu, Y. Q., Bianco, F. B., & Graur, O. 2016, ApJ, 832, 108
Moe, M. & Di Stefano, R. 2017, ApJS, 230, 15
Moreno Méndez, E., Brown, G. E., Lee, C.-H., & Park, I. H. 2008, ApJ, 689, L9
Neijssel, C. J., Vigna-Gómez, A., Stevenson, S., et al. 2019, MNRAS, 490, 3740
Neijssel, C. J., Vinciguerra, S., Vigna-Gómez, A., et al. 2021, ApJ, 908, 118
Nelson, D., Springel, V., Pillepich, A., et al. 2019, Computational Astrophysics and Cosmology, 6, 2
Nicholls, D. C., Sutherland, R. S., Dopita, M. A., Kewley, L. J., & Groves, B. A. 2017, MNRAS, 466, 4403
Nitz, A., Harry, I., Brown, D., et al. 2019, gwastro/pycbc: PyCBC Release v1.14.4
Nugis, T. & Lamers, H. J. G. L. M. 2000, A&A, 360, 227
Paczyński, B. 1998, ApJL, 494, L45
Patton, R. A. & Sukhbold, T. 2020, MNRAS, 499, 2803
Paxton, B., Bildsten, L., Dotter, A., et al. 2011, ApJS, 192, 3
Paxton, B., Cantiello, M., Arras, P., et al. 2013, ApJS, 208, 4
Paxton, B., Marchant, P., Schwab, J., et al. 2015, ApJS, 220, 15
Paxton, B., Schwab, J., Bauer, E. B., et al. 2018, ApJS, 234, 34
Paxton, B., Smolec, R., Schwab, J., et al. 2019, ApJS, 243, 10
Pejcha, O. & Thompson, T. A. 2015, ApJ, 801, 90
Perley, D. A., Krühler, T., Schulze, S., et al. 2016, ApJ, 817, 7
Planck Collaboration, Ade, P. A. R., Aghanim, N., et al. 2016, A&A, 594, A13
Postnov, K. A. & Yungelson, L. R. 2014, Living Reviews in Relativity, 17, 3
Price-Whelan, A. M., Sipőcz, B., Günther, H., et al. 2018, The Astronomical Journal, 156, 123
Qin, Y., Fragos, T., Meynet, G., et al. 2018, A&A, 616, A28
Quast, M., Langer, N., & Tauris, T. M. 2019, A&A, 628, A19
Rodriguez, C. L., Zevin, M., Amaro-Seoane, P., et al. 2019, Phys. Rev. D, 100, 043027
Román-Garza, J., Bavera, S. S., Fragos, T., et al. 2021, ApJ, 912, L23
Sana, H., de Mink, S. E., de Koter, A., et al. 2012, Science, 337, 444
Sari, R., Piran, T., & Halpern, J. P. 1999, ApJL, 519, L17
Sasaki, M., Suyama, T., Tanaka, T., & Yokoyama, S. 2016, Phys. Rev. Lett., 117, 061101
Schneider, F. R. N., Podsiadlowski, P., & Müller, B. 2021, A&A, 645, A5
Schrøder, S. L., Batta, A., & Ramirez-Ruiz, E. 2018, ApJ, 862, L3
Smarr, L. L. & Blandford, R. 1976, ApJ, 207, 574
Spruit, H. C. 1999, A&A, 349, 189
Spruit, H. C. 2002, A&A, 381, 923
Sukhbold, T., Ertl, T., Woosley, S. E., Brown, J. M., & Janka, H. T. 2016, ApJ, 821, 38
Taylor, P. A., Miller, J. C., & Podsiadlowski, P. 2011, MNRAS, 410, 2385
Thorne, K. S. 1974, ApJ, 191, 507
Tout, C. A., Pols, O. R., Eggleton, P. P., & Han, Z. 1996, MNRAS, 281, 257
Tutukov, A. V. & Yungelson, L. R. 1993, MNRAS, 260, 675
van den Heuvel, E. P. J. 1976, in Structure and Evolution of Close Binary Systems, ed. P. Eggleton, S. Mitton, & J. Whelan, Vol. 73, 35
van den Heuvel, E. P. J., Portegies Zwart, S. F., & de Mink, S. E. 2017, MNRAS, 471, 4256
van den Heuvel, E. P. J. & Yoon, S. C. 2007, Ap&SS, 311, 177
Vink, J. S., de Koter, A., & Lamers, H. J. G. L. M. 2001, A&A, 369, 574
Virtanen, P., Gommers, R., Oliphant, T. E., et al. 2020, Nature Methods, 17, 261
Wong, T.-W., Valsecchi, F., Fragos, T., & Kalogera, V. 2012, ApJ, 747, 111
Woosley, S. E. 1993, ApJ, 405, 273
Woosley, S. E. & Bloom, J. S. 2006, ARA&A, 44, 507
Yoon, S. C., Langer, N., & Norman, C. 2006, A&A, 460, 199
Zevin, M., Bavera, S. S., Berry, C. P. L., et al. 2021, ApJ, 910, 152
Zevin, M., Spera, M., Berry, C. P. L., & Kalogera, V. 2020, ApJL, 899, L1
Zhao, X., Gou, L., Dong, Y., et al. 2021, ApJ, 908, 117

Appendix A: Population synthesis of CE, SMT, and CHE binary black holes

We model the evolution of binaries through CE and SMT with the POSYDON framework to combine the rapid population synthesis code COSMIC (Breivik et al. 2020) with detailed MESA (Paxton et al. 2011, 2013, 2015, 2018, 2019) stellar structure and binary evolution simulations (Bavera et al. 2021a). This hybrid approach is used to rapidly evolve millions of binaries from the zero-age main sequence (ZAMS) until the end of the second MT episode. For the last phase of the evolution, which determines the second-born BH spin (Qin et al. 2018; Bavera et al. 2020), we used detailed BH–Wolf-Rayet binary evolution simulations to model the tidal spin-up phase until the secondary star reached central carbon exhaustion. These simulations take into account differential stellar rotation, tides, stellar winds, and the evolution of the Wolf–Rayet stellar structure until carbon depletion. The core collapse is modeled as described in the next section. We consider disk formation during the collapse of highly spinning stars, mass loss through neutrinos, pulsational pair-instability and pair-instability supernova (PPISN & PISN) (Marchant et al. 2019), and orbital changes resulting from anisotropic mass loss and isotropic neutrinos mass loss (Kalogera 1996).

In our models, the first-born BHs in the SMT and CE channels are formed with a negligible spin because of the assumed efficient AM transport (Fragos & McClintock 2015; Qin et al. 2018; Fuller & Ma 2019). If AM transport were to be inefficient, this would lead to spinning BBHs (Belczynski et al. 2020), which are currently inconsistent with GWTC-2 observations. Moreover, we assume Eddington-limited accretion efficiency onto compact objects, resulting in a negligible amount of mass accreted onto the first-born BH during SMT. Hence, the first-born BH in the SMT channel avoids any spin-up during MT (Thorne 1974). Alternatively, if the accretion onto compact objects could reach highly super-Eddington rates, the binaries would not shrink enough to produce merging BBHs, leading to the suppression of the SMT channel (Bavera et al. 2021a). Hence, even though super-Eddington accretion efficiency strongly affects the yield of merging BBHs through the SMT channel, it will not affect LGRBs rates as the MT accretion spin-up occurs after BH formation. Finally, motivated by the model comparison between our models and GWTC-2 data (Bavera et al. 2021a), we assume inefficient common envelope ejection efficiencies, taken as $\alpha_{\rm CE} = 0.5$ in the $\alpha_{\rm CE} - \lambda$ CE parameterization theory (see, e.g. Ivanova et al. 2013, for a review) and adopt λ fits as in Claeys et al. (2014). Because the orbital separation post CE is approximately proportional to $\alpha_{\rm CE}$, inefficient CE ejection leads, on average, to a larger fraction of tidally spun-up BHs, but at the same time to a smaller overall number of BBH merger events compared to efficient CE ejection, $\alpha_{\rm CE} > 1$. Here, an $\alpha_{\rm CE}$ value grater than 1 does not mean that other sources of energy partake in the CE ejection, but more likely points to an inaccurate assumption of core-envelope boundaries. Indeed, multiple recent studies (Fragos et al. 2019; Quast et al. 2019; Klencki et al. 2021; Marchant et al. 2021) have shown that envelope stripping stops earlier than what currently assumed in population synthesis. We find that this model's uncertainty changes our LGRB rate estimate by $\mathcal{R}_{\rm LGRB}^{\alpha_{\rm CE}=0.5}$ at redshift $z = 0$ ($z = 2$) by +36% (+18%), −56% (−42%) and −68% (−54%) for $\alpha_{\rm CE} = 0.25, 1$ and 2, respectively, not changing our study's conclusion.

The binary evolution through CHE is modeled entirely with MESA until the carbon depletion of both stars (du Buisson et al. 2020). More precisely, we model the two stars simultaneously in a binary system where tidal interaction and mass transfer are taken into account. For consistency, the CE and SMT MESA models used identical input physics to the CHE ones, while simulations with the COSMIC code were also configured to be as consistent as possible (Bavera et al. 2021a; Zevin et al. 2021). Similar to the other channels, the stars' profiles' core collapse is done self-consistently with CE and SMT models using POSYDON. Because the CHE MESA grids assume a fixed mass ratio $q = 1$, both stars will reach core collapse simultaneously. In practice, we collapse one star after the other by applying a Blauw kick (Kalogera 1996) after each star has collapsed to account for the orbit adjustment resulting from PPISN and neutrinos mass loss, where we assume circularization after the formation of the first BH (du Buisson et al. 2020).

Initial binary conditions at ZAMS are drawn randomly from empirically constrained distributions. In CE and SMT, the ZAMS binaries are directly evolved with POSYDON while binaries in the parameter space leading to CHE are mapped to the nearest neighbor CHE MESA evolutionary track. Metallicities are sampled in the log-range $\log_{10}(Z) \in [-5, \log_{10}(2Z_\odot)]$. For the CE and SMT models the log-metallicity range is divided in 30 desecrate values from $\log_{10}(Z) = -4$ to $\log_{10}(1.5Z_\odot)$ where binaries with $\log_{10}(Z) \in [-5, -4]$ are mapped to the lowest metallicity bin (Bavera et al. 2021a). For the CHE models the log-metallicity range is sampled with 22 discrete values from $\log_{10}(Z) = -5.0$ to $\log_{10}(Z) = -2.375$, above which any binary evolves through the CHE channel (du Buisson et al. 2020). Primary masses follow the Kroupa initial mass function (IMF), a broken power law with coefficient $\alpha = -2.3$ (Kroupa 2001) in the sampled mass range $5\,{\rm M}_\odot \leq m_1 \leq 150\,{\rm M}_\odot$. The upper limit is an extrapolation of the original Kroupa IMF measured only up to $50\,{\rm M}_\odot$. The arbitrary maximum stellar mass is chosen to exclude BH formation above the upper mass gap of PISN, which we do not model (Heger et al. 2002). The mass distribution of the less massive secondary star is given by $m_2 = m_1 \times q$, where the initial mass ratio q is drawn from a flat distribution (Sana et al. 2012) in the range $q \in (0, 1]$. We assume that all binaries are born with circular orbits. Furthermore, we adopt a binary fraction of $f_{\rm bin} = 0.7$ (Sana et al. 2012) and assume that at birth the distribution of log-orbital periods follow a power law with coefficient $\pi = -0.55$ (Sana et al. 2012) in the range $\log_{10}(p/[\rm day]) \in [0.15, 5.5]$ and extrapolate down to the range $\log_{10}(p/[\rm day]) \in [\log_{10}(0.4/[\rm day]), 0.15]$ assuming a log-flat distribution (Bavera et al. 2021a). The portion of the parameter space with $q \in [0.8, 1]$ and $p \in [0.4, 4]$ days may lead to CHE (du Buisson et al. 2020). Notice that there are some uncertainties on the actual initial binary properties of mass ratios, periods, and eccentricities (see e.g. Moe & Di Stefano 2017), however, there are no constraints on them at low metallicities such as the one modeled here. Moreover, The extrapolation to low orbital periods causes us to sample systems Roche-lobe overflowing at ZAMS. Therefore, these systems have undergone MT during the pre-main sequence phase, which complicates the binary evolution and, a priori, might not lead to CHE. To remove these systems from the sampled distribution, we adopt ZAMS stellar radii fits (Tout et al. 1996), which we compare to the initial Roche-lobe radii of the binary (Eggleton 1983). The population synthesis will then result in a synthetic population of BBHs, which we distribute across the cosmic history of the Universe to compute rate densities. See the later section for a detailed description.

Appendix B: LGRB collapsar scenario

A massive star collapses under its own weight when nuclear reactions can no longer generate enough pressure to balance the pull of gravity. For the most massive stars, this occurs after the stars have formed iron cores. Due to computational constraints, our MESA simulations run until carbon depletion, which occurs less than a year before the actual core collapse. Because the remaining stellar evolutionary phase is so rapid compared to the star's total evolution, we can assume that the star's structure will not change drastically in the neglected portion of the evolution. The core collapse is modeled using fits to the results of 2D core-collapse models (Fryer et al. 2012). We also account for mass loss through PPISN or stellar disruption from PISN using fits to 1D stellar models targeting this evolution phase (Marchant et al. 2019). Depending on the carbon-oxygen core mass, $m_{\rm CO-core}$, the star might explode as a supernova and have a fraction of the ejected mass falling back onto the compact object or, if the star is massive enough, where $m_{\rm CO-core} \geq 11\,{\rm M}_\odot$, the star will collapse directly to form a BH (Fryer et al. 2012). Consequently, in our models, only stars with $m_{\rm CO-core} \leq 11\,{\rm M}_\odot$ can receive natal kicks, with magnitudes drawn from a Maxwellian distribution with $\sigma = 265$ km/s (Hobbs et al. 2005) and rescaled by one minus the fall-back mass fraction (Fryer et al. 2012). In this case, only a negligible fraction of such low mass merging highly spinning BBHs associated to LGRBs will be disrupted by natal kicks as they are in tight orbits (orbital periods of less than one day) and, hence, only a kick with magnitude larger than the corresponding orbital velocity $v_{\rm orb} > 500\,{\rm km/s}$ can disrupt the system. Furthermore, notice that newer studies on core-collapse physics (e.g. Pejcha & Thompson 2015; Sukhbold et al. 2016; Patton & Sukhbold 2020; Schneider et al. 2021) indicate that there is no such distinct monotonic relation between neutron-star (NS) and BH formation (for a detailed study of the impact of newer core-collapse mechanism prescriptions on the formation of merging BBH and BH-NS in our models, see Román-Garza et al. (2021)). In the collapse, we also account for up to $0.5\,{\rm M}_\odot$ mass loss through neutrinos (Zevin et al. 2020). If the collapsing star is rapidly rotating, an accretion disk might form during this process (Bavera et al. 2021a). Because our MESA simulations provide us with the star's profile at core collapse, we can estimate the amount of material that forms an accretion disk around the newly-formed BH and the spin of the final BH (Batta & Ramirez-Ruiz 2019). We assume that the innermost shells of the star form a central BH of mass $2.5\,{\rm M}_\odot$ through direct collapse, where we account for the mass and AM loss through neutrinos (Bavera et al. 2021a). The collapse of each subsequent shell happens on a dynamical timescale. We account for each shell's portion with enough specific AM to support disk formation instead of collapsing directly. The thin disk is subsequently accreted on a viscous timescale which we assume to be much smaller than the dynamical timescale. Hence the disk is accreted before the next shell collapses. Notice that the accretion problem might be more complex than what assumed, e.g. Taylor et al. (2011) 3D smoothed-particle hydrodynamics simulations showed that hydrodynamical instabilities in the accretion disk may result in intermittent accretion. If this is the case one would also need to account for feedbacks from the already-accreted disk to the rest of the in-falling material (see e.g. Bavera et al. 2021c) which we do not account here. When an accretion disk is formed, a fraction of its rest-mass energy can power the formation of a jet that pierces through the star and breaks out from its poles. This mechanism is known as the collapsar scenario and is thought to give rise to LGRBs (Woosley 1993; Paczyński 1998).

Appendix C: LGRB isotropic-equivalent energy calibration

The LGRB jet is powered by the accretion disk produced in the core-collapse, and only a fraction, $f_{\rm jet}$, of this rest-mass energy will power the jet, of which a fraction f_γ is observed in the γ-ray band $45 - 450\,{\rm keV}$. Moreover, when the jet breaks out from the poles, the star's outer layers, which have yet to collapse, could become unbound by the shock caused by the jet, using a fraction of the estimated energy to unbind the star while the rest escapes. Similarly, we can encompass this uncertainty in the parameter $1 - f_{\rm unbound}$. For simplicity, in our models, we parameterize our ignorance about these processes in the fixed efficiency parameter $\eta = f_{\rm jet} \times f_\gamma \times (1 - f_{\rm unbound})$. Hence, the total LGRB energy released in the γ-ray band by the BH formation process is then

$$E_{\rm LGRB} = \eta \Delta M_{\rm disk}\, c^2 \ \ {\rm ergs}, \tag{C.1}$$

where $\Delta M_{\rm disk} = \sum_i (1 - [1 - 2GM_{\rm BH}/(3c^2 r_{\rm ISCO,i})]^{1/2}) m_{\rm disk,i}$ is the total rest mass released as energy during the accretion process which depends on the radius of the innermost stable circular orbit (ISCO) of the accreting central BH, $r_{\rm ISCO}$ (Bardeen 1970; Thorne 1974). Here, $m_{\rm disk,i} = m_{\rm shell,i} \cos(\theta_{\rm disk,i})$ is the mass of the disk formed during the collapse of the ith shell with radius r where $\theta_{\rm disk,i}$ is the polar angle above which disk formation occurs. This quantity depends on the specific AM of the ISCO of the accreting BH, $j_{\rm ISCO}$, and the shell's specific AM, $\Omega(r) r^2$, as

$$\theta_{\rm disk,i} \equiv \theta_{\rm disk}(r) = \arcsin\left[\left(\frac{j_{\rm ISCO}}{\Omega(r) r^2}\right)^{1/2}\right]. \tag{C.2}$$

The jet escapes from the poles and is beamed with a half-opening angle $\theta_{\rm B}$. The chance of having the line of sight aligned with the jets is then $f_{\rm B} = 1 - \cos(\theta_{\rm B})$. The total isotropic-equivalent energy released by the LGRB jet is

$$E^{\rm iso}_{\rm LGRB} = f_{\rm B}^{-1} E_{\rm LGRB} = f_{\rm B}^{-1}\, \eta\, \Delta M_{\rm disk,\,rad}\, c^2 \ \ {\rm erg}\,. \tag{C.3}$$

We have two apparent free parameters, $f_{\rm B}$ and η, to determine. For simplicity, we assume that both parameters are constants. We can then use observations of luminous LGRBs from the SHOALS survey to calibrate the ratio $\eta/f_{\rm B} \propto E^{\rm iso}_{\rm LGRB}$ such that the peak of the modeled isotropic-equivalent energy distribution matches the observed one. In Figure 3 we show the result of this calibration, namely $\eta/f_{\rm B} = 0.2$. With this constraint, we can choose reasonable values of $f_{\rm B}$ and obtain a corresponding η. Under certain model assumptions, the jet opening angle can be estimated from the afterglow (Sari et al. 1999; Frail et al. 2001) or the prompt emission of LGRBs (Goldstein et al. 2016), with mean reported values being roughly in the range of approximately 3 to 20 degrees (corresponding to $f_{\rm B}$ of 0.001-0.06). For our fiducial model we chose $f_{\rm B} = 0.05$ and $\eta = 0.01$. Different choices of $f_{\rm B}$, given the calibration, result in different LGRB rate densities as shown in Figure C.1. Lower $f_{\rm B}$ values lead to a suppression of the rates as the chance of seeing these systems are directly proportional to $f_{\rm B}$, while the contrary is true for larger $f_{\rm B}$ values.

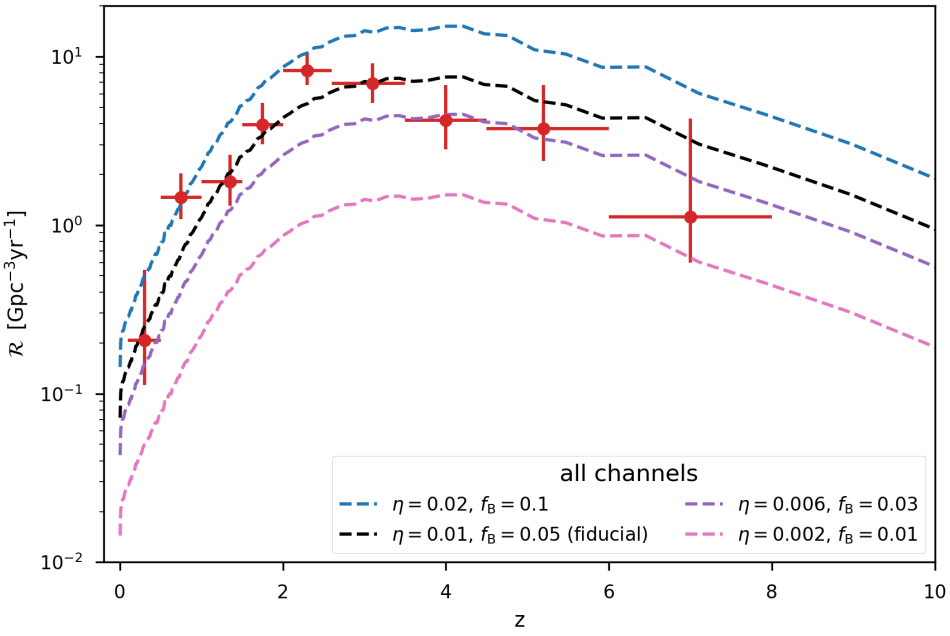

Fig. C.1: Modeled luminous LGRB rate densities as a function of redshift for all channels combined. The figure illustrates model uncertainties given an arbitrary choice of beaming fraction $f_B \in [0.01, 0.03, 0.05, 0.1]$. The LGRB energy efficiency η is obtained from the isotropic-equivalent energy calibration condition $\eta/f_B = 0.2$.

Appendix D: BBH and LGRB rate densities and detection rate

The BBH merger rate density $\mathcal{R}_{\rm BBHs}(z)$ is the number of BBHs mergers per comoving volume per year as a function of redshift. This quantity can be calculated (Bavera et al. 2021a) by convolving the redshift- and metallicity-dependent star-formation rate (SFR) density with the synthetic BBH population obtained sampling initial binary distributions. To conduct this calculation, we assume a flat ΛCDM cosmology with $H_0 = 67.7$ km s^{-1} Mpc^{-1} and $\Omega_m = 0.307$ (Planck Collaboration et al. 2016).

We assume a modeled redshift- and metallicity-dependent star formation rate, SFR$(z, \log_{10}(Z))$, from the TNG100 Illustris simulation (Nelson et al. 2019). Illustris is a state-of-the-art large-scale cosmological simulation of the Universe. This model tracks the expansion of the Universe assuming a flat ΛCDM cosmology, the gravitational pull of baryonic and dark matter onto itself, the hydrodynamics of cosmic gas, as well as the formation of stars. The simulated comoving volume of (100Mpc)^3 contains tens of thousands of galaxies captured in high detail. Illustris is calibrated to match the present-day ratio of the number of stars to dark matter for galaxies of all masses and the total amount of star formation in the universe as a function of time. Furthermore, the simulation also matches the galaxy stellar mass and luminosity functions.

The population synthesis predictions are performed in finite time bins of $\Delta t_i = 100$ Myr and log-metallicity bins ΔZ_j. Each binary k with BH masses $m_{1,k}$ and $m_{2,k}$ is placed at redshift of formation $z_{{\rm f},i}$ corresponding to the center of Δt_i and merging at redshift $z_{{\rm m},i,k}$ for its corresponding metallicity bin ΔZ_j. The BBH rate density is given by the Monte Carlo sum (Bavera et al. 2021a)

$$\mathcal{R}_{\rm BBHs}(z_i) = \sum_{\Delta Z_j} \sum_k f_{\rm corr} \frac{{\rm fSFR}(z_{{\rm f},i}|\Delta Z_j)}{M_{{\rm sim},\Delta Z_j}} \frac{4\pi c\, D_{\rm c}^2(z_{{\rm m},i,k})}{\Delta V_{\rm c}(z_i)} \Delta t_i \ \ {\rm Gpc^{-3}yr^{-1}}, \tag{D.1}$$

where $M_{{\rm sim},\Delta Z_j}$ is the simulated mass per log-metallicity bin ΔZ_j and $f_{\rm corr}$ the normalization constant which converts the simulated mass to the total stellar population (Bavera et al. 2020). Here, ${\rm fSFR}(z|\Delta Z_j) = \int_{\Delta Z_j} {\rm SFR}(z, \log_{10}(Z)) \log_{10} Z$ is the fractional SFR density corresponding to the log-metallicity bin ΔZ_j and $\Delta V_{\rm c}(z_i)$ is the comoving volume shell corresponding to Δt_i,

$$\Delta V_{\rm c}(z_i) \equiv \int_{\Delta z_i} \frac{1}{1+z} \frac{{\rm d}V_{\rm c}}{{\rm d}z} {\rm d}z = \frac{4\pi c}{H_0} \int_{\Delta z_i} \frac{D_{\rm c}^2(z)}{E(z)(1+z)} {\rm d}z\,, \tag{D.2}$$

where, Δz_i is the redshift interval corresponding to the formation time bin Δt_i, $D_c(z) = c/H_0 \int_0^z E(z')^{-1} dz$ is the comoving distance, $E(z) = \sqrt{\Omega_m (1+z)^3 + \Omega_\Lambda}$ and $\Omega_\Lambda = 1 - \Omega_m$.

A fraction of merging BBHs emit LGRBs at the compact object's formation, i.e., $z^l_{{\rm LGRB},i,k}$ where the dummy index $l = 1, 2$ indicates the first- or second-formed BH. In the case of CE and SMT channels, only the second-born tidally spun up BH can lead to a LGRB event, while for the CHE channel, we assume both stars can emit the LGRB at the same time $z^1_{{\rm LGRB},i,k} = z^2_{{\rm LGRB},i,k}$. We can therefore compute the LGRB rate density $R_{\rm LGRB}(z)$ by substituting $z_{{\rm LGRB},i,k}$ to $z_{m,i,k}$ in Eq. (D.1). Accounting for beaming, we

obtain the LGRB rate density visible to an observer as

$$\mathcal{R}_{\rm LGRB}(z) = \sum_{\Delta Z_j} \sum_{k} f_{\rm B} f_{\rm corr} \frac{{\rm fSFR}(z_{{\rm f},i}|\Delta Z_j)}{M_{{\rm sim},\,\Delta Z_j}} \frac{4\pi c\, D_{\rm c}^2(z_{{\rm LGRB},i,k})}{\Delta V_{\rm c}(z_i)} \Delta t_i \;\; {\rm Gpc^{-3}yr^{-1}}\,. \tag{D.3}$$

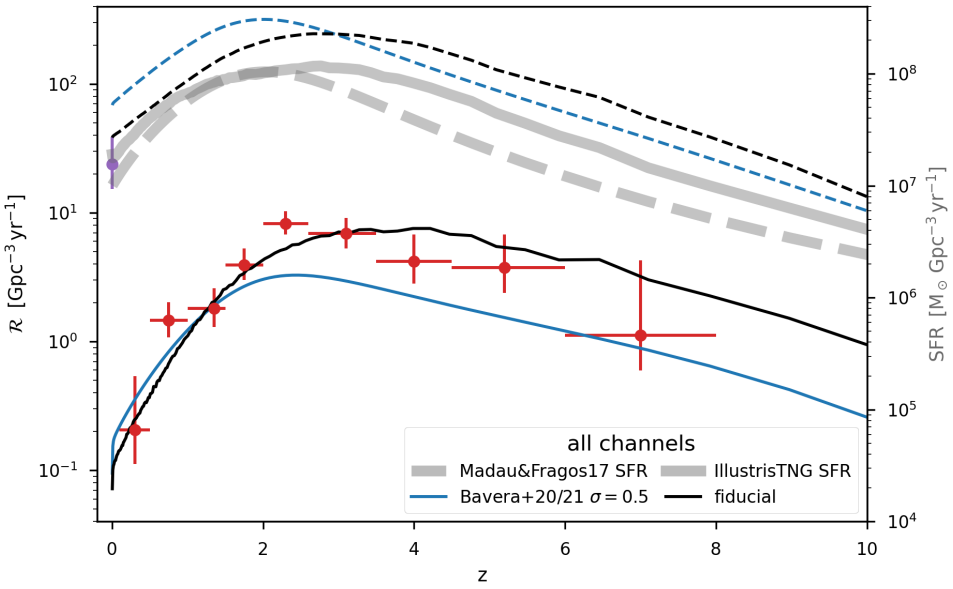

Fig. D.1: Modeled merging BBH (dashed lines) and luminous LGRB (solid lines) rate densities as a function of redshift for all channels combined. The figure illustrates model uncertainties given an alternative choice of SFR density (Madau & Fragos 2017) (dashed gray line) and assuming metallicities follow a truncated log-normal metallicity with $\sigma = 0.5$ dex as in (Bavera et al. 2020, 2021a), in blue, versus the fiducial assumption of IllustrisTNG SFR density (Nelson et al. 2019) (solid gray line), in black. The fiducial luminous LGRB rate estimate assumes the beaming fraction $f_{\rm B} = 0.05$ and LGRB energy efficiency $\eta = 0.0.01$, while the alternative model was calibrated against the empirical isotropic-equivalent energy to $f_{\rm B} = 0.02$ and $\eta = 0.002$.

To highlight the uncertainties in the SFR density and metallicity distribution which might bias our rate estimate, we compare our results given the fiducial SFR density choice (IllustrisTNG, Nelson et al. 2019) to an alternative SFR density (Madau & Fragos 2017) assumed in previous works (Bavera et al. 2020, 2021a) where it was assumed that metallicity follow a truncated log-normal distribution around the empirical mean of (Madau & Fragos 2017) with $\sigma = 0.5$ dex. In Figure D.1, we see that IllustrisTNG SFR density peaks at slightly higher redshift $z \in [2, 3]$ compared to Madau & Fragos (2017) SFR density which peaks at $z = 2$ while the latter shows a larger suppression at higher redshifts. Moreover, the alternative model predicts twice the fiducial BBH rate densities for $z < 2$. The difference lies in the metallicity distribution which in the alternative model predicts more low metallicity systems compared to the IllustrisTNG metallicity distribution. This difference is due to the truncation of the log-normal distribution centered around the empirical mean which shifts the distribution towards lower metallicity systems and, hence, leads to an overproduction of merging BBH systems compared to IllustrisTNG.

The BBH detection rate $R_{\rm BBHs}$ is the number of BBH mergers observed per year by a gravitational-waves detector network. Similarly to the rate density calculation, we can calculate the BBH detection rate with the Monte Carlo sum (Bavera et al. 2021a)

$$R_{\rm BBHs} = \sum_{\Delta t_i, \Delta Z_j, k} w_{i,j,k} = \sum_{\Delta t_i} \sum_{\Delta Z_j} \sum_{k} p_{{\rm det},i,k}\, f_{\rm corr} \frac{{\rm fSFR}(z_{{\rm f},i}|\Delta Z_j)}{M_{{\rm sim},\,\Delta Z_j}} 4\pi c\, D_{\rm c}^2(z_{{\rm m},i,k})\, \Delta t_i \;\; {\rm yr^{-1}}, \tag{D.4}$$

where $w_{i,j,k}$ is the contribution of the BBH k to the detection rate. Similarly to the rate density calculation, the binary k is placed at the time bin Δt_i with center the redshift of formation $z_{{\rm f},i}$ and merging at $z_{{\rm m},i,k}$ for its corresponding metallicity bin ΔZ_j. Here, $p_{{\rm det},i,k} \equiv p_{\rm det}(z_{{\rm m},i,k}, m_{1,k}, m_{2,k}, \mathbf{a}_{1,k}, \mathbf{a}_{1,k})$ is the detection probability which account for selection effects of the detector. Each BBH k is characterised by the masses $m_{1,k}$ and $m_{2,k}$, and by the dimensionless spin vectors $\mathbf{a}_{1,k}$ and $\mathbf{a}_{2,k}$. To compute $p_{{\rm det},i,k}$ (Bavera et al. 2021a) we assume a three detector configuration with a network signal-to-noise ratio threshold of 12 and "mid-high/late-low" sensitivity (Abbott et al. 2018), consistent with the third observing run of LIGO and Virgo detectors (Bavera et al. 2021a; Zevin et al. 2021).

The normalised weight $\tilde{w}_{i,j,k} = w_{i,j,k} / \sum_{\Delta t_{i'}, \Delta Z_{j'}, k'} w_{i',j',k'}$ is used to generate the gravitational-waves observable distributions of the detected BBH modeled population in the left panel of Figure 1. To generate the underlying (intrinsic) BBH merging distribution in Figure 1, i.e. what a detector on Earth with infinite sensitivity would observe, we weight the modeled population with $\tilde{w}^{\rm intrinsic}_{i,j,k} = \tilde{w}_{i,j,k}(p_{{\rm det},i,k} = 1)$. Finally the intrinsic distribution of BBH mergers associated with luminous LGRBs shown in the right panel of

Figure 1 is obtain by weighting the modeled population as

$$\tilde{w}_{i,j,k}^{\rm intrinsic,LGRB} = \begin{cases} \tilde{w}_{i,j,k}^{\rm intrinsic}, & E_{\rm LGRB}^{\rm iso} > 10^{51}{\rm erg} \\ 0, & \text{else} \end{cases} . \tag{D.5}$$

Appendix E: Luminous LGRB evidence in GWTC-2

The probability of a gravitational-wave event $\mathbf{x}$ to have emitted a luminous LGRB, given our model, is calculated as

$$\begin{aligned} p_{\rm LGRB}(\mathbf{x}) &= \int_{-1}^{1}\int_{0\,{\rm M}_\odot}^{100\,{\rm M}_\odot} f_{\rm GRB}(\chi_{\rm eff}, {\rm M}_{\rm chirp}) \times p(\chi_{\rm eff}, {\rm M}_{\rm chirp}|\mathbf{x})\, {\rm d}\chi_{\rm eff}\, {\rm dM}_{\rm chirp} = \\ &\approx \sum_l \sum_m f_{\rm LGRB}^{l,m} p(\Delta\chi_{\rm eff}^l, \Delta{\rm M}_{\rm chirp}^m) \Delta\chi_{\rm eff} \Delta{\rm M}_{\rm chirp}\,, \end{aligned} \tag{E.1}$$

where we approximated the integrals with a Riemann sum over the finite l- and m-bins of size $\Delta\chi_{\rm eff} = 0.05$ and $\Delta{\rm M}_{\rm chirp} = 2\,{\rm M}_\odot$, respectively. The gravitational-waves events' posterior probability density $p(\chi_{\rm eff}, {\rm M}_{\rm chirp}|\mathbf{x})$ is discretised and calculated at the center of each 2D bin ($\Delta\chi_{\rm eff}^l$,$\Delta{\rm M}_{\rm chirp}^m$). Here, $f_{\rm LGRB}$, is the probability density of an event with ($\chi_{\rm eff}$,${\rm M}_{\rm chirp}$) to have emitted a luminous LGRB at BBH formation. We approximate this probability, given our model, over the finite bins $\Delta\chi_{\rm eff}^l$ and $\Delta{\rm M}_{\rm chirp}^m$ as

$$f_{\rm LGRB}^{l,m} \equiv f_{\rm LGRB}(\Delta\chi_{\rm eff}^l, \Delta{\rm M}_{\rm chirp}^m) = \frac{\sum_{\Delta t_i, \Delta Z_j, k} w_{i,j,k}^{\rm intrinsic,LGRB}(\Delta\chi_{\rm eff}^l, \Delta{\rm M}_{\rm chirp}^m)}{\sum_{\Delta t_{i'}, \Delta Z_{j'}, k'} w_{i',j',k'}^{\rm intrinsic}(\Delta\chi_{\rm eff}^l, \Delta{\rm M}_{\rm chirp}^m)}\,, \tag{E.2}$$

where $w_{i,j,k}^{\rm intrinsic}$ is the weight contribution of each binary to the intrinsic detection rate and $w_{i,j,k}^{\rm intrinsic,LGRB}$ is conditioned against the luminous LGRB criteria similar to Eq. (D.5).

The probability $p_{\rm LGRB}$ of each event in GWTC-2 is summarised in Table E.1, where we also report as a reference the median $\chi_{\rm eff}$ and ${\rm M}_{\rm chirp}$ of each event.

Appendix F: Metallicity of LGRB progenitors

The maximal ZAMS metallicity of LGRB progenitors in our models is primarily dictated by the interplay of tides and Wolf-Rayet stellar winds (Nugis & Lamers 2000), which is the dominant phase of stellar wind mass loss and is taken to scale with metallicity as $\propto (Z/Z_\odot)^{0.85}$ (Vink et al. 2001). In our model, this threshold is at $Z_{\rm max} \approx 0.2\,Z_\odot$, where we adopt $Z_\odot = 0.017$ (Grevesse et al. 1996). As shown in Figure 4, this corresponds to the lower 16% bound of the metallicity distribution of newly formed stars at $z = 2$ in the IllustrisTNG simulation, which we use as input in our models. In the same figure we compare the progenitors' metallicities of modeled LGRBs to the sub-sample of the SHOALS LGRBs with 45 identified host galaxies which have measured metallicities for $z < 2.5$ (Graham et al. 2019). We have translated the reported $12 + \log_{10}({\rm O/H})$ to [Fe/H] using an empirical relation between [O/Fe] and [Fe/H] (Nicholls et al. 2017) and took the solar reference as $[{\rm O/H}]_{\rm ref} = 8.83$ (Grevesse & Sauval 1998). Explicitly, we numerically solve the equation [Fe/H] = [O/H]−[O/Fe]([Fe/H]) with respect to [Fe/H] where $[{\rm O/H}] = 12+\log_{10}({\rm O/H})-[{\rm O/H}]_{\rm ref}$ and (see Eq. (5) in Nicholls et al. 2017)

$$[{\rm O/Fe}]\,([{\rm Fe/H}]) = \begin{cases} +0.5, & -2.5 < [{\rm Fe/H}] \leq -1 \\ -0.5 \times [{\rm Fe/H}], & -1 < [{\rm Fe/H}] \leq 0.5 \\ -0.25, & [{\rm Fe/H}] > 0.5\,. \end{cases} \tag{F.1}$$

Typical values of [O/Fe] increase as [Fe/H] decreases due to the increased influence of Type II supernovae over Type Ia at lower metallicities. At face value, we find that 40% of the observed LGRB host galaxies have metallicities lower than $Z_{\rm max}$. However, when taking into account possible systematic uncertainties in the calibration of different metallicity measurement methods, we find that our model can be consistent between 18 and 86% of all observed luminous LGRBs, cf. Figure 4. These uncertainties can be as high as ± 0.35 dex on the measured abundance $\log_{10}({\rm O/H})$ (Kewley & Ellison 2008), where (Graham et al. 2019) determined metallicities using the R_{23} diagnostic scale of Kobulnicky & Kewley (2004) which are skewed towards larger values with respect to other calibration methods (cf. Figure 2 of Kewley & Ellison 2008).

EVENT	emitted LGRB chance in %	$<\chi_{\rm eff}>$	$<M_{\rm chirp}>$ $[M_\odot]$
GW190517_055101	86.85	0.52	26.6
GW190719_215514	59.82	0.31	23.4
GW190412	37.88	0.25	13.3
GW170729	28.37	0.37	35.4
GW190828_063405	26.93	0.19	25.0
GW190527_092055	19.00	0.11	24.3
GW190513_205428	18.89	0.11	21.6
GW190727_060333	15.36	0.11	28.7
GW151012	13.26	0.05	15.2
GW190424_180648	10.29	0.13	31.1
GW190620_030421	9.27	0.33	38.2
GW170823	7.68	0.09	29.2
GW190731_140936	6.39	0.06	29.6
GW190413_052954	5.94	-0.01	24.6
GW170809	5.57	0.08	24.9
GW190828_065509	4.20	0.08	13.3
GW190930_133541	4.15	0.14	8.5
GW190630_185205	3.44	0.09	24.9
GW190915_235702	2.96	0.02	25.3
GW190803_022701	2.54	-0.03	27.3
GW190909_114149	2.04	-0.06	30.6
GW151226	2.01	0.18	8.9
GW190706_222641	1.82	0.28	42.8
GW190413_134308	1.62	-0.04	32.9
GW170814	1.38	0.07	24.1
GW190929_012149	1.00	0.01	35.8
GW190519_153544	0.79	0.31	44.6
GW190512_180714	0.62	0.03	14.6
GW190421_213856	0.55	-0.06	31.2
GW190728_064510	0.49	0.12	8.6
GW170104	0.47	-0.04	21.4
GW190503_185404	0.44	-0.03	30.2
GW190521_074359	0.41	0.09	32.1
GW190720_000836	0.34	0.18	8.9
GW190514_065416	0.25	-0.19	28.7
GW170818	0.18	-0.09	26.6
GW190910_112807	0.15	0.02	34.3
GW190924_021846	0.09	0.03	5.8
GW170608	0.07	0.03	7.9
GW190408_181802	0.07	-0.03	18.3
GW190708_232457	0.07	0.02	13.2
GW190707_093326	0.00	-0.05	8.5
GW150914	0.00	-0.01	28.6
GW190602_175927	0.00	0.07	49.2
GW190521	0.00	0.03	69.2
GW190701_203306	0.00	-0.07	40.3
CUMULATIVE	383.66		

Table E.1: Probabilities of each BBH event in GWTC-2 to have emitted a luminous LGRB, $E^{\rm iso}_{\rm LGRB} > 10^{51}$ erg, at the formation of the BBH system. For comparison, we report the median $\chi_{\rm eff}$ and $M_{\rm chirp}$ for each event. The expected number of GWTC-2 events that had emitted a luminous LGRB is ≈4 out of 46.

4.1.3 Impact on the current field of research

The results obtained in this project are remarkable twofold. If indeed merging BBH progenitors are a dominant formation channel for luminous LGRBs, this would imply that LGRBs could be used as cosmological probes to empirically constrain BBH formation outside the current horizons of GW detectors such as *LIGO* and *Virgo* with horizons at $z \lesssim 1$. Additionally, independently from any rate estimate, Bavera et al. (2022b) found that the *LIGO-Virgo* detectors have already observed a BBH system associated with a LGRB at BBH formation. It is important to notice how this last result is independent of the relative contribution of this channel to the total population of LGRBs. It only depends on the ratio calibration between the disk energy-radiation efficiency and average beaming fraction, $\eta/f_{\rm B}$, against the distribution of isotropic equivalent luminous LGRB energies (see Figure 3 of Bavera et al. 2022b). In the following paragraphs, we summarise how the work presented in Bavera et al. (2022b) has impacted current high-energy astrophysics research.

Recently, Fuller & Lu (2022) studied tidal spun-up binaries using an updated model of the Tayler-Spruit dynamo (Spruit 2002; Fuller & Ma 2019) for efficient AM transport based on the Tayler instability (Spruit 1999; Fuller et al. 2019). The authors confirm the results presented in Chapter 2, where we found the BH-WR parameter space of orbital periods $p \lesssim 1\,$day leading to spun-up second-born BHs. Fuller & Lu (2022) explicitly confirms our results that the BH spin of systems with $p \lesssim 0.4\,$day approaches unity for BH masses $> 5\,M_{\odot}$. Following the procedure presented in Bavera et al. (2022b), Fuller & Lu (2022) investigates the possibility that tidally spun-up WR stars lead to LGRB production under the collapsar model. Once again, the authors reach a similar conclusion to the Bavera et al. (2022b) results finding that the binary channel may be able to account for most LGRBs of the Universe. However, Fuller & Lu (2022) points out that this evolutionary scenario cannot simultaneously explain the observed rate of Ic broad-line supernovae thought to occur from the discussed binary evolutionary scenario of LGRBs. Alternative models to explain Ic broad-line supernovae might also be possible. For example, the CHE channel leading to a wider BBH systems that do not merge within the age of the Universe, boosting Ic broad line supernovae rates without increasing BBH merger rates. Alternatively, the case A mass-transfer scenario also invoked for explaining the large inferred spins of BHs in high-mass X-ray binaries (HMXB; Liu et al. 2008, 2010; Gou et al. 2009, 2014) might be another possibility (Qin et al. 2019). For HMXBs like the one found in our own Galaxy (Cygnus X-1; Bowyer et al. 1965; Orosz et al. 2007, 2011; Miller-Jones et al. 2021), our current understanding of the future evolution of such systems is that they will avoid the formation of merging BBHs (Belczynski et al. 2011, 2012; Wong et al. 2012; Neijssel et al. 2021).

Inspired by Bavera et al. (2022b) results and with a different approach based on a phenomenological BBH delay time model and a statistical argument, Arcier & Atteia (2022) investigated whether BBH mergers and LGRBs are coming from the same population. The study finds that unless highly rotating BBH mergers have a long coalescence time of several Gyr (not supported by current models, see Bavera et al. 2020, 2021a, 2022b), the BBH and LGRB populations cannot have the same formation history. In spite of that, Arcier & Atteia (2022) analysis still supports the potential contribution of a few percent contaminant of the BBH merger channel to contribute to the LGRB population. It is important to notice that this study uses fiducial beaming fractions, which are $3 - 12$ times smaller than the fiducial

value used in Bavera et al. (2022b). Figure C1 of Bavera et al. (2022b) shows how uncertainties in this currently unconstrained parameter affect rate results. Indeed, for smaller values than the fiducial one assumed by Bavera et al. (2022b), these alternative models would lead to a smaller contribution of the BBH channel to LGRB formation. Hence, in this case, Bavera et al. (2022b) models agrees with Arcier & Atteia (2022)'s findings that other channels than isolated binary evolution might be responsible for producing the bulk of the observed LGRB population.

We finally mention that our results are also relevant to radio astronomy. For example, Lloyd-Ronning (2021) investigated the possibility that radio laud LGRBs result from the collapse of massive stars in interacting binaries. In contrast, the authors suggest that radio-quiet LGRBs are produced by the collapse of single massive, rapidly rotating stars. If such a scenario would turn out to be true in Nature, then radio follow-up observation of LGRBs may offer us a new and unique insight to constrain the underlying physics of these objects and eventually BBH formation.

4.2 On the electromagnetic counterpart observability of black-hole–neutron-star mergers

The chances of a BH-NS merger event emitting an EM counterpart depends on the compact object properties like masses, BH spin, and NS radius. An EM counterpart occurs if the NS tidal disruption radius is outside the ISCO of the BH. For a non-spinning BH and a NS of mass $1.4\,M_\odot$, this condition is met for BHs of mass $\lesssim 3.5\,M_\odot$ (Capano et al. 2020). The exact value depends on the NS radius, determined by the NS equation of state (Capano et al. 2020). If the BH is spinning, the ISCO moves closer to the BH event horizon, and the BH mass limit for an EM counterpart to occur moves to larger values of $\lesssim 20\,M_\odot$ for maximally spinning BHs ($a_{\rm BH} \simeq 1$; Foucart et al. 2018). Chapter 2 showed that tidal interactions in short-orbit BH-WR binaries can lead to the formation of highly rotating second-born BHs. Similar to the CE formation channel of BBHs, we could imagine an evolutionary formation channel for merging BH-NS systems where the NS is formed first and the WR stars in close NS-WR binaries tidally spin up to form highly rotating BHs.

To make qualitative statements about EM counterparts of BH-NS mergers, we need to extend our `MESA` BH-WR simulation library to sample the NS-WR parameter space where the BH is formed second and low mass BH-WR regime where the NS is formed second. Extending the parameter space of Bavera et al. (2021a) BH-WR simulations to cover NS star and low WR stellar masses is computationally expensive. This is due to two reasons. First, we want to sample multiple NS masses. Second, low mass WR stars, progenitors of NSs, expand from radii $\lesssim 1\,R_\odot$ at zero-age helium main sequence up to $100\,R_\odot$ during helium burning. Hence, this portion of the parameter space leads to mass transfer episodes (see, e.g., Figure 14 in Fragos et al. 2022). Given the mentioned computational constraints, we only expanded a subsample of 1/3 of the metallicities covered in Bavera et al. (2021a) to the considered mass regime, consisting of ten metallicities equally spaced in the log-range of $Z \in [0.0001, 0.0174]$. To the original sample of 11 BH masses taken in the log-range $[2.5, 54.4]\,M_\odot$, we simulate ten additional NS masses in the log-range $[1, 2.28]\,M_\odot$, assuming the NS can be treated as a point mass in the simulation similar to the BH. The original sample of 17 WR star masses in the log-range $[8, 80]\,M_\odot$ is extended with an additional

sample of 26 WR star masses in the range $[2.5, 12]\,M_{\odot}$. Finally, because the lowest mass WR stars can fit in a smaller orbit, we extend the 20 orbital periods sampled in the log-range $[0.09, 8]$ days by one extra period at 0.04 days. The subset of Bavera et al. (2021a) `MESA` simulations consisting of 37,400 models was extended to a total of $172,740$ `MESA` models. To highlight the computational effort and resources required in this task, we report that the new raw `MESA` simulation output of the grid extension accounts for ~ 3.7 TB (to be compared with the original grid size of ~ 2.5 TB).

The extended simulation grid was then used in Román-Garza et al. (2021) to study merging BH-NS formation channels associated with EM counterparts. In Appendix C, we present the mentioned project in detail and discuss it's impact on the current field of research. In addition to studying the fraction of merging BH-NS systems that will produce an EM counterpart from the tidal spin-up channel (constrained to be $\leq 10\%$), Román-Garza et al. (2021) also investigated the impact of newer core-collapse prescriptions on BBH and BH-NS merger rates. The newer predictions based on detailed core-collapse models indicate a stochastic relation between the explodability of massive stars and their pre-collapse core masses, which is in contrast to commonly used prescriptions in BH-NS rapid population synthesis (see §1.2.1).

Chapter 5

Back to the future

During the past few years, dozens of GW detections by the LVK Collaboration have revealed the existence of merging BBHs, starting the new era of multi-messenger astronomy. The improved sensitivity of the LVK detectors, and the development of the next generation of ground-based detectors, such as the *Einstein Telescope* and the *Cosmic Explorer*, and future space-based detectors like *LISA*, will increase detection rates by orders of magnitude. However, after more than half a decade since the first detection of GWs, the origin of merging BBHs remains an open question. This is not due to a lack of theoretical predictions, but rather because of model degeneracies and unconstrained astrophysical processes in the different BBH formation channels. The present thesis aimed at a deeper theoretical understanding of BBH formation through isolated binary evolution in galactic fields, focusing on the processes which affect the BH spins. Among other observable signatures, BBH spin distributions have the potential to disentangle the origin of merging BBHs. To this end, in preparation for future GW detections, we showcased the constraining power of hierarchical Bayesian model selection inference in constraining model uncertainties and quantifying the origin of merging BBHs.

5.1 Conclusions

The work presented in this thesis made contributions to different research fields and can be summarised in three distinct categories.

5.1.1 How do merging binary black holes form?

The models of isolated binary evolution presented in this thesis, distinguish themselves from others as they include accurate BBH spin estimates, which have already played a key role in shaping the current field of GW astrophysics. Such detailed simulations followed the BBH progenitor tidal spin-up phase and stellar core collapse, resulting in accurate BH spin estimates for LVK sources (Bavera et al. 2020, 2021a,b). Three distinct evolutionary pathways lead to merging BBHs within the isolated binary formation channel in galactic fields. Each of them is characterized by distinct binary interaction phases, affecting the BBH's observable properties such as BH mass, spin and the redshift of merger. These

pathways are (i) a stable mass transfer and a common envelope phase (CE channel; Bavera et al. 2020, 2021a, 2022a,b), (ii) double stable mass transfer (SMT channel; Bavera et al. 2021a, 2022a,b), or (iii) chemically homogeneous evolution (CHE channel; Bavera et al. 2022a,b). These model advancements are crucial because the BHs spin orientations and magnitudes are the keys to differentiate the isolated binary evolution pathways against other formation channels, and are currently poorly predicted in standard rapid population synthesis models. Combined predictions for the other formation channels and current GW events, the presented models favored a mixture of channel contributions over a single dominant pathway in the *LIGO-Virgo* detectable population of merging BBHs (Zevin et al. 2021a). Additionally, to further study BBH formation, we showed how one could use the SGWB to add an additional constraint to multi-channel hierarchical model selection (Bavera et al. 2022c). Finally, the introduced models of isolated binary evolution predict the existence of correlations between BBH spins and their merger redshift, which will be confirmed by the next generation of GW detectors (Bavera et al. 2022a).

5.1.2 Probing black hole merger formation with multi-messenger astrophysics

The discussed detailed models have a direct impact on multi-wavelength and multi-messenger observations. For example, we identified the subpopulation of highly spinning BBH mergers through isolated binary evolution as a significant contributor to the population of luminous LGRBs (Bavera et al. 2022b). We found two GW events in the second GW transient catalog (GWTC-2) with a probability more than 50% of being associated with a LGRB at the formation of the BBH system indecently of the rate contribution of the binary channel to LGRBs. The proposed link between LGRBs and the progenitors of spinning BBH mergers has the potential to probe the last well outside the horizon of current-generation GW observatories and out to cosmological distances. We also indirectly provided constraints on stellar core-collapse mechanisms by studying the relative fraction of EM counterparts to BH-NS merger events (Román-Garza et al. 2021). Detailed binary-evolution models are critical in determining whether the NS will be tidally disrupted by the BH, as spinning BHs increase the probability of EM counterparts produced by BH-NS mergers.

5.1.3 Software innovation and impact on the broader astrophysical community

During my Ph.D. research and, in part, through the work presented in this thesis, I contributed to the development of `POSYDON` (Fragos et al. 2022). The `POSYDON` software is a next-generation binary population synthesis code incorporating full stellar structure and binary evolution modeling, using the `MESA` code throughout the whole evolution of binaries. This allows `POSYDON` to employ self-consistent treatments of physical processes in stellar and binary evolution, including (i) realistic mass-transfer calculations and physical assessment of stability, (ii) internal angular-momentum transport and spin-orbit coupling for asynchronous binaries due to tides and mass-transfer, (iii) stellar core sizes, and central/surface abundances, which are calculated taking into account the effects of binary interactions, and (iv) compact object masses and spins that are based on the structure of stars as products of self-consistent binary evolution modeling. Such innovation in binary population synthesis modeling software has the potential

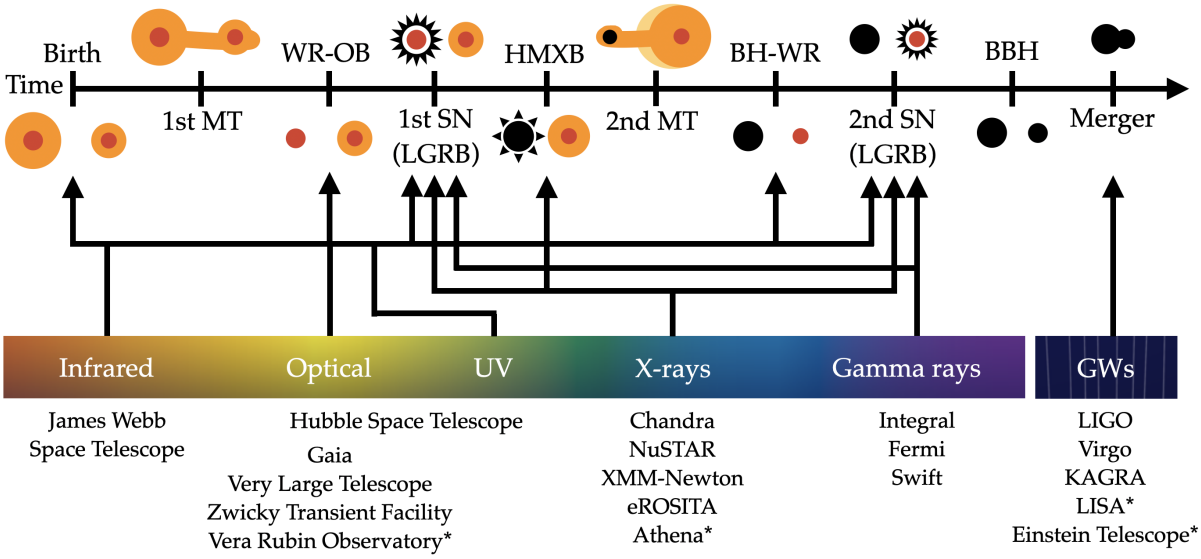

Figure 5.1: Diagram summarising all intermediate phases of the binary system evolving to become a GW source. Some of these phases can be probed with EM observations. The various space telescopes and ground observatories, each with different probing wavelengths of the EM spectrum, are indicated below the colored band. Future observatories are marked with an asterisk. We use the additional acronyms of mass transfer (MT) and supernova (SN) in the diagram.

to deeply impact the whole astrophysical community, well outside the field of GW science. For example, `POSYDON` has already been used to study stripped-envelope supernovae (Type IIb, Ib, Ic) in the context of single stellar evolution (Zapartas et al. 2021), demonstrating that massive, envelope-stripped, single stars, coupled with the state-of-the-art explodability prescriptions (implemented in `POSYDON`) are in tension with the observations of stripped-envelope supernovae, adding an independent physical argument toward an alternative channel, e.g., binary progenitors.

5.2 Final remarks and outlook

The formation pathways of merging BBHs are still surrounded by uncertainties related to stellar and binary evolution, which GW observations alone might not be able to constrain. Electromagnetic observations of intermediate phases of the binary systems along their pathways to become merging BBHs also have the potential to constrain these uncertainties. Ground-based and space telescopes provide rich information on the evolution of GW source progenitors. For example, ground observatories such as the *Very Large Telescope* can constrain initial binary conditions (Sana et al. 2012). Similarly, the binary state after the first mass transfer, composed of WR-OB stars, can be probed by multiple observatories and telescopes (e.g., van der Hucht 2001). High-mass X-ray binaries probe[1] the binary system after the

[1]The formation and future evolution of HMXBs is still a matter of active research. The current understanding of the future evolution of HMXBs is that they will avoid forming merging BBHs (e.g., Belczynski et al. 2011, 2012; Wong et al. 2012; Neijssel et al. 2021), however see Marchant et al. (2017). This intuition is mostly based on the rapid binary population synthesis approach. See Section 1.5.2 for the limitations of this technique which might affect such conclusions. Hence, for completeness, we indicate in Figure 5.1 when, hypothetically, the HMXB phase could occur during the evolution of a BBH progenitor.

first core-collapse (e.g., Vanbeveren et al. 2020), detections of which are carried out by X-ray telescopes like *Chandra, XMM-Newton, eROSITA, NuSATR* (e.g., Lazzarini et al. 2018) and *Athena* in the future (Barcons et al. 2017). Upcoming *GAIA* releases of astrometric data will provide BH-WR observations (e.g., Breivik et al. 2017; Mashian & Loeb 2017), which probe the binary phase following the second mass-transfer episode. Moreover, type Ib and Ic supernovae detected by surveys like the *Zwicky Transient Facility* (Perley et al. 2020) and the upcoming *Vera Rubin Observatory* (Ivezić et al. 2019) or *Fermi* (Atwood et al. 2009), and together with *SWIFT* LGRB observations (Perley et al. 2016), probe the first and second core collapse of the stars. Additional constraints on the environments of these transient events are obtained by detailed photometric and spectroscopic follow-up observations with the *Hubble Space Telescope* and *James Webb Space Telescope*. Figure 5.1 shows a diagram of all mentioned phases of a binary system evolving to become a merging BBH. Combining EM and GW observations with detailed binary population synthesis models in a full-scale hierarchical Bayesian model selection analysis, is a rich but uncharted territory that will advance the current understanding of isolated binary evolution, and shed light on the origin of merging double compact objects in general.

Appendix A

Suspicious siblings

A.1 The distribution of mass and spin across component black holes in isolated binary evolution

A.1.1 A brief introduction

The *LIGO-Virgo* collaboration reported the detection of BBHs systems with non-zero spins and systems like GW190412 with asymmetric mass ($q \simeq 0.28$) and spin residing in the heavier BH of the pair ($|\vec{\chi}_1| > 0.22$ at 95% credibility). The combination of BH masses and spins across binary components carry important clues about the formation history of the BBH system. As discussed in Section 1.3.1.1, under the paradigm that the angular-momentum transport inside stare is efficient, isolated binary evolution is expected to lead to the formation of the first-born BH with a negligible spin (Qin et al. 2018; Fuller & Ma 2019; Belczynski et al. 2020). Because the more massive star of the binary evolves faster, the first-born BH is *often* expected to form the more massive BH of the pair. Alternatively, appreciable accretion onto BHs (see §2.2) or mass ratio reversion during the first mass transfer episode followed by tidal spin up (see §2.1) can lead to highly spinning primary BHs. This project explored the viability of isolated binary evolution in forming asymmetric-mass, spinning primary BBH systems as observed by the LVK collaboration.

A.1.2 Manuscript

The conducted study Zevin & Bavera (2022) was published in *The Astrophysical Journal* in July 2022. The arXiv open-access version of the manuscript is presented in the following pages.

Draft version May 27, 2022
Typeset using LaTeX **twocolumn** style in AASTeX63

arXiv:2203.02515v2 [astro-ph.HE] 26 May 2022

Suspicious Siblings: The Distribution of Mass and Spin Across Component Black Holes in Isolated Binary Evolution

Michael Zevin[1, 2, *] and Simone S. Bavera[3]

[1] *Kavli Institute for Cosmological Physics, The University of Chicago, 5640 South Ellis Avenue, Chicago, Illinois 60637, USA*
[2] *Enrico Fermi Institute, The University of Chicago, 933 East 56th Street, Chicago, Illinois 60637, USA*
[3] *Département d'Astronomie, Université de Genève, Chemin Pegasi 51, CH-1290 Versoix, Switzerland*

ABSTRACT

The LIGO and Virgo gravitational-wave detectors have uncovered binary black hole systems with definitively non-zero spins, as well as systems with significant spin residing in the more massive black hole of the pair. We investigate the ability of isolated binary evolution in forming such highly spinning, asymmetric mass systems through both accretion onto the first-born black hole and tidal spin-up of the second-born black hole using a rapid population synthesis approach with detailed considerations of spin-up through tidal interactions. Even with the most optimistic assumptions regarding the efficiency at which an accreting star receives material from a donor, we find that it is difficult to form systems with significant mass asymmetry and moderate or high spins in the primary black hole component. Assuming efficient angular momentum transport within massive stars and Eddington-limited accretion onto black holes, we find that $< 1.5\%$ of systems in the underlying binary black hole population have a primary black hole spin greater than 0.2 and a mass asymmetry of greater than 2:1 in our most optimistic models, with most models finding that this criteria is only met in $\sim 0.01\%$ of systems. The production of systems with significant mass asymmetries and spin in the primary black hole component is thus an unlikely byproduct of isolated evolution unless highly super-Eddington accretion is invoked or angular momentum transport in massive stars is less efficient than typically assumed.

1. INTRODUCTION

Prior to the direct observation of compact binary coelescences via gravitational waves (GWs), the expected birth properties of black holes (BHs) relied primarily on highly-uncertain predictions from stellar population modeling and a limited number of indirect observations. The past half-decade has brought an observational sample of binary black hole (BBH) mergers that has not only provided invaluable insights into the birth properties of BHs, but also unveiled a number of unexpected systems that are in tension with the theoretical expectations of BH formation channels. Trends and features of the population as a whole are also becoming apparent, such as structure beyond a sharp cutoff in the BH mass distribution (e.g., Abbott et al. 2021a) and potential correlations between intrinsic parameters of BBH systems (e.g., Callister et al. 2021).

Certain BBH systems observed by the LIGO–Virgo–KAGRA Collaboration (LVK) collaboration show unexpected features not just in their masses or spins individually, but their distribution of mass and spin across the two binary components. For example, GW190412 was the first BBH to have been measured with definitively asymmetric component masses ($q \simeq 0.28$, where $q \coloneqq m_2/m_1$ with $m_2 \leq m_1$) and non-zero spin ($\chi_{\rm eff} > 0.14$ at 90% credibility, where $\chi_{\rm eff} \coloneqq (m_1 a_{1z} + m_2 a_{2z})/(m_1 + m_2)$ and a_z is the projection of the BH dimensionless spin aligned with the angular momentum) (Abbott et al. 2020). Because of the mass asymmetry in the signal, the component spin of the more massive primary BH was able to be disentangled from the leading-order spin term $\chi_{\rm eff}$, with the more massive BH having a dimensionless spin of $a_1 > 0.22$ at 95% credibility. More BBH systems with spinning component BHs have been identified in recent GW catalogs (e.g., Abbott et al. 2021b,c; Nitz et al. 2021; Olsen et al. 2022).

The combination of BH masses and spins across both binary components hold important clues about both the formation environment of BBH systems as well as the intricate physical processes occurring within and between their progenitor stars. In massive stars, angular momentum (AM) transport between the stellar core and envelope significantly impacts the expected spin of the resul-

michaelzevin@uchicago.edu

* NASA Hubble Fellow

tant BH. Models of AM transport in massive stars, such as the Taylor-Spruit magnetic dynamo (Spruit 2002), indicate AM transport to be highly efficient (Heger et al. 2005; Fuller et al. 2019). Under this paradigm, AM would thus be transported to the outer layers of the star during its giant phase and lost due to wind mass loss or Roche-lobe overflow (RLO) mass transfer (MT) onto a binary companion, resulting in a slowly-spinning core and upon collapse a BH with a dimensionless spin extremely close to zero (Qin et al. 2018; Fuller & Ma 2019, though see Belczynski et al. 2020 for variations in this mechanism that can lead to slightly larger spins of $a \simeq 0.1$). The low effective spins in most BBHs also observationally hint at efficient AM transport in their progenitors (Abbott et al. 2021a,d; Miller et al. 2020; Zevin et al. 2021), though certain systems are beginning to challenge the universality of quasi-isolated BHs having low spins at birth (e.g., Zevin et al. 2020a; Qin et al. 2021).

Even in the efficient AM transport paradigm, binary processes such as tides can induce high spins on stellar cores that can be preserved in their remnants. This can be accomplished in three general ways: (a) chemically homogeneous evolution, where two massive stars with near-equal masses in a tight binary system at zero-age main sequence (ZAMS) tidally interact on the main sequence, which induces strong rotational mixing that prevents expansion and AM loss, resulting in two massive, spinning BHs (Mandel & De Mink 2016; De Mink & Mandel 2016; Marchant et al. 2016); (b) Case A MT (i.e., while the donor is on the main sequence) for binaries on tight orbits of about a day or less, where the donor and accretor are tidally locked during MT and the envelope of the donor is stripped, leading the donor to never expand during its evolution into a Wolf-Rayet (WR) star (Qin et al. 2019); (c) tidal spin-up of a WR star (i.e., a naked helium star), either by an already-formed compact object following a stable or unstable MT event that hardens the binary to sub-day orbital periods (Detmers et al. 2008; Kushnir et al. 2017; Hotokezaka & Piran 2017; Zaldarriaga et al. 2018; Qin et al. 2018; Bavera et al. 2020; Olejak & Belczynski 2021; Steinle & Kesden 2021; Fuller & Lu 2022) or following a double-core common envelope (CE) scenario where two helium cores of supergiant stars are enveloped in the envelope of one or both of the supergiants and hardened through a CE phase to a point where the two cores can tidally interact (Brown 1995; Dewi et al. 2006; Hotokezaka & Piran 2017; Neijssel et al. 2019; Olejak & Belczynski 2021). Extremely metal-poor stars born in the early universe may also be able to retain a substantial hydrogen envelope and collapse into high-spinning BHs, though their contribution to the local merger population is likely small (Cruz-Osorio et al. 2021; Tanikawa et al. 2022). Following formation, a BH can also gain angular momentum through accretion, though any appreciable spin-up would require accretion to either be highly super-Eddington or transpire over timescales far longer than the evolutionary timescales of massive stars (van Son et al. 2020; Bavera et al. 2021b; Qin et al. 2022).

Systems with unequal masses and spinning primaries provide a challenge to the isolated binary evolution scenario. BBHs that result from chemically homogeneous evolution strongly favor near-equal-mass systems (Marchant et al. 2016; Mandel & De Mink 2016; du Buisson et al. 2020). The Case A MT scenario has been invoked for explaining the large inferred spins of BHs in high-mass X-ray binaries (Qin et al. 2019), though binary modeling finds high-mass X-ray binaries in the Milky Way are unlikely to form merging compact binary systems (Belczynski et al. 2011, 2012; Neijssel et al. 2021). The BH–WR tidal spin-up scenario is predicted to be common for post-CE binaries (Bavera et al. 2021b), though the efficiency of this pathway is highly dependent on CE ejection efficiency and can only impart spin on the second-born BH progenitor. Though the tidal spin-up of two WR stars following a double-core CE may lead to significant spins in both BHs (Olejak & Belczynski 2021), it typically leads to near-equal-mass mergers and operates at a much lower rate than the BH–WR tidal spin-up scenario (Neijssel et al. 2019). Lastly, though spinning up the first-born BH through accretion can be accomplished via highly super-Eddington MT, if accretion is pushed too high the rate of mergers from this channel can drop by orders of magnitude (Bavera et al. 2021b).

The BH–WR tidal spin-up scenario described above may be a valid explanation for the observed spins of primary BHs if the second-born BH can oftentimes be more massive than the first-born BH. In isolation, a more massive star at ZAMS will typically lead to a more massive remnant (though see e.g. Patton et al. 2022). However, binary interactions throughout the co-evolution of the two stars can alter this picture. In particular, since the more massive star at ZAMS will almost always evolve off the main sequence first, it will be the first to overflow its Roche lobe and transfer material onto its companion. The fraction of transferred mass deposited onto the companion depends on an uncertain MT accretion efficiency (Bouffanais et al. 2021b), and can potentially lead to a mass ratio reversal (MRR), where the star that was originally less massive at ZAMS has its mass inflated from the accreted material and leads to a more massive remnant (e.g., Olejak & Belczynski 2021;

Broekgaarden et al. 2022; Hu et al. 2022). The originally more massive star will still proceed through the remainder of its evolution quicker, and create the first compact object in the binary. Then, the originally less massive star can be stripped of its envelope and harden its orbit with the compact object companion during the second MT episode, and be tidally spun up as a WR star.

In this paper, we explore the viability of the MRR/tidal interaction and BH accretion spin-up scenarios for forming the asymmetric-mass, spinning-primary BBH systems observed by the LVK. In Section 2 we overview our populations models and the determination of BH spins through tidal spin-up and accretion. Analysis of these models, with a particular focus on mass ratios, MRR, and BH spins, is in Section 3. We contextualize our results with GW events and population properties in Section 4, and discuss broader implications and caveats in Section 5. Throughout this work we assume solar metallicity of $Z_\odot = 0.017$ (Grevesse & Sauval 1998) and *Planck 2018* cosmological parameters (Alves et al. 2020).

2. POPULATION MODELS

We use the open-source binary population synthesis code `COSMIC`[1] (Breivik et al. 2020) for modeling populations of BBH mergers. `COSMIC` is based on single-star evolutionary tracks from the `SSE` code (Hurley et al. 2000) and the binary star implementations of `BSE` (Hurley et al. 2002). A large number of updates have been made to the physical prescriptions used for initial conditions, winds, the onset of mass transfer and system evolution during RLO, remnant formation, and natal kicks. Rather than simulating a fixed number of systems with specific physical assumptions at a given metallicity, `COSMIC` samples systems until user-specified convergence criteria have been reached in the population.[2] Though we highlight physical assumptions pertinent to this work in the following section, we refer the reader to Breivik et al. (2020) for further details.

2.1. *Physical Assumptions*

A large number of physical uncertainties embed models of massive-star binary evolution, which have significant impacts on the population properties of their BBH remnants (e.g., Giacobbo et al. 2018; Giacobbo & Mapelli 2018; Kruckow et al. 2018; Bouffanais et al. 2019; Stevenson et al. 2019; van Son et al. 2020; Bavera et al. 2021b; Belczynski et al. 2021; Santoliquido et al. 2021; Zevin et al. 2021). Though recent studies have become increasingly thorough in their coverage of this highly uncertain parameter space (see Broekgaarden et al. 2021 for a recent overview), it is computationally expensive and can make interpretation difficult. We instead narrow our parameter space coverage to uncertainties that have the strongest effect on MRR and BH spin-up.

The main parameter varied between models is the accretion efficiency:

$$f_{\rm acc} = \frac{\dot{M}_{\rm acc}}{\dot{M}_{\rm don}} \in [0, 1] \tag{1}$$

where $\dot{M}_{\rm don}$ is the mass-loss rate of the donor during RLO and $\dot{M}_{\rm acc}$ is the mass accepted by the accretor. The additional mass $(1 - f_{\rm acc})\dot{M}_{\rm don}$ is lost from the system with an angular momentum as if it were a wind from the accretor. We simulate 5 variations for $f_{\rm acc}$: $[0.0, 0.25, 0.5, 0.75, 1.0]$ where $f_{\rm acc} = 0.0$ means that the accretor accepts no mass from the donor and $f_{\rm acc} = 1.0$ means that the accretor accepts all of the mass transferred by the donor. Though timescales pertinent to the response of the envelope to mass transfer may provide a more realistic description of the amount of material a star can accrete in a given amount of time, this simple parameterization can capture the extreme limits of accretion efficiency, which has an important impact on possible MRR during stable MT and subsequent tidal spin-up of the second-born BH. This parameter also impacts compact binary merger rates and mass spectra (see e.g., Kruckow et al. 2018), and has the promise of being constrained with GW data (Bouffanais et al. 2021b). The mass lost rate from the donor during RLO, $\dot{M}_{\rm don}$, follows the prescription of Hurley et al. (2002).

In addition, we simulate 2 separate assumptions for the amount at which BHs can accrete material above the Eddington rate, which impacts the accretion-induced spin-up of the first-born BH:

$$\dot{M}_{\rm BH}^{\rm max} \simeq \gamma_{\rm Edd} \times R_{\rm s} \times 2.08 \times 10^{-3}\, M_\odot {\rm yr}^{-1} \tag{2}$$

where $R_{\rm s}$ is the Schwarzschild radius of the BH in units of Solar radii and $\gamma_{\rm Edd}$ is a multiplicative factor that allows for super-Eddington accretion (i.e., $\gamma_{\rm Edd} = 1$ would limit accretion onto a BH to the Eddington rate). The maximum rate at which a BH can accrete is thus given by

$$\dot{M}_{\rm BH} = {\rm MIN}(f_{\rm acc}\dot{M}_{\rm don}, \dot{M}_{\rm BH}^{\rm max}) \tag{3}$$

Note that we allow $f_{\rm acc}$ to alter the accretion efficiency of compact objects as well as (non-degenerate) stars in

[1] cosmic-popsynth.github.io, Version 3.4

[2] We set the maximum number of simulated binaries for all runs to 10^8, and thus specified convergence criteria are sometimes not reached especially for high-metallicity populations where the BH formation efficiency is extremely low.

our models, and thus at $f_{\rm acc} = 0$ BHs will not gain mass through accretion. We choose two values for $\gamma_{\rm Edd}$: $[1, 10^5]$. The highly super-Eddington parameterization of $\gamma_{\rm Edd} = 10^5$ is extreme but chosen because it can lead to a significant number of BHs to be spun up through stable MT onto the BH, whereas lower values for $\gamma_{\rm Edd}$ are much less capable (see e.g. Bavera et al. 2021b).

The final parameter variations we explore govern the evolution through a CE phase. These affect both the survival of systems that evolve through a CE phase and post-CE orbital separations, thereby impacting the ability of the progenitors of the second-born BH to tidally spin up. We model 3 variations for the efficiency at which orbital energy of the inspiraling binary is transmitted into the energy needed to eject the envelope, assuming the $\alpha - \lambda$ formalism for energetics during CE evolution (Webbink 1984): $\alpha_{\rm CE} = [0.5, 1.0, 2.0]$. We use the variable prescription in Claeys et al. (2014) for determining the value of λ. Stellar type-dependent mass ratios that determine whether MT proceeds stably or unstably follow Neijssel et al. (2019), though we also run a subset of models that follow Belczynski et al. (2008) to investigate the impact this parameterization has on MRR and tidal spin-up (see Appendix B).

All models sample binary initial conditions independently following Kroupa (2001) and Sana et al. (2012), and assume a pessimistic CE scenario in which Hertzprung gap stars that experience unstable RLO merge in the CE and do not form compact binaries (see Belczynski et al. 2008). We assume a fixed binary fraction of $f_{\rm bin} = 0.7$, which only affects the arbitrary normalization during the resampling described in Section 2.3. Wind mass loss follows Hurley et al. (2002) with updates for O and B stars (Vink et al. 2001) and metallicity-dependent WR winds (Vink & de Koter 2005). Remnant masses are determined assuming the Delayed supernova engine prescription of Fryer et al. (2012) with neutrino mass loss as implemented in Zevin et al. (2020b). A maximum neutron star mass (and therefore minimum BH mass) of $3\,M_\odot$ is assumed. Supernova kicks, which can tilt the orbital plane and lead to BH spins that are misaligned from the orbital angular momentum, are drawn from a Maxwellian with a dispersion of $265\,{\rm km\,s^{-1}}$ (Hobbs et al. 2005) and are fallback modulated, leading to a suppression of kick strength as a function of BH mass (e.g., Rodriguez et al. 2016). BH masses as a result of pulsational pair instability and pair instability supernovae are treated using fits to the results of Marchant et al. (2019).

Population models only retain systems that result in a BBH that merges within a Hubble time. For each population model, we simulate 12 fixed metallicities spaced uniformly in log between $Z = [10^{-4}, 0.03]$. The permutation of all these model variations leads to $5\,[f_{\rm acc}] \times 2\,[\gamma_{\rm Edd}] \times 3\,[\alpha_{\rm CE}] \times 12\,[Z] = 360$ individual population sequences. Throughout this work, we present results that combine the 12 discrete metallicities for each model set according to the joint star formation and metallicity evolution of the universe (see Section 2.3).

2.2. *BH Spins*

Tracking the spin evolution of BH progenitors is difficult in rapid population synthesis, and typically relies on simplified prescriptions. This is because rapid population synthesis codes lack information about the internal structure of a star, and thus cannot accurately model the AM transport between binary components or back-reaction on the structure and evolution of each individual star. We assign spins to the first-born BH ($a_{\rm 1b}$) and second-born BH ($a_{\rm 2b}$) in our population during post-processing, assuming that angular momentum transport is highly efficient (Spruit 2002; Fuller & Ma 2019) such that the first-born BH can only attain nonzero spin through accretion after it becomes a compact object and the second-born BH can only attain nonzero spin through tidal spin-up of its WR progenitor. Thus, BHs born in quasi-isolation where their progenitors are not susceptible to tidal spin-up are assumed to be Schwarzschild BHs, though we examine the impact of relaxing this assumption on our results to account for other possible mechanisms for inducing spin in Section 5. We note that post-processing spins in this way leads to a slight inconsistency in our determination of inspiral times through GW emission, as spins aligned with the orbital angular momentum will slightly expedite the eventual merger. However, this has a minor effect for the timescales considered, since spin effects enter at a higher post-Newtonian order and do not impact the inspiral rate significantly until the binary is close to merger (Damour 2001).

The spin of the first-born BH is calculated assuming stable MT from a disk of material being accreted from the innermost stable circular orbit of the BH as in Thorne (1974):

$$a_{\rm 1b} = \begin{cases} \sqrt{\frac{2}{3}}\frac{M_{\rm i}}{M_{\rm f}}\left[4 - \sqrt{\left(\frac{18M_{\rm i}^2}{M_f^2} - 2\right)}\right] & 1 \leq \frac{M_{\rm f}}{M_{\rm i}} \leq \sqrt{6} \\ 1 & \frac{M_{\rm f}}{M_{\rm i}} > \sqrt{6} \end{cases} \tag{4}$$

where $M_{\rm i}$ is the mass of the BH prior to MT and $M_{\rm f}$ is the mass of the BH after MT has ceased. For the determination of $a_{\rm 1b}$, we only consider mass gained from RLO stable MT and neglect any potential mass gain from wind accretion. We also assume that the BHs gain no mass when inspiraling through a CE (though see e.g.

MacLeod & Ramirez-Ruiz 2015; Cruz-Osorio & Rezzolla 2020). The spin of the second-born BH is determined using the semi-analytic fits from Bavera et al. (2021a), which are based on detailed spin evolution of BH–WR systems during tidal spin-up using the `MESA` simulations (Paxton et al. 2011, 2013, 2015, 2018, 2019) under the `POSYDON`[3] framework (Fragos et al. 2022). Bavera et al. (2021a) found the spin of the second-born BH to be well-approximated by a quadratic function dependent on BH–WR log-orbital period $\log_{10}(p/\mathrm{day})$, which implicitly is dependent on the mass of the WR star $M_{\rm WR}$ at Helium depletion:

$$a_{2\rm b} = \begin{cases} f^{\alpha} \log_{10}\left(\frac{p}{\rm day}\right)^2 + f^{\beta} \log_{10}\left(\frac{p}{\rm day}\right) & 0.1 \leq \frac{p}{\rm day} \leq 1 \\ 0 & \frac{p}{\rm day} > 1 \end{cases} \tag{5}$$

where $f^{(\alpha,\beta)} = -c_1^{(\alpha,\beta)}/[c_2^{(\alpha,\beta)} + \exp(-c_3^{(\alpha,\beta)} M_{\rm WR}/M_\odot)]$ with coefficients $c_1^{(\alpha,\beta)}$, $c_2^{(\alpha,\beta)}$, and $c_3^{(\alpha,\beta)}$ determined through least-square minimization, see Bavera et al. (2021a). Since the grid of systems used for the fit only extended down to orbital periods of 0.1 day (given by the physical limit of RLO at zero-age helium main sequence in the `MESA` simulations), for systems in our population with $p < 0.1$ day we assume their orbital periods are 0.1 day when computing the fit. Across our population models, 0.2 − 2.9% of BH–WR systems have orbital periods of $p < 0.1$ day and are extrapolated in this manner.

We show the second-born BH spins for a single population model in Figure 1. For $M_{\rm WR} < 14\,M_\odot$ at low periods ($p < 0.3$ day) the resultant BH spin decays as a function of WR star mass. Such a trend is dictated by the core-collapse mechanism. For stars with carbon-oxygen core masses $m_{\rm CO-core} < 11\,M_\odot$, the Fryer et al. (2012) delayed prescription predicts mass ejection in the supernova event. The ejected mass will carry away the AM stored in the outer layers, lowering the fraction of AM transferred to the BH from the WR star. In the simulations of Bavera et al. (2021a), we also see a similar BH spin decay for BH–WR systems with $M_{\rm WR} > 40\,M_\odot$ and low orbital periods ($p < 0.3$ day). Such suppression is due to strong WR stellar winds and pulsations due to the pair instability process, which both cause the star to lose a non-negligible fraction of material from its envelope, depleting the WR AM reservoir.

One additional subchannel of BBH formation from isolated binary evolution that is present in our populations is the double-core CE channel, in which the helium cores of two supergiant stars proceed through a CE in one or both of the envelopes of the stars, leading to a tight WR–WR system where both binary components can be tidally spun up. Since this channel is sub-dominant and we currently lack simulation grids and fits to monitor this subdominant tidal spin-up scenario, we exclude such systems from our population and focus solely on the standard CE and stable MT channels that lead to tidal spin-up. This channel also typically forms near-equal-mass BBH systems and therefore does not strongly affect our key results. We comment more on our exclusion of this subchannel and implications in Section 5.

[3] posydon.org

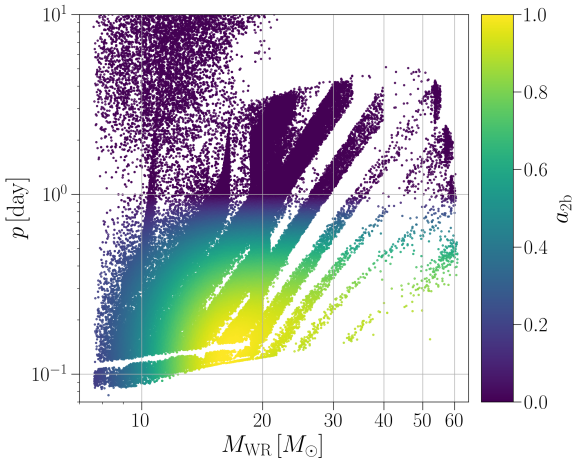

Figure 1. Dimensionless spin magnitudes of the second-born BH ($a_{2\rm b}$) determined using the fits from Bavera et al. (2021a) for a single population model as a function of the orbital period p and the WR-star mass at He-depletion $M_{\rm WR}$. This model assumes $f_{\rm acc} = 0.5$, $\gamma_{\rm Edd} = 1$, and $\alpha_{\rm CE} = 1$, with other model assumptions as specified in Section 2.1. Diagonal line-like features are the result of the set of discrete metallicities run for each population model, which are resampled according to the star-formation history and metallicity evolution of the Universe as described in Section 2.3.

2.3. *Star Formation and Metallicity Evolution*

As described in Section 2.1, for each model (parameterized by $f_{\rm acc}$, $\gamma_{\rm Edd}$, and $\alpha_{\rm CE}$), we simulate 12 discrete metallicities. Each binary is evolved for a full Hubble time $t_{\rm H}$. To get a population of merging BBHs that is representative of the underlying population in Universe, we resample 2×10^5 binaries from the metallicity runs and populate the binaries in redshift according to star formation history and metallicity evolution as predicted by the `Illustris-TNG` simulations (Nelson et al. 2015).

From `Illustris-TNG`, we have a grid of stellar mass formed over metallicity and lookback time in a 100 comoving Mpc^3 cube. Marginalizing over the metallicity axis provides the star formation rate density as a function of redshift, $\psi(z)$. However, though our population modeling tracks the total stellar mass sampled across all single stars and binaries, our population models only

retain systems of interest (i.e., those that form BBHs). Therefore, drawing birth redshifts for our target population according to this distribution does not account for the relative formation efficiency of our target population at each redshift, which is dependent on the metallicity distribution at each redshift. For each metallicity model $Z_{\rm sim}$ we have a formation efficiency

$$\zeta(Z_{\rm sim}) = \frac{N_{\rm BBH}(Z_{\rm sim})}{M_{\rm sample}(Z_{\rm sim})}, \quad (6)$$

where $N_{\rm BBH}$ is the number of BBHs formed and $M_{\rm sample}$ is the total mass sampled in the particular metallicity model, accounting for the entirety of the initial mass function and binary fraction. At a given redshift z, we can construct a distribution of metallicities from the cosmological model. The cumulative distribution function of this distribution can be used to determine the relative contribution of each discrete metallicity at a given redshift. We define $p_Z(Z|z)$ as the support of the metallicity cumulative distribution function at redshift z closest to a metallicity model $Z_{\rm sim}$ in log-space, such that $\sum_{Z\rm sim} p_Z(Z|z) = 1$. Combined, $\zeta(Z_{\rm sim})p_Z(Z_{\rm sim}|z)$ gives the number of systems per sampled stellar mass that should be drawn from each metallicity model at a given redshift.

The number of BBH systems formed per comoving volume at a particular discrete metallicity across all redshifts is thus

$$\frac{{\rm d}N}{{\rm d}V_{\rm c}}(Z_{\rm sim}) = \int_{z=0}^{z=\infty} \frac{\psi(z)\zeta(Z_{\rm sim})p_Z(Z_{\rm sim}|z)}{H_0(1+z)E(z)}{\rm d}z. \quad (7)$$

where we perform the change of variable ${\rm d}t = \frac{{\rm d}t}{{\rm d}z}{\rm d}z = (H_0(1+z)E(z))^{-1}{\rm d}z$ with $E(z) = \sqrt{\Omega_m(1+z)^3 + \Omega_k(1+z)^2 + \Omega_\Lambda}$. This integral gives us the total number of BBH systems formed per source-frame year in a comoving box at a discrete metallicity over the entire history of the Universe. At a given metallicity, we densely discretize redshifts and evaluate this integral between the bounds of our redshift bins, which gives a relative weight at a particular redshift and metallicity that we use when resampling our population models.

With the relative probability of drawing a system from our target population at a given redshift and metallicity in hand, we randomly draw the birth redshifts and metallicities of 2×10^5 systems for each population model set. We remove systems from our resampled population that merge after the present day; that is, systems that satisfy the condition $\tau(z) - t_{\rm delay} < 0$, where $t_{\rm delay}$ is the delay time (defined as the time between ZAMS and BBH merger) and $\tau(z)$ is the lookback time of a system born at redshift z. This eliminates $4-13\%$ of systems from our populations of merging BBHs. The codebase used for generating a metallicity and redshift resampled population based on `COSMIC` models using various star formation history and metallicity evolution assumptions is available on Github.[4]

3. RESULTS

We now investigate the viability of isolated evolution at forming systems with asymmetric masses and spinning primaries. We first look at the component spin distributions and mass ratio distributions individually for our array of population models to identify trends across our physical assumption variations in Sections 3.1 and 3.2. We then look at broader population properties in mass ratio–spin space in Section 3.3.

3.1. *Spin magnitudes of the first- and second-born BH*

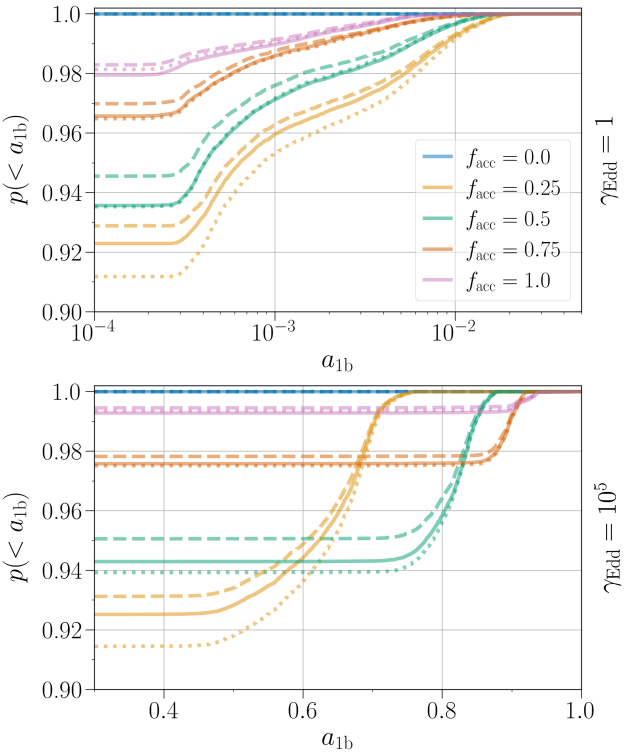

Figure 2. Spin magnitude distributions for first-born BHs. Non-zero spin magnitudes for the first-born BH population are the result of accretion onto the already-formed BH from stellar companions. Colors show distributions for different assumptions of the accretion efficiency $f_{\rm acc}$, with rows showing variations in the super-Eddington accretion parameter $\gamma_{\rm Edd}$. Dotted, dashed, and solid lines show the distributions for $\alpha_{\rm CE}$ values of 0.5, 1, and 2, respectively.

[4] https://github.com/michaelzevin/resample-population

Under the assumption of efficient AM transport in massive stars, spin in the first-born BH can be achieved through accretion via stable MT onto the already-formed BH by a stellar companion. Figure 2 shows the distribution of first-born BH spins a_{1b} across our various physical assumptions. The distributions transition from a flat region, which indicates the branching fraction of stable MT systems in each model, to a monotonically increasing behavior; the transition at $a_{1b} \sim 3 \times 10^{-4}$ in all models corresponds to the minimum accretion timescale found in our populations of ~ 0.01 Myr. Appreciable spin in the first-born BH can only be attained via accretion if the BH can accrete far above the Eddington limit. For Eddington-limited accretion onto the first-born BH, we find that no more than 0.9% of systems are spun up beyond $a_{1b} > 0.01$ across all population models. This is expected due to the short evolutionary timescales of the massive stars that are BH progenitors, which have post-main-sequence lifetimes of $\lesssim 1$ Myr and thus can only accrete at most a fraction of a Solar mass if accretion is limited to the Eddington rate. More systems proceed through this stable MT channel at lower accretion efficiencies ($\simeq$ 8% at $f_{acc} = 0.25$ compared to $\simeq$ 2% at $f_{acc} = 1$ in the Eddington-limited models), though higher values for the accretion efficiency lead to larger typical first-born spins when only considering the stable MT channel. Variations in the CE efficiency, shown with different linestyles in Figure 2, have a minor and indirect impact on the first-born spin distributions; these slight variations are due to the changes in the relative fraction of merging BBHs that proceed through a CE phase rather than stable MT.

Increasing the accretion limit onto BHs to 10^5 times the Eddington rate drives first-born BH spins to more extreme values. The differences in the transition between a flat behavior and monotonically increasing behavior for different accretion efficiency models in Figure 2 indicates that the maximum MT rate is now often imposed by the f_{acc} rather than the γ_{Edd}, with the transition happening at larger spins as f_{acc} increases. For non-zero accretion efficiencies $f_{acc} > 0$, a sizeable fraction of systems in our populations have first-born spins with $a_{1b} > 0.5$: $\approx$ 6% in our $f_{acc} = 0.5$ models. Almost no systems have first-born spins of $a_{1b} < 0.5$ in any of our super-Eddington accretion models. Though we do not explicitly consider BBH merger rates here, we note that significantly increasing the possible accretion rate onto BHs drives down the expected merger rate of systems with highly-spinning first-born BHs due to conservative MT not shrinking the orbit as efficiently as non-conservative MT (Bavera et al. 2021b). This is

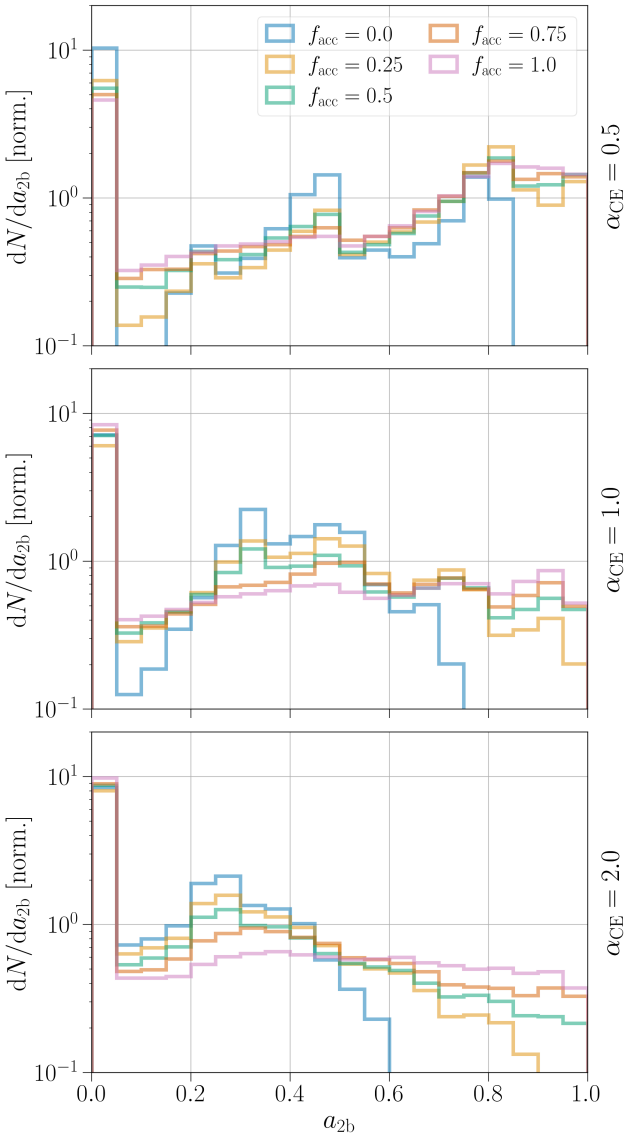

Figure 3. Spin magnitude distributions for the second-born BH. Non-zero spin magnitudes for the first-born BH population are the result of tidal spin-up of the WR progenitor. Colors show distributions for different assumptions of the accretion efficiency f_{acc}, with rows showing variations in CE efficiencies α_{CE}. Accretion is limited to the Eddington rate ($\gamma_{Edd} = 1$) for all plotted models.

seen in the bottom panel of Figure 2; though increasing the accretion efficiency does indeed lead to more highly-spinning BHs from the stable MT channel, the relative contribution of this channel compared to the full BBH population decreases.

In Figure 3, we show the spin distributions for the second-born BHs a_{2b} in our models, which is driven by tidal spin-up of He cores by the first-born BH. For all models, we find a broad range of spin magnitudes rang-

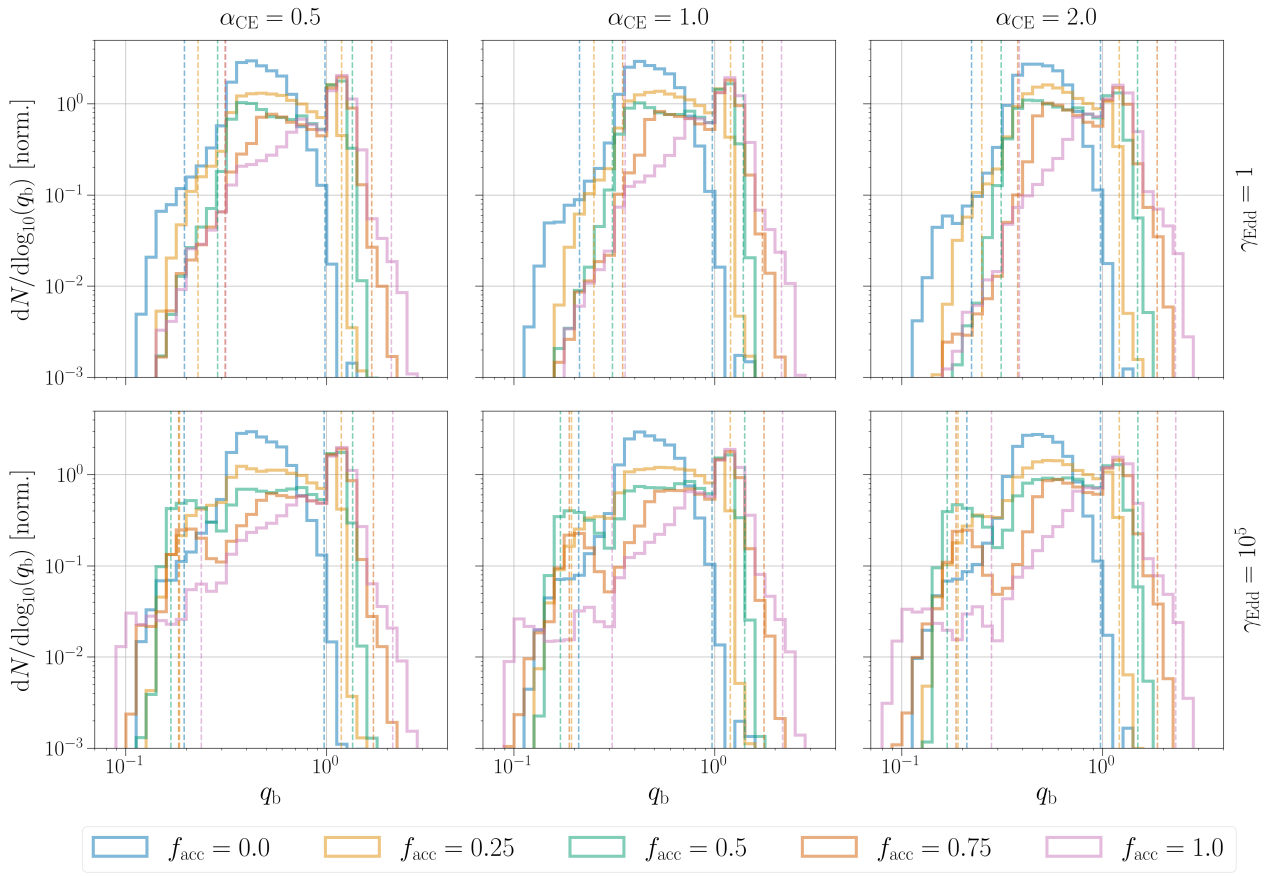

Figure 4. Distribution of mass ratios between the first-born BH and second-born BH. Values with $q_{\rm b} < 1$ indicate that the first-born BH is the more massive component, whereas values with $q_{\rm b} > 1$ indicate that the second-born BH is the more massive component. As in Figures 2 and 3, colors show distributions for different assumptions of the accretion efficiency $f_{\rm acc}$. Rows and columns show variations in CE efficiency $\alpha_{\rm CE}$ and super-Eddington accretion $\gamma_{\rm Edd}$, respectively. Vertical dashed lines mark the region in which 99% of all systems in the respective populations reside.

ing from non-spinning to maximally spinning, with little dependence on $\gamma_{\rm Edd}$ since the CE channel dominates over the stable MT channel in our models. The peak at $a_{\rm 2b} \simeq 0$ in all models is the result of systems that have orbital periods outside of the spin-up regime at WR–BH formation, see Figure 1. Across our models, we find that $22\% - 52\%$ of secondary spin magnitudes are $a_{\rm 2b} < 0.05$.

We find a general trend of second-born spin distributions pushing to larger values with increasing accretion efficiency and decreasing CE efficiency, in agreement with Bavera et al. (2021b). For $f_{\rm acc} = 0.5$ and $\alpha_{\rm CE} = 1$, 31% of systems have second-born BH spins of $a_{\rm 2b} > 0.5$. This fraction drops to 18% for $\alpha_{\rm CE} = 2$ and increases to 52% for $\alpha_{\rm CE} = 0.5$. The increase in high-spinning BHs with decreasing CE efficiency is due to less efficient CE phases leading to more hardened orbits post-CE, which makes the stripped He core more susceptible to tidal spin-up. At $\alpha_{\rm CE} = 1$, the fraction of systems with $a_{\rm 2b} > 0.5$ drops to 18% for $f_{\rm acc} = 0$ whereas at $f_{\rm acc} = 1$ it increases to 33%. This trend of increasingly high-spinning second-born BHs with increasing accretion efficiency is due to the progenitor of the second-born BH gaining more mass during the first stable MT phase; the post-CE separation scales inversely with the product of the total mass and envelope mass of the donor pre-CE.

3.2. *Mass ratios and Mass Ratio Reversal*

We now turn to the mass ratio distributions in our populations. Since the order at which BHs are born in a binary determines the mechanism responsible for their potential spin, we choose to define the birth mass ratio parameter $q_{\rm b} = m_{\rm 2b}/m_{\rm 1b}$, where $m_{\rm 1b}$ and $m_{\rm 2b}$ are the masses of the first-born BH and second-born BH, respectively. Thus, for values $q_{\rm b} > 1$, the system proceeded through a MRR that led to the less massive star at ZAMS forming in the more massive BH in the binary. Note that in our models the only mechanisms

for inducing spin on BH remnants are accretion onto the BH and tidal spin-up, and thus the first-born BH is only susceptible to the former and the second-born BH is only susceptible to the latter of these processes.

We show the population distributions of the mass ratio parameter q_b in Figure 4. The accretion efficiency f_{acc} has the largest impact in determining whether MRR ensues, as this parameters governs the amount of material the less massive star at ZAMS can accept from the initially more massive donor after it evolves off the main sequence and overflows its Roche lobe. For example, in our default model with $\alpha_{CE} = 1$ and $\gamma_{Edd} = 1$, we find 0.3% of merging BBH systems to have $q_b > 1$ for $f_{acc} = 0$, which rises to 47% at $f_{acc} = 0.5$ and 72% at $f_{acc} = 1$. Despite this, the second-born BH rarely reaches masses of more than $\simeq 3$ times the mass of the first-born BH; in our most optimistic MRR models, we find the birth mass ratio parameter to be constrained to $q_b < 2.2$ at 99% confidence, and never reach a value larger than $q_b = 3.7$.

Increasing the accretion limit onto BHs leads to more systems occupying the low-end tail of the q_b distribution. This is due to the first-born BH being able to gain significantly more mass from accretion relative to the Eddington-limited case, and can generate systems with mass ratios of $q_b \simeq 0.09$ in the most extreme cases. However, these extreme mass ratio systems are still rare in the context of the full population; at $f_{acc} = 0.5$ and $\alpha_{CE} = 1$, we find that 99% of systems have $q_b > 0.18$ for $\gamma_{Edd} = 10^5$, which raises to $q_b > 0.33$ for the Eddington-limited case with $\gamma_{Edd} = 1$. Thus, when considering all systems regardless if they proceeded through a MRR or not, we find that forming binaries with mass asymmetries of more than 3:1 is a rare occurrence unless super-Eddington accretion is invoked.

3.3. *Population properties*

We now examine both component spins and mass ratios simultaneously to make broader statements about the viability of generating asymmetric mass systems with spinning primaries. Figure 5 marks the fraction of systems in our full BBH population that satisfy particular criteria of interest. We specifically highlight systems that proceed through MRR ($q_b > 1$), systems that have significant asymmetries in their BH masses ($q_b > 2$ or $q_b < 0.5$), and systems that achieve a significant primary BH spin ($a > 0.2$).

As shown in Figure 4, the number of systems that proceed through a MRR is significantly enhanced with increasing accretion efficiency (blue and green lines). However, even for perfectly conservative MT where all of

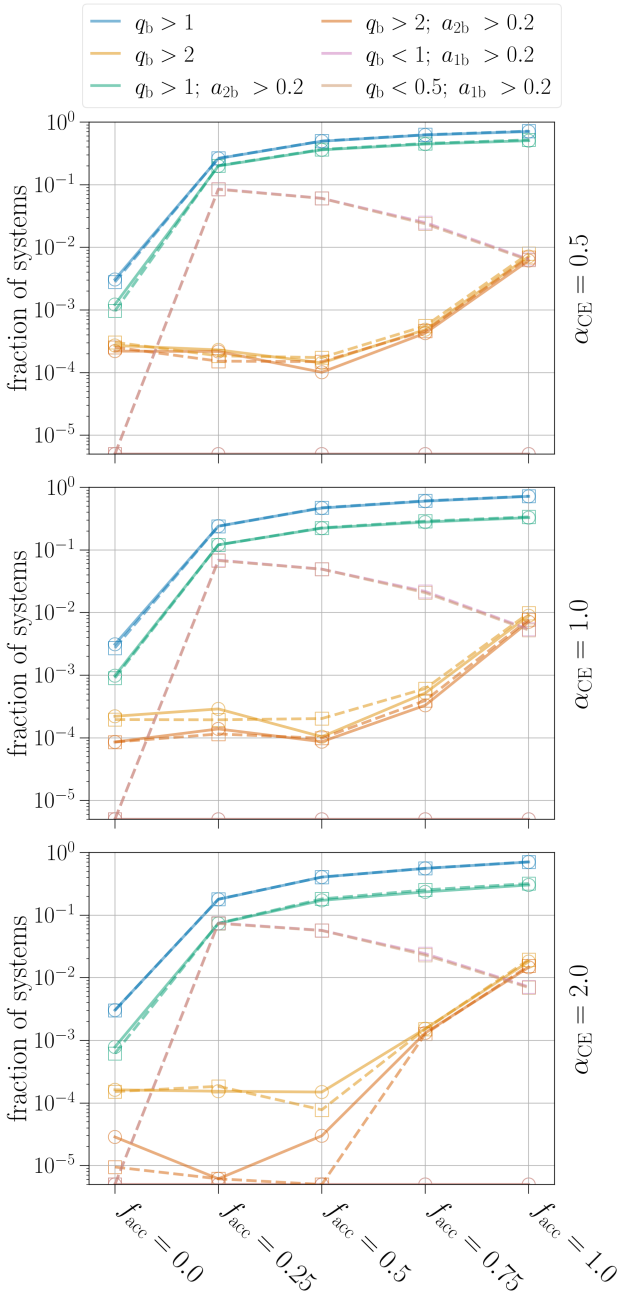

Figure 5. Fraction of systems that satisfy criteria based on mass ratios and component spins as a function of accretion efficiency f_{acc}. Different criteria are denoted with different colored lines as indicated in the legend, with solid lines with circular markers (dashed lines with square markers) showing the $\gamma_{Edd} = 1$ ($\gamma_{Edd} = 10^5$) populations and rows showing different values of α_{CE}. Points for models where no systems in the population satisfy a particular criteria are plotted on the horizontal axis. Note that the points for the pink ($q_b < 1$; $a_{1b} > 0.2$) and brown ($q_b < 0.5$; $a_{1b} > 0.2$) conditions are mostly overlapping.

the material from the donor is accepted by the accretor, the number of system that have significantly asymmetric masses and non-negligible spins in the primary BH are small (yellow and orange lines). Across our Eddington-limited population models, 0.6%−1.5% satisfy this criteria at $f_{\rm acc} = 1$; this number drops by and order of magnitude or more for lower values of $f_{\rm acc}$. Therefore, in the efficient AM transport paradigm, we find the formation of systems with asymmetric masses and spinning primary BHs to be inefficient even for the most optimistic assumptions about MT physics.

For our models that allow for highly super-Eddington accretion ($\gamma_{\rm Edd} = 10^5$), the percentage of systems with non-negligible primary BH spins and mass ratios greater than 2:1 can exceed 8% and drop to less than 0.5% depending on choice of accretion efficiency, so long as $f_{\rm acc} > 0$. When accretion onto BHs is Eddington limited, no systems in our population meet this criteria since the first-born BH spin-up is highly suppressed (see Figure 2). Thus, in either spin-up scenario, we find the fraction of systems that have significant mass asymmetries (> 2:1) and significant primary spins (> 0.2) to be percent-level at best, and requires highly conservative MT or highly super-Eddington accretion to achieve these numbers.

4. CONTEXTUALIZING WITH THE GRAVITATIONAL-WAVE POPULATION

In the previous section, we examined the efficiency of forming systems with asymmetric masses and spinning primary components, and found that such systems are relatively rare occurrences in the underlying population even when taking optimistic assumptions about mass transfer efficiency. We now turn to the implications of these results, both in the context of explaining individual events and general trends that are observed in the BBH population.

A number of systems in the current population of BBHs exhibit interesting combinations of mass ratio and spin. For example, GW190412 and GW190517_055101 are both high-confidence events with positive effective spins of $\chi_{\rm eff} = 0.25^{+0.08}_{-0.11}$ and $\chi_{\rm eff} = 0.52^{+0.19}_{-0.19}$, respectively, at 90% credibility (Abbott et al. 2021e). The primary BH in GW190412 is 3–4 time more massive than the secondary, with a mass ratio of $q = 0.28^{+0.12}_{-0.07}$ (Abbott et al. 2020), whereas the mass ratio of GW190517_055101 is more consistent with unity ($q = 0.69^{+0.27}_{-0.29}$, Abbott et al. 2021e). Because of the large measured effective spins and/or mass asymmetry, the spin magnitudes of the primary BH can be constrained to $a_1 = 0.44^{+0.16}_{-0.22}$ and $a_1 = 0.86^{+0.13}_{-0.35}$ for GW190412 and GW190517_055101, respectively, whereas the spin of the secondary BH is unconstrained.[5] The extended catalog for the first half of the third observing run uncovered the system GW190403_051519, and though it has a relatively low astrophysical probability compared to GW190412 and GW190517_055101 and a primary mass that is in tension with the maximum BH mass expected from the pair instability process, its significantly asymmetric masses ($q = 0.25^{+0.53}_{-0.11}$) and high primary spin ($a_1 = 0.92^{+0.07}_{-0.22}$) make it a system of interest. In the most recent GW catalog published by the LVK, the high-confidence event GW191109_010717 also has intriguing spin signatures with the primary BH spinning at $a_1 = 0.83^{+0.15}_{-0.58}$ (Abbott et al. 2021c), though its high mass and in-plane spin may be indicative of a dynamical formation scenario. Other GW catalogs outside the LVK have also uncovered additional systems with interesting configurations of spin and mass ratio that may help to probe viable spin-up mechanisms (e.g., Nitz et al. 2021; Olsen et al. 2022).

These BBHs, particularly GW190412, are potential exemplars of systems whose progenitors underwent a MRR where the more massive BH was born second and its progenitor was tidally spun up (Abbott et al. 2020; Zevin et al. 2020a; Olejak et al. 2020; Olejak & Belczynski 2021), or alternatively having the first-born primary BH spun up by super-Eddington accretion during the second stable MT episode (Bavera et al. 2021b). As we showed in Figure 3, population modeling predicts a significant number of systems that can have appreciable spins across the entire range of physical spin magnitudes in the underlying population. However, the formation of systems that can also achieve spinning primary components drops precipitously as the mass of the primary relative to the mass of the secondary increases, as shown in Figure 5. Though the mass ratio distribution of GW190517_055101 is too broad to definitively rule out this formation mechanism, we find the formation of GW190412 through MRR and tidal spin-up to be improbable. Taking the upper and lower values of GW190412's 90% symmetric credible interval for mass ratio and primary spin, respectively (i.e., taking values closest to non-spinning and equal mass), we find that < 0.1% of systems satisfy this criteria in our Eddington-limited accretion model even when we take the optimistic assumption of $f_{\rm acc} = 1$. For our highly super-Eddington models we find the formation of such systems

[5] Though strong astrophysical priors have been shown to lead to alternate interpretation in the distribution of spin between the primary and secondary components of GW190412 (Mandel & Fragos 2020), this interpretation is statistically disfavored relative to the system having a spinning primary (Zevin et al. 2020a).

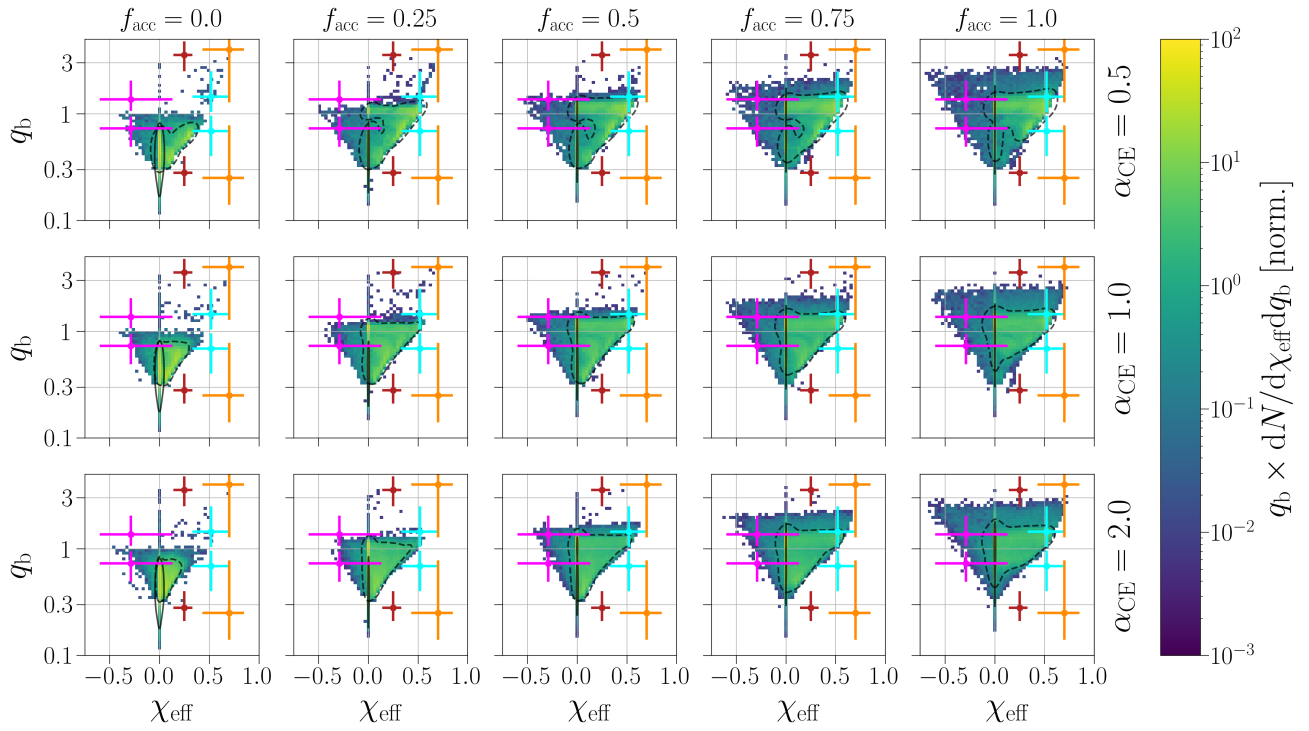

Figure 6. Joint distribution of mass ratio between the first-born and second-born BH, $q_{\rm b}$, and effective spin, $\chi_{\rm eff}$, for various assumptions regarding the accretion efficiency, $f_{\rm acc}$ (columns), and CE efficiency, $\alpha_{\rm CE}$ (rows). Values of $q_{\rm b} < 1$ indicate that the first-born BH is the more massive component, whereas $q_{\rm b} > 1$ indicate that the second-born BH is the more massive component. For all distributions in this figure, we show results for models that assume Eddington-limited accretion, with $\gamma_{\rm Edd} = 1$. Black dashed (solid) lines surround 90% of systems from the stable MT (CE) channel. Colored points show the 90% credible intervals for mass ratio and effective spin for a selection of GW events: GW190403_051519 (orange), GW190412 (red), GW190517_055101 (cyan), and GW191109_010717 (pink). Two points are shown for each event that are reflected over the boundary at $q_{\rm b} = 1$.

to be more likely, with up to 8% of systems satisfying this criteria.

We find the detection of asymmetric mass, spinning primary BH systems through the tidal spin-up scenario to be less likely when selection effects are accounted for, consistent with the findings of Bavera et al. (2021b). Since tidal spin-up of a WR star by a BH requires sub-day orbital periods (see Figure 1), these systems have short inspiral times when they form BBHs. Systems will more readily proceed through tidal spin-up at lower metallicities (and therefore higher redshifts) because WR stellar winds are weaker, which lessens orbital expansion and keeps the BH–WR system in the regime where tidal spin-up can still be efficient (Bavera et al. 2020). Therefore, many tidal spin-up systems will merge outside of the horizon of current ground-based GW detectors, and a lower fraction of systems in the detectable population are predicted to have high spins from tidal spin-up relative to the underlying population (e.g., Bavera et al. 2021b; Safarzadeh & Hotokezaka 2020). Applying selection effects to our population causes the probability of detecting systems similar to GW190412 through the MRR and tidal spin-up channel to further decrease by more than an order of magnitude. However, we find the super-Eddington accretion spin-up scenario to be less impacted by selection effects, still accounting for a percent-level number of systems in the detectable population. We describe our implementation of selection effects in Appendix A.

In addition to individual BBH systems in the GW-detected population having interesting parameter estimates, populations analyses are useful for uncovering trends and features in the data as a whole (see e.g., Mandel et al. 2019; Vitale et al. 2020). One example that is particularly pertinent to mass ratios and spins configurations is that the population of BBHs shows tantalizing signs of (anti-)correlations between mass ratio and effective spin (Callister et al. 2021; Abbott et al. 2021d). In Figures 6 and 7, we show joint distributions of the birth mass ratio parameter, $q_{\rm b}$, and effective spin, $\chi_{\rm eff}$, in our BBH populations for $\gamma_{\rm Edd} = 1$ and $\gamma_{\rm Edd} = 10^5$, respectively. A few GW events with interesting mass ratio and spin measurements are overplotted for comparison.

We find no strong indication of trends in effective spins as a function of mass ratio (for either $q_{\rm b} > 1$ or $q_{\rm b} < 1$) in our Eddington-limited population models shown in

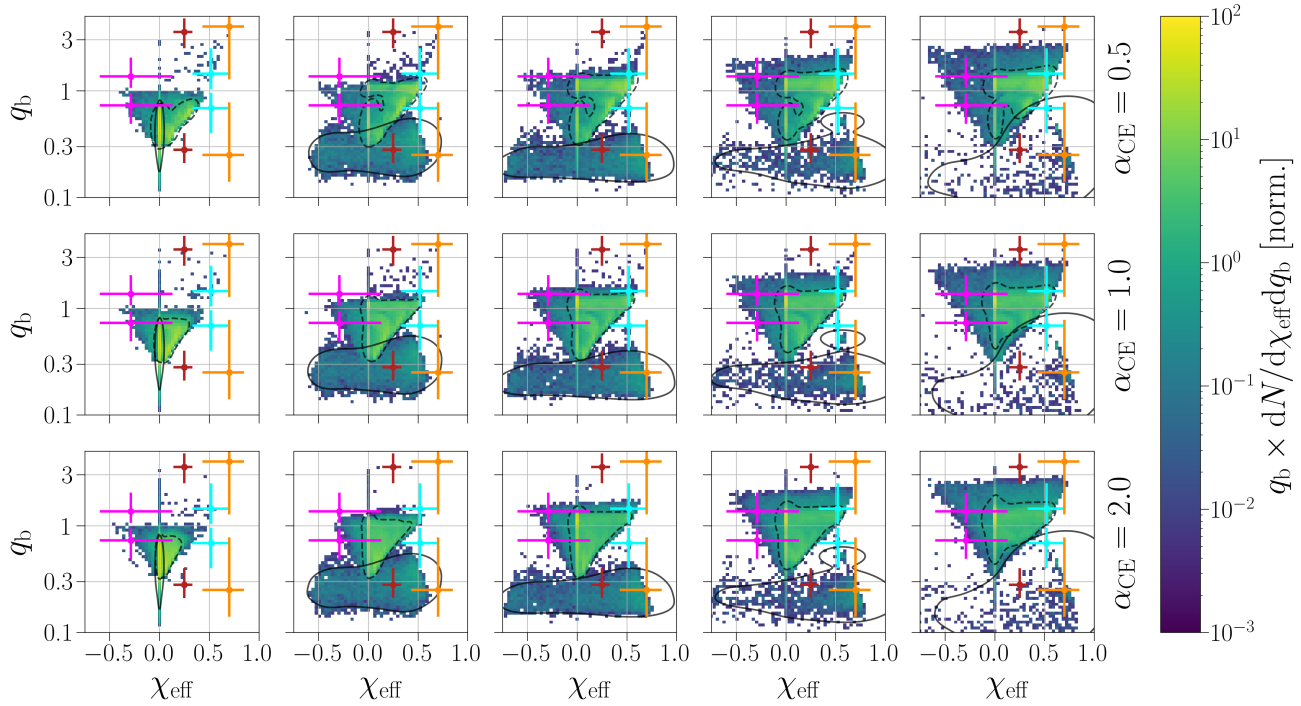

Figure 7. Same as Figure 6 except for models with a super-Eddington accretion parameter of $\gamma_{Edd} = 10^5$.

Figure 6. Effective spin distributions tend to narrow closer to $\chi_{eff} \simeq 0$ as mass ratios decrease from $q_b = 1$ to $q_b = 0$. For values of $q_b > 1$, effective spin distributions remain broad, but retain a peak in the distribution at $\chi_{eff} \simeq 0$.

This situation differs in the super-Eddington models, as shown in Figure 7. Significantly increasing the accretion limit onto BHs leads to the stable MT channel populating the region of parameter space with large effective spins and small mass ratios ($q_b \ll 1$). The combination of the bulk of systems dominating the low-spin and equal-mass regime, MRR and tidal spin-up accounting for mildly asymmetric masses and moderate spins, and stable MT with super-Eddington accretion producing low mass ratios and high spins can lead to an apparent trend between mass ratio and effective spin, and a potential means of generating the anti-correlation observed in GW data. Visually, the super-Eddington stable MT channel can populate regions of parameter space occupied by unique systems such as GW190412. We also see an increased number of systems with $q \ll 1$ and anti-aligned spins, which result from the second-born BH being lower mass and more susceptible to strong natal kicks that can significantly tilt the orbital plane. Though the relative fraction of BBHs formed via CE and stable MT channels may not be accurately captured by rapid population synthesis approaches (see Section 5 for further discussion), the combination of these isolated evolution subchannels may provide one explanation for anti-correlations between mass ratio and effective spin. However, our models find that extreme assumptions regarding the accretion rate onto BHs are required for such an interpretation.

It is interesting to note that certain analysis techniques can have a significant impact on measurements of spins in individual BH systems and the population of component spins. For example, rather than inferring the properties of the most massive and least massive BHs in a particular system, Biscoveanu et al. (2021) show that by instead inferring the parameters of the highest spinning and lowest spinning components of the system, spin magnitude measurements can be more informative especially for near-equal-mass systems. Such variations to standard analyses may be useful in better constraining component spin magnitudes, though it yields less differences in parameter estimates for unequal mass systems such as those considered in this work, due to the spin of the heavier BH playing a larger role in measured spin quantities such as the effective spin. Nonetheless, such techniques may uncover more component BHs with significant spin magnitudes in the broader population (Abbott et al. 2021d).

5. DISCUSSION AND CONCLUSIONS

In this work, we simulated a suite of population models to investigate the joint distribution of masses and

spins across an astrophysical population of BBHs. In particular, we focus on the ability of stellar progenitors to proceed through a MRR where the lighter star at ZAMS leads to the more massive compact object, and potential means of generating spin in BHs even with efficient AM transport in their stellar progenitors. Our key results are as follows.

1. Though the distribution is peaked near zero, the second-born BH can attain a range of spin magnitudes from near zero to maximally spinning through tidal spin-up, with less efficient CE phases leading to larger typical spins. Across our model variations, $4-57\%$ of systems have second-born BHs with spin magnitudes > 0.5 (Figure 3).

2. Assuming highly efficiency AM transport and Eddington-limited accretion, the spin of the first-born BH will naturally be small, with typical values $\ll 10^{-2}$. However, increasing the accretion rate to many orders of magnitude above the Eddington limit will lead to a sizeable fraction of first-born BHs with significant spin. Though higher accretion efficiencies lead to larger typical spins from this subchannel, it causes the contribution of this subchannel to drop relative to the full population (Figure 2).

3. Naturally, the number of systems that proceed through MRR is highly sensitive to the assumed accretion efficiency at which the accreting star accepts material from the donor star. Our parameterization choices for the accretion efficiency bracket the range of systems that have a more massive second-born BH to $0.3-72\%$, though even at a low accretion efficiency of $f_{\rm acc} = 0.25$ more than 18% of systems have a more massive second-born BH.

4. It is rare for systems to form with asymmetric masses and spinning primary BHs through MRR and tidal spin-up; across our various model assumptions with $f_{\rm acc} > 0$, $10^{-5}-10^{-2}$ of systems in the underlying population have second-born BHs that are twice as massive as their first-born counterparts and have spin magnitudes > 0.2. These numbers decrease by an order of magnitude or more when GW detector selection effects are considered due to the short delay times of this channel and lower efficiency of tidal spin-up at lower redshifts and higher metallicities. The number of systems where the first-born BH is twice as massive as the second-born BH and spinning at > 0.2 is negligible for our Eddington-limited models, though can account for $5 \times 10^{-3} - 8 \times 10^{-2}$ of systems in the underlying population for our models that assume highly super-Eddington accretion. We therefore find that the formation of BBH systems with asymmetric masses and spinning primary BHs, such as GW190412, is unlikely through the channels considered in this work unless highly super-Eddington accretion is invoked.

5. We find no indication of a correlation between mass ratio and effective spin in our model variations other than in models that assume highly super-Eddington accretion onto BHs.

Though we aim to survey the parameterizations of binary stellar evolution that most impact MRR and tidal spin-up, the vast array of physical uncertainties that embed binary population modeling prevent us from being completely exhaustive in our coverage of parameter space. We anticipate that the criteria determining the onset of unstable MT could lead to potential changes in our results. This is typically encoded in rapid population modeling via an array of stellar-type-specific critical mass ratio values, $\vec{q}_{\rm crit}$, where MT will be unstable if the donor mass is sufficiently more massive than the accretor mass. One variation in this parameter for a subset of our other model variations is described in Appendix B. However, it is possible that the values typically used in population synthesis are not representative of the true physical picture. For example, Gallegos-Garcia et al. (2021) found that rapid population synthesis may severely over-predict the number of systems that proceed through a successful CE phase and form BBH systems. In Figure 7, the high-density region at low mass ratios ($q_{\rm b} \ll 1$) and large, positive effective spins is populated almost exclusively through systems that do not proceed through CE evolution, and could potentially lead to a mass ratio–effective spin correlation in the full BBH population if the CE channel is suppressed, though this feature is only apparent in models that assume super-Eddington accretion onto BHs (see also Bavera et al. 2021b). In our Eddington-limited models, we find that the stable MT channel typically does not harden BH–WR binaries to orbital periods of less than 1 day, and thus is inefficient at spinning up the second-born BH progenitor through tides. However, we note that work investigating tidal spin-up in isolated evolution with other population synthesis codes, such as Olejak & Belczynski (2021), find that evolutionary sequences that do not involve a CE phase can still lead to an appreciable fraction of systems that are spun up via tides.

One subchannel present in our models though excluded in our analysis is the double-core CE channel, in which both helium cores can tidally interact and spin up before collapsing into BHs. This channel is excluded (a) because we lack detailed simulations grids following tidal spin-up in this scenario and (b) so our results are less opaque and the first-born BH can only attain spin through accretion following BH formation and the second-born BH can only attain spin through BH–WR tidal spin-up. Though subdominant, this channel contributes up to $\sim 10\%$ of our underlying population of merging BBHs in certain models, similar to the underlying populations of Neijssel et al. (2019). It does, however, contribute to a much smaller fraction of the detectable population (see e.g. Figure 12 of Neijssel et al. 2019). We anticipate that proper treatment of this spin-up process would lead to spinning first-born and second-born BHs and large, positive effective spins. However, in our models this channel favors the formation of near-equal-mass binaries, with $\sim 95\%$ of systems having mass ratios of $q > 0.75$. Therefore, though the inclusion and proper treatment of this channel would affect the formation of near-equal-mass systems with high effective spins, we find it to be inefficient at generating systems with spinning primaries and significantly asymmetric masses.

Another evolutionary scenario not explored in detail here that can induce spins in BH progenitors is through MT that occurs during the main sequence. In this Case A MT scenario, the primary star is in a tight binary with an orbital period at ZAMS of $\sim 0.5 - 1.2\,\mathrm{day}$ and is tidally locked when it overfills its Roche lobe on the main sequence. This strips the primary star of its envelope and causes it to become a fast-spinning WR star without any significant expansion. Though this channel has been shown to lead to the formation of high-mass X-ray binaries with appreciable BH spin, it will typically not lead to a merging BBH (Belczynski et al. 2012; Qin et al. 2019; Neijssel et al. 2021).

Throughout this work, we have assumed that AM transport in massive stars is highly efficient, leading to BHs formed from progenitors that do not undergo substantial tidal interaction to have near-zero spins. Though numerical simulations of AM transport in high-mass stars through Taylor-Spruit dynamo and the majority of spins in BBH systems being small hint at efficient AM transport, astroseismic measurements that encode this process are typically for low-mass stars. Furthermore, efficient AM transport may still lead to BH spins that are low but non-negligible ($a \simeq 0.1$, Belczynski et al. 2020), and processes such as supernova fallback may induce some spin on the resultant BH even if AM transport is highly efficient (Schrøder et al. 2018). As a simple approximation for less efficient AM transport, we set a floor on the minimum spin of BHs at birth:

$$a_{1\mathrm{b},2\mathrm{b}} = \begin{cases} a_{1\mathrm{b},2\mathrm{b}} & a_{1\mathrm{b},2\mathrm{b}} \geq a_{\min} \\ a_{\min} & a_{1\mathrm{b},2\mathrm{b}} < a_{\min} \end{cases} \tag{8}$$

where $a_{\min}$ is the minimum spin magnitude of quasi-isolated BHs at birth. With $a_{\min} = 0.2$, we find only minor changes in our main results regarding MRR and spinning primaries. For example, with all second-born BHs satisfying the criteria $a_{2\mathrm{b}} \geq 0.2$, we find that the percentage of systems in our most optimistic MT efficiency models with $q_{\mathrm{b}} > 2$ and $a_{2\mathrm{b}} \geq 0.2$ to raise from $\sim 0.6\% - 1.5\%$ to $\sim 0.7\% - 1.9\%$. However, setting the minimum natal spin magnitude of BHs has a larger impact on systems that do not proceed through a MRR, with upwards of 52% of systems satisfying $q_{\mathrm{b}} < 0.5$ and $a_{1\mathrm{b}} \geq 0.2$.

Of course, isolated evolution is only one of many proposed formation scenarios for generating BBH mergers, and the full population of BBH mergers may be the result of a combination of formation pathways (Bouffanais et al. 2021a; Wong et al. 2021; Zevin et al. 2021). Though we will not cover alternative potential formation pathways in detail here (see e.g. Mandel & Farmer 2018 for a review), we note that the formation of systems with spinning primaries and asymmetric masses may be the result of hierarchical mergers in dense stellar environments. However, the formation of GW190412-like systems still proves to be enigmatic in the standard hierarchical merger paradigm, as its primary BH component is unlikely to be the product of a second-generation merger in an environment such as a classical globular cluster since its primary spin is lower than what one would expect for the merger product of a two low-spinning BHs (Abbott et al. 2020). A number of other formation scenarios have been proposed such as third-generation mergers (Rodriguez et al. 2020), hierarchical systems (Hamers & Safarzadeh 2020), and formation in the disks of active galactic nuclei (McKernan et al. 2021; Tagawa et al. 2021). If systems such as GW190412 and GW190517_055101 result from sub-dominant formation scenarios it may impact the astrophysical interpretation of the apparent anti-correlation between mass ratio and effective spin, as the exclusion of these events in such analyses (slightly) reduces the statistical significance of such a correlation (Callister et al. 2021), and different formation pathways do not necessarily need to share correlations in their mass and spin parameters.

The population of BBH mergers observed via GW emission has already led to many astrophysical lessons.

In addition to the properties of systems as a whole, the distribution of mass and spin across the two components of the merging binary is enlightening when considering formation scenarios and physical processes. As always, the hundreds of anticipated BBH detections in the upcoming observing runs of the LVK interferometer network will help to determine whether such asymmetric mass, highly spinning systems are commonplace. Given the quantity and flexibility of proposed formation scenarios for compact binary mergers, we stress the importance of determining regions of parameter space that cannot be easily populated by astrophysical formation models in addition to regions that can. This will be equally as important for constraining merger rates and uncertain physical processes that embed the myriad of potential formation pathways.

ACKNOWLEDGMENTS

We thank Mario Spera for insightful discussion and a detailed read of this manuscript, Luke Kelley for providing processed Illustris-TNG data used in our population resampling, and Katie Breivik for useful conversations as well as pertinent developments to `COSMIC`. We also thank the anonymous referee whose comments improved this manuscript. Support for this work and MZ was provided by NASA through the NASA Hubble Fellowship grant HST-HF2-51474.001-A awarded by the Space Telescope Science Institute, which is operated by the Association of Universities for Research in Astronomy, Incorporated, under NASA contract NAS5-26555. SSB is supported by a Swiss National Science Foundation Professorship Grant (project number PP00P2_176868; PI Fragos)

Software: `Astropy` (Robitaille et al. 2013; Price-Whelan et al. 2018); `iPython` (Pérez & Granger 2007); `Matplotlib` (Hunter 2007); `NumPy` (Oliphant 2006; Van Der Walt et al. 2011); `Pandas` (McKinney 2010); `SciPy` (Virtanen et al. 2020).

APPENDIX

A. INCORPORATING SELECTION EFFECTS

The observation of compact binary coalescences via GWs is prone to selection effects, most notably that more massive systems are more luminous and thus can be seen out to higher luminosity distances. Current ground-based detectors are most sensitive at frequencies of $\sim 100\,\mathrm{Hz}$, and systems with redshifted total masses $\gtrsim 500\,M_\odot$ become unobservable since they merge at frequencies below the seismic floor (e.g., Mehta et al. 2021). Mass ratios and spins also impact the observability of compact binary mergers, with detectors being most sensitive to systems with near-equal masses and high, aligned spins. Selection effects must be accounted for in our population models to yield a fair comparison against the observed BBH population.

We use a semi-analytic treatment to incorporate selection effects in our population models, which relies on pre-computed detection probabilities over a grid of chirp masses $\mathcal{M}_\mathrm{c} = (m_1 m_2)^{3/5}/(m_1+m_2)^{1/5}$, mass ratios $q = m_2/m_1$ with $m_2 \leq m_1$, and redshifts z where m_1 and m_2 are the primary and secondary masses. We assume a three-detector network consisting of LIGO–Hanford, LIGO–Livingston, and Virgo operating at either `midhighlatelow` or `design` sensitivity (Abbott et al. 2018). Extrinsic parameters are sampled over, and systems with network signal-to-noise ratio of $\rho_\mathrm{thresh} = 10$ are considered detectable (Nitz et al. 2020; Abbott et al. 2021e), such that the detection probability p_det is given

$$p_\mathrm{det} = \frac{1}{N}\sum_j^N \mathcal{H}\left[\left(\sum_i \rho_i(\psi_j)\right)^{1/2} - \rho_\mathrm{thresh}\right] \tag{A1}$$

where ψ_j are the sampled extrinsic parameters, i defines the detector, and $\mathcal{H}$ is a Heaviside step function. Spin effects are ignored, as they have a minor effect on detection probabilities (Ng et al. 2018). The relative weight of each system in the population thus becomes

$$w = p_\mathrm{det}\frac{dV_\mathrm{c}}{dz}(1+z)^{-1} \tag{A2}$$

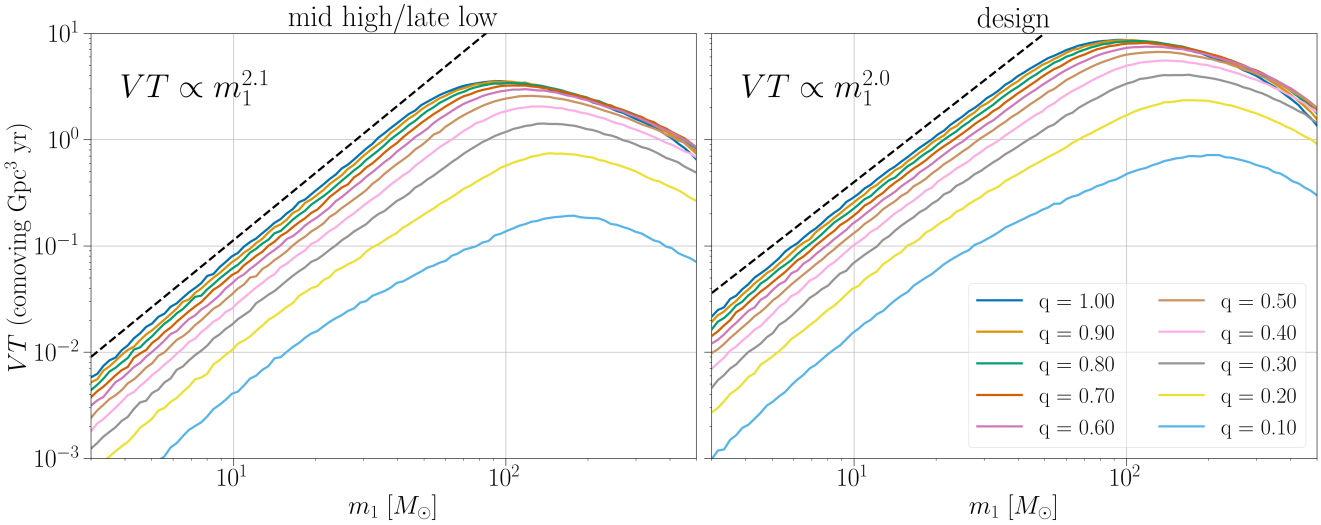

Figure 8. Sensitive redshifted spacetime volume, VT, as a function of primary mass m_1 and mass ratio q for a three-detector network consisting of LIGO-Hanford, LIGO-Livingston, and Virgo with fixed power spectral densities representative of the third observing run O3 (left) and at design sensitivity (right). Power spectral densities for all three interferometers are taken from Abbott et al. (2018). Colors show VT for mass ratios ranging from 10:1 to 1:1. Until the turnover in sensitivity at $m_1 \simeq 100\,M_\odot$, we find the scaling in VT to be well approximated by a power-law in m_1 with $VT \propto m_1^{2.1}$ for mid high/late low sensitivity and $VT \propto m_1^{2.0}$ for design sensitivity, similar to Fishbach & Holz (2017).

where $\frac{dV_c}{dz}$ is the differential comoving volume at the merger redshift and $dt_{\rm src}/dt_{\rm obs}(z) = (1+z)^{-1}$ is the time dilation between the merger and detectors. Detection probabilities for each system are determined using a k-nearest neighbors regressor trained on our detection probability grid.

Figure 8 shows the sensitive comoving spacetime volume, VT, for which a given search is sensitive to a BBH system with a particular primary mass and mass ratio, defined as

$$VT(m_1, q) = T \int \frac{dV_c}{dz} \frac{1}{1+z} p_{\rm det}(m_1, q, z) {\rm d}z \tag{A3}$$

where T is the observing time, which is fixed to 1 yr, and $p_{\rm det}(m_1, q, z)$ is the detection probability for a system merging at redshift z with primary mass m_1 and mass ratio q (see e.g., Fishbach & Holz 2017). Our grid of pre-computed detection probabilities is publicly available on Zenodo (Zevin 2021) and the associated codebase for applying selection effects is available on Github.[6]

B. VARYING THE ONSET OF UNSTABLE MT

Throughout this work, we have assumed that the critical mass ratios that govern the onset of unstable MT follow the prescription in Neijssel et al. (2019). Here, we briefly discuss how key results change with an alternative choice of critical mass ratios by adopting the values from Belczynski et al. (2008). Figure 9 shows the birth mass ratio versus effective spin distribution across our five simulated accretion efficiency ($f_{\rm acc}$) values, for a single model variation of CE efficiency ($\alpha_{\rm CE} = 1$) and super-Eddington accretion factor ($\gamma_{\rm Edd} = 1$). Overall, the mass ratio and effective spin distributions are similar between the two critical mass ratio models. The critical mass ratio parameterization of Belczynski et al. (2008) leads to slightly less systems proceeding through MRR and tidal spin-up. Compared to the critical mass ratios of Neijssel et al. (2019), at $f_{\rm acc} = 0.5$ the Belczynski et al. (2008) model decreases the percentage of systems with $q_{\rm b} > 1$ from 47% to 22%. The fraction of systems that proceed through MRR and have second-born spins of $a_{\rm 2b} > 0.2$ decrease by about a factor of 2.

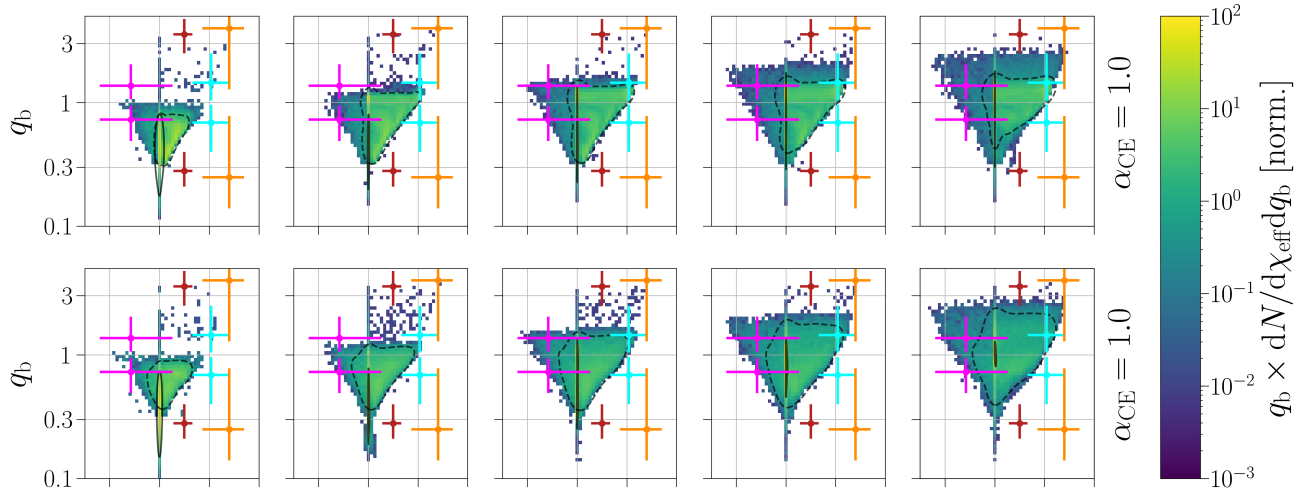

Figure 9. Same as Figure 6 except comparing the stellar-type-specific critical mass ratios of Neijssel et al. (2019) (N+19, used throughout the rest of this work) and Belczynski et al. (2008) (B+08). For the models shown here, the CE efficiency and super-Eddington factor are $\alpha_{\rm CE} = 1.0$ and $\gamma_{\rm Edd} = 1.0$, respectively.

[6] https://github.com/michaelzevin/selection-effects

REFERENCES

Abbott, B. P., Abbott, R., Abbott, T. D., et al. 2018, Living Reviews in Relativity, 21, 3, doi: 10.1007/s41114-018-0012-9

Abbott, R., Abbott, T. D., Abraham, S., et al. 2020, Physical Review D, 102, 43015, doi: 10.1103/PhysRevD.102.043015

—. 2021a, The Astrophysical Journal Letters, 913, L7, doi: 10.3847/2041-8213/abe949

—. 2021b, arXiv e-prints, doi: 10.1103/PhysRevX.11.021053

—. 2021c, arXiv e-prints, doi: 10.1103/PhysRevX.11.021053

—. 2021d, arXiv e-prints. https://arxiv.org/abs/2111.03634

—. 2021e, Physical Review X, 11, 21053, doi: 10.1103/PhysRevX.11.021053

Alves, J., Forveille, T., Pentericci, L., & Shore, S. 2020, Astronomy and Astrophysics, 641, 1, doi: 10.1051/0004-6361/202039265

Bavera, S. S., Zevin, M., & Fragos, T. 2021a, Research Notes of the American Astronomical Society, 5, 127. https://arxiv.org/abs/2105.09077

Bavera, S. S., Fragos, T., Qin, Y., et al. 2020, Astronomy & Astrophysics, 635, A97, doi: 10.1051/0004-6361/201936204

Bavera, S. S., Fragos, T., Zevin, M., et al. 2021b, Astronomy and Astrophysics, 647, A153, doi: 10.1051/0004-6361/202039804

Belczynski, K., Bulik, T., & Bailyn, C. 2011, Astrophysical Journal Letters, 742, 4, doi: 10.1088/2041-8205/742/1/L2

Belczynski, K., Bulik, T., & Fryer, C. L. 2012, arXiv e-prints. https://arxiv.org/abs/1208.2422

Belczynski, K., Kalogera, V., Rasio, F. A., et al. 2008, The Astrophysical Journal Supplement Series, 174, 223, doi: 10.1086/521026

Belczynski, K., Klencki, J., Fields, C. E., et al. 2020, Astronomy & Astrophysics, 104, 1, doi: 10.1051/0004-6361/201936528

Belczynski, K., Romagnolo, A., Olejak, A., et al. 2021, arXiv e-prints. https://arxiv.org/abs/2108.10885

Biscoveanu, S., Isi, M., Vitale, S., & Varma, V. 2021, Physical Review Letters, 126, 171103, doi: 10.1103/PhysRevLett.126.171103

Bouffanais, Y., Mapelli, M., Gerosa, D., et al. 2019, The Astrophysical Journal, 886, 25, doi: 10.3847/1538-4357/ab4a79

Bouffanais, Y., Mapelli, M., Santoliquido, F., et al. 2021a, Monthly Notices of the Royal Astronomical Society, 507, 5224, doi: 10.1093/mnras/stab2438

—. 2021b, Monthly Notices of the Royal Astronomical Society, 505, 3873, doi: 10.1093/mnras/stab1589

Breivik, K., Coughlin, S., Zevin, M., et al. 2020, The Astrophysical Journal, 898, 71, doi: 10.3847/1538-4357/ab9d85

Broekgaarden, F. S., Stevenson, S., & Thrane, E. 2022, arXiv e-prints. https://arxiv.org/abs/2205.01693

Broekgaarden, F. S., Berger, E., Neijssel, C. J., et al. 2021, arXiv e-prints. https://arxiv.org/abs/2103.02608

Brown, G. 1995, The Astrophysical Journal, 440, 270

Callister, T. A., Haster, C.-J., Ng, K. K. Y., Vitale, S., & Farr, W. M. 2021, The Astrophysical Journal Letters, 922, L5, doi: 10.3847/2041-8213/ac2ccc

Claeys, J. S. W., Pols, O. R., Izzard, R. G., Vink, J., & Verbunt, F. W. M. 2014, Astronomy & Astrophysics, 563, A83, doi: 10.1051/0004-6361/201322714

Cruz-Osorio, A., Lora-Clavijo, F. D., & Herdeiro, C. 2021, Journal of Cosmology and Astroparticle Physics, 2021, 32, doi: 10.1088/1475-7516/2021/07/032

Cruz-Osorio, A., & Rezzolla, L. 2020, The Astrophysical Journal, 894, 147, doi: 10.3847/1538-4357/ab89aa

Damour, T. 2001, Physical Review D, 64, 124013, doi: 10.1103/PhysRevD.64.124013

De Mink, S. E., & Mandel, I. 2016, Monthly Notices of the Royal Astronomical Society, 460, 3545, doi: 10.1093/mnras/stw1219

Detmers, R. G., Langer, N., Podsiadlowski, P., & Izzard, R. G. 2008, Astronomy and Astrophysics, 484, 831, doi: 10.1051/0004-6361:200809371

Dewi, J. D., Podsiadlowski, P., & Sena, A. 2006, Monthly Notices of the Royal Astronomical Society, 368, 1742

du Buisson, L., Marchant, P., Podsiadlowski, P., et al. 2020, Monthly Notices of the Royal Astronomical Society, 499, 5941, doi: 10.1093/mnras/staa3225

Fishbach, M., & Holz, D. E. 2017, The Astrophysical Journal, 851, L25, doi: 10.3847/2041-8213/aa9bf6

Fragos, T., Andrews, J. J., Bavera, S. S., et al. 2022, arXiv e-prints. https://arxiv.org/abs/2202.05892

Fryer, C. L., Belczynski, K., Wiktorowicz, G., et al. 2012, The Astrophysical Journal, 749, 14, doi: 10.1088/0004-637X/749/1/91

Fuller, J., & Lu, W. 2022, arXiv e-prints. https://arxiv.org/abs/2201.08407

Fuller, J., & Ma, L. 2019, The Astrophysical Journal Letters, 881, L1, doi: 10.3847/2041-8213/ab339b

Fuller, J., Piro, A. L., & Jermyn, A. S. 2019, Monthly Notices of the Royal Astronomical Society, 485, 3661, doi: 10.1093/mnras/stz514

Gallegos-Garcia, M., Berry, C. P. L., Marchant, P., & Kalogera, V. 2021, The Astrophysical Journal, 922, 110, doi: 10.3847/1538-4357/ac2610

Giacobbo, N., & Mapelli, M. 2018, Monthly Notices of the Royal Astronomical Society, 480, 2011, doi: 10.1093/mnras/sty1999

Giacobbo, N., Mapelli, M., & Spera, M. 2018, Monthly Notices of the Royal Astronomical Society, 474, 2959, doi: 10.1093/mnras/stx2933

Grevesse, N., & Sauval, A. J. 1998, Space Science Reviews, 85, 161, doi: 10.1023/A:1005161325181

Hamers, A. S., & Safarzadeh, M. 2020, The Astrophysical Journal, 99, 99, doi: 10.3847/1538-4357/ab9b27

Heger, A., Woosley, S. E., & Spruit, H. C. 2005, The Astrophysical Journal, 626, 350, doi: 10.1086/429868

Hobbs, G., Lorimer, D. R., Lyne, A. G., & Kramer, M. 2005, Monthly Notices of the Royal Astronomical Society, 360, 974, doi: 10.1111/j.1365-2966.2005.09087.x

Hotokezaka, K., & Piran, T. 2017, The Astrophysical Journal, 842, 111, doi: 10.3847/1538-4357/aa6f61

Hu, R.-C., Zhu, J.-P., Qin, Y., et al. 2022, arXiv e-prints. https://arxiv.org/abs/2201.09549

Hunter, J. D. 2007, Computing in Science and Engineering, 9, 99, doi: 10.1109/MCSE.2007.55

Hurley, J. R., Pols, O. R., & Tout, C. A. 2000, Monthly Notices of the Royal Astronomical Society, 315, 543, doi: 10.1046/j.1365-8711.2000.03426.x

Hurley, J. R., Tout, C. A., & Pols, O. R. 2002, Monthly Notices of the Royal Astronomical Society, 329, 897, doi: 10.1046/j.1365-8711.2002.05038.x

Kroupa, P. 2001, Monthly Notices of the Royal Astronomical Society, 322, 231, doi: 10.1046/j.1365-8711.2001.04022.x

Kruckow, M. U., Tauris, T. M., Langer, N., Kramer, M., & Izzard, R. G. 2018, Monthly Notices of the Royal Astronomical Society, 481, 1908, doi: 10.1093/MNRAS/STY2190

Kushnir, D., Zaldarriaga, M., Kollmeier, J. A., & Waldman, R. 2017, Monthly Notices of the Royal Astronomical Society, 467, 2146, doi: 10.1093/mnras/stx255

MacLeod, M., & Ramirez-Ruiz, E. 2015, Astrophysical Journal, 803, 41, doi: 10.1088/0004-637X/803/1/41

Mandel, I., & De Mink, S. E. 2016, Monthly Notices of the Royal Astronomical Society, 458, 2634, doi: 10.1093/mnras/stw379

Mandel, I., & Farmer, A. 2018, arXiv e-prints. https://arxiv.org/abs/1806.05820

Mandel, I., Farr, W. M., & Gair, J. R. 2019, Monthly Notices of the Royal Astronomical Society, 486, 1086, doi: 10.1093/mnras/stz896

Mandel, I., & Fragos, T. 2020, The Astrophysical Journal, 895, L28, doi: 10.3847/2041-8213/ab8e41

Marchant, P., Langer, N., Podsiadlowski, P., Tauris, T., & Moriya, T. 2016, Astronomy & Astrophysics, 588, A50, doi: 10.1051/0004-6361/201628133

Marchant, P., Renzo, M., Farmer, R., et al. 2019, The Astrophysical Journal, 882, 36, doi: 10.3847/1538-4357/ab3426

McKernan, B., Ford, K. E. S., Callister, T., et al. 2021, arXiv e-prints. https://arxiv.org/abs/2107.07551

McKinney, W. 2010, in Proceedings of the 9th Python in Science Conference, ed. S. van der Walt & J. Millman, 51–56, doi: 10.25080/Majora-92bf1922-00a

Mehta, A. K., Buonanno, A., Gair, J., et al. 2021, arXiv e-prints. https://arxiv.org/abs/2105.06366

Miller, S., Callister, T. A., & Farr, W. M. 2020, The Astrophysical Journal, 895, 128, doi: 10.3847/1538-4357/ab80c0

Neijssel, C. J., Vinciguerra, S., Vigna-Gómez, A., et al. 2021, The Astrophysical Journal, 908, 118, doi: 10.3847/1538-4357/abde4a

Neijssel, C. J., Vigna-Gómez, A., Stevenson, S., et al. 2019, Monthly Notices of the Royal Astronomical Society, 490, 3740, doi: 10.1093/mnras/stz2840

Nelson, D., Pillepich, A., Genel, S., et al. 2015, Astronomy and Computing, 13, 12, doi: 10.1016/j.ascom.2015.09.003

Ng, K. K., Vitale, S., Zimmerman, A., et al. 2018, Physical Review D, 98, 83007, doi: 10.1103/PhysRevD.98.083007

Nitz, A. H., Capano, C. D., Kumar, S., et al. 2021, arXiv e-prints, doi: 10.3847/1538-4357/ac1c03

Nitz, A. H., Schäfer, M., & Canton, T. D. 2020, The Astrophysical Journal Letters, 902, L29, doi: 10.3847/2041-8213/abbc10

Olejak, A., & Belczynski, K. 2021, The Astrophysical Journal Letters, 921, L2, doi: 10.3847/2041-8213/ac2f48

Olejak, A., Fishbach, M., Belczynski, K., et al. 2020, The Astrophysical Journal Letters, 901, L39, doi: 10.3847/2041-8213/abb5b5

Oliphant, T. E. 2006, A guide to NumPy (USA: Trelgol Publishing). https://web.mit.edu/dvp/Public/numpybook.pdf

Olsen, S., Venumadhav, T., Mushkin, J., et al. 2022, arXiv e-prints. https://arxiv.org/abs/2201.02252

Patton, R. A., Sukhbold, T., & Eldridge, J. J. 2022, Monthly Notices of the Royal Astronomical Society, doi: 10.1093/mnras/stab3797

Paxton, B., Bildsten, L., Dotter, A., et al. 2011, The Astrophysical Journal Supplement Series, 192, 3, doi: 10.1088/0067-0049/192/1/3

Paxton, B., Cantiello, M., Arras, P., et al. 2013, The Astrophysical Journal Supplement Series, 208, 4, doi: 10.1088/0067-0049/208/1/4

Paxton, B., Marchant, P., Schwab, J., et al. 2015, The Astrophysical Journal Supplement Series, 220, 15, doi: 10.1088/0067-0049/220/1/15

Paxton, B., Schwab, J., Bauer, E. B., et al. 2018, The Astrophysical Journal Supplement Series, 234, 34, doi: 10.3847/1538-4365/aaa5a8

Paxton, B., Smolec, R., Schwab, J., et al. 2019, The Astrophysical Journal Supplement Series, 243, 10, doi: 10.3847/1538-4365/ab2241

Pérez, F., & Granger, B. E. 2007, IEEE Journals & Magazines, 9, 21, doi: 10.1109/MCSE.2007.53

Price-Whelan, A. M., Sipocz, B. M., Günther, H. M., et al. 2018, The Astronomical Journal, 156, 123, doi: 10.3847/1538-3881/aabc4f

Qin, Y., Fragos, T., Meynet, G., et al. 2018, Astronomy & Astrophysics, 616, A28, doi: 10.1051/0004-6361/201832839

Qin, Y., Marchant, P., Fragos, T., Meynet, G., & Kalogera, V. 2019, The Astrophysical Journal, 870, L18, doi: 10.3847/2041-8213/aaf97b

Qin, Y., Shu, X., Yi, S., & Wang, Y.-Z. 2022, arXiv e-prints, doi: 10.1088/1674-4527/ac4ca4

Qin, Y., Yuan-Zhu, Wang, Dong-Hong, & Wu. 2021, arXiv e-prints. https://arxiv.org/abs/2108.04821

Robitaille, T. P., Tollerud, E. J., Greenfield, P., et al. 2013, Astronomy & Astrophysics, 558, A33, doi: 10.1051/0004-6361/201322068

Rodriguez, C. L., Zevin, M., Pankow, C., Kalogera, V., & Rasio, F. A. 2016, The Astrophysical Journal Letters, 832, 1, doi: 10.3847/2041-8205/832/1/L2

Rodriguez, C. L., Kremer, K., Grudić, M. Y., et al. 2020, The Astrophysical Journal, 896, L10, doi: 10.3847/2041-8213/ab961d

Safarzadeh, M., & Hotokezaka, K. 2020, The Astrophysical Journal, 897, L7, doi: 10.3847/2041-8213/ab9b79

Sana, H., De Mink, S. E., De Koter, A., et al. 2012, Science, 337, 444, doi: 10.1126/science.1223344

Santoliquido, F., Mapelli, M., Giacobbo, N., Bouffanais, Y., & Artale, M. C. 2021, Monthly Notices of the Royal Astronomical Society, 502, 4877, doi: 10.1093/mnras/stab280

Schrøder, S. L., Batta, A., & Ramirez-Ruiz, E. 2018, The Astrophysical Journal Letters, 862, L3, doi: 10.3847/2041-8213/aacf8d

Spruit, H. C. 2002, Astronomy & Astrophysics, 381, 923, doi: 10.1051/0004-6361

Steinle, N., & Kesden, M. 2021, Physical Review D, 103, 63032, doi: 10.1103/PhysRevD.103.063032

Stevenson, S., Sampson, M., Powell, J., et al. 2019, The Astrophysical Journal, 882, 121, doi: 10.3847/1538-4357/ab3981

Tagawa, H., Haiman, Z., Bartos, I., Kocsis, B., & Omukai, K. 2021, arXiv e-prints. https://arxiv.org/abs/2104.09510

Tanikawa, A., Yoshida, T., Kinugawa, T., et al. 2022, The Astrophysical Journal, 926, 83, doi: 10.3847/1538-4357/ac4247

Thorne, K. S. 1974, The Astrophysical Journal, 191, 507. https://arxiv.org/abs/arXiv:1011.1669v3

Van Der Walt, S., Colbert, S. C., & Varoquaux, G. 2011, Computing in Science and Engineering, 13, 22, doi: 10.1109/MCSE.2011.37

van Son, L. A. C., De Mink, S. E., Broekgaarden, F. S., et al. 2020, The Astrophysical Journal, 897, 100, doi: 10.3847/1538-4357/ab9809

Vink, J. S., & de Koter, A. 2005, Astronomy & Astrophysics, 442, 587, doi: 10.1051/0004-6361:20052862

Vink, J. S., de Koter, A., & Lamers, H. J. G. L. M. 2001, Astronomy & Astrophysics, 369, 574, doi: 10.1051/0004-6361

Virtanen, P., Gommers, R., Oliphant, T. E., et al. 2020, Nature Methods, 17, 261, doi: 10.1038/s41592-019-0686-2

Vitale, S., Gerosa, D., Farr, W. M., & Taylor, S. R. 2020, arXiv e-prints. https://arxiv.org/abs/2007.05579

Webbink, R. 1984, The Astrophysical Journal, 277, 355, doi: 10.1086/161701

Wong, K. W., Breivik, K., Kremer, K., & Callister, T. 2021, Physical Review D, 103, 83021, doi: 10.1103/PhysRevD.103.083021

Zaldarriaga, M., Kushnir, D., & Kollmeier, J. A. 2018, Monthly Notices of the Royal Astronomical Society, 473, 4174, doi: 10.1093/mnras/stx2577

Zevin, M. 2021, Semianalytic VT, Zenodo, doi: 10.5281/zenodo.5086359

Zevin, M., Berry, C. P. L., Coughlin, S., Chatziioannou, K., & Vitale, S. 2020a, The Astrophysical Journal, 899, L17, doi: 10.3847/2041-8213/aba8ef

Zevin, M., Spera, M., Berry, C. P. L., & Kalogera, V. 2020b, The Astrophysical Journal, 899, L1, doi: 10.3847/2041-8213/aba74e

Zevin, M., Bavera, S. S., Berry, C. P., et al. 2021, The Astrophysical Journal, 910, 152, doi: 10.3847/1538-4357/abe40e

A.1.3 Impact on the current field of research

The main results of Zevin & Bavera (2022) can be summered as follows. We found that depending on the assumed mass accretion efficiency onto stars and BHs, only a small fraction of $10^{-5} - 10^{-2}$ of underlying BBH systems underwent mass ratio reversal having the second-born BHs with more than twice the mass of the first-born counterparts and have spins of $|\vec{\chi}_2| > 0.2$. On the other hand, the fraction of systems with first-born BH being at least twice as massive as the second-born and spinning at $|\vec{\chi}_1| > 0.2$ is $5 \times 10^{-3} - 8 \times 10^{-2}$ of the systems in the underlying BBH population for super-Eddington accretion models. The present study has shown that BBHs such as GW190412 are unlikely to have formed from isolated binary evolution unless highly super-Eddington accretion onto BHs is invoked. Furthermore, we did not find a correlation between the mass ratio and effective spins other than for super-Eddington accretion models confirming Bavera et al. (2021a) results. In the reaming part of this section, we discuss the importance of these results in the current field of research.

Qin et al. (2022) also recently discussed the interpretation of GW190412-like systems in the context of the mass ratio reversal through the CE channel. The authors find that such systems are unlikely to be formed through the mentioned channel if angular momentum transport inside stars is assumed to be efficient. This independent study further corroborates the results of Zevin & Bavera (2022).

Recently, Shao & Li (2022) used detailed binary `MESA` simulations to study super-Eddington accrediting BHs. These detailed binary simulations corroborate our findings that super-Eddington accretion efficiency might lead to spun-up first-born BHs. In contrast to Zevin & Bavera (2022) results, Shao & Li (2022) models already show appreciable BH spin up at ten times the Eddington accretion limit. In Zevin & Bavera (2022), most of the super accreting BHs underwent case B mass transfer, while in Shao & Li (2022) most BHs underwent case A mass transfer which lasts longer. Hence, BHs can accrete more material and further spin up. We also point out that, compared to Zevin & Bavera (2022), the conclusion reached by Shao & Li (2022) about the importance of this BBH formation channel is pure speculation. A true statement for BBH merger rates cannot be made without accounting for the prior binary evolution until the second mass transfer episode. See, e.g., Bavera et al. (2021a), van Son et al. (2020), and Zevin & Bavera (2022) on how uncertainties during this prior binary evolution might affect BBH merger rate estimates of for the super-Eddington SMT channel.

Finally, Broekgaarden et al. (2022) performed a similar study to Zevin & Bavera (2022) studying the occurrence of mass ratio reversal with tidally spun-up second-born BHs assuming the Bavera et al. (2021b) BH spin fit. Broekgaarden et al. (2022) used a different rapid binary population synthesis code compared to Zevin & Bavera (2022) study, and explored additional model uncertainties including uncertainties about the cosmic star formation history In general, Broekgaarden et al. (2022) reached similar conclusions to Zevin & Bavera (2022).

Appendix B

One channel to rule them all?

B.1 Constraining the origins of binary black holes using multiple formation pathways

B.1.1 A brief introduction

Although past studies have attempted to leverage GW observations for characterizing the origin of BBHs or to constrain uncertain astrophysical processes governing their formation, they often restrict themselves to targeting a single channel or a small subset of channels. This is due to the high complexity and dimensional of the problem. Hierarchical model selection analysis is a technique that employs observational data to *simultaneously constrain multiple formation channels encompassing a wide range of prescriptions* for uncertain astrophysical processes, which can affect BBH population properties in highly degenerate ways. In principle, this Bayesian approach has the potential to quantify the origin of merging BBHs and constrain their model uncertainties. The current project aims to illustrate this formalism by leveraging existing data (GWTC-2). Even though the quantitative results presented in this project can be affected by uncertain assumptions in the assumed model predictions, the presented methodology can be extended to account for additional model uncertainties and to include other formation channels.

B.1.2 Manuscript

The conducted study Zevin et al. (2021a) was published in *The Astrophysical Journal* on April 2021. The arXiv open-access version of the manuscript is presented in the following pages.

Draft version April 8, 2021
Typeset using LaTeX **twocolumn** style in AASTeX63

arXiv:2011.10057v2 [astro-ph.HE] 6 Apr 2021

One Channel to Rule Them All? Constraining the Origins of Binary Black Holes Using Multiple Formation Pathways

Michael Zevin,[1,2,3,*] Simone S. Bavera,[4,2] Christopher P. L. Berry,[2,5] Vicky Kalogera,[1,2] Tassos Fragos,[4] Pablo Marchant,[6] Carl L. Rodriguez,[7] Fabio Antonini,[8] Daniel E. Holz,[3,9] and Chris Pankow[2]

[1] *Department of Physics and Astronomy, Northwestern University, 2145 Sheridan Road, Evanston, IL 60208, USA*
[2] *Center for Interdisciplinary Exploration and Research in Astrophysics (CIERA), 1800 Sherman Avenue, Evanston, IL 60201, USA*
[3] *Enrico Fermi Institute and Kavli Institute for Cosmological Physics, The University of Chicago, 5640 South Ellis Avenue, Chicago, Illinois 60637, USA*
[4] *Geneva Observatory, University of Geneva, Chemin Pegasi 51, 1290 Versoix, Switzerland*
[5] *SUPA, School of Physics and Astronomy, University of Glasgow, Glasgow G12 8QQ, UK*
[6] *Institute of Astrophysics, KU Leuven, Celestijnenlaan 200D, B-3001, Leuven, Belgium*
[7] *Department of Physics, Carnegie Mellon University, 5000 Forbes Avenue, Pittsburgh, PA 15213, USA*
[8] *Gravity Exploration Institute, School of Physics and Astronomy, Cardiff University, Cardiff, CF24 3AA, United Kingdom*
[9] *Department of Physics, Department of Astronomy & Astrophysics, The University of Chicago, 5640 South Ellis Avenue, Chicago, Illinois 60637, USA*

ABSTRACT

The second LIGO–Virgo catalog of gravitational-wave (GW) transients has more than quadrupled the observational sample of binary black holes. We analyze this catalog using a suite of five state-of-the-art binary black hole population models covering a range of isolated and dynamical formation channels and infer branching fractions between channels as well as constraints on uncertain physical processes that impact the observational properties of mergers. Given our set of formation models, we find significant differences between the branching fractions of the underlying and detectable populations, and that the diversity of detections suggests that multiple formation channels are at play. A mixture of channels is strongly preferred over any single channel dominating the detected population: an individual channel does not contribute to more than $\simeq 70\%$ of the observational sample of binary black holes. We calculate the preference between the natal spin assumptions and common-envelope efficiencies in our models, favoring natal spins of isolated black holes of $\lesssim 0.1$, and marginally preferring common-envelope efficiencies of $\gtrsim 2.0$ while strongly disfavoring highly inefficient common envelopes. We show that it is essential to consider multiple channels when interpreting GW catalogs, as inference on branching fractions and physical prescriptions becomes biased when contributing formation scenarios are not considered or incorrect physical prescriptions are assumed. Although our quantitative results can be affected by uncertain assumptions in model predictions, our methodology is capable of including models with updated theoretical considerations and additional formation channels.

1. INTRODUCTION

In less than five years the field of gravitational-wave (GW) astrophysics has evolved from speculating about the properties of compact binary coalescence events to having a substantial population primed for astrophysical inference. The recently released catalog of compact binary coalescences (GWTC-2), accumulated by the LIGO and Virgo GW detector network (Aasi et al. 2015; Acernese et al. 2015), has increased the number of confident detections reported by the LIGO Scientific and Virgo Collaboration (LVC) to 50 (Abbott et al. 2020b). As the endpoint of massive-star evolution, merging double compact objects can encode unique information about their progenitor systems, such as the types of galactic environments they were born in and their formation processes, the complex stellar evolution that persisted throughout their lives, and the physics of the supernovae that marked their deaths (Abbott et al. 2016a; Mandel & Farmer 2018; Vitale 2020). From this catalog, the rates of compact binary mergers in the local universe have been significantly constrained, features have been resolved in the binary black hole (BBH) mass spectrum, and a non-negligible fraction of systems have been found to have spins misaligned relative to the pre-merger orbital angular momentum by more than 90° (Abbott et al. 2020c).

* NASA Hubble Fellow
michaelzevin@uchicago.edu

Of the GWTC-2 observations, the vast majority (46) are confidently identified as BBH mergers (Abbott et al. 2020b). BBHs have a disparate array of proposed formation channels. The simple picture of two canonical BBH formation channels, the isolated evolution of a massive-star binary and dynamical assembly in a dense stellar environment, is now inadequate to capture the breadth of theoretical models proposed for BBH mergers. Both the isolated evolution and dynamical assembly paradigms have multiple subchannels with differing predictions for mass distributions, spin distributions, and the redshift evolution of BBH mergers, each with predicted local merger rates consistent with the empirical rate measured by the LVC of 15–40 $\mathrm{Gpc}^{-3}\,\mathrm{yr}^{-1}$ (90% credible interval; Abbott et al. 2020c).

On the isolated evolution side, the standard channel involves a phase of unstable mass transfer following the formation of the first black hole (BH), initiating a common envelope (CE) phase that hardens the binary via drag forces (Paczyński 1976; van den Heuvel 1976; Tutukov & Yungelson 1993) and leading to BBHs that can merge in less than the Hubble time (e.g., Bethe & Brown 1998; Belczyński et al. 2002; Dominik et al. 2012; Belczynski et al. 2016; Eldridge & Stanway 2016; Stevenson et al. 2017b; Giacobbo & Mapelli 2018). However, theoretical models have shown that hardened BBH systems merging within the Hubble time can also form through late-phase stable mass transfer (van den Heuvel et al. 2017; Neijssel et al. 2019). On the other hand, if the progenitor stars are born in a very tight orbital configuration, they may proceed through a chemically homogeneous evolution, in which rapid rotation of the stars attained through tidal interaction leads to strong mixing, replenishing the core with elements for nuclear burning and never leading to significant expansion of the progenitor stars (De Mink & Mandel 2016; Mandel & De Mink 2016; Marchant et al. 2016). Extremely low-metallicity Population III stars in binary systems have also been proposed to have formed the high-mass BBH mergers observed (Madau & Rees 2001; Kinugawa et al. 2014; Inayoshi et al. 2017).

On the dynamical side, following the formation of BHs from massive stars in a dense stellar environment such as a globular cluster (GC), nuclear star cluster (NSC), or young open star cluster, these BHs' mass segregate to the core of the cluster due to dynamical friction and create a dense subsystem dominated by BH interactions (Lightman & Shapiro 1978; Sigurdsson & Hernquist 1993). Strong gravitational encounters between BH systems act to produce hardened binaries, typically extracting orbital energy from the more massive components of the interaction by ejecting the lighter components (McMillan et al. 1991; Hut et al. 1992; Sigurdsson & Phinney 1993; Miller & Hamilton 2002; Gültekin et al. 2006; Fregeau & Rasio 2007) and leading to BBHs that can merge within the Hubble time (e.g., Portegies Zwart & McMillan 2000; O'Leary et al. 2006; Downing et al. 2010; Samsing et al. 2014; Ziosi et al. 2014; Rodriguez et al. 2015, 2016a; Antonini & Rasio 2016; Askar et al. 2017; Banerjee 2017; Samsing & Ramirez-Ruiz 2017). Different dynamical environments have unique predictions for the properties of merging BBHs, since stellar densities, escape velocities, and stellar mass budgets vary significantly between these environments.

To further complicate matters, a slew of formation scenarios for the synthesis of BBHs have been proposed that do not fit cleanly into the broad categorizations of isolated binary evolution and dynamical assembly. A significant number of massive stars form in high-order multiples such as triples and quadruples (Sana et al. 2014; Moe & Di Stefano 2017). If a BBH is the inner binary in a hierarchical system, eccentricity can be imparted into the inner BBH through the Lidov–Kozai mechanism (Kozai 1962; Lidov 1963). This process will expedite the inspiral time of the binary, allowing systems to merge as GW sources that would not typically merge within a Hubble time (Wen 2003; Antonini et al. 2017; Silsbee & Tremaine 2017; Fragione & Kocsis 2019; Vigna-Gómez et al. 2021). Galactic nuclei are also predicted to produce BBH mergers in a similar way, with the supermassive BH as the outer perturber (Antonini & Perets 2012). Another promising environment for facilitating BBH mergers is active galactic nuclei (AGNs); BHs are predicted to get caught in resonance traps of AGN disks, potentially proceeding through many hierarchical mergers due to the high escape velocity in the vicinity of the supermassive BH (McKernan et al. 2014; Bartos et al. 2017; Stone et al. 2017). Stellar-mass BBHs detected by LIGO–Virgo have also been proposed to originate from the merger of central BHs in extremely low-mass ultradwarf galaxies that merge at $z \gtrsim 1$ (Conselice et al. 2020). Ultrawide BH binaries and high-order systems in the galactic field that are perturbed from stellar flybys may also excite eccentricity in the BBH system and cause it to merge within the Hubble time (Michaely & Perets 2019, 2020). Finally, primordially formed BHs have also been proposed as sources of merging BBHs and have been suggested as candidates for dark matter (Bird et al. 2016; Sasaki et al. 2018; Clesse & Garcia-Bellido 2020).

Numerous attempts have been made to leverage GW observations for characterizing the branching fractions between these channels or constraining uncertain physical processes governing these channels (Stevenson et al.

2015; Rodriguez et al. 2016b; Farr et al. 2017a,b; Mandel et al. 2017; Stevenson et al. 2017a; Talbot & Thrane 2017; Vitale et al. 2017; Zevin et al. 2017; Barrett et al. 2018; Taylor & Gerosa 2018; Arca Sedda & Benacquista 2019; Powell et al. 2019; Roulet & Zaldarriaga 2019; Wysocki et al. 2019; Abbott et al. 2020c; Antonini & Gieles 2020a; Arca Sedda et al. 2020; Baibhav et al. 2020; Bavera et al. 2020a; Bouffanais et al. 2020; Farmer et al. 2020; Fishbach & Holz 2020; Hall et al. 2020; Kimball et al. 2020a,b; Roulet et al. 2020; Safarzadeh 2020; Wong et al. 2020, 2021; Bhagwat et al. 2021). However, due to the high complexity and dimensionality of the problem, these studies often restrict themselves to targeting a single channel or a small subset of channels. Though idealized model comparisons are enlightening, the most robust and unbiased constraints will come from considering *many prominent BBH formation channels* and encompassing *a wide range of prescriptions for uncertain physical processes*, which can affect BBH population properties in highly degenerate ways.

Given the rapidly growing catalog of BBHs, we are now at the stage where such high-dimensional, multi-channel model selection endeavors can be informative. We present a methodology for leveraging a suite of state-of-the-art BBH formation models to perform hierarchical inference using the catalog of GW events. We simultaneously consider the predicted BBH parameter distributions from five simulated populations, ensuring the models are as self-consistent as possible, and vary two uncertain physical parameters between these channels, namely the natal spins of isolated BHs and the efficiency of CE evolution. Though the models we consider do not cover the entire array of proposed formation channels, the infrastructure presented in this work can be expanded to include an arbitrary number of channels and uncertain physical prescriptions. We find that the current catalog of GWs strongly disfavors a single formation channel, indicating a more complex landscape of prominent channels for BBH formation.

In Section 2, we briefly overview the astrophysical models considered in this work, as well as the physical parameterizations we vary between these models. Section 3 details our hierarchical modeling procedure. In Section 4, we show the results of our analysis applied to the current catalog of GW observations of BBH mergers. We discuss the implications of our results and conclude in Section 5.

2. FORMATION MODELS

We consider five astrophysical models for BBH mergers, each with unique predictions for mass distributions, spin distributions, and the evolution of merger rate with redshift. Further details about these models and assumptions regarding cosmological evolution can be found in Appendix A.

2.1. *Isolated Evolution*

Three models are considered that fall under the broad categorization of isolated evolution in the galactic field: binaries that proceed through a late-phase CE (`CE`), binaries that only have stable mass transfer between the star and the already formed BH (`SMT`), and chemically homogeneous evolution (`CHE`).

The `CE` and `SMT` channels are modeled using the `POSYDON` framework (T. Fragos et al. 2021, in preparation), which, among other functionalities, stitches together different phases of binary evolution that are modeled using rapid population synthesis (`COSMIC`; Breivik et al. 2020) and detailed binary evolution calculations (`MESA`; Paxton et al. 2011, 2013, 2015, 2018, 2019). These models are described in detail in Bavera et al. (2020a), and the key ingredients are summarized in Appendix A.1.1. In this channel, the more massive star leaves the main sequence first and expands to become a supergiant star. At some point the star overfills its Roche lobe, typically leading to a stable mass-transfer event where the primary loses most of its hydrogen envelope before it undergoes core collapse and forms a BH. During the subsequent evolution the secondary expands, leading to a second mass-transfer episode. This can be either stable or unstable, with the latter leading to a CE phase that shrinks the orbit more efficiently. If the stripping of the secondary is successful, a BH–Wolf–Rayet system is formed, which can undergo a tidal spin-up phase. In general stable mass transfer leads to wider orbits compared to a CE, and hence, the system will avoid tidal spin-up (Bavera et al. 2020a). Eventually the secondary collapses to form a BH, and energy dissipation due to GW radiation leads to the merger.

The `CHE` models are adapted from du Buisson et al. (2020), who computed a large grid of simulations for binaries undergoing this evolutionary process. Although not discussed in the work of du Buisson et al. (2020), the simulations include predictions for the final spins of the BHs, which arise from tidal synchronization during core hydrogen burning. The final spin in these systems is determined by wind mass loss, which removes angular momentum and widens the binary. This leads to BBHs at wider separations and lower spins with increasing metallicity (Marchant et al. 2016).

2.2. *Dynamical Assembly*

We also consider two models for BBH mergers synthesized via dynamical assembly in dense stellar envi-

ronments: formation in old, metal-poor GCs (GC) and formation in NSCs (NSC).

The GC simulations are taken from a grid of 96 N-body models of collisional star clusters described in Rodriguez et al. (2019). The models were created using the Hénon-style cluster Monte Carlo code CMC (Hénon 1971a,b; Joshi et al. 2000; Pattabiraman et al. 2013). The 96 models consist of four independent grids of 24 models, each with different initial spins for BHs born from stellar collapse ($\chi_{\rm b} = 0$, 0.1, 0.2, and 0.5). Within each 24-model subgrid, the clusters span a range of realistic initial masses, metallicities, and half-mass radii consistent with observations of GCs in the Milky Way and nearby galaxies. The cluster birth times are taken from a cosmological model for GC formation (El-Badry et al. 2019), where we take into account the correlation between cluster metallicity and formation redshift (Rodriguez & Loeb 2018; Rodriguez et al. 2018a).

The NSC models are adapted from Antonini et al. (2019). For the evolution of the clusters we need the initial cluster mass M, half-mass radius $r_{\rm h}$, and BH masses. Since the formation history and evolution of NSCs is uncertain (Neumayer et al. 2020), we proceed with a number of simplifying assumptions. We assume that the properties of nuclear clusters today are representative of their properties at formation. Accordingly, M and $r_{\rm h}$ are sampled directly from the 151 NSCs in Georgiev & Böker (2014) with well-determined properties. For each cluster we use COSMIC to generate the BH masses from a single stellar population with metallicity of $0.01Z_{\odot}$, $0.1Z_{\odot}$, or $1Z_{\odot}$. We then evolve the clusters and their BHs using the semi-analytical approach described in Antonini et al. (2019). Finally, the BBH merger rate, masses, component spins, and redshift evolution are obtained by assuming that the formation epoch and metallicity of nuclear clusters evolve in the same way as their galactic hosts, using Madau & Fragos (2017). This procedure is repeated for four values of the initial BH spins, $\chi_{\rm b} = 0$, 0.1, 0.2 and 0.5.

2.3. *Physical Prescriptions*

The physical prescription we vary across all models above is the natal spin magnitude $\chi_{\rm b}$ of BHs that are born in isolation or in systems where binary interactions prior to the collapse of the helium core do not cause significant spin-up. Variations in the natal spin magnitudes act as a proxy for the efficiency of angular momentum transport in massive stars; if angular momentum is efficiently transported from the core to the envelope, the birth spins of BHs are predicted to be low (e.g., Fuller & Ma 2019). We use four models for the natal dimensionless spin magnitudes of isolated BHs in each channel: $\chi_{\rm b} \in [0.0, 0.1, 0.2, 0.5]$. These discrete values for $\chi_{\rm b}$ are chosen to match the natal spins assumed for the GC simulations in Rodriguez et al. (2019). However, this does not mean that all components of BBHs in these models are spinning at precisely these prescribed values.

In the field channels, tidal spin-up of the pre-collapse helium core or mass transfer following the birth of the primary BH can cause BHs to be born with or attain spin. For the CE channel, the helium core progenitor of the second-born BH can be spun up through tidal interactions with the already born BH. The degree at which the second-born BH is spinning depends on the post-CE separation and thus on the CE efficiency; lower CE efficiencies will lead to tighter post-CE binaries, increasing the effect of tides and therefore increasing the natal spin of the second-born BH (Qin et al. 2018; Zaldarriaga et al. 2018; Bavera et al. 2020a). The spin of the first-born BH can grow through stable mass transfer, though this is sensitive to assumptions regarding the maximum rate of accretion. Since we consider Eddington-limited accretion efficiency, the amount of spin-up that first-born BHs can acquire via accretion is minimal (Thorne 1974), and systems cannot tighten enough through this highly nonconservative mass transfer for tidal effects to be effective at spinning up the progenitor of the second-born BH (Bavera et al. 2020a). BBHs evolving through chemically homogeneous evolution are near-contact at birth, and strong tidal interaction between the stars leads to high rotations and substantial chemical mixing in both stars. This inhibits significant expansion of the stars, preventing efficient loss of angular momentum via accretion or loss of their envelopes. The natal spins of all BHs in our simulations self-consistently account for these effects, and for all three field channels considered, components spinning at $\chi < \chi_{\rm b}$ at BBH formation are given spins of $\chi_{\rm b}$. Thus, unless binary interactions such as tidal effects or mass transfer are efficient at spinning up the BH components, their spin magnitudes are assumed to be those that they would attain in isolation solely from the collapse of the stellar core.

For the dynamical channels, the natal spins of BHs play an important role in the evolution of the BBH subsystem in the cluster as a whole. In particular, the fraction of BBH merger products retained in a cluster is highly sensitive to the spins of the BHs in the natal population (Gerosa & Berti 2019; Rodriguez et al. 2019; Kimball et al. 2020a); as spin magnitudes increase, the higher degree of asymmetry in the merger leads to larger relativistic recoil kicks due to the anisotropic emission of GWs at merger (Peres 1962; Bekenstein 1973; Wiseman 1992; Favata et al. 2004; Baker et al. 2006; Koppitz et al. 2007; Pollney et al. 2007; Holley-Bockelmann

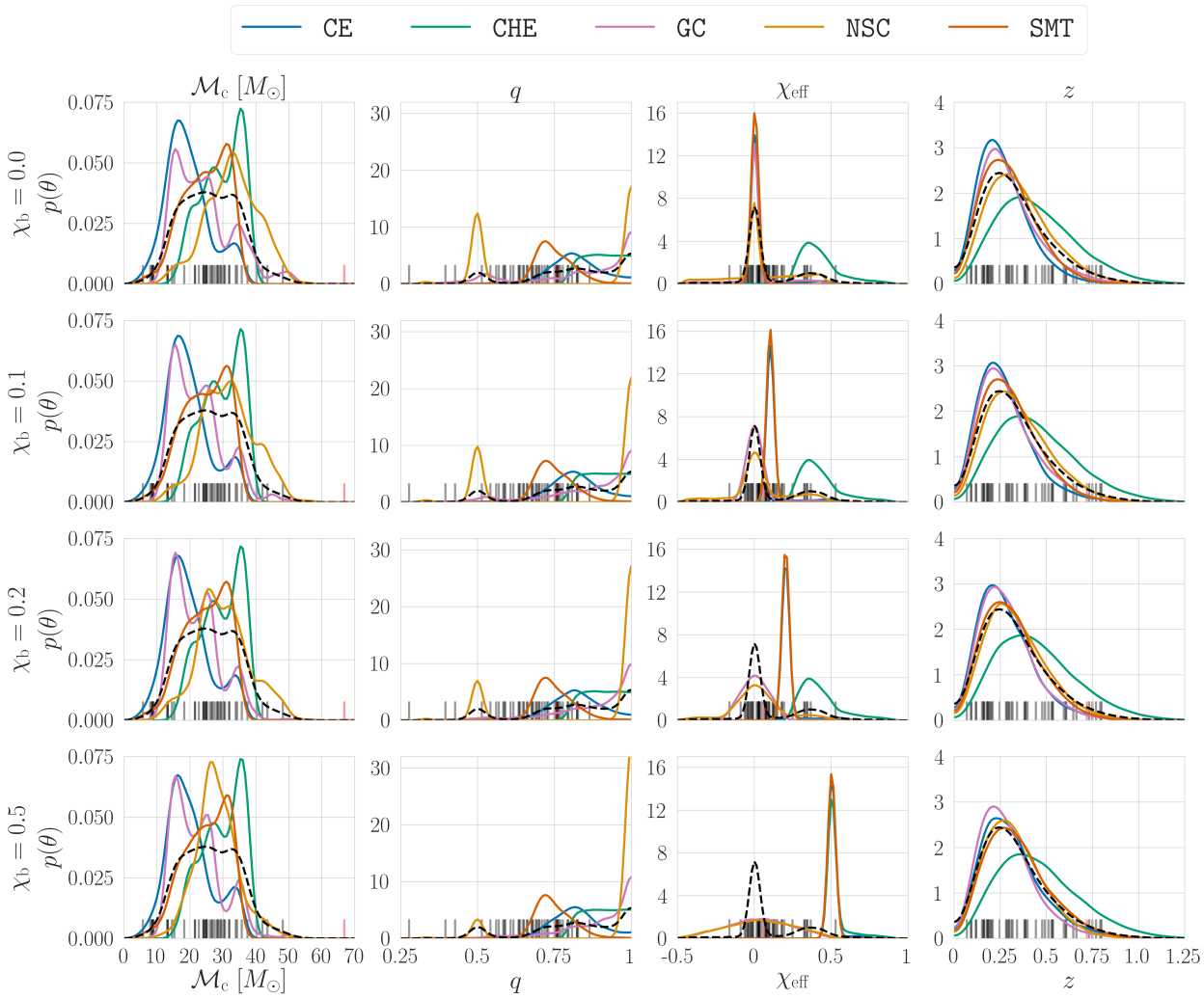

Figure 1. Marginalized detection-weighted distributions of BBH parameters for our five formation channels with varying natal spin prescriptions. The CE efficiency is fixed at $\alpha_{\rm CE} = 1.0$ for all models in this figure. Black ticks mark the median value of the posterior distribution for all confident BBHs in GWTC-2; GW190521, which is excluded from our analysis, is instead marked with a red tick. The dashed black line shows an example mixture model synthesized for the five channels, assuming equal detectable branching fractions and a true model with the values $\chi_{\rm b} = 0.0$ and $\alpha_{\rm CE} = 1.0$.

et al. 2008; Lousto et al. 2010; Blanchet 2014; Sperhake 2015). Thus, BBH merger products from spinning BHs' components are more efficiently kicked out of their host environments, preventing them from proceeding in subsequent hierarchical mergers (e.g., Rodriguez et al. 2019; Banerjee 2021; Fragione & Silk 2020). With higher natal spins, the mass spectrum of BBHs will thus be quenched at large values by the limitations of massive-star evolution, though the retention rate and frequency of hierarchical mergers are sensitive to the mass and escape velocities of the cluster in question (Antonini & Rasio 2016; Antonini et al. 2019; Gerosa & Berti 2019; Kimball et al. 2020a,b; Mapelli et al. 2020). Suites of cluster models with varying cluster properties and metallicities are thus run for the `GC` and `NSC` channels for all spin magnitude models considered. Though all BHs start with the prescribed spin magnitude, higher spins in BBH components can be attained through hierarchical mergers, which impart a spin on the newly formed BH of $\chi \sim 0.7$ for nearly equal-mass binary mergers with non-spinning components (Pretorius 2005; González et al. 2007; Buonanno et al. 2008).

In addition, we consider five assumptions for the efficiency of CEs: $\alpha_{\rm CE} \in [0.2, 0.5, 1.0, 2.0, 5.0]$. Values of $\alpha_{\rm CE} > 1.0$ (i.e. efficient CE evolution) mean that there is an energy source in addition to the orbital energy of

the binary acting to remove the envelope (e.g., Ivanova et al. 2013; Nandez & Ivanova 2016) or that some of the envelope material remains bound to the stellar core after the successful ejection of the CE (e.g., Fragos et al. 2019). These variations are assumed to affect only the `CE` channel, since the other field channels by definition do not proceed through late phases of unstable mass transfer and BBHs from dynamical channels are typically assembled after BHs form from isolated progenitor stars. The value of $\alpha_{\rm CE}$ in the `CE` channel impacts the resultant spin distribution significantly, since tighter post-CE binaries (lower $\alpha_{\rm CE}$) lead to more efficient tidal spin-up of the second-born BH.

We use a four-dimensional parameter distribution of the source-frame chirp mass $\mathcal{M}_{\rm c}$, mass ratio $q = m_2/m_1$, effective inspiral spin $\chi_{\rm eff}$, and merger redshift z in constructing the likelihoods of our population models given the GW observations. Marginalized detection-weighted distributions for our population models are shown in Figure 1. From these distributions, a variety of features from our population models can be seen. In the chirp mass and mass ratio distributions, varying assumptions for $\chi_{\rm b}$ primarily affect dynamical channels (`GC` and `NSC`); increasing $\chi_{\rm b}$ suppresses the high-mass bump in the chirp mass distribution and the asymmetric peak near $q \sim 0.5$, which are populated by hierarchical merger events that require lower recoil kicks and therefore lower component spins in the first-generation population. The asymmetric peak and high-mass bump are more pronounced in the `NSC` population than in the `GC` population since the potential well is deeper and merger products are more readily retained in the cluster. All formation channels show diversity in the $\chi_{\rm eff}$ distributions with varying $\chi_{\rm b}$. As $\chi_{\rm b}$ increases, we see broader distributions for $\chi_{\rm eff}$ in the `GC` and `NSC` models coming from their isotropically oriented spins. The `CE` and `SMT` channels are strongly peaked at the prescribed value of $\chi_{\rm b}$, with tails extending to higher $\chi_{\rm eff}$ in the `CE` channel due to systems that proceed through efficient tidal spin-up. The `CHE` channel typically has component spins greater than $\chi_{\rm b}$ and is therefore only affected in our most extreme spin scenario ($\chi_{\rm b} = 0.5$). The redshift distributions peak at slightly larger values and broaden with increasing $\chi_{\rm b}$ for the `CE` and `SMT` channels since higher aligned spins spend more time in-band and are preferentially detected.

3. POPULATION INFERENCE

Given our astrophysical models, we now establish how we place constraints on branching fractions and physical prescriptions using the current catalog of BBH observations. We use posterior and prior samples from the GWTC-1 (Abbott et al. 2019a) and GWTC-2 (Abbott et al. 2020b) analyses, publicly available from the Gravitational Wave Open Science Center (Abbott et al. 2019c). For GWTC-1 and GWTC-2, we use the `Combined` and `PublicationSamples` posterior samples, respectively, which combine posterior samples from different waveform approximants to marginalize over uncertainties in waveform modeling (Abbott et al. 2016b). The choice of prior on the event parameters is irrelevant since they are divided out during the inference. The detection probabilities for each sample in our populations are calculated assuming a detector network consisting of LIGO Hanford, LIGO Livingston, and Virgo operating at `midhighlatelow` sensitivity (Abbott et al. 2018) and assuming a network signal-to-noise ratio (SNR) threshold of $\rho_{\rm thresh} = 10$ (see Appendix B); these detection probabilities are used to construct the detection-weighted distributions in Figure 1. We only consider high-confidence GW events that are definite mergers of two BHs, thus excluding GW170817 (Abbott et al. 2017), GW190425 (Abbott et al. 2020a), GW190426 (Abbott et al. 2020b), and GW190814 (Abbott et al. 2020d). We also exclude GW190521 (Abbott et al. 2020e) from our analysis as it has vanishing support across our models and picks up on minute fluctuations in the kernel density estimates (KDEs) for certain population models. This event is either not explainable by our set of channels or requires updated physical prescriptions for our set of channels. For each event, we randomly draw 10^2 samples from its posterior distribution to evaluate in the population model KDEs, which are parameterized by $\chi_{\rm b}$, $\alpha_{\rm CE}$, and the formation channel. We provide additional details for our KDE generation in Appendix C.

We perform hierarchical modeling to place constraints on the parameters influencing our population models using a methodology similar to that of Zevin et al. (2017). Since we are only interested in the shape of the populations and not in the merger rate, we implicitly marginalize over the expected number of detections (e.g., Fishbach et al. 2018). The hyperparameters we wish to infer are the underlying branching fractions, $\vec{\beta} = [\beta_{\texttt{CE}}, \beta_{\texttt{CHE}}, \beta_{\texttt{GC}}, \beta_{\texttt{NSC}}, \beta_{\texttt{SMT}}]$, and the physical prescriptions assumed in each model, $\vec{\lambda} = [\chi_{\rm b}, \alpha_{\rm CE}]$. We assume an uninformative prior across $\vec{\beta}$, given by a Dirichlet distribution with equal concentration parameters and dimensions equal to the number of formation channels, and impose the constraints $(0 \leq \beta_i \leq 1)\,\forall\, i$ and $\sum_i \beta_i = 1$. Alternatively, this prior could be proportional to the predicted local merger rates for these channels; however, given the large uncertainties in the predicted merger rates we choose an uninformative prior

for this work. We assume a uniform prior across the physical prescription parameters $\vec{\lambda}$.[1] Since the $\chi_{\rm b}$ and $\alpha_{\rm CE}$ models are not mixed across formation channels (i.e. the `CE` channel cannot have $\chi_{\rm b} = 0.0$, while the `GC` channel has $\chi_{\rm b} = 0.1$), this results in $N_{\rm channel} + 1$ hyperparameters in our modeling: two physical prescriptions and $(N_{\rm channel} - 1)$ branching fractions, since one branching fraction is inferred given the constraint that the branching fractions sum to unity.

Given our model hyperparameters $\vec{\Lambda} = [\vec{\lambda}, \vec{\beta}]$ and the posterior samples of our event parameters $\vec{\theta} = [\mathcal{M}_{\rm c}, q, \chi_{\rm eff}, z]$, our hyperlikelihood $p(\vec{\theta}|\vec{\Lambda})$ is given by a mixture model of channels:

$$p(\vec{\theta}|\vec{\Lambda}) = \sum_j \beta_j p(\vec{\theta}|\mu_j^{\chi,\alpha}), \tag{1}$$

where $\mu_j^{\chi,\alpha}$ is the (underlying) population model associated with β_j, parameterized by a particular natal spin magnitude and CE efficiency. Using the discrete posterior samples for each event, the likelihood of the observed GW data $\mathbf{x} = \{\vec{x}_i\}_i^{N_{\rm obs}}$ given our model hyperparameters is

$$p(\mathbf{x}|\vec{\Lambda}) \propto \prod_{i=1}^{N_{\rm obs}} \frac{1}{S_i \tilde{\xi}^{\chi,\alpha}} \sum_j \beta_j \sum_{k=1}^{S_i} \frac{p(\vec{\theta}_i^k|\mu_j^{\chi,\alpha})}{\pi(\vec{\theta}_i^k)}, \tag{2}$$

where $N_{\rm obs}$ is the number of GW events, S_i denotes the posterior samples used for event i, $\pi(\vec{\theta}_k)$ is the prior weight for each posterior sample in the LVC analysis, and $\tilde{\xi}^{\chi,\alpha} \equiv \sum_j \beta_j \int P_{\rm det}(\vec{\theta}) p(\vec{\theta}|\mu_j^{\chi,\alpha})\, {\rm d}\vec{\theta}$ is the detection efficiency of each hypermodel (e.g., Mandel et al. 2019; Vitale et al. 2020). The hyperposterior is thus given by

$$p(\vec{\Lambda}|\mathbf{x}) = p(\mathbf{x}|\vec{\Lambda})\pi(\vec{\Lambda}), \tag{3}$$

where $\pi(\vec{\Lambda})$ is the prior on our hyperparameters.

In practice, the likelihood of Eq. (2) is evaluated by first moving in the (discrete) physical prescription parameter $\vec{\lambda}$ space, then moving in the (continuous) branching fraction $\vec{\beta}$ space, and evaluating if the jump proposal is accepted. Thus, Eq. (2) consists of evaluations from a mixture model of the underlying population KDEs for the given values of $\chi_{\rm b}$, $\alpha_{\rm CE}$, and $\vec{\beta}$ at a particular step in the sampler. We use the ensemble sampler from `emcee` (Foreman-Mackey et al. 2013) to sample this distribution, and perform 10^2 realizations of this inference with different random samplings from the event posteriors, creating a combined posterior distribution across these realizations. Further details can be found in Appendix D, and results from a mock injection study using this methodology can be found in Appendix E.

[1] In practice, we use a continuous dummy parameter to evaluate the discrete model space — see Appendix D.

4. APPLICATION TO GWTC-2

4.1. *Two-channel example*

We first consider a simplified picture to build intuition for the full analysis, assuming that the BBH population comes from only the `CE` and `GC` channels. The posterior distributions for the underlying branching fractions β are shown in Figure 2, with colored lines showing the contribution of various $\chi_{\rm b}$ models to the full posteriors for $\vec{\beta}$. In this simplified case, we already see some notable features. The Bayes factors $\mathcal{B}$ between models are given by the number of samples in one physical prescription model compared to another (i.e. the relative area under the colored curves in the top panels of Figure 2). We find a preference for our smallest natal spin model ($\chi_{\rm b} = 0.0$) relative to the higher $\chi_{\rm b}$ models considered. Compared to the highest natal spin model ($\chi_{\rm b} = 0.5$), the $\chi_{\rm b} = 0.0$ model is preferred by a Bayes factor of $\mathcal{B}^{\chi_{\rm b}=0.0}_{\chi_{\rm b}=0.5} \simeq 40$. However, once natal spin magnitudes are decreased to lower values, the preference becomes more marginal, $\mathcal{B}^{\chi_{\rm b}=0.0}_{\chi_{\rm b}=0.2} \simeq 7$ and $\mathcal{B}^{\chi_{\rm b}=0.0}_{\chi_{\rm b}=0.1} \simeq 4$, respectively. This is consistent with the population analysis associated with GWTC-2, which pushes to low component spins for the BBH population (Abbott et al. 2020c).

When marginalizing over all values of $\chi_{\rm b}$ and $\alpha_{\rm CE}$, the median and symmetric 90% credible interval of the posterior distributions for $\beta_{\texttt{CE}}$ and $\beta_{\texttt{GC}}$ are $0.89^{+0.07}_{-0.22}$ and $0.11^{+0.22}_{-0.07}$, respectively. The branching fractions are sensitive to the value of $\chi_{\rm b}$; we find a significant increase (decrease) in $\beta_{\texttt{GC}}$ ($\beta_{\texttt{CE}}$) for models with $\chi_{\rm b} \geq 0.1$. If we take our most extreme natal spin model, $\chi_{\rm b} = 0.5$, the inferred branching fractions reverse: $\beta_{\texttt{CE}} = 0.26^{+0.38}_{-0.23}$ and $\beta_{\texttt{GC}} = 0.74^{+0.23}_{-0.38}$. However, this model is strongly disfavored by the data. In the bottom panel of Figure 2, we also gauge the preference for a mixture of channels in the underlying population by evaluating the posterior distribution for $\beta_{\rm max}$, defined as the largest value of β across all channels. We find $\beta_{\rm max} \lesssim 0.95$ (0.97) at the 90% (99%) credible level when all spin models are considered. For this simplified case, if natal spins for BHs born in isolation are low, which is favored by the data, the `CE` channel dominates the underlying BBH population, though some contribution from the `GC` channel is still necessary. These results are for the underlying population of BBHs; we discuss the conversion to the detectable population in the following section.

4.2. *Five-channel analysis*

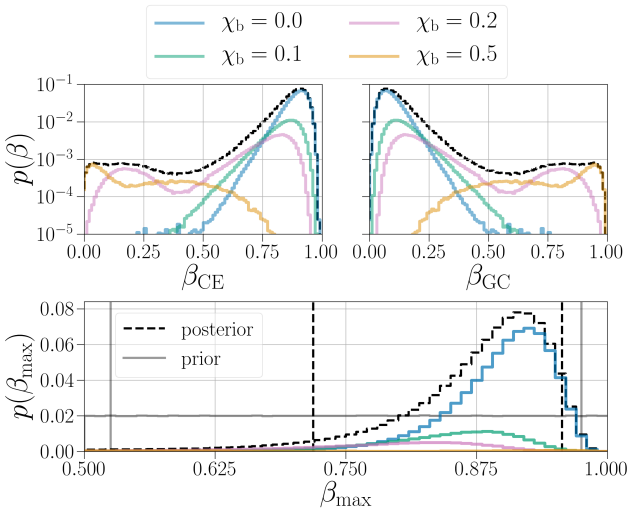

Figure 2. *Top row*: Branching fractions between `CE` and `GC` channels, under the assumption that only these two channels contribute to the BBH catalog. Black dashed lines show the posterior on the detected branching fractions β, marginalized over the χ_b and α_{CE} models. Colored lines show the contributions to the full β posterior from various χ_b models. *Bottom row*: Posterior distribution on $\beta_{max} = \max(\vec{\beta})$. The gray line shows the prior distribution for β_{max}; vertical lines mark the symmetric 90% credible interval for the fully marginalized posterior and prior distributions.

We now perform the same analysis but using all of our five formation models. In this case, we also consider the branching fractions for the detectable population $\vec{\beta}^{\rm det}$ which encodes the breakdown of formation channels to the population detected by LIGO–Virgo. To transform to such *detectable* branching fractions, we rescale the recovered underlying branching fractions by the detection efficiency of each population model, $\xi_j^{\chi,\alpha} = \int P_{\rm det}(\vec{\theta}) p(\vec{\theta}|\mu_j^{\chi,\alpha})\, {\rm d}\vec{\theta}$:

$$\vec{\beta}^{\rm det} = \left[\frac{\vec{\beta}\odot\vec{\xi}}{\tilde{\xi}}\right]_{\chi,\alpha}, \tag{4}$$

where $\vec{\xi}$ is a vector of detection efficiencies for all formation models j given a particular submodel χ, α and $\vec{\beta}\odot\vec{\xi}$ is the element-wise product of $\vec{\beta}$ and $\vec{\xi}$ for samples in the submodel χ, α. The posterior distributions for the underlying and detectable branching fractions are shown in Figures 3 and 4, respectively, with the top row breaking down the contribution from the various χ_b models and the bottom row breaking down the contribution from the various α_{CE} models.

Even when considering all five channels, the underlying populations may be dominated by the `CE` channel, though there is significant support for lower values of $\beta_{\texttt{CE}}$ and a non-negligible contribution from the other channels (see Figure 3). The median and 90% credible interval for the underlying branching fraction posteriors $\vec{\beta} = [\beta_{\texttt{CE}}, \beta_{\texttt{CHE}}, \beta_{\texttt{GC}}, \beta_{\texttt{NSC}}, \beta_{\texttt{SMT}}]$ are $[0.708^{+0.193}_{-0.604},\ 0.023^{+0.058}_{-0.018},\ 0.114^{+0.298}_{-0.091},\ 0.024^{+0.105}_{-0.021},\ 0.100^{+0.365}_{-0.090}]$. These correspond to relative measurement uncertainties on the underlying branching fractions of $\sim$ 80%–430% (90% credibility). Though most of the distributions are broad, the `CE` channel has the least support at $\beta = 0$; at least 2.4% of the underlying population is from the `CE` channel at 99% credibility.

As expected, we also find notably different inferred branching fractions and model preferences between the two-channel case and the five-channel case. For example, as compared to that in the two-channel analysis, in the five-channel analysis the median branching fraction for the `CE` channel decreases by 21% while the median branching fraction for the `GC` channel increases by 5%, and the $\chi_b = 0.1$ model is increasingly favored by a factor of $\mathcal{B}^{5-\rm channel}_{\chi_b=0.1}/\mathcal{B}^{2-\rm channel}_{\chi_b=0.1} \simeq 2.2$.

In certain formation channels, we see the branching fractions converge to different values when different physical prescriptions are assumed. The branching fractions for dynamical (isolated) channels push to larger (smaller) values with increasing χ_b; moving from $\chi_b = 0.0$ to $\chi_b = 0.5$ leads to an increase in the median recovered branching fraction of 0.51 for the `GC` channel. This is due to the effective inspiral spin distribution for the BBHs in the LVC catalog, which is near-symmetric about zero although slightly skewed toward positive values (Abbott et al. 2020c). As natal spins increase, the isotropic spin orientations in dynamical environments lead to broader and symmetric effective inspiral spin distributions, whereas the relatively aligned spins from isolated evolution channels lead to a strong peak in the effective inspiral spin distributions at positive values (see Figure 1). Thus, under the assumption of nonzero natal spins, the inferred relative branching fraction between channels will change, increasing the relative contribution from dynamical formation channels. Systematic shifts in the inferred branching fractions are also apparent for variations in the CE efficiency; for the `CE` channel, changing α_{CE} by an order of magnitude from 0.2 to 2.0 increases the median $\beta_{\texttt{CE}}$ by 0.63.

The posterior distributions on detectable branching fractions are shown in Figure 4. The median and 90% credible interval for the detectable branching fraction posteriors $\vec{\beta}^{\rm det} = [\beta^{\rm det}_{\texttt{CE}}, \beta^{\rm det}_{\texttt{CHE}}, \beta^{\rm det}_{\texttt{GC}}, \beta^{\rm det}_{\texttt{NSC}}, \beta^{\rm det}_{\texttt{SMT}}]$ are $[0.08^{+0.18}_{-0.07},\ 0.11^{+0.12}_{-0.08},\ 0.30^{+0.26}_{-0.22},\ 0.19^{+0.26}_{-0.16},\ 0.26^{+0.27}_{-0.24}]$. The detectable branching fractions for all channels other than `CE` increase relative to the underlying branching fractions, since the `CE` channel typically produces BBHs

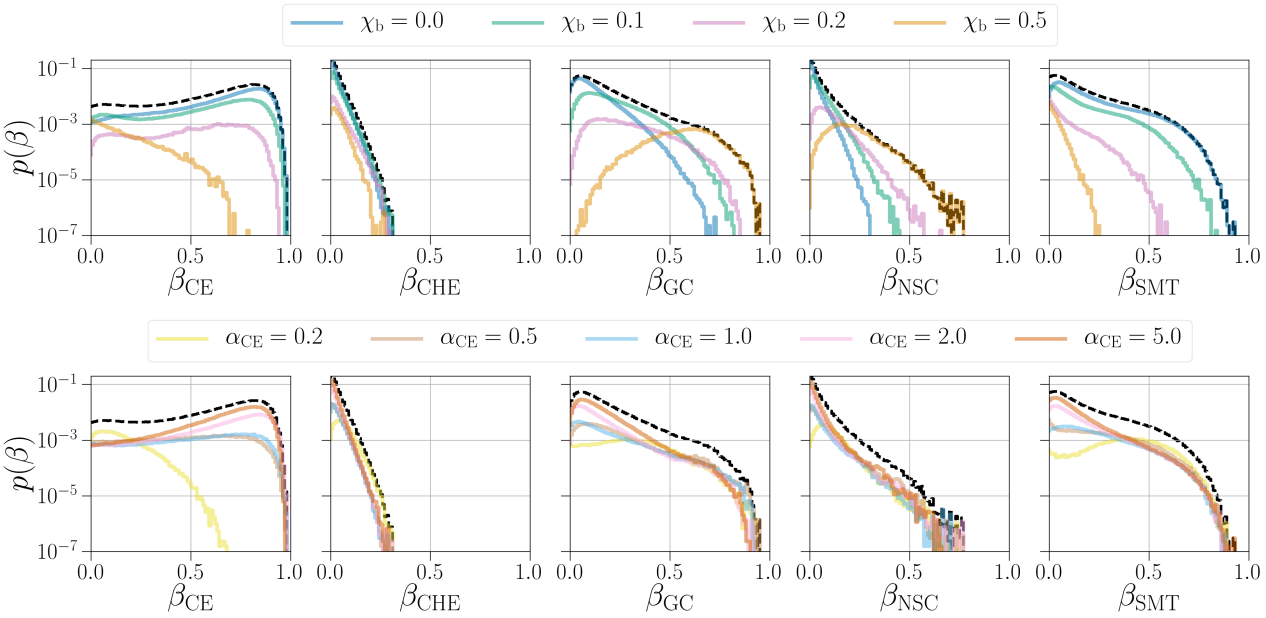

Figure 3. Branching fractions for all five channels inferred using the GWTC-2 BBHs. Colored lines show the contributions from various χ_b models marginalized over α_{CE} models (*top row*), and various α_{CE} models marginalized over χ_b models (*bottom row*). Black dashed lines show the full posterior on the branching fractions, marginalized over both χ_b and α_{CE} models.

with lower masses. This is due to the mass spectrum of these channels pushing to larger values, particularly for the favored $\chi_b = 0$ model, which leads to an increase in their detection efficiency. Given our astrophysical models, the `GC` channel contributes to the bulk of the detected population, making up $> 2.6\%$ of the observed population at 99% credibility. The most significant increases when converting to detectable branching fractions are in the channels whose mass spectra push to the largest values; given our set of formation models, the median detectable branching fraction for the `NSC` channel is almost an order of magnitude larger than the median underlying branching fraction.

Once again, the detectable branching fraction for isolated channels rises with decreasing natal spin magnitude. For example, the median value for $\beta^{\rm det}_{\tt SMT}$ increases by 24% when considering the $\chi_b = 0.0$ model relative to the fully marginalized models.

To further gauge whether a single channel or multiple channels are favored by the BBH population, we again show the posterior distribution on $\beta_{\rm max}$ in Figure 5, now with all five formation channels included. In this higher-dimensional case, the prior on $\beta_{\rm max}$ has a more complicated morphology; the prior volume near $\beta = 1$ for any one channel drops precipitously. However, we still see that the posterior on $\beta_{\rm max}$ significantly deviates from the prior, pushing to larger values of $\beta_{\rm max}$ and favoring one channel dominating the underlying population. For the underlying branching fractions, we find that $\beta_{\rm max}$ is constrained to be below 0.88 (0.93) at the 90% (99%) credible level, compared to 0.62 (0.79) for the prior. Conversely, we find a mixture of channels contributing to the detected population to be strongly preferred. For the detectable population, $\beta^{\rm det}_{\rm max} < 0.56$ (0.69) at 90% (99%) credibility compared to 0.75 (0.89) for the prior.

Another metric we can consider is the number of channels that dominate the branching fractions. We gauge this by examining the posterior distribution on the number of branching fractions that are simultaneously above a threshold value. Setting the threshold to $\beta = 0.1$ and marginalizing over all χ_b and α_{CE} models, we find that $\simeq 26\%$ of the posterior for the underlying branching fractions supports a single model contributing to more than 10% of the underlying population, and $> 95\%$ of the posterior supports a significant contribution from three or fewer channels. Though our `CE` model is favored, this indicates that there may still be an appreciable contribution from a couple of other formation channels to the underlying BBH population. This picture changes drastically for the detectable population. We find that there is a $> 99.8\%$ probability that more than one channel contributes to at least 10% of the detected population, with the bulk of the posterior support ($\simeq 79\%$) suggesting that three to four channels significantly contribute. Thus, given our astrophysical models, the de-

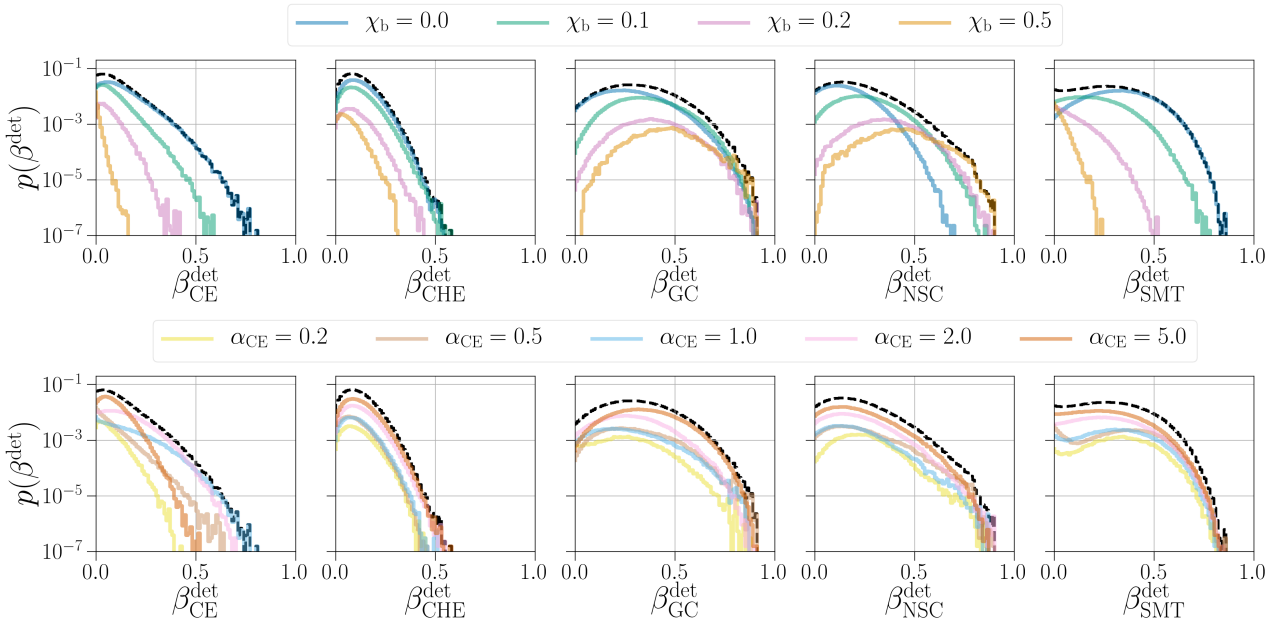

Figure 4. Same as Figure 3, but with detectable branching fractions instead of branching fractions for the underlying population.

tected catalog of BBHs comes from a diverse array of formation scenarios.

The Bayes factors between the physical prescriptions $\vec{\lambda} = [\chi_b, \alpha_{\rm CE}]$ are given in Table 1, analogous to the fully integrated colored curves in Figure 3. As with the two-channel case, we find moderate to strong preference for low natal spins of $\chi_b \lesssim 0.1$ relative to larger natal spins, in agreement with other work investigating natal spin distributions using the catalog of BBH events (Farr et al. 2017b; Abbott et al. 2020c; Kimball et al. 2020b; Miller et al. 2020). Spins of $\chi_b \lesssim 0.1$ are favored relative to models with $\chi_b \gtrsim 0.2$ by a Bayes factor of $\mathcal{B} \simeq 12.9$. The marginal preference for the no-spin $\chi_b = 0.0$ model compared to the low-spin $\chi_b = 0.1$ model ($\mathcal{B}^{\chi_b=0.0}_{\chi_b=0.1} \simeq 1.9$) indicates no strong discriminating power between the two.

We also marginally prefer high CE efficiencies of $\alpha_{\rm CE} \simeq 5.0$, which have Bayes factors of $\mathcal{B} \simeq 5$ relative to the $\alpha_{\rm CE} = 1.0$ model. Values of $\alpha_{\rm CE} = 1.0$ and $\alpha_{\rm CE} = 0.5$ show near-equal preference, and highly inefficient CEs with $\alpha_{\rm CE} = 0.2$ are disfavored relative to the most highly favored model ($\alpha_{\rm CE} = 5.0$) by a Bayes factor of $\gtrsim 10$. Though we use the `CE` and `SMT` models from Bavera et al. (2020a) in this work, we find the opposite results in terms of the inferred CE efficiency. In Bavera et al. (2020a), low CE efficiencies preferentially form more massive BBHs. Since only the `CE` and `SMT` channels are considered in Bavera et al. (2020a), the preference for low CE efficiencies comes from the necessity to produce these more massive systems to match the properties of the events in GWTC-2, whereas in this work such systems can be explained by alternative formation channels. We tested this hypothesis by considering two-channel inference that included only the `CE` and `SMT` channels, and also found a strong preference for CE efficiencies of $\alpha_{\rm CE} \simeq 0.5$, with no samples in the efficient ($\alpha_{\rm CE} > 1.0$) CE models.

Table 1. Bayes factors $\log_{10}(\mathcal{B})$ across χ_b models (columns) and $\alpha_{\rm CE}$ models (rows). Bayes factors are normalized against $\alpha_{\rm CE} = 1.0$ and $\chi_b = 0.0$ in the general case, against $\chi_b = 0.0$ when marginalizing over $\alpha_{\rm CE}$, and against $\alpha_{\rm CE} = 1.0$ when marginalizing over χ_b. The bottom row provides the Bayes factors for χ_b models marginalized over all $\alpha_{\rm CE}$ models, and the rightmost column provides the Bayes factors for $\alpha_{\rm CE}$ models marginalized over all χ_b models.

	χ_b				
	0.0	0.1	0.2	0.5	
0.2	−0.63	−0.56	−1.24	−1.71	−0.35
0.5	−0.06	−0.58	−0.96	−1.11	0.00
$\alpha_{\rm CE}$ 1.0	$\equiv 0$	−0.77	−1.02	−1.29	$\equiv 0$
2.0	0.34	0.05	−1.19	−1.15	0.42
5.0	0.56	0.39	−0.54	−0.87	0.70
	$\equiv 0$	−0.27	−1.11	−1.35	

5. DISCUSSION AND CONCLUSIONS

We analyze the recently bolstered catalog of BBH mergers using a suite of state-of-the-art models for astrophysical formation channels of BBHs. Our main findings are as follows:

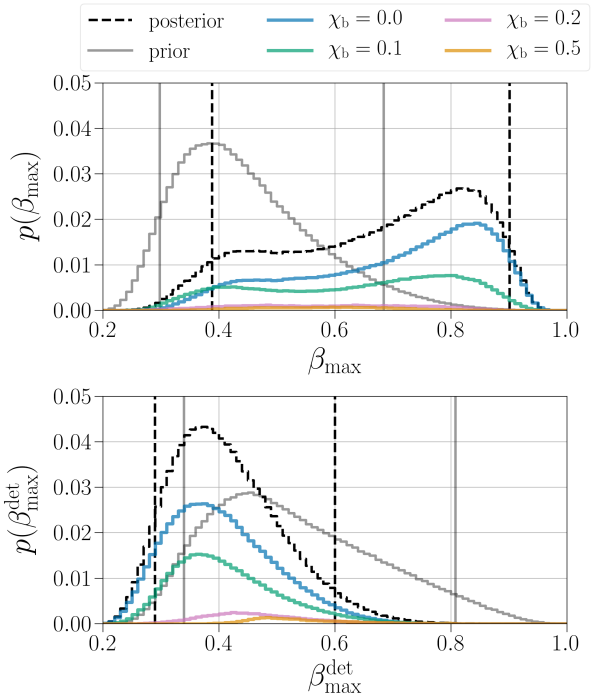

Figure 5. Posterior distribution for the maximum branching fractions of the underlying population $\beta_{\rm max}$ (*top row*) and detectable population $\beta^{\rm det}_{\rm max}$ (*bottom row*) when considering all five formation channel models. The black dashed line shows the fully marginalized posterior distribution, with colored lines showing the contribution to the posterior from the different $\chi_{\rm b}$ models marginalized over all $\alpha_{\rm CE}$ models. We also show the prior distributions for $\beta_{\rm max}$ and $\beta^{\rm det}_{\rm max}$ with gray lines; vertical black dashed lines and gray lines mark the symmetric 90% credible interval for the fully marginalized posterior and prior, respectively. There is a clear difference between the branching ratios in the detectable population and the underlying population. Since higher-mass binaries are more likely to be detected, the subpopulations that contribute to these channels are enhanced, making the detectable population much more diverse.

- Though the CE channel dominates the underlying BBH population in our models, a contribution from various formation channels is preferred over one channel dominating the detected population of BBH mergers. From the formation channels considered in this work, we find that no single channel contributes to more than 70% of the detectable BBH population at 99% credibility, and the probability that three to four channels each contribute to more than 10% of the detected BBH population is 79%.

- Small natal spins ($\chi_{\rm b} \lesssim 0.1$) for BHs born in isolation or without significant tidal influence from a binary partner are favored over larger natal spins ($\chi_{\rm b} \gtrsim 0.2$) by a Bayes factor of $\simeq 12.9$, indicating efficient angular momentum transport in massive stars.

- The CE efficiency, which scales roughly linearly with the post-CE separation, shows marginal preference for larger values ($\alpha_{\rm CE} \simeq 5.0$) relative to $\alpha_{\rm CE} \approx 1.0$ by a Bayes factor of ≈ 5, and stronger preference relative to highly inefficient CEs ($\alpha_{\rm CE} \simeq 0.2$) by a Bayes factor $\gtrsim 10$. This preference for efficient CE ejection may indicate that other energy sources are at play when ejecting CEs rather than solely the orbital energy of the binary (Ivanova et al. 2013).

- When incorrect physical prescriptions are assumed or formation channels contributing to the BBH population are not considered, estimates for the values of branching fractions and variables in physical parameterizations can be significantly biased.

Numerous studies have investigated how populations of compact-object mergers can help inform uncertainties in binary stellar evolution and compact-object formation. This is typically done with either phenomenological models or predictions from population models, though in the case of the latter, usually under the assumption that a single population model is exclusively contributing to the entire population. However, several studies have considered the relative contribution and population properties expected from dynamical channels versus isolated binary evolution (e.g., Rodriguez et al. 2016b; Farr et al. 2017b; Stevenson et al. 2017a; Vitale et al. 2017; Zevin et al. 2017; Bouffanais et al. 2019; Arca Sedda et al. 2020; Safarzadeh et al. 2020; Santoliquido et al. 2020; Wong et al. 2020). For example, when considering BBH mergers formed in isolation or dynamically in young stellar clusters, Bouffanais et al. (2019) found that branching fractions can be constrained to the $\sim$ 10% level with $\mathcal{O}(100)$ detections. With only $\sim$ 50 observations in GWTC-2 and the inclusion of additional formation channels, we see broader constraints on the precise values of branching fractions; investigating the convergence on branching fraction estimates when considering more channels will be investigated in future work. Wong et al. (2020) also analyzed the BBH population from GWTC-2 using models for the GC and CE channels. We find opposite results for the underlying branching fractions when we consider the simplified picture of only the `CE` and `GC` channels (see Figure 2); we find the majority of the underlying population ($\sim 90\%$) comes from the CE channel, whereas Wong et al. (2020) found $\sim 80\%$ of the underlying population comes from the GC channel. However, our detectable distributions

are in better agreement with the branching fractions presented in Wong et al. (2020); incorporating detectability increases the detectable branching fraction of GCs in the two-channel example to $\sim 70\%$. We also find a slight preference for efficient CEs and a stronger preference against highly inefficient CEs ($\alpha_{\rm CE} \simeq 0.2$), whereas the constraints for $\alpha_{\rm CE}$ in Wong et al. (2020) are broad but slightly favor inefficient CEs. The difference in our analyses may be due to our inclusion of spin information, since the CE efficiency has a stronger impact on the spin distributions of the CE channel compared to the mass spectrum. This emphasizes the importance of considering all observational information when constraining models.

Though we consider five distinct BBH formation models in this analysis, we can also investigate the broad two-channel categorization of formation in the galactic field and dynamical assembly in dense stellar environments. In Figure 6, we combine the branching fractions for the field channels (`CE`, `CHE`, `SMT`) against the dynamical channels (`GC`, `NSC`). With low spins ($\chi_{\rm b} \lesssim 0.1$), we find a strong preference for field channels comprising the majority of the underlying distribution. The field channels are dominated by the `CE` channel, which makes up the majority of the underlying population (see Figure 3). Marginalizing over all $\chi_{\rm b}$ and $\alpha_{\rm CE}$ models, we find the underlying branching fractions for the field channels and dynamical channels are $\beta_{\rm field} = 0.86^{+0.11}_{-0.36}$ and $\beta_{\rm dynamical} = 0.14^{+0.36}_{-0.11}$, respectively (90% credibility). The contribution from dynamical channels increases as natal spins increase due to the behavior of the effective inspiral spin distributions, since the effective inspiral spins of the BBH events in GWTC-2 are near-symmetric about zero (Abbott et al. 2020c) and incompatible with a highly spinning, aligned-spin population. At $\chi_{\rm b} = 0.5$, which is disfavored relative to $\chi_{\rm b} = 0$ by a Bayes factor of $\simeq 27$, the underlying branching fractions are $\beta_{\rm field} = 0.18^{+0.27}_{-0.12}$ and $\beta_{\rm dynamical} = 0.82^{+0.12}_{-0.27}$. In the bottom panel of Figure 6, we again use Eq. (4) to convert underlying branching fractions to detectable branching fractions. In the detectable population, the contribution from dynamical channels is amplified. Marginalizing over all $\chi_{\rm b}$ and $\alpha_{\rm CE}$ values, we find the inferred branching fractions of the detected populations to be $\beta^{\rm det}_{\rm field} = 0.50^{+0.25}_{-0.30}$ and $\beta^{\rm det}_{\rm dynamical} = 0.50^{+0.30}_{-0.25}$. Thus, given the formation models considered in this work, dynamical and field channels contribute similar numbers to the detected BBH population.

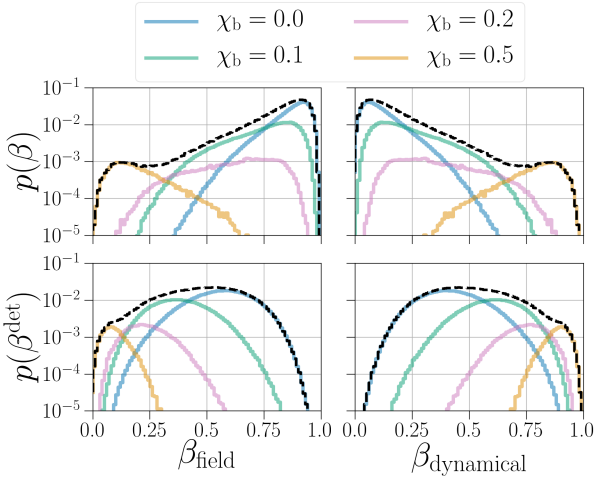

Figure 6. Branching fractions recovered for the combined field and dynamical channels. Colored lines show the contribution to the posterior from the different $\chi_{\rm b}$ models marginalized over all $\alpha_{\rm CE}$ models. In the top row we show the distribution for underlying branching fractions as in Figure 3, and in the bottom row we show the distribution for detectable branching fractions as in Figure 4.

Our analysis favors low natal spins for BHs born in isolation or without significant tidal spin-up. Analyses using phenomenological representations for the spin magnitude distribution show a preference for low spins (Farr et al. 2017b; Abbott et al. 2019b, 2020c; Kimball et al. 2020b; Miller et al. 2020), in agreement with the preference for low natal spins in this work. Low spins in the natal population will increase the rate of hierarchical mergers in dynamical environments (Rodriguez et al. 2019; Banerjee 2021; Fragione & Silk 2020; Fragione & Loeb 2021; Kimball et al. 2020a), pushing the BH mass spectrum to larger values, imparting large spin on the merger products, and accentuating the mass asymmetry of mergers in those populations.

We find a mild preference for efficient CEs in our modeling, which strongly disfavors highly inefficient CEs with $\alpha_{\rm CE} \simeq 0.2$. Inferred values for the CE efficiency $\alpha_{\rm CE}$ have more diversity than natal spins across the literature, from population modeling (e.g., Bavera et al. 2020a; Santoliquido et al. 2021; Zevin et al. 2020) to hydrodynamical simulations (e.g., Fragos et al. 2019) and theoretical considerations (e.g., Ivanova et al. 2013). Our results, which mildly favor high CE efficiencies, are in agreement with Santoliquido et al. (2021), who found high CE efficiencies are necessary to match the merger rate of binary neutron stars in their population models, and with Fragos et al. (2019), who modeled the spiral-in phase of CE evolution using hydrodynamic simulations and found a non-negligible fraction of the envelope remains bound to the core after the CE is successfully ejected. These results for $\alpha_{\rm CE}$ contrast with those from Bavera et al. (2020a), but we find that these conflicting results arise only from the consideration of more forma-

tion channels in this work; when considering contributions from only the `CE` and `SMT` channels, we also favor low CE efficiencies of $\alpha_{\rm CE} \simeq 0.5$. We also find similar detectable branching fractions for the `CE` and `SMT` channels, in agreement with Bavera et al. (2020a) who found the channels have comparable BBH detection rates in the local universe.

We have shown multiple times that failing to account for the broad array of formation channels or assuming incorrect physical prescriptions can severely bias inferences. For example, when only considering the `CE` and `SMT` channels in our inference, we find a preference for low CE efficiencies compared to the preference for high CE efficiencies when considering all five channels. When considering only the `CE` and `GC` channels, the recovered branching fractions differ significantly compared to when we consider all five channels (see Figures 2 and 3). Even when including our full array of formation channels, differing assumptions for physical prescriptions alter the recovered branching fractions (see Section 4.2).

While we consider more formation channels in this analysis than has been done before, the astrophysical models used in this work only comprise a subset of the proposed formation channels for BBHs,[2] and each channel is subject to a number of additional theoretical uncertainties that are not accounted for in this work. Therefore, as with any such model selection endeavor that is reliant on population modeling predictions, there are a number of inherent caveats associated with assumptions made for uncertain physical prescriptions. A few examples of such caveats are as follows: (a) since a massive-star binary in a CE phase has never been observed, the modeling of this phase is entirely theoretical, and the α–λ energy balance formalism with a fixed CE efficiency $\alpha_{\rm CE}$ across all stellar regimes may not be valid; (b) BH natal kick magnitudes and orientations relative to the spin axis of the exploding star are uncertain due to the limited observational sample of BH binaries with well-measured proper motions, and choosing a natal kick prescription other than the standard bimodal Maxwellian distribution with fallback-modulated kicks can affect both population properties and rates; (c) using a fixed natal spin for isolated BHs, which is a proxy for the efficiency of angular momentum transport, may instead be better described by a distribution of natal spins dependent on the properties of the collapsing star; and (d) in clusters, changes in the assumed binarity of the primordial population, cluster rotation, triaxiality, and the dynamical effect that would be caused by the presence of a massive BH may all have an impact on the properties of BBH mergers. This list of caveats is not exhaustive, but it provides a sense of the complexity of this model selection problem, especially when considering contributions from multiple formation scenarios that have both shared and independent physical uncertainties. Though our quantitative results may change with the inclusion of additional formation models or updated prescriptions for binary stellar evolution and compact-object formation, given the diversity of BBH detections to date we anticipate that the necessity for multiple channels significantly contributing to the detected BBH population is robust. Since the local BBH merger rate continues to become more constrained as the catalog of BBHs grows, predicted merger rates will also be crucial to include in these types of analyses and can be incorporated into branching fraction priors.

As statistical uncertainties get smaller, systematics become more important (Barrett et al. 2018), and failing to consider a more complete and comprehensive picture for the diversity of possible BBH formation channels will become increasingly dangerous. As the detected population of BBHs grows, our methodology can be expanded to include additional formation channels and uncertain physical prescriptions, which will lead to a more unbiased and complete understanding of the relative contribution from various astrophysical channels to the observed population of compact binary mergers. Only through these comprehensive analyses will we be able to accurately infer crucial aspects of BBH origins.

The population models and posterior samples from the hierarchical inference in this work are available on Zenodo (Zevin 2020). The codebase developed for this analysis, Astrophysical Model Analysis and Evidence Evaluation (`AMAZE`), is available on Github[3] along with notebooks for generating the numbers and figures in this paper.

[2] We welcome additional models that could be included in this framework.

[3] https://github.com/michaelzevin/model_selection

ACKNOWLEDGMENTS

The authors would like to thank Tom Callister and Maya Fishbach for their useful suggestions and to acknowledge the thoughtful comments from the anonymous referees, which helped improve this paper. Support for this work and for M.Z. was provided by NASA through the NASA Hubble Fellowship grant HST-HF2-51474.001-A awarded by the Space Telescope Science Institute, which is operated by the Association of Universities for Research in Astronomy, Inc., for NASA, under contract NAS5-26555. S.S.B. and T.F. are supported by a Swiss National Science Foundation professorship grant (project No. PP00P2 176868). This project has received funding from the European Union's Horizon 2020 research and innovation program under the Marie Sklodowska-Curie RISE action, grant agreement No. 691164 (ASTROSTAT). C.P.L.B. is supported by the CIERA Board of Visitors Research Professorship and National Science Foundation (NSF) grant PHY-1912648. V.K. is supported by a CIFAR G+EU Senior Fellowship and Northwestern University. P.M. acknowledges support from the FWO junior postdoctoral fellowship No. 12ZY520N. F.A. acknowledges support from a Rutherford fellowship (ST/P00492X/1) from the Science and Technology Facilities Council. D.E.H. was supported by NSF grants PHY-1708081 and PHY-2011997, the Kavli Institute for Cosmological Physics at the University of Chicago, and an endowment from the Kavli Foundation and also gratefully acknowledges a Marion and Stuart Rice Award. This work used computing resources at CIERA funded by NSF grant No. PHY-1726951 and resources and staff provided by the Quest high-performance computing facility at Northwestern University, which is jointly supported by the Office of the Provost, the Office for Research, and Northwestern University Information Technology. This document has been assigned LIGO document No. LIGO-P2000468.

Software: `Astropy` (Robitaille et al. 2013; Price-Whelan et al. 2018); `emcee` (Foreman-Mackey et al. 2013); `iPython` (Pérez & Granger 2007); `Matplotlib` (Hunter 2007); `NumPy` (Oliphant 2006; Van Der Walt et al. 2011); `Pandas` (McKinney 2010); `PyCBC` (Nitz et al. 2019); `SciPy` (Virtanen et al. 2020); `AMA`$\mathcal{Z}$`E` (this work).

APPENDIX

A. POPULATION MODELS

In this section, we provide further details for the population modeling in this work. In Appendix A.1, we discuss the formation channels used in our inference and the assumptions that were made to provide more self-consistency between models. In Appendix A.2, we discuss the distribution of systems across cosmic time for our five formation channels, as well as the assumed distribution of metallicities as a function of redshift.

A.1. *Formation Channels*

A.1.1. *Isolated Evolution through CE and Stable Mass Transfer*

The `CE` and `SMT` models are simulated with the `POSYDON` framework (T. Fragos et al. 2021, in preparation), which was used to combine the rapid population synthesis code `COSMIC` (Breivik et al. 2020) with `MESA` detailed binary evolution calculations (Paxton et al. 2011, 2013, 2015, 2018, 2019) as in Bavera et al. (2020a). `COSMIC` was used to rapidly evolve binaries from the zero-age main sequence until the end of the second mass-transfer episode. For the last phase of the binary evolution (BH–Wolf–Rayet), which determines the second-born BH spin (Qin et al. 2018; Bavera et al. 2020b), we used detailed stellar and binary simulations from `MESA`. These simulations take into account differential stellar rotation, tidal interaction, stellar winds, and the evolution of the Wolf–Rayet stellar structure, therefore allowing us to carefully model the tidal spin-up phase until the core collapse of the secondary.

These models assume the first-born BH is formed with a negligible spin $\chi_{\rm b} \simeq 0$ because of the assumed efficient angular momentum transport (Qin et al. 2018; Fuller & Ma 2019) and the Eddington-limited accretion efficiency onto compact objects; this also leads to small first-born BH spins for the `SMT` channel because the mass accreted onto BHs during the second mass- transfer is negligible (Thorne 1974). In this work we artificially varied the first assumption by changing the birth spins in post-processing. Assumptions for the efficiency of accretion onto BHs may affect the natal spins of the first-born BH in the `SMT` channel if it is highly super-Eddington, though Bavera et al. (2020a) showed that a highly super-Eddington accretion efficiency leads to the extinction of BBH mergers in the `SMT` channel and thus we do not consider variations in its value.

These simulations were designed as much as possible to match the same stellar and binary physical assumptions made in the `CHE` models; in fact, the `MESA` model is entirely self-consistent with that used in du Buisson et al. (2020). Consistency in the initial binary distributions was also a priority. For example, we assumed that log-initial orbital period distributions follow a Sana et al. (2012) power law in the range $[10^{0.15}, 10^{5.5}]$ days and extend down to 0.4 days assuming a flat-in-log distribution in order to sample the parameter space leading to a chemically homogeneous evolution (du Buisson et al. 2020). Finally, analogous to the `CHE` and `NSC` models, we used the same prescriptions for distributing the synthetic BBH populations across cosmic history (see Appendix A.2). To translate the underlying BBH population to the detected population in all channels, Bavera et al. (2020a) assumed the detection probabilities detailed in Appendix B but with a higher network SNR threshold of $\rho_{\rm thresh} = 12$. The estimated rate densities for the `CE` channel are in the range 17–113 $\mathrm{Gpc^{-3}\,yr^{-1}}$ depending on $\alpha_{\rm CE}$ (the smallest value corresponds to the model with $\alpha_{\rm CE} = 5.0$, while the largest value corresponds to $\alpha_{\rm CE} = 0.2$), and 25 $\mathrm{Gpc^{-3}\,yr^{-1}}$ for the `SMT` channel (Bavera et al. 2020a). For a detector network with `midhighlatelow` sensitivity and a network detection threshold of $\rho_{\rm thresh} = 12$, these values translate to a detection rate of 15–412 $\mathrm{yr^{-1}}$ and 86 $\mathrm{yr^{-1}}$ for `CE` and `SMT`, respectively.

A.1.2. *Chemically Homogeneous Evolution*

The `CHE` models are adopted from du Buisson et al. (2020) who computed a large grid of detailed `MESA` stellar and binary simulations undergoing this evolutionary process. For consistency with the other models, we restrict primary masses to the range $[0.01, 150]\,\mathrm{M_\odot}$, meaning that, compared to the original study, we ignore systems forming BBHs with components above the pair instability mass gap (e.g., Woosley 2017; Farmer et al. 2019; Marchant et al. 2019). The core collapse of the stars' profiles is done self-consistently in `CE` and `SMT` models using `POSYDON` (see Appendix D of Bavera et al. 2020a). The applied prescription takes into account disk formation during the collapse of highly spinning stars, mass loss through neutrinos, (pulsational) pair instability supernovae according to the fits of the detailed simulation of Marchant et al. (2019), and two Blaauw kicks (Blaauw 1961; Kalogera 1996) where we assume circularization after the first supernova (see du Buisson et al. 2020). The synthetic population of BBHs is distributed across the Universe cosmic history assuming the same initial binary distributions as in the `CE` and `SMT` models.

Since we have a regular grid of MESA simulations covering the initial binary distributions instead of sampling them with a Monte Carlo approach, we can directly calculate their phase space volume. Given a binary k with initial primary mass $m_{1,k}$, mass ratio q_k, and period p_k, the relative contribution of that system to the total population P_k is

$$P_k \equiv p(m_{1,k}, q_k, p_k) = p_{\rm IMF}(m_{1,k}, q_k, p_k) \times p_{\rm IQF}(m_{1,k}, q_k, p_k) \times p_{\rm IPF}(m_{1,k}, q_k, p_k), \tag{A1}$$

where IMF, IQF, and IPF designate the initial mass, mass ratio, and period functions. These probabilities are obtained by integrating the assumed initial distribution probability densities independently; for simplicity, we assume that the initial binary properties are independent of each other and of metallicity. For the initial mass function, we assume a Kroupa (2001) power law in the range $[0.01, 150]\,{\rm M}_\odot$; for the initial mass ratios, we assume a flat distribution in the range $[0, 1]$; and for the initial periods, we assume an extended Sana et al. (2012) log-power law as in Eq. (A.1) of Bavera et al. (2020a). For each binary the integration is performed around the initial values $m_{1,k}$, q_k, and p_k assuming a volume corresponding to the grid's resolution, namely, $\Delta \log_{10}(m_{1,k}/M_\odot) = 0.025$, $\Delta q_k = 0.2$, and $\Delta(p_k/{\rm day}) = 0.025$. Even though the simulations for the CHE channel were carried out at a fixed mass ratio value of $q = 1$, here we assume that they are representative of resultant BBH mass ratios within $[0.8, 1]$, and artificially smear the BBH mass ratios uniformly across this range while keeping the total mass of the binary fixed. This assumption is justified by the findings of Marchant et al. (2016).

Similar to Eq. (7) of Bavera et al. (2020a), the BBH merger rate density is calculated in finite-time bins of $\Delta t_i = 100$ Myr and log-metallicity bins ΔZ_j where each binary k is placed at the center of each time bin corresponding to the redshift of formation $z_{{\rm f},i}$ and merging at $z_{{\rm m},i,k}$. Therefore,

$$R_{\rm BBHs}(z_i) = \sum_{\Delta Z_j} \sum_k P_{i,j,k}\, f_{\rm bin} \frac{{\rm fSFR}(z_{{\rm f},i})}{\bar{m}_\star} \frac{4\pi c\, D_{\rm c}^2(z_{{\rm m},i,k})}{\Delta V_{\rm c}(z_i)} \Delta t_i \ {\rm Gpc^{-3}\,yr^{-1}}, \tag{A2}$$

where $f_{\rm bin} = 0.7$ (Sana et al. 2012) is the binary fraction, $\bar{m}_\star = 0.518\,M_\odot$ is the average system mass (computed as in Eq. (A.2) of Bavera et al. 2020b), fSFR is the star formation rate (SFR) per metallicity range ΔZ_j, $D_{\rm c}(z)$ is the comoving distance, and $\Delta V_{\rm c}$ is the comoving volume corresponding to Δt_i. Using a network detection threshold of $\rho_{\rm thresh} = 12$, we find a merger rate density of 32.9 ${\rm Gpc^{-3}\,yr^{-1}}$ and a detection rate for a detector network with midhighlatelow sensitivity of 360 ${\rm yr^{-1}}$. The rate found here is higher than the one found by du Buisson et al. (2020), 5.8 ${\rm Gpc^{-3}\,yr^{-1}}$, for two reasons: (i) The original study assumed a flat-in-log orbital period distribution over the range $[0.4, 365.25]$ days compared to the extended log-power law assumed here for consistency with the CE and SMT channels; when we assume the original distribution over the range $[0.4, 10^{5.5}]$ days, the rate density decreases to 10.6 ${\rm Gpc^{-3}\,yr^{-1}}$. (ii) du Buisson et al. (2020) assumed an SFR and metallicity distribution from the cosmological simulations of Taylor & Kobayashi (2015), which predicts less stellar mass formed at low metallicities compared to Madau & Fragos (2017), assuming the metallicities follow a truncated log-normal distribution around the empirical mean of Madau & Fragos (2017) and a standard deviation of 0.5 dex.

A.1.3. *Globular Clusters*

The GC models are simulated using the Hénon-style cluster Monte Carlo code CMC (Hénon 1971a,b; Joshi et al. 2000; Pattabiraman et al. 2013). CMC has been shown to reproduce both the global cluster properties and the BBH populations found in direct N-body cluster models in a fraction of the time (Rodriguez et al. 2016b). Each cluster model contains all of the necessary physics to describe the dynamical formation of BBHs. Each star and binary in the cluster is evolved with the Binary Stellar Evolution (BSE) package of Hurley et al. (2000, 2002) with updated prescriptions for stellar winds, compact-object masses, supernova natal kicks, and pulsational-pair instability physics consistent with COSMIC (Chatterjee et al. 2010; Rodriguez et al. 2016a, 2018b, and references therein). The three-body interactions between single stars that produce many BBHs are treated probabilistically using prescriptions from Morscher et al. (2013), which have been well tuned to direct N-body integrations. Furthermore, stars and binaries are allowed to interact through strong three- and four-body encounters, whose outcomes are directly integrated with Fewbody (Fregeau & Rasio 2007), a small-N dynamical integrator with relativistic corrections (Antognini et al. 2014; Amaro-Seoane & Chen 2016; Rodriguez et al. 2018b). BBHs that merge inside the cluster, either as isolated systems or due to prompt GW emission during three-body encounters, are given new masses, spins, and GW recoil velocities taken from numerical relativity-based fitting formulae (Rodriguez et al. 2018b, Appendix A).

As the natal spins of BHs are set at the start of the simulations, no post-processing is necessary across our $\chi_{\rm b}$ models. We do not consider differing $\alpha_{\rm CE}$ values in our GC models for two reasons: (i) Most BBHs that go on to merge

are processed dynamically and go through partner swaps throughout their evolution in the cluster and do not merge with their original partner; thus the post-CE separation has a minimal impact on the rates and properties of BBH mergers. (ii) Of the BHs in the cluster originally in a BBH system that formed from a massive-star binary progenitor, we find only a percent-level number that were at tight enough orbital configurations during the BH–Wolf–Rayet phase for tidal spin-up to be relevant. We therefore set the CE efficiency to our fiducial value of $\alpha_{\rm CE} = 1$ in the `GC` model.

The `GC` model is the only model that does not follow the standard star formation and metallicity evolution described in Appendix A.2, since cluster formation does not mimic the star formation history of the host galaxies. We instead follow the prescriptions in Rodriguez & Loeb (2018), which rely on detailed modeling of GC formation across cosmic time (El-Badry et al. 2019), and weight GCs of differing metallicities by the metallicity distribution of GCs observed in the Milky Way (Harris 2010).

A.1.4. *Nuclear Star Clusters*

The evolution of `NSC` models is determined using the semi-analytical approach of Antonini et al. (2019). In this method, we assume that the energy generated by the BH binaries in the cluster core is regulated by the process of two-body relaxation in the bulk of the system (Breen & Heggie 2013). This principle of balanced evolution (Hénon 1961) is used to compute the hardening and the merger rate of the core binaries. Moreover, we neglect mass loss from stellar evolution and the escape of BHs and stars, i.e. we assume a constant cluster mass (see Antonini & Gieles 2020b for caveats in this assumption). Each BBH formed dynamically in the cluster core is then evolved until it either merges inside the cluster or it is ejected from it. If the merger remnant is retained inside the cluster, we compute its spin and mass using the prescriptions in Rezzolla et al. (2008). We evolve the cluster until either all BHs have been ejected or a time of 13 Gyr has passed.

As with the `GC` model, we do not consider differing $\alpha_{\rm CE}$ values for the `NSC` model and assume the population properties are the same across all values of $\alpha_{\rm CE}$ (see discussion in Appendix A.1.3). In contrast to those in the `GC` model, we assume that star formation and metallicity evolution follow the same prescriptions as the `CE`, `CHE`, and `SMT` models (i.e. they trace the evolution of the host galaxy as a whole). There are arguments that the star formation histories of nuclear clusters are different from those of their galactic hosts (Neumayer et al. 2020). Given the uncertainties, however, we continue with the assumption above and sample from the three metallicity models ($0.01Z_\odot$, $0.1Z_\odot$, and $1Z_\odot$) according to the prescriptions described in Appendix A.2.

A.2. *Formation Rate and Metallicity Evolution*

All formation channels provide raw samples of BBH mergers for a given $\chi_{\rm b}$, $\alpha_{\rm CE}$, and metallicity. For all models other than `GC` (see Appendix A.1.3), we distribute the synthetic BBH populations across cosmic history assuming the SFR density in Madau & Fragos (2017):

$$\psi(z) = 10^{-2} \frac{(1+z)^{2.6}}{1+[(1+z)/3.2]^{6.2}}\, M_\odot\, {\rm yr}^{-1}\, {\rm Mpc}^{-3}. \tag{A3}$$

This determines the birth redshift of the BBH progenitor. For the `CE`, `CHE`, and `SMT` models, the merger redshift is then calculated using the BBH formation time ($t_{\rm birth} - t_{\rm BBH}$) and inspiral time ($t_{\rm insp}$), the latter of which is determined using the orbital properties of the binary following the birth of the second BH (Peters 1964). Thus, the merger redshift is

$$z_{\rm merge} = \mathcal{T}(t_{\rm birth} - t_{\rm BBH} - t_{\rm insp}), \tag{A4}$$

where $\mathcal{T}$ is the transformation function between the lookback time and redshift. For the `NSC` model, delay times ($t_{\rm delay} = t_{\rm BBH} + t_{\rm insp}$) are computed directly from the model and used to determine the merger redshift. For all models, we assume a ΛCDM cosmology with the *Planck 2015* cosmological parameters of $H_0 = 68\ {\rm km\,s^{-1}\,Mpc^{-1}}$, $\Omega_{\rm m} = 0.31$, and $\Omega_\Lambda = 0.69$ (Ade et al. 2016).

Each formation channel model is simulated across a range of metallicities. At a given redshift, metallicities are distributed following a truncated log-normal metallicity distribution around the empirical median metallicity from Madau & Fragos (2017) assuming a standard deviation of 0.5 dex (Bavera et al. 2020a, Section 2.2):

$$\log_{10}\langle Z/Z_\odot\rangle = 0.153 - 0.074 z^{1.34}, \tag{A5}$$

with a solar metallicity of $Z_\odot = 0.017$ (Grevesse & Sauval 1998). We use the SFR density, Eq. (A3), and metallicity distribution, Eq. (A5), to construct a full cosmological population for each submodel of the formation channels (parameterized by $\chi_{\rm b}$ and $\alpha_{\rm CE}$).

B. DETECTION PROBABILITIES

In our inference, detection probabilities are a key component of the detection efficiency ξ in the hyperlikelihood. From the cosmological populations of each channel, we calculate detection probabilities numerically. Though this is more computationally intensive than using analytical scaling relations that approximate the sensitive spacetime volume to leading order (e.g., Fishbach & Holz 2017), we choose to calculate detection probabilities numerically to better capture the influence that total mass, mass ratio, and spins have on selection effects.

Each system is characterized by its (source-frame) component masses, three-dimensional component spin vectors, and merger redshift. For every system in each population model, we first calculate the optimal SNR $\rho_{\rm opt}$ for LIGO Hanford, LIGO Livingston and Virgo operating at `midhighlatelow` sensitivity (Abbott et al. 2018) by assuming the system is directly overhead with a face-on inclination. We use the `IMRPhenomPv2` waveform approximant (Hannam et al. 2014; Khan et al. 2016) for determining SNRs, and detector response functions are constructed using the `PyCBC` package (Nitz et al. 2019). We approximate the optimal network SNR as the quadrature sum of the optimal SNRs from the three detectors,

$$\rho_{\rm net,\,opt} \lesssim \sqrt{\sum_i (\rho^2_{\rm i,\,opt})}, \tag{B6}$$

which will give us a conservative overestimate of the true optimal SNR of the network. We choose a network SNR threshold of $\rho_{\rm thresh} = 10$, consistent with the false-alarm-rate threshold of two per year, which is used as a criterion for events in GWTC-2 (Abbott et al. 2018; Nitz et al. 2020; Abbott et al. 2020b). If $\rho_{\rm net,\,opt} < \rho_{\rm thresh}$, we set the detection probability of the system to $\tilde{P}_{\rm det} = 0$. Otherwise, we consider the source potentially detectable and perform 10^3 Monte Carlo realizations of the extrinsic parameters, namely the right ascension, declination, inclination, and polarization angle. The detection probability of the system marginalized over the extrinsic parameters is then given by

$$\tilde{P}_{\rm det} = \frac{1}{N}\sum_{j=1}^{N} \mathcal{H}\left[\sqrt{\sum_i (\rho_i(\psi_j))^2} - \rho_{\rm thresh}\right], \tag{B7}$$

where N is the number of Monte Carlo realizations, i indexes over detectors, ψ_j denotes the extrinsic parameters drawn for the Monte Carlo sample j, and $\mathcal{H}$ is the Heaviside step function. These detection weights are used to construct the weighted KDE models in Figure 1.

C. KDES OF MODELS

We use an adaptation of the `gaussian_kde` class of `SciPy` to construct KDEs for each population model, which are 4-dimensional over the parameters $\vec{\theta}$. Our `gaussian_kde` class handles reflection over physical boundaries in the parameter space (i.e. $0 < q \leq 1$). To ensure an adequate choice of KDE bandwidth for our population models, we perform a holdout analysis where we construct the KDE using a subset of samples from the full population, draw samples from the KDE, and compare the one-dimensional marginalizations of the parameters $\vec{\theta}$ drawn from the KDE with another subset of samples. We find a bandwidth of ≈ 0.01 consistently matches the true distribution of parameters, whereas values lower and higher tend to overfit and underfit the data, respectively.

D. POPULATION INFERENCE

Our goal is to recover the posterior for our set of hyperparameters, $\vec{\beta} = [\beta_{\texttt{CE}}, \beta_{\texttt{CHE}}, \beta_{\texttt{GC}}, \beta_{\texttt{NSC}}, \beta_{\texttt{SMT}}]$ and $\vec{\lambda} = [\chi_{\rm b}, \alpha_{\rm CE}]$, given the set of (independent) GW observations of BBHs from GWTC-2, $\mathbf{x} = \{\vec{x}_i\}_i^{N_{\rm obs}}$. In the following, we are only interested in the shape of the populations and not the rate and implicitly marginalize out the rate term by assuming a $p(N) \propto 1/N$ prior on the number of detections (Fishbach et al. 2018).

Starting from the ground up, the probability of detecting a set of event parameters $\boldsymbol{\theta} = \{\vec{\theta}_i\}$ given the model hyperparameters $\vec{\Lambda} = [\vec{\beta}, \vec{\lambda}]$ from independent observations is

$$p(\boldsymbol{\theta}|\vec{\Lambda}) = \prod_{i=1}^{N_{\rm obs}} \frac{p(\vec{\theta}_i|\vec{\Lambda})}{\int p(\vec{\theta}|\vec{\Lambda}) P_{\rm det}(\vec{\theta})\,{\rm d}\vec{\theta}}, \tag{D8}$$

where $P_{\rm det}(\vec{\theta})$ is the detection probability for an event with parameters $\vec{\theta}$ (Chennamangalam et al. 2013; Farr et al. 2015; Mandel et al. 2019; Vitale et al. 2020). Marginalizing over event parameters, the probability of observing the

data for event $\vec{x}_i$ given our hyperparameters $\vec{\Lambda}$ is

$$p(\vec{x}_i|\vec{\Lambda}) = \int p(\vec{x}_i|\vec{\theta})p(\vec{\theta}|\vec{\Lambda})\,\mathrm{d}\vec{\theta}. \tag{D9}$$

By applying Bayes' theorem, we replace $p(\vec{x}_i|\vec{\theta})$ with $p(\vec{\theta}|\vec{x}_i)p(\vec{x}_i)/\pi(\vec{\theta})$. Assuming independent observations, we get

$$p(\mathbf{x}|\vec{\Lambda}) = \prod_{i=1}^{N_{\rm obs}} \frac{p(\vec{x}_i)}{\int p(\vec{\theta}|\vec{\Lambda})P_{\rm det}(\vec{\theta})\,\mathrm{d}\vec{\theta}} \int \frac{p(\vec{\theta}_i|\vec{x}_i)p(\vec{\theta}_i|\vec{\Lambda})}{\pi(\vec{\theta}_i)}\,\mathrm{d}\vec{\theta}, \tag{D10}$$

where $\pi(\vec{\theta})$ is the prior on the parameters $\vec{\theta} = [\mathcal{M}_{\rm c}, q, \chi_{\rm eff}, z]$ assumed in the original inference of $\vec{\theta}$, which is provided alongside the LVC posterior samples. We evaluate $\pi(\vec{\theta})$ at each point $\vec{\theta}_i$ in a 4-dimensional prior KDE constructed using the LVC prior samples. Since we use S_i posterior samples to approximate $p(\vec{\theta}_i|\vec{x}_i)$, we can rewrite this integral as a discrete sum over the posterior samples:

$$p(\mathbf{x}|\vec{\Lambda}) = \prod_{i=1}^{N_{\rm obs}} \frac{p(\vec{x}_i)}{S_i \int p(\vec{\theta}|\vec{\Lambda})P_{\rm det}(\vec{\theta})\,\mathrm{d}\vec{\theta}} \sum_{k=1}^{S_i} \frac{p(\vec{\theta}_i^k|\vec{\Lambda})}{\pi(\vec{\theta}_i^k)}. \tag{D11}$$

The hyperlikelihood $p(\vec{\theta}_i^k|\vec{\Lambda})$ is evaluated as a mixture model of the underlying KDEs in the current $\chi_{\rm b}$ and $\alpha_{\rm CE}$ model,

$$p(\vec{\theta}_i^k|\vec{\Lambda}) = \sum_j \beta_j p(\vec{\theta}_i^k|\mu_j^{\chi,\alpha}), \tag{D12}$$

where the summation is over the formation channels and $\mu_j^{\chi,\alpha}$ is the $\chi_{\rm b}$ and $\alpha_{\rm CE}$ model that the sampler is in at a given step in the chain. Thus, our hyperlikelihood from Eq. (D11) becomes

$$p(\mathbf{x}|\vec{\Lambda}) = \prod_{i=1}^{N_{\rm obs}} \frac{p(\vec{x}_i)}{S_i\tilde{\xi}^{\chi,\alpha}} \sum_j \beta_j \sum_{k=1}^{S_i} \frac{p(\vec{\theta}_i^k|\mu_j^{\chi,\alpha})}{\pi(\vec{\theta}_i^k)}, \tag{D13}$$

where for convenience we define $\tilde{\xi}^{\chi,\alpha} \equiv \sum_j \beta_j \xi_j^{\chi,\alpha}$ where

$$\xi_j^{\chi,\alpha} = \int p(\vec{\theta}|\mu_j^{\chi,\alpha})P_{\rm det}(\vec{\theta})\,\mathrm{d}\vec{\theta} \tag{D14}$$

is the detection efficiency for each formation channel model with natal spin χ and CE efficiency α. The channel-dependent detection efficiency $\xi_j^{\chi,\alpha}$ is evaluated using a Monte Carlo approach, since detection probabilities are already calculated for each sample in the population models. Finally, the posterior distribution on the hyperparameters, $p(\vec{\Lambda}|\mathbf{x}) = p(\mathbf{x}|\vec{\Lambda})\pi(\vec{\Lambda})/p(\mathbf{x})$, is

$$p(\vec{\Lambda}|\mathbf{x}) = \pi(\vec{\Lambda}) \prod_{i=1}^{N_{\rm obs}} \frac{1}{S_i\tilde{\xi}^{\chi,\alpha}} \sum_j \beta_j \sum_{k=1}^{S_i} \frac{p(\vec{\theta}_i^k|\mu_j^{\chi,\alpha})}{\pi(\vec{\theta}_i^k)}, \tag{D15}$$

where $\pi(\vec{\Lambda})$ is the prior on the hyperparameters.

For priors, we use a Dirichlet distribution with equal concentration parameters and dimensions equal to the number of formation channels as a prior for the branching fractions $\vec{\beta}$, imposing the constraints $(0 \leq \beta_i \leq 1)\,\forall\, i$ and $\sum_i \beta_i = 1$. In practice, the discrete $\chi_{\rm b}$ and $\alpha_{\rm CE}$ models are sampled using dummy index parameters that are defined on the range $[0, N_{\lambda,m}]$, where $N_{\lambda,m}$ is the number of $m = \chi_{\rm b}$ or $n = \alpha_{\rm CE}$ models, with a flat prior across this range and no support outside this range. The $\vec{\lambda}$ model considered at each step is given by the floor of the dummy parameter values that correspond to $\chi_{\rm b}$ and $\alpha_{\rm CE}$.

E. TESTING WITH MOCK OBSERVATIONS

In addition to examining constraints on the GW population, we can test our methodology using mock draws from the underlying population distributions. In Figures 7 and 8, we show the convergence on detectable branching fractions and physical prescriptions as the number of observations increases. In this mock sample, we set the true

physical prescriptions to $\chi_{\rm b} = 0.0$ and $\alpha_{\rm CE} = 1.0$ and the detectable branching fractions between channels to be $[\beta^{\rm det}_{\texttt{CE}}, \beta^{\rm det}_{\texttt{CHE}}, \beta^{\rm det}_{\texttt{GC}}, \beta^{\rm det}_{\texttt{NSC}}, \beta^{\rm det}_{\texttt{SMT}}] = [0.3, 0.1, 0.3, 0.1, 0.2]$. We draw systems from the underlying distributions of the various populations until $N_{\rm obs}\beta^{\rm det}_j$ detectable samples are drawn from channel j, where $N_{\rm obs}$ is the number of observed events for a particular mock realization. Figure 7 shows the contribution to branching fraction posteriors for different $\chi_{\rm b}$ models, marginalized over $\alpha_{\rm CE}$ models, and Figure 8 shows the contribution to branching fraction posteriors for different $\alpha_{\rm CE}$ models, marginalized over $\chi_{\rm b}$ models. For demonstration purposes, in these examples we assume no measurement uncertainty; in actuality the inclusion of mock measurement uncertainty will lead to less precise measurements. In this simplified example, we find our analysis recovers the injected model, with increasing Bayes factors for the correct physical prescription and increasing precision in the branching fraction measurement as the number of observations increases. As with our analysis using the GW observations, we see strong biases in the recovered branching fractions when the incorrect physical prescriptions are considered. A more investigative analysis with the inclusion of SNR-dependent measurement uncertainty will be explored in future work.

REFERENCES

Aasi, J., Abbott, B. P., Abbott, R., et al. 2015, Classical and Quantum Gravity, 32, 074001, doi: 10.1088/0264-9381/32/7/074001

Abbott, B. P., Abbott, R., Abbott, T. D., et al. 2016a, The Astrophysical Journal, 818, L22, doi: 10.3847/2041-8205/818/2/l22

—. 2016b, Physical Review Letters, 116, 241102, doi: 10.1103/PhysRevLett.116.241102

—. 2017, Physical Review Letters, 119, 161101, doi: 10.1103/PhysRevLett.119.161101

—. 2018, Living Reviews in Relativity, 21, 57, doi: 10.1007/s41114-018-0012-9

—. 2019a, Physical Review X, 9, 31040, doi: 10.1103/PhysRevX.9.031040

—. 2019b, The Astrophysical Journal, 882, L24, doi: 10.3847/2041-8213/ab3800

—. 2020a, The Astrophysical Journal, 892, L3, doi: 10.3847/2041-8213/ab75f5

Abbott, R., Abbott, T. D., Abraham, S., et al. 2019c, arXiv e-prints. https://arxiv.org/abs/1912.11716

—. 2020b, arXiv e-prints. https://arxiv.org/abs/2010.14527

—. 2020c, arXiv e-prints. https://arxiv.org/abs/2010.14533

—. 2020d, The Astrophysical Journal Letters, 896, L44, doi: 10.3847/2041-8213/ab960f

—. 2020e, Physical Review Letters, 125, 101102, doi: 10.1103/PhysRevLett.125.101102

Acernese, F., Agathos, M., Agatsuma, K., et al. 2015, Classical and Quantum Gravity, 32, 024001, doi: 10.1088/0264-9381/32/2/024001

Ade, P. A., Aghanim, N., Arnaud, M., et al. 2016, Astronomy and Astrophysics, 594, A13, doi: 10.1051/0004-6361/201525830

Amaro-Seoane, P., & Chen, X. 2016, Monthly Notices of the Royal Astronomical Society, 458, 3075, doi: 10.1093/mnras/stw503

Antognini, J. M., Shappee, B. J., Thompson, T. A., & Amaro-seoane, P. 2014, Monthly Notices of the Royal Astronomical Society, 439, 1079, doi: 10.1093/mnras/stu039

Antonini, F., & Gieles, M. 2020a, Physical Review D, 102, 123016, doi: 10.1103/PhysRevD.102.123016

—. 2020b, Monthly Notices of the Royal Astronomical Society, 492, 2936, doi: 10.1093/mnras/stz3584

Antonini, F., Gieles, M., & Gualandris, A. 2019, Monthly Notices of the Royal Astronomical Society, 486, 5008, doi: 10.1093/mnras/stz1149

Antonini, F., & Perets, H. B. 2012, The Astrophysical Journal, 757, 27, doi: 10.1088/0004-637X/757/1/27

Antonini, F., & Rasio, F. A. 2016, The Astrophysical Journal, 831, 1, doi: 10.3847/0004-637X/831/2/187

Antonini, F., Toonen, S., & Hamers, A. S. 2017, The Astrophysical Journal, 841, 77, doi: 10.3847/1538-4357/aa6f5e

Arca Sedda, M., & Benacquista, M. 2019, Monthly Notices of the Royal Astronomical Society, 482, 2991, doi: 10.1093/mnras/sty2764

Arca Sedda, M., Mapelli, M., Spera, M., Benacquista, M., & Giacobbo, N. 2020, The Astrophysical Journal, 894, 133, doi: 10.3847/1538-4357/ab88b2

Askar, A., Szkudlarek, M., Gondek-Rosińska, D., Giersz, M., & Bulik, T. 2017, Monthly Notices of the Royal Astronomical Society, 464, 36, doi: 10.1093/mnrasl/slw177

Baibhav, V., Gerosa, D., Berti, E., et al. 2020, Physical Review D, 102, 43002, doi: 10.1103/PhysRevD.102.043002

Baker, J. G., Centrella, J., Choi, D. I., et al. 2006, The Astrophysical Journal Letters, 653, 93, doi: 10.1086/510448

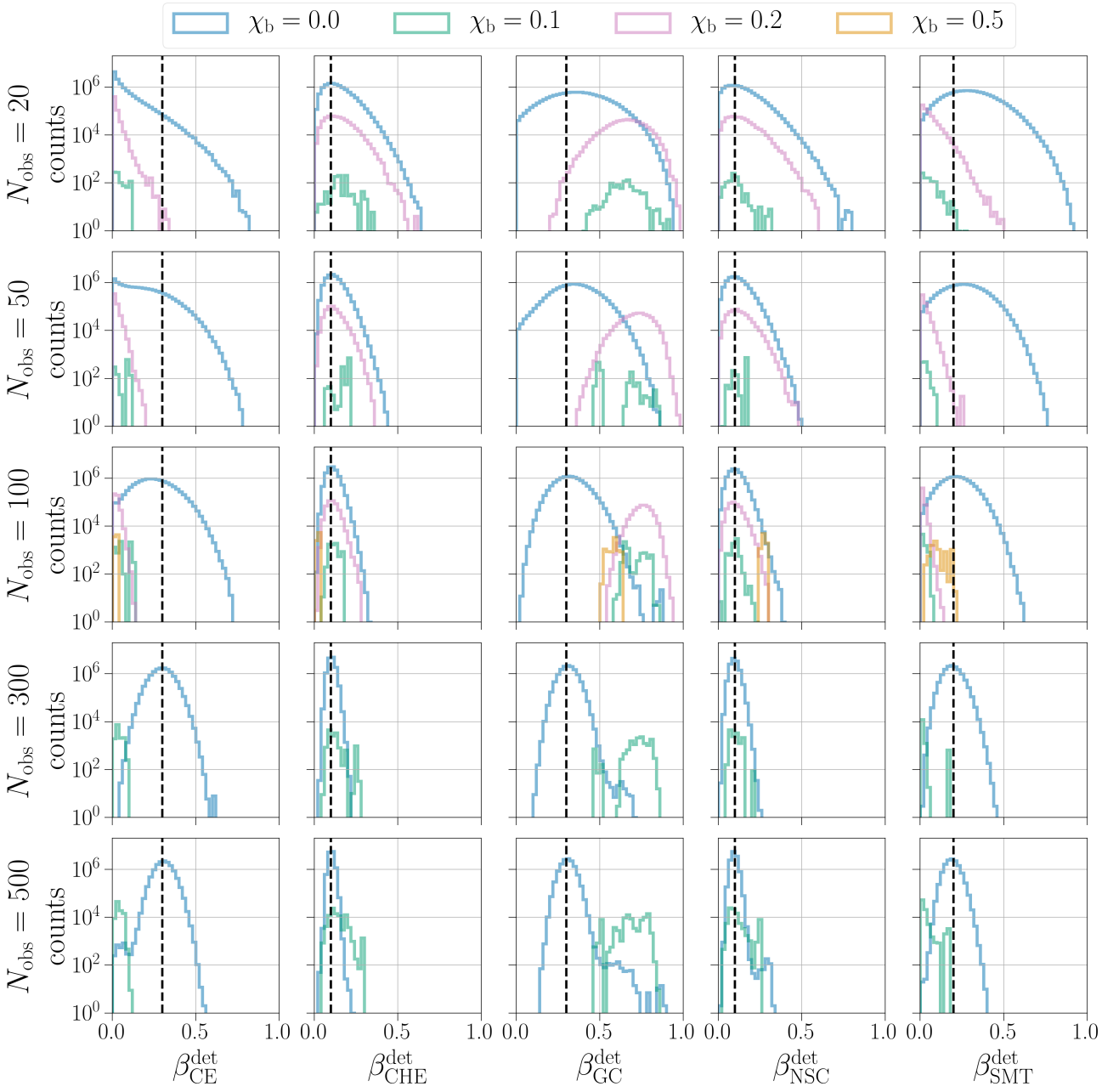

Figure 7. Convergence on underlying branching fractions using mock observations from the population models. In this example, the injected model has $\chi_b = 0$, $\alpha_{CE} = 1.0$, and $\vec{\beta}^{det} = [0.3, 0.1, 0.3, 0.1, 0.2]$. Different colors show the contribution of different χ_b models to the full branching fraction posteriors, marginalized over α_{CE} models; the injected χ_b model is shown with the blue curve. The Bayes factors between the physical models are the relative areas under the colored curves.

Banerjee, S. 2017, Monthly Notices of the Royal Astronomical Society, 467, 524, doi: 10.1093/mnras/stx2347

—. 2021, Monthly Notices of the Royal Astronomical Society, 500, 3002, doi: 10.1093/mnras/staa2392

Barrett, J. W., Gaebel, S. M., Neijssel, C. J., et al. 2018, Monthly Notices of the Royal Astronomical Society, 477, 4685, doi: 10.1093/mnras/sty908

Bartos, I., Kocsis, B., Haiman, Z., & Márka, S. 2017, The Astrophysical Journal, 835, 165, doi: 10.3847/1538-4357/835/2/165

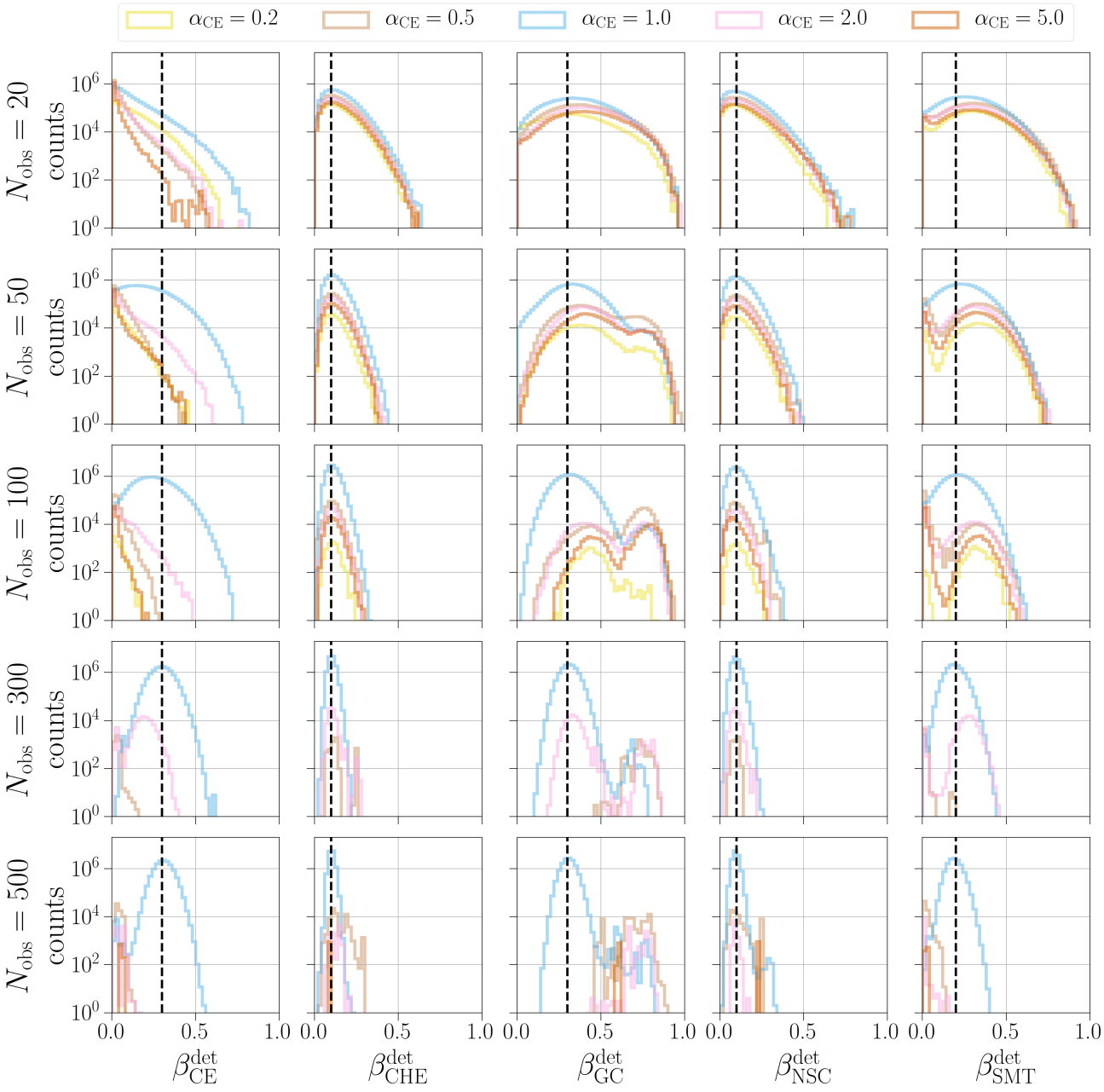

Figure 8. Same as Figure 7, but the different colors show the contribution of different $\alpha_{\rm CE}$ models to the full branching fraction posteriors, marginalized over $\chi_{\rm b}$ models. The injected $\alpha_{\rm CE}$ model is shown with the light blue curve.

Bavera, S. S., Fragos, T., Zevin, M., et al. 2020a, arXiv e-prints. https://arxiv.org/abs/2010.16333

Bavera, S. S., Fragos, T., Qin, Y., et al. 2020b, Astronomy & Astrophysics, 635, A97, doi: 10.1051/0004-6361/201936204

Bekenstein, J. D. 1973, The Astrophysical Journal, 183, 657, doi: 10.1086/152255

Belczyński, K., Kalogera, V., & Bulik, T. 2002, The Astrophysical Journal, 527, 407, doi: 10.1086/340304

Belczynski, K., Repetto, S., Holz, D. E., et al. 2016, The Astrophysical Journal, 819, 108, doi: 10.3847/0004-637X/819/2/108

Bethe, H. A., & Brown, G. E. 1998, The Astrophysical Journal, 506, 780, doi: 10.1086/306265

Bhagwat, S., de Luca, V., Franciolini, G., Pani, P., & Riotto, A. 2021, Journal of Cosmology and Astroparticle Physics, 2021, 037, doi: 10.1088/1475-7516/2021/01/037

Bird, S., Cholis, I., Muñoz, J. B., et al. 2016, Physical Review Letters, 116, 1, doi: 10.1103/PhysRevLett.116.201301

Blaauw, A. 1961, Bulletin of the Astronomical Institutes of the Netherlands, 15, 265

Blanchet, L. 2014, Living Reviews in Relativity, 17, 2, doi: 10.12942/lrr-2014-2

Bouffanais, Y., Mapelli, M., Gerosa, D., et al. 2019, The Astrophysical Journal, 886, 25, doi: 10.3847/1538-4357/ab4a79

Bouffanais, Y., Mapelli, M., Santoliquido, F., et al. 2020, arXiv e-prints. https://arxiv.org/abs/2010.11220

Breen, P. G., & Heggie, D. C. 2013, Monthly Notices of the Royal Astronomical Society, 432, 2779, doi: 10.1093/mnras/stt628

Breivik, K., Coughlin, S., Zevin, M., et al. 2020, The Astrophysical Journal, 898, 71, doi: 10.3847/1538-4357/ab9d85

Buonanno, A., Kidder, L. E., & Lehner, L. 2008, Physical Review D - Particles, Fields, Gravitation and Cosmology, 77, 026004, doi: 10.1103/PhysRevD.77.026004

Chatterjee, S., Fregeau, J. M., Umbreit, S., & Rasio, F. A. 2010, The Astrophysical Journal, 719, 915, doi: 10.1088/0004-637X/719/1/915

Chennamangalam, J., Lorimer, D. R., Mandel, I., & Bagchi, M. 2013, Monthly Notices of the Royal Astronomical Society, 431, 874, doi: 10.1093/mnras/stt205

Clesse, S., & Garcia-Bellido, J. 2020, arXiv e-prints. https://arxiv.org/abs/2007.06481

Conselice, C. J., Bhatawdekar, R., Palmese, A., & Hartley, W. G. 2020, The Astrophysical Journal, 890, 8, doi: 10.3847/1538-4357/ab5dad

De Mink, S. E., & Mandel, I. 2016, Monthly Notices of the Royal Astronomical Society, 460, 3545, doi: 10.1093/mnras/stw1219

Dominik, M., Belczynski, K., Fryer, C., et al. 2012, The Astrophysical Journal, 759, 52, doi: 10.1088/0004-637X/759/1/52

Downing, J. M. B., Benacquista, M. J., Giersz, M., & Spurzem, R. 2010, Monthly Notices of the Royal Astronomical Society, 407, 1946, doi: 10.1111/j.1365-2966.2010.17040.x

du Buisson, L., Marchant, P., Podsiadlowski, P., et al. 2020, Monthly Notices of the Royal Astronomical Society, 499, 5941, doi: 10.1093/mnras/staa3225

El-Badry, K., Quataert, E., Weisz, D. R., Choksi, N., & Boylan-Kolchin, M. 2019, Monthly Notices of the Royal Astronomical Society, 482, 4528, doi: 10.1093/mnras/sty3007

Eldridge, J. J., & Stanway, E. R. 2016, Monthly Notices of the Royal Astronomical Society, 462, 3302, doi: 10.1093/mnras/stw1772

Farmer, R., Renzo, M., de Mink, S., Fishbach, M., & Justham, S. 2020, The Astrophysical Journal Letters, 902, L36, doi: 10.3847/2041-8213/abbadd

Farmer, R., Renzo, M., de Mink, S. E., Marchant, P., & Justham, S. 2019, The Astrophysical Journal, 887, 53, doi: 10.3847/1538-4357/ab518b

Farr, B., Holz, D. E., & Farr, W. M. 2017a, The Astrophysical Journal Letters, 854, L9, doi: 10.3847/2041-8213/aaaa64

Farr, W. M., Gair, J. R., Mandel, I., & Cutler, C. 2015, Physical Review D - Particles, Fields, Gravitation and Cosmology, 91, 0230054, doi: 10.1103/PhysRevD.91.023005

Farr, W. M., Stevenson, S., Miller, M. C., et al. 2017b, Nature, 548, 426, doi: 10.1038/nature23453

Favata, M., Hughes, S. A., & Holz, D. E. 2004, The Astrophysical Journal, 607, L5, doi: 10.1086/421552

Fishbach, M., & Holz, D. E. 2017, The Astrophysical Journal, 851, L25, doi: 10.3847/2041-8213/aa9bf6

—. 2020, The Astrophysical Journal Letters, 891, L27, doi: 10.3847/2041-8213/ab7247

Fishbach, M., Holz, D. E., & Farr, W. M. 2018, The Astrophysical Journal, 863, L41, doi: 10.3847/2041-8213/aad800

Foreman-Mackey, D., Hogg, D. W., Lang, D., & Goodman, J. 2013, Publications of the Astronomical Society of the Pacific, 125, 306, doi: 10.1086/670067

Fragione, G., & Kocsis, B. 2019, Monthly Notices of the Royal Astronomical Society, 486, 4781, doi: 10.1093/mnras/stz1175

Fragione, G., & Loeb, A. 2021, Monthly Notices of the Royal Astronomical Society, 502, 3879, doi: 10.1093/mnras/stab247

Fragione, G., & Silk, J. 2020, Monthly Notices of the Royal Astronomical Society, 498, 4591, doi: 10.1093/mnras/staa2629

Fragos, T., Andrews, J. J., Ramirez-Ruiz, E., et al. 2019, The Astrophysical Journal, 883, L45, doi: 10.3847/2041-8213/ab40d1

Fregeau, J. M., & Rasio, F. A. 2007, The Astrophysical Journal, 658, 1047, doi: 10.1086/511809

Fuller, J., & Ma, L. 2019, The Astrophysical Journal Letters, 881, L1, doi: 10.3847/2041-8213/ab339b

Georgiev, I. Y., & Böker, T. 2014, Monthly Notices of the Royal Astronomical Society, 441, 3570, doi: 10.1093/mnras/stu797

Gerosa, D., & Berti, E. 2019, Physical Review D, 100, 41301, doi: 10.1103/PhysRevD.100.041301

Giacobbo, N., & Mapelli, M. 2018, Monthly Notices of the Royal Astronomical Society, 480, 2011, doi: 10.1093/mnras/sty1999

González, J. A., Sperhake, U., Brügmann, B., Hannam, M., & Husa, S. 2007, Physical Review Letters, 98, 2, doi: 10.1103/PhysRevLett.98.091101

Grevesse, N., & Sauval, A. J. 1998, Space Science Reviews, 85, 161, doi: 10.1023/A:1005161325181

Gültekin, K., Miller, M. C., & Hamilton, D. P. 2006, The Astrophysical Journal, 640, 156, doi: 10.1086/499917

Hall, A., Gow, A. D., & Byrnes, C. T. 2020, Physical Review D, 102, 123524, doi: 10.1103/PhysRevD.102.123524

Hannam, M., Schmidt, P., Bohé, A., et al. 2014, Physical Review Letters, 113, 1, doi: 10.1103/PhysRevLett.113.151101

Harris, W. E. 2010, arXiv e-prints. https://arxiv.org/abs/1012.3224

Hénon, M. 1961, Annales d'Astrophysique, 24, 369. https://ui.adsabs.harvard.edu/abs/1961AnAp...24..369H

—. 1971a, Astrophysics and Space Science, 14, 151, doi: 10.1007/BF00649201

—. 1971b, Astrophysics and Space Science, 13, 284, doi: 10.1007/BF00649159

Holley-Bockelmann, K., Gültekin, K., Shoemaker, D., & Yunes, N. 2008, The Astrophysical Journal, 686, 829, doi: 10.1086/591218

Hunter, J. D. 2007, Computing in Science and Engineering, 9, 99, doi: 10.1109/MCSE.2007.55

Hurley, J. R., Pols, O. R., & Tout, C. A. 2000, Monthly Notices of the Royal Astronomical Society, 315, 543, doi: 10.1046/j.1365-8711.2000.03426.x

Hurley, J. R., Tout, C. A., & Pols, O. R. 2002, Monthly Notices of the Royal Astronomical Society, 329, 897, doi: 10.1046/j.1365-8711.2002.05038.x

Hut, P., McMillan, S., Goodman, J., et al. 1992, Publications of the Astronomical Society of the Pacific, 104, 981, doi: 10.1086/133085

Inayoshi, K., Hirai, R., Kinugawa, T., & Hotokezaka, K. 2017, Monthly Notices of the Royal Astronomical Society, 468, 5020, doi: 10.1093/mnras/stx757

Ivanova, N., Justham, S., Chen, X., et al. 2013, Astronomy & Astrophysics Review, 21, 59, doi: 10.1007/s00159-013-0059-2

Joshi, K. J., Rasio, F. A., & Portegies Zwart, S. P. 2000, The Astrophysical Journal, 540, 969, doi: 10.1086/309350

Kalogera, V. 1996, The Astrophysical Journal, 471, 352, doi: 10.1086/177974

Khan, S., Husa, S., Hannam, M., et al. 2016, Physical Review D, 93, 044007, doi: 10.1103/PhysRevD.93.044007

Kimball, C., Talbot, C., L. Berry, C. P., et al. 2020a, The Astrophysical Journal, 900, 177, doi: 10.3847/1538-4357/aba518

Kimball, C., Talbot, C., Berry, C. P. L., et al. 2020b, arXiv e-prints. https://arxiv.org/abs/2011.05332

Kinugawa, T., Inayoshi, K., Hotokezaka, K., Nakauchi, D., & Nakamura, T. 2014, Monthly Notices of the Royal Astronomical Society, 442, 2963, doi: 10.1093/mnras/stu1022

Koppitz, M., Pollney, D., Reisswig, C., et al. 2007, Physical Review Letters, 99, 1, doi: 10.1103/PhysRevLett.99.041102

Kozai, Y. 1962, The Astronomical Journal, 67, 591, doi: 10.1086/108790

Kroupa, P. 2001, Monthly Notices of the Royal Astronomical Society, 322, 231, doi: 10.1046/j.1365-8711.2001.04022.x

Lidov, M. L. 1963, AIAA Journal, 1, 1985, doi: 10.2514/3.1983

Lightman, A. P., & Shapiro, S. L. 1978, Reviews of Modern Physics, 50, 437, doi: 10.1103/RevModPhys.50.437

Lousto, C. O., Campanelli, M., Zlochower, Y., & Nakano, H. 2010, Classical and Quantum Gravity, 27, 114006, doi: 10.1088/0264-9381/27/11/114006

Madau, P., & Fragos, T. 2017, The Astrophysical Journal, 840, 39, doi: 10.3847/1538-4357/aa6af9

Madau, P., & Rees, M. J. 2001, The Astrophysical Journal, 551, L27, doi: 10.1086/319848

Mandel, I., & De Mink, S. E. 2016, Monthly Notices of the Royal Astronomical Society, 458, 2634, doi: 10.1093/mnras/stw379

Mandel, I., & Farmer, A. 2018, arXiv e-prints. https://arxiv.org/abs/1806.05820

Mandel, I., Farr, W. M., Colonna, A., et al. 2017, Monthly Notices of the Royal Astronomical Society, 465, 3254, doi: 10.1093/mnras/stw2883

Mandel, I., Farr, W. M., & Gair, J. R. 2019, Monthly Notices of the Royal Astronomical Society, 486, 1086, doi: 10.1093/mnras/stz896

Mapelli, M., Santoliquido, F., Bouffanais, Y., et al. 2020, arXiv e-prints. https://arxiv.org/abs/2007.15022

Marchant, P., Langer, N., Podsiadlowski, P., Tauris, T., & Moriya, T. 2016, Astronomy & Astrophysics, 588, A50, doi: 10.1051/0004-6361/201628133

Marchant, P., Renzo, M., Farmer, R., et al. 2019, The Astrophysical Journal, 882, 36, doi: 10.3847/1538-4357/ab3426

McKernan, B., Ford, K. E., Kocsis, B., Lyra, W., & Winter, L. M. 2014, Monthly Notices of the Royal Astronomical Society, 441, 900, doi: 10.1093/mnras/stu553

McKinney, W. 2010, in Proceedings of the 9th Python in Science Conference, ed. S. van der Walt & J. Millman, 51–56, doi: 10.25080/Majora-92bf1922-00a

McMillan, S., Hut, P., & Makino, J. 1991, The Astrophysical Journal, 372, 111, doi: 10.1086/169958

Michaely, E., & Perets, H. B. 2019, The Astrophysical Journal, 887, L36, doi: 10.3847/2041-8213/ab5b9b

—. 2020, Monthly Notices of the Royal Astronomical Society, 498, 4924, doi: 10.1093/mnras/staa2720

Miller, M. C., & Hamilton, D. P. 2002, The Astrophysical Journal, 576, 894, doi: 10.1086/341788

Miller, S., Callister, T. A., & Farr, W. M. 2020, The Astrophysical Journal, 895, 128, doi: 10.3847/1538-4357/ab80c0

Moe, M., & Di Stefano, R. 2017, The Astrophysical Journal Supplement Series, 230, 55, doi: 10.3847/1538-4365/aa6fb6

Morscher, M., Umbreit, S., Farr, W. M., & Rasio, F. A. 2013, The Astrophysical Journal Letters, 763, 2006, doi: 10.1088/2041-8205/763/1/L15

Nandez, J. L., & Ivanova, N. 2016, Monthly Notices of the Royal Astronomical Society, 460, 3992, doi: 10.1093/mnras/stw1266

Neijssel, C. J., Vigna-Gómez, A., Stevenson, S., et al. 2019, Monthly Notices of the Royal Astronomical Society, 490, 3740, doi: 10.1093/mnras/stz2840

Neumayer, N., Seth, A., & Böker, T. 2020, Astronomy and Astrophysics Review, 28, 4, doi: 10.1007/s00159-020-00125-0

Nitz, A., Harry, I., Brown, D., et al. 2019, gwastro/pycbc: PyCBC Release v1.14.4, Zenodo, doi: 10.5281/zenodo.3546372

Nitz, A. H., Schäfer, M., & Canton, T. D. 2020, The Astrophysical Journal Letters, 902, L29, doi: 10.3847/2041-8213/abbc10

O'Leary, R. M., Rasio, F. A., Fregeau, J. M., Ivanova, N., & O'Shaughnessy, R. 2006, The Astrophysical Journal, 637, 937, doi: 10.1086/498446

Oliphant, T. E. 2006, A guide to NumPy (USA: Trelgol Publishing). https://web.mit.edu/dvp/Public/numpybook.pdf

Paczyński, B. 1976, in Eggleton P., Mitton S., Whelan J., eds, Proc. IAU Symp. 73, Structure and Evolution of Close Binary Systems. Reidel, Dordrecht, 75. https://ui.adsabs.harvard.edu/abs/1976IAUS...73...75P

Pattabiraman, B., Umbreit, S., Liao, W. K., et al. 2013, The Astrophysical Journal, Supplement Series, 204, 16, doi: 10.1088/0067-0049/204/2/15

Paxton, B., Bildsten, L., Dotter, A., et al. 2011, The Astrophysical Journal Supplement Series, 192, 3, doi: 10.1088/0067-0049/192/1/3

Paxton, B., Cantiello, M., Arras, P., et al. 2013, The Astrophysical Journal Supplement Series, 208, 4, doi: 10.1088/0067-0049/208/1/4

Paxton, B., Marchant, P., Schwab, J., et al. 2015, The Astrophysical Journal Supplement Series, 220, 15, doi: 10.1088/0067-0049/220/1/15

Paxton, B., Schwab, J., Bauer, E. B., et al. 2018, The Astrophysical Journal Supplement Series, 234, 34, doi: 10.3847/1538-4365/aaa5a8

Paxton, B., Smolec, R., Schwab, J., et al. 2019, The Astrophysical Journal Supplement Series, 243, 10, doi: 10.3847/1538-4365/ab2241

Peres, A. 1962, Physical Review, 128, 2471, doi: 10.1103/PhysRev.128.2471

Pérez, F., & Granger, B. E. 2007, IEEE Journals & Magazines, 9, 21, doi: 10.1109/MCSE.2007.53

Peters, P. C. 1964, Physical Review, 136, 1224, doi: 10.1103/PhysRev.136.B1224

Pollney, D., Reisswig, C., Rezzolla, L., et al. 2007, Physical Review D - Particles, Fields, Gravitation and Cosmology, 76, 1, doi: 10.1103/PhysRevD.76.124002

Portegies Zwart, S. F., & McMillan, S. L. W. 2000, The Astrophysical Journal Letters, 528, 17, doi: 10.1086/312422

Powell, J., Stevenson, S., Mandel, I., & Tiňo, P. 2019, Monthly Notices of the Royal Astronomical Society, 488, 3810, doi: 10.1093/mnras/stz1938

Pretorius, F. 2005, Physical Review Letters, 95, 1, doi: 10.1103/PhysRevLett.95.121101

Price-Whelan, A. M., Sipocz, B. M., Günther, H. M., et al. 2018, The Astronomical Journal, 156, 123, doi: 10.3847/1538-3881/aabc4f

Qin, Y., Fragos, T., Meynet, G., et al. 2018, Astronomy & Astrophysics, 616, A28, doi: 10.1051/0004-6361/201832839

Rezzolla, L., Barausse, E., Dorband, E. N., et al. 2008, Physical Review D - Particles, Fields, Gravitation and Cosmology, 78, 1, doi: 10.1103/PhysRevD.78.044002

Robitaille, T. P., Tollerud, E. J., Greenfield, P., et al. 2013, Astronomy & Astrophysics, 558, A33, doi: 10.1051/0004-6361/201322068

Rodriguez, C. L., Amaro-seoane, P., Chatterjee, S., et al. 2018a, Physical Review D, 98, 123005, doi: 10.1103/PhysRevD.98.123005

Rodriguez, C. L., Amaro-Seoane, P., Chatterjee, S., & Rasio, F. A. 2018b, Physical Review Letters, 120, 151101, doi: 10.1103/PhysRevLett.120.151101

Rodriguez, C. L., Chatterjee, S., & Rasio, F. A. 2016a, Physical Review D, 93, 084029, doi: 10.1103/PhysRevD.93.084029

Rodriguez, C. L., & Loeb, A. 2018, The Astrophysical Journal Letters, 866, L5, doi: 10.3847/2041-8213/aae377

Rodriguez, C. L., Morscher, M., Pattabiraman, B., et al. 2015, Physical Review Letters, 115, 051101, doi: 10.1103/PhysRevLett.115.051101

Rodriguez, C. L., Zevin, M., Amaro-Seoane, P., et al. 2019, Physical Review D, 100, 43027, doi: 10.1103/physrevd.100.043027

Rodriguez, C. L., Zevin, M., Pankow, C., Kalogera, V., & Rasio, F. A. 2016b, The Astrophysical Journal Letters, 832, 1, doi: 10.3847/2041-8205/832/1/L2

Roulet, J., Venumadhav, T., Zackay, B., Dai, L., & Zaldarriaga, M. 2020, Physical Review D, 102, 123022, doi: 10.1103/PhysRevD.102.123022

Roulet, J., & Zaldarriaga, M. 2019, Monthly Notices of the Royal Astronomical Society, 484, 4216, doi: 10.1093/mnras/stz226

Safarzadeh, M. 2020, The Astrophysical Journal, 892, L8, doi: 10.3847/2041-8213/ab7cdc

Safarzadeh, M., Farr, W. M., & Ramirez-ruiz, E. 2020, The Astrophysical Journal, 894, 129, doi: 10.3847/1538-4357/ab80be

Samsing, J., MacLeod, M., & Ramirez-Ruiz, E. 2014, The Astrophysical Journal, 784, 71, doi: 10.1088/0004-637X/784/1/71

Samsing, J., & Ramirez-Ruiz, E. 2017, The Astrophysical Journal Letters, 840, L14, doi: 10.3847/2041-8213/aa6f0b

Sana, H., De Mink, S. E., De Koter, A., et al. 2012, Science, 337, 444, doi: 10.1126/science.1223344

Sana, H., Le Bouquin, J. B., Lacour, S., et al. 2014, Astrophysical Journal, Supplement Series, 215, 15, doi: 10.1088/0067-0049/215/1/15

Santoliquido, F., Mapelli, M., Bouffanais, Y., et al. 2020, The Astrophysical Journal, 898, 152, doi: 10.3847/1538-4357/ab9b78

Santoliquido, F., Mapelli, M., Giacobbo, N., Bouffanais, Y., & Artale, M. C. 2021, Monthly Notices of the Royal Astronomical Society, 502, 4877, doi: 10.1093/mnras/stab280

Sasaki, M., Suyama, T., Tanaka, T., & Yokoyama, S. 2018, Classical and Quantum Gravity, 35, 063001, doi: 10.1088/1361-6382/aaa7b4

Sigurdsson, S., & Hernquist, L. 1993, Nature, 364, 423, doi: 10.1038/364423a0

Sigurdsson, S., & Phinney, E. S. 1993, The Astrophysical Journal, 39, 631, doi: 10.1086/173190

Silsbee, K., & Tremaine, S. 2017, The Astrophysical Journal, 836, 1, doi: 10.3847/1538-4357/aa5729

Sperhake, U. 2015, Classical and Quantum Gravity, 32, 124011, doi: 10.1088/0264-9381/32/12/124011

Stevenson, S., Berry, C. P. L., & Mandel, I. 2017a, Monthly Notices of the Royal Astronomical Society, 2811, 2801, doi: 10.1093/mnras/stx1764

Stevenson, S., Ohme, F., & Fairhurst, S. 2015, The Astrophysical Journal, 810, 58, doi: 10.1088/0004-637X/810/1/58

Stevenson, S., Vigna-Gómez, A., Mandel, I., et al. 2017b, Nature Communications, 8, 14906, doi: 10.1038/ncomms14906

Stone, N. C., Metzger, B. D., & Haiman, Z. 2017, Monthly Notices of the Royal Astronomical Society, 464, 946, doi: 10.1093/mnras/stw2260

Talbot, C., & Thrane, E. 2017, Physical Review D, 96, 023012, doi: 10.1103/PhysRevD.96.023012

Taylor, P., & Kobayashi, C. 2015, Monthly Notices of the Royal Astronomical Society, 448, 1835, doi: 10.1093/mnras/stv139

Taylor, S. R., & Gerosa, D. 2018, Physical Review D, 98, 83017, doi: 10.1103/PhysRevD.98.083017

Thorne, K. S. 1974, The Astrophysical Journal, 191, 507. https://arxiv.org/abs/arXiv:1011.1669v3

Tutukov, A. V., & Yungelson, L. R. 1993, Monthly Notices of the Royal Astronomical Society, 260, 675, doi: 10.1093/mnras/260.3.675

van den Heuvel, E. P., Portegies Zwart, S. F., & de Mink, S. E. 2017, Monthly Notices of the Royal Astronomical Society, 471, 4256, doi: 10.1093/mnras/stx1430

van den Heuvel, E. P. J. 1976, in Structure and Evolution of Close Binary Systems, ed. P. Eggleton, S. Mitton, & J. Whelan, 35. https://ui.adsabs.harvard.edu/abs/1976IAUS...73...35V

Van Der Walt, S., Colbert, S. C., & Varoquaux, G. 2011, Computing in Science and Engineering, 13, 22, doi: 10.1109/MCSE.2011.37

Vigna-Gómez, A., Haster, C.-j., & Riley, J. 2021, The Astrophysical Journal Letters, 907, L19, doi: 10.3847/2041-8213/abd5b7

Virtanen, P., Gommers, R., Oliphant, T. E., et al. 2020, Nature Methods, 17, 261, doi: 10.1038/s41592-019-0686-2

Vitale, S. 2020, arXiv e-prints. https://arxiv.org/abs/2011.03563

Vitale, S., Gerosa, D., Farr, W. M., & Taylor, S. R. 2020, arXiv e-prints. https://arxiv.org/abs/2007.05579

Vitale, S., Lynch, R., Sturani, R., & Graff, P. 2017, Classical and Quantum Gravity, 34, 03LT01, doi: 10.1088/1361-6382/aa552e

Wen, L. 2003, The Astrophysical Journal, 598, 419, doi: 10.1086/378794

Wiseman, A. G. 1992, Physical Review D, 46, 1517, doi: 10.1103/PhysRevD.46.1517

Wong, K. W. K., Breivik, K., Kremer, K., & Callister, T. A. 2020, arXiv e-prints. https://arxiv.org/abs/2011.03564

Wong, K. W. K., Franciolini, G., Luca, V. D., et al. 2021, Physical Review D, 103, 23026, doi: 10.1103/PhysRevD.103.023026

Woosley, S. E. 2017, The Astrophysical Journal, 836, 244, doi: 10.3847/1538-4357/836/2/244

Wysocki, D., Lange, J., & O'Shaughnessy, R. 2019, Physical Review D, 100, 43012, doi: 10.1103/PhysRevD.100.043012

Zaldarriaga, M., Kushnir, D., & Kollmeier, J. A. 2018, Monthly Notices of the Royal Astronomical Society, 473, 4174, doi: 10.1093/mnras/stx2577

Zevin, M. 2020, Constraining the Origins of Binary Black Holes using Multiple Formation Pathways, Zenodo, doi: 10.5281/zenodo.4448170

Zevin, M., Pankow, C., Rodriguez, C. L., et al. 2017, The Astrophysical Journal, 846, 82, doi: 10.3847/1538-4357/aa8408

Zevin, M., Spera, M., Berry, C. P. L., & Kalogera, V. 2020, The Astrophysical Journal, 899, L1, doi: 10.3847/2041-8213/aba74e

Ziosi, B. M., Mapelli, M., Branchesi, M., & Tormen, G. 2014, Monthly Notices of the Royal Astronomical Society, 441, 3703, doi: 10.1093/mnras/stu824

B.1.3 Impact on the current field of research

The presented manuscript had an important impact on the current field of GW astrophysics research, and was followed by other similar studies. Thanks to the tens of GW detections made by the LVK collaboration and ever-improving theoretical models of BBH formation channels, it is now possible to conduct full-scale model selection studies to quantify the origin of merging BBHs. This realm has marked a change of direction in the field of research aiming to study the origin of merging BBHs. Because the main findings of Zevin et al. (2021a) are summarised in Section 3.1, in the rest of this section, we limit ourselves to discussing the impact this paper had on the current field of research.

Multiple independent studies were either performed in parallel or followed the footsteps of Zevin et al. (2021a). For example, Wong et al. (2021) analyzed GWTC-2 accounting for models of isolated binary evolution in galactic fields through the CE and SMT channels and the dynamical formation of globular clusters. Because the models used by the authors did model BBH spins self consistently, their hierarchical model analysis only considered BH mass and redshift distributions. Similarly, Bouffanais et al. (2021a) also analyzed GWTC-2 BBH events but accounted for dynamical formation in young clusters instead of globular clusters. Overall, Wong et al. (2021) and Bouffanais et al. (2021a) conclusions agree with Zevin et al. (2021a) result that, given the employed BBH models, multiple formation channels are favored by the analyses over a single model dominating the formation of the observed BBH sample. Other studies have also looked for the potential contribution of other formation channels like PBHs (De Luca et al. 2021b; Franciolini et al. 2021; Hütsi et al. 2021), population III stars (Ng et al. 2021), and young star clusters (Mapelli et al. 2021, 2022). Zevin et al. (2021a) remains the most inclusive analysis that accounts for the largest number of formation channels and state-of-the-art model predictions BBH, including the self-consistent modeling of BH spins.

We repeat, here, that only by considering all model uncertainties and all active BBH formation channels in Nature once can obtain an unbiased and conclusive answer in hierarchical model selection. For example, Bouffanais et al. (2021b) used model selection to constrain mass-transfer accretion efficiency and the CE phase efficiency with GWTC-2 events. However, Bouffanais et al. (2021b) only accounted for the isolated binary evolution through the CE and SMT channels. The omission of other formation channels in the analysis might lead to biased results, similar to the contradicting result about CE efficiency found in Bavera et al. (2021a), which only considers the CE and SMT channels compared to the more inclusive Zevin et al. (2021a) model selection study.

The planned next generation of GW detectors such as *Einstein Telescope*, *Cosmic Explorer*, and *LISA* will bring order of magnitude new BBH detections. We foresee that the discussed Bayesian framework in comiatio with improved and more accurate BBH models will play a pivot role in the quest to understand the origin of merging BBHs (e.g., Maggiore et al. 2020; Tiwari 2022; Toubiana et al. 2021).

Appendix C

Shine like a diamond

C.1 The role of core-collapse physics in the observability of black hole neutron star mergers as multimessenger sources

C.1.1 A brief introduction

Current rapid binary population synthesis studies employ prescriptions to predict the final fates, explosion or implosion, and remnant masses of compact objects. These prescriptions are based on parameters at the evolutionary cutoff imposed by the code, usually at or near central carbon ignition. In doing this, rapid binary population synthesis studies disregard late-stage evolution's role in determining the final fate within the neutrino-driven explosion paradigm (see, e.g., Patton et al. 2022). The vast majority of these studies use the Fryer et al. (2012) "rapid" and "delayed" prescriptions, which predict a unique boundary in the core mass of the pre-core-collapse star that leads to the formation of a BH or an NS above or below that boundary, respectively. This is in contrast to recent core-collapse simulations, which show that there is no unique boundary in the core mass of the pre-core-collapse star that transitions between the formation of NSs and BHs. For example, Sukhbold et al. (2016); Ertl et al. (2020); Patton & Sukhbold (2020); Schneider et al. (2021) finds successive islands of successful and failed explosions leading to the formation of NSs and BHs via direct collapse, respectively (see §1.2.1). In this project, we explored the effects of newer core-collapse prescriptions on the formation of merging BH-NS systems and their potential observably as electromagnetic transients. We also discuss the impact of the newer core-collapse mechanisms on BBH merger rate models presented in Chapter 2.

C.1.2 Manuscript

The conducted study Román-Garza et al. (2021) was published in *The Astrophysical Journal Letters* in May 2021. The arXiv open-access version of the manuscript is presented in the following pages.

Draft version December 7, 2020
Typeset using LaTeX **twocolumn** style in AASTeX63

arXiv:2012.02274v1 [astro-ph.HE] 3 Dec 2020

The role of core-collapse physics in the observability of black-hole neutron-star mergers as multi-messenger sources

Jaime Román-Garza [1,*] Simone S. Bavera [1] Tassos Fragos [1] Emmanouil Zapartas [1] Devina Misra [1] Jeff Andrews [2] Scotty Coughlin [2] Aaron Dotter [2] Konstantinos Kovlakas [3,4] Juan Gabriel Serra [2] Ying Qin [2,5] Kyle A. Rocha [2] and Nam Hai Tran [6]

[1] *Observatory of Geneva, University of Geneva, Chemin Pegasi 51, 1290, Versoix, Switzerland.*
[2] *Center for Interdisciplinary Exploration and Research in Astrophysics (CIERA) and Department of Physics and Astronomy, Northwestern University, 1800 Sherman Avenue, Evanston, IL 60201, USA*
[3] *Physics Department, University of Crete, GR 71003, Heraklion, Greece*
[4] *Institute of Astrophysics, Foundation for Research and Technology-Hellas, GR 71110 Heraklion, Greece*
[5] *Department of Physics, Anhui Normal University, Wuhu, Anhui 241000, China*
[6] *DARK, Niels Bohr Institute, University of Copenhagen, Jagtvej 128, 2200 Copenhagen, Denmark*

(Received ...; Revised ...; Accepted ...)

Submitted to AJ

ABSTRACT

Recent detailed 1D core-collapse simulations have brought new insights on the final fate of massive stars, which are in contrast to commonly used parametric prescriptions. In this work, we explore the implications of these results to the formation of coalescing black-hole (BH) – neutron-star (NS) binaries, such as the candidate event GW190426_152155 reported in GWTC-2. Furthermore, we investigate the effects of natal kicks and the NS's radius on the synthesis of such systems and potential electromagnetic counterparts linked to them. Synthetic models based on detailed core-collapse simulations result in an increased merger detection rate of BH-NS systems ($\sim 2.3\,\mathrm{yr}^{-1}$), 5 to 10 times larger than the predictions of "standard" parametric prescriptions. This is primarily due to the formation of low-mass BH via direct collapse, and hence no natal kicks, favored by the detailed simulations. The fraction of observed systems that will produce an electromagnetic counterpart, with the detailed supernova engine, ranges from 2–25%, depending on uncertainties in the NS equation of state. Notably, in most merging systems with electromagnetic counterparts, the NS is the first-born compact object, as long as the NS's radius is $\lesssim 12\,\mathrm{km}$. Furthermore, core-collapse models that predict the formation of low-mass BHs with negligible natal kicks, such as the ones from detailed core-collapse studies, increase the detection rate of GW190426_152155-like events to $\sim 0.6\,\mathrm{yr}^{-1}$; with an associated probability of electromagnetic counterpart $\leq 10\%$ for all supernova engines. However, increasing the production of direct-collapse low-mass BHs also increases the synthesis of binary BHs, over-predicting their measured local merger density rate. In all cases, models based on detailed core-collapse simulation predict a ratio of BH-NSs to binary BHs merger rate density that is at least twice as high as other prescriptions.

Keywords: Gravitational waves – Stars: black holes – Stars: neutron – Supernovae: general – Stars: massive – Binaries

1. INTRODUCTION

The recently released catalogue of the LIGO Scientific and Virgo Collaboration (LVC), GWTC-2, includes for the first time an event, GW190426_152155, classified as a black hole (BH) – neutron star (NS) merger (Abbott et al. 2020a). In addition, GW190814, an extreme mass-ratio merger event, has an estimated mass of $2.59^{+0.08}_{-0.09}$ for the lower-mass compact object, making it unclear whether it is a binary BH (BBH) or a BH–NS (BHNS) merger (Abbott et al. 2020b). Due to the relatively low significance of GW190426_152155 and the unclear nature of GW190814, no BHNS merger rate density was estimated based on GWTC-2 (Abbott et al. 2020c), with

* jaime.roman@etu.unige.ch

the older estimates from GWTC-1 setting only an upper limit of $< 610\,\mathrm{Gpc^3\,yr^{-1}}$ (Abbott et al. 2019). Nevertheless, taking into account that the first half of the LVC's third observing run (O3a) included 177.3 days of data suitable for coincident analysis and assuming 1 or 2 detections, one can estimate a detection rate of $\sim$2–4 $\mathrm{yr^{-1}}$.

The first detection of a binary NS merger was accompanied by an electromagnetic counterpart (EMC), which was observed in the whole electromagnetic spectrum as a kilonova and a short Gamma-ray burst (Abbott et al. 2017b,a). The merger of a BH with a NS is also expected to be accompanied by a similar EMC, if the tidal disruption radius of the NS is outside the innermost stable circular orbit (ISCO) of the BH. The maximum mass of a non-spinning BH for this to happen, assuming a $1.4\,\mathrm{M_\odot}$ NS, is $\sim$3.5 $\mathrm{M_\odot}$, with the exact value depending on the adopted NS equation of state (e.g. Capano et al. 2020). If, however, the BH is spinning, then the ISCO moves closer to the BH and the corresponding BH mass limit becomes as high as $\sim 20\,\mathrm{M_\odot}$ for a maximally spinning BH (see Foucart et al. 2018), vastly increasing the probability of an electromagnetic counterpart.

Under the assumption of efficient angular momentum transport in the interior of stars, the first-born compact object in a binary is expected to be formed with negligible spin (Fragos & McClintock 2015; Qin et al. 2018). This is because as the progenitor star expands to become a supergiant, most of its angular momentum is transported to its outer layers, which are then removed via winds and Roche-lobe overflow. On the other hand, the immediate progenitor of the second-born compact object, in the isolated binary formation channels, is a stripped helium (He) star in a close orbit with its first-born compact-object companion. There, the He-star has a chance to be spun up via tides, and thus give rise to a compact object with a significant spin (e.g., Van den Heuvel & Yoon 2007; Qin et al. 2018; Bavera et al. 2020a,b). Hence, the only way to have a highly spinning BH in a BHNS system is to have the NS be the first-born compact object, which will then tidally spin up the BH's progenitor star.

Coalescing BHNSs formed via isolated binary evolution are thought to be sufficiently abundant, with theoretical estimates of their merger rate density covering the whole range of 0.1–1000 $\mathrm{Gpc^3\,yr^{-1}}$ (Giacobbo & Mapelli 2018; Belczynski et al. 2020; Drozda et al. 2020). Among them, however, BHNSs in which the NS is the first-born system should be rare for two main reasons: (i) the initially more massive primary star is typically the progenitor of the BH which tends to form first, and (ii) even if binary interactions reverse the pre-core-collapse mass of the primary and secondary, kicks imparted on newly-born NSs (Hobbs et al. 2005), which are typically higher than those on BHs, tend to disrupt the binary when the system is in a wide orbit, as is typically the case when the first compact object is formed.

The details of the general statements above depend crucially on the physics of core-collapse and compact object formation. The vast majority of binary population synthesis studies use the "rapid" and "delayed" mechanisms (Fryer et al. 2012) to prescribe the fate of massive stars. Both of them are parametric descriptions of the convection-enhanced supernova (SN) engine driven by neutrino losses (see Herant et al. 1994). In contrast to the "dealayed", the "rapid" prescription predicts a mass gap between BHs and NSs due to stronger convection which allows instabilities to grow rapidly and produces more energetic SN explosions. Furthermore, both mechanisms predict a unique boundary in the core mass of the pre-core-collapse star that leads to the formation of a BH or a NS, above or below that boundary respectively.

Detailed 1D core-collapse simulations, on the other hand, show that there is no unique boundary in the core mass of the pre-core-collapse star that transitions between the formation of NSs and BHs. Instead, these studies find successive islands of successful and failed explosions leading to the formation of NSs and BHs via direct collapse (e.g., Pejcha & Thompson 2015; Sukhbold et al. 2016; Ertl et al. 2020; Patton & Sukhbold 2020; Schneider et al. 2020; Ugliano et al. 2012; O'Connor & Ott 2011). This is the result of the non-monotonic behaviour between the central carbon-burning phase and the final core properties, linked to the convective episodes developed during the burning phase (e.g. Sukhbold et al. 2018). Another significant difference between these more recent calculations and the "rapid" and "delayed", is in the formation of BHs via successful explosions and significant fall-back. Whereas in the "rapid" and "delayed" prescriptions there is a wide range of pre-core-collapse core masses that lead to the formation of BHs via accretion of fall-back mass from a successful explosion. Detailed 1D simulations find that these cases are very rare and virtually all BHs are formed via direct collapse. The latter becomes important in the context of population synthesis studies, where the natal kicks imparted on BHs are most often normalized to the fraction of fall-back mass, while BHs formed via direct collapse receive no kick (e.g., Belczynski et al. 2008).

In this work we explore the effects of the core-collapse mechanism on the formation of coalescing BHNSs, such as GW190426_152155, and their potential observability as electromagnetic transients. For the first time we consider a core-collapse prescription based on detailed 1D core-collapse simulations and study the effect of non-

monotonic stellar explodability, with respect to the pre-collapse mass of the core. Finally, we discuss what we can learn in the future in terms of formation pathways, core-collapse physics and NS equation of state, once observations put a firmer constraints on the BHNS merger rate density and the fraction of them accompanied by an EMC.

2. METHODS

We use the software framework `POSYDON` (Fragos et al. 2021, in prep.) to evolve populations of binaries for this study. `POSYDON` allows, among other functionalities, to couple parametric population synthesis codes with such models for different phases of a binary's evolution. In this work, we coupled the parametric code `COSMIC` (Breivik et al. 2019) to evolve binaries from the zero-age main sequence (ZAMS) until the first compact object strips its companion; and a grid of ∼170,000 detailed binary evolution models ran with the `MESA` code (Paxton et al. 2011, 2013, 2015, 2018, 2019) to follow the final evolutionary phase of a BHNS progenitor, i.e. that of a binary consisting of stripped He-star and a compact object in a close orbit. This allows us to accurately predict the spin of the second born compact object (see Bavera et al. 2020b, for a detailed description of the simulation setup).

For all populations evolved, we consider the following initial binary properties: the mass of the most massive star m_1 is distributed by the Kroupa (2001) initial mass function in a mass range of $[5, 150]\,\mathrm{M}_\odot$. We assume the mass ratio at birth is distributed uniformly as $q \in [0, 1]$ (Sana et al. 2012). The initial orbital periods are distributed in the range $[0.4, 10^{5.5}]$ days as in Sana et al. (2012), extending the distribution for for low values with a flat distribution as in Bavera et al. (2020b). All binaries have zero birth eccentricity, and we assume an overall binary fraction $f_b = 0.7$ (see Bavera et al. 2020b; Sana et al. 2012). For each model, we evolve 5×10^6 binaries per metallicity, for 10 different metallicity values, $Z \in$ [0.0001, 0.0002, 0.0003, 0.0006, 0.001 , 0.0018, 0.0031, 0.0055, 0.0098, 0.0174]. This corresponds to a total stellar mass of $\sim 5 \times 10^8 \mathrm{M}_\odot$ for the underlying stellar population, per metallicity bin; and corresponds to a fraction of the initial mass function of $f_{\rm corr} = 0.212$.

We use the same set of physical model parameters as in Bavera et al. (2020b). Specifically, we adopt mass-transfer (MT) stability according to the values of $q_{\rm crit}$ as described there. Unstable MT is modelled with the classical $\alpha_{\rm CE}-\lambda$ common-envelope (CE) formalism (van den Heuvel 1976; Webbink 1984), where assume an $\alpha_{\rm CE} = 1$ and $\lambda_{\rm CE}$ fits from Claeys et al. (2014) without taking into account the ionization energy of the envelope. Moreover, we assume the pessimistic common-envelope scenario, namely all systems that start common envelope evolution with a star in the Hertzsprung's gap are considered to merge due to the unsuccessful envelope ejection (Ivanova & Taam 2004; Belczynski et al. 2007). The electron-capture SN (ECSN) prescription described in Podsiadlowski et al. (2004) is used, which maps Helium-core masses in the range $[1.4, 2.5]\,\mathrm{M}_\odot$ to remnant baryonic mass $1.38\,\mathrm{M}_\odot$ as in Giacobbo & Mapelli (2020). For the pair-instability and pulsational pair-instability SNe we consider the prescription by Marchant et al. (2019) which limits the maximum BH mass at $\sim 44\,\mathrm{M}_\odot$.

To model the core-collapse, in addition to the "rapid" and "delayed" mechanisms by Fryer et al. (2012), we implement a new prescription based on detailed 1D core-collapse simulations. We use the publicly available data on pre-SN models and the remnant properties produced by the N20 engine of Sukhbold et al. (2016). We consider the He-core mass of the star at the pre-SN phase, $M_{\rm He,\,core}$, to predict the remnant's baryonic mass, $M_{\rm rem,\,bar}$, taking into account whether the SN explosion is predicted to be successful or not. We only consider the successful explosions that will produce NSs, as the ones that produce BHs are rare. A complete description of the implementation of the engine in our population synthesis study is in the Appendix A.

For each mechanism three populations were produced with the assumptions described in Table 1. Our fiducial model, called STANDARD, considers a Maxwellian distribution with $\sigma_{\rm ECSN} = 20$ km/s for kicks imparted on NS formed from ECSN and $\sigma_{\rm FeCCSN} = 265$ km/s for Fe core-collapse SN (FeCCSN); the kicks in this model are fallback-weighted as in Fryer et al. (2012). The FULL-ECSN-KICK model considers that NS formed from ECSN and FeCCSN receive the same kicks ($\sigma_{\rm ECSN} = \sigma_{\rm FeCCSN} = 265$ km/s). Finally, the NO-BH-KICK model considers BHs receive no natal kicks, even if they are not produced by direct collapse.

While the evolution of binaries from ZAMS to the formation of a compact object plus a He-star was computed with the parametric code `COSMIC`, the last phase of the evolution of a close compact object plus He-star was performed by interpolating a grid constituted by 172,570 detailed `MESA` binary evolution models. This last step, allows us to derive accurate predictions of the second-born compact object's spin (Qin et al. 2018; Bavera et al. 2020a). The details on the grid and its interpolation are discussed in Appendix B.

We extract the BHNS mergers, systems that merge due to gravitational wave radiation emission in less time than the current age of the Universe, and compute the number of BHNS mergers per unit mass. The

Table 1. Definition of the models used to evolve the binary stellar populations.

Model name	$\sigma_{\rm ECSN}$ [km/s]	$\sigma_{\rm FeCCSN}$ [km/s]	NS kicks	BH kicks
STANDARD	20	265	fallback weighted	fallback weighted
FULL-ECSN -KICK	265	265	fallback weighted	fallback weighted
NO-BH -KICK	20	265	fallback weighted	No kicks

merging timescale, by gravitational wave radiation, is computed according to Peters (1964). Adopting the ΛCDM cosmology, we distribute the BHNS across the metallicity-dependent cosmic star-formation history; assuming metallicities follow a truncated log-normal distribution with standard deviation 0.5 dex around the empirical mean metallicity function derived by Madau & Fragos (2017). We compute the merger rate densities and detection rates as in Bavera et al. (2020b), assuming the simulated "mid high/late low" LVC O3 detector sensitivity (Abbott et al. 2018), by considering a single detector signal-to-noise ratio threshold > 8 that simulates a 2 network detector (see Barrett et al. 2018). Finally, we compute the fraction of events that produce EMCs. We assume that a BHNS merger will produce an electromagnetic counterpart if the mass outside the BH ISCO after the merger, $M^{\rm ejecta}$, is greater than zero. The detailed description on the computation of $M^{\rm ejecta}$ is described in Appendix C. Taking into account uncertainties in NS equation of state (e.g. Capano et al. 2020; Chatziioannou 2020, and references there in), we consider three different constant values for the NS readius, $R_{\rm NS} \in [11, 12, 13]$ km, to compute $M^{\rm ejecta}$ and, hence, predict the occurrence EMCs.

3. RESULTS

3.1. *The theoretical merger rates of BHNS*

The left panel of Fig. 1 shows the number of BHNS mergers per unit mass, namely the total evolved mass corrected by the initial mass function and the binary fraction, in terms of metallicity for the STANDARD model. In that panel the dashed lines represent the whole population of BHNSs for each core-collapse mechanism. While the shaded regions represent the subset of systems that will reproduce an EMC. The upper boundary of a shaded region is defined for $R_{\rm NS} = 13$ km, while the lower boundary is delimited by considering $R_{\rm NS} = 11$ km. By distributing the mergers on the cosmic star-formation history we find the merger density history in terms of redshift, shown in the right panel of Fig. 1. There, we see that the local merger density for all core-collapse mechanisms is consistent with the upper limit reported on GWTC-1 (see Abbott et al. 2019) and plotted as the gray shaded region. Furthermore, these results are consistent with other recent population synthesis studies (e.g. Giacobbo & Mapelli 2018; Neijssel et al. 2019; Drozda et al. 2020; Belczynski et al. 2020).

We show the detection rate of BHNSs for simulated O3 LIGO/Virgo sensitivity for all the populations in the upper panels of Fig. 2. The estimated BHNSs detection rates are plotted with unfilled diamonds, while the filled symbols represent the subset of systems that will produce an electromagnetic counterpart for different values of $R_{\rm NS}$. All the rates shown on the upper panels of Fig. 2 are also summarized in Table 2. The most striking feature of Fig. 2 is that detection rates from the N20 engine (the purple diamonds) are higher by a factor of $\sim 2-10$ with respect to the predictions for the "rapid" and "delayed" mechanisms in all models. This is because the N20 engine predicts the formation of low mass BHs by direct collapse. These BHs do not receive natal kicks, that would otherwise disrupt the binary, and they are produced by less massive stars whose number is favored by the initial mass function.

To explore further the role of BH natal kicks on the detection rates of BHNS mergers, we focus on the NO-BH-KICK model (upper right panel in the Fig. 2). The assumption of no BH kicks increases the detection rate for the "delayed" mechanism by a factor of ∼4 with respect to the STANDARD model. In contrast the rate for the "rapid" prescription does not have a significant increase between models. This difference is due to the fact that the pre-core-collapse He-core mass, $M_{\rm He,\,core}$, range where the "rapid" mechanism predicts BH formation via partial fall-back and non-zero kick velocities is smaller ($M_{\rm He,\,core} \in [9, 13]{\rm M}_\odot$) compared to the "delayed" mechanism ($M_{\rm He,\,core} \in [6, 13]{\rm M}_\odot$), as shown in Fig. 3. Furthermore, since this region is located at higher $M_{\rm He,\,core}$ values for the "rapid" mechanism, the steepness of the initial mass function results, in any case, in less BHs with non-zero kicks. Despite all of this, the N20 engine produces more than twice as many BHNS mergers, even when only considering the NO-BH-KICK models. This is explained by the fact that low mass BHs formed by the "delayed" mechanism in the NO-BH-KICK model are not produced by direct collapse. Meaning that only a fraction (as low as $\sim 30\%$) of the pre-SN mass of their progenitors will collapse and the orbit of the binary needs to be readjusted even if the BH does not receive a natal kick. The readjustment of the

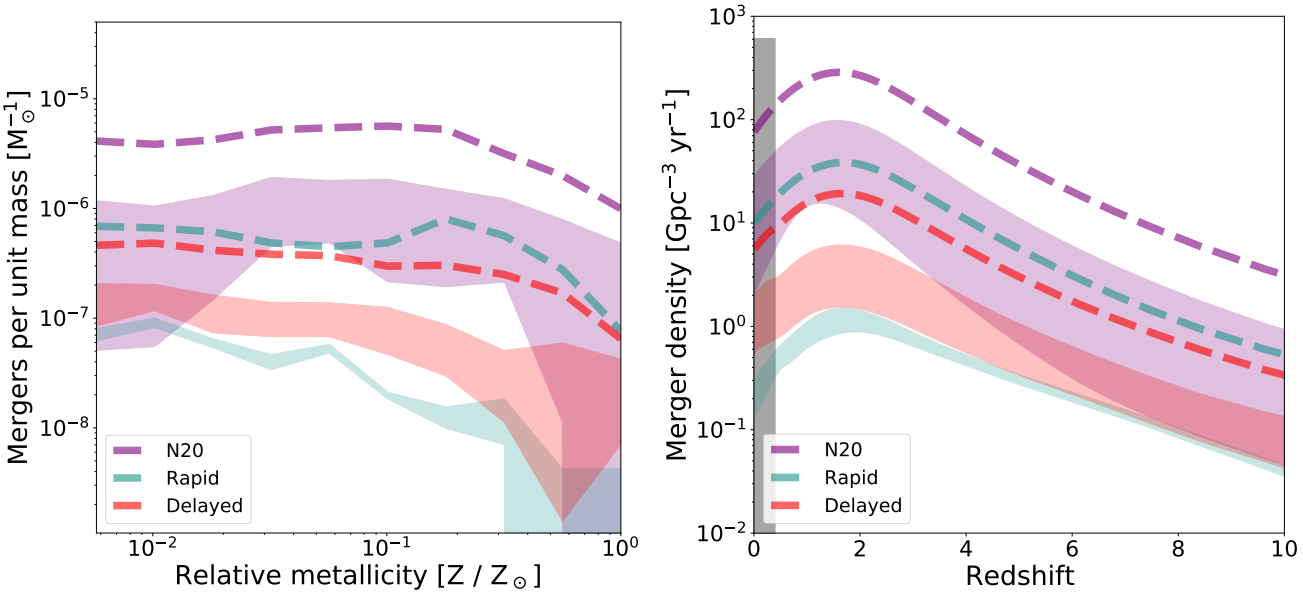

Figure 1. BHNS mergers per unit mass in terms of relative metallicity to the solar value (left) and its translation to the merger density rate history as a function of redshift z (right) for the STANDARD model. The dashed lines represent the whole population of BHNSs mergers, while the contours enclose the number of electromagnetic counterparts by considering the three values of NS radius as described in Sec. 2; where upper and lower boundaries of the contours are the predictions taking into account $R_{\rm NS} = 13$km and $R_{\rm NS} = 11$km respectively. In the right panel, the gray vertical bar is the 90% confidence interval of local BHNS merger density rate reported in GWTC-1.

orbit in such cases reduces the number of BHNS mergers with respect the amount expected if the low mass BHS were produced by direct collapse.

3.2. *Rates of electromagnetic counterparts linked to BHNS mergers*

The predicted rates of EMCs considering three different values for NS radii, 11, 12 and 13 km, are shown in the upper panels of Fig. 2 with the triangle, square and circle markers, respectively. The predicted EMC rates for the N20 engine in the STANDARD population remains higher than the ones predicted using the other core-collapse prescriptions and, for all NS radii. Note, however, that it is the "delayed" mechanism that has the largest fraction of BHNS mergers with EMCs. This can be understood from the fact that among the three mechanisms considered, it is only the "dalayed" that can produce low-mass BHs, in the range of $2.5 - 3.5\,{\rm M}_\odot$. These low-mass BHs, even when they are non-spinning, are able to disrupt a relatively compact ($\lesssim 12$ km) NS outside their ISCO.

For the "rapid" and N20 engines and assuming NS radii $\lesssim 12$ km, BHNS mergers with EMCs are only produced when the NS is the first-born compact-object which subsequently tidally spins up the BH progenitor star and produces a higly spinning BH. The bottom row of Fig. 2 shows that although the fraction of first-born NS in BHNS merges, for the "rapid" and N20 engines, is $\sim 10\%$, the fraction of BHNS mergers with EMC that had a first-born NS is close to 100%.

The formation of the first compact object occurs in a wide orbit. Since the probability of the binary to remain bound after a SN kick scales with the ratio of the orbital velocity over the kick velocity (Kalogera 1996), a NS formed via FeCCSN, that typically receives a natal kick of hundreds of km s^{-1}, will disrupt the binary. With the N20 engine, however, as BHs may be produced by $M_{\rm He,\,core}$ as low as $\sim 4.5\,{\rm M}_\odot$, a non-negligible fraction of first-born NSs may come from progenitors with low enough pre-core-collapse $M_{\rm He,\,core}$ that results to an ECSN. The low kicks associated with ECSN increase significantly the survivability of these relatively rare binary configurations.

The FULL-ECSN-KICK models allow us to quantitatively explore the role of ECSN on the formation of BHNS with EMCs, which as explained above affects models with the N20 engine. Increasing the ECSN kick velocities has primarily an impact on the systems with first-born NSs rather than the whole population of BHNSs. From Table 2, we see that the BHNS merger detection rate slightly decrease for N20 from STANDARD to FULL-ECSN-KICK. Contrarily, such rates for the other core-collapse mechanisms remain similar, as the fraction of first-born NSs from ECSN is negligible

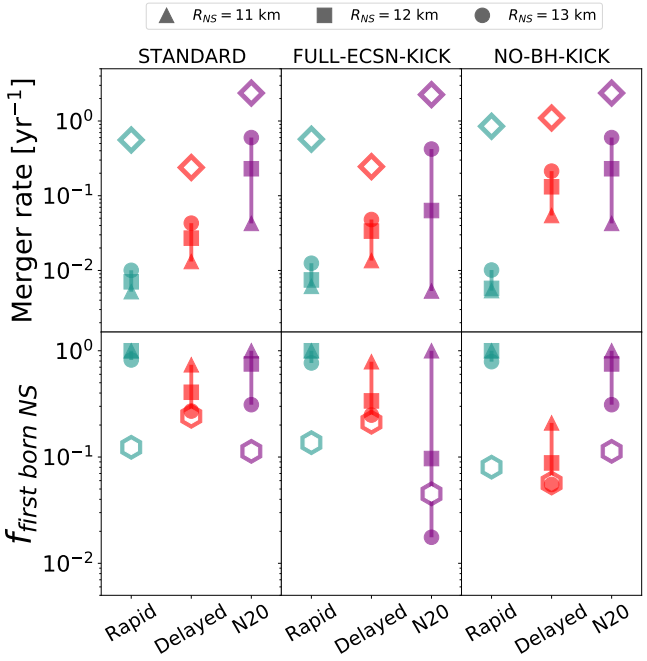

Figure 2. Predicted merger rate of BHNS populations for O3a (upper panels) and the fraction of systems with first-born NSs $f_{\text{first born NS}}$ (lower panels). This predicted rates are plotted each core-collapse mechanism mechanisms and each model respectively, see labels. In the upper panels, the unfilled diamonds indicate the predicted detection rate for the whole population of BHNSs, while the filled markers indicate the EMCs considering different NS radii, see legend above. In the lower panels, the unfilled hexagons denote the detected fraction of BHNSs with first-born NSs with respect to the whole population of detected mergers, while the filled markers are the fractions of EMC from systems with firstborn NSs with respect to all of them, see legend above for the shape description.

in those cases[1]. Most importantly though, high ECSN kicks decrease the rate of BHNS with EMCs, in the N20 engine by a factor of ~ 4, for NS with radii $\lesssim 12$ km, see Table 2.

Current constraints on the NS equation of state indicate that NS radii can be as high as 13 km (see Capano et al. 2020; Chatziioannou 2020, and references therein). This parameter has a crucial impact on the population of EMCs from BHNS mergers where the BH is the first-born compact object. In such cases the BH spin is negligible; therefore a $R_{\rm NS}$ on the high end of the allowed parameter space is crucial to achieve a NS tidal disruption (Foucart et al. 2018). In fact, for $R_{\rm NS} = 13$ km the maximum BH mass that can tidally disrupt a NS is below the minimum BH mass predicted by the N20 engine. This allows for BHNS mergers with EMCs originating from binaries with non-spinning, first-born BHs and translates to an increase by a factor of 15 and 2.5 of EMCs, compared to assumed $R_{\rm NS}$ of 11 km and 12 km, respectively.

[1] In fact, we do see a very small increase in the detection rate for those models, which is however above the Poisson error of our simulations. This very small increase may be explained by the fact that in those models some of the second-born NSs are produced by ECSN. Imparting a larger natal kick on those NSs will not disrupt the binary as its orbit is very close at that point in time, but will impart some eccentricity in the post-SN orbit which may shorten the time to merge due to GW emission. This in turn can have a small effect on the overall rate.

3.3. *The role of the SN engine on the synthesis of GW190426_152155-like events*

The estimation for the BHNS merger rate form the LVC O3a run, $2 - 4$ yr^{-1}, is closer to the results from the N20 engine on all populations, as well as for the "delayed" for the NO-BH-KICK population, favoring the engines that predict low-mass BHs with negligible SN kicks. We compute the merger rate of systems like GW190426_152155, the only observed system labeled as a BHNS merger (Abbott et al. 2020a), by considering the 90% confidence intervals of the event's measured total mass, chirp mass and the effective spin. Those results are shown in Table 2 as the population "GW190426-like". The detection of a system similar to GW190426_152155 is favored by the N20 engine in all populations and by the "delayed" mechanism in the NO-BH-KICK populations; while the "rapid" prescription predicts a rate of only $0.03 - 0.12$ yr^{-1}, indicating that the detection of an event with GW190426_152155-like properties is rare in such case.

We also computed the rate of GW190426_152155-like systems that will produce an EMC (population "GW190426 EMC" in Table 2). In all cases the rates of EMCs linked to events like GW190426_152155 are less than 0.1 yr^{-1}, translating to a probability of $0 - 25$ % of EMCs per observed system. This low rate agrees with the lack of an electromagnetic signal linked to the observed event.

3.4. *Comparison to BBH merger density rates*

In order to compare our models with measurements with better constraints, we compute the local BBH and BHNS merger density rates as shown in Table 3 of Appendix C. The N20 STANDARD model, which increases the likelihood of events like GW190426_152155, over-predicts the measured BBH merger density, as reported by Abbott et al. (2020a), by ~ 5 times compared to the other collapse mechanisms which over-predict the rate by < 2 times. Again, this is because the N20 engine assumes BH are born without kicks. Similarly,

Table 2. The predicted local detection rates, $\mathcal{R}^{\rm det}$ (detected mergers per year), for the LVC's third observing run. Results here are for the whole population of BHNSs (All) the electromagnetic counterparts (EMC), and for systems like GW190426_152155 (GW190426-like), and the subset of GW190425-like systems those systems that will produce an electromagnetic counterpart (GW190426 EMC) for each physical model.

		STANDARD			FULL-ECSN-KICK			NO-BH-KICK		
Population	$R_{\rm NS}$	$\mathcal{R}^{\rm det}_{\rm N20}$	$\mathcal{R}^{\rm det}_{\rm Rapid}$	$\mathcal{R}^{\rm det}_{\rm Delayed}$	$\mathcal{R}^{\rm det}_{\rm N20}$	$\mathcal{R}^{\rm det}_{\rm Rapid}$	$\mathcal{R}^{\rm det}_{\rm Delayed}$	$\mathcal{R}^{\rm det}_{\rm N20}$	$\mathcal{R}^{\rm det}_{\rm Rapid}$	$\mathcal{R}^{\rm det}_{\rm Delayed}$
All		2.37	0.56	0.24	2.25	0.57	0.25	2.37	0.85	1.10
EMC	11km	0.04	0.01	0.01	0.01	0.01	0.01	0.04	0.01	0.05
	12km	0.23	0.01	0.03	0.06	0.01	0.03	0.23	0.01	0.13
	13km	0.6	0.01	0.04	0.42	0.01	0.05	0.6	0.01	0.21
GW190426-like		0.56	0.03	0.06	0.55	0.05	0.07	0.56	0.12	0.42
GW190426 EMC	11km	0.00	0.00	0.00	0.00	0.00	0.00	0.00	0.00	0.00
	12km	0.01	0.00	0.00	0.00	0.00	0.00	0.01	0.00	0.00
	13km	0.05	0.00	0.02	0.03	0.00	0.01	0.05	0.00	0.03

"rapid" and "delayed" NO-BH-KICK over-predict the local BBH rate by the same amount. When looking carefully at the BBH's progenitor evolutionary pathway we find that it is the CE channel that produces the majority of these merging BBHs contributing to the observed local rate density. If, indeed, BHs are born without a kick then the models are overproducing the systems going trough and surviving CE and therefore the population of BBH, as we expect the mixture of all formation channels to contribute on the whole population, which is what recent studies suggests (e.g. Kruckow et al. 2016; Pavlovskii et al. 2017; Klencki et al. 2020).

4. DISCUSSION AND CONCLUSIONS

In this work, we present population synthesis models exploring the role of core-collapse prescriptions, including results of detailed 1D core-collapse simulations, and the associated natal kicks, on the observability of BHNS systems, events like GW190426_152155, and their EMCs. A parametric code has been used to model binary stars from ZAMS until the first-born compact object strips its companion star. From that stage, the evolution of the system until the formation of the second-born compact object was followed by detailed binary-evolution models, allowing for accurate predictions of the spin of the second-born compact object. The latter is critical in determining whether the NS will be tidally disrupted by the BH, as spinning BHs increase significantly the probability of EMCs produced by BHNS mergers.

We find that the N20 SN engine predicts BHNS merger rates higher by an order of magnitude compare to the "rapid" and "delayed" mechanisms. This is a consequence of the formation of low-mass BHs by direct collapse that are predicted by SN engines from detailed core-collapse simulations, such as N20. In addition, the N20 engine predicts higher rates of EMCs while being consistent with the lack of observations of such events to date.

Our models show that future, more stringent constraints on the NS equation of state will allow to distinguish between formation sub-channels of BHNSs. A mean NS radius closer to 11 km would indicate that the information from future observations of BHNS EMCs is linked to systems where the NS is the first-born compact object; as compact NSs are harder to disrupt by non-spinning BHs. In contrast, evidence of a larger radii (such as Abbott et al. 2020; Riley et al. 2019) will help us to infer information of low-mass BHs and possible natal kicks linked to their formation.

Finally, we find that the synthesis of events like GW190426_152155 is favored by SN engines that produce low-mass BHs with small or no SN kicks. The N20 engine predicts a rate of $\sim 0.6\,{\rm yr}^{-1}$ for such event, one order of magnitude higher than the predictions by the "rapid" and "delayed" mechanisms in the STANDARD model, and 30% larger than the result from "delayed" with the NO-BH-KICK model. However, such mechanisms overestimate the BBH local merger density rate, with most of the predicted merging BBHs going through the CE evolution channel. Detailed binary evolution calculations suggest that the source of this apparent discrepancy may be the parametrizations of mass-transfer stability criteria and envelope binding energy estimates, which, as implemented in most binary population synthesis codes may, severely over-predict the number of BBH progenitor systems going through and surviving the CE phase.

ACKNOWLEDGMENTS

The authors thank Vicky Kalogera and Christopher Berry for their thoughtful comments. This work was supported by the Swiss National Science Foundation Professorship grant (project number PP00P2 176868; PI Tassos Fragos). JRG is supported by UNIGE, JJA and SC are supported by CIERA and AD, JGSP, and KAR are supported by the Gordon and Betty Moore Foundation through grant GBMF8477. KK received funding from the *European Research Council under the European Union's Seventh Framework Programme (FP/2007-2013) / ERC Grant Agreement n. 617001. YQ acknowledges funding from the Swiss National Science Foundation under grant P2GEP2_188242. The computations were performed in part at the University of Geneva on the Baobab and Lesta computer clusters and at Northwestern University on the Trident computer cluster (the latter funded by the GBMF8477 grant). All figures were made with the free Python modules Matplotlib (Hunter 2007). This research made use of Astropy,[2] a community-developed core Python package for Astronomy (Robitaille et al. 2013; Price-Whelan et al. 2018).*

REFERENCES

Abbott, B., Abbott, R., Abbott, T., et al. 2020, The Astrophysical Journal Letters, 892, L3

Abbott, B. P., Abbott, R., Abbott, T. D., et al. 2019, Physical Review X, 9, 031040, doi: 10.1103/PhysRevX.9.031040

—. 2017a, ApJL, 848, L13, doi: 10.3847/2041-8213/aa920c

Abbott, B. P., Abbott, R., Abbott, T. D., Acernese, F., & Ackley, K. e. a. 2017b, ApJL, 848, L12, doi: 10.3847/2041-8213/aa91c9

Abbott, B. P., Abbott, R., Abbott, T., et al. 2018, Living Reviews in Relativity, 21, 3

Abbott, R., Abbott, T. D., Abraham, S., et al. 2020a, arXiv e-prints, arXiv:2010.14527. https://arxiv.org/abs/2010.14527

—. 2020b, ApJL, 896, L44, doi: 10.3847/2041-8213/ab960f

—. 2020c, arXiv e-prints, arXiv:2010.14533. https://arxiv.org/abs/2010.14533

Barrett, J. W., Gaebel, S. M., Neijssel, C. J., et al. 2018, Monthly Notices of the Royal Astronomical Society, 477, 4685

Bavera, S. S., Fragos, T., Qin, Y., et al. 2020a, A&A, 635, A97, doi: 10.1051/0004-6361/201936204

Bavera, S. S., Fragos, T., Zevin, M., et al. 2020b, arXiv e-prints, arXiv:2010.16333. https://arxiv.org/abs/2010.16333

Belczynski, K., Kalogera, V., Rasio, F. A., et al. 2008, ApJS, 174, 223, doi: 10.1086/521026

Belczynski, K., Taam, R. E., Kalogera, V., Rasio, F. A., & Bulik, T. 2007, ApJ, 662, 504, doi: 10.1086/513562

Belczynski, K., Klencki, J., Fields, C. E., et al. 2020, A&A, 636, A104, doi: 10.1051/0004-6361/201936528

Breivik, K., Coughlin, S. C., Zevin, M., et al. 2019, arXiv preprint arXiv:1911.00903

Capano, C. D., Tews, I., Brown, S. M., et al. 2020, Nature Astronomy, 1

Chatziioannou, K. 2020, arXiv preprint arXiv:2006.03168

Claeys, J., Pols, O., Izzard, R., Vink, J., & Verbunt, F. 2014, Astronomy & Astrophysics, 563, A83

Drozda, P., Belczynski, K., O'Shaughnessy, R., Bulik, T., & Fryer, C. 2020, arXiv preprint arXiv:2009.06655

Ertl, T., Woosley, S. E., Sukhbold, T., & Janka, H.-T. 2020, The Astrophysical Journal, 890, 51

Foucart, F., Hinderer, T., & Nissanke, S. 2018, Physical Review D, 98, 081501

Fragos, T., & McClintock, J. E. 2015, ApJ, 800, 17, doi: 10.1088/0004-637X/800/1/17

Fryer, C. L., Belczynski, K., Wiktorowicz, G., et al. 2012, The Astrophysical Journal, 749, 91

Giacobbo, N., & Mapelli, M. 2018, Monthly Notices of the Royal Astronomical Society, 480, 2011

—. 2020, The Astrophysical Journal, 891, 141

Herant, M., Benz, W., Hix, W. R., Fryer, C. L., & Colgate, S. A. 1994, The Astrophysical Journal, 435, 339

Hobbs, G., Lorimer, D., Lyne, A., & Kramer, M. 2005, Monthly Notices of the Royal Astronomical Society, 360, 974

Hunter, J. D. 2007, Computing in science & engineering, 9, 90

Ivanova, N., & Taam, R. E. 2004, ApJ, 601, 1058, doi: 10.1086/380561

Kalogera, V. 1996, The Astrophysical Journal, 471, 352

Klencki, J., Nelemans, G., Istrate, A. G., & Chruslinska, M. 2020, arXiv e-prints, arXiv:2006.11286. https://arxiv.org/abs/2006.11286

Kroupa, P. 2001, Monthly Notices of the Royal Astronomical Society, 322, 231

[2] http://www.astropy.org

Kruckow, M. U., Tauris, T. M., Langer, N., et al. 2016, A&A, 596, A58, doi: 10.1051/0004-6361/201629420

Madau, P., & Fragos, T. 2017, The Astrophysical Journal, 840, 39

Marchant, P., Renzo, M., Farmer, R., et al. 2019, The Astrophysical Journal, 882, 36

Neijssel, C. J., Vigna-Gómez, A., Stevenson, S., et al. 2019, MNRAS, 490, 3740, doi: 10.1093/mnras/stz2840

O'Connor, E., & Ott, C. D. 2011, The Astrophysical Journal, 730, 70

Patton, R. A., & Sukhbold, T. 2020, arXiv preprint arXiv:2005.03055

Pavlovskii, K., Ivanova, N., Belczynski, K., & Van, K. X. 2017, MNRAS, 465, 2092, doi: 10.1093/mnras/stw2786

Paxton, B., Bildsten, L., Dotter, A., et al. 2011, ApJS, 192, 3, doi: 10.1088/0067-0049/192/1/3

Paxton, B., Cantiello, M., Arras, P., et al. 2013, ApJS, 208, 4, doi: 10.1088/0067-0049/208/1/4

Paxton, B., Marchant, P., Schwab, J., et al. 2015, ApJS, 220, 15, doi: 10.1088/0067-0049/220/1/15

Paxton, B., Schwab, J., Bauer, E. B., et al. 2018, ApJS, 234, 34, doi: 10.3847/1538-4365/aaa5a8

Paxton, B., Smolec, R., Schwab, J., et al. 2019, ApJS, 243, 10, doi: 10.3847/1538-4365/ab2241

Pejcha, O., & Thompson, T. A. 2015, The Astrophysical Journal, 801, 90

Peters, P. C. 1964, Physical Review, 136, B1224

Podsiadlowski, P., Langer, N., Poelarends, A., et al. 2004, The Astrophysical Journal, 612, 1044

Price-Whelan, A. M., Sipőcz, B., Günther, H., et al. 2018, The Astronomical Journal, 156, 123

Qin, Y., Fragos, T., Meynet, G., et al. 2018, Astronomy & Astrophysics, 616, A28

Riley, T. E., Watts, A. L., Bogdanov, S., et al. 2019, The Astrophysical Journal Letters, 887, L21

Robitaille, T. P., Tollerud, E. J., Greenfield, P., et al. 2013, Astronomy & Astrophysics, 558, A33

Sana, H., De Mink, S., de Koter, A., et al. 2012, Science, 337, 444

Schneider, F., Podsiadlowski, P., & Müller, B. 2020. https://arxiv.org/abs/2008.08599

Sukhbold, T., Ertl, T., Woosley, S., Brown, J. M., & Janka, H.-T. 2016, The Astrophysical Journal, 821, 38

Sukhbold, T., Woosley, S. E., & Heger, A. 2018, ApJ, 860, 93, doi: 10.3847/1538-4357/aac2da

Ugliano, M., Janka, H., Arcones, A., & Marek, A. 2012, in Astronomical Society of the Pacific Conference Series, Vol. 453, Advances in Computational Astrophysics: Methods, Tools, and Outcome, ed. R. Capuzzo-Dolcetta, M. Limongi, & A. Tornambè, 91

Van den Heuvel, E., & Yoon, S.-C. 2007, Astrophysics and Space Science, 311, 177

van den Heuvel, E. P. J. 1976, in IAU Symposium, Vol. 73, Structure and Evolution of Close Binary Systems, ed. P. Eggleton, S. Mitton, & J. Whelan, 35

Webbink, R. F. 1984, ApJ, 277, 355, doi: 10.1086/161701

Zevin, M., Spera, M., Berry, C. P., & Kalogera, V. 2020, The Astrophysical Journal Letters, 899, L1

APPENDIX

A. IMPLEMENTATION OF THE N20 ENGINE

We consider the stellar models by Sukhbold et al. (2016), evolved in solar metallicity, to describe the baryonic mass of the final remnant. We apply the prescription deduced from their results to stars with different metallicity as we aim to explore the effect of the average non-monotonic explodability trends rather than predicting accurately the compactness of the core. Such non-monotonic trend is preserved for different metallicities (Patton & Sukhbold 2020).

Fig. 3 shows the baryonic remnant mass as a function of $M_{\rm He,\,core}$, for the N20 engine (Sukhbold et al. 2016), the "rapid" and "delayed" mechanisms (Fryer et al. 2012). On the same figure, each stellar model, collapsed with N20, is classified as a successful explosion or a direct collapse depending if the supernova shock is reactivated by the neutrino flux or not, respectively. In the case of the N20 engine, to predict if a star will undergo a successful explosion or direct collapse, we extract the result in terms of the nearest-neighbor of the star's $M_{\rm He,\,core}$ with respect to the results from Sukhbold et al. (2016). If the star is classified as a progenitor of a successful explosion, its $M_{\rm rem,\,bar}$ will have the same value of the remnant baryonic mass associated to the point with the nearest value for $M_{\rm He,\,core}$. Otherwise, if the star is classified as a progenitor of a direct collapse, then $M_{\rm rem,\,bar}$ is equal to the pre-SN mass of the star.

To determine if the remnant is a BH or a NS, we calculate the remnant gravitational mass considering the neutrino loss as in Zevin et al. (2020), where, here, the maximum mass loss by neutrinos is considered to be $0.5\,{\rm M}_\odot$. If the remnant gravitational mass is larger than $2.5\,{\rm M}_\odot$ we assume that the compact object is a BH, else a NS. For this work, the successful explosions that produce massive remnants that will end up as BHs were not considered, as such cases are rare (from Sukhbold et al. 2016, only 5 models from 105 successful explosions form a BH for the N20 engine).

B. GRIDS OF DETAILED NS/BH–HE-STAR MODELS

We use subset of detailed `MESA` models of BH–He-star systems of Bavera et al. (2020b) which we extend to cover the NS star and low He-star masses. These models treat the compact object as a point mass, hence, they can be applied to simulate NS–He-star systems. For simplicity, we assumed that all physical assumptions made in the BH–He-star regime applies also to the NS–He-star regime too, including an Eddington mass-accretion rate

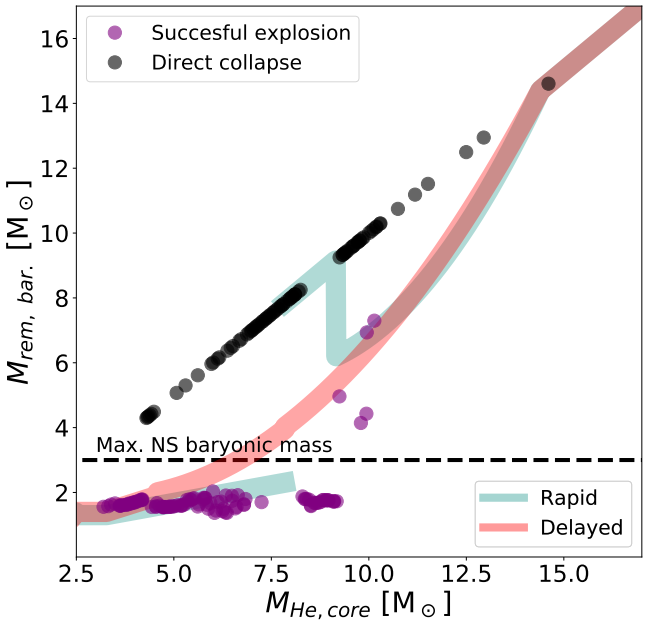

Figure 3. Baryonic remnant mass, $M_{\rm rem,\,bar}$, as a function of the He-core mass at the pre-supernova phase, $M_{\rm He,\,core}$, from N20 engine of Sukhbold et al. (2016) (circles); and for the "rapid" and "delayed" (red and turquoise thick lines) mechanisms from Fryer et al. (2012). For illustrative purposes we assume that the mass of the carbon-oxygen core is $0.76 M_{\rm He,\,core}$. Each model exploded with the N20 engine is labeled as a successful explosion or direct collapse (i.e. failed explosion), with purple and black colors, respectively. The black dashed line represents the maximum NS baryonic mass, in our model, which corresponds to a maximum NS gravitational mass of $2.5\,{\rm M}_\odot$.

limit of $\dot{M}_{\rm Edd} = 7.36\times10^{-8}\,(M_{\rm BH/NS}/{\rm M}_\odot)\ {\rm M}_\odot{\rm yr}^{-1}$. The selected subset of the original grid covers the initial parameter space of 10 metallicities, Z, in the log-range $[0.0001, 0.0174]$ in log-steps of $\Delta\log_{10}(Z)\simeq 0.25$, 11 BH masses in the log-range $[2.5, 54.4]\,{\rm M}_\odot$, 17 He-star masses in the log-range $[8, 80]\,{\rm M}_\odot$ and 20 binary periods in the log-range $[0.09, 8]$ days. We extend this dataset to cover 10 NS masses in the log-range $[1, 2.28]\,{\rm M}_\odot$, 26 He-star masses where 20 are in the log-range $[3, 12]\,{\rm M}_\odot$, 5 in the range $[3, 7]\,{\rm M}_\odot$ (only for BH masses) and one at $2.5\,{\rm M}_\odot$ and an extra period at 0.04 days. The smallest He-star mass is chosen to guarantee coverage of the parameter space down to white dwarf formation, while the maximum He-star mass and smallest orbital period were chosen to include the full range of compact object – He-star systems produced by our `COSMIC` models. The wide orbital period range ensures that we cover the pa-

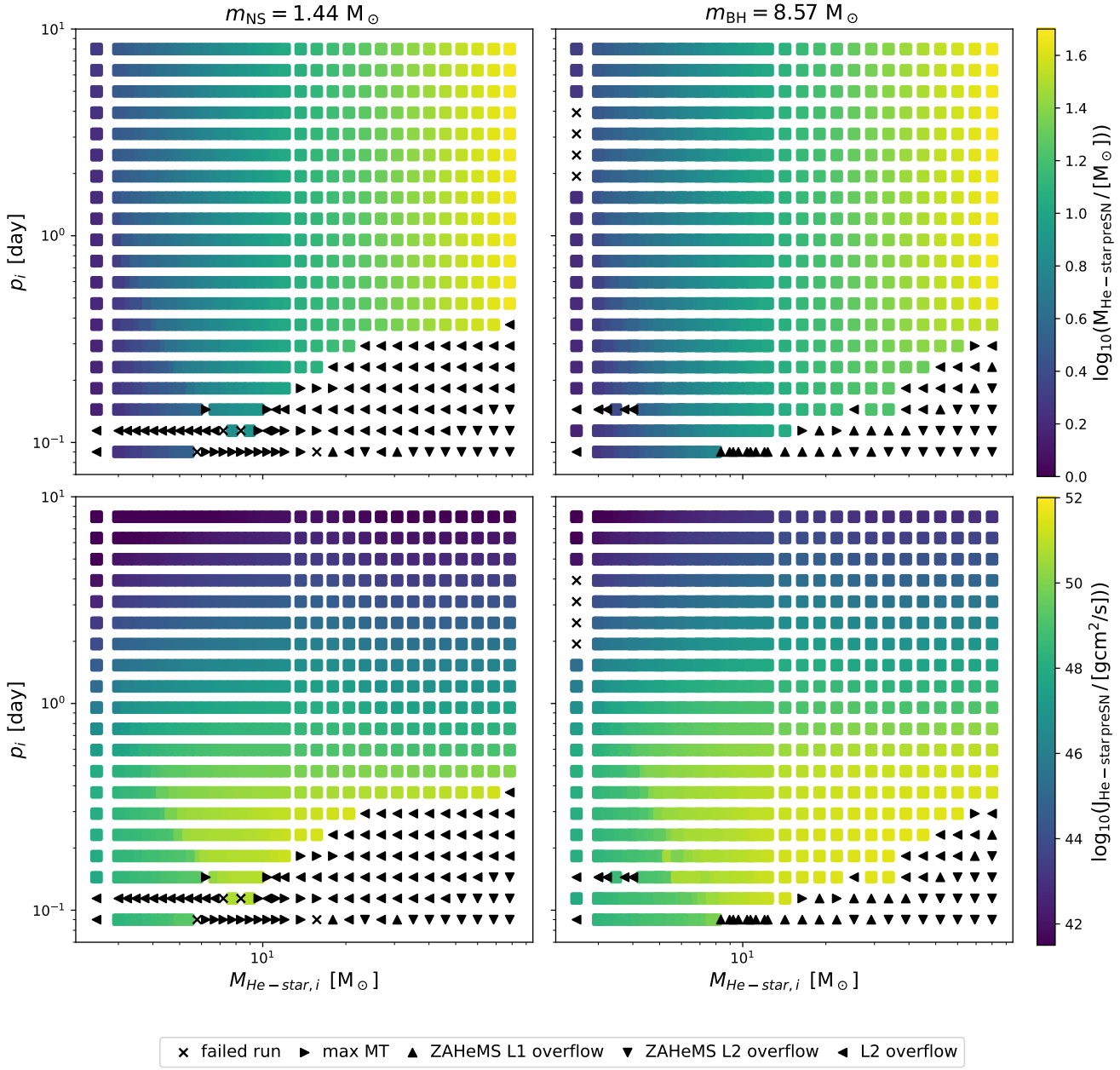

Figure 4. Two 2D slices of the 4D `MESA` grid for $Z = 0.00312$, and $m_{\rm NS} = 1.44\,{\rm M}_\odot$ and $m_{\rm BH} = 8.57\,{\rm M}_\odot$, respectively. The final He-star mass and angular momentum pre-SN values are colored for each successful track according to each color bar. Each successful run stopped because of carbon depletion or off-centre neon ignition (square markers), while other termination flags are shown in the bottom legend. For visualisation purposes, the models at $p = 0.04$ days were excluded from the figure which for these slices all runs resulted in ZAHeMS L1 or L2 Roche-lobe overflow.

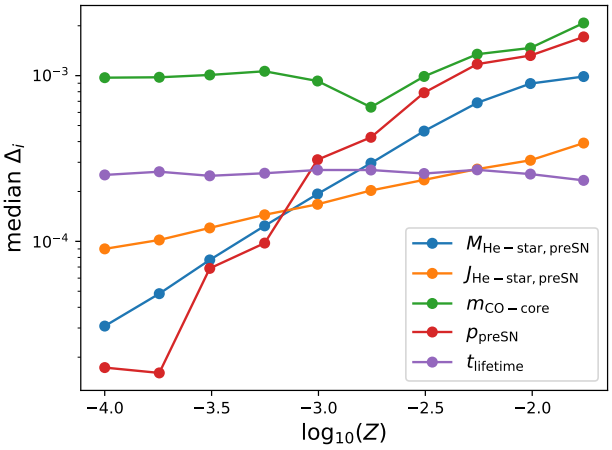

Figure 5. Median relative error as a function of metallicity of the log-transformed and re-scaled five quantities A_i: the He-star mass (blue), angular momentum (orange) and its carbon-oxygen core mass (green) before the supernova, the orbital period before the supernova (red) and the lifetime of the binary (green).

rameter space well past the point where any BHNS or BBH system will merge within the age of the Universe. The original grid subset consisting of 37,400 models was therefore extended to a total of 172,740 `MESA` models. The fraction of failed `MESA` runs vary from 0.6% to 1.5% depending on metallicity. In Figure 4 we show two 2D slices of the 4D parameter space sliced at $Z = 0.00312$ and, $m_{\rm NS} = 1.44\,{\rm M}_\odot$ and $m_{\rm BH} = 8.57\,{\rm M}_\odot$, respectively, where we indicate with a color the final He-star mass and angular momentum given initial orbital separation and He-star masses of the detailed simulations.

These grids were used to determine the final outcomes and final parameters of the late-end evolution stage of the binary systems through linear interpolation. Each metallicity is interpolated separately. We want to interpolate five quantities A_i: the He-star mass, angular momentum and its carbon-oxygen core mass, orbital period before the supernova, as well as the lifetime of the binary. Before interpolating each quantity, we log-transformed it and re-scale it to the interval $[-1, 1]$ to assign equal weight to each dimension during the interpolation. The interpolation itself relies on building a Delaunay triangulation of the input data points followed by barycentric linear interpolation over the vertices of the (hyper)triangle containing the location of interest. We test the accuracy of the interpolation computing relative errors of a test grid which is constituted of an arbitrary fraction (5%) of runs which we excluded from the train sample. To obtain a consistent estimate, we repeat this experiment 10 times for each metallicity and each interpolated quantity. If a point of an nonphysical region of the parameter space (e.g. zero age He main sequence (ZAHeMS) overflow, max MT or L2 overflow) is correctly interpolated to NaN (not a number) by the algorithm, we consider it to have a zero relative error. On the other hand, if a point is wrongly interpolated to NaN, we consider it to have a relative error of 1. In Fig. 5 we report the median relative error of each transformed and rescaled quantity $X_i \equiv \log_{10}(A_i)^{[-1,1]}$ as $\Delta_i = |X_{\rm true,i} - X_{\rm interp,i}|/X_{\rm true,i}$. Because of the large sample of data-points we find small interpolation errors. Most of the quantities show an increase of median relative error as a function of metallicity. This is caused by the fact that at high metallicity the grids show a less-linear behaviour than at low metallicity. This non-linearity is a direct consequence of He-star stellar winds which, in our models, scale as $(Z/Z_\odot)^{0.85}$. In these systems, the He-stars lose a non-negligible amount of mass and the orbits widen considerably. Moreover, NS–He-star in tight orbits have higher probability to initiate a mass transfer case due to the He-star tendency to expand more than at low metallicity.

C. BHNS ELECTROMAGNETIC COUNTERPART CONDITION

We consider the model of Foucart et al. (2018) to determine the mass of the NS that remains outside the BH ISCO after the tidal disruption, as

$$\left[\max\left(\alpha\frac{1-2C_{\rm NS}}{\eta^{1/3}} - \beta\hat{R}_{\rm ISCO}\frac{C_{\rm NS}}{\eta} + \gamma, 0\right)\right]^{\delta} M_{\rm NS} \quad \text{(C1)}$$

where α=0.406, β=0.139, γ=0.255, δ=1.761, $\hat{R}_{\rm ISCO} \equiv \frac{R_{\rm ISCO}c^2}{GM_{\rm BH}}$, $C_{\rm NS} = Q\frac{R_{\rm ISCO}}{\hat{R}_{\rm ISCO}R_{\rm NS}}$, $Q = \frac{M_{\rm BH}}{M_{\rm NS}}$, $\eta = Q/(1+Q)^2$. Here, $M_{\rm BH}$ is the mass of the BH, $M_{\rm NS}$ the mass of the NS, and $R_{\rm NS}$ is the radius of the NS. In this work we explore three values for $R_{\rm NS}$, as 11, 12, 13, km.

D. BBH AND BHNS MERGER RATE DENSITIES

To better understand the implication of the model physical modelling assumptions done in this study, we also calculate the BBH merger rate densities. The latter are much better constrained by GWTC-2, which finds the local merger rate density of BBH to be $23.9^{+14.9}_{-8.6}\,{\rm Gpc}^{-3}{\rm yr}^{-1}$ (Abbott et al. 2020c). The BBH rate densities rising from the common envelope (CE) and stable mass transfer (SMT) channels given the same set of assumption made here (STANDARD-Delayed) are presented in Bavera et al. (2020b). For an one-to-one comparison with BHNS rate densities of the different core-collapse and kick prescriptions considered in this work, we summarise the rate densities of BBHs and

Table 3. Predicted local rate density $\mathcal{R}$ (in units of $\mathrm{Gpc^{-1}yr^{-1}}$). Results here are shown for the common envelope (CE) and stable-mass transfer (SMT) channels sepratatly and combined for, both, the populations of BBH and BHNS for each model.

		STANDARD			FULL-ECSN-KICK			NO-BH-KICK		
	Channel	$\mathcal{R}_{\rm N20}$	$\mathcal{R}_{\rm Rapid}$	$\mathcal{R}_{\rm Delayed}$	$\mathcal{R}_{\rm N20}$	$\mathcal{R}_{\rm Rapid}$	$\mathcal{R}_{\rm Delayed}$	$\mathcal{R}_{\rm N20}$	$\mathcal{R}_{\rm Rapid}$	$\mathcal{R}_{\rm Delayed}$
BBH	CE	162.78	81.13	39.13	162.06	81.64	38.55	162.78	129.41	167.31
	SMT	39.73	33.05	31.27	41.43	33.6	31.08	39.73	31.38	26.36
	CE + SMT	202.51	114.18	70.4	203.49	115.24	69.63	202.51	160.79	193.67
BHNS	CE	74.96	7.28	2.59	66.36	7.59	2.93	74.96	14.66	30.18
	SMT	2.28	2.86	3.06	2.99	3.12	2.88	2.28	1.88	2.49
	CE + SMT	77.24	10.14	5.65	69.35	10.71	5.81	77.24	16.54	32.67

BHNS for the CE and SMT channels as well as their combination in Table 3.

In contrast to the original study done by Bavera et al. (2020b) the new models differ in the following ways. First, we simulated a (i) metallicity range with one third the resolution of Bavera et al. (2020b) but verified that this does not have a noticeable impact on the rate estimates by reanalysing Bavera et al. (2020b) models with the same metallicity sample resolution. Second, (ii) the core-collapse of the secondary is assumed to be direct where in the original study we followed the core-collapse of the `MESA` He-star profile at SN accounting for disk formation. When an accretion disk is formed only a fraction of its mass falls to the hole (see Appendix D in Bavera et al. 2020b) which, in practice, means that here tidally spin up highly spinning BHs are slightly more massive compared to Bavera et al. (2020b). Moreover, we only (iii) interpolate binary properties before the supernova while in the original work, which only investigated the delayed collapse mechanism, also interpolated the second born compact object mass and spin (the former has, on average, a larger interpolation error compared to the pre SN mass, see Fig. E.1 of Bavera et al. (2020b)). Finally, we also updated the condition which determines BH formation. We assume (iv) a BH is formed if the compact object gravitational mass is larger than the maximum NS mass ($2.5\,\mathrm{M_\odot}$) while in the previous work we assumed that a collapsing star leading to the formation of a BH had to have at least a carbon-oxygen core mass and a remnant baryonic mass of $3\,\mathrm{M_\odot}$ in order to form a BH (as $0.5\,\mathrm{M_\odot}$ where assumed to be lost because of neutrinos during the collapse of the proto-NS). We verified that this change has no impact on the results.

In Table 3 we can see that the STANDARD-delayed model predicts a comparable rate density $\sim 39\,\mathrm{Gpc^{-3}yr^{-1}}$ and $\sim 31\,\mathrm{Gpc^{-3}yr^{-1}}$ for CE and SMT channels, respectively. These values are in agreement with Bavera et al. (2020b) where the small deviation in the numbers is given by the changes explained in the previous paragraph. On the other hand, STANDARD-N20 overpredicts the CE+SMT rates compared to the observations by a factor of at least 5. This is because in the N20 engine all BHs are formed thorough direct collapse, without a kick. When assuming no natal kicks (other than the readjustment of the orbits because of neutrino mass loss) the NO-BH-KICK models with rapid and delayed predict similar rates to the N20 engine meaning that the discrepancy is a direct product of no BH kicks. In fact, if nature would to agree with the N20 engine, then the formation of merging BBH thorough the CE+SMT over-predicts the systems surviving these channels. When looking more carefully at the rate densities of these models we see that is the CE channel to over-predicting the constrains from merging BBH in the local universe. As recent studies have shown, the classical $\alpha_{\rm CE} - \lambda$ parameterization of CE and mass transfer stability parameterization ($q_{\rm crit}$) might over-predict the number of systems going thorugh and surviving this evolutionary phase (e.g. Kruckow et al. 2016; Pavlovskii et al. 2017; Klencki et al. 2020).

C.1.3 Impact on the current field of research

The main results of this project can be summarised in two parts. First, adopting newer core-collapse simulation results in the binary population synthesis leads to predicting one order of magnitude larger BH-NS merger rates than Fryer et al. (2012) prescriptions currently employed in other studies literature (e.g., Giacobbo & Mapelli 2018; Belczynski et al. 2020; Drozda et al. 2020). The increased rate is explained by the increased production of low-mass BHs produced by direct collapse. These results also positively impact the relative fraction of BH-NS EM counterparts. Second, assuming a stiff NS equation of states, our model predicts that BH-NS EM counterparts are linked to systems where the NS is the first-born compact object as such compact NSs (of $\sim 11\,\mathrm{km}$ in radius) are harder to disrupt by non-spinning BHs as discussed in Section 4.2. We now discuss how the results of Román-Garza et al. (2021) have impacted the current field of research.

The recent work of Fragione (2021) studied EM counterpart rates to BH-NS mergers considering different NS equations of state and BH birth spins as a proxy for angular-momentum transport. Fragione (2021) finds that only models with large BH birth spins ($|\vec{\chi}| \gtrsim 0.8$) would lead to more than 50% BH-NS mergers associated with an EM counterpart. Such results would invoke the existence of inefficient angular-momentum transport, which is currently excluded from asteroseismic observations and by GW observations, see Sections 1.3.1.1 and 3.1, respectively. The model variation of Fragione (2021) where the BH birth spins are small (inefficient angular-momentum transport) leads to similar results of Román-Garza et al. (2021) for both soft and stiff NS equation of state with one caveat. Fragione (2021) does not model the tidal spin-up of close NS-WR systems formed from the CE channel missing the EM channel for BH-NS mergers presented in Román-Garza et al. (2021).

Motivated by the lack of EM counterpart observation following the detection of BH-NS mergers GW200105 and GW200115 by the LVK collaboration (Abbott et al. 2021b), by follow up searches (e.g., Anand et al. 2021; Gompertz et al. 2020a,b; Kasliwal et al. 2020; Page et al. 2020), and by the lack of relevant research other than Román-Garza et al. (2021) on the BH-NS channel with fast-spinning BHs systems where the NS is first-born, recently, Hu et al. (2022) made a follow-up study. These authors corroborated Román-Garza et al. (2021) results that the mentioned channel can lead to highly rotating BHs and, hence, have an EM counterpart associated with BH-NS mergers. The lack of the observation of any EM counterparts to GW200105 and GW200115 is consistent with the model predictions of Román-Garza et al. (2021), which predicts the relative fraction of first-born NSs with tidal spun-up BHs to be small. However, Hu et al. (2022) points out that the relative fraction of the discussed BH-NS channel depends not only on the studied supernovae mechanism and natal kick magnitude uncertainties but also on other astrophysical uncertainties, which should be the subject of further investigation in the future (see, e.g., Broekgaarden et al. 2021a; Chattopadhyay et al. 2021).

A final interesting remark to make is that, in contrast to BBH formation, Román-Garza et al. (2021) showed that the BH-NS merger rate is approximately independent of metallicity up to $\sim 0.2 Z_{\odot}$ above, which then declines (see left panel of Figure 1 in Román-Garza et al. 2021). In contrast, BBH merger rates are strongly suppressed at large metallicities, see Chapter 2. Such difference rises from the fact that BH-NS systems typically form from lower mass stars than BBH mergers. Hence, these BH-NS

systems do not experience a boost in formation yields at low metallicities compared to the BBH mergers. These results are discussed in detail in Broekgaarden et al. (2021b) and are a direct consequence of the metallicity dependence of stellar-wind mass loss of massive stars.

Acknowledgements

I want to express my deepest gratitude to *Tassos*. You have been an excellent mentor to me, shaping my scientific intuition, driving my curiosity, and always pushing me to achieve more. Without your guidance and vision, I would not have been able to thrive in this new field of research. The successful scientific productivity I had during my Ph.D. would not have been possible without you. Other than a mentor, you have been a kind friend, and I will always be indebted to all that you did for me.

Thank you to all the group members who made my Ph.D. years enjoyable discussing science: *Devina, Jaime, Konstantinos, Manos, Nam,* and *Zepei*. A special word of gratitude to *Konstantinos*, who proofread this manuscript and made multiple suggestions on how to improve its quality.

I would also like to thank all the people I had the privilege to collaborate with during the past years: *Aldo, Chase, Christopher, Coan, Enrico, Gabriele, Giulia, Ilya, Jeff, Luke, Maya, Mike, Pablo, Simon, Toni, Vicky,* and *Ying*, all of whom helped me to become a better scientist. I also want to mention other members of the POSYDON collaboration that contributed to making my Ph.D. more enjoyable: *Aaron, Aggelos, Goce, Juanga, Kyle, Meng, Petter, Philipp, Prabin, Scotty, Shamal,* and *Xu*.

Moving on the personal side, I would like to thank my family and friends who always supported me during my studies well before the Ph.D. years.

One last special person I would like to thank is *Aurélie*, the love of my life, who shared this experience with me since the beginning, always supporting me. Without your love and encouragement, this journey would not have been possible.

I almost forgot ... a special thank you also to *Pixel*, who sat next to me on the kitchen table, keeping me company in the two years I worked from home during the COVID-19 pandemic.

Acronyms list

AGN	active galactic nuclei
BH	black hole
BBH	binary black hole
BNS	binary neutron star
CE	common envelope
CHE	chemically homogeneous evolution
EM	electromagnetic (counterpart)
CPU	central processing unit
GW	gravitational wave
GWTC	gravitational-wave transient catalog
HMXB	high-mass X-ray binaries
ISCO	innermost stable circular orbit
LVK	LIGO-Virgo-KAGRA (Collaboration)
LGRB	long-duration gamma-ray burst
NS	neutron star
BNS	binary neutron star
PBH	primordial black hole
PPISN	pulsational pair-instability supernova
PISN	pair-instability supernova
SMT	stable mass transfer
SGWB	stochastic gravitational-wave background
WR	Wolf-Rayet (star)

Bibliography

Aasi, J., Abadie, J., Abbott, B. P., et al. 2015a, Classical and Quantum Gravity, 32, 115012

Aasi, J., Abbott, B. P., Abbott, R., et al. 2015b, Classical and Quantum Gravity, 32, 074001

Abbott, B. P., Abbott, R., Abbott, T. D., et al. 2016a, Classical and Quantum Gravity, 33, 134001

Abbott, B. P., Abbott, R., Abbott, T. D., et al. 2016b, Physical Review X, 6, 041015

Abbott, B. P., Abbott, R., Abbott, T. D., et al. 2016c, Phys. Rev. Lett., 116, 131102

Abbott, B. P., Abbott, R., Abbott, T. D., et al. 2016d, Phys. Rev. Lett., 116, 061102

Abbott, B. P., Abbott, R., Abbott, T. D., et al. 2016e, Phys. Rev. Lett., 116, 241102

Abbott, B. P., Abbott, R., Abbott, T. D., et al. 2019a, ApJ, 882, L24

Abbott, B. P., Abbott, R., Abbott, T. D., et al. 2019b, Physical Review X, 9, 031040

Abbott, B. P., Abbott, R., Abbott, T. D., et al. 2020a, ApJ, 892, L3

Abbott, B. P., Abbott, R., Abbott, T. D., et al. 2020b, Classical and Quantum Gravity, 37, 055002

Abbott, B. P., Abbott, R., Abbott, T. D., et al. 2017a, ApJ, 848, L13

Abbott, B. P., Abbott, R., Abbott, T. D., et al. 2017b, Phys. Rev. Lett., 119, 161101

Abbott, B. P., Abbott, R., Abbott, T. D., et al. 2017c, ApJ, 848, L12

Abbott, B. P., Abbott, R., Abbott, T. D., et al. 2018, Phys. Rev. Lett., 120, 091101

Abbott, R., Abbott, T. D., Abraham, S., et al. 2021a, Physical Review X, 11, 021053

Abbott, R., Abbott, T. D., Abraham, S., et al. 2021b, ApJ, 915, L5

Abbott, R., Abbott, T. D., Abraham, S., et al. 2021c, ApJ, 913, L7

Abbott, R., Abbott, T. D., Abraham, S., et al. 2020c, Phys. Rev. D, 102, 043015

Abbott, R., Abbott, T. D., Abraham, S., et al. 2020d, Phys. Rev. Lett., 125, 101102

Abbott, R., Abbott, T. D., Abraham, S., et al. 2020e, ApJ, 896, L44

Abbott, R., Abbott, T. D., Abraham, S., et al. 2020f, ApJ, 900, L13

Abbott, R., Abbott, T. D., Acernese, F., et al. 2021d, arXiv e-prints, arXiv:2108.01045

Abbott, R., Abbott, T. D., Acernese, F., et al. 2021e, arXiv e-prints, arXiv:2111.03606

Abbott, R., Abbott, T. D., Acernese, F., et al. 2021f, arXiv e-prints, arXiv:2111.03634

Acernese, F., Agathos, M., Agatsuma, K., et al. 2015, Classical and Quantum Gravity, 32, 024001

Acernese, F., Agathos, M., Ain, A., et al. 2022, arXiv e-prints, arXiv:2205.01555

Adams, T., Buskulic, D., Germain, V., et al. 2016, Classical and Quantum Gravity, 33, 175012

Affeldt, C., Danzmann, K., Dooley, K. L., et al. 2014, Classical and Quantum Gravity, 31, 224002

Ajith, P. 2011, Phys. Rev. D, 84, 084037

Akutsu, T., Ando, M., Arai, K., et al. 2019, Nature Astronomy, 3, 35

Akutsu, T., Ando, M., Araya, A., et al. 2020, in Journal of Physics Conference Series, Vol. 1342, Journal of Physics Conference Series, 012014

Ali-Haïmoud, Y., Kovetz, E. D., & Kamionkowski, M. 2017, Phys. Rev., D96, 123523

Allen, B., Anderson, W. G., Brady, P. R., Brown,

D. A., & Creighton, J. D. E. 2012, Phys. Rev. D, 85, 122006

Alonso, D., Contaldi, C. R., Cusin, G., Ferreira, P. G., & Renzini, A. I. 2020, Phys. Rev. D, 101, 124048

Amaro-Seoane, P., Audley, H., Babak, S., et al. 2017, arXiv e-prints, arXiv:1702.00786

Anand, S., Coughlin, M. W., Kasliwal, M. M., et al. 2021, Nature Astronomy, 5, 46

Ando, M. & TAMA Collaboration. 2002, Classical and Quantum Gravity, 19, 1409

Antonini, F., Gieles, M., & Gualandris, A. 2019, MNRAS, 486, 5008

Antonini, F. & Merritt, D. 2012, ApJ, 745, 83

Antonini, F. & Perets, H. B. 2012, ApJ, 757, 27

Antonini, F. & Rasio, F. A. 2016, ApJ, 831, 187

Antonini, F., Toonen, S., & Hamers, A. S. 2017, ApJ, 841, 77

Arca Sedda, M. 2020, ApJ, 891, 47

Arca Sedda, M., Li, G., & Kocsis, B. 2021, A&A, 650, A189

Arcier, B. & Atteia, J.-L. 2022, arXiv e-prints, arXiv:2204.05013

Ashton, G., Hübner, M., Lasky, P. D., et al. 2019, ApJS, 241, 27

Askar, A., Szkudlarek, M., Gondek-Rosińska, D., Giersz, M., & Bulik, T. 2017, MNRAS, 464, L36

Aso, Y., Michimura, Y., Somiya, K., et al. 2013, Phys. Rev. D, 88, 043007

Atal, V., Blanco-Pillado, J. J., Sanglas, A., & Triantafyllou, N. 2022, arXiv e-prints, arXiv:2201.12218

Atwood, W. B., Abdo, A. A., Ackermann, M., et al. 2009, ApJ, 697, 1071

Aubin, F., Brighenti, F., Chierici, R., et al. 2021, Classical and Quantum Gravity, 38, 095004

Babak, S., Hewitson, M., & Petiteau, A. 2021, arXiv e-prints, arXiv:2108.01167

Balaji, S., Silk, J., & Wu, Y.-P. 2022, arXiv e-prints, arXiv:2202.00700

Banerjee, S. 2017, MNRAS, 467, 524

Banerjee, S. 2021, MNRAS, 503, 3371

Banerjee, S., Baumgardt, H., & Kroupa, P. 2010, MNRAS, 402, 371

Barcons, X., Barret, D., Decourchelle, A., et al. 2017, Astronomische Nachrichten, 338, 153

Barkat, Z., Rakavy, G., & Sack, N. 1967, Phys. Rev. Lett., 18, 379

Bartos, I., Kocsis, B., Haiman, Z., & Márka, S. 2017, ApJ, 835, 165

Batta, A. & Ramirez-Ruiz, E. 2019, arXiv e-prints, arXiv:1904.04835

Bavera, S. 2021, MESA Black-hole-Wolf-Rayet binary inlists used in "The impact of mass-transfer physics on the observable properties of field binary black hole populations", Zenodo

Bavera, S. S., Fishbach, M., Zevin, M., Zapartas, E., & Fragos, T. 2022a, arXiv e-prints, arXiv:2204.02619

Bavera, S. S., Fragos, T., Qin, Y., et al. 2020, A&A, 635, A97

Bavera, S. S., Fragos, T., Zapartas, E., et al. 2022b, A&A, 657, L8

Bavera, S. S., Fragos, T., Zevin, M., et al. 2021a, A&A, 647, A153

Bavera, S. S., Franciolini, G., Cusin, G., et al. 2022c, A&A, 660, A26

Bavera, S. S., Zevin, M., & Fragos, T. 2021b, Research Notes of the American Astronomical Society, 5, 127

Belczynski, K., Bulik, T., & Bailyn, C. 2011, ApJ, 742, L2

Belczynski, K., Bulik, T., & Fryer, C. L. 2012, arXiv e-prints, arXiv:1208.2422

Belczynski, K., Done, C., & Lasota, J. P. 2021, arXiv e-prints, arXiv:2111.09401

Belczynski, K., Heger, A., Gladysz, W., et al. 2016a, A&A, 594, A97

Belczynski, K., Holz, D. E., Bulik, T., & O'Shaughnessy, R. 2016b, Nature, 534, 512

Belczynski, K., Kalogera, V., & Bulik, T. 2002, ApJ, 572, 407

Belczynski, K., Kalogera, V., Rasio, F. A., et al. 2008, ApJS, 174, 223

Belczynski, K., Klencki, J., Fields, C. E., et al. 2020, A&A, 636, A104

Belczynski, K., Ryu, T., Perna, R., et al. 2017, MNRAS, 471, 4702

Bellovary, J. M., Mac Low, M.-M., McKernan, B., & Ford, K. E. S. 2016, ApJ, 819, L17

Benacquista, M. J. & Downing, J. M. B. 2013, Living Reviews in Relativity, 16, 4

Bird, S., Cholis, I., Muñoz, J. B., et al. 2016, Phys. Rev. Lett., 116, 201301

Biscoveanu, S., Callister, T. A., Haster, C.-J., et al. 2022, arXiv e-prints, arXiv:2204.01578

Biscoveanu, S., Isi, M., Varma, V., & Vitale, S. 2021, Phys. Rev. D, 104, 103018

Bisnovatyi-Kogan, G. S. 1993, Astronomical and Astrophysical Transactions, 3, 287

Biwer, C. M., Capano, C. D., De, S., et al. 2019, PASP, 131, 024503

Blaauw, A. 1961, Bull. Astron. Inst. Netherlands, 15, 265

Blinnikov, S., Dolgov, A., Porayko, N. K., & Postnov, K. 2016, JCAP, 1611, 036

Boersma, J. 1961, Bull. Astron. Inst. Netherlands, 15, 291

Bond, J. R., Arnett, W. D., & Carr, B. J. 1984, ApJ, 280, 825

Bouffanais, Y., Mapelli, M., Santoliquido, F., et al. 2021a, MNRAS, 507, 5224

Bouffanais, Y., Mapelli, M., Santoliquido, F., et al. 2021b, MNRAS, 505, 3873

Bowyer, S., Byram, E. T., Chubb, T. A., & Friedman, H. 1965, Science, 147, 394

Brandt, W. N., Podsiadlowski, P., & Sigurdsson, S. 1995, MNRAS, 277, L35

Breivik, K., Chatterjee, S., & Larson, S. L. 2017, ApJ, 850, L13

Breivik, K., Coughlin, S., Zevin, M., et al. 2020, ApJ, 898, 71

Breivik, K., Rodriguez, C. L., Larson, S. L., Kalogera, V., & Rasio, F. A. 2016, ApJ, 830, L18

Broekgaarden, F. S., Berger, E., Neijssel, C. J., et al. 2021a, MNRAS, 508, 5028

Broekgaarden, F. S., Berger, E., Stevenson, S., et al. 2021b, arXiv e-prints, arXiv:2112.05763

Broekgaarden, F. S., Stevenson, S., & Thrane, E. 2022, arXiv e-prints, arXiv:2205.01693

Bromm, V. & Yoshida, N. 2011, ARA&A, 49, 373

Brott, I., de Mink, S. E., Cantiello, M., et al. 2011, A&A, 530, A115

Brown, G. E. 1995, ApJ, 440, 270

Burrows, A. & Hayes, J. 1996, Phys. Rev. Lett., 76, 352

Bustillo, J. C., Sanchis-Gual, N., Torres-Forné, A., & Font, J. A. 2021, Phys. Rev. Lett., 126, 201101

Cabero, M., Lundgren, A., Nitz, A. H., et al. 2019, Classical and Quantum Gravity, 36, 155010

Callister, T., Fishbach, M., Holz, D. E., & Farr, W. M. 2020, ApJ, 896, L32

Callister, T. A., Farr, W. M., & Renzo, M. 2021a, ApJ, 920, 157

Callister, T. A., Haster, C.-J., Ng, K. K. Y., Vitale, S., & Farr, W. M. 2021b, ApJ, 922, L5

Callister, T. A., Miller, S. J., Chatziioannou, K., & Farr, W. M. 2022, arXiv e-prints, arXiv:2205.08574

Cantiello, M., Mankovich, C., Bildsten, L., Christensen-Dalsgaard, J., & Paxton, B. 2014, ApJ, 788, 93

Capano, C. D., Tews, I., Brown, S. M., et al. 2020, Nature Astronomy, 4, 625

Carr, B., Kohri, K., Sendouda, Y., & Yokoyama, J. 2020, arXiv e-prints, arXiv:2002.12778

Carr, B. & Kühnel, F. 2020, Annual Review of Nuclear and Particle Science, 70, 355

Carr, B. J. 1975, Astrophys. J., 201, 1

Chapline, G. F. 1975, Nature, 253, 251

Chatterjee, S., Rodriguez, C. L., & Rasio, F. A. 2017, ApJ, 834, 68

Chattopadhyay, D., Stevenson, S., Hurley, J. R., Bailes, M., & Broekgaarden, F. 2021, MNRAS, 504, 3682

Chen, Z.-C. & Huang, Q.-G. 2018, Astrophys. J., 864, 61

Choksi, N. & Gnedin, O. Y. 2019, MNRAS, 488, 5409

Choksi, N., Gnedin, O. Y., & Li, H. 2018, MNRAS, 480, 2343

Christensen, N. & Meyer, R. 1998, Phys. Rev. D, 58, 082001

Christensen, N. & Meyer, R. 2001, Phys. Rev. D, 64, 022001

Christensen, N. & Meyer, R. 2022, Reviews of Modern Physics, 94, 025001

Chruslinska, M., Nelemans, G., & Belczynski, K. 2019, MNRAS, 482, 5012

Chu, Q., Kovalam, M., Wen, L., et al. 2020, arXiv e-prints, arXiv:2011.06787

Clesse, S. & García-Bellido, J. 2017, Phys. Dark Univ., 15, 142

Clesse, S. & García-Bellido, J. 2018, Phys. Dark Univ., 22, 137

Clesse, S. & Garcia-Bellido, J. 2020, arXiv e-prints, arXiv:2007.06481

Conselice, C. J., Bhatawdekar, R., Palmese, A., & Hartley, W. G. 2020, ApJ, 890, 8

Covas, P. B., Effler, A., Goetz, E., et al. 2018, Phys. Rev. D, 97, 082002

Cucchiara, A., Levan, A. J., Fox, D. B., et al. 2011, ApJ, 736, 7

Dal Canton, T., Nitz, A. H., Lundgren, A. P., et al. 2014, Phys. Rev. D, 90, 082004

Davies, G. S., Dent, T., Tápai, M., et al. 2020, Phys. Rev. D, 102, 022004

Davis, D., Areeda, J. S., Berger, B. K., et al. 2021, Classical and Quantum Gravity, 38, 135014

Dayal, P., Rossi, E. M., Shiralilou, B., et al. 2019, MNRAS, 486, 2336

de Freitas Pacheco, J. A. 2020, arXiv e-prints, arXiv:2001.09663

De Luca, V., Desjacques, V., Franciolini, G., Pani, P., & Riotto, A. 2021a, Phys. Rev. Lett., 126, 051101

De Luca, V., Franciolini, G., Pani, P., & Riotto, A. 2020a, Phys. Rev. D, 102, 043505

De Luca, V., Franciolini, G., Pani, P., & Riotto, A. 2020b, JCAP, 04, 052

De Luca, V., Franciolini, G., Pani, P., & Riotto, A. 2021b, J. Cosmology Astropart. Phys., 2021, 003

de Mink, S. E. & Mandel, I. 2016, MNRAS, 460, 3545

de Mink, S. E., Pols, O. R., & Hilditch, R. W. 2007, A&A, 467, 1181

Deng, H. 2021, JCAP, 04, 058

Dewi, J. D. M., Podsiadlowski, P., & Sena, A. 2006, MNRAS, 368, 1742

Di Carlo, U. N., Giacobbo, N., Mapelli, M., et al. 2019, MNRAS, 487, 2947

Di Carlo, U. N., Mapelli, M., Bouffanais, Y., et al. 2020a, MNRAS, 497, 1043

Di Carlo, U. N., Mapelli, M., Giacobbo, N., et al. 2020b, MNRAS, 498, 495

Dominik, M., Belczynski, K., Fryer, C., et al. 2012, ApJ, 759, 52

Dominik, M., Belczynski, K., Fryer, C., et al. 2013, ApJ, 779, 72

Dominik, M., Berti, E., O'Shaughnessy, R., et al. 2015, ApJ, 806, 263

Dooley, K. L., Leong, J. R., Adams, T., et al. 2016, Classical and Quantum Gravity, 33, 075009

Downing, J. M. B., Benacquista, M. J., Giersz, M., & Spurzem, R. 2010, MNRAS, 407, 1946

Drozda, P., Belczynski, K., O'Shaughnessy, R., Bulik, T., & Fryer, C. L. 2020, arXiv e-prints, arXiv:2009.06655

du Buisson, L., Marchant, P., Podsiadlowski, P., et al. 2020, MNRAS, 499, 5941

Eggenberger, P., Montalbán, J., & Miglio, A. 2012, A&A, 544, L4

Eggleton, P. P. 1971, MNRAS, 151, 351

Eggleton, P. P. & Kiseleva-Eggleton, L. 2002, ApJ, 575, 461

Einstein, A. 1916, Annalen der Physik, 354, 769

Einstein, A. 1918, Sitzungsberichte der Königlich Preußischen Akademie der Wissenschaften (Berlin, 154

Eldridge, J. J., Stanway, E. R., Xiao, L., et al. 2017, PASA, 34, e058

Eldridge, J. J. & Tout, C. A. 2004, MNRAS, 353, 87

Eroshenko, Y. N. 2018, J. Phys. Conf. Ser., 1051, 012010

Ertl, T., Woosley, S. E., Sukhbold, T., & Janka, H. T. 2020, ApJ, 890, 51

Farmer, R., Renzo, M., de Mink, S. E., Fishbach, M., & Justham, S. 2020, ApJ, 902, L36

Farmer, R., Renzo, M., de Mink, S. E., Marchant, P., & Justham, S. 2019, ApJ, 887, 53

Farr, W. M., Stevenson, S., Miller, M. C., et al. 2017, Nature, 548, 426

Farrell, E., Groh, J. H., Hirschi, R., et al. 2021, MNRAS, 502, L40

Fishbach, M., Doctor, Z., Callister, T., et al. 2021, ApJ, 912, 98

Fishbach, M. & Holz, D. E. 2017, ApJ, 851, L25

Fishbach, M. & Holz, D. E. 2020, ApJ, 904, L26

Fishbach, M., Holz, D. E., & Farr, B. 2017, ApJ, 840, L24

Fishbach, M., Holz, D. E., & Farr, W. M. 2018, ApJ, 863, L41

Foucart, F., Hinderer, T., & Nissanke, S. 2018, Phys. Rev. D, 98, 081501

Fowler, W. A. & Hoyle, F. 1964, ApJS, 9, 201

Fragione, G. 2021, ApJ, 923, L2

Fragione, G. & Kocsis, B. 2018, Phys. Rev. Lett., 121, 161103

Fragione, G. & Kocsis, B. 2019, MNRAS, 486, 4781

Fragione, G., Loeb, A., & Rasio, F. A. 2020, ApJ, 902, L26

Fragione, G. & Silk, J. 2020, MNRAS, 498, 4591

Fragos, T., Andrews, J. J., Bavera, S. S., et al. 2022, arXiv e-prints, arXiv:2202.05892

Fragos, T. & McClintock, J. E. 2015, ApJ, 800, 17

Franciolini, G., Baibhav, V., De Luca, V., et al. 2021, arXiv e-prints, arXiv:2105.03349

Franciolini, G. & Pani, P. 2022, arXiv e-prints, arXiv:2201.13098

Fregeau, J. M. & Rasio, F. A. 2007, ApJ, 658, 1047

Fritschel, P. 2003, in Society of Photo-Optical Instrumentation Engineers (SPIE) Conference Series, Vol. 4856, Gravitational-Wave Detection, ed. M. Cruise & P. Saulson, 282–291

Fryer, C. L. 1999, ApJ, 522, 413

Fryer, C. L., Belczynski, K., Wiktorowicz, G., et al. 2012, ApJ, 749, 91

Fuller, J., Lecoanet, D., Cantiello, M., & Brown, B. 2014, ApJ, 796, 17

Fuller, J. & Lu, W. 2022, MNRAS, 511, 3951

Fuller, J. & Ma, L. 2019, ApJ, 881, L1

Fuller, J., Piro, A. L., & Jermyn, A. S. 2019, MNRAS, 485, 3661

Galaudage, S., Talbot, C., Nagar, T., et al. 2021, ApJ, 921, L15

Garcia-Bellido, J., Linde, A. D., & Wands, D. 1996, Phys. Rev. D, 54, 6040

García-Bellido, J., Nuño Siles, J. F., & Ruiz Morales, E. 2021, Physics of the Dark Universe, 31, 100791

Gerosa, D. & Berti, E. 2017, Phys. Rev. D, 95, 124046

Gerosa, D., Berti, E., O'Shaughnessy, R., et al. 2018, Phys. Rev. D, 98, 084036

Gerosa, D. & Fishbach, M. 2021, Nature Astronomy, 5, 749

Giacobbo, N. & Mapelli, M. 2018, MNRAS, 480, 2011

Giacobbo, N., Mapelli, M., & Spera, M. 2018, MNRAS, 474, 2959

Giersz, M., Leigh, N., Hypki, A., Lützgendorf, N., & Askar, A. 2015, MNRAS, 454, 3150

Gompertz, B. P., Cutter, R., Steeghs, D., et al. 2020a, MNRAS, 497, 726

Gompertz, B. P., Levan, A. J., & Tanvir, N. R. 2020b, ApJ, 895, 58

Goodman, J. & Tan, J. C. 2004, ApJ, 608, 108

Gou, L., McClintock, J. E., Liu, J., et al. 2009, ApJ, 701, 1076

Gou, L., McClintock, J. E., Remillard, R. A., et al. 2014, ApJ, 790, 29

Gow, A. D., Byrnes, C. T., Hall, A., & Peacock, J. A. 2020, JCAP, 01, 031

Green, A. M. & Kavanagh, B. J. 2021, Journal of Physics G Nuclear Physics, 48, 043001

Gröbner, M., Ishibashi, W., Tiwari, S., Haney, M., & Jetzer, P. 2020, A&A, 638, A119

Gültekin, K., Miller, M. C., & Hamilton, D. P. 2006, ApJ, 640, 156

Hall, A., Gow, A. D., & Byrnes, C. T. 2020, Phys. Rev. D, 102, 123524

Hannam, M., Brown, D. A., Fairhurst, S., Fryer, C. L., & Harry, I. W. 2013, ApJ, 766, L14

Harry, G. M. & LIGO Scientific Collaboration. 2010, Classical and Quantum Gravity, 27, 084006

Hartwig, T., Volonteri, M., Bromm, V., et al. 2016, MNRAS, 460, L74

Hawking, S. W. 1974, Nature, 248, 30

Heger, A. & Langer, N. 2000, ApJ, 544, 1016

Heger, A., Langer, N., & Woosley, S. E. 2000, ApJ, 528, 368

Heger, A. & Woosley, S. E. 2002, ApJ, 567, 532

Heger, A., Woosley, S. E., & Spruit, H. C. 2005, ApJ, 626, 350

Hirano, S., Hosokawa, T., Yoshida, N., et al. 2014, ApJ, 781, 60

Hobbs, G., Lorimer, D. R., Lyne, A. G., & Kramer, M. 2005, MNRAS, 360, 974

Hong, J., Vesperini, E., Askar, A., et al. 2018, MNRAS, 480, 5645

Hooper, S., Chung, S. K., Luan, J., et al. 2012, Phys. Rev. D, 86, 024012

Hotokezaka, K. & Piran, T. 2017, ApJ, 842, 111

Hu, R.-C., Zhu, J.-P., Qin, Y., et al. 2022, arXiv e-prints, arXiv:2201.09549

Hulse, R. A. & Taylor, J. H. 1975, ApJ, 195, L51

Hurley, J. R., Pols, O. R., & Tout, C. A. 2000, MNRAS, 315, 543

Hurley, J. R., Tout, C. A., & Pols, O. R. 2002, MNRAS, 329, 897

Hut, P. 1981, A&A, 99, 126

Hut, P., McMillan, S., Goodman, J., et al. 1992, PASP, 104, 981

Hütsi, G., Raidal, M., Vaskonen, V., & Veermäe, H. 2021, JCAP, 2103, 068

Hütsi, G., Raidal, M., Vaskonen, V., & Veermäe, H. 2021, J. Cosmology Astropart. Phys., 2021, 068

Hütsi, G., Raidal, M., & Veermäe, H. 2019, Phys. Rev. D, 100, 083016

Inayoshi, K., Haiman, Z., & Ostriker, J. P. 2016, MNRAS, 459, 3738

Inayoshi, K., Hirai, R., Kinugawa, T., & Hotokezaka, K. 2017, MNRAS, 468, 5020

Ioka, K., Chiba, T., Tanaka, T., & Nakamura, T. 1998, Phys. Rev. D, 58, 063003

Ivanov, P. 1998, Phys. Rev. D, 57, 7145

Ivanov, P., Naselsky, P., & Novikov, I. 1994, Phys. Rev. D, 50, 7173

Ivanova, N., Justham, S., Chen, X., et al. 2013, A&A Rev., 21, 59

Ivezić, Ž., Kahn, S. M., Tyson, J. A., et al. 2019, ApJ, 873, 111

Izzard, R. G., Dray, L. M., Karakas, A. I., Lugaro, M., & Tout, C. A. 2006, A&A, 460, 565

Izzard, R. G., Glebbeek, E., Stancliffe, R. J., & Pols, O. R. 2009, A&A, 508, 1359

Izzard, R. G., Tout, C. A., Karakas, A. I., & Pols, O. R. 2004, MNRAS, 350, 407

Janka, H.-T. 2013, MNRAS, 434, 1355

Janka, H. T., Langanke, K., Marek, A., Martínez-Pinedo, G., & Müller, B. 2007, Phys. Rep., 442, 38

Janka, H. T. & Mueller, E. 1994, A&A, 290, 496

Just, A., Yurin, D., Makukov, M., et al. 2012, ApJ, 758, 51

Kalogera, V., Belczynski, K., Kim, C., O'Shaughnessy, R., & Willems, B. 2007, Phys. Rep., 442, 75

Kasliwal, M. M., Anand, S., Ahumada, T., et al. 2020, ApJ, 905, 145

Kimball, C., Berry, C., & Kalogera, V. 2020, Research Notes of the American Astronomical Society, 4, 2

Kimball, C., Talbot, C., Berry, C. P. L., et al. 2021, ApJ, 915, L35

Kimura, R., Suyama, T., Yamaguchi, M., & Zhang, Y.-L. 2021, JCAP, 04, 031

Kinugawa, T., Inayoshi, K., Hotokezaka, K., Nakauchi, D., & Nakamura, T. 2014, MNRAS, 442, 2963

Kinugawa, T., Miyamoto, A., Kanda, N., & Nakamura, T. 2016, MNRAS, 456, 1093

Kinugawa, T., Nakamura, T., & Nakano, H. 2021, MNRAS, 501, L49

Klimenko, S., Vedovato, G., Drago, M., et al. 2016, Phys. Rev. D, 93, 042004

Köhler, K., Langer, N., de Koter, A., et al. 2015, A&A, 573, A71

Kouveliotou, C., Meegan, C. A., Fishman, G. J., et al. 1993, ApJ, 413, L101

Kozai, Y. 1962, AJ, 67, 591

Kremer, K., Spera, M., Becker, D., et al. 2020, ApJ, 903, 45

Kritos, K., De Luca, V., Franciolini, G., Kehagias, A., & Riotto, A. 2021, J. Cosmology Astropart. Phys., 2021, 039

Kruckow, M. U., Tauris, T. M., Langer, N., Kramer, M., & Izzard, R. G. 2018, MNRAS, 481, 1908

Kumamoto, J., Fujii, M. S., & Tanikawa, A. 2019, MNRAS, 486, 3942

Kumamoto, J., Fujii, M. S., & Tanikawa, A. 2020, MNRAS, 495, 4268

Kushnir, D., Zaldarriaga, M., Kollmeier, J. A., & Waldman, R. 2016, MNRAS, 462, 844

Langer, N. 1992, A&A, 265, L17

Langer, N. 2012, ARA&A, 50, 107

Langer, N., Schürmann, C., Stoll, K., et al. 2020, A&A, 638, A39

Laplace, E., Götberg, Y., de Mink, S. E., Justham, S., & Farmer, R. 2020, A&A, 637, A6

Laplace, E., Justham, S., Renzo, M., et al. 2021, A&A, 656, A58

Lattimer, J. M. & Yahil, A. 1989, ApJ, 340, 426

Lazzarini, M., Hornschemeier, A. E., Williams, B. F., et al. 2018, ApJ, 862, 28

Leigh, N. W. C., Geller, A. M., McKernan, B., et al. 2018, MNRAS, 474, 5672

Levin, Y. 2007, MNRAS, 374, 515

Lidov, M. L. 1962, Planet. Space Sci., 9, 719

Lightman, A. P. & Shapiro, S. L. 1978, Reviews of Modern Physics, 50, 437

Lipunov, V. M., Postnov, K. A., & Prokhorov, M. E. 1996, The scenario machine: Binary star population synthesis

Lipunov, V. M., Postnov, K. A., Prokhorov, M. E., & Bogomazov, A. I. 2009, Astronomy Reports, 53, 915

Liu, B. & Bromm, V. 2020a, MNRAS, 495, 2475

Liu, B. & Bromm, V. 2020b, ApJ, 903, L40

Liu, B. & Lai, D. 2021, MNRAS, 502, 2049

Liu, B., Meynet, G., & Bromm, V. 2021, MNRAS, 501, 643

Liu, J., McClintock, J. E., Narayan, R., Davis, S. W., & Orosz, J. A. 2008, ApJ, 679, L37

Liu, J., McClintock, J. E., Narayan, R., Davis, S. W., & Orosz, J. A. 2010, ApJ, 719, L109

Lloyd-Ronning, N. M. 2021, arXiv e-prints, arXiv:2109.14122

Loutrel, N. 2020, Classical and Quantum Gravity, 37, 075008

Lower, M. E., Thrane, E., Lasky, P. D., & Smith, R. 2018, Phys. Rev. D, 98, 083028

Madau, P. & Rees, M. J. 2001, ApJ, 551, L27

Maeder, A. 1987, A&A, 178, 159

Maggiore, M., Van Den Broeck, C., Bartolo, N., et al. 2020, J. Cosmology Astropart. Phys., 2020, 050

Mandel, I. & Broekgaarden, F. S. 2021, arXiv e-prints, arXiv:2107.14239

Mandel, I. & de Mink, S. E. 2016, MNRAS, 458, 2634

Mandel, I. & Farmer, A. 2022, Phys. Rep., 955, 1

Mandel, I., Farr, W. M., & Gair, J. R. 2019, MNRAS, 486, 1086

Mapelli, M. 2016, MNRAS, 459, 3432

Mapelli, M., Bouffanais, Y., Santoliquido, F., Arca Sedda, M., & Artale, M. C. 2022, MNRAS, 511, 5797

Mapelli, M., Giacobbo, N., Santoliquido, F., & Artale, M. C. 2019, MNRAS, 487, 2

Mapelli, M., Santoliquido, F., Bouffanais, Y., et al. 2021, Symmetry, 13, 1678

Marchant, P., Langer, N., Podsiadlowski, P., et al. 2017, A&A, 604, A55

Marchant, P., Langer, N., Podsiadlowski, P., Tauris, T. M., & Moriya, T. J. 2016, A&A, 588, A50

Marchant, P., Renzo, M., Farmer, R., et al. 2019, ApJ, 882, 36

Marigo, P., Girardi, L., Chiosi, C., & Wood, P. R. 2001, A&A, 371, 152

Marion, F. & VIRGO Collaboration. 2000, in American Institute of Physics Conference Series, Vol. 523, Gravitational Waves: Third Edoardo Amaldi Conference, ed. S. Meshkov, 110

Mashian, N. & Loeb, A. 2017, MNRAS, 470, 2611

McKernan, B., Ford, K. E. S., Bartos, I., et al. 2019, ApJ, 884, L50

McKernan, B., Ford, K. E. S., Bellovary, J., et al. 2018, ApJ, 866, 66

McKernan, B., Ford, K. E. S., Kocsis, B., Lyra, W., & Winter, L. M. 2014, MNRAS, 441, 900

McKernan, B., Ford, K. E. S., Lyra, W., & Perets, H. B. 2012, MNRAS, 425, 460

McKernan, B., Ford, K. E. S., O'Shaugnessy, R., & Wysocki, D. 2020, MNRAS, 494, 1203

McMillan, S., Hut, P., & Makino, J. 1991, ApJ, 372, 111

Messick, C., Blackburn, K., Brady, P., et al. 2017, Phys. Rev. D, 95, 042001

Michaely, E. & Perets, H. B. 2019, ApJ, 887, L36

Michaely, E. & Perets, H. B. 2020, MNRAS, 498, 4924

Miller, M. C. & Hamilton, D. P. 2002, ApJ, 576, 894

Miller, M. C. & Lauburg, V. M. 2009, ApJ, 692, 917

Miller, S., Callister, T. A., & Farr, W. M. 2020, ApJ, 895, 128

Miller-Jones, J. C. A., Bahramian, A., Orosz, J. A., et al. 2021, Science, 371, 1046

Mirabel, I. F., Dhawan, V., Mignani, R. P., Rodrigues, I., & Guglielmetti, F. 2001, Nature, 413, 139

Mirabel, I. F. & Rodrigues, I. 2003, Science, 300, 1119

Misra, D., Fragos, T., Tauris, T. M., Zapartas, E., & Aguilera-Dena, D. R. 2020, A&A, 642, A174

Moe, M. & Di Stefano, R. 2017, ApJS, 230, 15

Nakamura, T., Sasaki, M., Tanaka, T., & Thorne, K. S. 1997, Astrophys. J. Lett., 487, L139

Neijssel, C. J., Vigna-Gómez, A., Stevenson, S., et al. 2019, MNRAS, 490, 3740

Neijssel, C. J., Vinciguerra, S., Vigna-Gómez, A., et al. 2021, ApJ, 908, 118

Nelson, C. A. & Eggleton, P. P. 2001, ApJ, 552, 664

Nelson, D., Pillepich, A., Genel, S., et al. 2015, Astronomy and Computing, 13, 12

Ng, K. K. Y., Vitale, S., Farr, W. M., & Rodriguez, C. L. 2021, ApJ, 913, L5

Nitz, A. H., Capano, C. D., Kumar, S., et al. 2021a, ApJ, 922, 76

Nitz, A. H., Dent, T., Dal Canton, T., Fairhurst, S., & Brown, D. A. 2017, ApJ, 849, 118

Nitz, A. H., Kumar, S., Wang, Y.-F., et al. 2021b, arXiv e-prints, arXiv:2112.06878

O'Connor, E. & Ott, C. D. 2011, ApJ, 730, 70

Ogiya, G., van den Bosch, F. C., Hahn, O., et al. 2019, MNRAS, 485, 189

O'Leary, R. M., Rasio, F. A., Fregeau, J. M., Ivanova, N., & O'Shaughnessy, R. 2006, ApJ, 637, 937

Olejak, A. & Belczynski, K. 2021, ApJ, 921, L2

Olejak, A., Belczynski, K., & Ivanova, N. 2021, A&A, 651, A100

Olsen, S., Venumadhav, T., Mushkin, J., et al. 2022, arXiv e-prints, arXiv:2201.02252

Orosz, J. A., McClintock, J. E., Aufdenberg, J. P., et al. 2011, ApJ, 742, 84

Orosz, J. A., McClintock, J. E., Narayan, R., et al. 2007, Nature, 449, 872

Paczyński, B. 1998, ApJ, 494, L45

Page, K. L., Evans, P. A., Tohuvavohu, A., et al. 2020, MNRAS, 499, 3459

Palmese, A. & Conselice, C. J. 2021, Phys. Rev. Lett., 126, 181103

Patton, R. A. & Sukhbold, T. 2020, MNRAS, 499, 2803

Patton, R. A., Sukhbold, T., & Eldridge, J. J. 2022, MNRAS, 511, 903

Pavlovskii, K., Ivanova, N., Belczynski, K., & Van, K. X. 2017, MNRAS, 465, 2092

Paxton, B., Bildsten, L., Dotter, A., et al. 2011, ApJS, 192, 3

Paxton, B., Cantiello, M., Arras, P., et al. 2013, ApJS, 208, 4

Paxton, B., Marchant, P., Schwab, J., et al. 2015, ApJS, 220, 15

Paxton, B., Schwab, J., Bauer, E. B., et al. 2018, ApJS, 234, 34

Paxton, B., Smolec, R., Schwab, J., et al. 2019, ApJS, 243, 10

Pejcha, O. & Thompson, T. A. 2015, ApJ, 801, 90

Perets, H. B. & Kratter, K. M. 2012, ApJ, 760, 99

Périgois, C., Belczynski, C., Bulik, T., & Regimbau, T. 2021a, Phys. Rev. D, 103, 043002

Périgois, C., Santoliquido, F., Bouffanais, Y., et al. 2021b, arXiv e-prints, arXiv:2112.01119

Perley, D. A., Fremling, C., Sollerman, J., et al. 2020, ApJ, 904, 35

Perley, D. A., Krühler, T., Schulze, S., et al. 2016, ApJ, 817, 7

Peters, P. C. 1964, Physical Review, 136, 1224

Petrovich, C. & Antonini, F. 2017, ApJ, 846, 146

Pfister, H., Volonteri, M., Dubois, Y., Dotti, M., & Colpi, M. 2019, MNRAS, 486, 101

Piran, Z. & Piran, T. 2020, ApJ, 892, 64

Podsiadlowski, P., Rappaport, S., & Pfahl, E. D. 2002, ApJ, 565, 1107

Poisson, E. & Will, C. M. 1995, Phys. Rev. D, 52, 848

Pols, O. R., Tout, C. A., Eggleton, P. P., & Han, Z. 1995, MNRAS, 274, 964

Portegies Zwart, S. F., Dewi, J., & Maccarone, T. 2004, MNRAS, 355, 413

Portegies Zwart, S. F. & McMillan, S. L. W. 2000, ApJ, 528, L17

Portegies Zwart, S. F. & McMillan, S. L. W. 2002, ApJ, 576, 899

Portegies Zwart, S. F. & Verbunt, F. 1996, A&A, 309, 179

Postnov, K. A. & Yungelson, L. R. 2014, Living Reviews in Relativity, 17, 3

Punturo, M., Abernathy, M., Acernese, F., et al. 2010, Classical and Quantum Gravity, 27, 194002

Qin, Y., Fragos, T., Meynet, G., et al. 2018, A&A, 616, A28

Qin, Y., Marchant, P., Fragos, T., Meynet, G., & Kalogera, V. 2019, ApJ, 870, L18

Qin, Y., Wang, Y.-Z., Wu, D.-H., Meynet, G., & Song, H. 2022, ApJ, 924, 129

Racine, É. 2008, Phys. Rev. D, 78, 044021

Raghavan, D., McAlister, H. A., Henry, T. J., et al. 2010, ApJS, 190, 1

Raidal, M., Spethmann, C., Vaskonen, V., & Veermäe, H. 2019, JCAP, 02, 018

Rakavy, G. & Shaviv, G. 1967, ApJ, 148, 803

Rastello, S., Amaro-Seoane, P., Arca-Sedda, M., et al. 2019, MNRAS, 483, 1233

Rastinejad, J. C., Gompertz, B. P., Levan, A. J., et al. 2022, arXiv e-prints, arXiv:2204.10864

Reitze, D., Adhikari, R. X., Ballmer, S., et al. 2019, in Bulletin of the American Astronomical Society, Vol. 51, 35

Renzo, M., Farmer, R. J., Justham, S., et al. 2020, MNRAS, 493, 4333

Repetto, S., Davies, M. B., & Sigurdsson, S. 2012, MNRAS, 425, 2799

Repetto, S., Igoshev, A. P., & Nelemans, G. 2017, MNRAS, 467, 298

Riley, J., Agrawal, P., Barrett, J. W., et al. 2022, ApJS, 258, 34

Riley, J., Mandel, I., Marchant, P., et al. 2021, MNRAS, 505, 663

Rizzuto, F. P., Naab, T., Spurzem, R., et al. 2021, MNRAS, 501, 5257

Rodriguez, C. L., Amaro-Seoane, P., Chatterjee, S., et al. 2018, Phys. Rev. D, 98, 123005

Rodriguez, C. L., Chatterjee, S., & Rasio, F. A. 2016a, Phys. Rev. D, 93, 084029

Rodriguez, C. L. & Loeb, A. 2018, ApJ, 866, L5

Rodriguez, C. L., Morscher, M., Pattabiraman, B., et al. 2015, Phys. Rev. Lett., 115, 051101

Rodriguez, C. L., Zevin, M., Amaro-Seoane, P., et al. 2019, Phys. Rev. D, 100, 043027

Rodriguez, C. L., Zevin, M., Pankow, C., Kalogera, V., & Rasio, F. A. 2016b, ApJ, 832, L2

Román-Garza, J., Bavera, S. S., Fragos, T., et al. 2021, ApJ, 912, L23

Romero-Shaw, I., Lasky, P. D., & Thrane, E. 2021, ApJ, 921, L31

Romero-Shaw, I., Lasky, P. D., Thrane, E., & Calderón Bustillo, J. 2020, ApJ, 903, L5

Romero-Shaw, I. M., Lasky, P. D., & Thrane, E. 2022, arXiv e-prints, arXiv:2206.14695

Roulet, J., Chia, H. S., Olsen, S., et al. 2021, Phys. Rev. D, 104, 083010

Roulet, J. & Zaldarriaga, M. 2019, MNRAS, 484, 4216

Röver, C., Meyer, R., & Christensen, N. 2006, Classical and Quantum Gravity, 23, 4895

Roškar, R., Fiacconi, D., Mayer, L., et al. 2015, MNRAS, 449, 494

Safarzadeh, M., Farr, W. M., & Ramirez-Ruiz, E. 2020, ApJ, 894, 129

Safarzadeh, M. & Haiman, Z. 2020, ApJ, 903, L21

Salpeter, E. E. 1955, ApJ, 121, 161

Samsing, J. & D'Orazio, D. J. 2018, MNRAS, 481, 5445

Samsing, J. & Hotokezaka, K. 2021, ApJ, 923, 126

Samsing, J., MacLeod, M., & Ramirez-Ruiz, E. 2014, ApJ, 784, 71

Samsing, J. & Ramirez-Ruiz, E. 2017, ApJ, 840, L14

Sana, H., de Mink, S. E., de Koter, A., et al. 2012, Science, 337, 444

Sana, H., Le Bouquin, J. B., Lacour, S., et al. 2014, ApJS, 215, 15

Sasaki, M., Suyama, T., Tanaka, T., & Yokoyama, S. 2016, Phys. Rev. Lett., 117, 061101, [erratum: Phys. Rev. Lett.121,no.5,059901(2018)]

Sasaki, M., Suyama, T., Tanaka, T., & Yokoyama, S. 2018, Class. Quant. Grav., 35, 063001

Sathyaprakash, B. S. & Dhurandhar, S. V. 1991, Phys. Rev. D, 44, 3819

Schmidt, P. 2020, Frontiers in Astronomy and Space Sciences, 7, 28

Schneider, F. R. N., Podsiadlowski, P., & Müller, B. 2021, A&A, 645, A5

Schneider, R., Ferrara, A., Ciardi, B., Ferrari, V., & Matarrese, S. 2000, MNRAS, 317, 385

Secunda, A., Bellovary, J., Mac Low, M.-M., et al. 2019, ApJ, 878, 85

Sesana, A., Gair, J., Berti, E., & Volonteri, M. 2011, Phys. Rev. D, 83, 044036

Sesana, A., Gair, J., Mandel, I., & Vecchio, A. 2009, ApJ, 698, L129

Shao, Y. & Li, X.-D. 2022, arXiv e-prints, arXiv:2203.14529

Siess, L., Izzard, R. G., Davis, P. J., & Deschamps, R. 2013, A&A, 550, A100

Sigurdsson, S. & Hernquist, L. 1993, Nature, 364, 423

Sigurdsson, S. & Phinney, E. S. 1993, ApJ, 415, 631

Silsbee, K. & Tremaine, S. 2017, ApJ, 836, 39

Smarr, L. L. & Blandford, R. 1976, ApJ, 207, 574

Socrates, A., Blaes, O., Hungerford, A., & Fryer, C. L. 2005, ApJ, 632, 531

Spera, M., Mapelli, M., & Bressan, A. 2015, MNRAS, 451, 4086

Spera, M., Mapelli, M., Giacobbo, N., et al. 2019, MNRAS, 485, 889

Spruit, H. C. 1999, A&A, 349, 189

Spruit, H. C. 2002, A&A, 381, 923

Stacy, A. & Bromm, V. 2013, MNRAS, 433, 1094

Stancliffe, R. J. & Eldridge, J. J. 2009, MNRAS, 396, 1699

Steinle, N. & Kesden, M. 2021, Phys. Rev. D, 103, 063032

Stevenson, S. 2022, ApJ, 926, L32

Stevenson, S., Sampson, M., Powell, J., et al. 2019, ApJ, 882, 121

Stevenson, S., Vigna-Gómez, A., Mandel, I., et al. 2017, Nature Communications, 8, 14906

Stone, N. C., Küpper, A. H. W., & Ostriker, J. P. 2017a, MNRAS, 467, 4180

Stone, N. C., Metzger, B. D., & Haiman, Z. 2017b, MNRAS, 464, 946

Suijs, M. P. L., Langer, N., Poelarends, A. J., et al. 2008, A&A, 481, L87

Sukhbold, T. & Adams, S. 2020, MNRAS, 492, 2578

Sukhbold, T., Ertl, T., Woosley, S. E., Brown, J. M., & Janka, H. T. 2016, ApJ, 821, 38

Szécsi, D., Langer, N., Yoon, S.-C., et al. 2015, A&A, 581, A15

Tagawa, H., Haiman, Z., & Kocsis, B. 2020, ApJ, 898, 25

Tagawa, H., Kocsis, B., Haiman, Z., et al. 2021, ApJ, 908, 194

Talbot, C. & Thrane, E. 2017, Phys. Rev. D, 96, 023012

Tamfal, T., Capelo, P. R., Kazantzidis, S., et al. 2018, ApJ, 864, L19

Tanikawa, A. 2013, MNRAS, 435, 1358

Tanikawa, A., Kinugawa, T., Yoshida, T., Hijikawa, K., & Umeda, H. 2021, MNRAS, 505, 2170

Tanikawa, A., Yoshida, T., Kinugawa, T., et al. 2022, ApJ, 926, 83

Taylor, J. H. & Weisberg, J. M. 1982, ApJ, 253, 908

Thorne, K. S. 1974, ApJ, 191, 507

Tiwari, V. 2022, ApJ, 928, 155

Tokovinin, A. 2014, AJ, 147, 87

Toonen, S., Boekholt, T. C. N., & Portegies Zwart, S. 2021, arXiv e-prints, arXiv:2108.04272

Toonen, S., Hamers, A., & Portegies Zwart, S. 2016, Computational Astrophysics and Cosmology, 3, 6

Toonen, S., Nelemans, G., & Portegies Zwart, S. 2012, A&A, 546, A70

Toonen, S., Portegies Zwart, S., Hamers, A. S., & Bandopadhyay, D. 2020, A&A, 640, A16

Toubiana, A., Wong, K. W. K., Babak, S., et al. 2021, Phys. Rev. D, 104, 083027

Tremmel, M., Governato, F., Volonteri, M., & Quinn, T. R. 2015, MNRAS, 451, 1868

Tutukov, A. V. & Yungelson, L. R. 1993, MNRAS, 260, 675

Ugliano, M., Janka, H.-T., Marek, A., & Arcones, A. 2012, ApJ, 757, 69

Unnikrishnan, C. S. 2013, International Journal of Modern Physics D, 22, 1341010

Usman, S. A., Nitz, A. H., Harry, I. W., et al. 2016, Classical and Quantum Gravity, 33, 215004

Vajente, G., Gustafson, E. K., & Reitze, D. H. 2019, Advances in Atomic Molecular and Optical Physics, 68, 75

van den Heuvel, E. P. J. 1976, in Structure and Evolution of Close Binary Systems, ed. P. Eggleton, S. Mitton, & J. Whelan, Vol. 73, 35

van den Heuvel, E. P. J., Portegies Zwart, S. F., & de Mink, S. E. 2017, MNRAS, 471, 4256

van der Hucht, K. A. 2001, New A Rev., 45, 135

van der Sluys, M., Raymond, V., Mandel, I., et al. 2008a, Classical and Quantum Gravity, 25, 184011

van der Sluys, M. V., Röver, C., Stroeer, A., et al. 2008b, ApJ, 688, L61

van Son, L. A. C., De Mink, S. E., Broekgaarden, F. S., et al. 2020, ApJ, 897, 100

van Son, L. A. C., de Mink, S. E., Callister, T., et al. 2021, arXiv e-prints, arXiv:2110.01634

Vanbeveren, D., De Donder, E., Van Bever, J., Van Rensbergen, W., & De Loore, C. 1998a, New A, 3, 443

Vanbeveren, D., De Loore, C., & Van Rensbergen, W. 1998b, A&A Rev., 9, 63

Vanbeveren, D., Mennekens, N., van den Heuvel, E. P. J., & Van Bever, J. 2020, A&A, 636, A99

Vaskonen, V. & Veermäe, H. 2020, Phys. Rev. D, 101, 043015

Veitch, J., Raymond, V., Farr, B., et al. 2015, Phys. Rev. D, 91, 042003

Veitch, J. & Vecchio, A. 2010, Phys. Rev. D, 81, 062003

Venumadhav, T., Zackay, B., Roulet, J., Dai, L., & Zaldarriaga, M. 2020, Phys. Rev. D, 101, 083030

Vigna-Gómez, A., Toonen, S., Ramirez-Ruiz, E., et al. 2021, ApJ, 907, L19

Vink, J. S., de Koter, A., & Lamers, H. J. G. L. M. 2001, A&A, 369, 574

Vitale, S., Gerosa, D., Farr, W. M., & Taylor, S. R. 2020, arXiv e-prints, arXiv:2007.05579

Wang, S., Terada, T., & Kohri, K. 2019, Phys. Rev. D, 99, 103531

Wang, S., Wang, Y.-F., Huang, Q.-G., & Li, T. G. F. 2016, arXiv e-prints, arXiv:1610.08725

Wen, L. 2003, ApJ, 598, 419

Willke, B., Aufmuth, P., Aulbert, C., et al. 2002, Classical and Quantum Gravity, 19, 1377

Wong, K. W. K., Breivik, K., Kremer, K., & Callister, T. 2021, Phys. Rev. D, 103, 083021

Wong, K. W. K., Franciolini, G., De Luca, V., et al. 2021, Phys. Rev., D103, 023026

Wong, T.-W., Valsecchi, F., Fragos, T., & Kalogera, V. 2012, ApJ, 747, 111

Woosley, S. E. 1993, ApJ, 405, 273

Woosley, S. E. 2017, ApJ, 836, 244

Woosley, S. E. 2019, ApJ, 878, 49

Woosley, S. E., Blinnikov, S., & Heger, A. 2007, Nature, 450, 390

Woosley, S. E. & Heger, A. 2006, ApJ, 637, 914

Woosley, S. E. & Heger, A. 2015, in Astrophysics and Space Science Library, Vol. 412, Very Massive Stars in the Local Universe, ed. J. S. Vink, 199

Woosley, S. E., Heger, A., & Weaver, T. A. 2002, Reviews of Modern Physics, 74, 1015

Wu, Y. 2020, Phys. Rev., D101, 083008

Wysocki, D., Lange, J., & O'Shaughnessy, R. 2019, Phys. Rev. D, 100, 043012

Yang, Y., Bartos, I., Gayathri, V., et al. 2019a, Phys. Rev. Lett., 123, 181101

Yang, Y., Bartos, I., Haiman, Z., et al. 2019b, ApJ, 876, 122

Yoon, S. C. & Langer, N. 2005, A&A, 443, 643

Yoshida, T., Umeda, H., Maeda, K., & Ishii, T. 2016, MNRAS, 457, 351

Zackay, B., Dai, L., & Venumadhav, T. 2018, arXiv e-prints, arXiv:1806.08792

Zahn, J. P. 1977, A&A, 57, 383

Zajacek, M. & Tursunov, A. 2019, The Observatory, 139, 231

Zaldarriaga, M., Kushnir, D., & Kollmeier, J. A. 2018, MNRAS, 473, 4174

Zapartas, E., Renzo, M., Fragos, T., et al. 2021, A&A, 656, L19

Zel'dovich, Y. B. & Novikov, I. D. 1967, Soviet Astron. AJ (Engl. Transl.),, 10, 602

Zevin, M. 2021, The Astrophysical Journal, 910, 152, New version following referee process and minor changes.

Zevin, M. & Bavera, S. S. 2022, ApJ, 933, 86

Zevin, M., Bavera, S. S., Berry, C. P. L., et al. 2021a, ApJ, 910, 152

Zevin, M., Romero-Shaw, I. M., Kremer, K., Thrane, E., & Lasky, P. D. 2021b, ApJ, 921, L43

Zevin, M., Samsing, J., Rodriguez, C., Haster, C.-J., & Ramirez-Ruiz, E. 2019, ApJ, 871, 91

Zevin, M., Spera, M., Berry, C. P. L., & Kalogera, V. 2020, ApJ, 899, L1

Ziosi, B. M., Mapelli, M., Branchesi, M., & Tormen, G. 2014, MNRAS, 441, 3703